3D Printed Microfluidic Systems
Towards Biomedical and Diagnostic Applications

by

Eric C Sweet

A dissertation submitted in partial satisfaction of the

requirements for the degree of

Doctor of Philosophy

in

Engineering - Mechanical Engineering

in the

Graduate Division

of the

University of California, Berkeley

Committee in charge:

Professor Liwei Lin, Chair
Professor Dorian Liepmann
Professor Lisa Pruitt

Fall 2019

3D Printed Microfluidic Systems
Towards Biomedical and Diagnostic Applications

by

Eric C Sweet

Abstract

3D Printed Microfluidic Systems
Towards Biomedical and Diagnostic Applications

by

Eric C Sweet

Doctor of Philosophy in Engineering - Mechanical Engineering

University of California, Berkeley

Professor Liwei Lin, Chair

Integrated microfluidic systems enable manipulation of fluids at the submillimeter length-scale, which offers particular advantages for various chemical, biological and biomedical testing applications. Conventional technologies based upon micromachining approaches are inherently planar in nature, therefore alternative approaches for the construction of microfluidic systems *via* additive manufacturing or *three-dimensional (3D) printing* gave drawn great interest in the field of microfluidic device engineering. This dissertation presents the Multijet 3D printing approach - a layer-by-layer, multi-material micro-scale deposition method - towards the development of geometrically and functionally-unique submillimeter microfluidic structures, resulting in new classes of *three dimensionally*-complex integrated microfluidic platforms to address challenges currently faced by conventional microfluidics in relevant biomedical and diagnostic applications.

Homogenous mixing of co-laminar fluids inside conventional microchannels, especially under low Reynolds Number conditions ($Re \leq 1$) continues to be a primary issue for the efficient *on-chip* mixing of reagent and analytes. In the first part of this dissertation, various 3D μ-mixer prototypes capable of inducing fluidic motion and chaotic advection in *three-dimensions* to promote mixing quality enhancement over a range of *Re*'s ($\sim 0.1 \leq Re \leq \sim 10$) have been engineered. Theoretical simulations and experimental characterization demonstrate that greater mixing per-unit microchannel length is achieved utilizing intra-channel fabricated 3D μ-mixers ($\sim$148% increase in mixing quality is achieved at $Re \sim 0.1$ using a 4mm long 3D μ-mixer) as compared to smooth-walled 3D printed microchannels.

Microfluidic concentration gradient generators (μ-CGG) are incapable of generating symmetric gradients of more than two fluids simultaneously. In the second part of this dissertation, two different 3D microchannel network designs which accomplish 3D fluidic routing impossible to achieve using planar fabrication methods in order to generate *symmetric three-fluid* gradients are demonstrated. Fabricated prototypes output discrete μ-drug cocktails containing certain potentially experimentally-useful concentrations of each input fluidic species ($\sim$100%, 76%, 50%, 32%, 11%,

10% & 0% and ∼100%, 70%, 50%, 33%, 30% & 0%, respectively). Furthermore, incorporating 3D μ-mixer structures to improve the simulated accuracy of the generated gradient up to ∼88% is demonstrated. The biomedical application of both fabricated 3D μ-CGG prototypes is demonstrated through single, pair-wise and three-antibiotic susceptibility testing experiments involving multiple clinically-relevant antibiotic drugs against antibiotic-resistant *Escherichia coli* bacteria.

In the third part of this dissertation, entirely-3D printed modular human-powered microfluidic actuators are proposed to serve as easy-to-operate, portable and completely electrical power-free sources of fluidic actuation. A new 3D fluidic one-way valve concept employing a dynamic bracing mechanism is presented, demonstrating enhancement in diodicity from ∼95.4 to ∼1117.4 and significant reduction in back-flow in the system. As result, fabricated prototypes demonstrate experimental fluid flow rates from 600 to 3000 μL/min, without the use of electricity. Furthermore, the *on-chip* integration of human-powered actuators into larger 3D printed microfluidic networks is demonstrated in the form of single finger-actuated pressure source to enable an integrated two-fluid pulsatile mixer prototype.

The fourth and final part of this dissertation proposes the concept of an entirely-3D printed, hand-held microfluidic device to enable human-powered fluid sample collection and entirely *on-chip* enrichment and multiplexed pathogenic detection. A custom drop-casting procedure is developed and experimentally-optimized to pre-treat fabricated prototypes with nutrients and bacteria-specific colorimetric reagents for *on-chip* biological enrichment and practical optical pathogen detection. The quantitative limit-of-detection of the employed proof-of-concept colorimetric detection scheme is experimentally determined to be $\sim$1x10^6 cells/mL in 6 hours, a result validated by the demonstration of collection, enrichment and detection of *E. coli* bacteria in model drinking water using the actual fabricated prototype device.

For Joel Sweet
My inspiration in every way, notably to become the second Doctor in the CA Sweet family.
The mechanical engineering bug lives on in yet another generation!

Kevin and Suzanne Sweet
My incredible parents who have given me the greatest love and support - mentally, emotionally and physically - for the past 27 years, without whom I could not have done any of this.

and Adriana Sweet
My other-half, my everything. I simply would not be where I am today without you.
Here's to the next chapter in our lives together, as two Dr. Sweet's!

Acknowledgments

To say that my time at UC Berkeley has been life changing is more accurate than I could have ever imagined. If you would have told me 8 years ago whilst sitting in Freshman year Physics 7A lecture in LeConte Hall, having moved out to Berkeley from Concord, Massachusetts in 2011 and not even quite sure exactly what I wanted to study, that I'd now be sitting here, next to my wife, putting the finishing touches on my 300 page Mechanical Engineering dissertation... I never would have believed you!

First, I want to acknowledge that you, Dear Reader, would not be reading this if it weren't for the genuinely incredible support from Professor Liwei Lin, which has enabled me to be where I am today. I have the utmost respect and admiration for Prof. Lin as a man and a mentor, who over the past 6 years has entrusted in me an enormous amount of responsibility and freedom to pursue my own research directions, whilst also providing me critical guidance and advice towards enhancing the quality of my research projects, as well as achieving my larger academic and professional goals. I am also incredibly grateful for the ability to have represented the Lin Lab alongside Prof. Lin at various conferences around the world, from Las Vegas, NV (MEMS 2017) and Kaohsiung, Taiwan (Transducers 2017) to Seoul, South Korea (MEMS 2019) and Berlin, Germany (Transducers 2019). Prof. Lin's confidence in my abilities as a researcher and communicator encouraged me to pursue my Masters and PhD degrees, and it was only through his dedication that I was able to do so here at Cal.

Second, I would also not be where I am today if it weren't for the incredible efforts of Professor Ryan D. Sochol (University of Maryland) who, way back in 2013 as a post-doctoral researcher in the Lin Lab, took me under his wing as an undergraduate student researcher and inspired me to fall in love with all-things additive manufacturing and to pursue my own academic research projects. Prof. Sochol is genuinely one of the most interesting and motivated people I've ever had the privilege to know and work with, and I would not have been able to grow and develop into the independent researcher that I am today if it weren't for his example and his support of me along the way. I would also like to thank Professor Dorian Liepmann and Professor Lisa Pruitt, my two additional doctoral committee members who's guidance and feedback before and during my Qualifying examination inspired me to dive even deeper into my research, and who's patience in reviewing this dissertation up until mid-December whilst I am concurrently working full-time cannot be overstated. Furthermore, I will always cherish the memories of being a student in Prof. Pruitt's materials courses, from ME108 as an undergraduate to MEC223 and MEC215 as a graduate student, which were genuinely the most interesting, useful and inspiring courses that I've ever taken. Additionally, if I ever find myself as an educator in any capacity in the future, if I am able to achieve anywhere close to effectiveness of Prof. Pruitt's communication and teaching style, as well as her incredible dedication to her students, I would be absolutley honored.

The projects presented in this dissertation would also not have been possible without the amazing contributions of all of the undergraduate student researchers that I have had the privilege to mentor and work with as director of the Micro-Mechanical Methods for Biology (M3B) Research Program, a sub-division of the Liwei Lin Laboratory founded by none-other than Ryan Sochol, and the initial research group that I initially joined. Particularly, I'd like to thank Josh Chen, Rudra Mehta, Brenda Yang and Yifan Xu, who's creativity, coding expertise and experimental protocol know-how enabled the quality biological demonstrations and quantitative analysis featured throughout this work. I would also like thank all of the various UC Berkeley staff who've made all of the work in this dissertation possible; notably, Paul Lum, director of the Biomolecular Nanotechnology Center (BNC) in Stanley Hall, who's wit, wisdom and genuine support is most cherished; the staff of the Jacobs Hall Makerspace, who's advice and instruction allowed me to explore and gain experience with an amazing array of fabrication equipment, including state-of-the-art FDM, SLA and Polyjet 3D printers and laser cutters, which have been integral to various aspects of my projects; Professor Robert Full and the members of the Center for Integrative Biomechanics in Education and Research (CiBER) Lab in VLSB, who allowed me to use their 3D printers and lab equipment to fabricate essentially all of the devices that you're about to see in this work; and all of the members of the Berkeley Sensors and Actuators Center (BSAC), especially Richard Lossing, Dalene Schwartz Corey and Kim Ly, who've made being a BSAC researcher an incredible experience over the past 6 years. It has also been an absolute honor to be able work along side my friends from the Lin Lab, particularly Casey Glick, Emmeline Kao, Jaqueline Elwood, Ilbey Karakurt, Sedat Pela, Junwen Zhong, Neil Ramierez and Nate Liu, who's emotional and mental support, inspiration and genuine friendships have been one of the most valuable assets of my time at Cal. And to of all my friends that I've made in my new home in CA, especially at our Friday VIP meetings, Darren!; you've made my life here at Cal truly special)'(

Moreover, UC Berkeley has given me something even more precious than my B.S., M.S. and Ph.D. degrees. How could I have ever have dreamt back in that Physics 7A lecture in Freshman year that the cute girl whom I gradually sat nearer and nearer to over the course of the semester would eventually become my wife? Adriana Sweet, words cannot express my love and devotion to you, nor my appreciation for your undying support on this wild and crazy ride of ours. Come May 2020 we will both have our those Ph.D. degrees hanging on our wall! We have done this together, and I will cherish every memory that we've made together here at Cal for the rest of my life. I also genuinely could not have done this without the rest of my family. Kevin and Suzanne Sweet, thank you for encouraging and supporting me every single day; living in Berkeley with you has been the most precious experience, and I could not have done this without your love. I have also appreciated having my sisters, Zoe and Elizabeth Sweet, living right across the Bay Bridge, a lot more than I ever thought I would, ha! Carmen and Adrian Ureche and Tina Caloianu, my parents and auntie-in-law, and Uncle Jim and Grammy, your support has meant the world to me. Finally, thank you Grandpa Joey and Grandma Rita for supporting Adriana and I, we've treasured every single day we've spent with you in Nevada City; I finally did it, Grandpa! I love you all!

Eric Christopher Sweet

Ph.D. Candidate

ericsweet@berkeley.edu
http://m3b.me.berkeley.edu

1974 Thousand Oaks Blvd, Berkeley, CA, 94707
(978) 996-6799

EDUCATION

UNIVERSITY OF CALIFORNIA, BERKELEY — Berkeley, CA

Ph.D. in Mechanical Engineering — 08/2016 - 12/2019 (Expected)
MEMS/Nano (*Major*), Bioengineering (*Minor*)

M.S. in Mechanical Engineering — 08/2015 – 05/2016

B.S. in Mechanical Engineering — 08/2011 – 05/2015

RESEARCH AND INTERNSHIP EXPERIENCE

BERKELEY SENSORS AND ACTUATORS CENTER (BSAC) — Berkeley, CA

Graduate Student Researcher, The Liwei Lin Laboratory — 05/2015 – Present
Director, *Micro Mechanical Methods for Biology (M^3B) Research Program*
Co-Director, *M^3B Research Program* — 01/2013 – 05/2015

- **Entirely-3D Printed Microfluidic Platform For On-Site Detection Of Drinking Waterborne Pathogens**
  - Presented at *MEMS 2019 Conference*, Seoul, South Korea, January 28th, 2019
- **Three-Dimensional, Three-Fluid Microfluidic Gradient Generator Bacteria-Antibiotic Drug Screening**
  - Engineering of entirely-3D printed devices; demonstrating application on antibiotic-resistant bacteria (*e.g.* E. coli)
- **3D Printed, Finger-Powered Microfluidic Actuators**
  - Designing, optimizing & fabricating entirely 3D printed power-less microfluidic pumps and control systems
- **Low-Reynolds Number Mixing using Microscale 3D Printed Microfluidic Devices**
  - Designing & fabricating 3D fluidic mixers using multi-jet, ultra-high resolution (~40 μm) 3D printers
  - Characterizing chaotic and diffusion mixing of 2- & 3-phase low-Reynolds number fluids in 3D printed fluidics
- **Investigation of Multijet-Modeling for Microscale 3D Printed Integrated Microfluidic Circuitry**
  - Manufacturing 3D microfluidic circuit components (*e.g.*, 3D transistors, capacitors, diodes, *etc.*) in Solidworks
  - Characterizing 3D printed integrated fluidic circuits and components (*e.g.*, full-wave rectifiers and pressure-gain valves) using pressure control pumps, flow rate sensors, SEM/optical microscopy & image analysis

TERALYTIC – A SOIL HEALTH COMPANY — Berkeley, CA

Product Development Engineer, *Research & Development* — 05/2019 – Present
Engineering Consultant — 11/2018 – 05/2019

- Teralytic's wireless probes employ an array of sensors to provide the most detailed soil quality data available, reporting soil moisture, salinity, and NPK at three different depths, as well as aeration, respiration, temp, light, and humidity
- Designing, fabricating & evaluating sensor electronics, physical hardware for commercial sensor platform development
- Managing sensor calibration and manufacturing evaluation experiments using 3D printed and laser-cut hardware

UNIVERSITY OF TOKYO, DEAN'S FORUM LECTURE PROGRAM ON MICRO/NANO FLUIDICS FOR BIO-MEDICAL APPLICATIONS — Tokyo, Japan — 09/2015

- Presented Master's thesis project in micro/nano-fludics research
- Studying the mathematics of viscous-dominant micro/nanofluidic flow and bio-medical applications

MAKO GLOBAL TRADING DERIVATIVES, LONDON — London, England

Software Development Intern, *Quantitative & Automated Trading Division* — 05-08/2013

- **High-speed Trading Systems: Data Management & Network Response Time Improvement**
  - Utilizing C++, MATLAB, BASH & network navigation to automatically collect high-speed trading data
  - Developing UNIX scripts to help improve high-speed trading network response time between server centers

SPACE SCIENCES LABORATORY, UC BERKELEY — Berkeley, CA

Undergraduate Researcher, *Neutron Detector Hardware Development Project* — 01-05/2013
Program Advisor: Dr. Anton Tremsin

- **Hardware Development for Space-bound Neutron Detector**
  - Designing neutron detector's exterior & interior housings for an extraterrestrial environment using Solidworks
  - Refining designs for thermal-contraction & tensile strength, mechanical, material & machinability properties

PUBLICATIONS AND PRESENTATIONS

Journal Publications and Peer-Reviewed Conference Proceedings

- ***(ORAL) E. Sweet**, N. Liu, J. Chen, and L. Lin, "Entirely-3D Printed Microfluidic Platform For On-Site Detection Of Drinking Waterborne Pathogens" *Proc. International Conference on Micro Electro Mechanical Systems (MEMS) 2019, Seoul, South Korea,* 2019.
- ***E. Sweet**, R. R. Mehta, Y. Xu, N. Liu, K. Korner, C. Glick and L. Lin, "3D-Printed Chaotic Mixer For Low Reynolds Number Microfluidics" *Proc. International Conference on Solid-State Sensors, Actuators and Microsystems (Transducers) 2019, Berlin, Germany,* 2019.
- J. Chen, C. Liu, X. Wang, **E. Sweet**, N. Liu, X. Gong, and L. Lin, " 3D printed microfluidic devices for circulating tumor cells (CTCs) isolation," *Biosensors and Bioelectronics*, 111900, 2019. https://doi.org/10.1016/j.bios.2019.111900
- R. D. Sochol, **E. Sweet**, C. C. Glick, S.-Y. Wu, C. Yang, M. Restaino, Liwei Lin, "3D printed microfluidics and microelectronics". *Microelectronic Engineering*, vol. 189, pp. 668-678, 2018. https://doi.org/10.1016/j.mee.2017.12.010
- ***(ORAL) E. Sweet**, J. C.-L. Chen, I. Karakurt, A. T. Long, and L. Lin, "3D Printed Three-Flow Microfluidic Concentration Gradient Generator for E.Coli.-Antibiotic Drug Screening," *Proc. International Conference on Micro Electro Mechanical Systems (MEMS) 2017, Las Vegas, NV, USA,* 2017. ***Outstanding Paper Award Winner*** (out of 700 papers)
- ***E. Sweet**, R. Mehta, R. Lin, and L. Lin, "Finger-Powered, 3D Printed Microfluidic Pumps" *Proc. International Conference on Solid-State Sensors, Actuators and Microsystems (Transducers) 2017, Kaohsiung, Taiwan,*2017.
- I. Karakurt, J. Elwood, L. Beker, X. Li, L. Beker, **E. Sweet**, W. Cai, and L. Lin, "Membraneless Microfluidic Redox Battery For Wearable Electronics Applications", *Proc. International Conference on Solid-State Sensors, Actuators and Microsystems (Transducers) 2017, Kaohsiung, Taiwan,* 2017.
- R. D. Sochol, **E. Sweet**, C. C. Glick, S. Venkatesh, A. Avetisyan, K. F. Ekman, *et al.*, "3D printed microfluidic circuitry via multijet-based additive manufacturing," *Lab on a Chip*, vol. 16, pp. 668-678, 2016. http://dx.doi.org/10.1039/C5LC01389E

Conference Presentations - *Berkeley Sensor and Actuator Center* (BSAC) *Industrial Advisory Board* (IAB), UC Berkeley

- "3D Printed Biomedical and Diagnostic Systems" (Spring 2019 – Fall 2016)
- "Applications of 3D Printed Integrated Microfluidics: Circuitry, Finger-Powered Pumps and Mixers" (Spring 2019 – Fall 2016)
- "Low-Reynolds Number Mixing using Microscale 3D Printed Microfluidic Devices" (Spring 2016 – Fall 2015)
- "Integrated Microfluidic Circuitry *via* Microscale 3D Printing" (Spring 2016 – Fall 2015)
- "Development of 3D Printed Integrated Fluidic Circuitry via Multijet Modeling" (Spring 2015 – Fall 2014)

Other Oral Presentations

- "Investigating Multijet Modeling for 3D Printed IFCs", *Univ. of Tokyo, Dean's Forum Lecture Series*, Tokyo, Japan, 09/2015

AWARDS, HONORS AND PROFESSIONAL ACTIVITIES

- **Outstanding Paper Award Winner (out of 700 papers)** – IEEE MEMS 2017 Conference, Las Vegas, NV — January 2017
- *"M3B Researcher of the Year Award"* – UC Berkeley — Fall 2014 & Spring 2015
- *Dean's Honor List* – UC Berkeley College of Engineering — 2014 - 2015
- *American Society of Mechanical Engineers (ASME)* – Professional Dev. Member — 2013 - 2015
- *Berkeley Institute of Design @ Cal* – Product Design Team — Fall 2012 – Spring 2015
- Volunteer Teacher of CAD & 3D Printing to Bay Area High School Students — Summer 2013
- *Certified Solidworks Associate Accreditation (SCAA)* — Fall 2012 - Present

TECHNICAL SKILLS

- **Computer Programming / Software:** Solidworks (*CSA Accreditation 12.2012*) | AutoCAD | COMSOL Multiphysics | LaTex MATLAB/Simulink | C++ | UNIX (Bash) Shell Scripting | LabVIEW | Python | ImageJ
- **3D Printing:** *FormLabs* Form 3,2 (SLA) | *Stratasys* Objet260 Connex3 (Polyjet) | *3D Systems* ProJet HD 3000 (MultiJet) | *Asiga* Pico (SLA) | *Makerbot* Replicator (FDM) | *Stratasys* Dimension 1200es (FDM) | *Carbon3D* M1 (SLA)
- **MEMS/Nano-Fabrication Equipment:** Scanning Electron Microscope (SEM) | Conformal Vapor Deposition (CVD) | Oxygen Plasma/DRIE Etching | Soft-lithography (PDMS)
- **Machine Shop:** Laser Cutter | CNC & Manual Mill/Lathe | Water Jet | Drill Press | Band Saw | Composites Manufacturing
- **Additional Spoken Languages:** German (*Basic*)

Contents

List of Figures

Chapter 1

Introduction

The field of microfluidics is best characterized as the study and manipulation of fluids at sub-millimeter length scales [1]. Control over fluids at such scales has numerous applications in chemical and biological fields, including biomedical research [2], clinical diagnostics [3] and pharmaceutical drug discovery [4]. Scaling-down the physical geometric length-scales of physical *microfluidic* hardware to below 1 mm presents numerous unique fluidic handling potentials, such as reduction in reagent volumes [5] with high surface are-to-volume ratios [6], more rapid thermal [7] and molecular diffusion [8], laminar flows [9], membrane-less microparticle filtering [10], precision handling of microparticles [11] and control of microenvironments [12] and the replication of biophysiological-scale stress and strain states [13, 14]. Microfluidic-based analysis often demonstrates advantages over conventional fluid handling methods, such as confined chemical and biological reactions [15] resulting in higher throughput fluidic processing in low-cost platforms [16], lower interference from background noise [17] and higher analytical sensitivity and selectivity [18, 19]. Furthermore, integrated *lab-on-a-chip* and micro total analytical system (μTAS) microfluidic platforms are capable of performing semi-automated fluidic processing steps *on-chip* [20, 21], resulting in analytical multiplexing and a reduction of the number of independent time- and labor-intensive fluid handling operations, which has far reaching benefits towards biomedical and diagnostic applications [22–24].

Researchers in various fields originally adapted micromachining methods initially developed for the microelectromechanical systems (MEMS) and semiconductor industries to fabricate microscale fluidic platforms [25], etching and machine microscale features onto the surface of materials commonly-employed in such industry-based applications, such as glass and silicon [26]. As an alternative manufacturing solution to avoid some of the challenges of employing such materials towards many microfluidic applications, Duffy *et. al* [27] introduced the elastomeric replication technique of *soft-lithography* [28], which is used to cast and bond the poly(dimethylsiloxane) (PDMS) silicone elastomer. Quake *et. al* [29], in particular, expanded the functionality of PDMS-based microfluidic components beyond static microstructures to employ pneumatically-controlled dynamic *on-chip* valving and pumping mechanisms for a variety of logic control and lab-on-a-chip applications [30–32]. The diversity of integrated PDMS-bases fluidic operators has made soft-lithography the predominant microfluidic fabrication technique for use in research-based applications; whereas thermoplastic polymer-based microfluidic fabrication techniques such as injection molding and hot embossing are better suited for higher-scale production of microfluidics [33].

Such conventional microfluidic fabrications approaches have, however, demonstrated some critical limitations towards the effective scaling of microfluidic systems, as well as the innovation of functional-complex and geometrically-intricate designs. Fundamentally, the *two-dimensionality* of conventionally-fabricated microstructures inherently limits the freedom for geometric dimensional complexity in the third spatial dimension; as a result, fabrication of complex three-dimensional geometries is practically impossible to acheive using conventional microscale fabrication techniques [34–38]. Additionally, microfluidic systems demonstrating higher-level functionalities than flow around passive microstructures in static microchannels must be fabricated from multiple layers of material subject to highly-sensitive manual alignment and inter-layer leak-free bonding *via* oxygen plasma [39, 40] or adhesive [41] treatments, which frequently results in device leaking and relatively high degrees of fabrication imprecision and irreproducibility [42]. Furthermore, multiple manual labor- and time-intensive manufacturing procedures are often required utilizing expensive equipment operated by highly-trained personnel in well-equipped fabrication facilities [43–45]. As a result, such conventional fabrication processes have historically limited the ability to develop novel *three-dimensionally*-complex microfluidic platforms with a relatively-low throughput of microfluidic design iteration, prototype fabrication and device innovation [46–48].

Of significant interest in the field of microfluidic device engineering over the past decade has therefore been research into strategies to overcome some of the fundamental limitations of conventional manufacturing approaches in the form of alternative approaches for the construction of microfluidic systems *via* additive manufacturing or *three-dimensional (3D) printing* approaches [49–53], used to fabricate microfluidic structures *via* automated layer-by-layer deposition of polymer materials. These methods employ an entirely-alternative 3D solids modeling approach to design 3D printable microfluidic device designs, incorporating truly *three-dimensionally*-complex microstructural elements only manufacturable using additive manufacturing-based approaches, which are created using computer aided design software and then uploaded to the 3D printing hardware [54]. This dissertation presents the development of various new classes of *three dimensionally*-complex, integrated microfluidic platforms utilizing *Multijet* 3D printing - a layer-by-layer, multi-material micro-scale deposition method - towards the engineering of geometrically and functionally-unique submillimeter microfluidic structures which are only made possible using an additive manufacturing approach. Moreover, entirely-3D printed prototype microfluidic platforms are employed to address specific challenges currently faced by conventional microfluidics in relevant biomedical and diagnostic applications.

1.1 Microfluidic Fabrication Techniques

1.1.1 Conventional MEMS-based Approaches

1.1.1.1 Soft-lithography

The soft-lithography process first entails fabrication of a microfabricated master in order to micromold a single layer of PDMS (**Fig. 1.1a**). This process consists of (*i*) spin coating photoresist (*e.g.* SU-8 [55]) onto a silicon wafter; (*ii*) defining the 2D geometry of the desired microscale structures using the photolithography process (*i.e.* exposing the photoresist to UV light excitation through a photomask); (*iii*) chemically-developing and removing the undesired portions of the photoresist. Once the master mold is fabricated, as illustrated in **Fig. 1.1c** the remaining steps in the soft-lithography process involve (*iv*) pouring liquid PDMS onto the master mold, serving as a negative master defining the final microstructures (*e.g.* microchannels), and curing the PDMS until hardened; (*v*) removing the cured PDMS from the mold; (*vi*) bonding the PDMS structure to a substrate (*e.g.* rigid glass or silicon wafer, or an additional layer of cured PDMS) *via* oxygen plasma, UV ozone or adhesive treatments; and (*vii*) punching microchannel inlets and outlets for *off-chip* interfacing hardware to be installed [39, 41, 56–58].

PDMS is valued for its strength, optical transparency, cost and manufacturability, as well as its biocompatibility and gas-permeability, a particular advantage towards many biological and chemical fluidic handling applications [59–62]. Furthermore, soft-lithography as a fabrication technique can be further extended to a process known as *multi-layer soft-lithography* [29, 63], a method by which multiple discrete micromolded PDMS layers are aligned, bonded and assembled together to create microfluidic devices with each layer possessing a different behavior, to enable overall device functionalities beyond those possible with single layer microfluidic devices [62]. For example, thin membrane-like layers assembled between two rigid layers comprising microchannels can be used to create dynamic microvalve structures and fluidic operators serving as hydrodynamic allegories of electrical circuitry components [64–66]. Additionally, various physical and mechanical properties of PDMS can be modified by adjusting the ratio of base-to-curing agent in the uncured PDMS formulation, enabling dynamic components with relatively-tailorable mechanical behaviors [59, 67–69]. Moreover, different assembled PDMS layers can be designed with specific biochemical properties, such as membranes with increased porosity for semi-permeable boundaries separating two fluids for studying diffusive biochemical transport in biological applications [70–72].

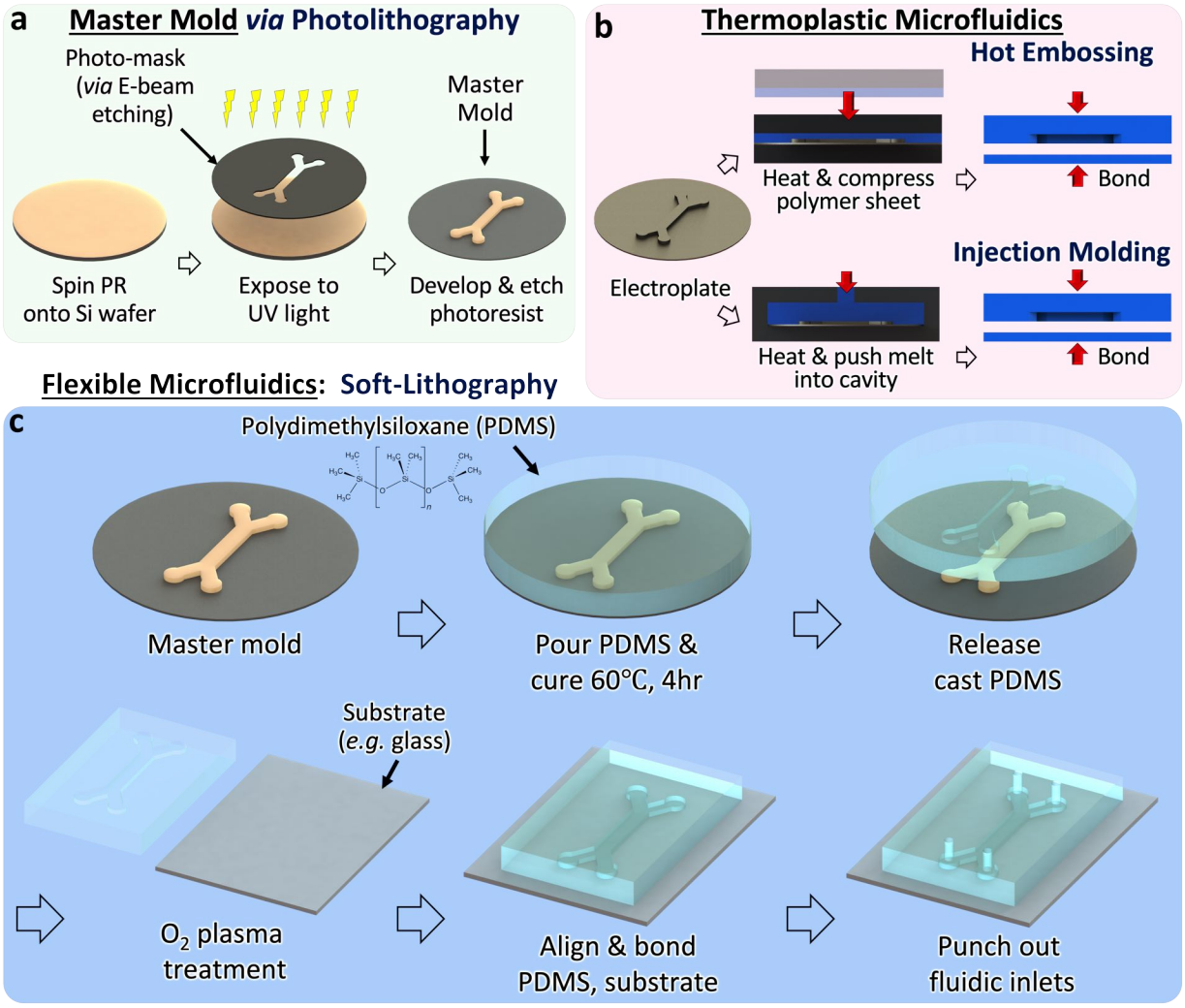

Figure 1.1: Conceptual illustrations of the MEMS-based fabrication processes used to fabricate conventional microfluidic devices. **(a)** All processes begin with the creation of a master mold, most often photolithography is used to create a mold comprised photoresist on a silicon wafer which defines the functional microstructures in the final device. **(b)** Thermoplastic-based microfluidic systems typically involve either hot embossing or injection molding, which uses heat and pressure to form stock polymer material around an electroplated master mold, after which the micro-molded polymer is bonded to a substrate (*e.g.* glass, polymer). **(c)** The soft-lithography process is used to fabricate microfluidic systems from polydimethylsiloxane (PDMS), which involves bonding of a micro-molded PDMS structure to a substrate (typically *via* O_2 plasma treatment) to form enclosed microchannels comprising the final operational device.

1.1.1.2 Injection Molding and Hot Embossing

Injection molding [73] and hot embossing [74] are two additional manufacturing methods commonly used to fabricate microfluidic devices. As illustrated in **Fig. 1.1b, *left***, both injection molding and hot embossing processes utilize a master mold which can be fabricated using photolithography (**Fig. 1.1a**) or using subtractive manufacturing-based micromachining techniques (*e.g.* micro-CNC milling) for more high-volume production, although micromachining lacks the sub-micron resolution of the photolithography-based master mold fabrication approach [75]. In the instance of utilizing a photolithography-fabricated master mold, the master mold is first plated with a metallic layer *via* electrodeposition methods in order to lend the structure higher robustness and reusability for low- to medium-volume production [76]. The master mold is then placed into injection molding or hot embossing equipment which encloses the microstructured surface in a hollow cavity, into which thermoplastic, melted to a liquid state inside a compressor, is compressed (in hot embossing) or injected (in injection molding) under heat; allowed to cool, and is subsequently removed from the mold then bonded to a substrate to form an enclosed microfluidic device [33].

Both injection molding and hot embossing pose fairly-significant reductions in material and operating cost, manufacturing complexity and manual labor intensiveness as compared to soft-lithography [77], and are compatible with a wide range of available thermoplastic polymers, including poly(methyl methacrylate) (PMMA), polycarbonate (PC), polystyrene (PS) and polyvinyl chloride (PVC) [78]. Furthermore, hot embossing demonstrates a potential advantage over injection molding in that microstructures can be replicated with sightly higher accuracy, as less viscous flow over the mold is requited and less material shrinkage is encountered upon thermoplastic cooling with hot embossing [79]. The geometric-complexity of injection molding and hot embossing -manufacturable designs, however, is limited by the inability for the micromold to possess any physical structures with undercutting structures or large features which would otherwise pose issues for reliable feature resolution upon removal from the master mold [80, 81]. Furthermore, as typical microfluidic structures fabricated *via* injection molding and hot embossing generally lack the complexity and functionality of 3D fluidic operator-integrated microfluidic systems fabricated *via* soft-lithography [33, 82], the primary focuses of microfluidic fabrication research are in further development of such techniques in order to integrate more complex fluid handling mechanisms into existing injection molding and hot embossing manufacturable designs and to reduce the cost and time of mold fabrication [83]. Regardless, these two manufacturing methods are currently deemed more rapid, mass-producible and suitable conventional manufacturing approaches than soft-lithography for the translation of primarily research-based microfluidic designs towards certain commercial applications [16, 84, 85].

1.1.1.3 Fundamental Limitations

Despite the demonstrated advantages of the aforementioned conventional microfluidic fabrication approaches, certain limitations inherent to such methods exist towards the effective scaling of microfluidic systems, the innovation of geometrically-complex and functional designs and the commercializability of the technology in most chemical and biological applications [34]. Practically, the soft-lithography process in particular requires numerous cost, time and manual labor-intensive procedures [37] which quite often must be performed by highly-trained personnel working in well-equipped facilities (*e.g.* clean room-based facilities for the processing of silicon wafer devices) utilizing expensive manufacturing equipment [43–45], which can be challenging for organizations outside of the engineering community [77]. Furthermore, construction of dynamic physical fluid manipulation elements with higher-level functionalities requires the highly-sensitive manual alignment and inter-layer leak-free bonding of multiple microscale fabricated layers of material together in order to assemble complete enclosed devices; consequentially, leaking and overall device failure often result in devices with fairly high degrees of assembled imprecision and irreproducibility, which furthermore reduces the commercializability of microfluidic devices [35, 42, 86]. Perhaps most significantly however, these conventional fabrication approaches are monolithic in nature and therefore are only capable of fabricating inherently *planar* structures with geometric complexity in two-dimensions, yet lack practically any geometric complexity in the third-dimension [87] (*i.e.* fabrication results from lithography have low aspect ratios, microchannel heights $\sim 10^{-2}$ mm, microchannel widths $\sim 10^{-1}$ μm & channel lengths $\sim 10^{1}$ μm [55, 88]); thus rendering the construction of complex three-dimensional geometries (*e.g.* circular inner diameter channels, over-hanging and enclosed structures) impractical if not impossible to accomplish using conventional microscale fabrication techniques [34–38]. As a result, these fundamental limitations of such conventional fabrication processes have historically limited the ability to develop novel *three-dimensionally*-complex microscale structures, as well as provide for a relatively-low throughput of microfluidic device iteration, fabrication and innovation [46–48].

1.1.2 Additive Manufacturing for *Three Dimensional* Microfluidics

Additive manufacturing - otherwise referred to as *three-dimensional (3D) printing* - encompasses different layer-by-layer material deposition processes used to construct 3D physical structures, and offers significant promise for the innovation of microfluidics in various applications [89]. Generally, 3D printable designs are modeled using computer aided design (CAD) software and imported (*i.e.* in the form of an .STL file) into computer aided manufacturing (CAM) software, which translates the 3D model into 3D printer instruction (*i.e.* in the form of G-code) for autonomous 3D printing. Truly-micro/nanoscale 3D printing techniques most suitable for the fabrication of lab-on-a-chip microfluidic systems can be categorized into three fundamental approaches: (*i*) Fused Deposition Modeling (FDM), (*ii*) Stereolithography (SLA), and (*iii*) Multijet modeling.

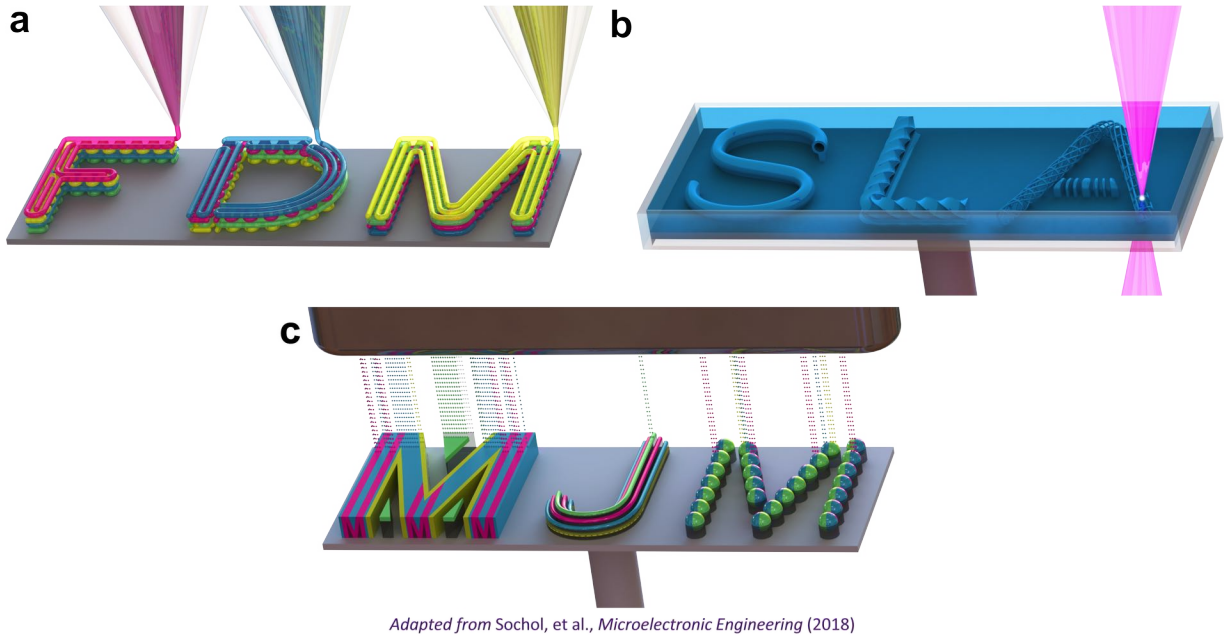

Figure 1.2: Conceptual illustrations of state-of-the-art additive manufacturing approaches for the fabrication of *3D printed*, three-dimensional microfluidic systems. *(a)* Fused Deposition Modeling (FDM), one of the most common examples of extrusion-based processes (in addition to direct-laser writing, DLW) whereby solid polymeric stock material is heated until softened, then deposited in a layer-by-layer procedure (simultaneous multi-material extrusion is possible), typical X-Y resolution limit is approximately 100's of μm. *(b)* Stereolithography (SLA), involving selective laser curing of photocurable polymer liquid resin, only a single material is used at a time and no support material used, resolution above approximately 50μm resolution is common. *(c)* Multijet Modeling (MJM), whereby micro-droplets (approximately 10's of μm in diameter) of multiple materials (photocurable polymers and usually sacrificial support polymer-based materials) are simultaneously deposited in an inkjet-like deposition process, followed by flash curing using UV light in layers, with a typical resolution of approximately 10's of μm. Adapted from [49].

1.1.2.1 Fused Deposition Modeling (FDM)

The concept of extrusion-based additive manufacturing by which a 3D object is created from softened material extruded from dispensing nozzles was first patented by S. Scott Crump in 1992 [90]. Since the expiration of Crump's original patent in the 2010's, multiple hardware companies have been founded and every year continue to manufacture lower cost, more compact desktop-sized extrusion-based 3D printing equipment and expanding the world-wide access to reasonably affordable 3D printing technologies. Fused Deposition Modeling (FDM) (**Fig. 1.2a**) is an extrusion-based 3D printing process entailing the deposition of a wide variety of thermoplastic polymers, including acrylonitryl butadiene styrene (ABS), polylactic acid (PLA) and polyethylene terephthalate (PET), which are manufactured into long (*e.g.* 1 kg) spools of solid polymer filaments. In

the FDM process, as the polymer spool is fed into and softened by the deposition head, material is extruded and deposited (at a speed dependent on the feed rate into the deposition head) onto the substrate with approximately 100's of μm resolution [89] in the X-Y plane. The substrate then moves in the Z-direction, enabling the layer-by-layer deposition of polymer. As polymer layers are deposited upon previous layers and cool to room temperature at different rates, FDM deposition is often characterized by fairly low-bond strength and non-isotropic material properties; furthermore, most FDM-compatible polymers feature lower density and higher porosity than injection molding-compatible polymers, for example [36]. Similar additive manufacturing methods entailing isothermal deposition of materials (*e.g.* inks and hydrogels), referred to as *direct ink writing* (DIW) techniques, are also attractive extrusion-based approaches [91].

FDM-based approaches have demonstrated relatively-limited application for most submillimeter-scale microfluidics due to the requirements of feature resolution often well below 100 μm and for the need for support material to fabricate fully-enclosed structures [92]. DIW has therefore been the predominant extrusion-based technique utilized in various microfluidic applications, primarily for the deposition of sacrificial inks which can be physically-removed for the fabrication of 3D networks of hollow microchannels in inside large gel-like volumes [93–96], and have been extended for various bio-printing of extra cellular matrix hydrogels for *on-chip* cell culture applications [97–99] as well as 3D printing of wax-based supports for the soft-lithography casting of PDMS to generate non-planar PDMS-based microchannel constructs [100] and multi-material extrusion of functional membranes integrated into FDM-fabricated microchannels [38]. Furthermore, the inherently-high surface roughness (average $\sim$600 μm tall surface abnormalities) of FDM-fabricated microchannels has been utilized as an advantage for the enhanced mixing of laminar fluids, therefore FDM-fabricated microfluidics should be restricted to use in applications where fluidic mixing is desired [84].

1.1.2.2 Stereolithography (SLA)

The strategy for creating solid polymer structures by exposing liquid photo-curable polymer resin to UV light in a layer-by-layer approach was first developed in 1981 by Hideo Kodama [101], but wasn't first patented until 1984 by Charles hull [102], termed *Stereolithography* (SLA) (**Fig. 1.2b**). In the SLA method, photo-curable material is solidified, either by continuous (*e.g.* laser-based) or discrete (*e.g.* CDC pixel-based) UV light excitation, as the build plate is linearly-extruded out of a bath of liquid resin in incremental steps, the distance of which defines the layer thickness (*e.g.* $\sim$25 μm) of the fabricated 3D part [102]. During the course of the development of SLA technology, Hull also introduced the .STL file format, which is nearly-universally used by CAM software to dictate 3D printing G-code. Furthermore, an extension of SLA technology, known as *direct laser writing* (DLW) utilizes two-photon absorption to enable highly spatially-controlled, point-by-point photo-polymerization of liquid photo-curable polymer with resolution down to $\sim$100 nm [88, 103].

SLA-based fabrication approaches have been extensively demonstrated towards microfluidic device manufacturing over the past few years [104–106]. SLA 3D printed microchannels have been shown to more accurately-replicate as-designed dimensions (within $\sim$26 μm) with smoother surface texture than both FDM (within $\sim$109 μm) or Multijet (within $\sim$40 μm) 3D printing approaches [84]. SLA-fabricated systems have been demonstrated towards microfluidic applications requiring hardware with high degrees of optical clarity [86], limited laminar flow mixing for diffusive filtering [107, 108] and *on-chip* cell culture using photocurable biocompatible polymers (*e.g.* PEG-DA-250) [109]; furthermore, 3D printed automation accomplished *via* SLA-fabricated deformable membranes and valves [105], 3D gradient generator structures [110], reconfigurable modular microchannel elements for laminar flow mixing and microdroplet generation and processing [106], and the *in-situ* fabrication of ultra-high resolution dynamic 3D microstructures with dimensions on the order of $\sim$25 μm inside microchannels [88] have been demonstrated. Typical reliable SLA-fabricated microchannel widths fabricated using commercially-available SLA-compatible polymers are on the order of $\sim$100 μm [36, 111]; however customization of the chemistry of photo-curable polymers compatible with SLA 3D printers has resulted in the smallest enclosed microchannel dimensions of any 3D printing approach, with widths as low as $\sim$20 μm [112], with DLW-approaches demonstrating the overall highest resolution of any 3D printing approach [88, 113]. However, SLA-based technologies are inherently limited by the requirement for structures to be self-supporting, as SLA is a single-material technique with the inability to print sacrificial support materials, therefore SLA-fabricated structures must utilize fabricated structural supports which must be physically-removed after fabricated, a challenging and in many cases impossible task for most fully-enclosed structures [114, 115].

1.1.2.3 Multijet Modeling

The inkjet-based deposition of multiple photo-curable or thermo-curable polymers in a layer-by-layer process was first invented in the 1990's by Yamane *et. al* [116] and was later extended for the simultaneous deposition of both structural and sacrificial support support materials to fabricate truly-3D overhanging structures [117], which formed the basis of the Multijet modeling technique (**Fig. 1.2c**) (currently patented by *3D Systems*, SC, USA; whereas the related *Polyjet* modeling technique is patented by *Stratasys*, MN, USA). Multijet 3D printing techniques employ large arrays of inkjet nozzles to deposit microdroplets ($\sim$10's μm in spherical diameter) of various photo-curable polymers on a build substrate as the print head linearly-scans the substrate in X-direction, as the nozzles are selectively-actuated such that the 3D printed component is fabricated with geometric complexity in the X-Y plane plane, as the build substrate lowers down in the Z-direction to enable fabrication of 3D components. Subsequently, post-processing methods are used to remove the sacrificial support (*e.g.* water-soluble gel-based or meltable wax-based materials) in order to yield truly *three-dimensionally*-complex enclosed structures [115, 118, 119].

The sacrificial support material 3D printing capability of Multijet modeling enables the fabrication of the most *three-dimensionally*-complex physical microfluidic geometries of any additive manufacturing approach [49] which have been demonstrated towards many diverse research applications [120], as exemplified by discrete microfluidic circuitry operators and integrated circuitry networks [115], 3D finger-actuated systems [121], 3D gradient generating networks [122] and functional 3D printed intra-channel membranes [38]. Furthermore, the multi-material capabilities of Multijet 3D printing have also been demonstrated towards the fabrication of integrated materials digitally-tailored to have material composition between hard, rigid materials and soft, flexible, rubber-like materials [123, 124]. Various strategies have also been introduced for the integration of interfacing hardware directly with Multijet 3D printed components, such as functional membrane inserts and non-3D printed O-rings [120, 125].

Even though Multijet modeling is particularly-advantageous for many microfluidic applications due to its relatively-high resolution ($\sim$16 μm), rapid printing speeds, large build volumes, multi-material integration and sacrificial support material printing capabilities [92, 105, 115], one of the inherent drawbacks of Multijet 3D printing is the fairly-limited selection of proprietary materials manufactured by 3D printing companies to be the only materials compatible with their hardware, for which detailed information (*e.g.* precise chemical composition, mechanical and thermal properties) is not published by the manufacturers [51, 126]. Therefore, the material and mechanical properties of most Multijet 3D printable polymers are usually first independently investigated in the context of different end-applications in order to empirically-determine the suitability of the material towards the desired application, due to the lack of comprehensive documented material properties for most proprietary materials. Conveniently however, common Multijet-compatible 3D printing materials including Visijet M3 (*Stratasys*), the 3D printing material predominantly featured in this work, have been previously researched, characterized and demonstrated towards various microfluidic device applications in multiple fields [115, 118, 121, 122, 127–133]. In instances where certain Multijet 3D printing materials are found to be inherently non-suitable for certain applications, various material post-processing techniques can be employed to enhance certain material properties, for example by encapsulating the interior of inherently non-biocompatible 3D printed microchannels with PDMS or PS coatings to prevent the leaching of cytotoxic monomers into the enclosed fluid, thereby improving *on-chip* cell adhesion and proliferation [70, 118, 134].

Moreover, as with most 3D printing methods, the removal of sacrificial support material from within enclosed Multijet 3D printed microfluidic channels with different internal volumes is one of the primary considerations when implementing different Multijet 3D printing techniques [119], as certain post-processing procedures are more effective at removing certain support material compositions from the interior of microchannels. For example, a multi-step heated mineral oil method was developed to efficiently melt and remove wax-based support material from within complex integrated microfluidic circuitry networks [115], and various physical [135] and diffusion-based [84] methods to remove water-soluble gel-based support materials from within microchannels have been demonstrated. Multijet 3D printing techniques implementing wax-based support materials generally permit more flexibility in 3D microfluidic design than comparable techniques utilizing

water-soluble gel-based support materials, as since the diffusion-dominant time necessary to remove gel-based support is directly related to the length, and inversely-related to the characteristic length (*e.g.* diameter), of the enclosing microchannel, microfluidic devices fabricated using gel-based support material must usually be designed comprising linear microchannels with millimeter-scale characteristic lengths, limited 3D complexity of enclosed geometries, as well as additional device inlets which facilitate easier support material removal which can be permanently plugged following post-processing [49].

In summary, 3D printing approaches demonstrate various advantages for microfluidics manufacturing *versus* conventional methods. The additive manufacturing-nature of 3D printing enables fabrication of complex *three dimensional* geometries and microfluidic constructs with unique functional capabilities as compared to *two-dimensional* microstructures. Various 3D printing techniques enable effective universal scaling of fluidic operators (exemplified by 3D integrated fluidic circuitry [115]), accomplished *via* monolithic, automated fabrication using compact equipment which demonstrates higher-throughput prototyping of microfluidic designs. Additionally, 3D printing enables simplification, even outright elimination, of device assembly and packaging processes [108]. Furthermore, 3D printing equipment decreases in price and increasing in resolution every year, which extends the availability of commercially-viable and accessible technologies to biomedical researchers and microfluidic device engineers around the world, those which can be operated by untrained personnel. The remaining challenges with 3D printing for microfluidics fabrication include the development of efficient support material removal procedures as well as the relatively-limited commercially-availability of materials, compatible with SLA and Multijet modeling especially, although 3D printable polymeric materials are generally decreasing in price and increasing in variety and availability every year, demonstrating the capability for more rapid printing with higher resolutions [119]. Finally, a useful comparison between various microfluidic device fabrication methods, including soft-lithography and 3D printing (adapted from [84]), is illustrated in Appendix **Fig. 7.2**. Furthermore, a summary of the various 3D printing technologies and materials pursued in this work is presented in Appendix **Fig. 7.3**.

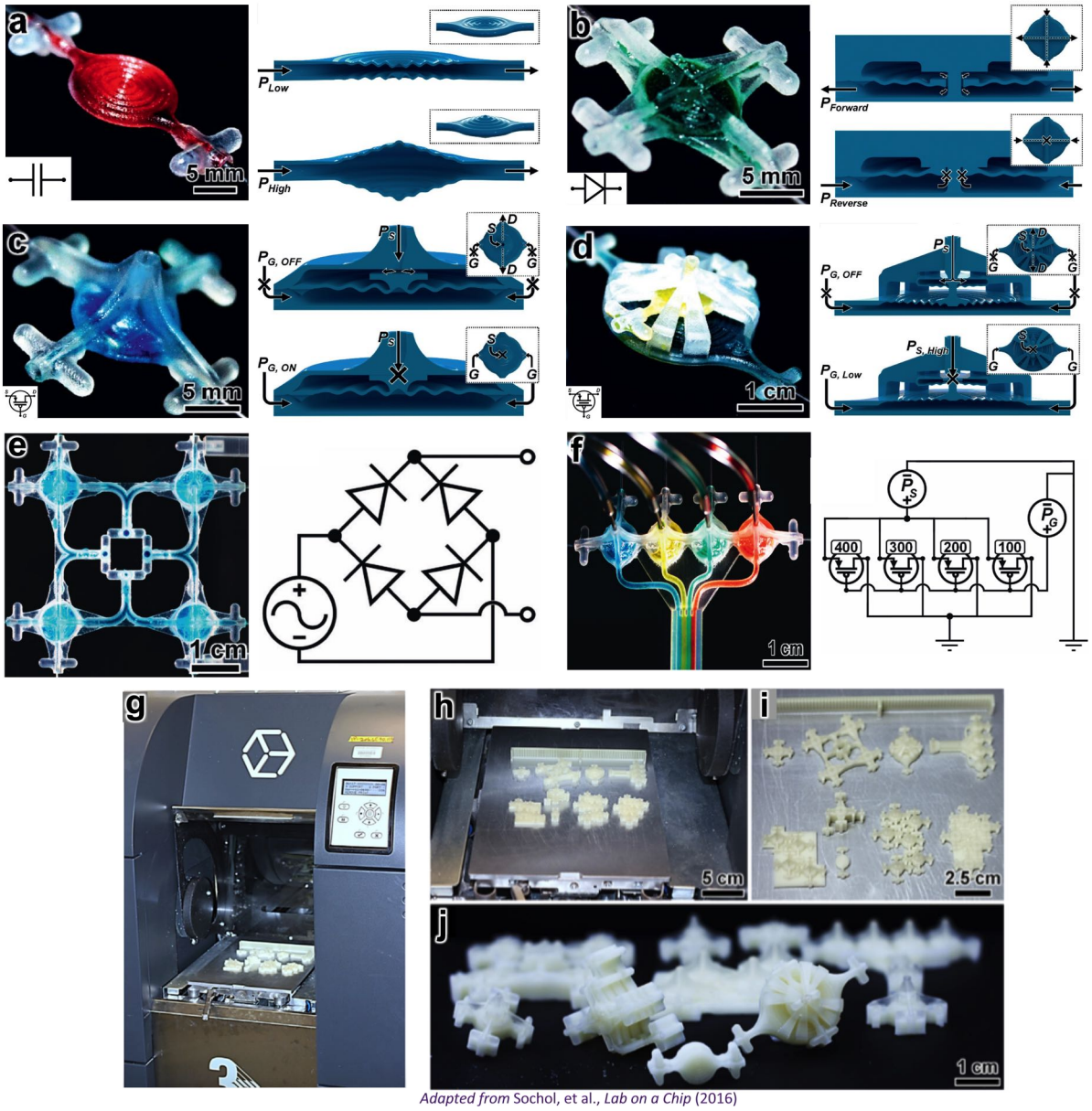

Figure 1.3: Examples of previously-demonstrated 3D printed integrated fluidic circuitry (IFC) *via* Multijet 3D additive manufacturing. **(a)** 3D fluidic capacitor, post-processed prototype (*left*) and operational diagram (*right*). **(b)** 3D fluidic diode. **(c)** 3D fluidic transistor. **(d)** 3D fluidic pressure gain transistor. **(e)** 3D full-wave fluidic rectifier circuitry comprised of four integrated 3D fluidic diodes. **(f)** 3D multi-fluid perfusion controller comprised of four integrated 3D fluidic transistors with a single-input control source. **(g)** 3D printing system used to fabricate all 3D IFC prototypes (Projet 3000UHD, *3D Systems, SC, USA*). **(h-j)** Examples of various prototypes 3D IFC prototypes comprised of structural polymer (in white) and sacrificial support polymer (in yellow). Images adapted from previous work featured in [115].

1.1.2.4 Example of 3D Printed Integrated Microfluidic Circuitry (3D IFC)

Inspired by the advent of integrated electronic circuitry, researchers have previously demonstrated physical *on-chip* PDMS-based *integrated microfluidic circuitry* operators, including fluidic capacitors [136], transistors [137] and diodes [136, 138], used to autonomously execute basic fluidic routines [139], replacing high-powered and bulky powered *off-chip* external equipment [140, 141]. However, proper functionality of these fluidic circuitry components is highly dependent on the precision of manual alignment and assembly of the PDMS layers as part of the soft-lithography fabrication process, which frequently results in a high probability of device failure due to errors in manual assembly. In previous work in our group [115], we investigated the use of Multijet additive manufacturing towards the development of entirely-3D printed modular 3D fluidic operators. This work presents the first demonstration of fabricated dynamic as well as static truly-3D intra-channel microstructures (*e.g.* 3D corrugated dynamic membranes, one-way valves for flow rectification, dynamic pistons for fluidic logic switching) comprising 3D fluidic circuit components, including 3D fluidic capacitors, diodes and transistors using a Multijet additive manufacturing technique. This 3D printing approach, in particular, was found to be most suitable for the fabrication of truly *three-dimensionally*-complex, intra-channel microstructures, due to the multi-material nature of the structural and support material deposition method. Furthermore, the microscale fabrication resolution and accuracy demonstrated using the 3D printing system (Projet 3000UHD 3D printer, *3D Systems, SC, USA*) were proved to be sufficient to fabricate modular 3D fluidic circuitry operator prototypes, as well as fully-integrated 3D fluidic circuits, including full-wave rectifiers (consisting of four integrated fluidic diodes) and single input-actuated multi-fluid perfusion platforms (consisting of four unique fluidic transistors). Additionally, images of prototype devices before and after the implementation of the custom-developed post-processing procedure to remove the wax-based support material from the exterior of the fabricated prototypes are shown in Appendix **Fig. 7.1**. Finally, this work also serves as the inspiration for the further exploration of Multijet additive manufacturing, as is demonstrated with the multiple comprehensive projects presented in this dissertation.

1.2 Dissertation Outline

This dissertation presents the Multijet 3D printing approach towards the development of geometrically and functionally-unique submillimeter microfluidic structures, resulting in new classes of *three dimensionally*-complex integrated microfluidic platforms to address specific challenges currently faced by conventional microfluidics in relevant biomedical and diagnostic applications.

In **Chapter 2**, the technique of employing intra-channel, 3D micro-mixing structures (μ-mixers) to enhance low-Reynolds Number co-laminar fluid mixing is presented. The fundamental challenge of homogenous mixing at low Reynolds Numbers is presented, followed by an overview of prior efforts to enhance low-Reynolds Number mixing, including implementing conventional μ-mixers. Two distinct 3D μ-mixer designs are described: (*i*) the *3D Rifled μ-Mixer*, employing 3D split-and-recombination and axial fluidic rotation, and (*ii*) the *3D Bulbous μ-Mixer*, utilizing 3D axial fluidic rotation and undulation, in order to passively induce chaotic advective fluidic mixing in *three dimensions* and enhance mixing efficiency in shorter microchannel lengths. The design and fabrication of modular two-fluid 3D μ-mixer prototypes are discussed. Computational fluid dynamics simulation results used to qualitatively and quantitatively demonstrate the theoretical mixing performance of each design, as compared diffusion-limited mixing inside smooth-walled microchannels, are presented. The experimental methods for observing and quantifying fluidic mixing inside each fabricated prototype are detailed. Experimental results of mixing performance *versus* Reynolds Number and *versus* device unit μ-mixer-length are presented and discussed, followed by comparisons between the theoretical and experimental results. Furthermore, the experimental results in this work are contextualized by comparison with the mixing efficiencies demonstrated by conventional 2D and 3D μ-mixing approaches from the literature.

In **Chapter 3**, the technique of multi-fluid concentration gradient generation in *three dimensions* is presented. An overview of prior microfluidic efforts to improve clinical antimicrobial susceptibility testing to combat antimicrobial-resistant infections is presented, including prior uses of microfluidic concentration gradient generator (μ-CGG) microchannel networks. The design, fabrication, theoretical and experimental validation of gradient generation characteristics for two distinct three-fluid 3D μ-CGG prototype designs are presented: (*i*) a *layer*-based 3D microchannel network design capable of generating 15 discrete output μ-drug cocktails, and (*ii*) an improved *tetrahedral*-based microchannel network design capable of geometrically-symmetric 3D fluid routing generating 13 discrete output μ-drug cocktails including one consisting of equivalent-proportions of all three input fluidic species. Furthermore, the improvement in gradient generation *via* integration of 3D rifled μ-mixer-based intra-channel structures into the *tetrahedral*-based microchannel network is theoretically-demonstrated. The methods associated with the experimental procedures, data acquisition, and quantitative analyses are detailed. Moreover, the biomedical application of both prototypes towards antibiotic susceptibility testing to treat antibiotic-resistant bacterial infections, in particular, is demonstrated through bacteriological studies used to determine

single-antibiotic minimum inhibitory concentration (MIC) values, as well as pair-wise and three-antibiotic combination drug screening (CDS) studies for clinically-relevant antibiotic compounds targeting an antibiotic-resistant strain of *E. coli* bacteria as a model.

In **Chapter 4**, the methodology of entirely-3D printed modular human-powered microfluidic actuators serving as low-cost and portable sources of electrical power-free pressure-driven flow for microfluidic devices, is presented. An overview of microfluidic applications demanding portable, low-powered systems is provided, in addition to limitations currently faced by conventional platforms in terms of the need for high-powered and bulky laboratory-based interfacing hardware. The design and fabrication of entirely-3D printed prototype human-powered microfluidic actuators are discussed. The methods associated with the experimental procedures, data acquisition, and quantitative analyses are presented. Experimental results characterizing the forward driven-fluid flow behavior for each prototype, with respect to pushing frequency, are presented and discussed. Examples of four prototype designs are presented: (*i*) a single-fluid actuator employing previously-demonstrated one-way fluid flow rectification; (*ii*) a single-fluid actuator employing improved one-way fluid rectification, reduced back-flow throughout the system and higher output flow rates; (*iii*) a single-fluid actuator employing improved one-way fluid rectification and in-line finger-actuated pressure generation, resulting in even higher output flow rates; and (*iv*) an integrated two-fluid modular pulsatile microfluidic mixer employing two independent single-fluid actuators sharing a common finger-actuated pressure source.

Finally in **Chapter 5**, the methodology of employing entirely-3D printed human-powered hand-held microfluidic platforms enabling completely-*on-chip* finger-actuated fluid sample collection, biological sample enrichment and multiplexed pathogen detection targeting entirely-*on-site* pathogenic contamination for point-of-need applications is presented. Prior efforts in utilizing microfluidic systems as portable point-of-need diagnostic tools are discussed. A derived multiplexed design methodology, the 3D solids modeling and fabrication of an entirely-3D printed finger-actuated prototype hardware are discussed. A custom drop-casting procedure developed to pre-treat *on-chip* biological enrichment and detection chambers with nutrients and colorimetric metabolic-indicator compounds which enable a straight-forward and practical optical pathogen detection scheme, along with the device operational procedure, are presented. Furthermore, the fluid uptake characteristics of the fabricated prototype are experimentally-verified. Moreover, results for the experimental optimization of the chamber pre-treatment chemistry and determination of the limit of detection of the employed proof-of-concept pathogen detection scheme are presented. Finally, the application of the prototype for human-powered sample collection, biological enrichment and optical detection of *E. coli* bacteria in model drinking water is experimentally-demonstrated.

Conclusions for the dissertation are discussed in **Chapter 6**. The unique capabilities of microfluidic mixing, fluidic routing and gradient generation in *three dimensions*, as well as the benefits of finger-actuated fluidic actuation and *on-site* pathogen detection utilizing entirely-3D printed portable human-powered microfluidic platforms, are summarized. Future directions and applications for the presented technologies are discussed.

Chapter 2

Low Reynolds Number 3D Micromixers

2.1 Introduction

2.1.1 Challenge of Low Reynolds Number Mixing in Microfluidics

Control over the of mixing of fluids inside microfluidic devices is one fundamental challenge of all multi-fluid handling microfluidic platforms, regardless of the applications [142–144]. In the fields of biological testing [145, 146], pharmaceutical drug discovery [147, 148] and chemical synthesis [149, 150], homogenous inter-fluidic species mixing in certain regions is often required [151, 152]. In clinical biomedical and diagnostic applications the homogenous mixing of microscale volumes of target analyte and analytical reagent solutions ensures that chemical reactions or biological interactions occur reliably and thoroughly, resulting in expedited reaction rates, higher analytical throughput and increased analytical sensitivity and accuracy [18, 19]. For example, this is an essential requirement for complex micro total analytical systems (μTAS) and lab-on-a-chip microfluidic platforms for semi-automated fluidic processing steps *on-chip* [20], such as biomedical microfluidic immunoassay systems previously-demonstrated towards point-of-care blood plasma screening [22], detection of bloodborne-pathogenics *via* microfluidic nucleic acid analysis [23] and *on-chip* whole blood cell lysis for proteomic analysis [24]. These characteristics make microfluidic systems advantageous over conventional analytical methods, yet present a persistent and fundamental challenge for nearly all microfluidic devices: achieving complete homogenous co-laminar fluidic mixing in microchannels.

The Navier-Stokes equation defines the conservation of momentum of an incompressible Newtonian fluid inside a microchannel (a reasonable assumption for most microfluidic reagents in general applications), balancing the rate of change of momentum within the fluid due to all convective, viscous, pressure and externally-applied forces, as defined by **Eq. 2.1**,

$$\rho(\frac{\partial \overrightarrow{u}}{\partial t} + \overrightarrow{u} \cdot \overrightarrow{\nabla}\overrightarrow{u}) = -\overrightarrow{\nabla p} + \mu\overrightarrow{\nabla}^2\overrightarrow{u} + \overrightarrow{F} \tag{2.1}$$

where ρ is the density of the fluid, $\overrightarrow{u}$ is the flow velocity, $\overrightarrow{p}$ is the pressure acting upon the fluid, μ is the dynamic viscosity of the fluid and $\overrightarrow{F}$ is the sum of the body forces acting upon the fluid. The lefthand-side of the equation takes into account the inertial acceleration of the fluid ($\frac{\partial \overrightarrow{u}}{\partial t}$ is the time dependent term representing the change in fluid velocity with time; and the non-linear inertial $\overrightarrow{u} \cdot \overrightarrow{\nabla} \overrightarrow{u}$ term represents momentum change due to convection). Furthermore, the righthand-side of the equation takes into account the effects of the various forces acting upon the fluid (the $\overrightarrow{\nabla} p$ term represents the pressure differential between the beginning and end of the section of fluid; the $\mu \overrightarrow{\nabla}^2 \overrightarrow{u}$ term represents diffusion; and the $\overrightarrow{F}$ term represents the body forces acting upon the fluid). [153]

Due to the complexity of analytical solutions for the Navier-Stokes equation, analysis of microfluidic systems and understanding of the behavior of fluids inside microchannels are often made simpler by considering certain *dimension-less* parameters. For example, microfluidic flows are often characterized using the Reynolds Number (*Re*), which is used to describe the relative importance of inertial forces as compared to viscous forces in a given fluidic state, or specifically, the importance of particle momentum transferred *via* convection relative to particle momentum transferred *via* viscous diffusion as presented in **Eq. 2.2** [154],

$$Re = \frac{\rho v L_c}{\mu} \tag{2.2}$$

where ρ is the density of the fluid, v is the flow velocity, L_c is the characteristic length (*e.g.* the width of planar microchannels or inner diameter of circular cross-section microchannels) and μ is the dynamic viscosity. Microfluidic devices fabricated *via* high-resolution MEMS-based processes have typically very small characteristic length scales (*i.e.* width, *e.g.* $\sim$150 μm) and an even smaller channel height (*e.g.* $\sim$50 μm), and thus, a large surface area-to-volume ratio (*e.g.* $\frac{2*length*(width+height)}{width*length*height}$ = 2*($\frac{width+height}{width*height}$) $\approx$ 2*($\frac{(150\mu m+50\mu m)}{(150\mu m*50\mu m)}$) $\approx$ 2*($\frac{200}{7500}$) $\approx$ 5*10^{-2}) [155]. In addition, typical fluidic flow rates used in devices as required by most microfluidic applications are on the order of $\sim$100's of μL/min or less [156]. As a result, at these length-scales the effects of gravity on the microchannel-constricted fluids is negligable, while the effects of surface forces (*e.g.* surface tension, surface roughness interactions, van der Waals forces, etc.) become more predominant (the relative importance of the acting forces can be approximated as: interfacial forces >> viscous forces > inertial forces > buoyancy) [157, 158]. Therefore *Re* values in conventional microfluidics applications are typically $\leq$ 100 [93]. In this, the *laminar* regime (*Re* $\leq \sim$2300), viscous forces dominate over inertial forces (as opposed to in the *turbulent* regime, *Re* $>$ 4000, experienced in most everyday *macro-fluidic* conditions). Furthermore at even lower *Re*'s in the *low Re regime* or *Stoke's flow* (*Re* $<$ 1), lateral convective forces are practically-negligable. As a result, in the *low Re regime* since the convective forces can be neglected, the $\overrightarrow{u} \cdot \overrightarrow{\nabla} \overrightarrow{u}$ term on the lefthand-side of the Navier-Stokes equation (**Eq. 2.1**) can be eliminated. Therefore, the Navier-Stokes equation can be reduced to the Stokes equation as shown in **Eq. 2.3**,

$$\rho(\frac{\partial \overrightarrow{u}}{\partial t}) = -\overrightarrow{\nabla p} + \mu \overrightarrow{\nabla}^2 \overrightarrow{u} + \overrightarrow{F} \tag{2.3}$$

which is linear and the analytical solutions are easier to find. Furthermore, external body forces on the righthand-side of this equation are usually neglected, since gravitational effects are negligible, and the $\rho(\frac{\partial \overrightarrow{u}}{\partial t})$ term can also be eliminated since the fluids are usually assumed to be incompressible. Therefore, the reduced form of the Stokes equation as shown in **Eq. 2.4**,

$$\overrightarrow{\nabla p} = \mu \overrightarrow{\nabla}^2 \overrightarrow{u} \tag{2.4}$$

reflects the fact that the fluid velocity vectors and streamlines of fluid motion are effectively all parallel to one another and point normal to the microchannel inlets and outlets for steady state incompressible flow in a linear smooth-walled microchannel, thus the streamlines do not interfere [15, 143]. Furthermore, the Péclet Number (*Pe*) is another dimension-less parameter often used to describe the relative importance of convection to diffusion for particle mixing, in other words, the time required for diffusive mass transport relative to the time required for convective mass transport as presented in **Eq. 2.5** [159],

$$Pe = \frac{vL_c}{D} \tag{2.5}$$

where v is the average fluid velocity, L_c is the characteristic length (*e.g.* the width of planar microchannels or inner diameter of circular cross-section microchannels) and D is the diffusivity coefficient[1] which describes the speed of molecular diffusion for a given species. Diffusion is an inherently very slow process, as reflected by typical values of D on the order of $\sim 10^3$ $\mu m^2 s^{-1}$ for small chemical molecules ($\leq$1 nm), $\sim 10^2$ $\mu m^2 s^{-1}$ for larger molecules such as proteins ($\sim$5 nm), $\sim 10^{-1}$ $\mu m^2 s^{-1}$ for nanoparticles ($\leq$1 μm) and $\sim 10^{-2}$ $\mu m^2 s^{-1}$ for single-cellular organisms such as bacteria ($\sim$10 μm) [160, 161]. Furthermore, according to **Eq. 2.7** which relates *Pe* to *Re*, in the case of water at 25° C ($\mu \approx 1*10^{-3}$ Pa*s; $D_{water} \approx 10^{-9}$ $m^2 s^{-1}$), *Pe* $\approx$ 1000**Re* [159].

[1] It should be noted that the diffusivity coefficient is not a *constant* value, as the diffusivity coefficient is in fact *temperature-dependent* according to the Stokes-Einstein equation as shown in **Eq. 2.6** [160],

$$D(T) = \frac{kT}{6\pi\eta(T)r} \tag{2.6}$$

whereby D is the diffusivity coefficient as a function of temperature, k is the Boltzmann constant ($\approx 1.3807*10^{-23}$ JK^{-1}), η(T) is the viscosity of the medium as a function of temperature and r is the approximate hydrodynamic radius of the species particle of interest. Therefore, anywhere in this text where a single D value is mentioned, this is in actual fact referring to the approximate value of D at 298 K in water as tabulated or plotted from cited experimental studies, unless otherwise specified in the text.

$$\frac{Pe}{Re} = \frac{\mu}{D} \tag{2.7}$$

Laminar flow is typically characterized by *Pe*'s $\approx 10^4$. In the laminar regime, therefore below *Pe* $\approx 10^6$, mass transport *via* diffusion dominates over mass transport *via* convection [162]. As a result, an inherent characteristic of fluidic processing at this microscale, especially at or approaching the low *Re* regime, is that inter-fluid mixing of molecular species in co-laminar flow is heavily dominated by molecular diffusion [163, 164].

In general, biological and chemical reaction rates and efficiency are usually physically enhanced by increasing the contact area between the various molecular species; therefore, thorough fluidic mixing is required. However, as a result of the aforementioned physical and operational parameters of conventional microfluidic channels and applications, the only inter-fluid mixing between two conceptual fluidic species solutions under co-laminar flow conditions occurs across a single flat inter-fluid interface, the fluid boundary layer, which remains constant in hydrodynamic steady-state. In this state, an inter-fluid concentration gradient exists in the *transverse* direction (*i.e.* normal to the boundary layer) across both fluids. [154]

The time required for complete diffusive mass transport across L_c (complete homogenous mixing) in the transverse direction can be described by **Eq. 2.8**,

$$t_{diff} = \frac{L_c^2}{D} \tag{2.8}$$

In a conceptual microchannel with $L_c \approx 150$ μm for example, t_{diff} for fluorophore solutions commonly used as fluid tracer dyes (D $\approx 10^2$ $\mu m^2 s^{-1}$) [165, 166] is on the order of $\sim$4 minutes, whilst for larger particles such as bacteria (D $\approx 10^{-2}$ $\mu m^2 s^{-1}$) t_{diff} is on the order of 13 days. In general, complete homogenous mixing in such microchannels (duration of t_{diff}) usually takes an impractically-long time, in general hours-to-days depending on the size of L_c and the scale of the molecule or species in question [158].

In light of this challenge, one of the most simple and frequently-used approaches to enhance microfluidic mixing inside conventional microchannels is to increase the length of the microchannel, maximizing the surface area between the co-laminar flows and allowing the fluids sufficient time inside the microchannel for diffusion to take place. The minimum path length of this channel, that which is required to achieve complete homogenous mixing, can be found using **Eq. 2.9**,

$$z_{diff} = v * t_{diff} = v * (\frac{L_c^2}{D}) = Pe * L_c \tag{2.9}$$

Using the same examples as previously proposed both given a velocity of 100 μm/s, the required z_{diff}'s would be 2.25cm & 225m, respectively. As these two examples demonstrate, the value of z_{diff} is prohibitively-long in most cases [158]. Furthermore typical aspect ratios between z_{diff} and L_c ($z_{diff} : L_c$) are on the order of $\sim$100:1 and above [167]. Since the objective of most microfluidic systems is to minimize the overall size of microchannel structures, the ability to fabricate compact microchannels in which mixing will occur is therefore fundamentally limited by the rate of molecular diffusion. This fundamental limitation is illustrated in **Fig. 2.1a**.

2.1.2 Approaches to Enhance Microfluidic Mixing

Instead of fabricating microchannels of path length z_{diff} to allow for purely-diffusive mixing across a steady-state planar inter-fluid boundary layer, many microfluidics studies have pursued alternative strategies to reduce the overall microchannel length required for homogenous mixing. These approaches can be broadly classified into two categories: active (utilizing external energy to agitate fluid flow) or passive (utilizing physical geometries to alter fluid dynamics without the need for input of external energy) [154]. Active mixing approaches typically take the form of external disturbances created using powered hardware to actively generate various forms of fluidic pressure, temperature and electrohydrodynamical sources which dynamically disturb the boundary layer; however, conventional sources of active mixing tend to necessitate the demand of costly and bulky external laboratory-based equipment which are often difficult to operate and maintain [164].

Passive mixing approaches namely pertain to the development of physical microfluidic mixer (μ-mixer) elements which are used to passively-induce enhanced microfluidic mixing. Conceptually, μ-mixers are physical fabricated microstructures that lend an alternative morphology to a microchannel (*i.e.* other than linear, smooth-walled channels) which is used to physically-induce *transverse* (non-axial) components of fluid velocity. As a result of this non-linear, transverse fluid motion, volumes of fluid are stretched and folded over each other as seen on fluidic planes on the cross-section of the microchannel and the surface area of the boundary layer is significantly increased, thereby provided a larger area for diffusion to act across, enhancing the mixing rate and quality inside a microchannel [167]. Furthermore, these passive elements can be more simply fabricated and employed than active mixing approaches, as they do not require any form of external power under which to operate and can be directly incorporated into the design of the physical microfluidic body itself [18].

2.1.2.1 Conventional μ-Mixing Approaches

Various μ-mixer structural designs have been previously-demonstrated in planar microchannels comprising conventional (*i.e.* PDMS-based) microfluidic platforms. These μ-mixer designs usu-

ally take the form of *unit* elements of a single design incorporated into a microchannel body, and multiple μ-mixer unit elements are usually combined in-series in order to study the effect of the overall effective μ-mixer unit length on the mixing enhancement inside a microchannel. Overall, different μ-mixer designs are typically employ one of the main principles to enhance mixing quality, hydrodynamic focusing, flow separation, split-and-recombination of flows and induction of chaotic advection [20]. Hydrodynamic focusing techniques typically are used to create uneven pressure-driven flow, whereby a single input fluid (*e.g.* sample fluid) is sandwiched in between two different sources of the same input fluid (*e.g.* reagent fluids) which are both driven at higher pressures and thereby compress the sample fluid into a very thin lamellae, increasing the surface area-to-volume ratio and overall diffusion distance of this sample fluid [168, 169]. Flow separation approaches typically utilize non-linear microchannels, such as those comprised of periodic recesses made possible by a converging-diverging microchannel side-wall shape which generates non-axial pressure gradients, and as a result transverse fluid velocities, along the microchannel wall, inducing separation of the fluid streamlines and fluidic recirculation zones with increased boundary layer surface area at *Re*'s as low as $\sim$10 [170, 171]. Split-and-recombination (SaR) of fluids is a technique often made possible by creating *quazi-three dimensional* microchannel paths constructed from multiple assembled layers of microchannel bodies, which are typically used to split co-laminar flow perpendicular to the boundary layer and *via* non-planar fluidic routing recombine the fluidic paths in a different orientation (*e.g.* 90 degrees shifted from the original arrangement), thereby increasing the fluidic lamellae and doubling the boundary layer surface area, through which multiple SaR units in-series can significantly increase the surface area and thereby mixing [18, 159, 164]. Some of the limitations of the aforementioned approaches are that hydrodynamic focusing employs occasionally complex multi-channel pressure-driven fluid flow rate control and uses microchannel flow focusing nozzle designs and structures which can be difficult to fabricate; microchannel wall geometries used to induce flow separation tend to be limited in their complexity due to the planar nature of conventional fabrication methods, in addition to the fact that recirculating flows with higher degrees of chaotic motion are observed at *Re*'s above those in the low *Re* regime (on the order of $\sim$100's); and SaR microchannel structures, while effective at exponentially-increasing boundary layer folding using multiple units in-series, usually require multiple labor-intensive assembly and bonding steps in order to fabricate the typically geometrically-complex multi-layer μ-mixer element designs [18, 20, 172].

Chaotic mixing, however, might possibly represent the passive mixing approach with the greatest freedom in the uniqueness of the μ-mixer design, as well as the overall practicality and effectiveness of the method. On a macro-scale (*i.e.* turbulent fluidic regime), stirring of fluids can be used to induce mixing. If multiple stationary stirring bodies are used, for example in a container of liquid, this provides the basis for mathematically-integrable particle motion which has been shown to result in low fluidic mixing efficiency; however, if the stirring bodies are active in a time-dependent manner (*e.g.* the stirring bodies are periodically turned on and off and rotate in different directions over time), the fluid volume stretches and folds significantly, thereby exponentially increasing in mixing surface area with time, and, as can be mathematically-shown, inducing chaotic particle motion and significantly-enhanced particle mixing [173].

The translation of the phenomenon of *chaotic advection* to the micro-scale does exist. Steady state fluid flows with two degrees of freedom of motion (*i.e.* 2D or planar fluid flows experienced in conventional planar microchannels) do not exhibit chaotic fluid motion; however, fluid motion with three degrees of freedom, as well as unsteady (*i.e.* time dependent) 2D flows, can exhibit chaotic fluid motion [15]. Therefore, chaotic advection in low-*Re* microfluidic flows is made possible by using physical structures of various morphologies to induce fluid velocities *transverse* to the normal direction of axial fluid flow, thereby generating secondary helical fluid recirculation patterns with three degrees of freedom in the fluid and which increases boundary layer stretching and folding, followed by combining multiple different mixing modes in-series to increasing the degree of chaotic fluid and particle motion over the length of the microchannel [174]. For example, curvilinear channels with an alternating serpentine path can be used to generate secondary recirculation flow and vortical fluid flow patterns, thereby inducing chaotic advective mixing using a non-linear microchannel path in 2D space [175]. As an alternative approach, one fundamental example of integrating discrete physical μ-mixer unit elements into conventional microchannels was first demonstrated by Stroock et al. [167, 176], whereby so-called staggered herringbone-shaped grooves are integrated into the bottom and top surfaces of a planar linear microchannel. These grooves are tilted at different angles with respect to the microchannel path length such that when pressure-driven fluid flows over the surfaces, an asymmetric pressure gradient is generated along the direction of the grooves and asymmetrically reverses as the direction of the grooves change. This pressure gradient induces transverse fluid velocities, helical recirculating fluid flow and chaotic advection as seen on cross-section fluidic profiles, which exponentially stretches and folds the boundary layer along the length of the main microchannel. As a result, chaotic advective mixing is demonstrated which increases the mixing efficiency inside the channel at $Re \leq 10$, including in the low *Re* regime.

2.1.2.2 Additive Manufacturing-Based μ-Mixing Approaches

Moreover, the degree of chaotic mixing within a microchannel can itself be enhanced by either introducing a time-dependent element to the fluid flow (*e.g.* time-dependent pressure-driven flow) or by utilizing geometries which take advantage of the the third spatial-dimension (truly three-dimensionally-complex structures) to induce properly *three-dimensional* chaotic fluid particle motion [177]. Regarding the latter point, the planar nature of conventional fabrication methods used to manufacture 2D microfluidic systems (*i.e.* microchannel heights restricted to $< \sim 100$ μm) limits the geometric complexity of microchannels and microchannel-constrained physical μ-mixer element designs to *two dimensions*. Thus, the freedom in generating transverse fluid flows and highly chaotic fluid motion is inherently limited, mainly in the direction in-plane with fluid flow (*i.e.* not truly in the third dimension, out-of-plane with the axial direction of fluid flow, perpendicular to the bottom surface of the microchannel) [178, 179].

Despite considerable recent advancements in additive manufacturing technologies (*e.g.* higher resolution, wider material variability, greater commercial accessibility to different types of equipment [49]), only a few fundamental 3D μ-mixer designs have been fabricated using additive manufacturing approaches and demonstrated in recent years [142]. Of these previously-demonstrated 3D μ-mixer designs, the majority have comprised three-dimensionally-arranged networks of microchannels consisting of smooth-walled (*e.g.* circular inner diameter) microchannels in condensed in 3D space, effectively compacting an overall long microchannel length inside spatially-compact 3D μ-mixing *regions* of a 3D microchannel network [93]. Only a few examples of 3D μ-mixer development work have attempted instead *linearly-compact* 3D μ-mixer unit elements, thereby shorter μ-mixer channels lengths. For example, Shallan et al. [110] employed a stereolithography-based 3D printer (Miicraft) to fabricate compact 3D SaR μ-mixer units comprised of 500 μm-wide cross-section linear microchannels, demonstrating the ability to fabricate 3D printable μ-mixer-integrated microfluidic systems using transparent, low cost materials, yet did not provide any quantified measurements of mixing quality at any reported *Re*'s. Furthermore, Plevniak et al. [22] used a Multijet 3D printing approach (ProJet 1200, *3D Systems*) to fabricate different 3D printed μ-mixer channel designs comprised of various non-linear microchannel paths (*i.e.* complex 3D serpentine and circular curved structures) designed to enhance mixing *via* flow separation and SaR techniques, and demonstrated prototypes towards passive *on-chip* mixing of sample and reagent fluids targeting blood-based point-of-care diagnostic applications. Additionally, Lee et al. [180] reported an entirely-3D printed microfluidic device, fabricated using SLA 3D printing (Viper SL, *3D Systems*) which employs a trapezoidal cross-section channel with spirals in a circular 3D helical pattern, generating Dean vortices to first passively mix a bacteria sample solution and a reagent solution containing bacterial enzyme-targeted nano-particle cultures, then separate the bacteria-attached nano-particle clusters using inertial focusing. Finally in a recent study, Enders et al. [142] created five different 20mm-long 3D μ-mixing channels, each comprised of unique 3D networks of (500 μm by 400 μm rectangular cross-section) microchannels, using Multijet 3D printing (Projet MJP 2500 Plus, *3D Systems*), in order to find an optimal 3D μ-mixer design of the same microchan-

nel length; yet this study only demonstrated homogenous mixing inside all designs at a relatively high $Re \sim 37$. This latter study established, however, that the mixing performances of new and unique 3D μ-mixer prototype designs are possible following well-established protocols used to quantify the mixing performance of conventional μ-mixer devices.

Most conventional 2D and 3D μ-mixer designs however, including all of those examples mentioned heretofore in this section, demonstrate higher degrees of mixing enhancement in the moderately-low *Re* range of $1 \leq Re \leq 100$; thus, demonstrating consistent and definitive effective co-laminar fluid mixing in the low *Re* regime ($Re \leq 1$) is still a challenge faced by nearly all μ-mixer designs [18]. Moreover, all of the aforementioned examples of recent works demonstrating 3D μ-mixer development *via* additive manufacturing approaches focus entail design and fabrication of primarily 3D networks of microchannels which lack any actual substantial intra-channel 3D μ-mixer geometries. Therefore, this chapter presents the exploration of the potential to utilize Multijet additive manufacturing to fabricate 3D intra-channel μ-mixer structures designed to passively-induce *three-dimensional* chaotic mixing, a truly-3D μ-mixing approach, to demonstrate mixing enhancement in the low *Re* regime for entirely-3D printed point-of-care and point-of-need biomedical and diagnostic-based microfluidic platforms.

2.2 Design of Intra-Channel 3D Micro-mixer Structures

In order to demonstrate the unique advantages of the Multijet additive manufacturing approach in tackling the challenge of low-*Re* microfluidic mixing, the concept of incorporating entirely 3D printed microstructures as intra-channel *3D μ-mixer units*, only possible to fabricate using an additive manufacturing approach, is illustrated in **Fig. 2.1b**. These 3D microstructure geometries can be fabricated at any arbitrary location along the length of a linear microchannel as part of the monolithic 3D printing process used to manufacture the entire 3D printed microfluidic platform in a single-step, in order to enhance localized mixing efficiency (at that particular location along the microchannel) by inducing chaotic advective mixing in *three-dimensions*. The overall objective of this approach is to create more compact linear microchannels for the complete mixture of co-laminar fluids inside entirely-3D printed microfluidic platforms.

As explained in **Section 2.1**, one method to produce chaotic particle motion in microfluidic flow is to subject a volume of fluid flowing down the path length of a microchannel to repeated sequences of fluidic helical motion, stretching, expansion and rotational motion [167]. Thus, two unique 3D μ-mixer unit designs were created, the solids models of each are illustrated in **Fig. 2.1c**, which utilize different 3D elements to perform 3D fluidic manipulation in distinct manners, resulting in two different approaches to induce chaotic fluidic mixing in *three-dimensions*.

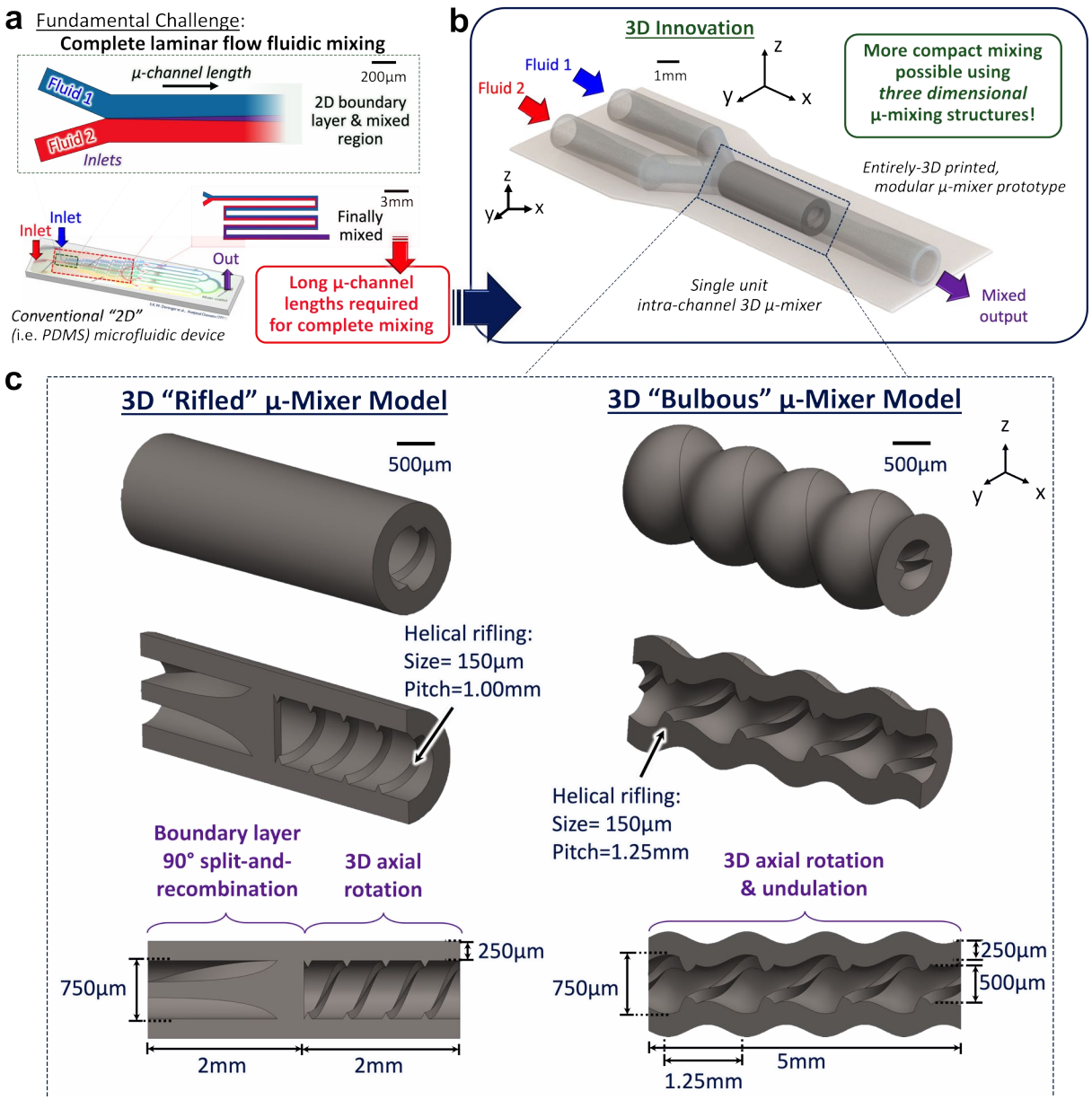

Figure 2.1: Conceptual illustrations of the two unique 3D intra-channel μ-mixer models, integrated into entirely-3D printable modular mixing prototype devices. **(a)** Conventional *2D* microfluidic device (*e.g.* PDMS-based *via* soft-lithography) in which mixing of co-laminar fluids is a fundamental challenge for most microfluidic applications; therefore, conventional μ-channels typically require μ-channel length ($\sim$cm) $>>$ width ($\sim$0.1 mm) to provide sufficient time for mixing. **(b)** Prototype, entirely-3D printable two-fluid modular mixing device model showing a single-unit integrated intra-channel structure. **(c)** The two unique 3D μ-mixer designs featured in this work - the 3D *rifled* μ-mixer (*left*) and 3D *bulbous* μ-mixer (*right*) - utilize truly three-dimensional structures with characteristic length scales of 750 μm intended to induce chaotic advection in three dimensions and increase mixing efficiency in shorter μ-channel lengths.

2.2.1 3D Rifled Micromixer

The 3D *rifled* μ-mixer design as illustrated to the left of **Fig. 2.1c** is based on the foundation of a 4mm unit-length section of microchannel with a smooth-walled circular cross-section and a wall thickness of 250 μm. The inner diameter of this 3D circular microchannel base is 750 μm, which is also the characteristic length of this design, as the intra-channel 3D microstructures are entirely enclosed by this dimension. This design incorporates two different forms of 3D microstructural elements to perform two different fluidic manipulation steps, in-series. The two fluids, once combined forming co-laminar flow, enter the μ-mixer unit from the left side and flow from left-to-right as viewed on the model. The first 2mm of the design contains a 225 μm thick structure which bisects the combined fluid perpendicular to the boundary layer, and uses a helical twist to rotate the two halves of the fluid flow by 90° and recombine the separate fluids, stretching and folding the boundary layer. This action increases the surface area for boundary layer diffusion and decreases time for complete inter-fluid species transport diffusion. This fluidic manipulation is in a sense a 3D allegory of the split-and-recombination (SaR) technique previously employed by various different conventional 2D μ-mixing approaches [164, 181, 182], but employs a monolithically-fabricated helical microstructure (termed the *3D SaR helix*), only possible by using additive manufacturing. The latter 2mm long section of the design contains a 3D rifling structure along the side wall of the microchannel consisting of an equilateral triangular cross-section with side walls 150 μm long and repeats with a pitch length of 1mm. This structure manipulates the fluid in a truly 3D fashion, which is a 3D extension of a previously-adopted approach employing 2D micro-ridges fabricated on the bottom of planar microchannels to induce transverse velocity and helical secondary flow in planar microchannels [167, 177]. The 3D helical rifling provides increased resistance to fluid flow along the axial direction of the microchannel which induces an axial pressure gradient parallel to the rifling, causing transverse fluid velocity following the direction of the rifling in *three-dimensions*. As a result, 3D helical fluid rotation is induced which enhances the quality of chaotic advective mixing in and out of the plane of fluid flow along the rifled length of the microchannel.

2.2.2 3D Bulbous Micromixer

The 3D *bulbous* μ-mixer design, as illustrated to the right of **Fig. 2.1c**, employs an overall alternative form of 3D fluidic manipulation, for comparison. Similar to the 3D rifled μ-mixer design, the 3D bulbous μ-mixer has a wall thickness of 250 μm and employs the same geometry 3D rifling structure along the side wall of the microchannel but with a pitch length of 1.25mm. This design is instead based on the foundation of a 5mm unit-length microchannel with a truly 3D cross-section comprised of hollow spherical regions with a maximum inner diameter of 750 μm and minimum diameter of 500 μm and repeating with a period of 1.25mm. The characteristic length is an average of 750 μm. Employing such a 3D undulating microchannel side wall geometry is a technique representiing a 3D extension of approaches previously employed in conventional planar

microchannels utilizing asymmetric side wall shapes to induce transversal fluid velocities parallel to the bottom of 2D microchannels and induce chaotic mixing in-plane with the direction of flow [20, 170]. During fluid flow along the axis of the microchannel, the 3D rifling produces similar 3D helical fluid rotation as induced by the 3D rifled μ-mixer design; however, the undulating side wall generates asymmetric pressure gradients and periodic converging-diverging fluid velocities in textitthree-dimensions, which periodically compress and expand the co-laminar boundary layer, contributing further stretching and folding of the boundary layer and increasing chaotic mixing in- and out-of the plane of fluid flow.

2.2.3 Conceptual Modular Low Reynolds Number Two-Fluid Mixer

As a tangible demonstration of the ability to incorporate an arbitrary number of 3D μ-mixer units into the digital solids model design of any arbitrary 3D printed microfluidic system, as well as to design a manufacturable platform which enables the analytical testing of 3D printed μ-mixer prototypes, a modular two-fluid microfluidic mixer device is designed and illustrated in **Fig. 2.1b**. This entirely-3D printed prototype routes two independent fluidic inputs *via* smooth-walled circular profile microchannels into a 3D Y-junction, replicating the basic principle of combining two fluids for diffusive mixing in a single linear microchannel [183], but using 3D cross-section microchannels. Immediately after the Y-junction, the two fluids physically contact one another and form a single planar co-laminar fluidic diffusion boundary layer. The combined fluids flow through a single microchannel of an arbitrary length, into which the designs of 3D μ-mixer units are incorporated, and the resulting fluid output is routed away from the device *via* a single microchannel outlet. The result is an an entirely monolithically-3D printable modular prototype which can be used to perform and observe mixing of two co-laminar fluids to evaluate the effectiveness of multiple unit-length μ-mixers comprised of the different 3D microstructure designs as featured in **Fig. 2.1c**. This modular two-fluid μ-mixer design represents the model of the fabricated prototypes employed in the experimental fluidic testing that is presented in this chapter.

2.3 Materials and Methods

2.3.1 Three Dimensional Modeling

All of the 3D μ-mixer concepts were designed using Solidworks (*Dassault Systemes*, Velizy-Villacoublay, France) solids modeling computer aided design (CAD) software. The portions of each design intended to enable device-to-world interfacing for post-processing and device operation were made possible by designing standard inlets and outlet geometries (as described in **Section**

2.3.3.2) to facilitate universal interfacing with a 20 gauge stainless steel interconnecting catheter couple. This design is saved as a modular part in Solidworks (.SLDPRT file). The main functional (device-specific) design of each device (*i.e.* the microchannel sections containing the intra-channel 3D microstructures) is saved as a modular part file, as well. These parts are then physically mated in 3D space to form a complete Solidworks assembly (.SLDASM file). The conceptual illustrations shown in **Fig. 2.1** were created using the Solidworks PhotoView 360 rendering plugin tool. Finally, the .SLDASM file is exported to a manufacturable sterolithography (.STL) file for fabrication of the actual prototype.

2.3.2 Theoretical Simulations of Mixing Profile

Theoretical simulations using COMSOL Multiphysics (Version 4.5a, *COMSOL, Inc.*, CA, USA) finite element analysis software were performed to visualize qualitatively, as well as determine quantitatively, the theoretical mixing performance of each of the following 3D models:

- 3D rifled μ-mixer, 1 unit long
- 3D rifled μ-mixer, 3 units long
- 3D rifled μ-mixer, 5 units long
- 3D bulbous μ-mixer, 1 units long
- 3D bulbous μ-mixer, 3 units long
- 3D bulbous μ-mixer, 5 units long
- Control μ-channel, 1 unit long
- Control μ-channel, 3 units long
- Control μ-channel, 5 units long

A negative solids model (the hollow region inside each microchannel in the original model becomes the new solid body; the impression of the 3D microstructures is reflected on the outer surface of the model) of each of the designs is created in Solidworks, only for use in the COMSOL studies. On the face of this model representing the inlet of the microchannel, two thin solid bodies, separated by a distance of ten microns, are extruded by one micron in order to subdivide the face, reflecting the geometry where each of the two fluidic inlets to the microchannel merge. Each of these negative solids model part files are imported into separate COMSOL files to perform each

individual study, after which a physics-controlled mesh with a normal element size ($\sim$5 μm side-length triangular meshing geometries) is applied to the model. The physics of the study are defined using Eulerian fluid mechanics and approximated using laminar and incompressible fluid flow assumptions to solve built-in fluid hydrodynamic equations. Each of the two faces on the model for the fluid inlets are selected as input fluid boundary condition surfaces representing the regions where two theoretical fluid inputs are defined as entering the fluidic system with only normal velocity to the surface. Similarly, the face on the model representing the outlet of the microchannel is selected as the only fluid outlet boundary condition surface and the pressure difference from ambient conditions is set to zero. All other surfaces are selected for the no-slip solid wall boundary condition. Standard material properties of water as shown in Appendix **Table 7.1** were chosen and modeled for the input fluids.

The ultimate objective of each study is to simulate the distribution of two distinct input species contained in either of the two input fluids at every location, especially at the outlet of the device. Therefore, transport of dilute species physics is also implemented and solved along with the hydrodynamics equations at each location assuming species mixing *via* convection and diffusion (fundamentally, the incompressible Navier-Stokes equations for each fluid are first solved to find the fluid velocity field at every point, then the velocity field is mapped to the convective mass-transport term of the convection diffusion equation) to calculate a steady-state solution. Each of the two faces selected for each of the distinct fluidic inputs are also selected to couple one of two input species, C_1 & C_2, respectively, both defined using the diffusivity constant of fluorescein molecule in water at 25 $^\circ$ C ($D_{fluorescein}$ = 4.25x10^{-6} cm^2 s^{-1}), to model the diffusivity of the florophore dye solutions that will be used in experimental measurement. The initial concentration of each species ($C_{1,o}$ & $C_{2,o}$) is defined as 1 mol/m^3. In order to quantify the degree of species mixing, a unit-less metric of localized mixing, the mixing index (*M*) [184], is defined according to Eq. 2.10,

$$M = 1 - \left| \frac{c_1}{c_{1,0}} - \frac{c_2}{c_{2,0}} \right| \tag{2.10}$$

The mixing index is a unit-less value and ranges in magnitude from 0 (corresponding to 0% species mixing, *i.e.* at that location the concentration of either species is 0% while the concentration of the other species is 100%) to 1 (corresponding to 100% species mixing, *i.e.* the concentrations of both species at that location are exactly 50% each). Finally, a parameter sweep of discrete input flow rates corresponding to a range input Reynolds Numbers from 0.01 to 50 was selected. All of the programmed input flow rates were selected to produce the total input flow rate values where the inter-species boundary layer first forms, along with their corresponding Reynolds and Péclet Numbers, calculated using Eqs. 2.2 and 2.5, respectively, as listed in Appendix **Table 7.2**.

When the simulation is run, the physical equations are solved and the mixing index is calculated at every location inside the solids model. The resulting physical distribution of mixing index solutions can then be visualized on the outer surfaces (along the inner wall of the actual microchannel), on the outlet face (on the fluid profile at the outlet of the actual microchannel) and on discrete profiles perpendicular to and running along the central axis of the model (on any fluid profile anywhere along the length of the actual microchannel). Visualizations of select simulation results for different models, all at an equivalent input Reynolds Number of Re = 1, are featured in **Section 2.4.1** and are used to qualitatively compare the mixing performance of each of the simulated 3D μ-mixer designs to the control μ-channel design. In these visualizations, 100% of both C_1 & C_2 are represented by the color blue, and any amount of mixing is represented as a color in a gradient between blue and red, with 100% species mixing (50% of both C_1 & C_2 at that location) is represented as red. The single quantitative value calculated by each simulation is defined to be the average mixing index value on the fluid flow profile on the face of the terminus of the fluidic outlet on the solids model. This represents the average mixing index in an infinitesimally-small volume of fluid at the outlet of the microchannel of the actual device. Upon completion of each simulation, one mixing index value is produced for each flow rate simulated as defined in the parameter sweep. These simulation results are plotted and the quantitative analysis results are shown in **Sections 2.4.2, 2.4.3**.

2.3.3 Fabrication and Post-Processing

In this section, the Multi-jet fabrication process, materials, and the mineral oil-based post-processing procedure are described in detail. These procedures were used to fabricate not only the devices presented in this chapter, but in fact also to fabricate all of the devices in **Chapters 3 - 5**. The information in this section can therefore be referred back to when reading subsequent chapters for a reminder of the details of the device fabrication process.

2.3.3.1 Fabrication *via* Multi-jet 3D Printing

The Multi-jet 3D printing approach was used to manufacture all of the 3D microfluidic designs presented in this work, because multi-jet 3D printing technology was determined to be a suitable manufacturing approach to successfully fabricate the featured devices. The Multi-jet 3D printing equipment available at the time of this work satisfied these requirements more thoroughly than any of the available SLA or FDM-based 3D printing equipment, namely: has sufficiently high resolution (a limit of no higher than 100 μm; FDM and SLA did not reliably print with this fine of resolution) in order to fabricate the intricate 3D structures enclosed inside microchannels; employs multi-material 3D printing (FDM and SLA 3D printers present only single-material printing capability), specifically prints using sacrificial support material in order to successfully fabricate long

enclosed 3D microchannels as well as the complex 3D arrangement of microchannels suspended in 3D space (see **Chapter 3**); and the ability to fabricate larger-scale hand-held devices with large internal volumes enclosed with mechanically-functional membranes (see **Chapters 4 & 5**).

The Multi-jet 3D printing equipment used in this work is the Projet 3000UHD 3D printer (*3D Systems, SC, USA*), available from the Center for Interdisciplinary Biological Inspiration in Education and Research (CiBER) laboratory (Principle Investigator Professor Robert Full, Department of Integrated Biology, Valley Life Sciences Building, UC Berkeley), as well as the Center for Information Technology Research in the Interest of Society (CITRIS) Invention Lab (Sutardja Dai Hall, UC Berkeley). The Multi-jet 3D printing approach entails layer-by-layer inkjet-like deposition of micro-droplets of photocurable materials roughly 32μm in diameter onto an aluminum build plate. Once each layer of materials is deposited in the X-Y horizontal plane, a UV light source flash cures the materials so that they cure, harden to their final mechanical properties and cool sufficiently such that the build plate can be lowered in the Z direction and the subsequent layer deposited on top of the previous layer. The 3D printing materials have a gel-like solid form when contained inside the commercially-available material cartridges, and are heated inside the deposition head in order to lower the viscosity sufficiently for deposition.

Throughout this work, the structural material used is Visijet M3 crystal (*3D Systems*), which is a urethane-based polymer matte white in appearance (see Appendix **Fig. 7.6**), and while the exact composition of this polymer is proprietary, basic information is provided in the material data sheet; the polymer consists of approximately 20-40$\%$ urethane acrylate oligomers, 15-35$\%$ ethoxylated bisphenol A diacrylate and 1.5-3$\%$ tri(propyleneglycol) diacrylate which acts as a curing agent [185–187]. This material was chosen because at the time of this work, it is the most readily commercially available and most affordable material offered by and compatible with the Projet 3000UHD 3D printer, which does have the ability to print using different structural material (albeit one type of structural material can be loaded into the equipment at a time). This material, when cured, is mechanically rigid with an elastic modulus given in the material data sheet as 1.159 GPa [187]; however as previous work from our group has demonstrated, the elastic modulus has been experimentally found to lower, roughly 58-116 MPa [185]. The cured polymer has proven sufficiently ductile to produce robust deformable thin-walled mechanical membranes (thickness roughly 200 μm) capable of repeatable deformations simply using manual force applied by a human finger [115, 121, 127].

In addition to the structural material, the 3D printer also deposits a support material, Visijet S100 (*3D Systems*), the only support material compatible with *Stratasys* 3D printers, which is a hydroxylated wax-based polymer [185, 188] which is yellow in appearance once cured and can be melted into liquid-phase at temperatures around 50°C and removed from the structural material comprising the device during the post-processing procedure [115]. The resulting 3D printed devices appear translucent white-clear on the exterior surfaces, and hollow regions filled with the solid support material appear an opaque yellow, as visualized in Appendix **Fig. 7.1**. A particular advantage of using the Visijet M3 material to fabricate all of the devices in this work is its useful-

ness towards microfluidic applications, as the material is sufficiently translucent that thin-walled structures allows visualization of fluids inside microchannels, especially when dyed with a color. This ability to visualize the internal fluids inside such 3D printed microfluidic devices can permit fluorescence imaging and optical microscopy of the contained fluid through the material, which is a particular advantage for fully enclosed device in applications where such analytical measurement techniques are necessary.

As an aside regarding 3D printer-compatible polymer chemistry, the exact composition of both of the aforementioned materials is proprietary and is not revealed on material data sheets. Maintaining the exact material composition a closely-guarded trade secret is a common practice in the 3D printing industry, as for many if not all of the commercial SLA and Multi-jet companies produce equipment that is most suitable, and in some cases only compatible, with the material which the company itself produces and sells to the end users of the equipment. From a business-perspective, this logic allows commercial companies to ensure a steady source of income in terms of material costs from their customers after the equipment is purchased, but also ensures that the equipment can produce the manufacturing specifications (*e.g.* resolution, material finish, material properties, build speed, reliability of the printing mechanisms) promised to the end user, as the equipment can be well-calibrated in the factory to specific materials produced and controlled by the company, ensuring customer satisfaction.

The Projet 3D printer has a feature resolution (in ultra-high definition printing mode, which was the only setting used) of approximately 32μm in Z, which corresponds to the physical height of the printed layers, limited by the size and volume of the deposited micro-droplets, as well as a lateral resolution of approximately 39μm [189]. The calibration of the 3D printer deposition head is the other predominant factor determining the feature resolution of the 3D printer. Additionally, the build volume of 127mm x 178mm x 152mm (X x Y x Z directions) and speed of the deposition process enable the simultaneous fabrication of multiple individual microfluidic devices, depending on the size and type of devices being fabricated in roughly four to six hours. It was also experimentally observed that the predominant factors determining total fabrication time were experimentally found to be the overall height of the devices (as it was determined that the printer deposits features faster in the X-Y horizontal plane than in the Z direction; orientation of a given design on the build plate therefore potentially has a significant effect on fabrication time) and the packing density of the devices on the build plate (a more compact arrangement of devices results in a shorter transition time for the print heads to traverse the area in the horizontal plane).

A custom 3D printing software provided by *3D Systems* is used to interface with the 3D printer. Briefly, the 3D printable 3D CAD model in Solidworks (file extension .SLDPRT or .SLDASM) is first meshed by the software, creating a stereolithography file (extension .STL), which is a universally-compatible file for software developed to interface with different fabrication technologies, such as various forms of additive manufacturing systems and CNC milling tools [106]. The .STL file is then uploaded into the 3D printing software, which displays a physical surface of the model and allows the user to position it anywhere on the build plate (default position is contacting

the build plate, however the user can also choose to fabricate the devices elevated off the build surface). Multiple .STL files can be added to the digital build plate area in one build. The user can typically also select user-defined print settings such as build quality (higher qualities entail slower deposition times, likely to ensure that the deposited material has the highest accuracy in the X-Y horizontal plane and smoother textured horizontal surfaces), build time (sacrifices build quality) and layer height resolution (more layers printed results in a higher in the Z direction accuracy and smoother textured vertical surfaces, but has a significant effect on fabrication time). Additionally, the software for the Projet 3000UHD 3D printer automatically senses which materials are loaded into the printer itself (using RFID-tags on every material cartridge), and so programs appropriate print settings in the software which are optimized for the given material, which presumably are slightly differently calibrated for various materials.

When ready to print, the user sends the command to the software, which automatically calculates where in the model support material is necessary, using a proprietary algorithm. Areas where the software decides support material is necessary is underneath any overhanging structures, inside enclosed features such as cavities and microchannels and on the bottom of each part between the build plate and the structure, forming a roughly 2mm thick raft which can be broken off of the build plate to remove the part without damaging the structure itself. After automatically placing the support material in the build plate model (which is visualized before submitting the print job), some 3D printing software will allow the user to selectively add or remove support material from different areas on the build plate, however the Projet 3000UHD 3D printer software does not offer the user this ability. The software then creates G-code instructions, the coding language used nearly-universally by manufacturing equipment, which is interpreted by the equipment as instructions for depositing each layer of material. Finally, after a clean, dry aluminum build plate is loaded into the printer, the user selects a command on the equipment itself to begin the printing job. Once the fabrication is finished, the build plate is removed from the 3D printer and placed into a -4°C freezer for 10-15 minutes until the support material forming the raft underneath each part contracts sufficiently (the wax-based support material has a larger coefficient of thermal expansion than both the aluminum and structural material) to weaken the attachment of the support material on the build plate, enabling the user to simply lift off the 3D printed parts. The fabricated parts are then ready for post-processing.

2.3.3.2 Support Material Removal *via* Mineral Oil-Based Post-Processing

One of the most significant advantages of Multi-jet modeling over other 3D printing technologies is the multi-material printing capability which enables the use of a sacrificial support material. This support material is used to produce a physical foundation akin to a scaffold upon which complex geometries enclosed inside cavities or channels, as well as large hollow volumes, can be reliably fabricated without material warpage during fabrication, which would occur without the use of a support material. The mechanical properties of support materials vary fairly significantly,

however, from wax-based to hydrogel-based materials [49]. Therefore different post-processing techniques must be developed and applied to successfully and completely remove the different formulations of support materials from inside and around 3D printed components. For example, the support material used by the *Stratasys* Objet line of Polyjet 3D printers (SUP705/706, *Stratasys*) is a hydrogel-based material which is most readily dissolvable in a heated KOH solution subjected to consistent mechanical agitation and/or sonification over the course of a few hours.

The advantage of the wax-based support material used in this work is its ability to be easily melted into a liquid state. Our research group developed a custom protocol to remove the sacrificial support material from both the exterior and the interior of the 3D printed components [115], which has been extensively demonstrated in our group's previous work [121, 122, 127, 128, 185, 190]. Briefly, this process entails heating 2 250mL beakers containing commercially-available food-grade mineral or vegetable oil (*e.g.* Bayes High-Performance Food Grade Mineral Oil Wood & Bamboo Conditioner) to roughly 50°C, as the support material is found to be soluble in many tested brands of food grade oils around this temperature [185]. Separate beakers of soapy water (roughly 10:1 water-soap mixture) and clean water are also heated up, concurrently. While the beakers are heating up, the 3D printed components are placed into an oven pre-heated to 75°C for 15-20 minutes, until all of the exterior support material is melted and removed from the exterior, especially the bottom surface, of each 3D printed part. Placing the 3D printed parts on top of a tray lined with 4-5 sheets of standard paper towel assists in wicking away the melted wax from the exterior of the devices, expediting the process. Once the wax is visibly removed from all of the exterior surfaces, the 3D printed components are then transferred to the heated beaker and submerged in the mineral oil, which within 2-5 minutes liquifies the remaining support material on the interior of the 3D printed devices, turning the interior of the devices (which can be visualized through the thin-walled material) translucent yellow in color.

At this point, the wax-mineral oil solution can then be flushed out from the interior of hollow channels. All 3D printed components are designed with a custom-shaped channel inlet interface design (diameter 550μm, for detailed geometry see Appendix **Fig. 7.44**), designed and fabricated onto the end of every exposed microchannel on each device, which facilitates support material removal [115] and universal interfacing with a 20 gauge stainless steel interconnecting couple (model SC20/15, *Instech*, USA outer dimeter 910μm, length 15 mm). In order to physically force the wax solution out of the enclosed regions of the devices, a 10mL hand-held syringe (*Cole-Palmer*) which is attached to a 20-gauge Luer stub (model LS20, *Instech*, needle length 12mm) connected to a length of Tygon microbore tubing (model #06420-03, *Cole-Palmer*, IL, USA) with the other end connected to the steel couple, is filled with the heated oil. The couple at the end of the tubing is connected to the inlet of the 3D printed device microchannel and steady pressure is applied by and the syringe (up to 4 ATM [185] to maintain a physical, leak-free seal between the 3D printed inlet and the couple). This pressurized flow of oil dissolves the wax to form a heated wax-oil solution, which is subsequently flushed out of the inlet on the opposite end of the microchannel. This process is repeated up to three times until the oil inside the 3D printed device is no more yellow in color than the surround oil bath, indicating the wax is fully removed.

Afterwards, to ensure that no wax remains inside of the device, clean heated mineral oil from the appropriate beaker is flushed through the device up to three times. In order to remove all remaining oil, heated soapy water from the appropriate beaker is flushed through the device up to three times, followed by a final flush with heated clean water. At this point, the 3D printed device is allowed to cool back to room temperature and the post-processing procedure is complete.

On the potential effects of the heating up of the structural polymer throughout the post-processing procedure, the glass transition temperature of the structural polymer is listed in the material data sheet as 52.5°C [187], so the temperature of the oil is kept within 50-55°C as to preserve the 3D printed structures. Above this temperature range, the structural material becomes opaque white in color, slightly more ductile and rougher in texture, although when allowed to cool back to room temperature the material retains its original appearance and mechanical properties. Furthermore, experiments have shown that above roughly 80°C, especially when comprising thin-walled membranes and other delicate thin features, permanent plastic deformation and physical damage may occur due to compression, forcing liquid through the device at high manual pressures and poking with sharp tweezers. Therefore by keeping the temperature of the liquids below 55°C at all times, the integrity of the 3D printed components is preserved.

2.3.4 Experimental Setup

Fluorescent imaging of the steady-state low Reynolds Number co-laminar fluid flow inside the fabricated 3D μ-mixer and μ-channel prototype devices, which is later used to quantify the mixing efficiency of each device design, is made possible using the experimental setup as illustrated in **Fig. 2.2**. All of the constituent fluidic elements in the experimental setup were interconnected using the Tygon tubing (*Cole-Palmer*) and steel couples (*Instech*) as previously described in **Section 2.3.3**, and all experiments were performed under standard ambient environment room temperatures of roughly 20-25°C.

To isolate the fluorescent imaging experiments from sources of background light interference and to achieve the highest contrast fluorescence images as possible, a comprehensive light-isolation fluorescence imaging setup was fabricated. The main component, the light-isolation box (actual images and detailed descriptions of the construction are shown in Appendix **Figs. 7.15,7.16**) consists of a plastic container with the lid attached and placed bottom-up on a bench top, with a hole cut into the side (the panel re-attached using hinges to form an access door) and black felt material lining every interior surfaced (attached using glue). The result is an interior space for which all sources of external light are blocked, and internal light reflection is minimized by the use of the light-absorbent felt. A hole is drilled into the top of the box and a custom-cut rubber PVC pipe fitting used to securely mount a 10 megapixel DSLR digital camera (Canon EOS 1000D, *Canon*, Tokyo, Japan) facing downwards with the lens inserted vertically into the interior of the box. Two additional holes are drilled into the side of the box and used to mount two UV light bulbs which

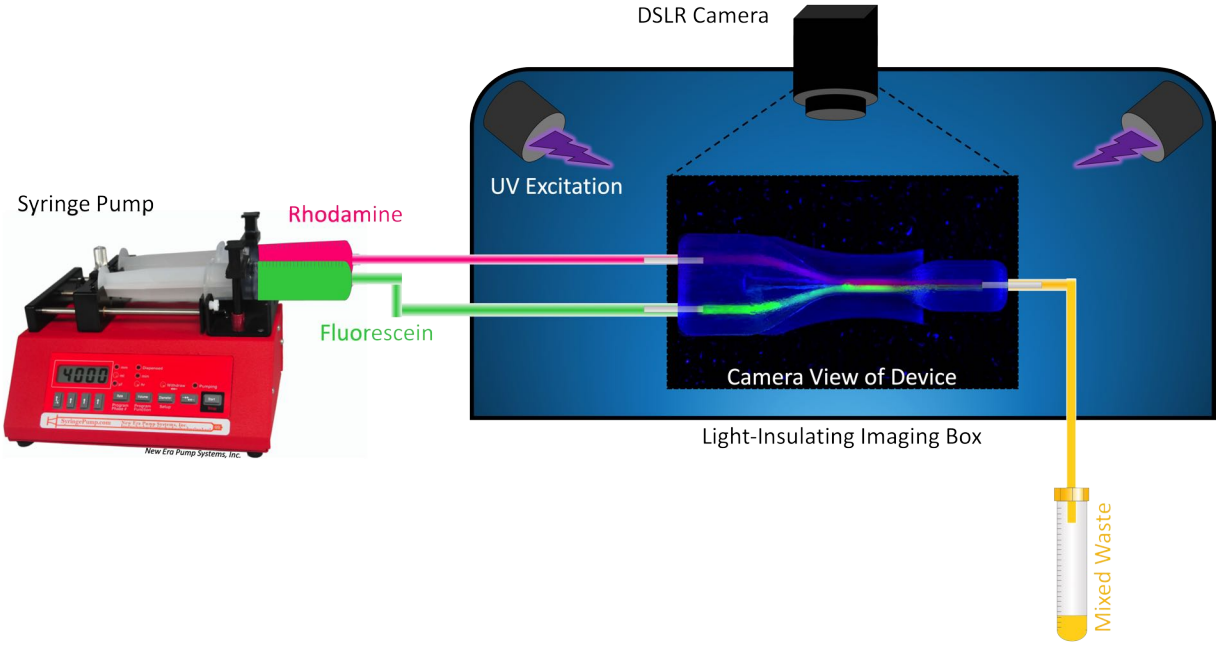

Figure 2.2: Conceptual illustration of the complete experimental setup created to capture the fluorescent images of the steady-state low Reynolds Number co-laminar fluid flow inside the fabricated 3D μ-mixer and μ-channel prototype devices. A light-isolation box isolates the prototype being tested during the fluorescent imaging experiments from sources of background light interference to achieve the highest contrast fluorescence images as possible. A syringe pump is used to drive fluorescein (*green*) and rhodamine (*red*) fluorescent dyes from two syringes concurrently at the same input flow rate through a network of tubing (*purple*) and steel couples (*silver*), into the box, through the fabricated prototype device and in view of the camera, and from the device to a waste container on the exterior of the box. UV light bulbs excite the fluorescent dyes and images of the fluorescence emission are captured using a DSLR camera.

serve as fluorescent excitation light sources.

Two syringes containing fluorescein and rhodamine dye solutions, respectively, are then loaded into an electronic syringe pump (NE-4000 Programmable 2 Channel Syringe Pump, *New Era Pump Systems, Inc.*, NY, USA), secured in place with masking tape and then each attached to a segment of tubing which extends into the light-isolation box through holes drilled into the lid of the box (resting on the bench top). The fabricated prototype to be imaged for a given experiment is then placed inside the box on a custom-made level stand made from taped cardboard and covered entirely with black felt, which elevates the sample to within around 8 inches of the camera lens. The ends of the tubing that extend from the two syringes, with steel couples attached to the free ends, are then attached to the fabricated prototype, the tube from the rhodamine syringe into the top microchannel inlet (as seen from the camera view) and the tube from the fluorescein syringe

into the bottom microchannel inlet. An additional segment of tubing is attached to the single microchannel outlet on the device and routes through a hole in the lid to a waste fluid collection container on the exterior of the box.

2.3.5 Data Acquisition and Quantitative Analysis

2.3.5.1 Data Acquisition

To reiterate, each of the following fabricated 3D device prototypes were tested using the experimental setup shown in **Fig. 2.2**: one prototype each of 1, 3 & 5 units in length for the 3D Rifled μ-Mixers, 3D Bulbous μ-Mixers and control μ-channels designs (9 prototypes in total). For each of the 9 prototype devices, one set of multiple experimental images are necessary to calculate the mixing quality of the device under different steady state fluid flow conditions. Four different Reynolds Number conditions were chosen to be experimentally produced for each prototype, and were created by creating pressure-driven flow using the syringe pump to drive fluids through each prototype device at 5.4 μL/min (Re $\approx$ 0.1), 10.4 μL/min (Re $\approx$ 0.3), 20.4 μL/min (Re $\approx$ 0.6) & 310.4 μL/min (Re $\approx$ 10), requiring a total of 36 separate experiments (different input flow rates for each prototype device) in order to collect the full set of experimental data for analysis.

The experimental operation and data acquisition procedures used to capture the fluorescent images for each individual experiment are as follows. These steps are then repeated at each of the four input fluid flow rates for all nine total prototypes. To begin, the chosen prototype is loaded into the experimental setup and is interfaced with the fluidic system as described in the previous section. The UV light bulbs are then turned on, and the DSLR camera is turned on and set from Automatic to Manual photography settings. The manual focus of the DSLR camera is then adjusted manually using the camera eye piece, focusing the image on the microchannel section of the prototype. During image capture, the only setting adjusted is the exposure setting, as two images were taken at exposures of 0.5 seconds and 1 second (camera aperture f-stop of 1/5.6 and ISO 800 were held constant), see example of the camera view during imaging in Appendix **Fig. 7.18**). It was subsequently determined, however, during image analysis that 1 second exposure produces brighter images (the magnitudes of all sources of captured light from the system are higher) than 0.5 second exposure. It was decided therefore that these images deliver stronger distinct fluorescent light intensities from both dyes, which more accurately reflect the qualitative observation of light intensity and difference in observed mixing from image to image, therefore only these images were used in the upcoming image analysis.

As described in the following paragraphs and in Appendix Protocol *Image Analysis Protocol For Producing Raw Data From Experimental Fluorescent Images of μ-Mixers*, images of two different experimental states are necessary for calculation of the mixing index for a given device under specific steady state fluidic conditions: one image of the device empty, without any fluids inside of the microchannels, and one image under steady state fluid flow conditions inside the device. Therefore images of the empty device are captured first. Then, to capture the images of the device under steady state fluid flow conditions, the syringe pump is turned on and the number for the desired forward flow rate is set. The syringe pump is then activated by pressing the *Go* button, which depresses the plungers on both syringes simultaneously, producing a constant fluid flow rate out of the syringes. The two fluids are routed through a series of tubing at the same input flow rate into the device, across the view of the camera, then out of the device through the tubing directed to the waste container. The pump is left to operate for at least 30 seconds to let the fluids reach steady state inside of the prototype device. It is observed that, other than physically disturbing the syringe pump, experimental box, table top or tubing, the appearance of the fluids inside the device as viewed through the camera remain constant, indicating a steady state fluidic system, ready for imaging. Both images at that fluid flow rate are then taken.

The order of fluid flow rate experiments performed were from lowest to highest volumetric flow rate, 5.4 μL/min, 10.4 μL/min, 20.4 μL/min & 310.4 μL/min. After performing the initial experiment at 5.4 μL/min, the syringe pump flow rate setting is then changed to 10.4 μL/min, the fluids are left to flow for an additional 30 seconds to reach steady state, then the next series of images are taken. This procedure is then repeated for flow rates of 20.4 μL/min & 310.4 μL/min. When all 4 sets of experimental images (in addition to the one set of images of the empty device) are taken for a given prototype, the syringe pump and UV lights are turned off, the top of the imaging box is lifted and the prototype device is replaced with the next prototype for testing. The above procedure is then repeated until all 9 prototypes have been tested. In total, 90 images were taken, of which 45 are used for quantitative processing.

2.3.5.2 Quantitative Processing

The quantitative processing procedure is briefly summarized below. For further details regarding the quantitative image analysis protocol, see Appendix **Section 7.2**, Protocols *Image Analysis Protocol For Producing Raw Data From Experimental Fluorescent Images of μ-Mixers* and *Protocol For Calculating Mixing Index From Experimental Fluorescent Images of μ-Mixers* and Appendix **Fig. 7.4** for further illustrations.

The quantitative metric used in this work to determine the mixing quality for each of the experimental images is defined using the Relative Mixing Index value (RMI, alternatively referred to in this text as *M*), which has been demonstrated extensively by previous work [159, 164, 184, 191–194] to be one of the standard metrics to use when performing fluorescent fluids and image

analysis to quantify the mixing quality inside microchannels of various morphologies. The RMI value is determined using image analysis of experimental images of steady state fluid flow conditions inside a microchannel, which is sufficiently translucent in order to enable visualization of the fluids inside the device, at a user-defined position where the fluids are assumed to be in an unmixed state, as well as at a user-defined position where the two fluids are assumed to be in a mixed state (the location where the mixing quality will be determined).

All image analysis performed in this work uses the open-source Fiji image processing software. For each set of experimental images of a given device at a given steady state fluid flow rate (consisting of one image of the empty device and one image of the device under steady state fluid flow conditions), the two bounding rectangles are first manually drawn on the experimental image of the device under steady state fluid flow conditions, one rectangle at the inlet of the microchannel and one rectangle at the outlet of the microchannel. The rectangle at the microchannel inlet captures both inlet fluids in their unmixed state (region of σ_o in Appendix **Fig. 7.4**), therefore it is manually drawn sufficiently wide to contain only the region where both input fluids have combined into co-laminar flow before entering the length of the single device-long channel and sufficiently tall to only capture the region containing fluid whilst not capturing any of the background device. The rectangle at the microchannel outlet captures the output fluid from the device in its most mixed state (region of σ in Appendix **Fig. 7.4**), therefore it is drawn with the same height as the inlet rectangle but sufficiently wide to capture the final segment of fluid flow before the fluids enter the steel couple and leave the 3D printed prototype device, see Appendix **Fig. 7.4** for illustrations. After defining both rectangles on the image of the device under steady state fluid flow, the same two rectangles are duplicated (using the copy-and-paste geometry feature in Fiji) in the same positions on the image of the empty device as shown in Appendix **Fig. 7.4a**.

The intensities of the pixels across the area of each of the user-defined geometries drawn on each image are then measured and stored in a matrix (either using Python programming, Excel data sheets, *etc.*). In this work, a Python script was created to interface with the Macros programming interface of the Fiji software and, after manually selecting which rectangle for analysis, export the X and Y pixel location and the intensity of the red, green and blue wavelengths of each pixel to a .csv data file. This process is then repeated for each of the rectangles in both images for each device. Although this protocol is equally as applicable for experiments using non-fluorescent fluid dyes, most experiments intending to utilize image analysis to calculate mixing characteristics employ fluorescent-dyed fluids, since the wavelengths of light emitted from fluorescent dyes typically produce images with greater contrast in specific wavelengths, which can be isolated using image processing, and result in more accurate visualizations of the distribution of specific dyed fluids at any given location inside the device, and therefore a more accurate quantification of mixing quality [174]. This distinction can be visualized by splitting an image into an RGB stack, which isolates the red, green and blue color channels from the original image and transforms each into greyscale. The result, as shown in Appendix **Fig. 7.4b**, reveals that the wavelength of light which shows the greatest difference in fluorescent intensity emitted between the two fluids from this work, Fluorescein (nearly pure green emission), background (mostly blue reflection) and Rhodamine (nearly

pure red emission), is the green wavelength. The magnitude of green wavelength data for each pixel is therefore the sole data selected for further analysis in the following protocol, and will henceforth be referred to as the *intensity* of each pixel. An additional Python script was created that accesses the data stored in each .csv file (two rectangles for each image, two images, therefore four rectangles in total) and uses the data to perform the following data processing procedures. For each image in the set for a given experiment (a total of one image of the device empty and three images of the device containing steady state fluid flow at a given flow rate), the script calculates the following values:

- The intensity of each pixel inside the drawn rectangle at the outlet of the microchannel (*i.e.* fluids in the *mixed state*, σ as illustrated in Appendix **Fig. 7.4a**), I_i
- The average value of the local pixel intensities in said rectangle, $< I >$
- The number of the pixels inside the drawn rectangle, N
- The intensity of each pixel inside the drawn rectangle at the inlet of the microchannel (*i.e.* fluids in the *unmixed state*, σ_o as illustrated in Appendix **Fig. 7.4a**), I_{io}
- The average value of the local pixel intensities in said rectangle, $< I_o >$
- The number of the pixels inside the drawn rectangle, N_o

The first step is to eliminate the contribution of background noise caused by light reflected by the 3D printed material itself. As is illustrated in Appendix **Fig. 7.4b**, this light is apparent in the green stack image of the empty device. Therefore, the final variables (those used in Eq.) for each experimental image of steady state fluid flow are calculated by subtracting the measured values from each rectangle in the image of the empty device (entirely to background noise, $I_{i,noise}$, $I_{io,noise}$, $< I_{noise} >$ & $< I_{o,noise} >$) from the measured values from each rectangle in the image of steady state fluid flow ($I_{i,fluid}$, $I_{io,fluid}$, $< I_{fluid} >$ & $< I_{o,fluid} >$), as shown in Eq. 2.11-2.14,

$$I_i = I_{i,fluid} - I_{i,noise} \tag{2.11}$$

$$I_{io} = I_{io,fluid} - I_{io,noise} \tag{2.12}$$

$$< I >=< I_{fluid} > - < I_{noise} > \tag{2.13}$$

$$< I_o >=< I_{o,fluid} > - < I_{o,noise} > \tag{2.14}$$

Finally, the RMI value is then computed for each image of steady state fluid flow as the ratio of the standard deviation of the pixel intensities in the mixed region (σ as illustrated in Appendix **Fig. 7.4a**) to the standard deviation of the pixel intensities in the unmixed region (σ_o as illustrated in Appendix **Fig. 7.4a**), as represented by Eq. 2.15 [184],

$$RMI = 1 - \frac{\sigma}{\sigma_o} = 1 - \frac{\sqrt{\frac{1}{N}\sum_{i=1}^{N}(I_i - < I >)^2}}{\sqrt{\frac{1}{N_o}\sum_{i=1}^{N_o}(I_{io} - < I_o >)^2}} \tag{2.15}$$

The RMI value therefore quantifies the mixing quality as a decimal value 0 to 1, where a value of 0 corresponds to completely unmixed fluids (at the inlet to the co-laminar flow microchannel) while a value of 1 corresponds to fluids in a completely mixed state. Finally, in order to account for any inconsistencies in the process of manually defining and drawing each bounding rectangle on each image and errors generated therein, the aforementioned quantitative processing procedure is repeated in triplicate, producing three RMI and standard deviation values for each set of experimental images, and an average RMI and average standard deviation value calculated. The data and error bars shown in **Fig. 2.7, 2.8** represent these average values calculated for a given steady state fluid flow condition for each prototype device. Finally for clarity, a distinction must be made regarding the language used throughout this chapter to describe the *mixing* of two co-laminar fluidic species. The quantifiable metric used to define mixing as calculated in this work is the mixing index (referred to in various figures as *M*), once again a unit-less number. However, the discussion of most results usually uses the terms *mixing quality* or *mixing performance*, which will be stated in terms of a percentage (*i.e.* mixing quality of 60%). This simply refers to *M* as a percentage (100**M*), to describe the quality of mixing as in *how well mixed is the fluid compared to being 100% completely mixed (quantitatively defined in quantitative processing), relative to the 0% mixing of the two initially-discrete fluidic species*. Furthermore, the concept of *mixing efficiency* is defined as follows: for the same degree of mixing and *Re* conditions, higher mixing efficiencies are achieved in more compact devices (*i.e.* shorter microchannel lengths) [155].

2.3.6 Preparation of Experimental Reagents

For all experiments, solutions of two different organic fluorophores, fluorescein and rhodamine b, are used as fluorescent dyes to enable visualization of fluidic mixing through the thin-walled surface of each fabricated prototype device under different steady state low Reynolds Number fluid flow conditions. Both molecules are often employed in fluorescent tracing in a variety of

applications on both the micro-scale, such as in forensic microscopy and serology, as well as the macro-scale, such as for the tracing of environmental contaminants in fluid bodies and networks. Fluorescein has an excitation energy 494nm and a strong fluorescent emission energy peak at 512 nm, thus in fluorescent microscopy when excited with a 494nm laser beam, or in fluorescent imaging when excited with UV light, a solution of fluorescein will fluoresce yellow-green, which can be imaged and the normalized fluorescent intensity used to determine the concentration of the molecules in a given fluidic sample [195]. Similarly, rhodamine is an organic fluorophore which is often used in fluorescent tracing, and has an excitation energy peak at 540 nm and emission peak at 625 nm [196]. The fluorescein and rhodamine solutions are each formulated by adding 50 drops of fluorescein solution (0.1% Fluorescent Green Aqueous Solution, Fluorescein Water - 60mL, *OnlineScienceMall*) and 50 drops of rhodamine solution (0.04% Fluorescent Red Dye, Aqueous Solution, Rhodamine B Solution, 60mL, *OnlineScienceMall*), respectively, to separate beakers containing 50 mL of DI water. Each solution is then used to fill two separate 10mL syringes (*Cole-Palmer*), and the fluorescent solution beakers are then wrapped in aluminum foil and stored inside a closed drawer isolated from background light to preserve the fluorescent sensitivity of the remaining fluorescent solutions for later use.

2.4 Results and Discussion

2.4.1 Visualization of Simulation Results

Fig. 2.3a-c illustrate select qualitative results of the theoretical simulations performed on the 1 unit, 3 unit and 5 unit-length 3D rifled μ-mixer, 3D bulbous μ-mixer and control μ-channel designs. All visualizations present the theoretical calculation of Mixing Index distribution (see **Eq. 2.10**) for *Re* = 1, whereby 100% concentration of either input fluidic species (C_1 and C_2) is shown in *blue*, and 100% mixing of both species (*i.e.* 50% concentration of both C_1 and C_2) is shown in *red*, and any intermediate degree of mixing is shown as a color on a gradient between the two colors. The *left-hand*) side of each sub-figure presents an isometric view of this theoretical distribution in single unit-length models for each device (the axial direction of each model from microchannel inlet towards the outlet is from left-to-right). On the *right-hand*) side, the distribution on the 2D fluidic profile at the outlet of each microchannel (perpendicular to the microchannel axis) is presented for the 1 unit, 3 unit and 5 unit-length devices (from left-to-right).

The visualizations of the 3D rifled μ-mixers (**Fig. 2.3a**) clearly demonstrate the effect of both 3D intra-channel microstructures on the fluid and mixing dynamics along the length of the device. Initially, both two fluids combine at the microchannel inlet, forming a single planar co-laminar fluid boundary layer. The 3D SaR helix structure is shown to bisect the two fluids perpendicular to the boundary layer (1^{st} fluid profile), twisting and folding the boundary layer such that the two

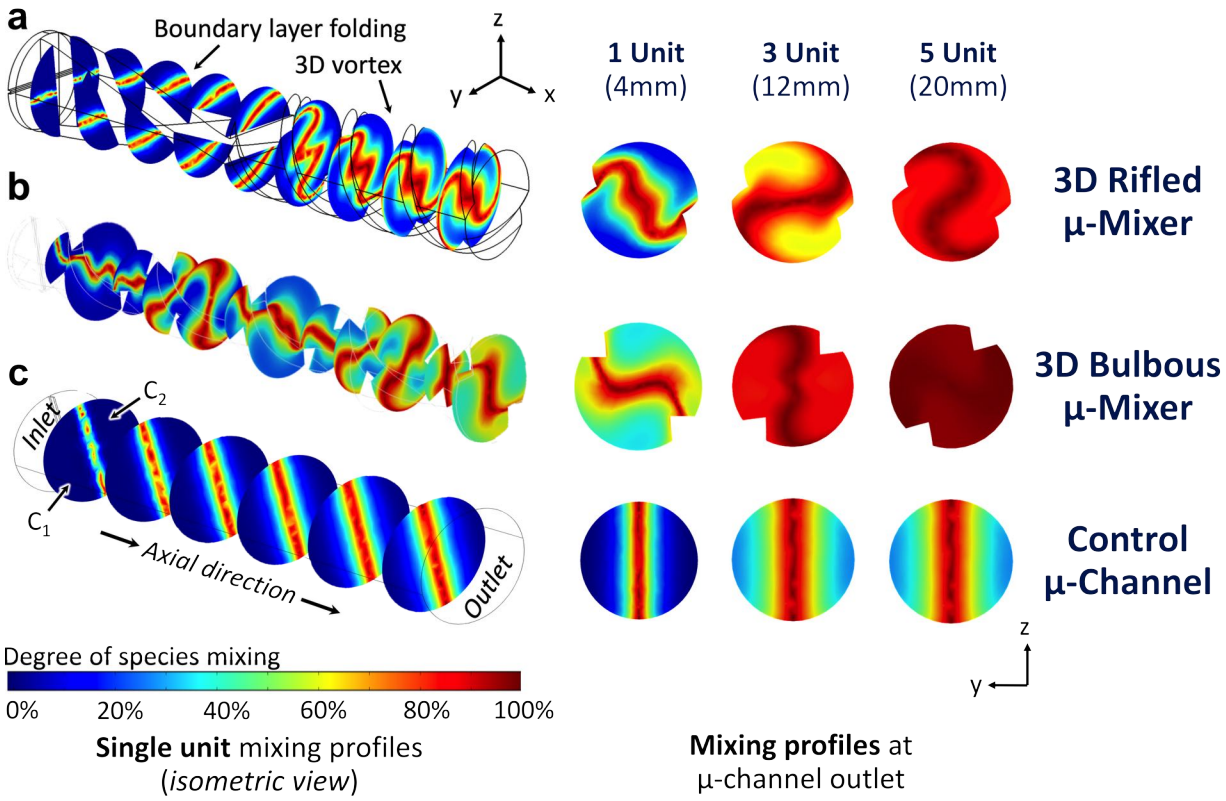

Figure 2.3: Select visualizations of COMSOL simulation results used to qualitatively compare the mixing performance of the 3D rifled μ-mixer, 3D bulbous μ-mixer and control μ-channel designs. All results show species Mixing Index distribution (see Eq. 2.10) for Re = 1. *Blue* represents 100% of either input fluid concentration (C_1 and C_2), *red* represents 100% mixing (50% of both C_1 and C_2), and any color on a gradient between the two represents partial mixing. (*Left*) Single unit-length models shown in isometric view; (*right*) fluid profiles at the outlet of each device perpendicular to the microchannel axis for 1, 3 and 5 unit-length devices. Results show increasing mixing performance with increasing device length. **(a)** 3D rifled μ-mixer model induces boundary layer folding, followed by rotational motion and chaotic advection perpendicular to the axial direction, greater mixing per-unit length than control μ-channel design. **(b)** 3D bulbous μ-mixer model induces undulation, rotational motion and chaotic advection generation perpendicular to the axial direction, greater mixing per-unit length than both 3D rifled μ-mixer and control μ-channel designs. **(c)** Control, smooth-walled μ-channel model maintains parallel co-laminar flow and diffusion-dominant mixing across the parallel boundary layer, lowest degree of mixing.

fluidic sections recombine at 90° (6^{th} fluid profile), increasing the boundary layer surface area for diffusion to occur across. The effect of the subsequent 3D helical rifling microstructure can then be seen (from 6^{th} fluid profile onwards), as a fluidic pressure gradient is generated along the direction of the 3D rifling, which induces transverse fluid velocity in *three-dimensions*. As a result, the edges of the twisted boundary layer are observed to twist, following along the surface 3D rifling at the side walls (due to the no-slip condition of the fluid at the surface). This action serves to

cause bulk 3D helical rotation in the fluid about the central microchannel axis, which increases the degree of chaotic advection in the fluid, resulting in an enhancement in chaotic mixing towards the microchannel outlet. Furthermore, adding multiple of these unit-length 3D rifled μ-mixer structures in-series clearly increases the degree of mixing, as demonstrated on the fluid profiles for the different unit-length designs due to the increasing proportion of red in each subsequent profile, as can be reasonably surmised.

Likewise, the 3D bulbous μ-mixer prototype 3D intra-channel microstructures (**Fig. 2.3b**) exhibit similar chaotic mixing inducing effects on the fluids along the length of the device. As soon as both input fluids combine at the microchannel inlet (1^{st} fluid profile), the 3D rifling microstructures begin to rotate the co-laminar fluid boundary layer, and the 3D undulating microchannel structure induces an asymmetric pressure gradient, causing the fluids follow along the side-wall of the hollow spherical-shaped regions and inducing converging-diverging fluid velocities in textitthree-dimensions, periodically compressing and expanding the co-laminar fluid boundary layer (2^{nd} fluid profile onwards). This action continues along the length of the microchannel, stretching and folding the boundary layer and increasing the degree of chaotic advective mixing. Furthermore as the fluid profiles for the different unit-length designs demonstrate, increasing the number of μ-mixer designs in-series increases the mixing efficiency, as indicated by the deep concentration of red in the latter fluid profiles.

The results for the control μ-channel (**Fig. 2.7c**), however, demonstrate the axial fluid flow and diffusion-dominant mixing dynamics that can be expected from a smooth-walled linear microchannel. Since there are no intra-channel 3D microstructures to obscure the fluid flow, the fluid streamlines remain parallel to each other and the microchannel axis and normal to the microchannel inlets and outlets. As a result, the co-laminar fluid boundary layer (evident from the 1^{st} fluid profile onwards) remains planar along the entire length of the microchannel, permitting mixing only *via* diffusion across the boundary layer, which is evident as the concentrations of green and red increase along the length of the microchannel and on the outlet fluid profiles as the unit-length of the device increases.

The 3D rifled μ-mixer induces chaotic advection predominantly due to the 3D twisting motion of the fluid induced by the 3D rifling, apparent as the boundary layer remains highly twisted along the length of the microchannel and is more twisted at the outlet of the microchannel as the unit-length of the device increases. The 3D bulbous μ-mixer on the other hand induces chaotic advection more predominantly due to the converging-diverging fluid motion induced by the 3D undulating side-wall, evidenced by the higher concentration of green, yellow and red on fluid profiles at the same length along the microchannel as compared to those concentrations at the same positions along the length of the 3D rifled μ-mixer. Moreover, the predominance of the converging-diverging fluid velocities over the 3D rifling along the length of the 3D bulbous μ-mixer results in a boundary layer which exhibits less twisting, adopting a higher-frequency, lower-amplitude waveform-like appearance, as the unit-length of the device increases. The 3D bulbous μ-mixer as a result appears to demonstrate greater chaotic advective mixing per-unit length than the 3D rifled

μ-mixer. Finally, compared the control μ-channels, both μ-mixers exhibit significantly enhanced to the chaotic advective mixing, per-unit length.

2.4.2 Simulation Results, Mixing Index *versus* Reynolds Number

In order to quantitatively-analyze the entirety of the COMSOL theoretical simulation results, **Fig. 2.4a-e** present the theoretical results for mixing index *versus* Reynolds Number (from $0.01 \leq Re \leq \sim 50$) for the 3D rifled μ-mixer (*red*), 3D bulbous μ-mixer (*blue*) and control μ-channel (*green*) designs, on plots for devices of 1 unit, 2 unit, 3 unit, 4 unit & 5 unit-length, respectively. In these plots, the individual simulation results are shown as data points (*circles*) connected by dotted lines shown for visualization purposes only. The quantitative threshold mixing value used in this work to determine when the mixing index is *sufficient* to signify *practically complete* mixing is defined as 90%, which is a conventionally-established threshold used in various previously-demonstrated works featuring the development of μ-mixer device[167, 192, 197, 198]. **Fig. 2.4a-e** reflect this 90% mixing threshold value as a black horizontal dotted line.

Analyzing the quantitative trends in the simulated data between the three different designs, for example for the 1 unit-length models in **Fig. 2.4a**, a similar trend in mixing index magnitude is exhibited for all three designs. For each model, the rate of change in mixing index (approximated by the visual slope of the line connecting the data points) is roughly constant as the *Re* increases from $\sim$0.01 to $\sim$0.1. The reason for this behavior is that such low flow rates under these conditions ($Pé \approx 10^1$-10^2) permit the fluids to remain inside the devices long enough for diffusion-dominant mixing to generate a comparatively-high degree of mixing above 50%. Once the *Re* reaches $\sim$0.1 however, the degree of mixing remains nearly constant, due to the a limited amount of mixing inherent to the geometries of the microchannels and the fact that the flow rates are high enough to allow minimal time for diffusive mixing to occur between the fluids whilst flowing through the microchannel. Most interestingly, once the *Re* reaches $\sim$10, while the mixing index for the control μ-channel remains roughly constant (due to the continued dominance of limited diffusive mixing), the rates of change of the mixing index for the 3D rifled and 3D bulbous μ-mixers both increase, up to $Re \approx 50$. One likely explanation for this observed behavior is that the at these *Re*'s above the low *Re* regime, the effects of 3D chaotic advection induced by the specific 3D intra-channel microstructures of both μ-mixer designs become sufficiently-predominant over the effects of diffusion as to induce significantly-higher inter-fluidic species mixing and thus a higher mixing index, as compared to in the low *Re* regime. The most obvious difference between the performances of the three designs, however, is that the 3D bulbous μ-mixer achieves higher mixing indices, thereby improved mixing performance, than both the 3D rifled μ-mixer and the control μ-channel at all simulated *Re*'s, especially in the low *Re* regime ($\sim 0.1 \leq Re \leq \sim 1$) where mixing is the most challenging. The aforementioned trends are observed for all unit-length devices.

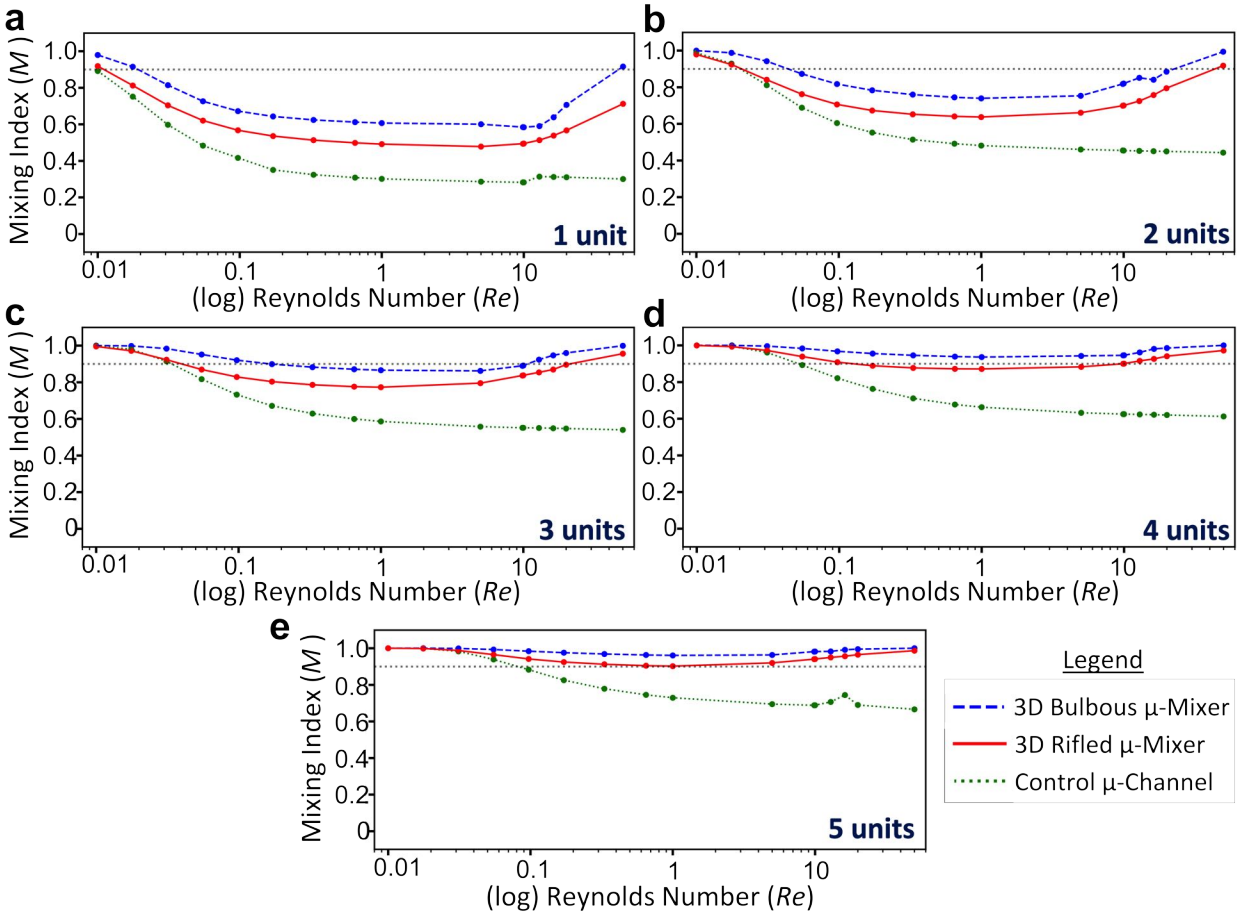

Figure 2.4: Theoretical COMSOL simulation results of Mixing Index *versus* Reynolds Number, $0.01 \leq Re \leq \sim 50$, for 3D rifled and 3D bulbous μ-mixers and control μ-channels. Individual simulated data points (*circles*) connected by dotted lines for **(a)** 1 unit, **(b)** 2 unit, **(c)** 3 unit, **(d)** 4 unit, **(e)** 5 unit-length devices. Established 90% mixing threshold shown as a *black* dotted line. Both 3D bulbous μ-mixer (*blue*) and 3D rifled μ-mixer (*red*) designs exhibit better mixing performances than those of the control μ-channel (*green*) at all *Re*, especially in the low *Re* regime, $\sim 0.1 \leq Re \leq \sim 1$, where mixing is the most challenging.

2.4.3 Simulation Results, Mixing Index *versus* Device Length

The theoretical simulation results can also be analyzed from an alternative perspective, by looking at mixing index *versus* device length for all unit-length 3D rifled μ-mixers and 3D bulbous μ-mixers as compared to the control μ-channels, as is presented in **Fig. 2.5a,b**. Furthermore, the percent increase of the mixing index demonstrated by both μ-mixer designs over the control μ-channel design for all unit-length devices are visualized in **Fig. 2.5c**. On these plots, the individual simulation data points are represented as *colored bars* and the 90% mixing threshold is shown as a *black* dotted line.

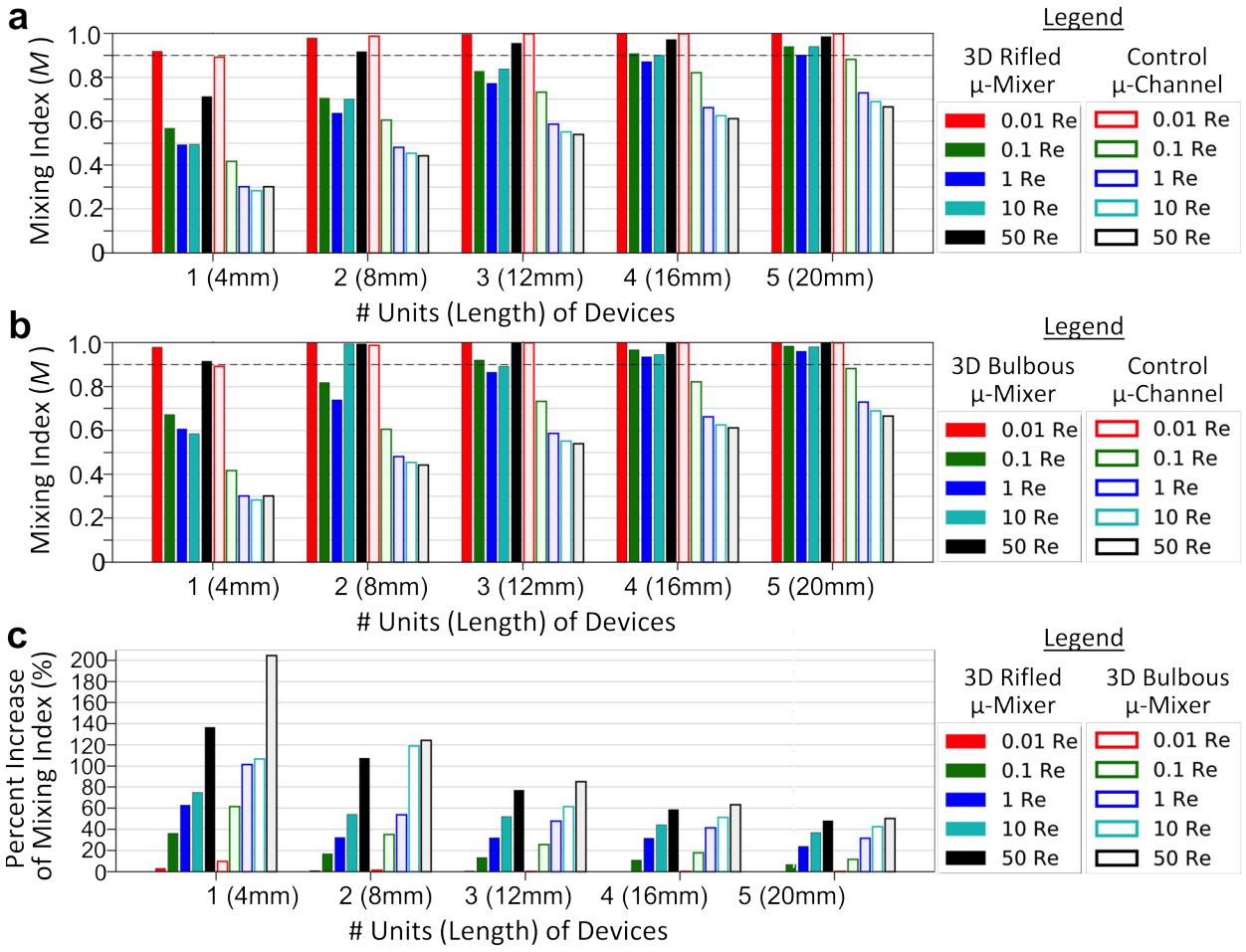

Figure 2.5: Theoretical COMSOL simulation results of Mixing Index *versus* Device Length for 1-5 unit-length 3D rifled and 3D bulbous μ-mixers, as well as percent increase of mixing index as compared to control μ-channels. Individual simulated data points represented as *colored bars*, 90% mixing threshold shown as a *black* dotted line. **(a)** Comparison between mixing index *versus* device length for the 3D rifled μ-mixers (*solid bars*) and control μ-channels (*solid outline bars*), likewise **(b)** for the 3D bulbous μ-mixers (*solid bars*) and control μ-channels (*solid outline bars*). Both plots demonstrate enhanced mixing performance of the μ-mixers and increasing mixing with device length. **(c)** Percent increase of mixing index between the 3D rifled μ-mixers and control μ-channels (*solid bars*), as well as 3D bulbous μ-mixers and control μ-channels *solid outline bars*). Percent increase in mixing index increases for all length devices with at higher *Re*'s, and remains higher for the 3D bulbous μ-mixers than for the 3D rifled μ-mixers.

As is illustrated in **Fig. 2.5a,b**, at the lowest simulated *Re* (*Re* = 0.01), all 1, 2, 3, 4 & 5 unit-length designs achieve 90% mixing. At the highest simulated *Re* (*Re* = 50), the 1, 2, 3, 4 & 5 unit-length 3D rifled and 3D bulbous μ-mixers all achieve 90% mixing (except in the instance of the 1 unit-long 3D rifled μ-mixer which only achieves $\sim$71% mixing). These *Re* values are too low and too high, respectively, to be of practical experimental use in the experimental characterization

studies to follow, and thus their relevance for any further study or comparison with the experimental prototypes is insignificant. The designs that first approach or surpass 90% mixing at all *Re*'s simulated are the 3 unit-length 3D bulbous μ-mixer and the 4 unit-length 3D rifled μ-mixer. At 5 unit-length, both μ-mixer designs surpass 90% mixing under all simulated *Re* conditions. The control μ-channel design, however, does not reach or surpass 90% mixing at any unit-length for any *Re* greater than $\sim$0.1. Therefore, both both μ-mixer designs exhibit superior theoretical performance over the control μ-channel design in the low *Re* regime of greatest interest.

Additionally, the trends illustrated in **Fig. 2.5c** reveal that in the low *Re* regime, the percent increases in mixing index for both 3D rifled and 3D bulbous μ-mixers over the control μ-channel increase with increasing *Re* for all length devices. This is the due to the fact that higher *Re*'s increase the predominance of the effects of 3D chaotic advection induced by the 3D intra-channel microstructures over the effects of diffusion, thereby increasing the degree of co-laminar mixing as compared to the control. At *Re* = 1 for example, the percent increase in mixing index is higher than 20% for both μ-mixers of all unit-lengths. The highest percent increase in mixing index in the low *Re* regime ($\sim 0.1 \leq Re \leq \sim 1$) is between $\sim$35% and 60% for the 1 unit-length 3D rifled μ-mixers and between $\sim$ 60% and 100% for the 1 unit-length 3D bulbous μ-mixers. As the unit-length of both devices increase, however, the overall magnitude of percent increase of mixing index decreases for each *Re*. This makes intuitive sense, as the mixing indices for the μ-mixers approach and seemingly converge at values above 90% mixing for the longer unit-length devices. Therefore once mixing above 90% is achieved by a given unit-length device at a certain *Re*, further increasing the unit-length will see roughly the same degree of resulting mixing, and therefore a smaller percent increase of mixing index.

2.4.4 Visualization of Experimental Results

In this project, the following designs were 3D printed on a single build plate following the protocols discussed in **Section 2.3.3**: one prototype each of 1 unit, 3 units and 5 unit-length 3D rifled μ-mixer, 3D bulbous μ-mixer and control μ-channel designs, a total 9 fabricated prototype devices. The fabricated prototypes were then post-processed according to the protocols discussed in **Section 2.3.3.2**. Images of post-processed prototypes for visualization purposes are shown in Appendix **Fig. 7.6**. All of the prototype devices were then integrated into the experimental setup as detailed in **Section 2.3.4** for experimental characterization using fluorescence imaging according to the protocols discussed in **Sections 2.3.5** and **2.3.5.2**. Example experimental fluorescence images are visualized in **Fig. 2.6**, as well as in Appendix **Fig. 7.8**. These images enable a qualitative analysis of the experimental performance of each of the prototypes. The images each feature a top-down view of the distribution of fluorescein (*green*) and rhodamine (*red*) solutions used as fluorescence tracers to enable visualization of the fluid and mixing dynamics inside each prototype device. Cross-sections of the 3D solids models are displayed along with select experimental images of 1 unit, 3 unit and 5 unit-length versions of all fabricated prototype devices at $Re \approx 0.6$.

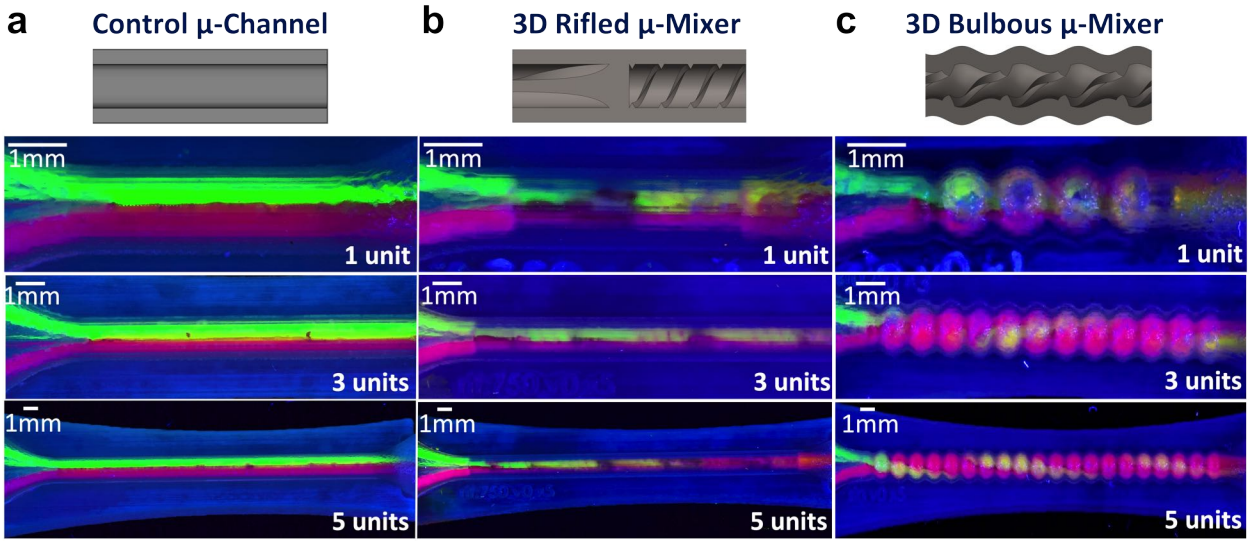

Figure 2.6: Experimental fluorescence image examples from the fluidic characterization of actual 3D printed prototypes using fluorescein (*green*) and rhodamine (*red*) solutions demonstrating co-laminar fluid mixing. 3D cross-section models (*top*) and experimental images (*below*) of 1 unit, 3 unit and 5 unit-length prototypes (at $Re \approx 0.6$). **(a)** Control μ-channel images, co-laminar flow is visible at all lengths. **(b)** 3D rifled μ-mixer images, split-and-recombination and rotation of fluids is clearly visible with increasing unit length devices, fluid mixing is most apparent in the 1 unit-length device, 3D rifling and 90 $^\circ$ twist microstructures are visible. **(c)** 3D bulbous μ-mixer images, fluid rotation, the effect of the 3D undulating rifling microstructures, is clearly visible with increasing unit length devices, fluid mixing is most apparent in the 1 unit-length device.

The images of the control μ-channel prototypes (**Fig. 2.6a**) reveal that the as-fabricated surface roughness is low enough and the inner-microchannel wall is smooth enough to maintain co-laminar flow of both fluids over the entire length of each device, even in the 25mm long, 5 unit-length prototype. Very little, if any, mixing between the two fluids is qualitatively observed.

Furthermore, images of the 3D rifled μ-mixers (**Fig. 2.6b**) show very different results, however. The image of the 1 unit-length 3D rifled μ-mixer shows the apparent effect of the split-and-recombination action of the 3D helical SaR microstructure (towards the left-hand side of the microchannel) indicated by the dark patch in the channel, followed by the effect of the 3D rifling microstructures as indicated by the blurring of the two distinct colors forming a region of fluid more yellow or orange in appearance (towards the right-hand side of the microchannel). This is an indication of the stretching, folding and rotation of the boundary layer, so clearly apparent in the images in **Fig. 2.6a** of the control μ-channel prototypes, inducing chaotic fluidic mixing. The images of the 3 unit and 5 unit-length 3D rifled μ-mixers show increased blurring of the two colors, and hence even greater degrees of fluidic mixing, farther down the length of each microchannel, culminating in a very monochrome orang, pink color at the outlet of the 5 unit-length 3D rifled

μ-mixer, indicative of a very high degree of mixing. Interestingly, the image of the 3 unit-length 3D rifled μ-mixer best visualizes the actual 3D printed 3D rifling structures, apparent as darker streaks (most predominantly visible in the fluorescein fluid towards the left-hand side and middle of the microchannel). See Appendix **Fig. 7.9** for an additional example experimental image which best enables the visualization of the actual fabricated 3D rifled microstructures inside the 3D rifled μ-mixer prototypes.

Finally, images of the 3D bulbous μ-mixers (**Fig. 2.6c**) show similar fluidic mixing as observed in the images of the 3D rifled μ-mixers. The 1 unit-length 3D bulbous μ-mixer image shows the definitive effect of the 3D rotation of the two fluids induced by the 3D rifling microstructures, as well as more blurring of the two colors as was seen in the images of the 3D rifled μ-mixers, which indicates the additional chaotic mixing enhancement due to the 3D undulating side-wall of the microchannel. The images of the 3 unit and 5 unit-length 3D bulbous μ-mixers more clearly show the induced 3D rotation of the two fluids, which is more pronounced than seen in the images of the 3D rifled μ-mixers. The color of the 3D rotated fluids, in these images becomes more blurred, monochrome orange-ish, pink-ish in color at the outlet of the 5 unit-length 3D rifled μ-mixer especially, indicative of a very high degree of chaotic mixing. The physical 3D undulating interior side-wall of the microchannels is very clearly observed in all of these images. Additionally, see Appendix **Fig. 7.9**), again, for a further example image which better enables the visualization of the actual fabricated 3D rifling microstructures inside the 3D bulbous μ-mixer prototypes.

The visualization of the morphologies of the actual fabricated 3D intra-channel microstructures is presented in Appendix **Fig. 7.37** with high-resolution 3D laser scans of cross-sections of the fabricated prototypes taken using scanning laser microscopy (*Keyence*, Osaka, Japan). Appendix **Fig. 7.5** shows images taken using scanning electron microscopy (Bio-Nanotechnology Center, UC Berkeley).

2.4.5 Experimental Results, Mixing Index *versus* Device Length

The image analysis procedure as described in **Section 2.3.5.2** was employed to generate the data presented in **Fig. 2.7**. Each experimental data point represents the average of three separate RMI values calculated for the experimental images for each steady state fluid flow condition in each prototype device, following the quantitative processing as described in **Section 2.3.5.2**. The error bars denote the standard deviation of each individual RMI calculation from the mean. Additionally, colored lines are shown interconnecting the data points for visualization purposes and do not represent and any predictive trend in the experimental data. **Fig. 2.7a-c** illustrate the mixing index as calculated for 3D rifled μ-mixer, 3D bulbous μ-mixer and control μ-channel prototype devices, respectively, *versus* device length, for 1 unit, 3 unit & 5 unit-length μ-mixer and channel structures. Each data set and line represents the mixing index at a given *Re* condition in different length devices, for $Re \approx 0.1$, 0.3, 0.6 & 10.

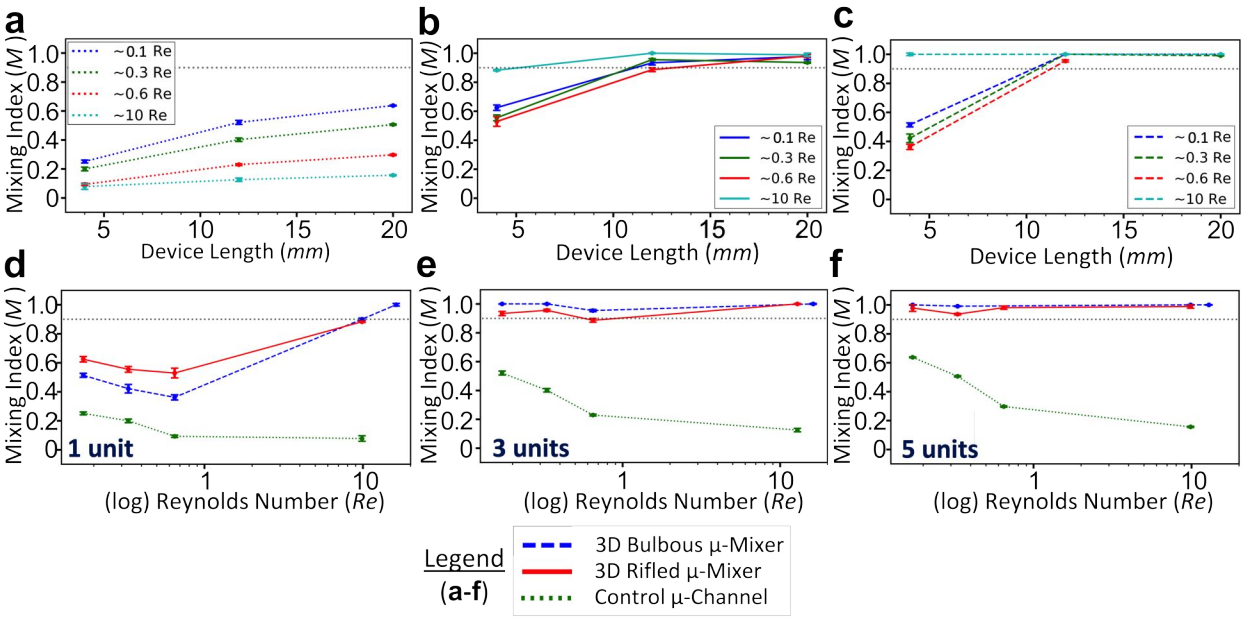

Figure 2.7: Experimental results for Mixing Index *versus* both Device Length and Reynolds Number, from fluorescence image analysis of actual 3D printed prototypes. Individual data points (*circles*) connected by lines represent the average of three RMI measurements performed for each experiment (error bars denote standard deviation of these measurements), and the established 90% mixing threshold shown as a *black* dotted line. Mixing Index *versus* Device Length for 1-5 unit-length **(a)** control μ-channels, **(b)** 3D rifled μ-mixers and **(c)** 3D bulbous μ-mixers for various *Re*'s (*different colored data points and lines*). Mixing Index *versus* Reynolds Number for **(d)** 1 unit, **(e)** 3 unit & **(f)** 5 unit-length 3D rifled μ-mixer (*red*), 3D bulbous μ-mixer (*blue*) and control μ-channel (*green*) prototypes. Both the 3D rifled and 3D bulbous μ-mixer prototypes demonstrate enhanced mixing performance *versus* the control μ-channel throughout, achieving the 90% mixing threshold for all *Re*'s tested at 3 unit-lengths and longer, whilst none of the control μ-channel prototypes of any length achieve 90% mixing for any of the *Re*'s tested.

2.4.5.1 Control μ-Channel Prototype

For the control μ-channel (**Fig. 2.7a**), increasing *Re*'s result in lower mixing quality at the outlet of the device. Since mixing is purely diffusion-dominant for all of the *Re*'s in the smooth-walled μ-channel, higher flow rates result in shorter residence times inside the μ-channel and therefore less time for diffusion to occur, resulting in less mixing. Furthermore, the degree of mixing slightly increases with increasing μ-channel lengths, since for the same *Re* and flow rate, the additional length increases residence time, resulting in greater mixing. This trend is reflected for all *Re*'s tested, and is the most significant at the lowest *Re* tested, $Re = \approx 0.1$ since this conditions gives the two co-laminar fluids the longest residence time for mixing (slowest flow rate in the longest μ-channel).

2.4.5.2 3D Rifled μ-Mixer Prototype

The 3D rifled μ-mixers (**Fig. 2.7b**) consistently demonstrate higher mixing indices than the control μ-channels of the same length at the same *Re*'s, with the 1 unit-length 3D rifled μ-mixer at the low *Re* conditions tested ($Re \approx 0.1$ to 0.6) producing roughly the same mixing quality as the 5 unit-length control μ-channel in roughly the same low *Re* regime. The 3D rifled μ-mixer prototype therefore demonstrates a similar quality of mixing ($\sim$ 52%-62%) as the control μ-channel in a more compact device, roughly 5x shorter length. Furthermore, the 3 unit-length prototype approaches (within $\sim$2.4%) or surpasses the 90% mixing threshold for all *Re*'s tested. Finally, the 5 unit-length prototype exhibits nearly the same range of mixing indices, all above 90%, as the 3 unit-length prototype. As a result, the 3 unit-length design would be the minimum-length device of this design necessary to generate *sufficiently complete* mixing (as relative to the 90% mixing threshold) of two co-laminar fluids at under any operational *Re* conditions from $Re \approx 0.1$ to 10.

2.4.5.3 3D Bulbous μ-Mixer Prototype

The 3D bulbous μ-mixer prototypes of each unit-length (**Fig. 2.7c**) exhibit similar mixing index enhancement *versus* the control μ-channel prototypes of the same length at the same *Re*'s as the 3D rifled μ-mixer prototypes. The 1 unit-length 3D bulbous μ-mixer produces slightly lower quality of mixing ($\sim$ 36%-51%) than the 1 unit-length 3D rifled μ-mixer ($\sim$52%-62%) in the low *Re* regime, albeit still greater than the 1 unit-length control μ-channel in the same regime ($\sim$9%-25%). Both the 3 and 5 unit-length prototypes, however, do surpass the 90% mixing threshold for all *Re*'s tested. The 3 unit-length 3D bulbous μ-mixer design would be the minimum length of this specific design required to achieve complete mixing between $Re \approx 0.1$ & 10.

2.4.6 Experimental Results, Mixing Index *versus* Reynolds Number

For an alternative, and perhaps more intuitive, visualization of the experimental data, the mixing index data for 3D rifled μ-mixer (*red*), 3D bulbous μ-mixer (*blue*) and control μ-channel (*green*) prototype devices *versus* Reynolds Number are shown in **Fig. 2.7d-f**, plotted for 1 unit, 3 unit & 5 unit-length devices, respectively.

2.4.6.1 1 Unit-length Prototypes

The data for all 1 unit-length prototype devices (**Fig. 2.7d**) reflect the aforementioned trend that the 3D rifled μ-mixer produces greater mixing quality than the 3D bulbous μ-mixer and control

μ-channel do in the low *Re* regime conditions tested (again, *Re* $\approx$ 0.1, 0.3 & 0.6). However as is more apparent viewing the 1 unit-length device data in this manner, both prototype μ-mixers, exhibit the same trend as with the control μ-channel of decreasing mixing index magnitude with increasing flow rate for *Re* $\approx$ 0.1, 0.3 & 0.6; yet at *Re* $\approx$ 10, the mixing index considerably increases to $\sim$0.9. This is likely an indication of the 3D 90 $^\circ$ split-and-recombination and axial rotation microstructures in the 3D rifled μ-mixer and the 3D undulation and axial rotation microstructures in the 3D bulbous μ-mixer generating a sufficiently amount of chaotic advection as to contribute predominantly to inter-fluidic species mixing dynamics and hence produce a higher mixing index, as compared to those at lower *Re*'s. (Both 3D rifled and 3D bulbous μ-mixers each exhibit a $\sim$67% and $\sim$148% *increase* in mixing index, respectively, as compared to the $\sim$16% *decrease* in mixing index exhibited by the control μ-channel, from *Re* $\approx$ 0.6 to 10). This eludes to the fact that likely at some *Re* between $\sim$0.6 and $\sim$10 (possibly around a transitionary *Re* between the low, *Re* $\approx$ 1, and moderately-low, *Re* $\approx$10, regimes) there exists a fluidic state at which the effect of 3D chaotic advection due to the geometry of the fabricated 3D intra-channel microstructures of both μ-mixer designs becomes sufficiently dominant over the effect of diffusion as to significantly enhance the mixing enhancement to such a degree. Finally, out of all of the fludic conditions experimentally created in this work, complete mixing is the most difficult to achieve for the 1 unit-length prototypes at *Re* $\approx$ 0.1. Under these conditions, the 3D rifled μ-mixer demonstrates the best mixing index ($\sim$62.5%), surpassing that of the 3D bulbous μ-mixer ($\sim$51.4%) and control μ-channel ($\sim$25.1%).

2.4.6.2 3 Unit-length Prototypes

The data for the 3 unit-length prototypes (**Fig. 2.7e**) demonstrate that throughout the range of *Re*'s tested, all prototypes show roughly the same trend in mixing quality for increasing *Re*'s as was exhibited by the 1 unit-length prototypes, albeit the differences in mixing index are all very small. At nearly all *Re*'s tested, the 3D rifled and 3D bulbous μ-mixer prototypes both generate above 90% mixing (the only exception is for the 3D rifled μ-mixer which generated $\approx$ 88.6% mixing), whilst the control μ-channel prototypes remain well below the 90% mixing threshold for all *Re*'s, exhibiting a maximum of $\sim$52% mixing at *Re* $\approx$ 0.1. Furthermore, seeing as both μ-mixers achieve over 90% mixing at the lowest *Re* tested, *Re* $\approx$ 0.1, a shorter critical length (*e.g.* 2 unit-length) μ-mixer would conceptually produce 90% mixing at some intermediate *Re* value.

2.4.6.3 5 Unit-length Prototypes

This pattern is similarly reflected in the data for the 5 unit-length devices (**Fig. 2.7f**). The control μ-channel prototype exhibits the same decreasing trend in mixing index with increasing *Re*, and demonstrates an overall experimental maximum mixing index magnitude at *Re* $\approx$ 0.1 of $\sim$63.7%

mixing. The mixing indices for both 3D rifled and 3D bulbous μ-mixer prototypes on the other hand remain above 90% mixing and exhibit less variation in mixing quality for all *Re*'s tested.

2.4.7 Experimental and Simulation Results Compared

The experimental and simulation results for all devices over the range of *Re*'s experimentally tested ($\sim 0.01 \leq Re \leq \sim 10$) are compared in **Fig. 2.8a-c**. For all *Re* tested, the control μ-channel prototypes of each unit-length generate lower mixing indices than those theoretically predicted by the simulation; the magnitude of experimental mixing quality is a minimum of 28.3% (1 unit-length, $Re \approx 0.1$) and a maximum of $\sim$76.5% (5 unit-length, $Re \approx 10$) smaller than the simulated mixing quality. Both experimental and simulated data for each unit-length device follow the same trend of decreasing mixing quality with increasing *Re*, however. As shown in **Fig. 2.8a**, the 1 unit-length 3D rifled μ-mixer prototype performs slightly better than is predicted, whilst the 1 unit-length 3D bulbous μ-mixer prototype performs slightly worse than is predicted. At $Re \approx 10$, however, both 1 unit-length 3D μ-mixer prototypes perform significantly (average of $\sim$59.7%) better than simulated. **Figs. 2.8b,c** demonstrate a consistent trend for the 3 unit and 5 unit-length prototypes, respectively, that both 3D μ-mixers perform better (average of $\sim$17.1% for the 3 unit-length prototypes and $\sim$5.1% for the 5 unit-length prototypes) than those from simulated results.

The discrepancy between the experimental and simulated mixing results demonstrated in this work suggests that there might be potential room for optimization of certain experimental and simulation parameters in order to refine future mixing quality analysis of 3D μ-mixer prototype devices. Regarding the theoretical simulation parameters used in this study, the 3D models imported and analyzed by the simulation feature smooth surfaces and geometrically-well defined microstructures. It can be reasonably surmised, however, that due to the presence of surface roughness and the limits to dimensional accuracy and feature resolution of Multijet 3D printing (see a more detailed argument for the importance of these factors in **Section 3.3.5**), the discrepancy of the actual fabricated morphology of the 3D microstructures and prototype from the 3D model is not insignificant. A likely consequence is that actual fabricated geometries possess a more random morphology than is designed in the 3D solids model, as suggested by the laser scanning microscopy images of actual 3D printed prototype cross-sections shown in Appendix **Fig. 7.37**. As a result, the degree of chaotic mixing induced at higher *Re*'s ($Re \approx 10$) might be more significant than anticipated, resulting in even greater mixing in the fabricated prototypes than those of the theoretical simulations. Such a behavior likely explains the increased mixing efficiency of both 1 unit-length 3D μ-mixer prototypes at $Re = \approx 10$. At the present time, the standard theoretical modeling approach, using COMSOL for example, does not take into account any geometrical abnormalities or surface roughness accurately replicating the as-fabricated morphology of 3D printed prototypes [52, 132, 166, 199]. One reason is that the randomness of as-fabricated 3D printed structures is very hard to model or even predict. One potential approach to address this problem would be to take high-resolution laser scans of fabricated intra-channel 3D microstructures, using for example the

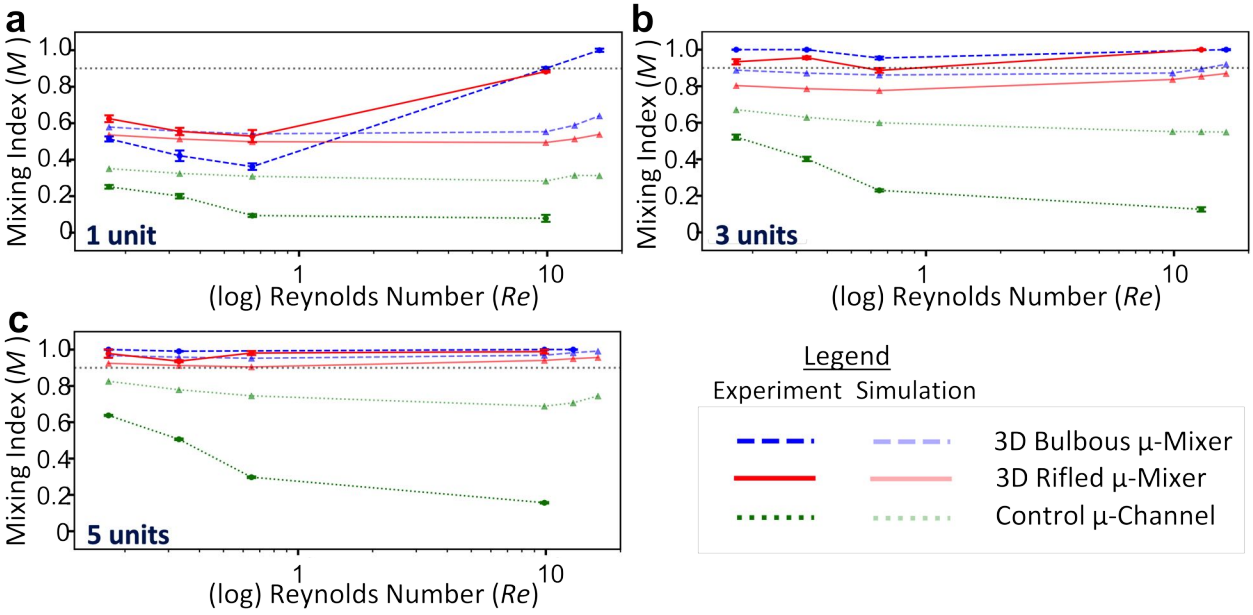

Figure 2.8: Comparison between experimental and simulation results for Mixing Index *versus* Reynolds Number, for $\sim 0.01 \leq Re \leq \sim 50$. Individual data points connected by lines represent the average RMI calculation for a given experiment (error bars denote standard deviation from the mean), and the established 90% mixing threshold shown as a *black* dotted line. Experimental (*opaque*) and simulation (*semi-transparent*) data for the 3D rifled μ-mixers (*red*), 3D bulbous μ-mixers (*blue*) and control μ-channels (*green*).
(a) 1 unit, **(b)** 3 unit and **(c)** 5 unit-length devices shown.

equipment employed in this work to capture the aforementioned prototype cross-section images, then use this data to build a 3D solids model (*i.e.* in Solidworks) to more accurately represent the as-fabricated surfaces and structural elements of actual 3D printed prototypes. This new solids model could then be used to perform (*i.e.* in COMSOL) more accurate theoretical studies of the performance of 3D printed device designs.

From the experimental data collection and quantitative processing perspective, the physical morphology of most 3D printed prototypes is distinct from most conventional planar microfluidic systems, upon which the experimental analysis protocol demonstrated in this work was based. For example, most microchannels as observed from above are rectangular, and fluorescence imaging generally captures fluids a relatively-2D plane at the top of the microchannel. Additionally, conventional mixing image analysis is performed using smooth (surface roughness as low as $\sim$1's nm [200]), optically-transparent (*i.e.* PDMS) materials, minimizing light diffraction and scattering. Factors affecting light transmittance through material include surface roughness ($\sim$10's μm), the transmissivity of the material itself, and physical surface morphology (100's μm) [134]. The fabricated prototypes demonstrated in this work feature 3D curvature in the top surface of the circular 3D printed microchannel through which the enclosed fluids are image, potential inducing non-normal light diffraction or scattering, and the surface roughness of the 3D printed material is roughly on the order of an average of 20-30 μm [185]. Furthermore, the fluorescence emission peaks of fluorescein and rhodamine are 512 nm and 625 nm, respectively, and the thickness of the thin-walled microchannel top surface is $\sim$250 μm. Conveniently, the bulk optical transmittance of the Visijet M3 crystal material, the material used throughout this work, has been experimentally determined as $\sim$0.33 for 512nm and $\sim$0.35 for 625nm through a section of $\sim$250 μm thick material [126], which is relatively low compared to the high $\sim$0.98 transmittance of PDMS [201]. Therefore increasing transmissivity of light in the setup (despite the fact that the quantitative processing procedure employed in this work does normalize the fluorescence intensity in the mixed region to the initial intensity in the unmixed region), whether by decreasing the microchannel wall thickness, smoothing out the surface to reduce surface roughness or imaging fluids though an optically-transparent material section of the experimental setup [202] (*e.g.* through the device outlet tubing), would be of benefit. An alternative image capture procedure that has been previously employed for microfluidic fluorescence image capture is confocal scanning microscopy [178], which can capture images of the distribution of experimental fluorescent fluids on planes perpendicular to the path length axis of the microchannel. This approach would offer significant benefits for the visualization of truly 3D distributions of fluids on these planes, as illustrated in **Fig. 2.2**. Two significant requirements of this imaging method are for the microchannel construct for imaging to be made from a material with a very high optical transparency and very low surface roughness and to have a thickness (between the exposed upper surface of the microfluidic body and the upper surface of the microchannel) of no more than 100 μm [192]. For the reasons discussed here, the 3D printed constructs and material featured in this work would be incompatible with this analytical imaging method.

2.4.8 Results Compared with Conventional Micro-mixing Approaches

Considering the experimental mixing performance of the fabricated 3D rifled and 3D bulbous μ-mixer prototypes in the context of other previously demonstrated conventional μ-mixing approaches serves as an interesting topic of discussion. As mentioned in **Section 2.1**, mixing effi-

ciency is usually defined as mixing quality achieved relative to the microchannel or μ-mixer device length (*i.e.* higher mixing efficiencies are defined for the same degree of mixing and *Re* conditions in the most compact the μ-mixer or shortest microchannel). For example, the experimental results in this work demonstrated a higher mixing efficiency for the 3 unit-length μ-mixer prototypes at all *Re*'s than the 5 unit-length μ-mixer prototypes (all over $\sim$90% mixing achieved).

An additional approach has also been used in recent μ-mixer development studies to analyze mixing efficiency relative to the unit-less parameter *z'/Pé*, which is defined according to Eq. 2.16,

$$\frac{z'}{Pe} = (\frac{z}{L_c}) * (\frac{D}{\mu L_c}) = \frac{\frac{z}{\mu}}{L_c^2 D} = \frac{t_{flow}}{t_{diffusion}} \tag{2.16}$$

Here, the z' parameter is used to normalize the path length of the microchannel (from the inlet to the outlet),z, by the characteristic length of the microchannel, L_c. Thus, various microfluidic platforms with different characteristic lengths (*i.e.* conventional 2D microfluidic channels manufactured *via* planar fabrication methods, $L_c \approx 100$ μm, and 3D μ-mixers fabricated *via* additive manufacturing, $L_c \approx 1$ mm) can be directly compared. Additionally, by normalizing z' by the Péclet Number (*Pe*), the mixing performance demonstrated by the aforementioned devices at various fluidic conditions can all be compared directly, on one plot. Furthermore as shown in Eq. 2.16, the z'/Pé parameter also represents the ratio of the time required for fluid to flow along the path length of the microchannel (from inlet to outlet) to the time required for complete intra-fluid species mixing to occur solely *via* diffusion in the transverse direction [159]. Since diffusion time is much longer than most operational fluid flow rates, the magnitude of the z'/Pé parameter for most work is $\leq \sim$1.

Fig. 2.9 compares the experimental mixing performance demonstrated by both 3D rifled and 3D bulbous μ-mixer prototypes in this work to the experimental mixing performances achieved by various previously-demonstrated examples of 2D and 3D μ-mixers, fundamental in the field of microfluidic mixing. This comparison is visualized in the low *Re* regime ($\sim 0.01 \leq Re \leq \sim 2$) and in the moderate-low *Re* regime ($\sim 5 \leq Re \leq \sim 20$) in **Fig. 2.9a** and **Fig. 2.9b**, respectively, in terms of experimental mixing index relative to the z'/Pé parameter. To create both of these plots, the experimental data for the 3D rifled and 3D bulbous μ-mixer prototypes first presented in **Fig. 2.7** are used, and experimental mixing index data, characteristic length, path length and fluid flow parameters from each of the various previously-demonstrated μ-mixer publications are extracted, and the z'/Pé value for each set of experimental data is manually calculated. For comparison, data from examples of fundamental conventional PDMS-based 2D μ-mixer approaches (Bhagat 2007 [18], Fang 2009 [164], Lim 2011 [203], Ou 2007 [177], Park 2004 [178], Stroock 2002 [167]), as well as additive manufacturing-based 2D μ-mixer and 3D μ-mixer approaches (Therriault 2003 [93]), are presented. In general, complete mixing is harder to achieve at lower z'/Pé values (higher *Pe*'s, shorter z, larger L_c). Microfluidic devices fabricated *via* MEMS-based processes have typ-

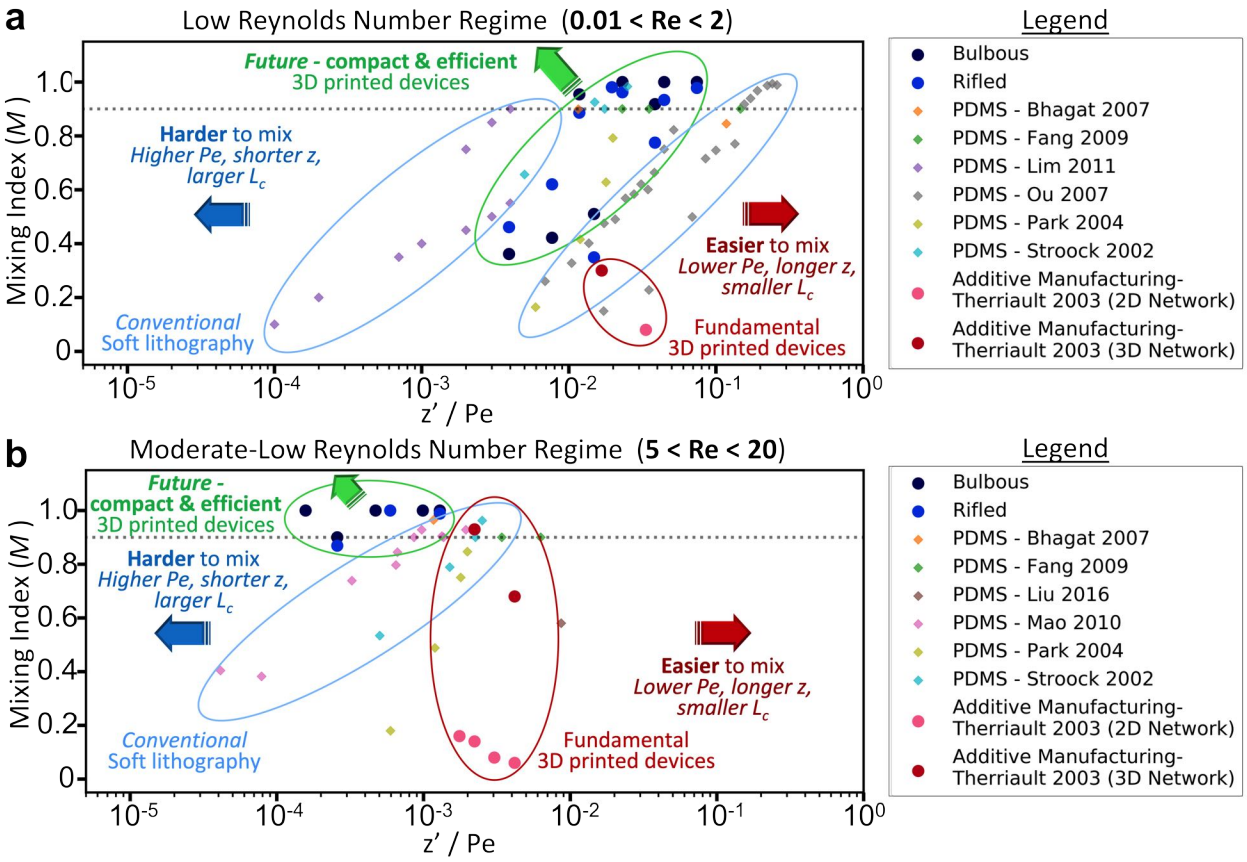

Figure 2.9: Comparison between the experimental mixing results demonstrated in this work and conventional μ-mixing approaches, in both **(a)** the low *Re* ($\sim$0.01 $\leq$ *Re* $\leq$ $\sim$2) regime and **(b)** the moderate-low *Re* ($\sim$5 $\leq$ *Re* $\leq$ $\sim$20) regime. Mixing Index *versus* the *z'/Pé* metric. In general, co-laminar fluidic mixing is harder to achieve at lower z'/Pé values (higher *Pe*'s, shorter path length, larger characteristic length), as indicated by *blue arrows*. Conversely, mixing is easier at higher z'/Pé values (lower *Pe*'s, longer path length, smaller characteristic length), as indicated by *red arrows*. The performance of future high mixing efficiency 3D printed μ-mixer devices is indicated by *green arrows*. The 3D rifled and bulbous μ-mixer prototype devices in this work (*blue circle data points*) feature better mixing performances than various examples of conventional microfluidic prototypes fabricated *via* soft-lithography (*diamond data points*) and fundamental microfluidic prototypes fabricated *via* additive manufacturing (*red circle data points*) at lower *z'/Pé* values. Data from each class of microfluidic device are roughly illustrated by colored circles on each plot.

ically have very small L_c values ($L_c \leq 100$ μm), but require long z values ($\sim$ cm's) in order to achieve complete mixing and at higher z'/Pé values [159]. In the low *Re* regime (**Fig. 2.9a**), the experimental mixing quality demonstrated by the 3D rifled μ-mixer and 3D bulbous μ-mixer prototypes approach or surpass 90% mixing more efficiently than conventional soft-lithography-based μ-mixer devices [18, 164, 177, 178] at higher z'/Pé values, as well as more frequently than examples [167, 203] at lower z'/Pé values. Furthermore, compared to those results demonstrated by both

2D and 3D μ-mixer devices manufactured *via* additive manufacturing [93], the results in this work produce significantly higher mixing efficiencies at comparative z'/Pé values. In the moderate-low *Re* regime (**Fig. 2.9b**), the performance of the 3D printed μ-mixer prototypes in this work proves to be even more efficient than the highlighted conventional soft-lithography-based μ-mixer device examples [18, 164, 167, 178, 179, 204] at comparable or slightly higher z'/Pé values, as well as more definitively more efficient than the example 2D and 3D μ-mixer devices manufactured *via* additive manufacturing [93] at higher z'/Pé values, by surpassing 90% mixing at most data points.

Finally, in light of the current trends in the improvement of 3D printing technology (*e.g.* improvement in ultimate resolution and the ability to fabricate larger-scale devices with intricate sub-millimeter structures with increased speed) [49], the projected performance of future compact and high mixing efficiency 3D printed μ-mixer devices relative to their z'/Pé value can be roughly described as indicated by the green arrows in **Fig. 2.9a,b**, starting from the basis of the experimental 3D printed intra-channel μ-mixer prototype performances demonstrated in this work.

Since mixing is diffusion-dominant in conventional planar microfluidic channels (*e.g.* PDMS-based devices *via* soft-lithography), typical characteristic length scales $\approx$100 μm require often impractically-long path lengths on the order of $\sim$cm's to achieve complete mixing [167]; therefore, the aspect ratio between the path length required for complete mixing and the characteristic length ($z_{diff} : L_c$) is typically $\sim$100:1. The 3D rifled μ-mixer prototypes experimentally demonstrated in this work, however, achieve or surpass 90% mixing at all *Re* tested ($0.1 \leq Re \leq \sim 10$), especially in the low *Re* regime ($Re \leq \sim 1$) at 3 unit-lengths (12mm), therefore demonstrate a $\frac{z}{L_c}$ aspect ratio of only $\sim$16:1, a six-fold improvement. Hence, the 3D printed prototypes demonstrate an overall $\sim$84% improvement in aspect ratio, which can also be considered as an $\sim$84% enhancement in the compactness of the microfluidic system, required for complete low *Re* mixing. Furthermore, the compactness of the 3D μ-mixer prototypes experimentally demonstrated in this work in **Fig. 2.9** shows that the 1 unit-length 3D rifled μ-mixer prototypes (4mm long) exhibited 90% mixing at $Re \approx 10$, resulting in a $\frac{z}{L_c}$ aspect ratio of only $\sim$5.3:1; whereas at the same *Re*, fundamental conventional 2D PDMS-based μ-mixer prototypes demonstrate a minimum aspect ratio of 10:1 [20, 167] and fundamental 3D additive manufacturing-fabricated μ-mixer prototypes demonstrate a minimum aspect ratio of $\sim$80:1 [93]. The 3D printed prototypes demonstrated in this work therefore achieve an overall $\sim$47% enhancement in compactness over conventional 2D PDMS-based microfluidic examples and $\sim$93.4% enhancement in compactness over 3D additive manufacturing-fabricated microfluidic examples.

Chapter 3

Microfluidic Concentration Gradient Generators for Antimicrobial Drug Screening

3.1 Introduction

Antimicrobial resistance (AMR) is one of the most critical global health concerns today. Prolonged hospitalizations due to AMR-related infections caused by a multitude of pathogens places a significant economic burden on worldwide healthcare costs, estimated at upwards of $35 billion per year in the United States alone, and since the late 2010's has been the cause of death of over 700,000 people each year worldwide, a number which projected to surpass 10 million people by the year 2050 [205]. AMR is most often applicable in the context of bacterial antibiotic resistance, as the US Centers for Disease Control and Prevention has identified more than 18 distinct (*super-bug*) bacterial strains which have developed resistance to at least one of the developed-world's essential antibiotic agents used as the first-line-of-defense in treating AMR infections, posing degrees of risks to human health from *concerning* to *urgent* [206].

Antibiotics are chemotherapeutic compounds which are used to treat bacterial infections by inhibiting the growth and replication of pathogenic bacteria, thereby helping the immune system to kill off the remaining bacterial population and fight the infection within the body [207]. The specific mechanisms behind the inhibition of bacterial growth are not perfectly well understood for every antibiotic compound. however with most antibiotics, it is generally-accepted that a single bacterium will metabolically processes an antibiotic molecule, reducing it into a series of intermediate molecules, one or some of which will bind to its DNA and proteins responsible for cell division, inhibiting the bacterium's cell division [208, 209]. Bacterial strains do develop antibiotic-resistant bio-physiological pathways through natural selection and genetic mutations, which has been attributed to multiple human-induced factors including the extensive over-prescription of broad-spectrum antibiotics in medicine and in the industrial agriculture industry, patient non-compliance with prescribed antibiotic regimens and a general lack of robust antibiotic stewardship programs in developing nations, in particular [210]. As a result, the efficacy of many

clinically-relevant antibiotics is significantly diminished worldwide towards treatment of many different antibiotic-resistant bacterial infections. Despite this rise in antibiotic-resistance, development of new antibiotic compounds has been practically stalled entirely in developed nations, as only two new classes of antibiotics have been developed and introduced in the past three decades, which are themselves only moderately-effective in treating most bacterial infections [211]. The rate of new antibiotic development and significant advances in the management and prevention of infectious diseases was at an all-time high by the middle of the 20th century; however, the late 20th century witnessed drastic decline in interest on part of the pharmaceutical industry in the development of new classes antibiotics. One contributing factor to this decline is that in order to bring a single new antibiotic compound to market today, pharmaceutical companies must invest on average $\sim$\$800 million in research and development, a process which takes at least $\sim$10 years on average, and which demonstrates a considerably lower rate of return in terms of profit as compared to developing novel drugs targeting chronic diseases. [212]

3.1.1 Antimicrobial Susceptibility Testing (AST)

One of the primary clinical methods employed in order to tackle AMR-related bacterial infections in the biomedical community today is Antimicrobial/Antibiotic Susceptibility Testing (AST), which encompasses a variety of different clinical approaches through which the susceptibility of a given antimicrobial-resistant organism to pre-existing antibiotics are determined. Different AST methods are often employed in order to determine the most effective dosage of a single antibiotic, or in order to find novel combinations of existing antibiotics which can be used to combat pre-existing and emerging AMR-related infections. Modern clinical settings have therefore become heavily-reliant on AST methods, performed on isolated patient bodily fluid samples or laboratory-standard cultured bacterial strains, in order to deliver fast and reliable determinations of antibiotic resistance and the efficacy of different antibiotic dosages and combinations as to best recommend the most optimal course of treatment for the infection. [213, 214]

In practice, different strains of bacteria evolve varying degrees of sensitivity to certain concentrations of antibiotic compounds at different rates; thus, the nature of clinical AST is such that whenever a definitive evaluation of antibiotic sensitivity is desired, the most medically-rigorous course of action is to perform AST *on-site* in the clinical setting on a sample of that particular bacteria using specific antibiotics available at hand (*i.e.* a patient is admitted to a hospital with symptoms of a suspected type of infection, a bodily fluid sample is collected, and the healthcare professional would like to confirm the appropriate dose of the most effective antibiotic before administering the treatment, taking caution not to inadvertently prescribe an ineffective treatment or prolong patient hospitalization). This course of action is particularly commonplace in the example of the treatment of urinary tract infections (UTI's), which are a healthcare concern worldwide and can lead to serious health complications if not treated effectively with antibiotics. UTI's in humans are caused by strains of bacteria such as *Escherichia coli* (*E. coli*), *Escherichia faecalis*

(*E. faecalis*), *Klebsiella pneumoniae* (*K. pneumoniae*),*Staphylococcus aureus* (*S. aureus*) and *Proteus mirabilis* which demonstrate varying degrees of sensitivity to most commonly-administered antibiotics. In suspected cases of UTI outbreaks, especially in low resource areas, clinical AST evaluation is routinely performed on urine samples in order to identify the particular strain of bacteria by its sensitivity profiles to single antibiotics and to determine the most effective dose of each antibiotic which could be used to treat the infection. In these AST methods, the degree of sensitivity to individual antibiotics, as indicated by the inhibition of bacterial proliferation in a cultured sample in the presence of different concentrations of the given antibiotic, is typically separated into three categories: *Resistant*, *Intermediate Resistance* and *Sensitive*. For example, a recent study by Sabir et al. [215] revealed that out of 500 clinical samples taken from patients with suspected cases of UTI's in a developing nation (performed using the disk diffusion method), *E. coli* was the most prevalent bacteria identified and demonstrated the highest resistance to penicillin (100% of samples tested) and amoxicillin (100%), an intermediate resistance to tetracycline (69.4%), doxycycline (66.6%) and ciprofloxacin (54.2%), and high sensitivity to treptomycin (30%), kanamycin (19.9%) and amikacin (12.7%). Therefore, UTI treatment in this instance with kanamycin or amikacin, which are both of the same family [216], would be the only advisable treatment. Moreover, since $\sim$81% of the samples tested in this study were resistant to multiple classes of antibiotics, this study recommends testing combinations of multiple antibiotics to find the most optimal treatment. However as this study discusses, the *E. coli* antibiotic sensitivity profile demonstrated in this instance is different from those evaluated for *E. coli* in other parts of the world (*e.g.* UTI's in the developing world can be treated with penicillin and amoxicillin, as those antibiotics are not as heavily-prescribed in those regions than they are in developing nations). Therefore, this study demonstrates the need for consistent region-specific AST evaluations on a case-by-case (more practically outbreak-by-outbreak) basis in clinical settings; thus, the frequency of AST and the need for higher throughput analysis is critically needed. [215, 217]

Conventional AST methods generally involve measuring the growth of bacteria, either in the form of solid films or in solution in liquid culture media, when incubated under the optimal growth conditions in the presence of different antibiotic compounds. For example, one standard clinical AST approach using solid bacteria culture is the *Kirby-Bauer* or *disk diffusion* method [218], which involves plating a bacteria culture onto the surface of an agar (solid growth media) plate and then selectively-placing disks of solid antibiotics onto the surface. Upon incubation, the antibiotic diffuses outwards into the agar and bacteria solution and the growth of the bacteria on the surface is inhibited within an *inhibition zone*. The size of this zone is then physically-measured (units of mm) after at least $\sim$24 hours. Comparing zone sizes for disks of different concentrations of the same antibiotic (typically in units of μg), a given strain of bacteria is usually reported as being susceptible, intermediate, or resistant to a certain concentration of that antibiotic. Alternatively, comparing zone sizes for disks of the different antibiotic types, comparable degrees of susceptibility for a given strain of bacteria can be determined for different antibiotics. The other standard clinical AST method used is the *broth dilution* method [219, 220], which involves a series of manual-labor intensive fluid handling procedures involving the culture of bacteria in liquid media, but which usually requires less incubation time than using solid growth media. This method

involves creating an overnight bacterial inoculation in growth media, diluting the concentration to a known bacterial density (typically in units of cell forming units per milliliter of solution, cfu/μL), then incubating the culture in the presence of various concentrations of liquid antibiotic solution (typically in units of μg/L) for up to $\sim$24 hours. Then, detection and quantification of bacterial density growth, and inhibition thereof, in different doses and combinations of antibiotic solutions can then be performed qualitatively (*i.e.* looking for increasing *cloudiness*, indicating an increase in bacterial density) or quantitatively using a variety of analytical methods, most often by measuring turbidity (*i.e.* optical transmissivity) of the solution using spectrophotmetry. [221]

3.1.1.1 Minimum Inhibitory Concentration (MIC) Metric

The clinical *gold standard* AST metric used to determine the susceptibility of a given bacterial strain to a specific antibiotic compound is the *minimum inhibitory concentration* (MIC) value, which is defined as the lowest dose of the antibiotic that is required to inhibit the visible proliferation of a bacteria samples overnight ($\sim$16-24 hours) and is typically reported as a concentration in units of mg/L [208, 222]. As **Fig. 3.1a** illustrates, determination of the MIC value is typically performed using the broth dilution method, whereby multiple volumes (*e.g.* test tubes) of bacterial solution (with an initial bacteria cell density $\sim 10^5$ cfu/mL [223], which can originate from a patient's bodily fluid sample or from a laboratory standard culture) are incubated at 37° C in the presence of growth media and different dilute concentrations of an antibiotic solution (*i.e.* typically starting from a high concentration, *e.g.* $\sim$1000 μg/L, with intermediate concentrations diluted by one-half, down to a low concentration *e.g.* $\sim$10's of μg/L [222]). Conceptually, after a certain incubation time, typically 16-24 hours [224], the optical properties of each of the volumes are observed, which is often performed qualitatively using the naked eye, or can be measured quantitatively. In volumes containing antibiotic concentration *below* the MIC value (*i.e.* the antibiotic concentration is insufficient to stop the proliferation of the bacteria), the increased bacterial density is apparent as the solution turns cloudier and darker. The decreased magnitude of transmission of specific wavelengths of light through the medium can be optically measured and correlated to bacterial population density. See **Section 3.3.7** for a detailed description of the spectrophotometric method used in this work to measure optical cell density. However in those culture volumes in which the concentration of antibiotic is *above* the MIC value, the proliferation of bacteria was inhibited over the course of incubation, and thus the cloudiness of the solutions remain unchanged. Quantitative measurements of optical transmissivity of these samples can be used to confirm the lack of cellular proliferation. The known concentration of antibiotic in solution inside the fluid volume where the inhibition of bacterial proliferation is first observed (*i.e.* the lowest concentration) represented the MIC value for that given antibiotic and bacterial strain. The MIC value provides healthcare providers with a minimum dosage recommendation that would be necessary to inhibit growth of the bacteria inside a patient's body and treat the infection whilst not exposing the bacteria to a higher concentration to which the bacteria could evolve resistance [225]. Examples of documented experimentally-determined MIC values for particular bacterial strains and antibiotic

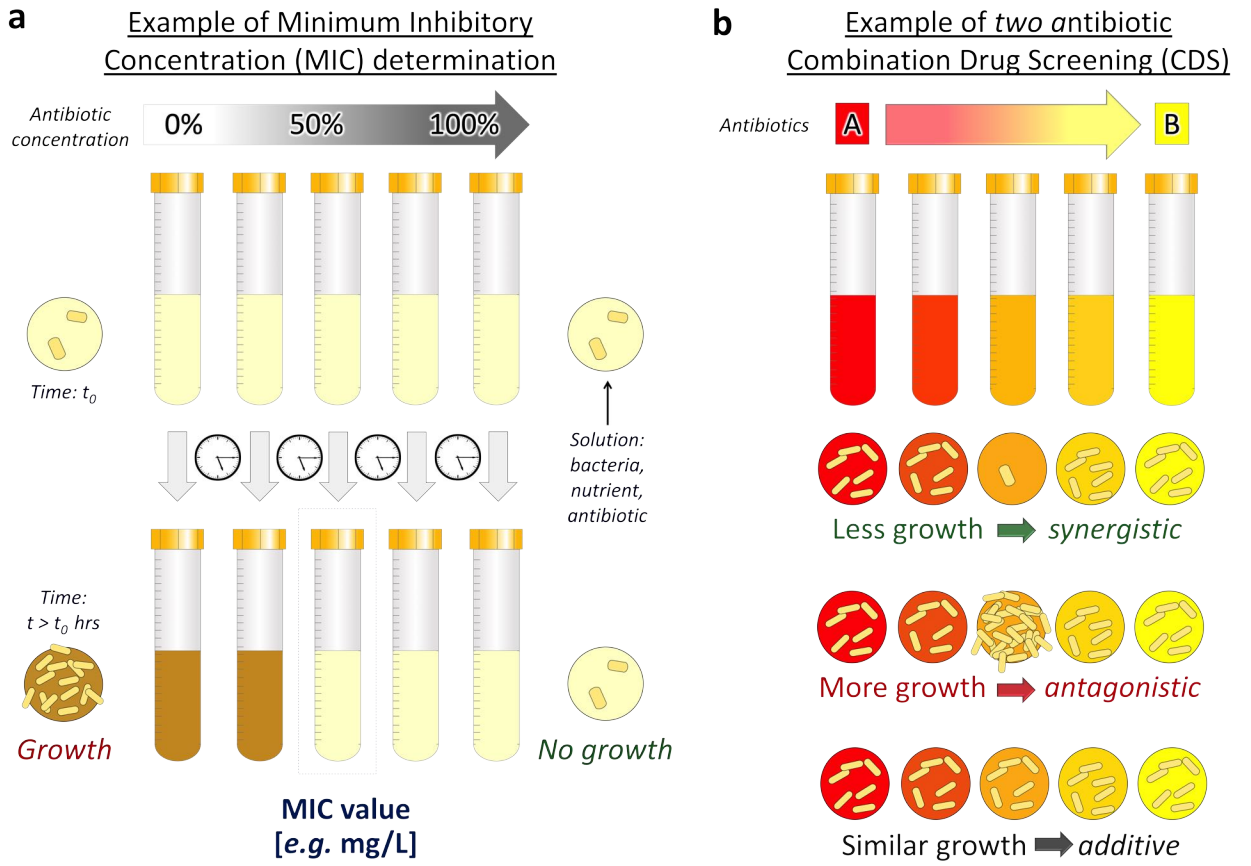

Figure 3.1: Conceptual illustrations of conventional antibiotic drug testing protocol standards. **(a)** Minimum Inhibitory Concentration (MIC) testing is used to determine the minimum concentration of a single antibiotic in solution (typical units of *mg/L*) needed to inhibit the growth of a specific bacterial colony. **(b)** Combination Drug Screening (CDS) involves combining multiple antibiotics into discrete drug cocktails, comprised of different concentration ratios of the antibiotics, and is used to determine the effects of the certain antibiotics on bacterial colony growth when combined in specific ratios, *i.e.* more effective (*synergistic*), less effective (*antagonistic*) or no noticeable difference (*additive*). Conventional clinical techniques used to perform these assessments typically involve long incubation times, large reagent volumes and manual-labor intensive procedures (*e.g.* bulk macro-dilution involving test tube incubation and qualitative optical measurements, and micro-dilution involving 96-well plates and quantitative microscopy).

compounds can be found in the literature; however as previously discussed, the inherent antibiotic sensitivity profile for different strains of bacteria varies between strain type and evolves over the course of the lifetime of the bacterium. Therefore, individual AST evaluations are recommended to be performed each time a definitive evaluation of the MIC values for a certain strain of bacteria for a given antibiotic is desired.[208, 222, 225, 226]

3.1.1.2 Combination Drug Screening (CDS) Clinical Studies

Many existing strains of bacteria have developed total resistance to specific antibiotic compounds, however, rendering those antibiotics functionally-useless in treating infections caused by those bacteria in any concentration. The only effective chemotherapeutic treatment against these multi-drug resistant (MDR) bacteria is in the form of a combination of antibiotics. *Combination drug screening* (CDS) is therefore a highly relevant AST method used in both clinical laboratory-based and drug development research facility-based drug screening applications. Specific combinations of two or more antibiotic compounds are known to induce different and unique cellular reproduction inhibiting pathways, and thus can demonstrate enhanced bacterial proliferation inhibitory effects in combination than each antibiotic exhibits on its own. For example, certain combinations of up to four antibiotics are some of the only known effective treatments against *Mycobacterium tuberculosis* infections, and multiple-antibiotic combinations are required to treat many bacterial urinary tract infections. (Interestingly, multi-drug combinations have also proven the most effective treatment against different forms of cancers, viral infections such as HIV and parasitic infections such as malaria) Therefore multiple-antibiotic CDS remains a critical pursuit in the field of AST for MDR-bacterial infections. [227, 228]

Despite the apparent inherent appeal of multiple-antibiotic combination treatments, adverse side effects are in fact possible between certain antibiotics, which can even encourage proliferation as well as the overall antibiotic resistance characteristics of certain strains of MDR bacteria; therefore, comprehensive screening of various concentrations of different antibiotics must be performed in CDS experiments, which poses a considerable limitation on the clinical throughput and cost of screening more than two antibiotics at a time [229, 230].

As illustrated in **Fig. 3.1b**, to perform CDS on two antibiotic solutions using the commonplace broth dilution method, for example, different combinations between the two antibiotics must be manually created in test tubes through serial dilutions of both antibiotics (*i.e.* from a high to a low concentration of one antibiotic solution in the presence of the opposite concentration of the other antibiotic solution), which is a very time and manual labor-intensive process to perform conventionally. Solutions of bacterial culture and nutrient media are then added to each test tube and are incubated at 37 $^{\circ}$ C for up to 24 hours [224]. Bacterial proliferation can then be observed and quantified using the same methods as described for the MIC determination. [231]

Conceptually, certain combinations of the antibiotics will be *more* effective at inhibiting bacterial proliferation than either of the two antibiotics on their own (*i.e.* a *synergistic* combination), therefore least amount of bacterial proliferation will be observed in that volume. Furthermore, certain antibiotic combinations will be *less* effective at inhibiting bacterial proliferation than either of the two antibiotics on their own (*i.e.* an *antagonistic* combination), therefore most amount of bacterial proliferation will be observed in that volume. The other case is that the inhibitory effects of certain antibiotic combinations will be somewhere in between those of the two antibiotics on

their own. Any additive combination represents an acceptable dosage which can be used when any chance of inducing or enhancing bacterial resistance to one of the antibiotics on its own needs to be avoided; any synergistic combination represents a recommended dosage which can be used as an effective treatment against MDR infections; and any antagonistic combination represents a dosage which should be avoided as it would prove detrimental to the treatment of MDR infections. [232] As with the case with MIC determination, examples of documented experimentally-determined CDS results for particular bacterial strains and antibiotic combinations can be found in the literature [227, 233, 234], however since the inherent antibiotic sensitivity profile for different strains of bacteria varies between strain type and constantly evolves, individual AST evaluations are recommended to be performed each time a definitive evaluation of the CDS profile for a certain strain of bacteria for combinations of certain antibiotics is desired. [235, 236]

Overall, the aforementioned conventional AST techniques used in clinical laboratory or biomedical research settings are well-established, relatively inexpensive to perform and have been proven reliable and instrumental in treating bacterial infections; yet, they are manual labor-intensive, operators must strictly adhere to complicated testing standards, and their use requires laboratories with the hardware needed to perform multiple independent fluidic handling procedures and quantifiable detection schemes with varying degrees of complexity. In order to address this, different commercially-available AST instruments have been developed which can perform semi-automated fluidic handling, for example preparation and analysis of standard 96 well-plates for micro-broth dilution and automated detection, which can deliver accurate results in under 24 hours, depending on the AST method. However, adoption of these technologies, which are often quite expensive to purchase and maintain, is fairly limited especially in low-resource clinical settings. [213]

The fundamental limitation inherent to these conventional AST methods is that most usually involve a minimum of $\sim$24-48 hours for sample incubation followed by $\sim$24-72 hours for the actual AST analysis to take place, depending on the analytical method used. The most time-intensive aspects of conventional AST approaches are the bacterial incubation steps required to enrich the bacterial population density sufficiently (to $\sim 10^7$ cfu/mL) as to enable optical density-based measurements ($\sim$24 hours to create the initial inoculation, followed by $\sim$24+ hours for analysis). Therefore in clinical settings, AST results usually take anywhere from two days to one week from the time of sample collection to deliver definitive analytical results (*e.g.* 18-24 hours for the most rapid methods [208]). A standard clinical procedure whilst clinical AST methods are being performed is for a clinician to prescribe a large dose of a broad-spectrum antibiotic in hopes of ensuring that the patient receives a larger dose than would be minimally-required to inhibit the growth of the bacteria and stop the infection from worsening. This very practice, however, often contributes to the emergence and propagation of AMR in the first place. [221, 237, 238]

3.1.2 Microfluidic-Based AST Approaches

Alternative *microfluidic*-based approaches have therefore been developed towards AST applications evaluating highly clinically-relevant *antimicrobial drugs* in point-of-need clinical laboratories and in pharmaceutical research and development settings [238, 239], which has demonstrated the potential for this technology to significantly-decrease the mortality rate and healthcare costs associated with treating AMR-related infections [240]. The primary objective of implementing microfluidic-based platforms in these applications is to miniaturize various fluidic handing, cell culture and analysis processes into *on-chip* platforms in order to: (*i*) increase overall analytical throughput and decrease the duration of drug development through *on-chip* multiplexed analysis [241, 242]; (*ii*) to decrease the necessary working volumes of occasionally-very expensive experimental antimicrobial drug compounds and produce a more overall economical drug development cycle [243, 244]; (*iii*) to study the antimicrobial effects of compounds in submillimeter-scale fluid environments without needing to perform *in-vivo* trials and case studies involving actual patients towards the development of new antimicrobial compounds [211, 245]; and (*iv*) to provide for antimicrobial dosage recommendations to treat microbial infections in truly-point-of-need and point-of-care clinical applications [246–249]. A higher throughput of clinical AST analytical results also has the potential to provide potentially-life saving effective antibiotic treatment recommendations to treat infections caused by unknown bacteria harvested from patient samples. [213]

3.1.2.1 Concentration Gradient Generator-Based Methods

One of the more widely-adopted classes of microfluidic devices used towards these applications are microfluidic *concentration gradient generators* (CGG's). These devices are typically comprised of individual microchannel nodal units used to combine, mix and split fluid samples which are fabricated into *christmas tree*-like branched microchannel networks that produce a concentration gradient between the fluidic species input into the device [14, 250] which represent useful concentrations of the input species, such as linear and logarithmic stepwise combinations [251]. Further details on the working principles of CGG microchannel networks are discussed in **Section 3.1.2.2**. One of the first demonstrations of the inherent advantages of CGG microfluidic devices was performed by Zigmond and Sullivan [252], who employed one possible type of concentration gradient, a *continuous* or *spatio-temporal* gradient, comprised of specific chemotactic peptide solutions which were used to show that polymorphonuclear leukocyte cells cultured within the gradients exhibited transient changes in morphology and locomotion with preferential growth in certain concentrations of the peptide fluid flows, which proved to be one of the fundamental studies of chemotactic factors on leukocyte chemotaxis. A spatio-temporal gradient often formed by combining the individual fluidic outlets from a branched gradient-generating microchannel network together and established *via* inter-fluidic species diffusion. The gradient is then maintained in a localized region of the device thereby permitting *on-chip* cell culture or chemical reaction studies in

the presence of the fluids. Many examples of biomedical applications for spatio-temporal concentration gradients have followed, including those used to study various effects of different growth factor, hormone and chemokine environments on a variety of other single- and multi-cellular microorganisms [213]. An alternative type of concentration gradient is a *discrete* gradient, which is not continuous, but rather a concept represented by the collection of discrete fluidic elements from the CGG microchannel network itself, each containing certain discrete combinations and proportions of each of the input fluidic species [153, 253]. In microfluidic drug-screening applications, these fluid outputs can be referred to as discrete *μ-drug cocktails* [254].

Several examples of microfluidic CGG-based devices employing discrete gradient generation, predominantly, have been demonstrated towards AST applications in the contexts of both single-antibiotic MIC determination and CDS studies [223, 229]. In these applications, the discrete μ-drug cocktail solutions can be routed from the CGG microchannel network to discrete ($\sim$nL-μL volume) regions of the device in order to perform localized *on-chip* bacteria culture in the presence of the antibiotic solutions. Alternatively, the μ-drug cocktail solutions can be routed to discrete microchannel outlets on the device which permit the collection of ($\sim\mu$L volume) individual antibiotic solution samples for further use in *off-chip* bacteriological experiments [213]. For example, these devices have been used to perform AST evaluations of a multitude of clinically-relevant antibiotics against bacterial strains cultured in the laboratory as analytical standards [255], bioengineered strains for genomic therapy studies [348] and cells harvested from biological fluid samples [256], such as *Escherichia coli*, *Staphylococcus aureus*, *Klebsiella pneumoniae*, and *Listeria monocytogenes* [211, 223]. The overall objective of these microfluidic CGG-based AST studies, accomplished to varying degrees, is to achieve MIC and CDS values comparable to those found using the conventional AST methods mentioned in this section, such as the broth dilution method. As a result, many microfluidic CGG-based AST approaches have demonstrated gradient generation in seconds-minutes using *on-chip* CGG microchannel networks and *on-chip* multiplexing [257], increased experimental reliability and higher measurement sensitivity by analyzing smaller incubation volumes and lower cell densities ($\sim$1x10^5 cfu/mL is the standard diluted inoculation density employed by most assays) [258], and reduced overall biological incubation and analysis times due to smaller ($\sim$10's-100'sμL volume) bacteria culture volumes [229]. The standard timeframe for *rapid* results in the AST field today has been established as $\sim$6-8 hours (after the overnight bacterial inoculation is created) [259].

3.1.2.2 Limitations of Conventional 2D Gradient Generators

Despite these previous demonstrations of conventional CGG-based microfluidic platforms in AST applications, the development of higher-complexity CGG microchannel network designs is fundamentally limited by the *two-dimensionality* of MEMS-based manufacturing techniques, in addition to the tediousness and manual-labor intensiveness of such procedures. Therefore, the physical nature of these devices is restricted to two-spatial dimensions of geometric freedom, and the resulting

2D fluidic routing *via* planar microchannel constructs is only able to generate *symmetric* gradients of only two distinct input fluidic species at a time. A concentration gradient can be defined as *symmetric* if it captures all possible combinations of each of the input fluidic species (*e.g.* a continuous linear gradient between two distinct fluidic species), which is possible to accomplish using two fluidic input planar microfluidic CGG devices, as illustrated in **Fig. 3.2a**. Therefore conventional CGG-based microfluidic devices for AST applications are fundamentally limited to producing μ-drug cocktails that capture the greatest range of possible combinations of only two antibiotics, simultaneously. As a result, since symmetric gradients of three or more antibiotics are impossible to achieve, such multiple-antibiotic microfluidic CDS procedures must be performed manually and have much lower throughput, which could be the primary contribution to the fact that comprehensive clinical CDS studies of combinations of three or more clinically-relevant antibiotics are so limited in the biomedical community today.

Traditionally, planar CGG-based microfluidic devices have been developed in order to handle more than two input fluidic species. As **Fig. 3.2b** illustrates a linear gradient can be produced between all (*e.g.* three) fluidic input species (*i.e.* a continuous linear gradient is possible between species #1 & #2 and between #2 & #3); however, such gradients do not capture any combinations of the first and the last input species (*i.e.* any combinations of species #1 & #3). This resulting gradient, therefore, must be defined as being *non-symmetric*. One potential approach to produce the aforementioned absent combinations of species (*i.e.* #1 & #3) would be add an additional fluidic input containing the same fluidic species as used in Input #1; hence an additional linear gradient can be produced (*i.e.* between species #1 & #3). Accomplishing this task presents some practical issues, however, including the need to double the volume of one of the (potentially expensive) fluidic species, adding an additional independent source of (potentially complex) forward-driving fluidic control, increasing the geometric complexity of the microchannel network design and potentially increasing the complexity and duration of the fabrication process. Moreover, even using these technique, it is impossible to generate fluidic combinations of all input fluidic species (*i.e.* #1, #2 & #3), which is a fundamental limitation of planar fluidic routing in conventional CGG microfluidic systems. [250]

One additional previously-demonstrated approach used to generate gradients between more than two input fludic species at a time is the establishment of a spatio-temporal gradient. The first demonstration of this technique by Atencia et al. [165] involves a planar PDMS-based *microfluidic palette* system employing a circular-shaped analytical chamber to generate a spatio-temportal gradient of three fluidic inputs, which is used to demonstrate gradient generation between one drug solution, one buffer solution and one solution of bacteria media, *on-chip*, to study the chemotactic behavior of bacteria. Despite the planar nature of the 2D PDMS-based microchannel structures, the geometric symmetry of the analytical chamber permits the input of multiple fluidic input species, three or more in theory; however, the resulting diffusive gradient is still *non-symmetric*, as it is still linear between all of the species along the circumference of the circular analysis chamber. Furthermore, the freedom to select and isolate discrete portions of the generated gradient is lacking, as the diffusive gradient is continuous between all of the input fluidic species. Moreover, the only portion

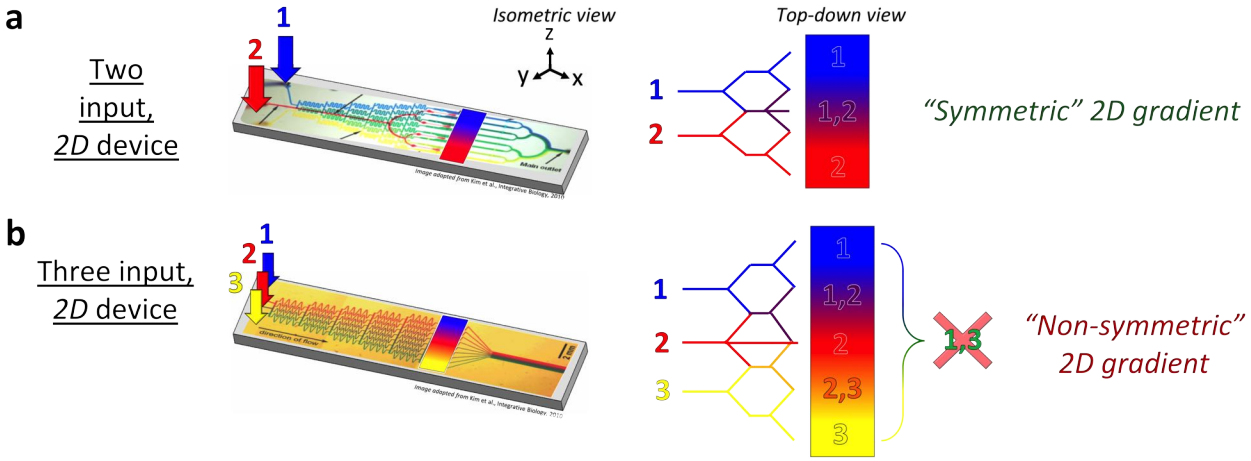

Figure 3.2: Concept of microfluidic concentration gradient generator (μ-CGG) systems, and the limitation of conventional two-dimensional μ-CGG's, *i.e.* the inability to generate symmetric fluidic gradients of three or more fluidic inputs. **(a)** Conventional two input, two-dimensional μ-CGG's (*e.g.* PDMS-based systems fabricated *via* soft-lithography) can generate a *symmetric* gradient between both input fluids (*i.e.* creates fluid outputs that capture combinations of all possible input fluidic species). **(b)** However when a third (or more) input fluid is added to three (or greater) input μ-CGG's, the resulting gradient is *non-symmetric* (*i.e.* no combinations of fluid inputs 1&3 are generated) due to the two-dimensionality of the microchannel network construct, the result of the planar nature of conventional microfluidic fabrication approaches.

of the generated gradient which contains a combination of three or more fluidic species is directly in the center of the device, containing some portion of every single input species; therefore, the ability to generate a specific desired combination of more than two input fluidic species without the interference from any of the other species is also lacking which limits analytical throughput. Additionally, entire experimental environment is contained *on-chip* and is difficult to dynamically change for different experiments, therefore no portion of the generated gradient can be collected and used in any further *on-chip* analysis down-stream in a different region of the device (thereby limiting the ability of this type of gradient to be incorporated into a larger, more functionally-complex lab-on-a-chip system) or in any form of *off-chip* experimental study, if so desired by the application.

Furthermore, alternative manufacturing approaches have been demonstrated in order to increase the complexity of planar microchannel structures, for example by aligning, layering and bonding multiple (*i.e.* PDMS-based) layers together, thereby generating *quazi-3D* microchannel structures; however, this often proves to be a laborious, tedious and often error-prone process which, in addition to numerous geometric limitations inherent to the simple layering of discrete planar microchannel designs on top of one another, has limited the geometric complexity of conventional CGG designs [260, 261]. Therefore in light of current trends in the improvement of 3D printing technology, additive manufacturing-based techniques have seen recent interest towards

developing more *three dimensionally*-complex microfluidic CGG systems using various 3D printing techniques to demonstrate simple monolithic fabrication, cheap material and equipment costs relative to those inherent to soft-lithography-based processes and compact 3D device geometries [4, 110, 262]; yet, most of these studies have demonstrated fairly-limited characterization towards AST applications. In particular, none of these examples have demonstrated generation of more than two antibiotic concentration gradients, simultaneously.

Finally, these aforementioned fundamental limitations of conventional CGG microfluidic platforms have critical ramifications for the field of microfluidic-based AST, in that such platforms are inherently restricted to evaluating a maximum of two distinct antibiotic species in a single experimental operation. As a consequence, the throughput of MIC testing, and moreover CDS of three or more clinically-relevant antibiotics, is fundamentally-limited [229, 263].

3.2 Design of 3D Concentration Gradient Generators *via* Additive Manufacturing

In light of these fundamental limitations of conventional 2D μ-CGG devices, the objective of this project is to design, fabricate and demonstrate *three-dimensional* μ-CGG structures capable of generating truly *symmetric* multi-fluid gradients. The only way of accomplishing such a symmetric gradient of three or more fluids is to utilize the *third spatial dimension* and perform fluidic routing and mixing in a truly-*three-dimensional* fashion, a task which is fundamentally hindered by the limitations of conventional planar fabrication methods. As a means to this end, this work demonstrates the use of a Multijet 3D printing to fabricate entirely-3D printed 3D μ-CGG prototypes which utilize unique *three-dimensionally*-arranged microchannel networks only possible to fabricate *via* an additive manufacturing-based fabrication approach. As **Fig. 3.3a** illustrates, by utilizing the additive manufacturing nature of 3D printing, the *third-spatial dimension* is now available in which to fabricate microchannel structures that perform the 3D fluidic routing necessary to create combinations of fluidic species input to Inlets #1 & #2, Inlets #2 & #3, Inlets #1 & #3, and most critically, Inlets #1, #2 & #3 of the device. As a result, the conceptual gradient of all three input fluidic species is inherently *symmetric*, as all possible combinations of all three input fluidic species are generated, simultaneously.

In this work, two distinct 3D microchannel networks are proposed and designed. The first design utilizes a 3D microchannel network comprised of thin-walled microchannel elements arranged into horizontal triangular-shaped layers interconnected by vertical microchannels, and is referred to henceforth as the *layer-based* μ*-CGG* design (**Fig. 3.3b**). Due to the unique 3D layer-based arrangement of these microchannels, this proposed device is able to generate a discrete gradient of all three input fluidic species, producing 15 unique output fluid samples representing this

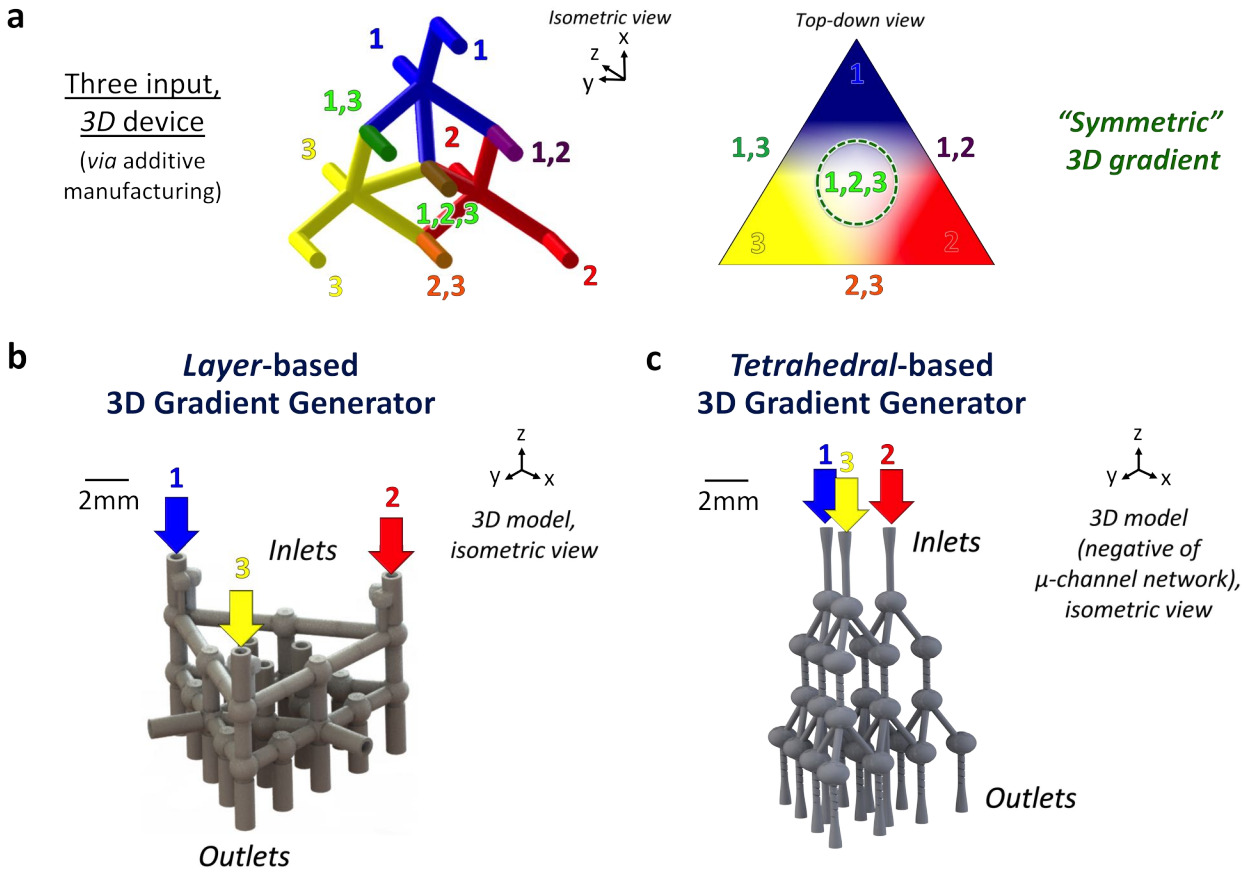

Figure 3.3: Concept of microfluidic concentration gradient generation in *three dimensions*. **(a)** A truly 3D microchannel network (*left*) is able to generate combinations of all possible fluid inputs (*i.e.* 1&2; 3&3; 1&3; and 1,2&3), resulting in a truly symmetric three-fluid gradient (*right*). Two specific proposed designs for 3D μ-CGG devices, which can achieve fluidic routing in three dimensions that is impossible to achieve using conventional devices manufactured *via* planar fabrication methods, are featured in this work: **(b)** a *layer*-based microchannel arrangement, and **(c)** a *tetrahedral*-based microchannel arrangement, both generate discrete fluid outputs (15 and 13, respectively) from three input fluidic species.

gradient, most critically three outlets which contain proportional concentrations of all three input species. These fluid outputs can be collected using interfacing hardware to perform further experiments. The second design utilizes a 3D microchannel network comprised of hollow microchannel elements fabricated into a solid structure which are arranged into tetrahedron-based units interconnected by vertical microchannels, forming layers which grow in size the further down the 3D network similar to an overall tetrahedron in shape, and is referred to henceforth as the *tetrahedral-based μ-CGG* design (**Fig. 3.3c**). Due to the unique symmetry of the 3D arrangement of these microchannels, this proposed device is able to generate a discrete gradient of all three input fluidic species, producing 13 unique output fluid samples, most critically one output fluid which contains

an equivalent proportion of all three input species concentrations. Likewise, these fluid outputs can be collected and used to perform further experiments.

3.2.1 Analytical Design Methodology

Comprehensive presentations on the analysis of pressure-driven microfluidic networks using electric circuit analogies behind the design of concentration gradient generator microfluidic networks are published in seminal reviews by Oh et al. [264] and Toh et al. [153], respectively. During the conceptualization and design of both 3D microchannel network arrangements, mathematical approaches derived from these works, traditionally used in the design of conventional 2D CGG's [250, 265], were extended for the purposes of this project in *three-dimensions* in order to analytically-determine the expected flow rates and concentrations of each fluidic input species at each fluidic outlet of the 3D microchannel network design. Due to the symmetry in the 3D microchannel network geometry (*i.e.* the fluid paths between device Inlets #1 & #2 to each device outlet are identical to those between Inlets #1 & #3 and Inlets #2 & #3), nodal analysis calculations were performed along the fluidic paths between Inlets #1 & #2, and at any location where contribution from the species from Inlet #3 was present, the concentration of that species was determined from the reflection of the geometry over the plane of geometric symmetry and the value that was used was the value of the species from Inlet #2. For clarity, an example of the actual analytical calculations performed by hand, step-by-step, for the *layer*-based 3D μ-CGG design are shown in Appendix **Fig. 7.28**.

Briefly, each location in the 3D fluidic network design where fluids combine and split from a hollow bulb is treated as an individual *nodal unit*. At this point, significant assumptions are made in the nodal analysis. For the *layer*-based 3D μ-CGG design, the assumptions are made that all fluids that enter each hollow bulb from the input microchannels homogeneously mix inside the hollow bulb before splitting off and exiting the hollow bulb at equivalent flow rates through all of the outlet microchannels. By making these assumptions, the hollow bulb of each nodal unit can be treated as a control volume and nodal analysis can then be performed using the following calculations and analytical steps in order to determine the fluid flow rate and species concentrations of the input fluids to, and output fluids from, each control volume.

For the *tetrahedral*-based 3D μ-CGG design, the assumptions are made that all fluids that enter the upper hollow bulb (as indicated in Appendix **Fig. 7.23**) from the input microchannels and flow through the vertical microchannel are homogeneously mixed by the time that they enter the lower hollow bulb and split off and exit at equivalent flow rates through all of the outlet microchannels. By making these assumptions, the group consisting of the upper and lower hollow bulbs and vertical microchannel of each nodal unit can be treated as a control volume and nodal analysis can then be performed using the following calculations and analytical steps in order to determine the fluid flow rate and species concentrations of the input fluids to, and output fluids from, each control

volume. For both designs, nodal analysis proceeds from the top of the microchannel network (*i.e.* at the fluidic inlets) to each subsequent nodal unit, and ending at the bottom of the network (*i.e.* at the fluidic outlets) where the final values are calculated and reported (*i.e.* the total fluidic flow rate, Q, and the total concentration of each input species, C_1, C_2 & C_3, contained in the fluidic volume.

Nodal analysis begins at the two outer-most hollow bulbs on the first layer for both designs. The flow rate and concentration of the input fluidic species into each initial nodal unit are known (Q_1 and C_1 into Inlet #1; Q_2 and C_2 into Inlet #2). Each of these control volumes therefore sees a single input and multiple outputs. Each of the fluid output therefore contains 100% concentration of the input fluidic species and, for example, have flow rates of exactly one half of the input flow rate. For all subsequent control volumes with multiple fluidic inputs, the following nodal analysis procedure is performed.

First, the hydraulic resistances of each of the microchannels exiting the control volume are calculated using **Eq. 3.1**, which is defined as the value of hydraulic resistance from the Hagen-Pouisse Equation [264] for a circular cross-section, smooth-walled microfluidic channel,

$$R = \frac{8\mu L}{\pi r^4} \tag{3.1}$$

where μ is the dynamic viscosity of the fluid (assumed for water at 25°C, 8.9x10^{-4} Pa s), L is the length of the microchannel and r is the hydraulic radius of the microchannel. Afterwards, the total equivalent hydraulic resistance of all fluids exiting the control volume *via* the outlet microchannels, $R_{out,total}$, is calculated using **Eq. 3.2**,

$$\frac{1}{R_{out,total}} = \sum_{i=1}^{n} (\frac{1}{R_{out,i}}) \tag{3.2}$$

which is the hydrodynamic-equivilent of the Parallel Resistors equation used to calculate the effective total electrical resistance of resistors in parallel where $R_{out,i}$ represents each of the individual hydraulic resistances of the outlet microchannels (as previously calculated from **Eq. 3.1**). The total volumetric flow rate into the control volume, $Q_{in,total}$, is then calculated by taking the sum of all volumetric flow rates from the input microchannels into the control volume. Each volumetric flow rate that leaves the control volume *via* each of the individual output microchannels ($Q_{out,i}$) can then be calculated using the Conservation of Momentum equation in **Eq. 3.3**,

$$Q_{out,i} = (\frac{R_{out,total}}{R_{out,total} + R_{out,i}}) Q_{in,total} \tag{3.3}$$

Then Conservation of Mass equation is then solved using **Eq. 3.4**,

$$Q_{total}C_{total} = \sum_{i=1}^{n}(Q_iC_i) \tag{3.4}$$

where Q_i and C_i are defined as the flow rate (as a function of the proceeding flow rates) and concentration (as a function of the proceeding concentrations) of each of the input fluids into the control volume, respectively (*i.e.* $\sum_{i=1}^{n}(Q_{in,i}C_{in,i})$). Once $Q_{total}C_{total}$ is calculated as a function of the proceeding known input values, this quantity can be defined as equivalent to the total mass leaving the control volume *via* the outlet microchannels (*i.e.* $\sum_{i=1}^{n}(Q_{out,i}C_{out,i})$), and **Eq. 3.4** is used once more to solve for the flow rate (as a function of the input flow rates) and concentration (as a function of the input concentrations) of each of the output fluids leaving the control volume. Finally, following this convention throughout the 3D microchannel nodal network, the flow rate and concentration of each of the fluids exiting the microchannel network *via* the device outlet microchannels can then be mathematically defined in terms of the initial input flow rates (Q_1, Q_2 in units of μL/min) and concentrations (C_1, C_2 in units of μg/L) of each of the input fluidic species, and subsequently analytically calculated in order to quantify each of the values.

3.2.2 *Layer-Based* 3D Microchannel Network

The *layer*-based 3D μ-CGG design is illustrated in **Fig. 3.4**. This particular 3D arrangement of microchannels arose from the conceptualization of a microchannel network which would feature symmetric fluidic routing between three input fluidic species; thus, symmetrical horizontal layers of microchannels with a triangular arrangement (as viewed from the top-down), interconnected by vertical microchannels, was adopted. The horizontal microchannels on the first layer are all 7.5mm long in order to provide for the same fluidic resistance inside all microchannels. Following the same logic, all horizontal microchannels on the second layer are 3mm long, and all vertical microchannels are 3.5mm long. As a result, theoretically-equivalent fluid flow rates and symmetric flow dynamics are produced in each horizontal layer. Regarding the morphology of the microchannels, this design features thin-walled microchannel elements with a thickness of 375 μm suspended in 3D space. The fluid division principle follows a pattern whereby each fluid flow is split and combined with that from an adjacent fluid flow. For example, the first layer of this design is intended to split and combine half of the volume of each of the input fludic species, generating new fluid flows with 50% concentrations of all possible pairs of input fluidic species, and routing this fluid along with 100% of each input species to the secondary later, where the 50% concentration fluids all mix with the 100% fluids once more, and those fluid flows furthermore mix with each other, creating complex combinations of all three species. As a result, the outlet microchannels generate 15 discrete fluid samples capturing the distinct gradient between all three

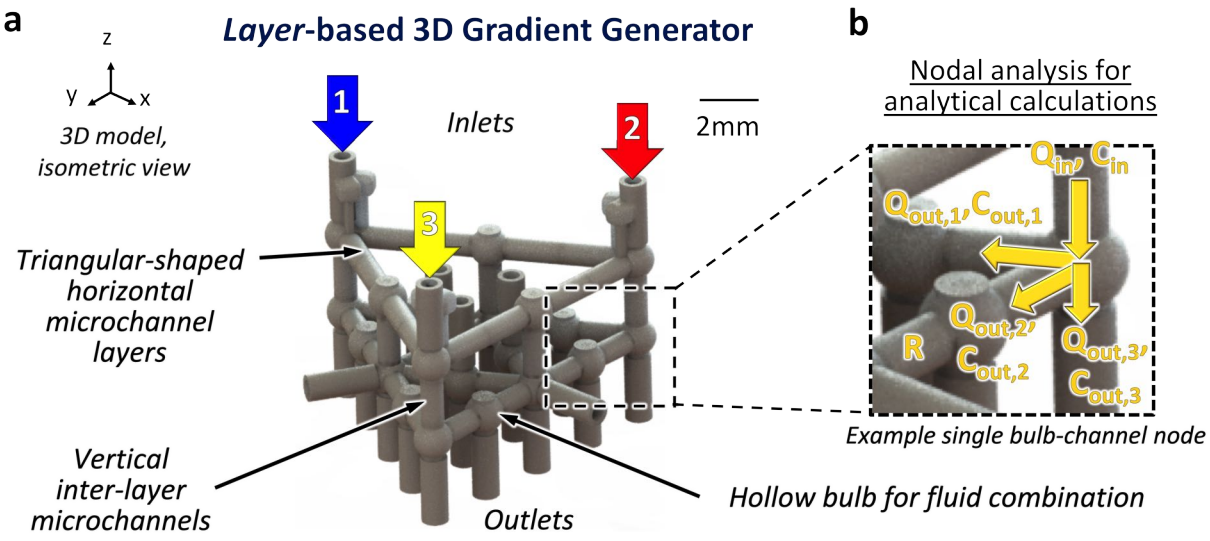

Figure 3.4: Design of the *layer*-based 3D μ-CGG device. **(a)** Isometric view of the Solidworks computer aided design (CAD) 3D model of the 3D network of hollow microchannels. The microchannels are arranged in triangular-shaped horizontal layers interconnected by vertical microchannels. All junctions between microchannels are comprised of hollow bulbs for fluid combination before splitting off to subsequent hollow bulbs. All microchannels have an inner diameter of 750μm and all bulbs have an inner diameter of 1.25mm. The length of all horizontal microchannels on the first layer is 7.5mm, 3mm for all horizontal microchannels on the second layer, and 3.5mm for all vertical microchannels. **(b)** Illustration of a single nodal microchannel unit used to perform nodal analysis, consisting of one hollow mixing bulb and all associated microchannels which lead into and out of the bulb. The input and output fluid flow rates (Q_{in}, Q_{out}) and species concentrations (C_{in}, C_{out}) into and out of the nodal unit are illustrated. For the analytical results of the nodal analysis calculations, see **Fig. 3.8b**.

input fluidic species, intended to be collected using interfacing hardware and incorporated into further experiments. Moreover, due to the compact arrangement of horizontal microchannels on the second layer, the three fluid outputs *via* the microchannel outlets in the middle of the layer are ultimately produced from fluidic contributions of all three fluidic input species, and thus contain different proportional concentrations of each of the three input species, a unique capability of the truly-3D fluidic routing accomplished by this design. **Section 3.4.1** presents the analytical, theoretical and experimental characterization of the *layer*-based 3D μ-CGG design, followed by its demonstration as a biomedical tool towards various MIC determination and CDS evaluation experiments evaluating clinically-relevant antimicrobial agents against antibiotic-resistant bacteria. This portion of the project was completed before moving onto the development of the *tetrahedral*-based 3D μ-CGG design. Therefore as will be discussed, feedback regarding the performance of this design resulted in design modifications and improvements which were subsequently implemented into the conceptualized design and modeling of the *tetrahedral*-based 3D μ-CGG.

3.2.3 *Tetrahedral*-Based 3D Microchannel Network

Specifically, modifications were made to the 3D microchannel network comprising the *tetrahedral*-based 3D μ-CGG design (as illustrated in **Fig. 3.5**) in order to improve the symmetry of the flow dynamics inside the network, with the end goal of producing different concentrations of each input fluidic species at each device outlet. Furthermore, one objective of this 3D symmetry is to produce a single fluidic outlet which contains an equivalent concentration (*i.e.* $\sim$33%) of each of the three inlet species, which is impossible to achieve with the *layer*-based 3D microchannel arrangement.

The *tetrahedral*-based 3D μ-CGG design is illustrated in **Fig. 3.5**. The 3D modeling process used to create this specific design was slightly different from that used to model the *layer*-based design. Briefly, a negative of the 3D arrangement of the hollow microchannels was initially modeled (**Fig. 3.5a**), which is geometrically-symmetric in all three dimensions. Each nodal microchannel unit (**Fig. 3.5b,c**) is comprised of an upper hollow bulb where fluids enter and are combined, a vertical microchannel (the illustrated design incorporates vertical 3D rifled μ-mixer structures into the side-wall to enhance fluidic mixing quality at the exit of the microchannel, see **Section 3.4.2.1.1** for further details), and a lower hollow bulb[1] where the fluid flow is then symmetrically-split *via* a tetrahedron shape-based arrangement of microchannels at equivalent angles ($\sim$120 °). All microchannels throughout this design are 5mm in length. The nodal units are arranged into what can be defined as two tiers, or layers. After the first layer, the nodal units which produce ($\sim$50%) of each pair of inlet fluidic species, in addition to routing the combined fluid flow to the next layer, also consist of a long vertical microchannel, termed the *dropdown outlet*, which generates a collectable-fluidic outlet. A more detailed description of the layered nodal unit arrangement, as well as a derived design methodology which can be used to analytically predict the fluid output concentrations at each outlet, are presented in Appendix **Fig. 7.23**.

Moreover, this 3D microchannel arrangement also improves upon the *layer*-based 3D μ-CGG design, in that the outermost nodal units on the first horizontal layer of the *layer*-based design featured vertical inlet and outlet microchannels in a linear arrangement, as well as the additional outlet microchannel oriented 90° from each microchannel branching off of the hollow bulb. This arrangement generates a linear path for the input fluid to travel along through the nodal unit, *i.e.* the pressure drop into the linearly-positioned outlet microchannel is lower than that into the horizontally-positioned outlet microchannel; thus, more fluid likely exits the nodal unit towards the next horizontal layer than flows horizontally, which causes uneven fluid flow and gradient generation on each horizontal layer than flows in the vertical direction. However in the *tetrahedral*-based 3D μ-CGG design, due to the total geometric-symmetry of all microchannel lengths, angles and 3D nodal-unit spatial arrangement, this design features theoretically-equivalent fluid flow rates and symmetric flow dynamics throughout the entire device, eliminating the uneven dis-

[1]The bulbs featured in this design are 3 mm in diameter. Upon initial fluid flow through the network, the potential exists for air bubbles to be trapped near the microchannel inlets to the bulbs. Therefore further proposed design modification would entail reduction of the bulb diameter to reduce the chance for air trapping.

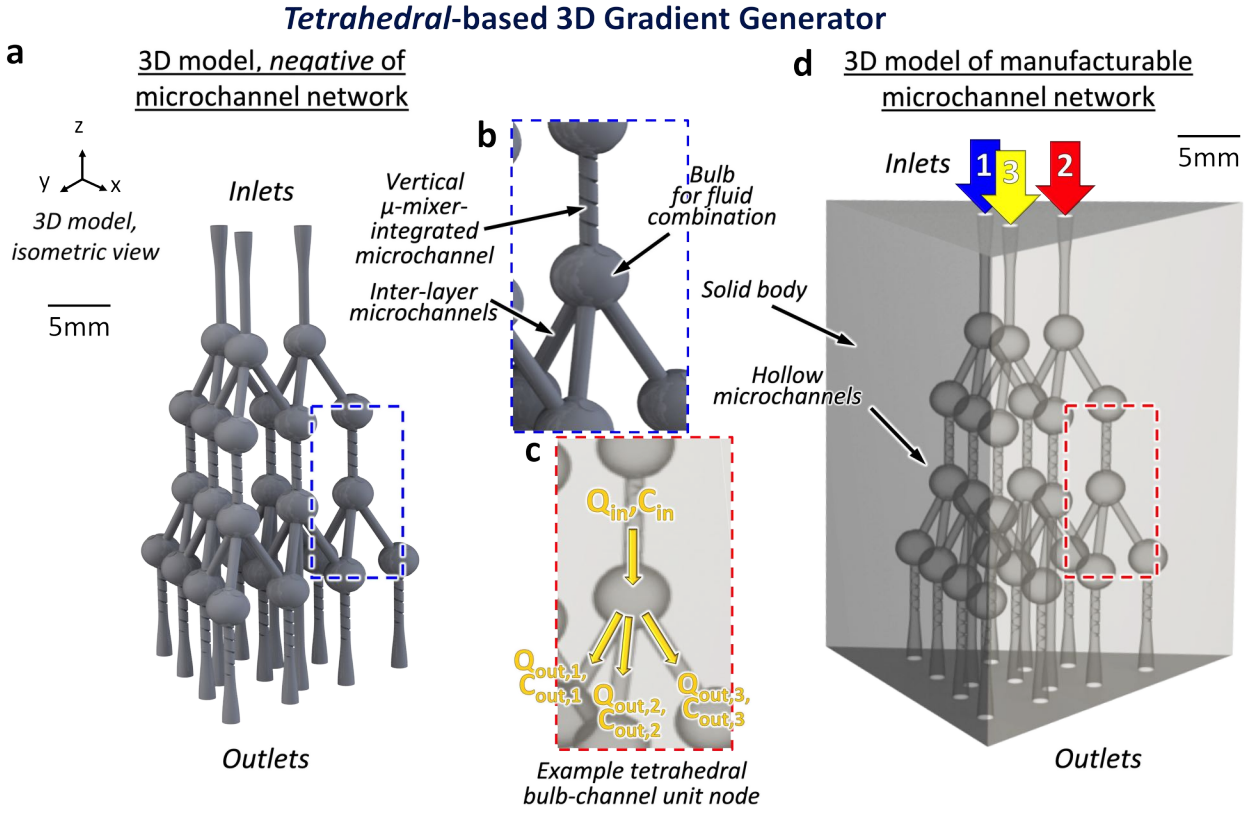

Figure 3.5: Design of the *layer*-based 3D μ-CGG device. **(a)** Isometric view of the Solidworks computer aided design (CAD) 3D model of the network of positive-features which define the inside of all hollow microchannel structures. **(b)** All junctions between microchannels are comprised of hollow bulbs for fluid combination before splitting off again. The microchannel network is comprised of tetrahedron-shaped units arranged in layers, and interconnected by vertical microchannels. This figure illustrates a model with 3D Rifled μ-Mixer elements incorporated into each vertical microchannel to enhance mixing quality of the input solution into each subsequent hollow bulb. All microchannels have an inner diameter of 750μm and 5mm in length. All bulbs have an inner diameter of 1.25mm. **(c)** Example of nodal analysis showing the input and output fluid flow rates (Q_{in}, Q_{out}) and single species concentrations (C_{in}, C_{out}) into and out of each nodal unit, consisting of an upper hollow bulb and lower hollow bulb interconnected by a vertical microchannel and all associated microchannels which lead out of the lower bulb. For analytical results of the nodal analysis calculations, see **Fig. 3.14**. **(d)** Isometric view of the actual 3D printable device with hollow microchannels, the negative of positive microchannel model, illustrating hollow microchannels and a solid structural body.

tribution of fluid flow between layers experienced in the *layer*-based design. As a result, the outlet microchannels generate 13 discrete fluid samples capturing the distinct gradient between all three input fluidic species, likewise intended to be collected and used in further experiments. Moreover, a single fluid output *via* the microchannel outlet in the middle of the outlet arrangement is pro-

duced from equivalent fluidic contributions of all three fluidic input species, an inherent capability of the truly-3D symmetric fluidic routing accomplished by this specific design. Finally, an actual manufacturable (*i.e.*3D printable) design is modeled, consisting of a solid construction containing hollow microchannels which represent the reciprocal of the negative microchannel model (**Fig. 3.5d**). See **Section 3.3.1** for a detailed description of the 3D modeling processes used to create all of the 3D designs. Finally, **Section 3.4.2** presents the analytical, theoretical and experimental characterization of the *layer*-based 3D μ-CGG design, followed by demonstrations of its utility as a tool towards further bacteriological drug screening applications.

3.3 Materials and Methods

3.3.1 Three Dimensional Modeling

All of the 3D μ-mixer concepts were designed using Solidworks, as described in **Section 2.3.1**. Each of the individual inlet/outlet geometries, smooth-walled and 3D μ-mixer-incorporated microchannels and hollow bulbs were all designed as individual part files. For the *layer*-based 3D μ-CGG design as shown in **Fig. 3.4**, these components were designed as thin-walled structures (thickness of 375 μm) with hollow regions defining the microchannels themselves. For the *tetrahedral*-based 3D μ-CGG design however, as shown in **Fig. 3.5a**, the negative of the microchannel network design itself was first modeled (whereby the hollow regions inside each microchannel and bulb in the conceptual microchannel network become the new solid body; the impression of any intra-channel 3D microstructure is reflected on the outer surface of the model). Each individual node (comprised of one hollow bulb, one vertical microchannel and multiple smooth-walled microchannels from individual part files) was first assembled as a sub-assembly. Then, the nodal sub-assemblies were all mated into one primary assembly, which is subsequently saved as a new single part file. This model can be directly imported into the theoretical simulation software, as is described in the next section. Finally, to create the manufacturable *tetrahedral*-based 3D μ-CGG model as illustrated in **Fig. 3.5d** from the main microchannel network part file, a single solid triangular-shaped body as shown in the figure is first designed and saved as separate part. Then, the two parts are mated in an assembly, and the *cavity* feature in Solidworks is used to perform a Boolean subtraction of the microchannel network part file from the main body part file, creating a 3D hollow microchannel network which is saved as separate part file.Conceptual illustrations of all models were created using PhotoView 360 from an aforementioned final design part file, which were also used to export the .STL files for fabrication.

3.3.2 Theoretical Simulations of Flow Rate and Concentration Distribution

Theoretical simulations using COMSOL were performed to visualize qualitatively, as well as determine quantitatively, the mixing quality at all of the discrete fluid outlets on each of the following 3D μ-CGG device models:

- *Layer*-based 3D μ-CGG device (model shown in **Fig. 3.4**)
- *Tetrahedral*-based 3D μ-CGG device with *smooth-walled* vertical channels (**Fig. 3.13b**)
- *Tetrahedral*-based 3D μ-CGG device with integrated 3D *bulbous* μ*-mixers* (**Fig. 3.13c**)
- *Tetrahedral*-based 3D μ-CGG device with integrated 3D *rifled* μ*-mixers* (**Fig. 3.5**)

A negative solids model of each of the designs is created in Solidworks, only for use in the COMSOL studies. Each of these negative solids model part files are imported into separate COMSOL files to perform each individual study, after which a physics-controlled mesh with a normal element size is applied to the model.

The physics coupling, equations and parameters implemented in each simulation are identical to those described for the theoretical simulations of the 3D μ-mixer devices. For these simulations, however, each of the three horizontal faces on the three protruding inlet microchannel regions on the top of the microchannel network model are selected as input fluid boundary condition surfaces representing the regions where three theoretical fluid inputs are defined. Each face on the bottom of the model representing the outlet each microchannel is selected as the only fluid outlet boundary condition surfaces, and all other faces are selected as surfaces for the no-slip solid wall boundary condition. To assign input concentration species, one distinct input species (C_1) is assigned to one of the three fluidic inlet surfaces (referred to as *Inlet #1*), and another input species (C_2) is assigned to both of the two remaining fluidic inlet surfaces (referred to as *Inlet #1* and *Inlet #2*, respectively). As with the previously presented μ-mixer devices simulations, the standard material properties of water as shown in Appendix **Table 7.1** were chosen and modeled for the input fluids, and the two input species are defined with the diffusivity constant of fluorescein molecule in water at 25 $^\circ$ C with initial concentrations $C_{1,o}$ = 1 mol/m^3 and $C_{2,o}$) = 0 mol/m^3. Finally, a parameter sweep of discrete input flow rates from 10 to 4000 μL/min as shown in Appendix **Table 7.3**, was assigned to all three input fluids

The ultimate objective each study is to quantify the concentration of C_1 present at every location, especially at each of the outlets of the device. To this end, a unit-less metric of normalized concentration (N) is introduced as defined by Eq. 3.5,

$$N = \left| \frac{c_1}{c_{1,0}} \right| \tag{3.5}$$

The effect of the combination, mixing and splitting of each of the three input fluids at each node upstream in the gradient generator microchannel network results in various distributions of C_1 at each outlet, which is reflected by the normalized concentration ranging in magnitude from N = 1 (textiti.e. at that location the concentration of C_1 = $C_{1,o}$) to N = 0 (a complete absence of C_1, *i.e.* C_1 = 0). Alternatively, the normalized concentration of C_1 can also be presented in the form of a percentage of $C_{1,o}$, (*e.g. 69% C_1 at a given device output*), and is referred to as such in **Fig. 3.8,3.10,3.14,3.16-3.19**.

When the simulation is run, the physical equations are solved and the normalized concentration is calculated at every location inside the solids model. The resulting physical distribution of normalized concentration solutions can then be visualized on the outer surfaces (along the inner wall of the actual microchannels), on the outlet faces (on the fluid profiles at the outlets of the actual microchannels) and on discrete profiles perpendicular to the axial fluid flow inside the model.

Visualizations of select simulation results, all at input flow rates of 1 mL/min, are presented. The result of the simulation of the *layer*-based 3D μ-CGG device is presented in **Fig. 3.8** and discussed in **Section 3.4.1.1**. The results of the simulations of various *tetrahedral*-based 3D μ-CGG devices are presented in **Fig. 3.13** and discussed in **Section 3.4.2.1**. These visualizations are used to qualitatively compare the distribution of species C_1 throughout the microchannel networks. A critical assumption was made when undertaking the theoretical study of all of the models developed in this work, that due to the symmetry of all of the microfluidic networks designed, the results for the normalized concentration of C_1 when assigned to microchannel Inlet #1 will be identical to the results when C_1 is assigned to Inlets #2 & #3. Therefore in this work, only one input species arrangement was assigned and tested, that is C_1 assigned as the input to Inlet #1. In all of these visualizations, a 100% concentration C_1 at any location inside the microchannel network is represented by the color red, 0% concentration C_1 is represented by the color blue and any diluted concentration of C_1 is represented as a color in a gradient between blue and red. The single quantitative value calculated by each simulation is defined as the average normalized concentration value on the entire face of each outlet on each of the microchannels in the model. This represents the average normalized concentration of C_1 in an infinitesimally-small volume of fluid at the outlet of the microchannel of the actual device. Upon completion of each simulation, one normalized concentration value is produced for each flow rate simulated as defined in the parameter sweep. These simulation results are plotted and the quantitative analysis shown in **Sections 3.4.1.1, 3.4.2.1**.

3.3.3 Fabrication and Post-Processing

Both of the 3D μ-CGG designs featured in this work were fabricated from the same materials, using the same equipment and were processed using the same post-processing procedure as previously detailed in **Section 2.3.3**. To assist in the post-processing procedure to remove the wax-based support material from the interior of the *layer*-based 3D μ-CGG prototype (as seen in **Fig. 3.9**) microchannel network, horizontally-arranged microchannel outlets on the exterior of the vertical channels, specifically designed for the purposes of wax removal, permitted easy access to the high density of microchannels and hollow mixing bulbs on the second horizontal layer of the device, and proved instrumental in enabling complete removal of the support material from the fabricated prototype device during post-processing. Upon completion of the post-processing procedure, these inlets were subsequently plugged using stainless steel catheter plugs (SP20/12, *Instech*) and permanently sealed using JB Weld epoxy (*The J-B Weld Company*, GA, USA). The microchannel network comprising the *tetrahedral*-based 3D μ-CGG design, on the other hand, features a symmetric arrangement of tetrahedral-based microchannel nodal units. The symmetry of this microchannel network produces more symmetric fluidic resistance layer-to-layer than the microchannel network comprising the *layer*-based 3D μ-CGG design. This symmetry of fluidic resistance permits more uniform and symmetric fluid flow from each of the inlets, throughout the fluidic network and out the outlets of the prototype (as seen in **Fig. 3.15**); therefore, the addition of superfluous inlets to assist in post-processing were deemed unnecessary and not designed in the prototype, which was confirmed to be an accurate assessment, as all of the support material was removed from the fabricated prototype during post-processing.

3.3.4 Experimental Setup

In order to assess the efficacy of various concentrations of antimicrobial drugs on bacteria metabolism, the experimental procedure involves three sequential procedures: *(i)* generating a gradient of antimicrobial drug solutions using the fabricated 3D μ-CGG device, collecting the fluid samples and adding bacteria metabolism indicator and bacteria culture solutions; *(ii)* incubating the samples to facilitate bacteria metabolism; and *(iii)* fluorescent imaging and data analysis to quantify the magnitude of bacteria colony growth.

3.3.4.1 Device Operation and Fluid Collection

Fig. 3.6a shows a conceptual rendering of the *layer*-based 3D μ-CGG device incorporated into the setup for visualization purposes, however this setup was used throughout all of the experimental testing of both the *layer*-based and the *tetrahedral*-based 3D μ-CGG device designs. Images of

the actual fabricated experimental fluidic testing setups are shown in Appendix **Fig. 7.11** for the *layer*-based 3D μ-CGG device and in Appendix **Fig. 7.12-7.18** for the *tetrahedral*-based 3D μ-CGG device. All of the constituent fluidic elements in the experimental setup were interconnected using the tubing and steel couples as previously described in **Section 2.3.4**, and similarly all experiments were performed at temperatures of roughly 20 to 25 °C. The MAESFLO microfluidic pressure controller system (*Fluigent*, Paris, France), which is comprised of both the Microfluidic Flow Control System (MFCS) micro-controller and the FLOWELL microfluidic flow sensor platforms and is programmable using the MAESFLOW-dedicated software (*Fluigent*) installed on the computer at the work station, reduces high air pressure delivered from a building source of pressurized air at roughly 7 ATM and delivers precisely-controlled air pressure to three independent fluid reservoirs. Each reservoir contains one of three distinct fluidic species (*e.g.* illustrated in the figure as three distinct antibiotic species) and is interconnected to one of the three respective inlets to the prototype device. Before running each experiment, FLOWELL microfluidic flow sensors (*Fluigent*) controlled using the Microfluidic Flow Control System (MFCS) by Fluigent were placed in-series with fluidic tubing between the fluid reservoirs and the tubing routing to the device. Air pressure was then generated and delivered to the fluid reservoirs, measured by the flow rate sensors, and the air pressure value adjusted until the measured pressure-driven volumetric flow rate reached 1000 μL/min. This air pressure is slightly different each time in the experiments due to various factors including the orientation of all routing tubing, the length of tubing used and the height of the outlet tubing interface relative to the bench top, therefore the appropriate air pressure value found before running each experiment is fixed for the duration of that experiment. This single operational volumetric flow rate was chosen because it was observed during initial testing of both prototypes that around this value, the fluid flow through the prototypes was sufficient to fill all of the interconnected fluid collection tubing attached to each outlet of the device in approximately 30-60 seconds. Slower input flow rates (down to around 500 μL/min) resulted in longer times needed to fill all of the fluid collection tubing which extended the operational time longer than one minute and was deemed too time-intensive. At even slower flow rates (below 500 μL/min) the fluidic resistance of the fluid collection tubing added sufficient resistance as to stop the flow of fluids out of select outlets, which would negatively impact the flow dynamics within the gradient generation network itself. At higher fluid flow rates (larger than 1000 μL/min), waste volume was produced out of the outlets which experienced the highest output flow rates while the outlets which experienced the lowest output flow rates needed longer time to fill the fluid collection tubing, which was deemed too wasteful. Therefore, throughout the numerous experiments on both prototype devices the pressure-driven volumetric flow rate from the fluid reservoirs to the inlets of the to the device was maintained at 1000 μL/min.

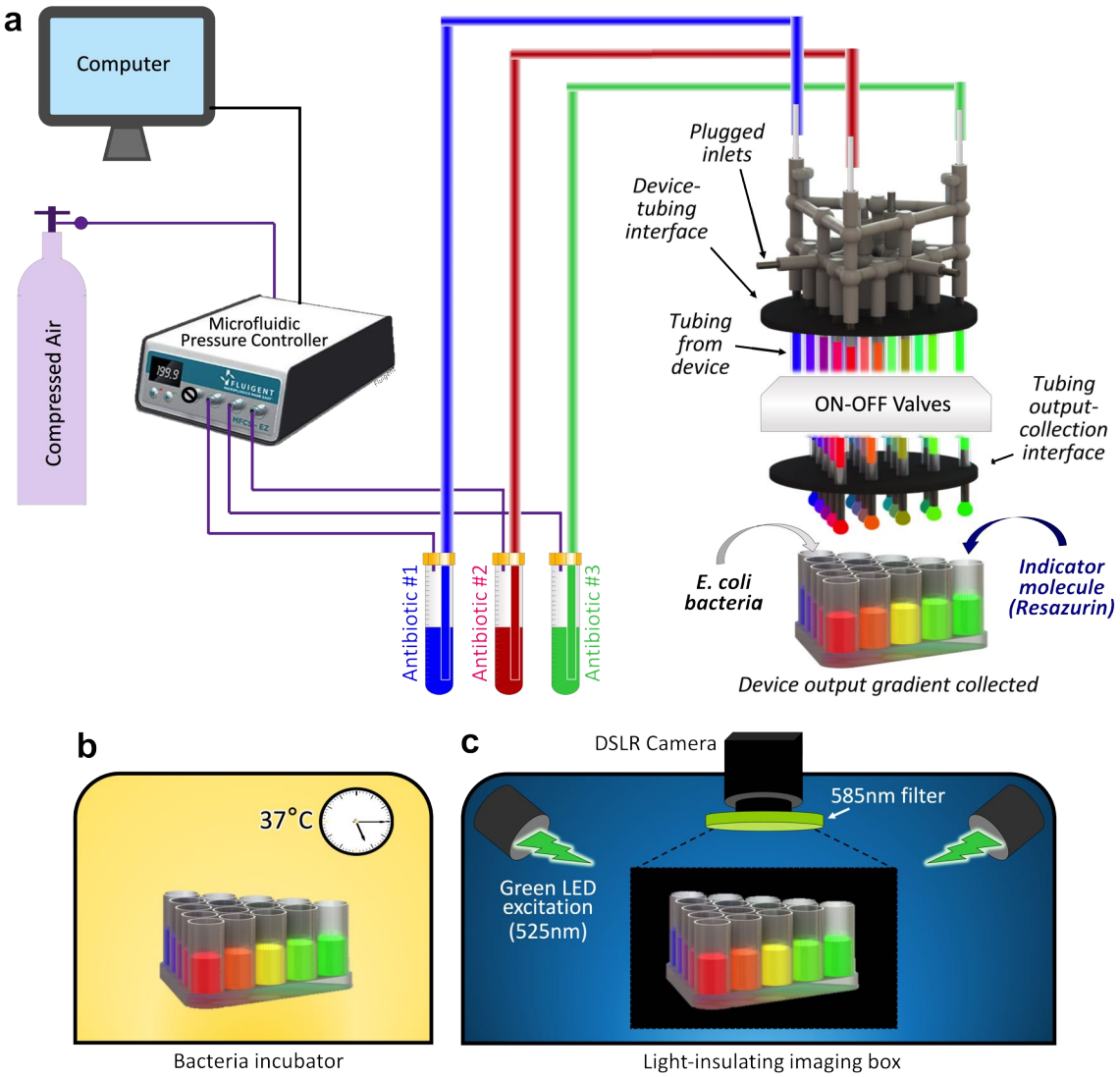

Figure 3.6: Conceptual illustrations of the experimental setup used to perform operation of both the *layer*-based (shown for visualization purposes) and the *tetrahedral*-based 3D μ-CGG devices, bacterial incubation and fluorescent imaging. **(a)** Tubing (*purple*) and steel couples (*silver*) are used to interconnect all independent elements of the fluidic system. A microfluidic pressure controller drives fluids in three independent reservoirs at a constant flow rate into the three inlets of the 3D printed microfluidic prototype device. The discrete concentration gradient outputs from the device are routed to corresponding wells on a fluid collection receptacle. Prepared bacteria metabolism indicator and antibiotic-resistant *E. coli*) bacteria culture solutions are then pipetted into each well. **(b)** The fluid collection receptacle is then incubated at 37°C in a bacteria incubator. (**c**) Finally, the receptacle is placed inside the light-isolation imaging box setup, employing using a green LED excitation light source and optical filter, to perform fluorescent imaging used to quantify the magnitude of bacteria growth in the presence of different concentrations of various antibiotics.

The horizontal exposed microchannel outlets on the *layer*-based 3D μ-CGG device serve the function in the post-processing procedure of removal of the wax-based support material. They were plugged using catheter plugs (*Instech*) and permanently sealed using JB Weld epoxy (*The JB Weld Company*, GA, USA). The *tetrahedral*-based 3D μ-CGG device did not incorporate these additional post-processing inlets. Each 3D μ-CGG prototype is then integrated into a hardware mechanism designed to physically hold the device fixed in place so that the inlet tubing, the microchannel network, and the outlet tubing is maintained in a vertical orientation. Images of the actual fabricated experimental hardware used to interface with each prototype are shown in Appendix **Fig. 7.11** and in Appendix **Fig. 7.13-7.18** for the *layer*-based 3D μ-CGG device and the *tetrahedral*-based 3D μ-CGG device setups, respectively.

During operation, the fluids are driven from the source fluid reservoirs at 1 mL/min under a constant pressure, through the device, and the resulting fluid gradient is routed through outlet tubing which is spatially arranged using different orientating hardware designed to align the tubing with different fluid collection receptacles for each prototype design, and the fluids permitted to drain into a waste receptacle for one minute. This time is to allow the fluid flow throughout the gradient generating microchannel network to reach steady state conditions and for the produced fluid outputs to flush through the entirety of each outlet tubing, ensuring that each outlet tubing contains the volume of fluid from a single experimental operation. After one minute of steady fluid flow, the forward driving pressure is shut off and the fluids stop flowing through the device, as a vacuum is generated in the fluidic network, originating inside the fluid reservoirs with the only exposed end of the fluidic network being the outlet of each segment of output tubing.

For the *layer*-based 3D μ-CGG device, a 3D printed triangular-shaped collection receptacle (15-wells of volume 200 μL each, fabricated using the same material and post-processing protocol as used to create the 3D μ-CGG device itself) is used to collect the fluid outputs, and each of the ends of the output tubing are manually aligned with and positioned over each of the respective outlets. The orientation of the device outputs with specific wells on the collection receptacle are recorded in a lab notebook for reference during image analysis. For the *tetrahedral*-based 3D μ-CGG device the ends of the output tubing are orientated using a 3D printed tray such that each aligns with the center of a single well on a standard 96-well plate, as shown in Appendix **Fig. 7.15**. A standard 96-well plate is used to collect the fluid outputs, in lieu of the custom-fabricated fluid collection receptacle.

A crucial operational requirement for both experimental setup designs is the use of some mechanism to function as a form of *on-off valves*, which is used to prevent back-flow throughout the network of tubing and through the device itself, whilst allowing the fluids to drain from each of the outlet tubes into the the fluid collection receptacle. If such a mechanism was not employed, for example if the three inlet tubes were suddenly physically removed from the top of the prototype, the vacuum holding the fluids inside the network is broken and as fluid drains from one segment of tubing it is replaced by fluid farther up from the fluidic network inside the prototype itself, contaminating the purity of the steady-state gradient generator output samples originally contained in each

of the tubes. Therefore this mechanism of *on-off valves* must be placed after an initial segment of tubing leading from the outlets of the prototype itself, as illustrated in **Fig. 3.6**.

This was made possible for the *layer*-based 3D μ-CGG device by attaching two segments of tubing in-series to each of the outlets of the device (the joint between these two segments, accomplished using a steel couple between the two ends of the tubing, for each of the output tubing elements is hidden from view by the white styrofoam holder as shown in Appendix **Fig. 7.11**). After the fluid flow through the device is stopped, the end of each of the tubes is aligned with its dedicated well on the 3D printed collection chamber, the two segments of tubing are separated from one another and the fluid drains from the now-independent segment of tubing into the chamber, yet the vacuum is maintained in the fluidic network. This procedure is then repeated until all fluids are collected in the receptacle. The volume output from each of the latter segments of tubing from each outlet was controlled by cutting each segment of tubing to the same length, in order to contain 30 μL volume.

To experimentally test the *tetrahedral*-based 3D μ-CGG device, an improved experimental setup was designed and constructed, as seen in the images and descriptions of the actual setup used as shown in Appendix **Fig. 7.12-7.15**. This setup employs a more proper form of a mechanical *on-off valve* mechanism. As shown in Appendix **Fig. 7.14**, a 3D printed T-junction was designed with 13 independent microchannel elements (a linear microchannel with an outlet in the center oriented outwards at 90 °, all inner diameters 750 μm) incorporating an inlet (from tubing routing from each outlet of the device) and an outlet (to the latter segment of tubing leading to the fluid collection receptacle). Steel couples are inserted into all 39 inlets to this component and all segments are sealed using hot glue for water-tightness. During operation, a solid block of 3D printed material with 13 holes designed to be aligned with, and fit tightly around, all of the 13 exposed steel couples is attached to the T-junction, effectively shutting *off* these microchannel outlets and creating effectively-linear microchannels. The 3D printed block is shown as attached to the T-junction in Appendix **Fig. 7.14**. Therefore when forward fluid driving air pressure is shut off, the vacuum in the fluidic setup is created. When the 3D printed block is removed, however, all 13 microchannel elements suddenly gain an additional outlet which is exposed to ambient pressure, which permits all of the fluids to drain from the now-exposed latter segments of tubing into the 96-well plate for fluid collection. Employing this approach, as compared to the approach used in the *layer*-based 3D μ-CGG device experimental setup, involves significantly less manual labor and expedites the fluid collection procedure, reducing the time to collect all of the device outputs from around 10 minutes to only about 5 seconds. The orientation of the outlet tubing routing to the wells on the 96-well plates is illustrated in the diagram shown in Appendix **Fig. 7.19**.

Between each experiment where different antibiotic species are used as inputs into the device, both fluidic reservoirs are filled with a 70% ethanol solution and run through the fluidic network, removing any residue of previous solid species from inside the device. For the experiments pertaining to the *tetrahedral*-based 3D μ-CGG device, each fluid collection experiment for a specific combination of input fluidic samples was performed in triplicate and collected on two 96-well

plates. Prior to the bacteriological experiments, however, flow verification experiments are performed on each prototype in order to empirically validate the fluid flow characteristics of each of the concentration gradient generation microchannel networks (as will be described in the following sections). To do so, the exact same device operation and fluid collection procedure is followed. For the flow verification experiments performed on the *layer*-based 3D μ-CGG device, however, one solution of fluorescein in de-ionized (DI) water and two solutions of pure DI water are used as the fluidic inputs, and a green optical filter is used in front of the camera lens. Similarly, for those experiments performed on the *tetrahedral*-based 3D μ-CGG device, one solution of rhodamine in DI water and two solutions of pure DI water are used, and a red optical filter is used.

3.3.4.2 Bacterial Incubation

For the bacteriological experiments, after all of the fluidic outlets from the 3D μ-CGG device (30 μL each) are collected in their corresponding wells, two pre-prepared solutions (in aliquots of 30 μL each) are manually-pipetted into each well: *(i)* a solution of a bacterial metabolic indicator molecule called *resazurin* and *(ii)* an inoculation of ampicillin-resistant *E. coli* bacteria.

Resazurin is most frequently available as a sodium salt powder, dark blue in appearance, and serves the function of an oxio-reduction indicator, as the cellular electron receptors that are used in metabolic activity chemically-reduce the molecule to produce the molecule resofurin, which is bright pink in appearance. The rate of reduction of resazurin into resorufin occurs proportionally to the rate of respiration of cells in the medium, therefore the use of resazurin is proven to be a simple, accurate and reproducible method to quantifiably assess the metabolic activity of organisms including animal cells, fungi and bacteria during both aerobic and anaerobic respiration, having been previously demonstrated in numerous cell viability, culture and proliferation assay protocols. [240, 266–268] Additionally, the resazurin oxio-reduction process has been shown to be more sensitive to slighter changes in bacterial density or metabolic conditions than accomplished using conventional optical density-based measurement methods, and therefore is often accepted as a higher-sensitivity method to indicate cellular metabolism than optical analysis in many bacterial viability assays [205].

For example, a conceptualized cell viability assay for MIC determination using resazurin is illustrated in **Fig. 3.7**. Here, bacteria and resazurin solutions are each added to two separate wells on the fluid receptacle containing two different concentrations of antibiotic solutions, in one well antibiotic below its MIC value for that specific bacteria (*top*) and in one well antibiotic higher than its MIC value (*bottom*). Upon incubation, the bacteria in the *top* well proliferate in the presence of the sub-MIC value concentration of antibiotic and therefore metabolize the resazurin in the solution, eventually reducing all of the resazurin into resorufin and turning the color of the entire solution visibly pink (due to the color of the resorufin molecule). The proliferation of the bacteria in the *bottom* well is inhibited, however, by the antibiotic, therefore over the same course of time

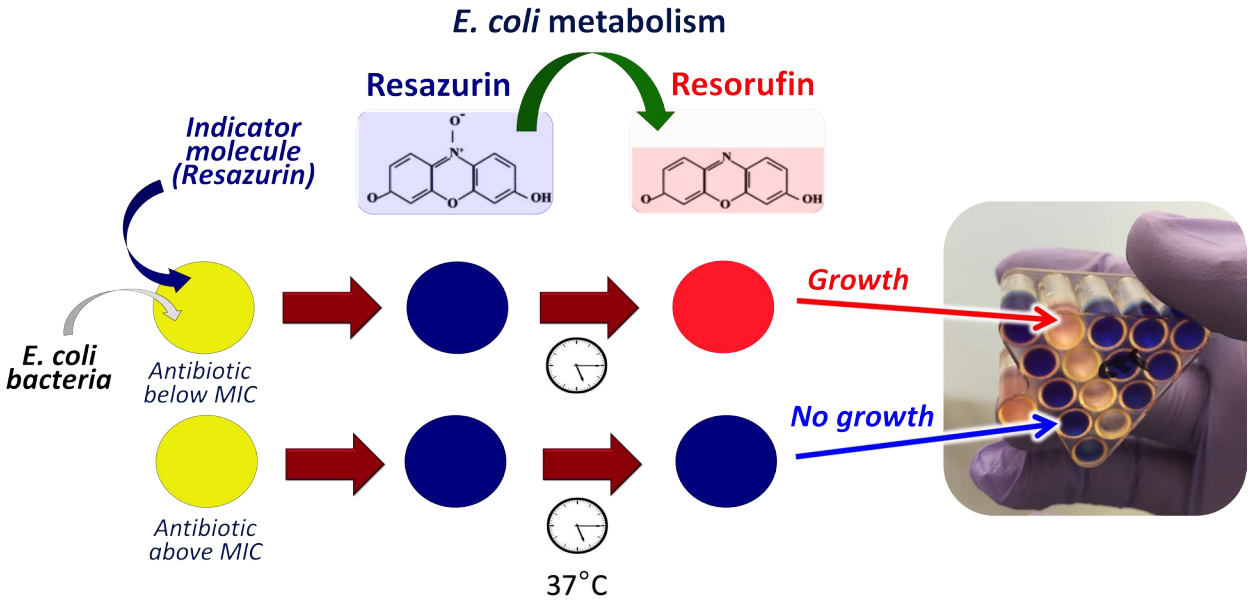

Figure 3.7: Conceptualized cell viability assay for MIC determination of a specific antibiotic for a specific strain of bacteria, showing the reduction of resazurin into resorufin during incubation and the associated color change of the fluid samples in two wells with two different concentrations of antibiotic solutions: below the MIC value in the *top* well, where uninhibited bacterial proliferation signified by the reduction of resazurin turning the fluid sample from blue to red; and above the MIC value in the *bottom* well, where no resorufin is produced keeping the well blue. Also shown is an image (*far right*) of an actual demonstration experiment employing a 3D printed fluid receptacle where the labeled wells contained antibiotic below the MIC value, the rest contained antibiotic above the MIC value, showing the potential for the resazurin method to be used as a qualitative *growth-no growth* metric of cell viability.

during incubation none of the resazurin is reduced and the well remains visibly blue. This color change is often used as a qualitative *growth-no growth* metric in basic cell viability assays, as can be seen on the *righthand* side of **Fig. 3.7** showing an image of an actual experiment employing a 3D printed fluid receptacle where the four labeled wells contained antibiotic below the MIC value, the rest contained antibiotic above the MIC value. Once the three fluid solutions are added to the wells, the fluid receptacle is placed inside a temperature- and CO_2-controlled bacteria incubator and incubated at 37 ° C in 4% CO_2 as illustrated in **Fig. 3.6b**. The duration of incubation of $\sim$100 μL volumes of bacteria solutions in standard micro-broth dilution resazurin protocols typically varies from $\sim$3 hours [266] to $\sim$12 hours [269], and can be as high as 24 hours using conventional macro-broth dilution techniques [270]. In the protocol used in this work, the fluid receptacles are incubated an average of $\sim$5 hours, until a visible gradient of colors is observed, as can be seen in actual images of the experimental results from *layer*-based 3D μ-CGG device testing in Appendix **Fig. 7.22b,c,e** and from *tetrahedral*-based 3D μ-CGG device testing in Appendix **Fig. 7.22f** and Appendix **Fig. 7.31**. A fluid sample containing 30 μL of bacteria culture solution, 30 μL of resazurin solution and 30 μL of nutrient solution (representing 0% antibiotic) was loaded onto

wells on each of the fluid receptacles and used as a control; incubation was considered completed when a color gradient was observed from dark blue to bright pink.

3.3.4.3 Fluorescent Imaging

In all verification experiments, for the *layer*-based 3D μ-CGG device, fluorescein distribution amongst the device output fluid samples is imaged using a green bandpass optical filter (43MM X 10MM, W6307, *Omega Optical*) placed in front of of the optical lens of the DSLR camera protruding into the box in order to isolate the fluorescence emission of fluorescein. Additionally, for the *tetrahedral*-based 3D μ-CGG device, rhodamine distribution amongst the device output fluid samples is imaged using a red bandpass optical filter (43MM X 6MM, W6308, *Omega Optical*) in order to isolate the fluorescence emission of rhodamine. A custom-designed optical filter holder was designed, 3D printed and attached to the front of the camera lens, used to suspend the inserted optical filters in front of the lens itself, covering the full view of the camera. In all bacteriological experiments, after incubation the fluid receptacle is transferred to the fluorescent imaging experimental setup as illustrated in **Fig. 3.6c**, and placed inside the light-isolation box as described in **Section 2.3.4** (actual images and detailed descriptions of the setup's construction are presented in Appendix **Fig. 7.15,7.16**), which serves to block out all external background light. Resazurin cell viability protocols are also well suited for quantitative analysis *via* fluorescent microscopy [268], because whereas resazurin is a weakly-fluorescent molecule, resofurin, which is highly-fluorescent with a peak excitation energy at $\sim$579 nm and peak emission energy at $\sim$584 nm. Therefore for all bacteriological experiments, a strip of green LED lights attached to the ceiling of the box serves as a source of top-down excitation of resorufin in the fluid samples using green light [266]. Since the peak fluorescence emission energy of resorufin is $\sim$584 nm, a 585 nm optical filter [271] (*Omega Optical*, VT, USA) is placed in front of of the optical lens of the camera. The filter serves to best isolate any interference caused by the fluorescence of resazurin, the fluid receptacle itself and background light noise. (Appendix **Fig. 7.30** summarizes the optical properties, including emission and excitation wavelengths, bandpass range, of all chemicals, fluorophores, emission sources and optical filters used throughout this work.) Finally, the lens focus is manually-adjusted every time that a fluid receptacle is placed into the box, and the image settings are manually-adjusted to create optimum brightness and contrast in the images (camera aperture f-stop of 1/5.6, ISO 800 and exposure of 0.25 seconds, see example camera view in Appendix **Fig. 7.18**).

3.3.5 Data Acquisition and Quantitative Analysis

As previously mentioned regarding the flow verification experiments performed on the *layer*-based 3D μ-CGG device, one solution of fluorescein and two solutions of DI water are used as the fluidic inputs. It must be noted that a critical assumption was made during the planning and performing of

these experiments. Due to the symmetry of the microfluidic design, the distribution of one species when input into microchannel Inlet #1 will be identical to that achieved when inputting said species into Inlets #2 & #3. Thus working under this assumption, the fluid verification experiments for this fabricated prototype design were only performed by inputting the fluorescein solution into one of the prototype device inlets and inputting the DI water into the other two inlets, collecting and analyzing the results of the fluorescein distribution (as presented in **Section 3.4.1.3**), and assuming that this distribution is symmetric for all three input species. The results of this experiment are presented in **Fig. 3.10**.

During the phase of this project entailing the development of the *tetrahedral*-based 3D μ-CGG device, however, upon further consideration, it was decided that such an assumption cannot be reasonably made, since the nature if the 3D printing process itself, like practically every manufacturing process to some degree, will introduce some form of physical structural or material asymmetries inside the physical fabricated prototype (*e.g.* randomized reductions in the hydraulic diameter in random locations in microchannels due to polymer deposition error or material warpage during printing). Since the upper limit of resolution of the 3D printer is stated as on the order of 10's of μm, a conservative estimation of the geometrical inaccuracies can be assumed to be on the order to 50-100 μm, an average of 75 μm, which is roughly 10% of the scale of the as-designed hydraulic diameter of the microchannels, and is roughly 50% of the size of the 3D rifling microstructures used inside the 3D rifled μ-mixer-incorporated channels in the fabricated prototype design. It was therefore surmised that such errors are more than likely to induce even slight asymmetries in the distribution of the three distinct fluidic input species throughout the microchannel network. Thus, three separate flow verification experiments were performed on the *tetrahedral*-based 3D μ-CGG prototype device in order to analyze the distribution of each of the three inlet fluids separately. To this end, one solution of rhodamine in DI water and two solutions of pure DI water are used; each of the three separate experiment entailed using the rhodamine as the fluidic input to one of the microchannel inlets and DI water as the input to the other inlets, such that separate rhodamine distributions were collected when using rhodamine as the input to microchannel Inlets #1, #2 & #3. The results of these experiments are presented in **Fig. 3.16**.

For any experiment, when imaging any fluid receptacle, one image is taken with the center of each well aligned with alignment mark on the center of the camera eyepiece. The fluid receptacle is manually re-positioned for each image. The number of the well (position on the fluid collection receptacle) for each image and the image file name (as read off of the camera display) are both recorded in a lab notebook. All experimental images are analyzed using Fiji image processing software, pursuant slightly different image analysis protocols involving: (*i*) flow verification experimental imaging of rhodamine and fluorescein and (*ii*) resazurin-based bacteriological experimental imaging of resorufin. The data acquisitoin and quantitative processing procedures used for each type of experiment are briefly summarized below.

3.3.5.1 Flow Verification Experimental Fluorescent Image Analysis

For further details of the image analysis protocol, see Appendix **Section 7.3**, *Protocol For Producing Normalized Fluorescent Concentration Values from Flow Verification Experimental Fluorescent Image Analysis* and Appendix **Fig. 7.33**.

The sets of images analyzed from the *layer*-based μ-CGG design experiments are as follows:

- Fluorescein into device Inlet #1 (DI water into all other inlets)
- Separate well containing a 30 μL aliquot of pure DI water (0% control well)
- Separate well containing a 30 μL aliquot of pure fluorescein solution (100% control well)

The sets of images analyzed from the *tetrahedral*-based μ-CGG design experiments are as follows:

- Rhodamine into device Inlets #1 (DI water into all other inlets)
- Rhodamine into device Inlet #2 (DI water into all other inlets)
- Rhodamine into device Inlet #3 (DI water into all other inlets)
- Separate well containing a 30 μL aliquot of pure DI water (0% control well)
- Separate well containing a 30 μL aliquot of pure rhodamine solution (100% control well)

Briefly, for each image using Fiji: (*i*) a circle is drawn to fully enclose the fluid sample well in the center of the image, (*ii*) the green (for fluorescein) or red (for rhodamine) RGB stack channel (best enhancing the contrast of the fluorescence intensity of the emission from the respective florophore from the background) is selected, and (*iii*) the average pixel intensity inside the circular area is calculated and stored as raw data.

The metric used to quantify the amount of florophore in each well will be called the Normalized Fluorescent Concentration value (arbitrary units), and is calculated for each device output fluid sample from a given collection of experimental images. This metric is defined by normalizing the magnitude of fluorescence intensity (amount of florophore fluorescent emission) of a given well containing the fluid sample generated from the gradient generator device and containing a certain percentage of the input florophore concentration, to that present in the 100% control well (maximum concentration of florophore) [266].

To calculate this value, the raw data is put into an Excel workbook and the software used to calculate the Normalized Fluorescent Concentration for a given well of interest as the magnitude of the average pixel intensity from said well, minus the average pixel intensity from the 0% control well representing background fluorescence noise, divided by the magnitude of the average pixel intensity from the 100% control well representing the pure concentration of florophore emission, minus the average pixel intensity from the 0% control well. This calculation is performed on all cells representing the raw fluorescent magnitude values in fluid receptacle wells. For the data from the experimental tests of the *tetrahedral*-based μ-CGG design, an average and standard deviation of the Normalized Fluorescent Concentration values previously calculated are taken. These data can now be plotted using Excel.

3.3.5.2 Bacteriological Experimental Fluorescent Image Analysis

For further details of the image analysis protocol, see Appendix **Section 7.3**, *Protocol For Producing Normalized Growth Values from Bacteriological Experimental Fluorescent Image Analysis*.

The images analyzed from the *layer*-based μ-CGG experiments are as follows:

- Nitrofurantoin into device Inlet #1 (LB media into all other inlets)
- Tetracycline into device Inlet #1 (LB media into all other inlets)
- Trimethoprim into device Inlet #1 (LB media into all other inlets)
- Nitrofurantoin into device Inlet #1, Tetracycline into device Inlet #2, Trimethoprim into device Inlet #3
- Separate well containing a 30 μL aliquot of pure LB media (0% control well)
- Separate well containing 30 μL LB media, 30 μL resazurin solution and 30 μL antibiotic solution (100% control well)

The images analyzed from the *tetrahral*-based μ-CGG experiments are as follows:

- Tetracycline into device Inlet #1 (LB media into all other inlets)
- Ciprofloxacin into device Inlet #1 (LB media into all other inlets)
- Amikacin into device Inlet #1 (LB media into all other inlets)
- Tetracycline into device Inlet #1, Ciprofloxacin into device Inlet #2

- Amikacin into device Inlet #1, Ciprofloxacin into device Inlet #2
- Tetracycline into device Inlet #1, Amikacin into device Inlet #2
- Amikacin into device Inlet #1, Ciprofloxacin into device Inlet #2, Tetracycline into device Inlet #3
- Separate well containing a 30 μL aliquot of pure LB media (0% control well)
- Separate well containing 30 μL LB media, 30 μL resazurin solution and 30 μL antibiotic solution (100% control well)

Briefly, for each image using Fiji a similar procedure to that described in **Section 3.3.5.1** is followed, whereby the average pixel intensity on the green stack image of the region defining each well is calculated and stored as raw data. Bacterial proliferation in each well is quantified using the metric of the Normalized Growth value (arbitrary units), and is calculated for each device output fluid sample from a given collection of experimental images by normalizing the magnitude of fluorescence intensity (from the amount of resorufin produced) of a given well containing a certain percentage of the input antibiotic concentration, to that present in the 100% control well, in this case the maximum growth present in the case where no antibiotic is present [266]. To calculate this value, the raw data is imported into an Excel workbook and the software used to calculate the Normalized Growth value for a given well of interest as the magnitude of the average pixel intensity from said well, minus the average pixel intensity from the 0% control well representing background fluorescence noise, divided by the magnitude of the average pixel intensity from the 100% control well representing the maximum concentration of resorufin produced possible, minus the average pixel intensity from the 0% control well. This calculation is performed on all cells representing the raw fluorescent magnitude values in fluid receptacle wells.

3.3.6 Preparation of Experimental Reagents

The flow verification experiments involve the use of two solutions of organic fluorophores, fluorescein and rhodamine b. Fluorescein has an excitation energy 494nm and a strong fluorescent emission energy peak at 512 nm, and rhodamine b has an excitation energy peak at 540 nm and emission peak at 625 nm [196]. The fluorescein and rhodamine solutions are formulated following the same procedure as discussed in **Section 2.3.6**, by adding 50 drops each of fluorescein and rhodamine solutions separately to 50 mL of DI water in separate beakers. Similarly, the solutions are then wrapped in aluminum foil and stored inside a closed drawer isolated from background light to preserve the fluorescent sensitivity of each solution.

In all bactriological experiments, the three primary constituent fluids used in the bacteria incubation and fluorescent imaging studies consist of: (*i*) antibiotic solutions, (*ii*) resazurin indicator

molecule solution and (*iii*) bacteria cell culture solution. Description of the preparation and formulation of solutions (*i*) and (*ii*) are described in this section and of solution (*iii*) is described in the following section.

The base liquid used to create all fluidic solutions in this work (*e.g.* cell culture stock solution, antibiotic and buffer solutions used as inputs into the microfluidic device and resazurin solution) is a bacteria-specific nutrient-rich solution, Lysogeny Broth growth medium (henceforth referred to simply as *LB medium*), prepared by dissolving commercially-available LB broth powder (LB Broth, Miller, item #L3522, *Sigma-Aldrich*, MO, USA) in de-ionized (DI) water to make a $25g/L$ solution in a 1000mL Pyrex beaker (*ThermoFiser-Scientific*). The beaker is then autoclaved at 120 $^\circ$ C for 25 minutes to encourage the solids to thermally dissolve into the liquid and to sterilize the stock solution. Batches of at least 2 liters of LB media are created each time the autoclave is used. Whenever solids are added to liquids or multiple solutions are combined to create new solutions, sterile 50 mL conical polypropylene centrifuge tubes (339652, *ThermoFisher Scientific*, MA, USA) are used. Once all species are combined, the tubes are aggravated using a vortex mixer (Vortex-Genie 2, *Scientific Industries*, NY, USA) in bursts of 5 seconds for roughly 30 seconds to ensure solution mixing.

To formulate each antibiotic solution, the required mass of each antibiotic powder (all acquired from *Sigma-Aldrich*) is added to a beaker containing 500 mL of LB media to create the desired concentration of stock antibiotic solution. For the exact concentrations of each antibiotic stock solution used in testing of the *layer*-based μ-CGG design (nitrofurantoin, tetracycline and trimethoprim) and in testing of the *tetrahedral*-based μ-CGG design (amikacin, tetracycline and ciprofloxacin), see the Stock Solution data presented in Appendix **Fig. 7.32**. The resorufin salt solution is prepared to a concentration of $\sim$4.4 mM by adding $\sim$5 mg of resazurin salt powder to 50 mL of LB medium. When kept for short-term use during experiments in any given week, the antibiotic solutions (up to two days) and the resazurin solution (up to five days) are kept cold in a -4 $^\circ$ C refrigerator.

3.3.7 Preparation of Cell Suspension

The specific terminology used to describe the growth of bacteria must be clarified. In this work wherever the use of the phrase *bacteria growth* is used, this refers to the increase in the density of bacteria cells in a given volume of liquid bacterial culture media, usually presented in units of colony forming units per milliliter of liquid bacterial stock solution, *cfu/mL*. Here, a single colony forming unit is defined as an individual viable bacterium cell in the given sample, *viable* referring to the ability of each of said cell to reproduce and form a new colony population of cells under the appropriate conditions. [272, 273].

In all experiments, ampicillin-resistant strains of BL21(DE3) gram-negative *Escherichia coli* (*E. coli*) bacteria are used as the target organism (acquired from *New England BioLabs*, MA, USA [274] for the experiments involving the *layer*-based prototype; and from *Agilent Technologies*, CA, USA [275] for the experiments involving the *tetrahedral*-based prototype) , as the antibiotic-resistance of this bacteria is an ideal model to add clinical-relevance to the experiments performing antimicrobial drug testing on antibiotic-resistant pathogens that were demonstrated in this work. The stock bacteria cultures are received on dry ice in 2 mL cryovials in the form of frozen glycerol bacteria stock, and are subsequently stored frozen-down in a -80 ° C freezer. Each time that a series of experiments is planned to take place over a period of 3-4 weeks, a fresh inoculation must be prepared. To make the inoculation, a sterile pipet tip is used to transfer a scraping from the top of one of the glycerol stock tubes and is then placed inside of a 25 mL Nunc Non-treated T25 EasYFlask with breathable filter cap (169900, *ThermoFisher Scientific*) filled with 10 mL of LB medium and incubated in the bacteria incubator overnight. The next day, when retrieved, the solution will be cloudy indicating cellular proliferation. At this point, the bacteria is transferred to an agar plate to create a solid bacteria colony stock and stored in a -4 ° C refrigerator for use up to one month. For details regarding the protocols used for how to make the aforementioned agar plates and agar plate solid bacteria colony stock, see Appendix **Section 7.3**, *Agar Plating Protocols*.

Following the standard set as previously demonstrated by most laboratory-based bacteria cell viability assays [180, 276, 277], antimicrobial drug testing studies in particular [223, 240, 266, 278, 348], a bacterial solution with a cell density of around 10^5 cfu/mL is used in all of the experiments featured in this work. Each time a new round of experiments is planned, a fresh liquid bacteria culture stock must be created. This process begins by harvesting a single colony of bacteria from the solid agar plate media using a sterile pipet tip and placing it into a 25 mL flask filled with 10 mL of LB medium, which is then incubated in the bacteria incubator overnight at 37° C until cloudy, indicating that the bacteria have reached the plateau growth phase and the density is around 10^8 cfu/mL. At this point, the two primary laboratory-based protocols conventionally can be used to quantify the density of bacteria in the sample, the agar plate counting (solid culture) method and the spectrophotometric (liquid culture) method. The agar plate counting method is a time-intensive procedure and can only quantify the population density of a given sample after-the-fact, around 24 hours after an initial sample is taken for analysis, but can quantify density with an accuracy as high as roughly 10's of cfu/mL. The spectrophotometric, or OD600, method employs a spectrophotometer to quantify the absorbance of each wavelength of light transmitted through a liquid culture (known as turbidity) and can provide instantaneous measurements of optical bacterial density (most commonly by measuring the absorptivity of the medium at 600nm, resulting in a measurement known as OD600), but the relationship between turbidity and cell density is only accurately correlated for cell suspensions of around 10^7 cfu/mL and greater. [273]

The method used throughout this work to quantify the initial density of the overnight culture[2] of liquid bacteria stock is the spectrophotometric method [224]. A Vernier UV-VIS Spectrophotometer (*Vernier*, OR, USA) is used to take the OD600 measurement of $\sim$2 mL of the medium (spectrophotometer is initally calibrated to an equal volume of sterile LB media), and an online calculator (E. coli Cell Concentration from OD600 Calculator, *Agilent Genomics*, CA, USA) is used to correlate the raw OD600 measurement from the spectrophotometer (unitl-less value) to a relevant cell density value for *E. coli* in cfu/mL. Once the initial cell density of the overnight culture is quantified, to create the required bacterial solution with a density of around 10^5 cfu/mL, a serial dilution of the high concentration media is performed. For further details regarding the protocol used in this work to measure cell density using the spectrophotometric method and for the serial dilution of the liquid cell culture media to prepare the appropriate 10^5 cfu/mL starting concentration of bacteria stock solution for each experiment, see Appendix **Section 7.3**, *Spectrophotometric Bacteria Density Calculation and Growth Media Preparation Protocols*. Additionally, for details regarding the alternative agar plating method [208], see Appendix **Section 7.3**, *Agar Plating Protocols*. The experimental images shown in this protocol were taken from an experiment performed at the very beginning of this project before the experiments were performed in order to confirm the ampicillin resistance of the cultures strain of bacteria, whereby following standard protocol [280] a concentration of 100 mg/L ampicillin antibiotic stock solution was created and incorporated into the molten agar mixture prior to cooling and bacteria plating. Indeed, proliferation of this strain of bacteria was observed on these agar plates, confirming the ampicillin resistance of the bacteria.

[2] Bacteria, such as *E. coli*, nearly-universally undergo five distinct, well studied, phases of population growth. Bacteria are asexual organisms and reproduce by binary fission. In well-controlled laboratory settings, when a single individual colony forming unit is added to fresh nutrient-rich growth media, after the (*i*) "lag phase" where the organism is adjusting to the chemical dynamics of the new environment, the bacterium begins to reproduce and the population of bacteria increases roughly exponentially, referred to as the (*ii*) "logarithmic phase" of the population growth. In this growth phase, the population of many known strains of *E. coli* doubles approximately every 20 to 30 minutes. Even in initially nutrient-rich media however, after roughly 12 to 24 hours, the depletion of available nutrients eventually stymies bacterial growth, the rate of cellular reproduction and death roughly equilibrate, and the population growth enters the (*iii*) "plateau phase" or "stationary phase", saturating at approximately 10^8 cfu/mL for roughly 24 hours. The eventual accumulation of toxic byproducts of cellular metabolism causes the population to enter the (*iv*) "death phase", where the population will decrease by two to three orders of magnitude, eventually saturating once more due to the availability of nutrients released from the cellular rupture upon the death of most of the population, and remaining constant during the (*v*) "long-term stationary phase. Throughout this phase, which can last weeks to months, some of the surviving cells begin to mutate and the viability of most cells in the population is not assured. Therefore when creating a useful bacterial stock for bacteriological experiments, the standard protocol is to create a bacterial inoculation after overnight incubation to use the bacteria population whilst still in the "stationary" phase, where both the consistency of the population density and the viability of the cells are reasonably assured. [279]

3.4 Results and Discussion

3.4.1 *Layer*-Based 3D Microchannel Network

3.4.1.1 Theoretical Output Concentration Distribution

The predicted gradient generation performances of the *layer*-based 3D μ-CGG design are presented in **Fig. 3.8**. The numbering convention used to label each of the outlets of the device for use in the upcoming experiments is shown in **Fig. 3.8a**, superimposed over a bottom-up view of a rendering of the device design. The equations presented in **Section 3.2.1** were used to analytically calculate the normalized concentration of a single input fluidic species (flow rate Q_1, concentration C_1) at each outlet of the conceptual μ-CGG design (calculations make the critical assumption of complete mixing inside each of the nodal units of the microfluidic network, and are therefore independent of the input fluidic flow rate into the device). The results of these calculations, presented as a percentage of C_1, which was assumed to be input into the microchannel inlet directly

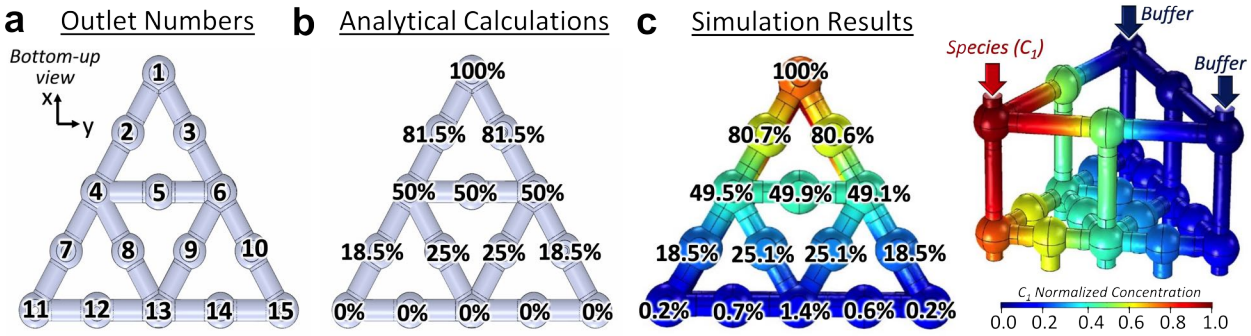

Figure 3.8: Analytical calculations and theoretical simulation results for the distribution of a single input fluidic species concentration at each outlet of the *layer*-based 3D μ-CGG design. **(a)** Map showing the numbering convention of each of the device outlets superimposed over a bottom-up view of the 3D solids model of the device. **(b)** Analytical calculations for the concentration of a single fluidic species (input into device Inlet #1, directly above Outlet #1) at each outlet of the device, superimposed over a bottom-up view of the 3D solids model of the device; concentrations calculated include 100%, 81.5%, 50%, 25%, 18.5% & 0%. **(c)** Theoretical COMSOL simulation results for the concentration of a single fluidic species input into device Inlet #1(*left*) at each outlet of the device, superimposed over a bottom-up view of the visualization of the COMSOL results throughout the device, concentrations simulated include ~100%, ~80.7%, ~80.6%, ~49.9%, ~49.5%, ~49.1%, ~25.1%, ~18.5% & 0%.; and (*right*) an isometric view of a visualization of the COMSOL results for the theoretical distribution of the single input fluidic species throughout the device with symmetric input flow rates of 1000 μL/min, simulating the species of interest (C_1, *red*) input into Inlet #1 and buffers input into Inlets #2 & #3 (*blue*).

above Outlet #1, are shown in **Fig. 3.8b**. Furthermore, a COMSOL theoretical simulation was performed on the solids model of the negative of the microchannel network, pursuant to the protocols as detailed in **Section 3.3.2**. Simulation results for the normalized concentration of a given input species (C_1 input to Inlet #1, buffer solution input to Inlets #2 & #3) at each device outlet at a flow rate of 1000 μL/min are shown in **Fig. 3.8c**. Normalized concentration values as percentages of C_1 are superimposed over a bottom-up view of the distribution of C_1 inside the model (*left*), and an isometric view the distribution for visualization purposes (*right*). The analytical and theoretical results indicate that the fluid outputs of the device, all capturing discrete elements of the generated gradient, represent potentially useful approximate fractional concentrations of C_1 (*i.e.* $\sim\frac{10}{10}$, $\sim\frac{8}{10}$, $\sim\frac{5}{10}$, $\sim\frac{2}{10}$). Moreover, device Outlets #5, #8 & #9 each contain proportions of each of the three input fluidic species (*i.e.* $\sim$50% of the fluidic species from Inlet #1 and $\sim$25% of the fluidic species from both Inlets #2 & #3). This demonstrates the inherent innovation of the 3D fluidic routing accomplished using the 3D fluidic routing capabilities of this particular *layer*-based arrangement of microchannels comprising the *layer*-based 3D μ-CGG design. Finally, as the theoretical normalized concentrations at all outlets are within 10% of the analytically-predicted values, this design is deemed sufficient to move forward with in order to perform experimental characterization of a fabricated prototype.

3.4.1.2 Fabrication Results

In this project, three copies of the *layer*-based 3D μ-CGG design were fabricated on a single build plate, then post-processed, following the procedures as discussed in **Section 3.3.3**. The decision was made to fabricate three different prototypes because it was considered that the thin-walled microchannel structures (thickness of 375 μm) might be so fragile that, upon removal from the build plate or inside the hot mineral oil solution during post-processing, some of the structures might fracture and the prototype damaged beyond repair. Therefore it was decided that fabricating multiple prototypes would increase the chances of yielding a fully-functional device ultimately after the post-processing procedure was complete. This cautionary decision was proven sound, as none of the prototypes broke when being release from the build plate, but various components, an average of one inlet and two outlet microchannel structures, broke off two of the three prototype devices during post-processing. It was observed that during wax removal, the temperature of the mineral oil was sufficiently high as to soften the 3D printed polymer such that the microchannel structures became soft and pliable, and as a result highly vulnerable to fracture. These results motivated the decision to modify the design of the next version of the 3D μ-CGG to eliminate the thin-walled structures and instead fabricate the microchannels as hollow regions inside a solid polymer body, as to lend the prototype structural integrety and robustness during post-processing and testing. This improved design became the *tetrahedral*-based 3D μ-CGG design.To illustrate the concept of the Multijet 3D printing approach used to fabricate the prototypes in this work, **Fig. 3.9a** shows a conceptual rendering of the layer-by-layer inkjet-like procedure during the fabrication of the 3D microchannel network. The print head sweeps in the X-Y plane, selectively

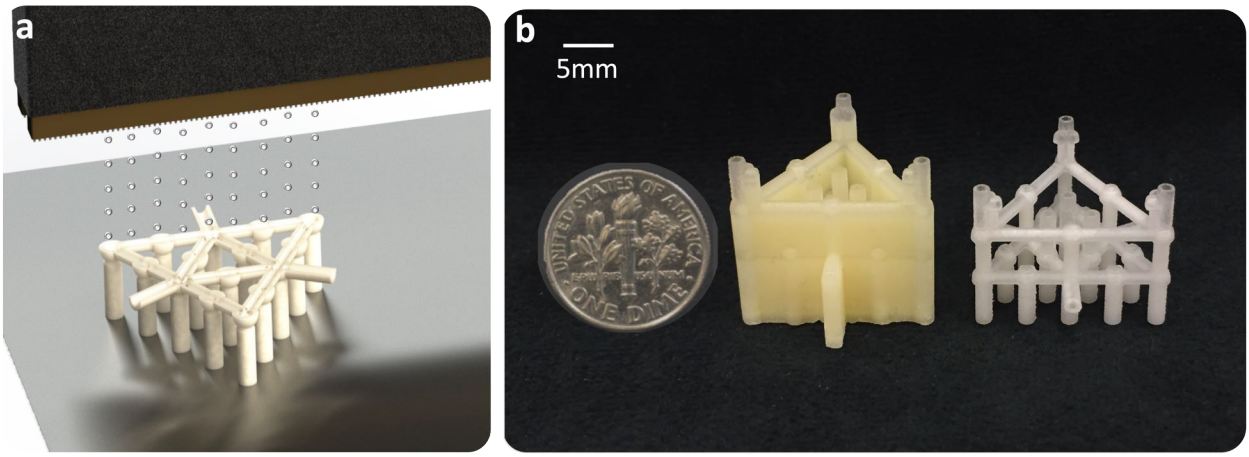

Figure 3.9: Fabrication results, *layer*-based 3D μ-CGG device. **(a)** Illustration of the Multijet fabrication process, conceptualizing micro-droplets of photocurable resin (*silver spheres*) ejected from a print head (*top black and gold rectangle*) onto the 3D printer build plate (*lower grey platform*) to fabricate the partially-constructed *layer*-based 3D μ-CGG device (*in white*). **(b)** Examples of fabricated *layer*-based 3D μ-CGG device prototypes, with a US dime for scale (*left*), pre-post processing (*middle*) with sacrificial wax-based support material (*yellow*), and after post-processing (*right*) revealing stand-alone microchannel structures.

depositing structural polymer micro-droplet (*silver spheres*), then sweeps in the opposite direction to flash-UV cure the polymer. This image shows the second horizontal microchannel layer (*white*) half-constructed. The sacrificial support material is deposited along with the structural material in each layer, but that material is not shown in the rendering.

The results of the 3D printing fabrication process and post-processing procedure are shown in **Fig. 3.9b**, with a U.S. dime (*left*) for scale. The prototype before post-processing (*middle*) is shown exactly as the prototype appears once it is removed from the 3D printer build plate. The yellow wax-based support material is clearly visible, as it was deposited underneath all overhanging structural elements. Since the sides of the prototype are comprised of thin-walled microchannel structures suspended in space, support material is required in practically every location at the base of the device. Additionally, the microchannel inlet meant for the post-processing removal of the support material from within the microchannels is evident on the front side of the prototype and support material is visible underneath. The successfully-post-processed fabricated prototype device is also shown (*right*). This device is white in appearance (*i.e.* the color of the structural polymer itself), signifying the successful removal of all support material from the interior and exterior of the device. The suspended thin-walled microchannel structures are visible. Both prototypes are positioned with the three inlets facing upwards and all 13 outlets facing downwards.

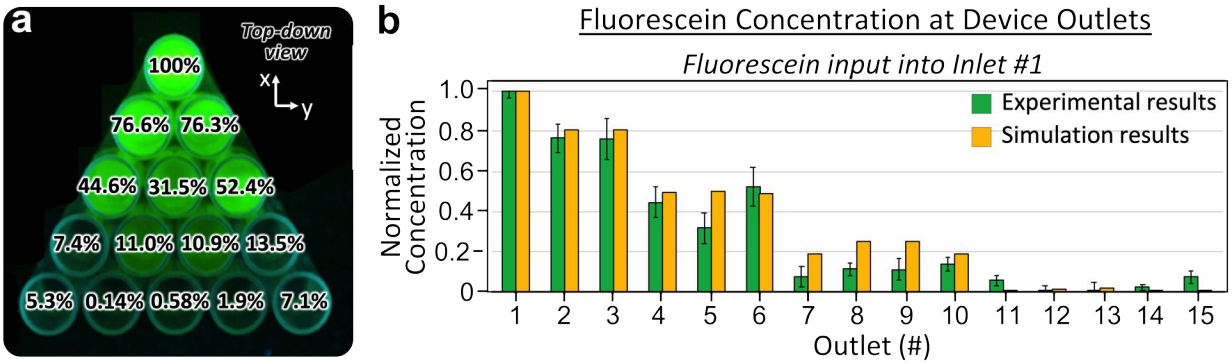

Figure 3.10: Experimental flow verification results for the concentration of a single input fluidic species concentration generated at each of the outlets of the fabricated *layer*-based 3D μ-CGG prototype device, compared to the theoretical COMSOL simulation results. **(a)** Example experimental results for the concentration of a single fluidic species (fluorescein dye solution input into Inlet #1, de-ionized (DI) water input into Inlets #2 & #3) in the collected fluid samples from each device outlet superimposed over a top-down fluorescence image of the fluid outputs collected in custom-designed 3D printed collection receptacle under UV excitation. Mean normalized concentration values for each of the fluids are calculated from experiments performed in triplicate. **(b)** Quantitative comparison the experimental mean normalized concentration results (*green*) with the theoretical COMSOL simulation results (*yellow*), error bars on the experimental result bars signify the standard deviation of the normalized concentration values calculated from three experiments from the displayed mean.

3.4.1.3 Flow Verification Experiment

The post-processed *layer*-based 3D μ-CGG prototype was then integrated into the experimental testing setup as illustrated in **Fig. 3.6**. The actual experimental hardware used in all experiments involving the *layer*-based 3D μ-CGG prototype is shown in Appendix **Fig. 7.11**. The prototype device was then operated to generate a gradient of fluorescein dye solution input into Inlet #1 and DI water solutions input into Inlets #2 & #3 following the procedures described in detail in **Section 3.3.4**. The collected fluid outputs serve as results for the experimental flow verification experiment, performed in order to experimentally-characterize the gradient generation performance of the fabricated prototype device. Details for the data acquisition and image analysis procedures performed during this experiment are presented in **Section 3.3.5**.

The raw experimental image used for fluorescence image processing to yield quantitative analytical results is shown in **Fig. 3.10a** (shown is one of three experimental images taken, one for each of three fluid collections, in order to perform the experiment in triplicate). This image shows a top-down view of the custom-designed and fabricated 3D printed fluid collection receptacle containing the experimentally-collected collected fluid outputs from the device. The receptacle

is shown under excitation by UV light, and the resulting fluorescence emission of the fluid samples (*green*) is clearly visible. Each fluid sample contains a specific concentration of the fluorescein dye solution, and hence a gradient of this fluidic species can be observed qualitatively. Superimposed over each fluid sample well is the experimental result of the quantitative analysis procedure, representing the mean normalized concentration of fluorescein dye solution contained in the fluid sample and output from the corresponding outlet on the prototype device (calculated from experiments performed in triplicate). As a result, a gradient of fluorescein solution from an overall high concentration of $\sim$100% in Well #1 to overall low concentration of $\sim$0% in Well #12 is observed.

The plot in **Fig. 3.10b** quantitatively compares the theoretically-simulated data (*yellow*, also shown in **Fig. 3.8c**) and experimental data (*green*), showing mean normalized concentration *versus* Outlet # on the *layer*-based 3D μ-CGG prototype, following the numbering convention illustrated in **Fig. 3.8a**. The error bars over each experimental data set signify the standard deviation of the normalized concentration values calculated from three experiments from the mean for that well. The experimental normalized concentrations of fluorescein from Outlets #5, #7-#9 & #10 are all statistically-lower than theoretically-predicted (*i.e.* the mean value and upper standard deviation bound are all lower than the value from the theoretical simulation), whist the concentrations from Outlets #11 & #15 are both statistically-higher than theoretically-predicted (*i.e.* the mean value and lower standard deviation bound are all higher than the value from the theoretical simulation). Finally, the theoretically-predicted concentrations for Outlets #1-#4, #6 & #12-#14 are all within the standard deviation of the experimental results.

One probable contributing factor to the observed discrepancy in the mean experimental values and theoretical results could be that the physical morphology of the prototype microchannel network is different enough from the 3D model used in the COMSOL simulation (*e.g.* if residual support material is present at any location inside the microchannel network or if the inner dimensions of the microchannels suffered warpage during fabrication), the hydrodynamics of the fluid flow inside the network could be altered sufficiently as to produce fluid flow patterns different from those simulated resulting in an inaccurate gradient. An additional factor could be that the short lengths of most microchannels and nodal mixing units which simply utilize a hollow mixing bulb (and do not incorporate any mixing enhancement microstructures, for example) result in incomplete fluidic mixing in each node in the gradient generation network; this incomplete mixing would compound the effects of any physical morphological inaccuracies on the flow dynamics, and resulting in consistently inaccurate overall gradient generation results. In order to evaluate these potential causes further, the experimental accuracy and precision of multiple fabricated prototype devices would need to be evaluated (three prototypes would be required to produce a statistically-satisfactory sample size).

Nevertheless, satisfactory precision of the fluid collection procedure and device gradient generation operation are demonstrated, as the range of standard deviations deviate by no more than 10% from the mean value for all experimental data points collected (a maximum deviation $\sim$9.6% for Outlet #6 is observed). Overall, experimental fluid outputs are generated which contain approxi-

mate proportional concentrations of each input fluidic species roughly representing an average of $\sim$100%, 75%, 50%, 10% & 0% along each edge of the device outlet arrangement. Moreover, fluids from Outlets #5, #8 & #9 each contain proportions of each of the three input fluidic species, $\sim$32% of the fluidic species from Inlet #1 and $\sim$11% of the fluidic species from both Inlets #2 & #3. Thus, the inherent innovation of the 3D fluidic routing accomplished by the *layer*-based arrangement of microchannels comprising this 3D μ-CGG design is experimentally validated. Finally, from an operational perspective, due to the demonstrated precision of the experimental flow verification results, this prototype was deemed acceptable to use in demonstrative bacteriological experiments, as described in the following section.

3.4.1.4 *Single-Antibiotic* MIC Determination Experiments

The capability of the theoretically and experimentally-characterized *layer*-based 3D μ-CGG prototype to serve as a microfluidic AST platform is first demonstrated through the determination of single-antibiotic sensitivity towards antibiotic-resistant bacteria. An ampicillin-resistant strain of BL21(DE3) *E. coli* bacteria was used as a demonstrative model, as discussed in **Section 3.3.7**. The resistance of this strain to ampicillin was confirmed and demonstrated through manually-performed MIC determination experiments, the results of which are shown in Appendix **Fig. 7.21**. The experimental procedure described in **Section 3.3.4** was used to perform the following experiments, which were performed in triplicate in order to determine a mean MIC value for Nitrofurantoin, Tetracycline and Trimethoprim, three different clinically-relevant antibiotic compounds commonly used to combat AMR-related infections [222].

For each set of MIC determination experiments involving one of the studied antibiotic compounds, a stock solution of the chosen antibiotic in LB media was prepared following the protocols outlined in **Section 3.3.6**, with a starting concentration of approximately double that of the approximate documented MIC value for that antibiotic against related *E. coli* strains, experimentally-determined by previous studies and published in the literature. Appendix **Fig. 7.32** tabulates all of the stock solution concentrations used, MIC values for different *E. coli* strains from the literature[3] and experimental MIC values as determined from all experiments involving the fabricated prototypes from this work. The antibiotic solution is input into Inlet #1 of the device, which is

[3]Bacterial sensitivity to specific antibiotics varies between strain type and usually evolves over the lifetime of the bacterium [222, 225]. As a result, the experimentally-determined MIC values reported in the literature for a given antibiotic compound can vary, often fairly significantly, between different bacterial strains and even study-to-study for the same strain of bacteria [208, 226]. Therefore, a range of documented MIC values for each antibiotic are listed in Appendix **Fig. 7.32**. Moreover, an antibiotic concentration double that of the *highest* reported MIC value from the literature was chosen for the input antibiotic stock concentration such that the "middle" of the generated gradient will represent the approximate MIC value. As discussed in **Section 3.1.1**, AST is recommended each time a definitive evaluation of the MIC values for a certain strain of bacteria and antibiotic is desired. Therefore, discrepancies between the experimental MIC values from this work and those documented in the literature are likely due to the variable bacterial strain-dependent antibiotic sensitivity characteristics of the strains used.

directly above Outlet #1 as seen on the bottom of the device. Furthermore, two solutions of LB media are used as buffers and input into the other two Inputs #1 & #3, directly above device Outlets #11 & #15, respectively. Thus, the 3D μ-CGG prototype is used to generate a gradient of the single antibiotic represented by discrete μ-drug cocktails which (pursuant to the protocol described in **Section 3.3.4.2**) are collected by the interfacing hardware and routed to corresponding wells on the custom-3D printed fluid collection receptacle, which are then filled with bacteria culture solution and resazurin indicator solution and incubated.

The color change in the fluidic solutions in the 3D printed receptacles inside the incubator are monitored about every hour until a visible gradient of colors is observed, which was an average duration of $\sim$5 hours across all of the experiments. Then, the data acquisition and quantitative analysis procedures presented in **Section 3.3.5.2** are used to quantify the normalized fluorescence intensity of resorufin emission inside the liquid sample inside each well on the fluid receptacle, producing the Normalized Growth value (with arbitrary units) of the bacteria in the presence of the fluid output from each of the outlets on the device (*i.e.* the amount of bacterial proliferation in the given fluid sample as compared to that in the control fluid sample containing no antibiotic, and therefore the maximum amount of bacterial proliferation over the course of the experiment).

Thus, the inhibitory effects of the different antibiotic concentrations comprising each discrete μ-drug cocktail can be determined [269, 281]. The Normalized Growth values of the μ-drug cocktails produced from the device outlets along one edge of the device representing a gradient from 100% antibiotic to 100% buffer are then compared. The fluid sample corresponding to the MIC value of the antibiotic is represented by the first μ-drug cocktail to exhibit a step-wise enhancement in growth inhibition. The concentration of the input antibiotic species in this fluid sample is quantified using the experimental normalized concentration value of fluorescein from that device outlet as determined from the flow verification experiment (as shown in **Fig. 3.10**). Thus, the MIC value is calculated as a proportion of the input antibiotic concentration contained in the MIC-corresponding fluid sample and reported as a concentration in mg/L.

Fig. 3.11a-c presents all results for the three MIC value determination experiments. For each antibiotic evaluated, the Normalized Growth values in each of the fluid outputs from device Outlets #1, #3, #6, #10 & #15 are plotted, along with the device outlet numbering convention and indication of the outlets containing 100% antibiotic and 100% buffer solutions superimposed over a rendering of the 3D model of the device.

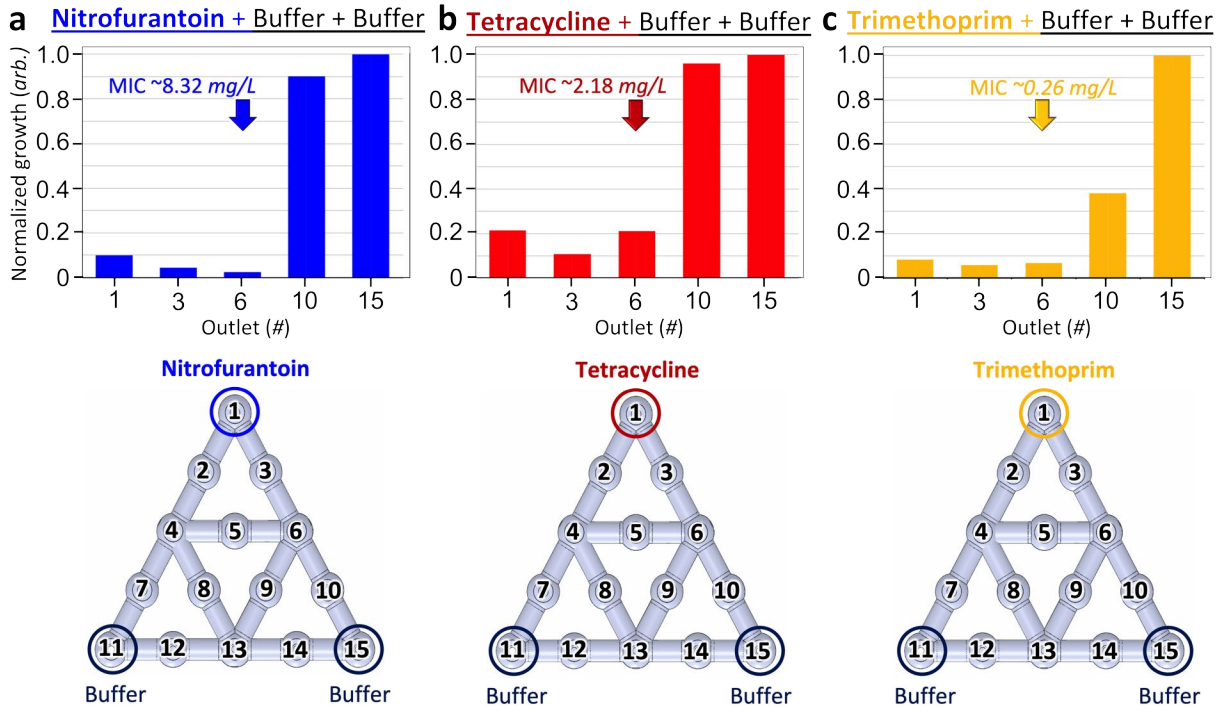

Figure 3.11: Experimental single-antibiotic MIC determination results demonstrated for the *layer*-based 3D μ-CGG prototype device with the antibiotic solution input into Inlet #1 (LB input into Inlets #2 & #3), device outputs were collected in a custom-3D printed fluid receptacle. Each subfigure shows (*top*) the calculated Normalized Growth value of the fluid outputs from the device outlets along one edge of the device representing a gradient from 100% antibiotic to 100% buffer, as well as (*bottom*) the outlet numbering convention and indication of the outlets containing 100% antibiotic and 100% buffer solutions. Results involving **(a)** Nitrofurantoin (MIC outlet indicated by the *blue* arrow), **(b)** Tetracycline (MIC outlet indicated by the *red* arrow) and **(c)** Trimethoprim (MIC value indicated by the *yellow* arrow) compounds.

3.4.1.4.1 *Nitrofurantoin*-Buffer-Buffer

Nitrofurantoin is an antibiotic which has been used since the mid-20th century to combat infections caused by bacteria such as *E. coli*, *E. faecalis* and *K. pneumoniae*. The mechanism of action of this synthetic antibiotic compound is such that, through high-affinity absorption and chemical-reduction by bacterium, nitrofurantoin disrupts synthesis of DNA, proteins and cell wall membranes, which has the overall effect of slowing the growth of the bacteria rather than outright killing the cells. Furthermore, the natural concentration of Nitrofurantoin in the renal system when absorbed by the body makes it an effective first-line-of-defense antibiotic in the treatment of UTI's; moreover, the low rate of bacterial resistance to nitrofurantoin, relative to that of other broad-spectrum antibiotics, has led to its increasing use over the past few decades, therefore effective AST is needed to ensure AMR is not developed towards this antibiotic. [217, 234, 282].

The Normalized Growth values for the featured fluid outputs representing the nitrofurantoin concentration gradient (**Fig. 3.11a**) indicate that the MIC value is apparent for the μ-drug cocktail from Outlet #6 (exhibiting normalized growth of below $\sim$5%), which corresponds to a nitrofurantoin concentration of $\sim$8.32 mg/L ($\sim$52% of the concentration of the input nitrofurantoin stock solution). The fluid outputs containing higher concentrations of nitrofurantoin show roughly the same amount of growth (below $\sim$10%), whereas those containing lower concentrations of nitrofurantoin show drastically-increased amounts of growth ($\sim$90% & 100%, respectively), when compared to the control. This drastic difference in observable growth in fluid outputs containing concentrations higher and lower than in Outlet #6 justifies the decision to assign the MIC value to this μ-drug cocktail. Therefore, the specific strain of ampicillin-resistant *E. coli* bacteria evaluated in these experiments is deemed susceptible to nitrofurantoin above concentrations of $\sim$8 mg/L, which is in fact in agreement with the documented range of nitrofurantoin MIC values for alternative strains of *E. coli*, $\sim$4-8 mg/L [222, 226].

3.4.1.4.2 *Tetracycline*-Buffer-Buffer

Tetracycline is a naturally-derived antibiotic class which been available as a generic medication since the 1970's and has been one of the safest and effective broad-spectrum medications used to treat serious conditions such as syphilis, cholera, malaria and the plague, but is also commonly-prescribed to treat more benign conditions such as acne. Tetracycline works by interfering with protein synthesis in bacterial cells, and most AST-evaluated bacterial strains, with the exception of *Pseudomonas aeruginosa* (*P. aeruginosa*) and *Proteus mirabilis*, have demonstrated naturally low-to-intermediate sensitivity towards tetracycline. Tetracycline is also a useful antibiotic in multi-drug treatments used to treat AMR-related infections, such as bacterial peptic ulcers [234, 283]

The Normalized Growth values for the featured fluid outputs representing the tetracycline concentration gradient (**Fig. 3.11b**) indicate that the MIC value is also apparent for the μ-drug cocktail from Outlet #6 (exhibiting normalized growth of $\sim$20%), which corresponds to a tetracycline concentration of $\sim$2.18 mg/L ($\sim$52% of the concentration of the input tetracycline stock solution). The fluid outputs containing higher concentrations of tetracycline show roughly the same amount of growth (below $\sim$20%), whereas those containing lower concentrations of tetracycline show drastically-increased amounts of growth ($\sim$100%), when compared to the control. This drastic difference in observable growth, similar to that observed in the case of nitrofurantoin, justifies the decision to assign the MIC value to this μ-drug cocktail. Therefore, the ampicillin-resistant *E. coli* bacterial strain evaluated in these experiments is deemed moderately susceptible to tetracycline above concentrations of $\sim$2 mg/L, which is in fact in agreement with the documented range of tetracycline MIC values for similar known AMR-resistant strains of *E. coli*, $\sim$1-2 mg/L [215, 222].

3.4.1.4.3 *Trimethoprim*-Buffer-Buffer

Trimethoprim has been considered since the 1960's a safe and effective antibiotic, primarily used to treat bladder, urinary tract and middle-ear infections as well as chronic diarrhea. The working mechanism of trimethoprim, as with many broad-spectrum antibiotics, is by inhibiting bacterial DNA synthesis. Most evaluated common bacterial strains, such as *E. coli*, *Proteus mirabilis*, *K. pneumoniae* and *Streptococcus pneumoniae* (*S. pneumoniae*), as well as the hazardous influenza-causing bacteria *Haemophilus influenzae* (*H. influenzae*), demonstrate moderate levels of susceptibility to trimethoprim; however, cases of trimethoprim-resistant bacterial infections are increasing, specially in the developing world where the antibiotic is commonly used as a first-line-of-defense treatment against many infections. As a result, routine AST evaluation of trimethoprim, among other broad-spectrum antibiotics, against patient samples to identify accurate MIC dosage is recommended in clinical settings around the world. [222, 234, 283]

The Normalized Growth values for the featured fluid outputs representing the trimethoprim concentration gradient (**Fig. 3.11c**) indicate that the MIC value is similarly apparent for the μ-drug cocktail from Outlet #6 (exhibiting normalized growth of $\sim$5%), which corresponds to a trimethoprim concentration of $\sim$0.26 mg/L ($\sim$52% of the concentration of the input trimethoprim stock solution). Of the fluid outputs containing lower concentrations of trimethoprim, Outlet #10 (consisting of around $\sim$14% of the concentration of the input trimethoprim stock solution, $\sim$0.07 mg/L) exhibits a higher amount of growth (around $\sim$40%), and the fluid output from Outlet #15 (consisting of $\sim$100% input buffer solution) exhibits a drastically-increased amount of growth ($\sim$100%), when compared to the control. Despite the fact that a trimethoprim concentration of $\sim$0.07 mg/L results in normalized growth below 50%, the MIC value is defined in this context for less growth, $\sim$5%, which was first exhibited by the μ-drug cocktail from Outlet #6. Therefore, the ampicillin-resistant *E. coli* evaluated in these experiments is deemed susceptible to tetracycline above concentrations of $\sim$0.25 mg/L, which is in agreement with the documented range of trimethoprim MIC values for alternative strains of *E. coli*, $\sim$0.25-1 mg/L [222].

3.4.1.5 *Three-Antibiotic* CDS Experiment

Nitrofurantoin, tetracycline and trimethoprim have all been previously used in various clinical capacities to create two-antibiotic (*i.e.* pair-wise) combination treatments to combat certain AMR-related bacterial infections; furthermore, previously-demonstrated CDS studies from the literature have established known pair-wise interactions between each of the antibiotic combinations, mostly towards cultured strains of common bacteria such as *E. coli*. Nitrofurantoin and trimethoprim have demonstrated generally-*synergistic* effects (*i.e.* more effective) in combination; nitrofurantoin and tetracycline have demonstrated generally-*additive* effects (*i.e.* no more nor less effective) in combination; and tetracycline and trimethoprim have demonstrated generally-*antagonistic* effects (*i.e.* less effective) in combination. [235, 284]

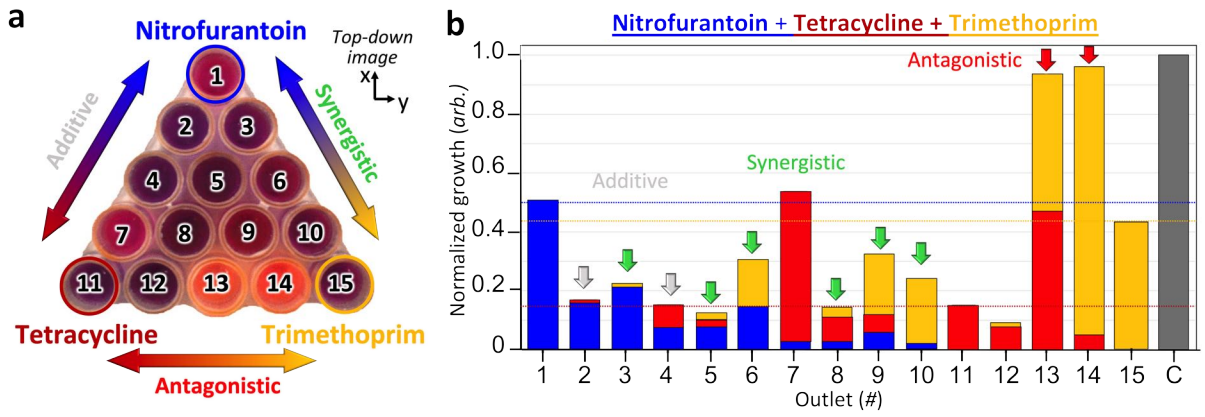

Figure 3.12: Experimental *three-way* CDS results demonstrated for the *layer*-based 3D μ-CGG prototype device with antibiotic solutions input into Inlets #1, #2 & #3, device outputs were collected in a custom-3D printed fluid receptacle. **(a)** Experimental top-down image of the incubated fluid receptacle superimposed with outlet numbering convention and indication of the outlets containing 100% of each of the antibiotics. **(b)** Calculated Normalized Growth values (represented by bars with colors representing the proportional concentrations of each antibiotic calculated from the flow verification data in **Fig. 3.10**) for the fluid outputs from all of the device outlets. Colored horizontal lines indicate the normalized growth for 100% nitrofurantoin (*blue*) in Outlet #1, 100% tetracycline (*red*) in Outlet #11 and 100% trimethoprim (*yellow*) in Outlet #15. Outlets that demonstrate pair-wise interactions between each two antibiotics which agree with those documented in the literature are indicated by colored arrows, *i.e. synergy* between Nitrofurantoin+Trimethoprim in *green*, *additivity* between Tetracycline+Nitrofurantoin in *grey*, and *antagonism* between Tetracycline+Trimethoprim in *red*. Normalized Growth value for the control well is indicated by the grey bar.

Fig. 3.12 presents the experimental results of a three-antibiotic CDS demonstration of AST evaluation of the combinatorial effects of all three antibiotic compounds, simultaneously, from a single experimental single operation of the prototype device. The inherent advantageous capabilities of this 3D μ-CGG prototype are apparent by analyzing the different types of gradients that are produced in a single fluid collection receptacle from a single operation of the device, as analysis of just a single image of the fluid receptacle from a single experiment represents data for 15 μ-drug cocktails which capture three discrete approximately pair-wise antibiotic gradients and one three-antibiotic gradient. The high-throughput capability of this device is experimentally demonstrated, the device generates three distinct pair-wise studies of two antibiotics, simultaneously. For example, the μ-drug cocktails generated from Outlets #1, #3, #6, #10 & #15 represent an approximately pair-wise gradient between nitrofurantoin and trimethoprim; those generated from Outlets #1, #2, #4, #7 & #11 represent an approximately pair-wise gradient between nitrofurantoin and tetracycline; and those generated from Outlets #11, #12, #13, #14 & #15 represent an approximately pair-wise gradient between tetracycline and trimethoprim.

The expected *synergistic* effect of nitrofurantoin and trimethoprim in combination is demonstrated by the fact that the μ-drug cocktails from Outlets #3, #6 & #10 all demonstrate lower normalized growth than both the 100% nitrofurantoin from Outlet #1 and the 100% trimethoprim from Outlet #15. The expected *additive* effect of nitrofurantoin and tetracycline in combination is demonstrated by the fact that the μ-drug cocktails from Outlets #2 & #4 demonstrate intermediate normalized growth between the 100% nitrofurantoin from Outlet #1 and the 100% tetracycline from Outlet #11. Finally, the expected *antagonistic* effect of tetracycline and trimethoprim in combination is demonstrated by the fact that the μ-drug cocktails from Outlets #13 & #14 all demonstrate significantly higher normalized growth than both the 100% tetracycline from Outlet #11 and the 100% trimethoprim from Outlet #15.

Interestingly, a few unexpected approximately-pair-wise antibiotic effects are also demonstrated in these results. For example, an *antagonistic* effect of nitrofurantoin and tetracycline in combination is demonstrated by the fact that the μ-drug cocktail from Outlet #7 demonstrates more normalized growth than those of either the 100% nitrofurantoin or the 100% tetracycline. Assuming that this fluid sample was not contaminated by an organism other than the *E. coli*, the gradient generator produced the intended fluidic output, and this μ-drug cocktail represents an approximate pair-wise combination of only nitrofurantoin and tetracycline (ignoring the minute quantity, $\sim$2%, of trimethoprim present in this sample), this pair-wise chemistry demonstrates *antagonistic* effects as compared to the 100% solutions of both antibiotics, therefore this specific chemistry would be *heavily avoided* in treating an infection caused by the ampicillin-resistant *E. coli* strain demonstrated in this work. If instead the minute quantity of trimethoprim present in this sample is not ignored, this three-antibiotic chemistry should similarly be avoided. In addition, a *synergistic* effect of tetracycline and trimethoprim in combination is demonstrated by the fact that the μ-drug cocktail from Outlet #12 demonstrates less normalized growth than both the 100% tetracycline and the 100% trimethoprim. Assuming that this μ-drug cocktail represents an approximate pair-wise combination of only tetracycline and trimethoprim (ignoring the minute quantity, $\sim$0.14%, of trimethoprim present in this sample), this specific pair-wise chemistry would therefore be *recommended* in treating an infection caused by the ampicillin-resistant *E. coli* strain demonstrated in this work. If, instead, the contribution of the minute addition of nitrofurantoin in the sample was not ignored, this three-antibiotic chemistry would be likewise recommended in treating such an infection due to the enhanced degree of synergy demonstrated.

Moreover, the novel 3D fluidic routing capability of the 3D μ-CGG prototype device is also demonstrated by the generated μ-drug cocktails produced from Outlets #5, #8 & #9 which all contain different proportions of all three antibiotics in significant proportions, three-antibiotic combinations which are otherwise impossible to generate using planar fluidic routing inherent to conventional CGG-based microfluidic devices. The μ-drug cocktail from Outlet #9 ($\sim$32% trimethoprim, $\sim$11% tetracycline & $\sim$11% nitrofurantoin) demonstrates *synergistic* effects as compared to the 100% solutions of nitrofurantoin and trimethoprim, but approximately the same effect as the μ-drug cocktail from Outlet #6 ($\sim$50% nitrofurantoin + $\sim$50% trimethoprim). Additionally, the μ-drug cocktail from Outlet #9 demonstrates *additive* effects as compared to the 100% solutions

of nitrofurantoin and trimethoprim, but approximately the same effect as the μ-drug cocktail from Outlet #6 ($\sim$50% nitrofurantoin + $\sim$50% trimethoprim). Therefore from both standpoints, this three-antibiotic chemistry demonstrates no significant improvement in efficacy than the pair-wise nitrofurantoin and trimethoprim μ-drug cocktail from Outlet #6 against the bacterial strain demonstrated in this work. On the other hand, the μ-drug cocktails from Outlets #5 ($\sim$32% nitrofurantoin, $\sim$11% tetracycline & $\sim$11% trimethoprim) & #8 ($\sim$32% tetracycline, $\sim$11% nitrofurantoin & $\sim$11% trimethoprim) both demonstrate *synergistic* effects as compared to the 100% solutions of all antibiotics, therefore these specific three-antibiotic chemistries would be *recommended* in treating an infection caused by the ampicillin-resistant *E. coli* strain demonstrated in this work.

3.4.2 *Tetrahedral*-Based 3D Microchannel Network

3.4.2.1 Theoretical Output Concentration Distribution

3.4.2.1.1 Study of 3D μ-Mixer-Integrated Microfluidic Networks

One functional requirement of CGG devices is that all fluids that enter each combination-mixing-splitting nodal unit of a gradient generation network should be well-mixed before the resulting fluid volume is routed to the next units the fluidic network. This ensures that the generated concentrations from each unit are consistent with the analytical calculations made during nodal analysis, which assumes complete fluidic mixing at each node in the network. The accuracy (of the generated concentration gradient to the analytical calculations of concentration at each device outlet) demonstrated by any CGG design or actual fabricated CGG prototype device is therefore critically dependent the mixing efficiency of each nodal unit in the fluidic network. The previously demonstrated *layer*-based 3D μ-CGG design, for example, simply featured one hollow bulb in the design of each nodal unit in which the input fluids combined and almost immediately thereafter split off to the next nodal unit, and therefore did not incorporate any form of mixing-enhancement elements. The resulting ineffectiveness of the fluidic mixing inherent to each nodal unit in this design could be a contributing factor to the discrepancy between the experimental and simulated performances of this specific 3D μ-CGG design.

To address this limitation, the effect of integrating 3D μ-mixer structures into each tetrahedral μ-mixing nodal unit comprising the the *tetrahedral*-based 3D μ-CGG fluidic network design was investigated. A vertical smooth-walled channel placed between the *upper* hollow bulb (where fluids combine) and the *lower* hollow bulb (where the fluids split off to the next nodal unit) in the design of each tetrahedral μ-mixing unit in the microchannel network serves as linear microchannel region in which diffusive mixing of the combined can occur. Thus, a design incorporating these smooth-walled vertical channels was constructed and used as a *control* design. The additional diffusive mixing inside each nodal unit will present mixing enhancement over a conceptual

design utilizing a single hollow bulb. Furthermore, two additional designs were created, one incorporating a 3D rifled μ-mixer-based element and one incorporating a 3D bulbous μ-mixer-based element, both in place of the vertical microchannels. The 3D rifled μ-mixer integrated μ-CGG design features microstructures of the same design as comprises the rifled portion of the 3D rifled μ-mixer design as presented in **Chapter 2**. The 3D bulbous μ-mixer integrated μ-CGG design features the microstructures identical to the 3D bulbous μ-mixer design from **Chapter 2**, as well. The experimental results demonstrated in **Chapter 2** reinforce the concept that incorporating such 3D microstructural elements into each fluidic nodal unit will enhance mixing efficiency.

COMSOL theoretical simulations were performed in order to compare the theoretical gradient generation performance of the various μ-CGG designs, pursuant to the protocols as detailed in **Section 3.3.2**. The theoretical results for the normalized concentration of a given input species (defined as input to device Inlet #1, while buffer solution at 0% concentration is input into Inlets #2 & #3) at each device outlet *versus* flow rate input into each of the device inlets from 0 to 4000 μL/min are presented for each design on the plots in **Fig. 3.13b-d**. Each of these plots reveals that the normalized concentrations at each outlet become independent of input flow rate for all devices around $\sim$1000 μL/min; therefore only the normalized concentration values at $\sim$1000 μL/min are selected for comparison between devices. Accompanying each plot is an isometric view of the simulated distribution of a single fluidic species (defined as input to device Inlet #1, while buffer solution at 0% concentration is input into Inlets #2 & #3) at 1000 μL/min flow rate. Furthermore, the theoretical results and analytical calculations for all normalized concentrations at an input flow rate of $\sim$1000 μL/min, along with the percent error between the two calculations, are tabulated in **Fig. 3.13e**. (Additionally, the average percent error of the pixels on the fluidic profile representing normalized concentrations from the average value calculated on each Outlet face are shown in Appendix **Fig. 7.25**.) A conventionally-accepted metric for *acceptability* in the error of generated gradients from CGG platforms (*i.e.* the variation between the actual and intended concentrations of each input fluidic species at any outlet of a CGG network), specifically for antibiotic susceptibility testing applications, is a maximum of 10% [153, 213]. Therefore in this study, theoretical normalized concentration values that are within 10% of the analytical concentration are deemed as *acceptable* being useful for experimental study and are highlighted in green, while those results greater than 10% error are highlighted in red in **Fig. 3.13e**.

The analytical calculations for normalized concentration at each outlet of the conceptual μ-CGG design are independent of fluidic flow rate into the device, as is reflected on the plot in **Fig. 3.13a** (since the equations use the glaring assumption that mixing is 100% effective in each nodal unit). These values are also tabulated at the top of **Fig. 3.13e**, for reference. Furthermore, the theoretical simulation of the smooth-walled vertical channel control μ-CGG design, results shown in **Fig. 3.13b**, indicate that the normalized concentrations at Outlets #2 & #3 exhibit $\sim$24% error as compared to the analytically-predicted concentrations. Furthermore, the normalized concentrations at Outlets #6 & #8 exhibit $\sim$57% error. The discrepancy between these results is evidence of the inefficient co-laminar fluidic mixing inside the smooth-walled linear microchannels which is successfully simulated by the theoretical model.

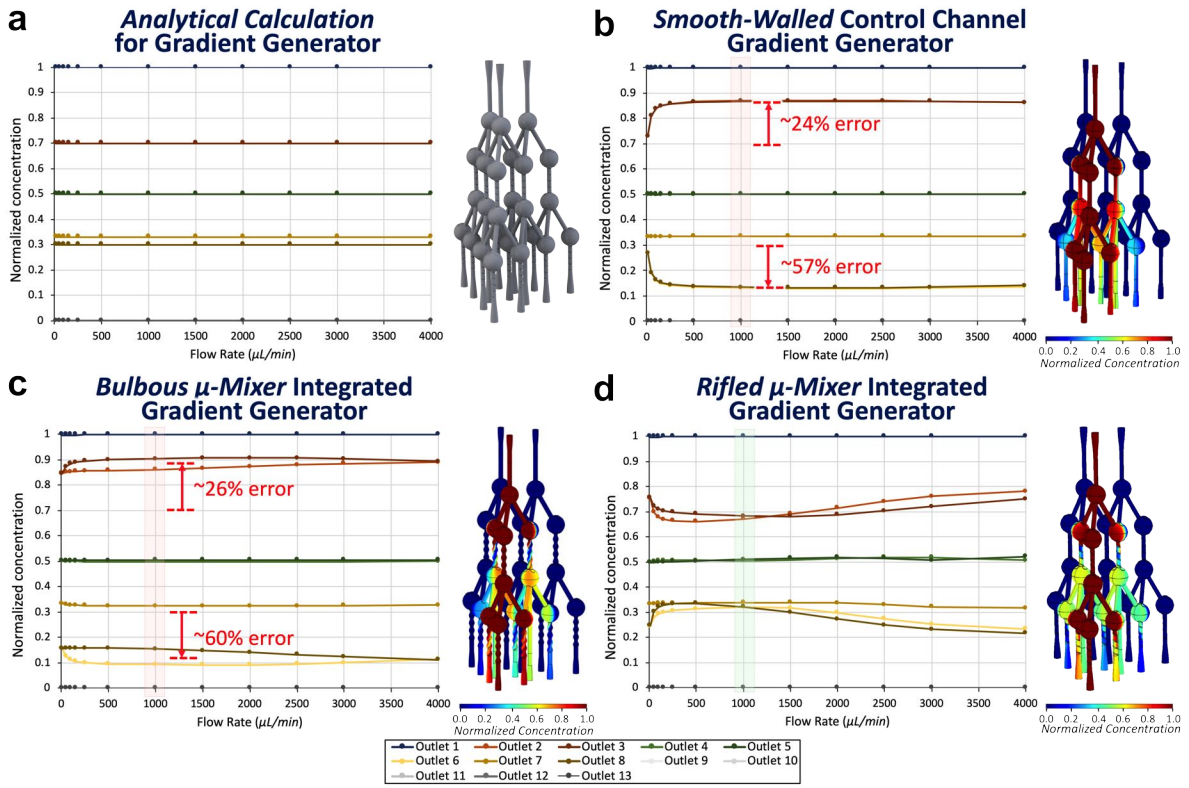

e % Mix	1	2	3	4	5	6	7	8	9	10	11	12	13
Analytical	1.00	0.70	0.70	0.50	0.50	0.30	0.33	0.30	0	0	0	0	0
Rifled μ-Mixer Simulation	1.00	0.69	0.68	0.50	0.51	0.32	0.34	0.32	0	0	0	0	0
% Error	0%	1.4%	2.9%	0%	2.0%	6.7%	6.7%	3.0%	0%	0%	0%	0%	0%
Bulbous μ-Mixer Simulation	1.00	0.86	0.90	0.50	0.50	0.09	0.32	0.15	0	0	0	0	0
% Error	0%	22.8%	28.6%	0%	0%	70.9%	3.0%	50.0%	0%	0%	0%	0%	0%
Control Channel Simulation	1.00	0.87	0.87	0.50	0.50	0.13	0.34	0.13	0	0	0	0	0
% Error	0%	24.3%	24.3%	0%	0%	56.7%	6.7%	56.7%	0%	0%	0%	0%	0%

Figure 3.13: Theoretical COMSOL simulations evaluating the effect of integrating 3D μ-mixer structures into the *tetrahedral*-based 3D μ-CGG design. Plots (*left*) present normalized concentration *versus* input flow rate from 0 to 4000 μL/min; visualization (*right*) of the simulated distribution of a single fluidic species from each COMSOL simulation. **(a)** Analytical calculations are independent of fluidic flow rate as reflected on the plot. Theoretical COMSOL simulated results for the **(b)** smooth-walled control vertical channel-integrated 3D μ-CGG design, **(c)** 3D bulbous μ-mixer-integrated 3D μ-CGG design and **(d)** 3D rifled μ-mixer-integrated 3D μ-CGG design. The data for all 13 Outlets are shown on each graph, however many Outlets produce very similar values, therefore some data is overlapping. All results at $\sim$1000 μL/min are tabulated in **(e)**. The 3D rifled μ-mixer-integrated 3D μ-CGG produces all output concentrations with the lowest error (within 10%, *green*) from the analytical predictions, therefore is the sole design selected for prototyping, experimental characterization and bacteriological demonstration.

The 3D bulbous μ-mixer integrated μ-CGG design, theoretical simulation results as shown in **Fig. 3.13c**, exhibits an even more severe degree of inaccuracy, as the normalized concentrations at Outlets #2 & #3 exhibit $\sim$23% & $\sim$29% error, respectively; Outlets #6 & #8 exhibit $\sim$71% & $\sim$50% error, respectively, as well. One potential reason for this discrepancy is could be due to the fact that each 3D microstructure design generates incomplete fluidic mixing, resulting in an error which compounds as the fluids move throughout the fluidic network, ultimately producing inaccurate output concentrations. Additional error is produced when the still-laminar fluids split inside each hollow bulb in each nodal unit, as each outlet microchannel routing to the next nodal unit in-series will contain a higher proportion of one of the physical fluids than the others. These results are summarized in **Fig. 3.13e**. The theoretical simulation for the 3D rifled μ-mixer integrated μ-CGG design as shown in **Fig. 3.13d**, on the other hand, demonstrates the most accurate results, as the normalized concentration at all outlets is within 10% of the predicted values, as illustrated in **Fig. 3.13e**. The 3D rifling μ-mixer microstructure therefore demonstrates the most efficient mixing performance in the 3D fluidic network.

3.4.2.1.2 Optimal 3D Rifled μ-Mixer-Integrated Design

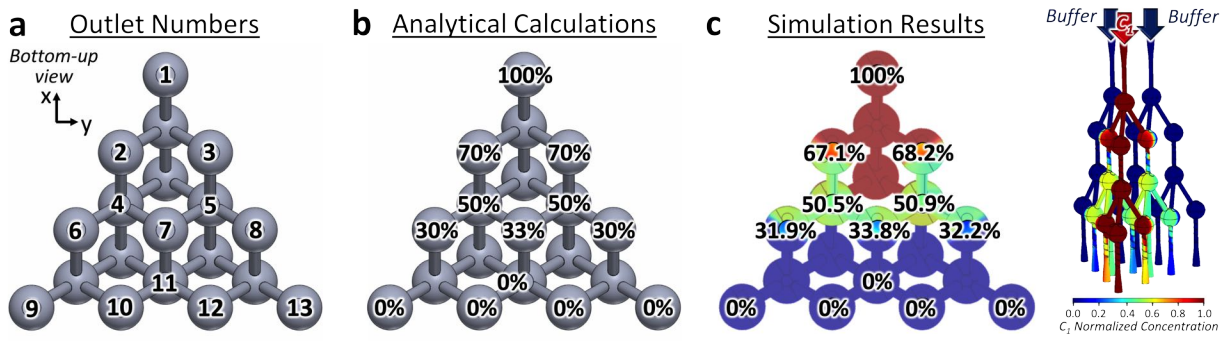

Figure 3.14: Analytical calculations and theoretical simulation results for the distribution of a single input fluidic species concentration at each outlet of the *tetrahedral*-based 3D μ-CGG design. **(a)** Map showing the numbering convention of each of the device outlets superimposed over a bottom-up view of the 3D solids model of the device. **(b)** Analytical calculations for the concentration of a single fluidic species (input into device Inlet #1, directly above Outlet #1) at each outlet of the device, superimposed over a bottom-up view of the 3D solids model of the device; concentrations calculated include 100%, 70%, 50%, 33%, 30% & 0%. **(c)** Theoretical COMSOL simulation results for the concentration of a single fluidic species input into device Inlet #1(*left*) at each outlet of the device, superimposed over a bottom-up view of the visualization of the COMSOL results throughout the device, concentrations simulated include $\sim$100%, $\sim$68.2%, $\sim$67.1%, $\sim$50.9%, $\sim$50.5%, $\sim$33.8%, $\sim$32.2%, $\sim$31.9% & 0%.; and (*right*) an isometric view of a visualization of the COMSOL results for the theoretical distribution of the single input fluidic species throughout the device with symmetric input flow rates of 1000 μL/min, simulating the species of interest (*red*) input into Inlet #1 and buffers input into Inlets #2 & #3 (*blue*).

Based on the results of the theoretical study presented in **Section 3.4.2.1.1**, the 3D rifled μ-mixer-integrated *tetrahedral*-based 3D μ-CGG is selected design to be used for prototype fabrication and for all experimental characterization and bacteriological demonstrations. Therefore, regarding the terminology used throughout the rest of this chapter, the descriptively-accurate term *3D rifled μ-mixer-integrated tetrahedral*-based 3D μ-CGG is shortened to simply *tetrahedral*-based 3D μ-CGG design. **Fig. 3.14a** presents the device outlet numbering scheme used hereon-in for characterization of the *tetrahedral*-based 3D μ-CGG design, as well as summaries of the analytical calculations **Fig. 3.14b** and theoretical results from the COMSOL simulation representing the normalized concentrations predicted at each device outlet **Fig. 3.14c**, all shown as percentages of a given input species (C_1 input to Inlet #1, buffer solution input to Inlets #2 & #3). The theoretical results, also shown in **Fig. 3.13d,e**, validate the generation of normalized concentrations at all outlets within 10% of the analytically-predicted values (as mentioned in **Section 3.4.2.1.1**). Overall, the results of the analytical and theoretical studies of this specific 3D μ-CGG design indicate that, due to the inherent symmetry of the tetrahedron-based nodal units, the fluid outputs of the device, all capturing discrete elements of the generated gradient, represent potentially more useful fractional concentrations of the input fluidic species (*i.e.* $\sim$1, $\sim\frac{7}{10}$, $\sim\frac{5}{10}$ & $\sim\frac{3}{10}$) than were generated by the *layer*-based 3D μ-CGG. Moreover, device Outlet #7 contains a nearly-equal proportion of all three input fluidic species ($\sim\frac{1}{3}$). This latter output is only achievable using the geometrically-symmetric microchannel network, enabled by tetrahedron-based mixing nodal units which are themselves geometrically-symmetric, featured in the design of the *tetrahedral*-based 3D μ-CGG. Finally, as the theoretical normalized concentrations at all outlets are within 10% of the analytically-predicted values, this design is deemed sufficient to move forward with in order to perform experimental characterization of a fabricated prototype. Furthermore, Appendix **Fig. 7.24** presents the conceptualization, 3D modeling and preliminary analytical and theoretical characterization of an extension of this *tetrahedral*-based 3D μ-CGG design consisting of an additional nodal unit layer and 22 fluidic outlets. The theoretical results demonstrate that with an additional layer of fluidic routing, further useful approximate fractional concentrations of the input fluidic species (*i.e.* $\sim$1, $\sim\frac{3}{4}$, $\sim\frac{6}{10}$, $\sim\frac{1}{2}$, $\sim\frac{3}{10}$, $\sim\frac{1}{4}$, & $\sim\frac{1}{3}$) can be generated. Development of this design was not pursued beyond theoretical characterization in this work. However, the basic results are presented to illustrate the effect of additional layers of 3D fluidic routing, as an example of the capability to design much more complex 3D microchannel arrangements based off of a 3D symmetric, *tetrahedral*-based 3D design methodology.

3.4.2.2 Fabrication Results

Three copies of the *tetrahedral*-based 3D μ-CGG design were fabricated on a single build plate, then post-processed, following the procedures as discussed in **Section 3.3.3**. Multiple prototypes were fabricated since the ease of sacrificial support material removal from within the fabricated microchannels was uncertain. The overall effective lengths of the microchannel networks from the inlets to the outlets are longer than those comprising the *tetrahedral*-based 3D μ-CGG design

and therefore have higher fluidic resistance. Additionally, it was uncertain if the absence of post-processing-dedicated lateral microchannel outlets would make support material removal difficult. Since any manufacturing defects in any of the prototypes could compound the difficulty of material removal, it was surmised that fabricating three prototypes would increase the probability of yielding a successfully fabricated and post-processed prototype for testing. Upon post-processing, it was instead found that all three fabricated prototypes were successfully fabricated and support material removal was performed without significant difficulty. The actual 3D printed and post-processed *tetrahedral*-based 3D μ-CGG prototype device is visualized in **Fig. 3.15**, shown held between this Doctoral Candidate researcher's fingers, for scale, demonstrating the compactness and portability of this microfluidic platform. The three inlet microchannels are visible on the flush to surface of the device. Furthermore, the entirety of one side of the hollow microchannel network

Figure 3.15: Fabrication results, *tetrahedral*-based 3D μ-CGG device after post-processing revealing hollow microchannel structures visible through the translucent material comprising the body of the device. The prototype is shown held between this Doctoral Candidate researcher's fingers, for scale.

is visible through the translucent material comprising the structural body of the device. In this image, the 3D rifled μ-mixer structures integrated into the vertical microchannels are difficult to see clearly; however, Appendix **Fig. 7.10b** shows an image of the fabricated prototype at another angle, one in which the 3D rifling is clearly visible. The solid-nature of prototype, containing the hollow microchannel structures, proved much more robust and easy to handle during removal from the 3D printer build plate and during post-processing.

3.4.2.3 Flow Verification Experiment

The post-processed *tetrahedral*-based 3D μ-CGG prototype was then integrated into the experimental testing setup as illustrated in **Fig. 3.6**. The actual experimental hardware used in all experiments involving the *tetrahedral*-based 3D μ-CGG prototype is shown in Appendix **Fig. 7.12**. The prototype device was then used to perform flow verification experiments in order to experimentally-characterize of the gradient generation performance of the fabricated prototype device. The experimental procedures followed are described in detail in **Section 3.3.4**. Briefly, nine different flow verification experiments were performed; fluid collections were performed in triplicate for the fluidic input conditions listed in **Section 3.3.5.1**, using rhodamine dye solution input into each of the three microchannel inlets in separate experiments. This represents an improvement over the experimental flow verification study undertaken for the *layer*-based 3D μ-CGG prototype as presented in **Section 3.4.1.3**, as these experiments enable the characterization of the distribution of all three input fluidic species at every outlet of the device, without needing to make any assumptions about the inherent fluid dynamic symmetry inside the microchannel network, as were made for the demonstration of the *layer*-based 3D μ-CGG prototype. Details for the data acquisition and image analysis procedures employed throughout this experiment are presented in **Section 3.3.5**. Experimental images (one for each fluid collection, for three fluidic collections, each for three different input fluid arrangements) enabled observation, and furthermore quantification, of the gradient of rhodamine dye solution output from the device on a 96-well plate, an example image of which is shown on the far righthand side in Appendix **Fig. 7.22f**.

The experimental results quantifying the normalized concentration of rhodamine in each fluid sample from the fluorescence imaging of each of the fluid collections are compared to the results from the theoretical simulation for each device outlet in **Fig. 3.16**. Data for the different configurations of input fluidic species into the prototype are presented as follows: rhodamine solution into Inlet #1 and DI water into Inlets #2 & #3 (**Fig. 3.16a**), rhodamine solution into Inlet #2 and DI water into Inlets #1 & #3 (**Fig. 3.16b**) and rhodamine solution into Inlet #3 and DI water into Inlets #1 & #2 (**Fig. 3.16c**). Each subfigure shows the mean experimental normalized concentration value, shown as a percentage of the input concentration (100%) rhodamine solution, for each fluid sample contained in discrete wells on a 96-well plate, superimposed over the corresponding outlet on the prototype device (*left*). In addition, the theoretical simulation data (*yellow*) and experimental data (*green*) data are compared on the adjacent plots (*right*), showing the mean normalized concentra-

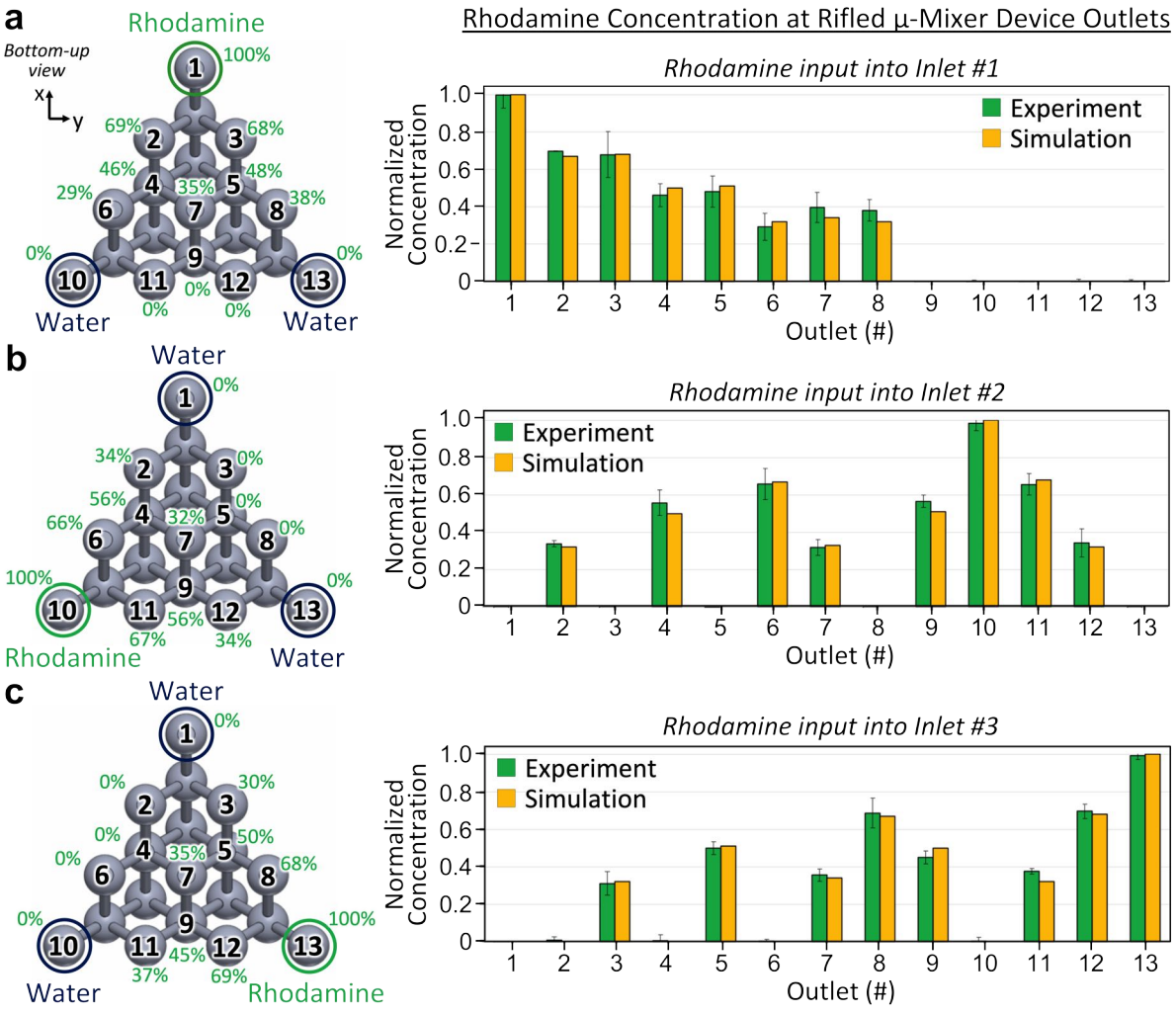

Figure 3.16: Experimental flow verification results for the concentration of the three input fluidic species at each of the outlets of the fabricated *tetrahedral*-based 3D μ-CGG prototype device, compared to the theoretical COMSOL simulation results. **(a)** Experimental results for the concentration of rhodamine solution input into Inlet #1 (DI water input into Inlets #2 & #3) at each device outlet (*left*) superimposed over a bottom-up view of the 3D solids model of the device with outlet numbering labeled. Device outlets were collected on a standard 96-well plate and fluorescence imaging used to calculate the mean normalized concentration value, normalizing the fluorescence magnitude in each fluid to the fluorescence of a DI water, from experiments performed in triplicate. (*Right*) Quantitative comparison the experimental mean normalized concentration results (*green*) with the theoretical COMSOL simulation results (*yellow*), error bars on the experimental result bars signify the standard deviation of the normalized concentration values calculated from three experiments from the displayed mean. **(b)** Same data format, instead for rhodamine solution input into Inlet #2 (DI water input into Inlets #1 & #3). **(c)** Same data format, but instead for rhodamine solution input into Inlet #3 (DI water input into Inlets #1 & #2).

tion *versus* device Outlet number (following the numbering convention for the well/device outlet shown on the rendering of the device on the *left*). The error bars over each experimental data set signify the standard deviation of values calculated from three experiments from the mean for the fluids output from that outlet.

For the configuration of rhodamine input into Inlet #1 (**Fig. 3.16a**), the theoretically-predicted concentrations for all outputs are statistically-within the standard deviations of the experimental results (average standard deviation of $\sim$4.8%). Additionally, the mean normalized concentration values for all outputs are within 10% concentration of the theoretically-predicted values (a maximum of $\sim$6.0% variation for Well #8, and an average variation of $\sim$2.0% across all of the wells). Furthermore, for the configuration of rhodamine input into Inlet #2 (**Fig. 3.16b**), the theoretically-predicted concentrations for all outputs, except for that from Outlet #9, are statistically-within the standard deviations of the experimental results (average standard deviation of $\sim$3.9%). However, the mean normalized concentration values for all outputs are within 10% concentration of the theoretically-predicted values (a maximum of $\sim$5.6% variation for Outlet #9, and an average variation of $\sim$3.0% across all of the wells). Finally, for the configuration of rhodamine input into Inlet #3 (**Fig. 3.16c**), the theoretically-predicted concentrations for all outputs, except for Outlets #9 & #11, are statistically-within the standard deviations of the experimental results (average standard deviation of $\sim$3.1%). However, the mean normalized concentration values for all outputs are within 10% concentration of the theoretically-predicted values (a maximum of $\sim$4.9% variation for Outlet #9, and an average variation of $\sim$1.7% across all of the outlets).

The overall experimental performance of the tested prototype demonstrates that, practically, this prototype can be used to generate useful fluid outputs which contain useful concentrations of each of the three input fluidic species into the device. For example, 100% of each input fluidic species (with 0% of each of the other species) can be collected from the outputs from the outlets on the vertices of the bottom of the device. Furthermore, a gradient between two of the three fluidic species (and 0% of the other species) can be collected from the device outputs from the outlets on each of the sides of the bottom of the device. Additionally, the outputs from device Outlets #4, #5 & #9 can be used to collect $\sim$50% of two of the three input fluidic species with 0% of the other species present. (Of note, the output from device Outlet #9 experiences the most significant deviation from the theoretically-predicted value, likely the result of a slight manufacturing abnormality causing a consistent unexpected alteration in the flow dynamics within the prototype microchannel network. Regardless, the total deviation is a maximum of $\sim$5.6% for the fluidic species input into Inlet #2. As a consequence, the fluid output from device Outlet #9, theoretically-predicted to contain $\sim$50.9% of fluidic species from Inlet #2 and $\sim$50.1% of fluidic species from Inlet #3, contains a slightly altered proportion of each fluid, $\sim$56% of fluidic species from Inlet #2 and $\sim$45% of fluidic species from Inlet #3). Most significantly, the fluid output from Outlet #7 generates a nearly-equal proportion of each of the three input fluidic species ($\sim$35% of the fluidic species from Inlet #1, $\sim$32% of the fluidic species from Inlet #2 and $\sim$35% of the fluidic species from Inlet #3), demonstrating an experimental validation of the advantage of the 3D fluidic routing accomplished by the *tetrahedral*-based arrangement of microchannels comprising this 3D μ-CGG

design. Finally, from an operational perspective, due to the demonstrated precision and relative accuracy (all concentrations within 10% of the theoretical predictions) of the experimental flow verification results, this prototype was deemed acceptable to use in demonstrative bacteriological experiments, as described in the following section.

3.4.2.4 *Single-Antibiotic* MIC Determination Experiments

The capability of the theoretically and experimentally-characterized *tetrahedral*-based 3D μ-CGG prototype to serve as a microfluidic AST platform is first demonstrated through experiments evaluating single-antibiotic sensitivity of the same ampicillin-resistant strain of *E. coli* bacteria used in the demonstrative bacteriological experiments in **Section 3.4.1**. Similarly to those experiments, the procedure described in **Section 3.3.4** was used and performed in triplicate in order to determine the mean MIC value for Tetracycline, Ciprofloxacin and Amikacin, three different clinically-relevant antibiotic compounds also commonly used to combat AMR-related infections [222].

Appendix **Fig. 7.32** tabulates all of the stock solution concentrations used, documented MIC values for different *E. coli* strains from the literature and experimental MIC values as determined from all experiments involving the fabricated prototypes from this work for all antibiotic compounds evaluated. Likewise with the MIC determination experiments for the *layer*-based 3D μ-CGG prototype for each antibiotic compound, a stock solution of the chosen antibiotic in LB media[4] is input into Inlet #1 of the device, which is directly above Outlet #1 as seen on the bottom of the device. Furthermore, two solutions of LB media are used as buffers and input into the other two Inputs #1 & #3, directly above device Outlets #9 & #13, respectively. Thus, the 3D μ-CGG prototype is used to generate a gradient of the single antibiotic represented by discrete μ-drug cocktails which (pursuant to the protocol described in **Section 3.3.4.2**) are collected by the interfacing hardware and routed to corresponding wells on a standard 96-well plate, which are then filled with bacteria culture solution and resazurin indicator solution and incubated for what until a visible gradient of colors is observed, which ended up being an average duration of $\sim$5 hours across all of the experiments. Then, the data acquisition and quantitative analysis procedures presented in **Section 3.3.5.2** are used to quantify the normalized fluorescence intensity of resorufin emission inside the liquid sample inside each well on the fluid receptacle, producing the Normalized Growth value (with arbitrary units) of the bacteria in the presence of the fluid output from each of the Outlets on the device (*i.e.* the amount of bacterial proliferation in the given fluid sample as compared to that in the control fluid sample containing no antibiotic, and therefore the maximum amount of

[4]Images showing experimental studies of pair-wise combinations of all antibiotics (performed by manually-plating all fluids, *i.e.* the micro-broth dilution method [225]) are shown in Appendix **Fig. 7.31**. The results of these experiments, performed before any experiments involving gradients generated using the fabricated *tetrahedral*-based 3D μ-CGG prototype, were used to determine the approximate starting concentrations of each antibiotic for use in the *single-antibiotic* MIC determination experiments and in the *two-antibiotic* and *three-antibiotic* CDS experiments, as well as to produce the *MIC Bulk* data in Appendix **Fig. 7.32**.

bacterial proliferation over the course of the experiment). Thus, the inhibitory effects of the different antibiotic concentrations comprising each discrete μ-drug cocktail can be determined [269, 281]. The Normalized Growth values of the μ-drug cocktails produced from the device outlets along one edge of the device representing a gradient from 100% antibiotic to 100% buffer are then compared. The fluid sample corresponding to the MIC value of the antibiotic is represented by the first μ-drug cocktail to exhibit a step-wise enhancement in growth inhibition. The concentration of the input antibiotic species in this fluid sample is quantified using the experimental normalized concentration value of rhodamine from that device outlet as determined from the flow verification experiment (as shown in **Fig. 3.16**). Thus, the MIC value is calculated as a proportion of the input antibiotic concentration contained in the MIC-corresponding fluid sample and reported as a concentration in mg/L.

Fig. 3.17a-c presents all results for the three MIC value determination experiments. For each antibiotic evaluated, the Normalized Growth values in each of the fluid outputs from device Outlets #1, #3, #5, #7, #8 & #13 are plotted, along with the device outlet numbering convention and indication of the outlets containing 100% antibiotic and 100% buffer solutions superimposed over a rendering of the 3D model of the device. Furthermore, the corresponding concentrations of the antibiotic solution from Inlet #1 (in *light blue*) at each device outlet are presented in **Fig. 3.19d**.

3.4.2.4.1 *Tetracycline*-Buffer-Buffer

Background on the bacterial sensitivity and working mechanism of tetracycline is discussed in **Section 3.4.1.4.2**. The Normalized Growth values for the featured fluid outputs representing the tetracycline concentration gradient (**Fig. 3.17a**) indicate that the MIC value is apparent for the μ-drug cocktail from Outlet #5 (exhibiting normalized growth of $\sim$20%), which corresponds to a tetracycline concentration of $\sim$0.26 mg/L ($\sim$48% of the concentration of the input tetracycline stock solution). The fluid outputs containing higher concentrations of tetracycline show roughly the same or lower amounts of growth (below $\sim$20%), whereas those containing lower concentrations of tetracycline show increased amounts of growth (between $\sim$60%-100%), when compared to the control. This difference in observable growth above and below $\sim$0.26 mg/L justifies the decision to assign the MIC value to this μ-drug cocktail concentration, which is close to the documented range of tetracycline MIC values for similar strains of *E. coli*, $\sim$1-2 mg/L [215, 222]. Interestingly, the tetracycline MIC result found using the *layer*-based prototype in **Section 3.4.1.4.2** is in better agreement with the the MIC range in the literature than the MIC value as determined in this experiment. One explanation for this discrepancy is that the two tetracycline experiments utilized different strains of the same bacteria acquired from different sources as discussed in **Section 3.3.7**, therefore the specific bacteria procured for use in this experiment might have possessed a higher degree of susceptibility to tetracycline; alternatively, this could also be an indication that the bacteria might have developed a higher degree of sensitivity to trimethoprim over the course of culture for use in these experiments.

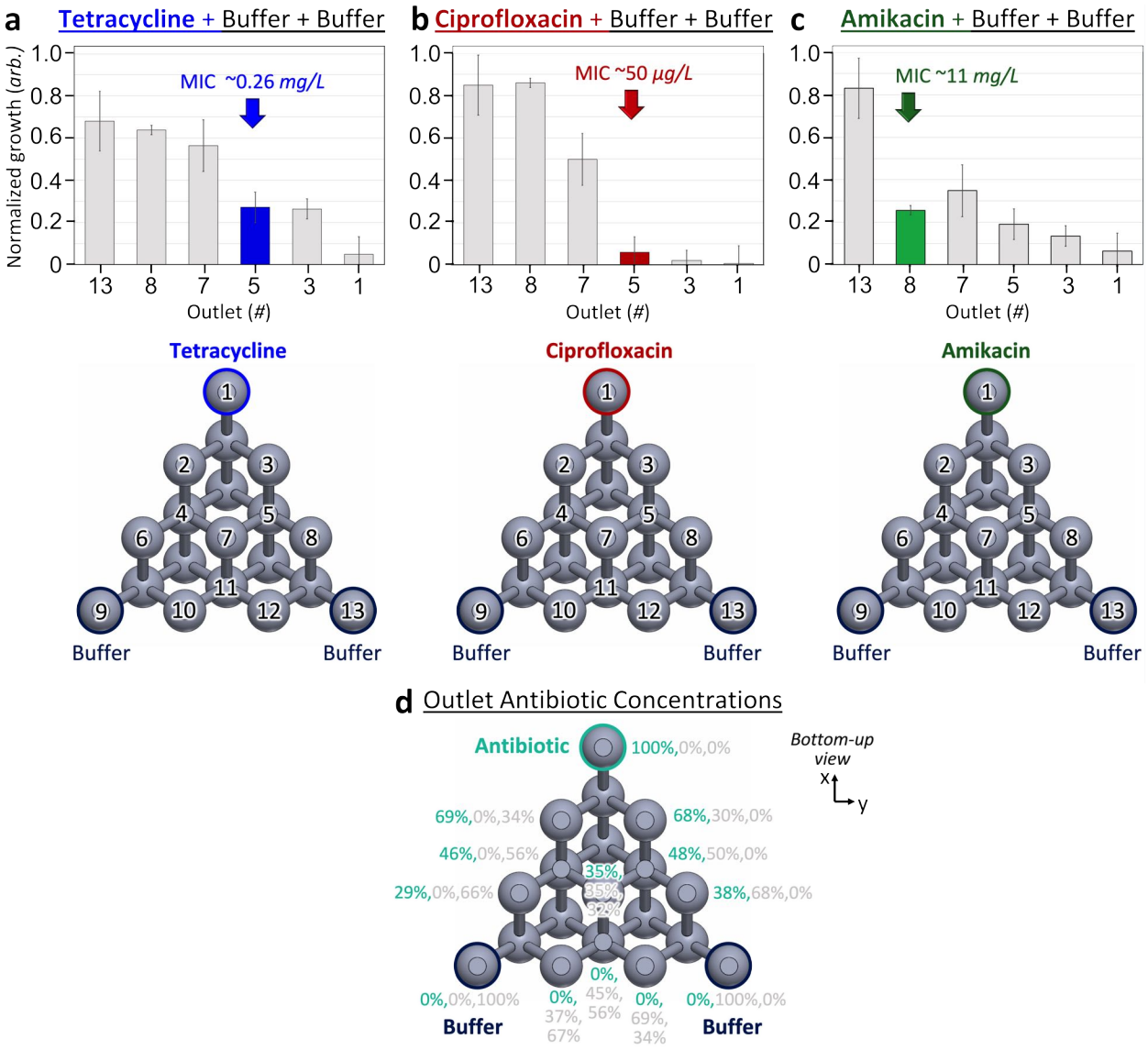

Figure 3.17: Experimental single-antibiotic MIC determination results demonstrated for the *tetrahedral*-based 3D μ-CGG prototype device with the antibiotic solution input into Inlet #1 (LB input into Inlets #2 & #3), device outputs were collected on a standard 96-well plate. Each subfigure shows (*top*) the mean value and standard deviation error bars of Normalized Growth values calculated from experiments performed in triplicate of the fluid outputs from the device outlets along one edge of the device representing a gradient from 100% antibiotic to 100% buffer, as well as (*bottom*) the outlet numbering convention and indication of the outlets containing 100% antibiotic and 100% buffer solutions. Results involving **(a)** Tetracycline (MIC value in *blue*), **(b)** Ciprofloxacin (MIC value in *red*) and **(c)** Amikacin (MIC value in *green*) compounds. **(d)** Corresponding concentration of the antibiotic solution at each device outlet (in *light blue*).

3.4.2.4.2 *Ciprofloxacin*-Buffer-Buffer

Ciprofloxacin has been a clinically-available antibiotic since the late 1980's, and is used today to combat UTI's, respiratory infections, gastroenteritis, endocarditis and typhoid fever caused by bacteria such as *E. coli*, *E. faecalis* and *Salmonella enterica*. The working mechanism of ciprofloxacin is by inhibiting the DNA replication and cellular reproduction. Since ciprofloxacin is widely commercially-available and inexpensive to produce, it has historically been used worldwide over the past few decades to treat relatively-minor bacterial infections which would be easily-treatable with other more narrow-spectrum classes of antibiotics; thus, many strains of the aforementioned bacteria have developed low susceptibility, and in some cases very strong resistance, towards ciprofloxacin. In fact, developed-AMR towards ciprofloxacin has been observed even over the course of treatment of a single instance of an infection. The most commonly ciprofloxacin-resistant bacteria are UTI-causing strains of *E. coli*, therefore the prescription of ciprofloxacin to treat UTI's is usually precluded by AST evaluation on patient samples used to identify effective MIC values for non-AMR bacterial strains. Ciprofloxacin is often useful in combination with other antibiotics to treat common otherwise AMR-related bacterial infections including UTI's, however, so CDS involving ciprofloxacin is of great clinical importance. [227, 230, 233, 285]

The Normalized Growth values for the featured fluid outputs representing the ciprofloxacin concentration gradient (**Fig. 3.17b**) indicate that the MIC value is also apparent for the μ-drug cocktail from Outlet #5 (exhibiting normalized growth of $\sim$5%), which corresponds to a ciprofloxacin concentration of $\sim$50 μg/L ($\sim$52% of the concentration of the input ciprofloxacin stock solution). The fluid outputs containing higher concentrations of tetracycline show roughly the same amount of growth (below $\sim$5%), whereas those containing lower concentrations of ciprofloxacin show increased amounts of growth (between $\sim$50%-100%), when compared to the control. This drastic difference in observable growth justifies the decision to assign the MIC value to this μ-drug cocktail. Therefore, the ampicillin-resistant *E. coli* bacterial strain evaluated in these experiments is deemed susceptible to ciprofloxacin above concentrations of $\sim$50μg/L, which is in agreement with the documented range of ciprofloxacin MIC values for similar known multi-drug AMR strains of *E. coli*, $\leq \sim$1 mg/L [215, 217].

3.4.2.4.3 *Amikacin*-Buffer-Buffer

Amikacin is generally considered a safe and highly clinically-useful antibiotic first introduced in the 1970's, and is particularly effective in antibiotic combination treatments used to treat otherwise AMR-related bacterial infections such as serious UTI's, tuberculosis and bacterial meningitis caused by bacteria such as *E. coli*, *Enterobacter cloacae*, *S. pneumoniae*, *P. aeruginosa* and *Proteus mirabilis*, by interfering with RNA synthesis. Most bacteria demonstrate susceptibility towards amikacin, mainly when in combination with other classes of antibiotics, but some AMR strains of bacteria such as AMR-related UTI-causing *E. coli* demonstrate intermediate resistance

to the antibiotic on its own. As a result, AST evaluation of amikacin, especially CDS of pair-wise combinations including amikacin, is highly-recommended in clinical and drug development settings around the world. [216, 217, 227, 286, 287]

The Normalized Growth values for the featured fluid outputs representing the amikacin concentration gradient (**Fig. 3.17c**) indicate that the MIC value is apparent for the μ-drug cocktail from Outlet #8 (exhibiting normalized growth of $\sim$30%), which corresponds to a ciprofloxacin concentration of $\sim$11 mg/L ($\sim$38% of the concentration of the input ciprofloxacin stock solution). The fluid outputs containing higher concentrations of amikacin show roughly the same or lower amount of growth (normalized growth from Outlet #8 is within the statistical deviation of the normalized growth from Outlet #7), whereas Outlet #13 which contains 100% of the concentration of the input amikacin stock solution shows the highest amount of growth (statistically up to $\sim$100%), when compared to the control. This difference in observable growth justifies the decision to assign the MIC value to the μ-drug cocktail in Outlet #8. Therefore, the ampicillin-resistant *E. coli* bacterial strain evaluated in these experiments is deemed susceptible to amikacin above concentrations of $\sim$11 mg/L, which is close to the documented range of amikacin MIC values for similar strains of *E. coli*, $\sim$16-20 mg/L [215, 284, 287], if not a little lower, indicating that the evaluated bacterial strain is slightly more sensitive to the amikacin solution used in this work.

3.4.2.5 *Two-Antibiotic* CDS Experiment

In addition to MIC determination for single antibiotics, the fabricated 3D μ-CGG prototype can also be used as a clinically-relevant AST tool to perform individual *pair-wise* CDS studies. **Fig. 3.18a-c** presents three distinct sets of experimental results for the AST evaluation of generated gradients between two antibiotics simultaneously. For each two-antibiotic combination evaluated, the Normalized Growth values in each of the fluid outputs from device Outlets #1, #3, #5, #7, #8 & #13 are plotted, along with the device outlet numbering convention and indication of the outlets containing 100% antibiotic solutions and 100% buffer solution superimposed over a rendering of the 3D model of the device. Furthermore, the corresponding concentrations of the antibiotic solutions from Inlet #1 (in *light blue*) and Inlet #2 (in *purple*) at each device outlet are presented in **Fig. 3.19c**. Two-antibiotic combinations of amikacin, ciprofloxacin and tetracycline have all been previously used in various clinical combination treatments to combat certain AMR-related bacterial infections; furthermore, previously-demonstrated CDS studies from the literature have established the known pair-wise interactions of each antibiotic combinations, mostly towards cultured strains of common bacteria such as *E. coli*. In general, amikacin and ciprofloxacin have demonstrated *synergistic* effects in combination [227, 249]; amikacin and tetracycline have demonstrated *additive* effects in combination [288, 289]; and tetracycline and ciprofloxacin have demonstrated *antagonistic* effects in combination [233].

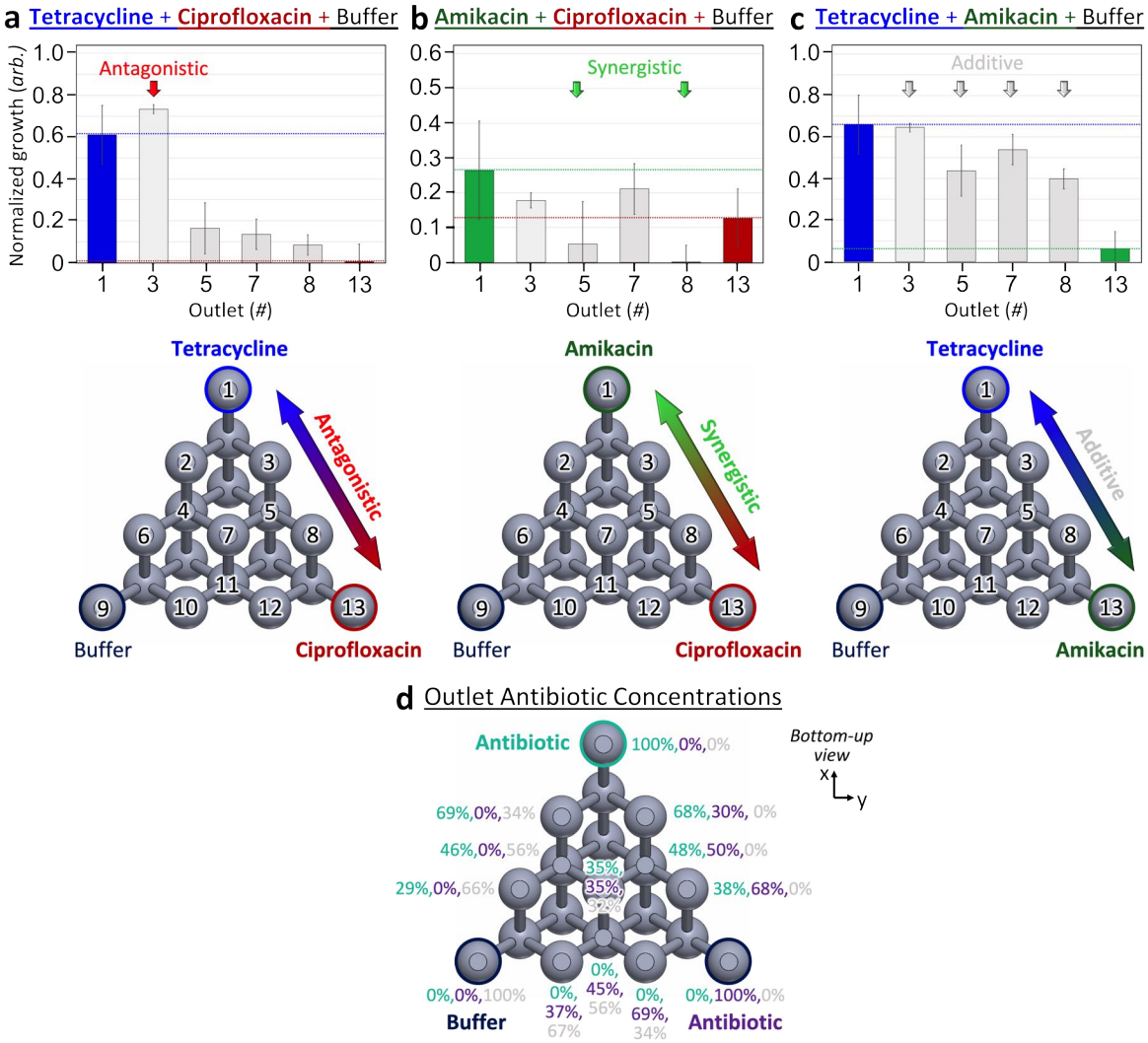

Figure 3.18: Experimental *pair-wise* CDS results demonstrated for the *tetrahedral*-based 3D μ-CGG prototype device with antibiotic solutions input into Inlets #1 & #3 (LB input into Inlets #2), device outputs were collected on a standard 96-well plate. Each subfigure shows (*top*) the calculated mean and standard deviation of Normalized Growth values of the fluid outputs from the device outlets along one edge of the device representing a gradient from 100% of one antibiotic to 100% of the other antibiotic calculated from experiments performed in triplicate, colored horizontal lines and bars indicate the Normalized Growth values for 100% amikacin (*green*), 100% ciprofloxacin (*red*) and 100% tetracycline (*blue*), colored arrows also indicate outlets which demonstrate pair-wise interactions between the two antibiotics which agree with those documented in the literature; as well as (*bottom*) outlet numbering convention and indication of the outlets containing 100% of each of the antibiotics. Results involving **(a)** Tetracycline+Ciprofloxacin (*antagonistic* interaction indicated in *red*), **(b)** Amikacin+Ciprofloxacin (*synergistic* interaction indicated in *green*) and **(c)** Tetracycline+Amikacin (*additive* interaction indicated in *grey*). **(d)** Corresponding concentrations of the antibiotic solutions from Inlet #1 (in *light blue*) and Inlet #3 (in *purple*) at each device outlet.

The expected *antagonistic* effect of tetracycline and ciprofloxacin in combination (**Fig. 3.18a**) is demonstrated by the μ-drug cocktail from Outlet #3 which demonstrates more normalized growth than both the 100% tetracycline from Outlet #1 and the 100% ciprofloxacin from Outlet #13. This specific chemistry would therefore be *highly avoided* in treating an infection caused by the ampicillin-resistant *E. coli* strain demonstrated in this work. The specific chemistries of the μ-drug cocktails from Outlets #5, #7 & #8 on the other hand demonstrate *additive* effects between the two μ-drug cocktails of 100% of each antibiotic, therefore none of these μ-drug cocktail chemistries would be recommended in treating such infections. Furthermore, the expected *synergistic* effect of amikacin and ciprofloxacin in combination (**Fig. 3.18b**) is demonstrated by the μ-drug cocktails from Outlets #3 & #8 which demonstrate less normalized growth than both the 100% amikacin from Outlet #1 and the 100% ciprofloxacin from Outlet #13. These specific chemistries would therefore be *highly recommended* in treating an infection caused by the ampicillin-resistant *E. coli* strain demonstrated in this work. The specific chemistries of the μ-drug cocktails from Outlets #3 & #7 demonstrate *additive* effects between the two μ-drug cocktails of 100% of each antibiotic, rather, therefore none of these μ-drug cocktail chemistries would be recommended in treating such infections. Finally, the expected *additive* effect of tetracycline and amikacin in combination (**Fig. 3.18c**) is demonstrated by the μ-drug cocktails from Outlets #3, #5, #7 & #8 which demonstrate intermediate normalized growth between the 100% tetracycline from Outlet #1 and the 100% amikacin from Outlet #13. These specific chemistries would therefore not be recommended in treating an infection caused by the ampicillin-resistant *E. coli* strain demonstrated in this work.

3.4.2.6 *Three-Antibiotic* CDS Experiment

Fig. 3.19 presents the experimental results of a three-antibiotic CDS demonstration of AST evaluation of the combinatorial effects of all three antibiotic compounds, simultaneously, from a single experimental single operation of the prototype device. The inherent advantageous capabilities of this 3D μ-CGG prototype are apparent by analyzing the different types of gradients that are produced from a single operation of the device, as analysis of just a single image of the 96-well plate from a single experiment represents data for 13 μ-drug cocktails which capture three discrete pairwise antibiotic gradients and a single μ-drug cocktail which contains a nearly-identical proportion of all three-antibiotic, a unique capability demonstrated by the symmetric 3D fluidic routing accomplished using the *tetrahedral*-based 3D microchannel arrangement featured in this design. The outlet numbering convention used in the experiments and indication of the outlets containing 100% of each of the antibiotics are illustrated in **Fig. 3.19b**. Furthermore, the corresponding concentrations of the antibiotic solutions from Inlet #1 (in *light blue*), Inlet #2 (in *yellow*), and Inlet #3 (in *purple*) at each device outlet are presented in **Fig. 3.19c**.

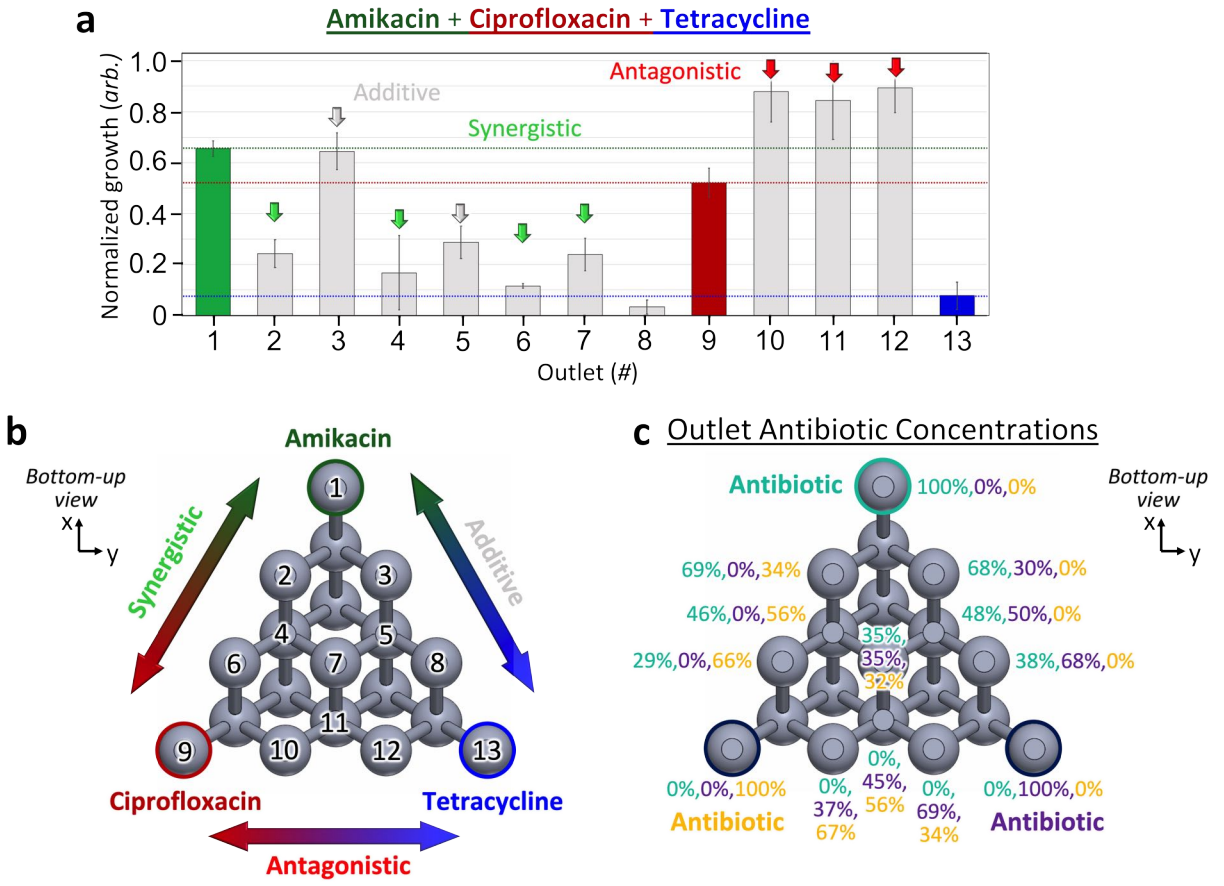

Figure 3.19: Experimental *three-way* CDS results demonstrated for the *tetrahedral*-based 3D μ-CGG prototype device with antibiotic solutions input into Inlets #1, #2 & #3, device outputs were collected on a standard 96-well plate. **(a)** Calculated mean and standard deviation of Normalized Growth values of the fluid outputs from all of the device outlets from experiments performed in triplicate represented by bars. Colored horizontal lines and bars indicate the normalized growth for 100% amikacin (*green*) in Outlet #1, 100% ciprofloxacin (*red*) in Outlet #9 and 100% tetracycline (*blue*) in Outlet #13. Colored arrows indicate the outlets which demonstrated pair-wise interactions between each two antibiotics which agree with those documented in the literature, *i.e. synergy* between Amikacin+Ciprofloxacin in *green*, *additivity* between Tetracycline+Amikacin in *grey*, and *antagonism* between Tetracycline+Ciprofloxacin in *red*. **(b)** Outlet numbering convention and indication of the outlets containing 100% of each of the antibiotics. **(c)** Corresponding concentrations of the antibiotic solutions from Inlet #1 (in *light blue*), Inlet #2 (in *yellow*), and Inlet #3 (in *purple*) at each device outlet.

Similar to the three-antibiotic demonstration of the *layer*-based 3D μ-CGG prototype in **Section 3.4.1.5**, the high-throughput capability of this device is experimentally demonstrated as three distinct pair-wise studies of two antibiotics are simultaneously generated. For example, the μ-

drug cocktails generated from Outlets #1, #3, #5, #8 & #13 represent a pair-wise gradient between amikacin and tetracycline; those generated from Outlets #1, #2, #4, #6 & #9 represent a pair-wise gradient between amikacin and ciprofloxacin; and those generated from Outlets #9, #10, #11, #12 & #13 represent a pair-wise gradient between ciprofloxacin and tetracycline.

The expected *additive* effect of amikacin and tetracycline in combination is demonstrated by the fact that the μ-drug cocktails from Outlets #3 & #5 demonstrate intermediate normalized growth between the 100% amikacin from Outlet #1 and the 100% tetracycline from Outlet #13. The expected *synergistic* effect of amikacin and ciprofloxacin in combination is demonstrated by the fact that the μ-drug cocktails from Outlets #2, #4 & #6 all demonstrate lower normalized growth than both the 100% amikacin from Outlet #1 and the 100% ciprofloxacin from Outlet #9. Finally, the expected *antagonistic* effect of ciprofloxacin and tetracycline in combination is demonstrated by the fact that the μ-drug cocktails from Outlets #10, #11 & #12 all demonstrate significantly higher normalized growth than both the 100% ciprofloxacin from Outlet #9 and the 100% tetracycline from Outlet #13. The only unexpected pair-wise antibiotic effect is demonstrated by the observed *synergism* between the amikacin and tetracycline in combination in the μ-drug cocktail from Outlet #8, which demonstrates less normalized growth than either the 100% amikacin or the 100% tetracycline. This specific chemistry would therefore be *recommended* in treating an infection caused by the ampicillin-resistant *E. coli* strain demonstrated in this work.

Moreover, the novel 3D fluidic routing capability of the 3D μ-CGG prototype device is also demonstrated by the generated μ-drug cocktail produced from Outlet #7 which contains a nearly-identical proportion of each of the three input antibiotic compounds ($\sim$35% amikacin, $\sim$32% ciprofloxacin & $\sim$35% tetracycline). This μ-drug cocktail demonstrates *synergistic* effects as compared to the 100% solutions of amikacin and ciprofloxacin and the 100% solutions of amikacin and ciprofloxacin, but *additive* effects as compared to the 100% solutions of amikacin and tetracycline and the 100% solutions of amikacin and ciprofloxacin. Overall, the μ-drug cocktails generated by Outlets #2, #4, #5, #6, #8 & #13 demonstrate more effective inhibition of bacterial proliferation, therefore the specific three-antibiotic μ-drug cocktail chemistry would not be a recommended dosage for treatment of an infection caused by the ampicillin-resistant *E. coli* strain demonstrated in this work. Regardless, this specific symmetric three-antibiotic combination is the result of a unique capability demonstrated by the symmetric 3D fluidic routing accomplished only by the geometrically-symmetric *tetrahedral*-based 3D microchannel arrangement featured in the *tetrahedral*-based 3D μ-CGG design, and which is otherwise impossible to generate using planar fluidic routing inherent to conventional CGG-based microfluidic devices.

Chapter 4

Integrated Finger-Powered Microfluidic Actuators

4.1 Introduction

Biomedical and diagnostic platforms for *on-site* sample processing and analysis are important tools for *point-of-need* or *point-of-care* applications. Outbreaks of antimicrobial-resistant infections, for example, encourage the development of rapid and accurate diagnostic tools [17]. Most point-of-need devices used in the biomedical community today, such as immunoassay test strips for the qualitative detection of various biomolecules (*e.g.* glucose, blood coagulants, recreational drugs, stress and pregnancy hormones) are used to perform bodily fluid analysis at the patient's bedside, thus eliminating the need to collect and transport a patient's sample to an *off-site* biological laboratory for comprehensive analysis; yet, the vast majority of these approaches lack analytical precision, sensitivity and selectivity [290]. Specific demands of truly capable point-of-need diagnostic platforms therefore are for relatively low cost, portable and compact hardware, preferably with a low-power demand in many applications, which can be readily used to perform rapid and precise diagnostic analysis in low-resource settings such as in rural healthcare clinics and at isolated locations of potential outbreaks of disease [291–293].

Microfluidic technologies such as *lab-on-a-chip* and *micro-total analytical system* (μ-TAS) platforms demonstrate the ability to miniaturize conventional laboratory-based fluid processing methods onto compact physical devices. As a result, microfluidic approaches often enable a reduction in overall equipment size and cost, as well as required fluidic operating volumes and reagent expenses. Additionally, many systems demonstrate the capability for *on-chip* automation of fluidic routines which often results in reduced requirements for highly-trained personnel, as well as the reduction of procedural errors. Furthermore, microfluidic-based approaches often demonstrate more rapid fluidic analysis (*e.g.* by reducing necessary biological incubation times due to the handling of sub-mL bacteria culture volumes) with increased sensitivity, selectivity and reproducibility towards the detection of target analytes. Therefore, microfluidic-based analytical methods have been proposed and demonstrated, especially in the last decade or so, towards many point-of-need biomedical and applications [294–296]. The majority of microfluidic-based techniques, however,

involve multiple independent time and manual labor intensive analytical procedures which must be performed by highly-skilled trained personnel and use expensive, bulky and high-powered interfacing equipment [297]. In particular, conventional microfluidic platforms rely upon high-powered and non-portable *off-chip* sources of fluidic actuation, such as air pressure-driven microfluidic controllers or electrically-driven mechanical pumps which limit most microfluidic technologies to well-equipped laboratory-based settings [3, 298, 299]. Therefore most conventional *lab-on-a-chip* microfluidic devices are very much *chips-in-a-lab*, which limits the portability and applicability of such systems for truly-point-of-need biomedical and diagnostic applications.

In order to reduce the need for such conventional fluidic actuators, various microfluidic designs have demonstrated alternative sources of passive or electrical power-free fluidic actuation, such as integrated low-power micro-pumps [300, 301] and passive vacuum pressure-driven flow utilizing the porosity of PDMS for whole blood separation [302]. Additionally, *on-chip* integrated *finger-powered fluidic actuators* have been previously-demonstrated, constructed *via* soft-lithography from multiple assembled layers of PDMS and *via* injection molding from molded thermoplastic sheets [77], enabling entirely human-powered generation of predicable pressure waves used to perform *on-chip* fluidic routines in electrical power-free microfluidic applications such as the *on-chip* generation of micro-droplets and single-cell handling [303], as well as concentration gradient generation [304]. Moreover, additive manufacturing approaches have been recently employed to fabricate *on-chip* integrated dynamic micro-valves and micro-pumping systems [105, 108, 305], yet these 3D printed systems still rely upon externally-powered *off-chip* air pressure sources and microfluidic controllers. The development of monolithically-manufacturable and easily-tailorable finger-powered microfluidic actuators which can be directly incorporated into the 3D digital design of any entirely-3D printable microfluidic device therefore represents a promising approach to eliminating the requirement for bulky, high-powered microfluidic control interfaces and fluid actuation hardware, which is necessary to expand the applicability of microfluidic platforms out of the laboratory and into truly point-of-need settings.

4.2 Design of 3D Printable Finger-Powered Actuators

4.2.1 Concept of On-Chip Integrated 3D Fluidic Networks

The concept of designing integrated 3D fluidic operator networks to accomplish finger-powered fluidic actuation at any arbitrary location in the entirely-3D printed microfluidic device is illustrated in **Fig. 4.1**. As previously demonstrated, the Multijet additive manufacturing approach enables the straightforward monolithic fabrication of intricate static and dynamic 3D microstructural elements, such as dynamic 3D corrugated membranes with fluidic capacitor-like functionalities, as well as dynamic 3D corrugated membranes with a central aperture enclosed by upper and lower fluidic channels, to generate scalable 3D capacitor-like and diode-like fluidic operators, respectively [115, 121, 127]. The proposed so called *3D printed finger-powered actuator* (FPA) concept (**Fig. 4.1a**) consists of a 3D fluidic network which can be integrated into any arbitrary location of the 3D solids model of a 3D printable microfluidic device where fluid actuation is desired.

In the proposed FPA design, a finger-actuated 3D corrugated membrane encloses an air reservoir which is connected to an air channel. The air channel is isolated from a separate fluid channel by an additional corrugated membrane inside a fluidic reservoir. As the finger-actuated membrane is depressed, the pressure force generated by the evacuation of the air in the air reservoir is transduced to the other corrugated membrane, which displaces upwards into the fluidic reservoir. This action reduces the volume of the fluidic reservoir, forcing the fluid volume through a network of two fluidic one-way valves to generate a net fluid flow in the direction of the forward-facing (*rightmost* in the illustration) fluidic diode. The flexibility of the 3D solids modeling process enables the integration of a single air channel with multiple independent fluid channels *on-chip* (**Fig. 4.1b**), serving as a common source of fluidic actuation which can be used to drive multiple fluids at the same input fluidic flow rate through a larger, more complicated microfluidic network. Moreover, the conceptual FPA design can also be fabricated as a modular system (**Fig. 4.1c**), serving as a completely independent, hand-held source of fluidic actuation, which can interface between a source fluid reservoir and a stand-alone microfluidic chip, fabricated either entirely using additive manufacturing or conventional MEMS-based fabrication processes. Overall, the proposed 3D printed FPA approach serves to eliminate the need for multiple *off-chip*, bulky and high-powered independent fluidic actuation sources for point-of-need and point-of-care biomedical and diagnostic applications.

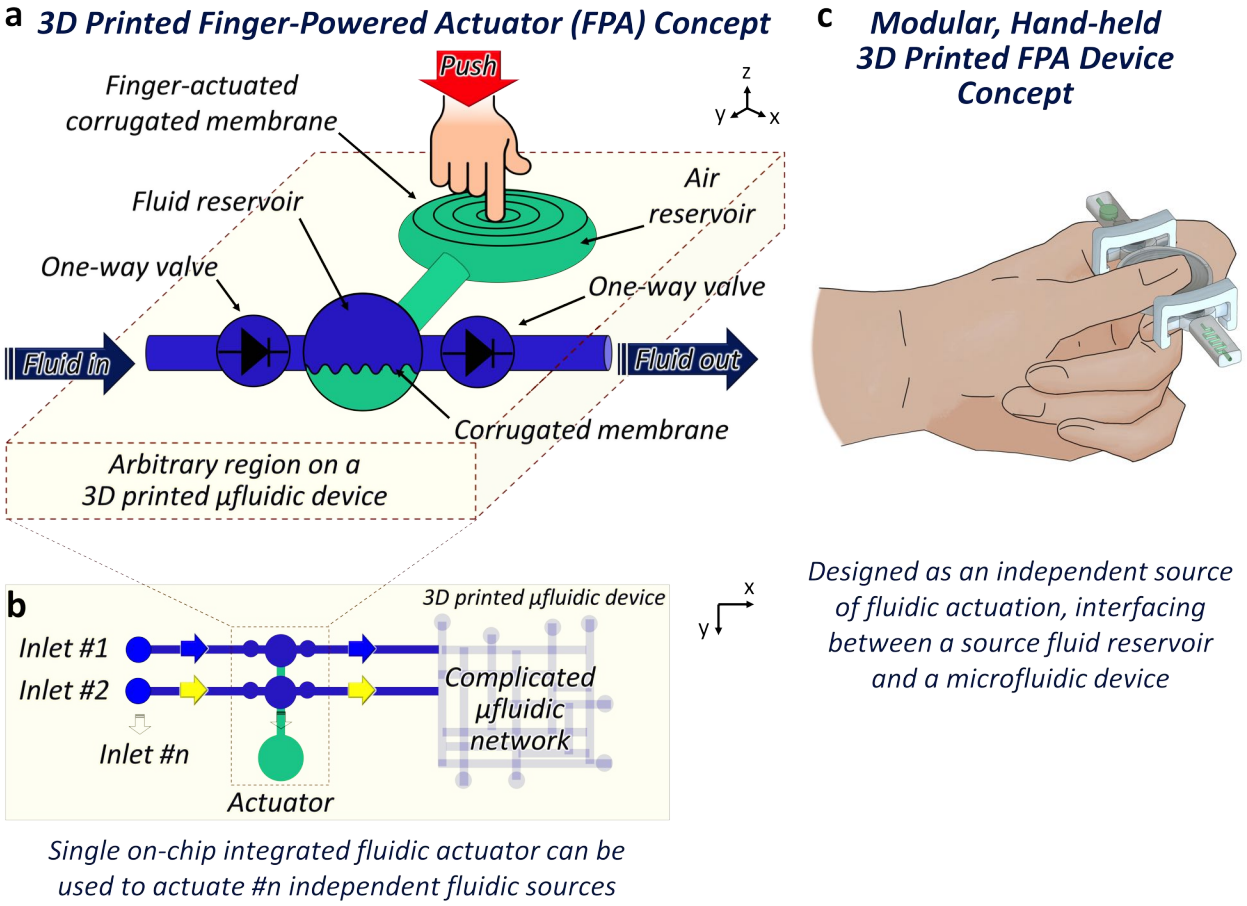

Figure 4.1: Conceptual illustrations of the proposed 3D Printed Finger-Powered Actuator (FPA) microfluidic design. **(a)** An integrated network of 3D fluidic operators is comprised of two isolated channels, a fluid channel (*blue*) and an air channel (*green*), and can be integrated into the 3D solids model of a 3D printable microfluidic device at any arbitrary location where fluid actuation is desired. When depressed by the operator's finger, the finger-actuated corrugated membrane generates a positive pressure inside the air channel, causing the corrugated membrane to expand, driving the fluid through two fluidic one-way valves in-series, producing a new-forward fluid flow in the direction of the fluidic outlet channel. **(b)** The air channel can be integrated into multiple isolated fluid channels to simultaneously actuate multiple fluids through an arbitrarily-complicated microchannel network down-stream on a 3D printed microfluidic device. **(c)** The proposed FPA design can also be fabricated as a modular, hand-held 3D printed device used to interface between a fluid source and an additional microfluidic device (constructed *via* conventional or additive manufacturing approaches) to serve as an independent source for human-powered fluidic actuation.

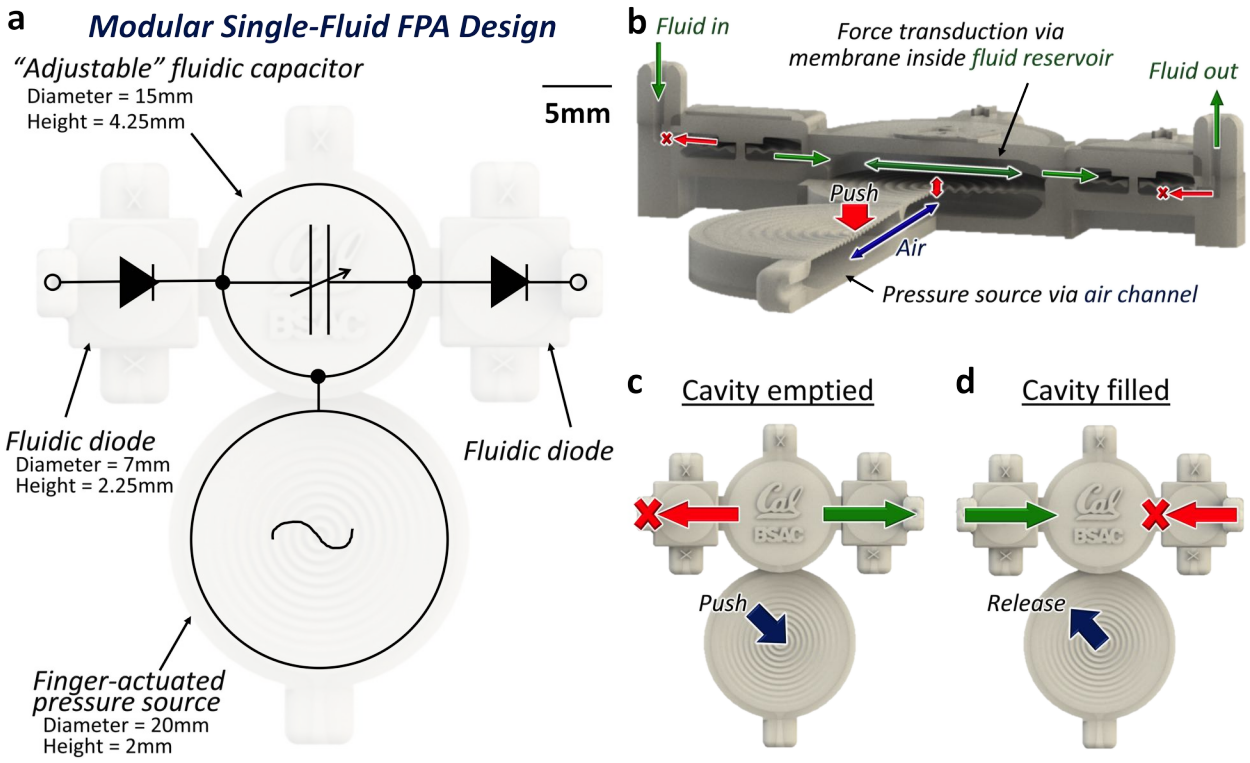

Figure 4.2: Schematic and working principle of the proposed modular single-fluid 3D Printed FPA prototype. **(a)** Top-down rendering of the 3D solids model superimposed with a fluidic circuitry schematic. **(b)** Cross-section rendering indicating forward (*green arrows*) and prevented directions (*red arrows*) of fluid actuation inside the device. When corrugated membrane comprising the *finger-actuated pressure source* is depressed by the operator's finger, a positive pressure is generated inside the air channel, causing the corrugated membrane inside the fluid reservoir (which behaves akin to an *adjustable fluidic capacitor*) to expand and transduce the force to the fluid volume inside the reservoir, which forces the fluid through two one-way *fluidic diodes* in-series, producing a net-forward fluid flow. **(c)** Top-view rendering indicating operational principle. When the finger-actuated membrane is pushed, the fluid volume inside the reservoir is driven in the net-forward direction through the right-most fluidic diode. **(d)** When the finger-actuated membrane is released, fluid volume fills the reservoir from the fluid source connected to the left-most fluidic diode.

4.2.2 Design of Modular Single-Fluid Finger-Powered Actuator (FPA)

In this work, modular single-fluid FPA prototypes were designed and fabricated in order to characterize their fluid actuation characteristics, experimentally. The basic design and working principle of the fundamental modular single-fluid 3D printed FPA are illustrated in **Fig. 4.2**. The design schematic (**Fig. 4.2a**) reveals that the finger-actuated corrugated membrane (3D cross-sectional profile based off the 2D damped sinusoidal function previously developed by our group towards 3D fluidic capacitor membranes [115]) and air reservoir function akin to a sinusoidal pressure source,

which transduces the force of membrane depression to the fluidic reservoir, which acts akin to an *adjustable* fluidic capacitor as the internal membrane expands and contracts. The two fluidic one-way valves are made possible by two 3D fluidic diodes, the design of which, for the FPA_{V1} model, is adapted from that previously demonstrated by our group [115]. The cross-sectional illustration of the fluid and air channels (**Fig. 4.2b**) helps to visualize the fluid motion inside each 3D fluidic operator during device operations.

When the finger-actuated membrane is depressed (**Fig. 4.2c**), a positive pressure is generated as air is forced from the pressure source via the air channel to underneath the membrane inside the fluid reservoir, which transduces the force applied by the operator's finger to the fluid reservoir membrane. The expansion of this membrane reduces the volume of the hollow upper region which forces fluid into the lower channel of the left-most fluidic diode and into the upper channel of the right-most fluidic diode. A more detailed explanation of the working mechanism behind this 3D fluidic diode design is presented in **Section 4.4.4**; briefly, each fluidic diode is comprised of a diaphragm with a damped sinusoidal profile which contains circular aperture in the center, allowing fluid to flow from the upper channel, through the center aperture, to the lower channel under forward fluid flow conditions. Under reverse flow conditions, the diaphragm deforms upwards and contacts the static upper surface of the interior, serving to obstruct fluid flow. Therefore, the right-most diode permits net fluid flow forward through to the outlet of the device, whereas the left-most diode prevents most fluid flow in the reverse direction.

When the finger-actuated membrane is released (**Fig. 4.2d**), the positive pressure on the membrane inside the fluid reservoir is relaxed, permitting the membrane to contract and producing a vacuum pressure inside the fluid reservoir. Due to the arrangement of the fluidic diodes, this creates a forward-driving fluid flow through the left-most fluidic diode from the device inlet, dominating any back-flow through the right-most diode, in order to fill the fluid reservoir and return the device back to its initial state. This aforementioned operation represents one complete *fluid actuation cycle*. The frequency and duration of the repeated fluid actuation cycles will have a direct effect on the effective fluid flow rate produced at the outlet of the modular FPA_{V1} device.

4.3 Materials and Methods

4.3.1 Three Dimensional Modeling

All of the 3D microfluidic operator elements were designed as individual parts using Solidworks, following the example discussed in **Section 2.3.1**. Specific modular operator elements featured in this work are based off of the initial fluidic operator designs featured in our group's previous work [115]. The improved fluidic diode, dynamic bracket element and the air-fluid cavity (*i.e.* fluid reservoir) designs, along with the concepts of the human-powered elements and integrated fluid+air fluidic networks are all developments inherent to this project. Each of the individual 3D fluidic operators solids model parts were assembled into a single assembly (with modification of each individual part file to create and remove interconnecting holes) in order to form continuous 3D integrated fluidic circuits comprising the various modular, hand-held device designs. The conceptual illustrations shown in **Figs. 4.2, 4.3c, 4.4-4.9a,4.10a,c** were all created using PhotoView 360 and were used to export individual .STL files for fabrication.

4.3.2 Fabrication and Post-Processing

The prototype devices featured in this work were fabricated from the same materials, using the same equipment and were processed using the same post-processing procedure as previously detailed in **Section 2.3.3**. The wax-based support material was removed from the microchannel network by manually forcing heated mineral oil solution through each of the exposed microchannel inlets in the device, taking care not to apply so much pressure as to cause observable deformation in the finger-actuated membrane.

4.3.3 Experimental Setup

To evaluate the fluid actuation performance of each fabricated FPA prototype, a bench top setup was constructed and used to visualize the forward-driven fluid output from each device upon actuation of the finger-actuated pressure source membrane. An example of the experimental setup used to test the fabricated FPA_{V1} prototype is shown in Appendix **Fig. 7.36**. Before each experiment involving the single-fluid FPA prototypes, blue dyed solution (formulated by filling a 10mL glass petri dish with DI water and adding and incorporating 10 drops of blue food-grade color dye) was manually loaded onto the prototype device, filling the entirety of the fluid network. In the experiments involving the two-fluid $\text{FPA}_{V1,2fluid}$ prototype, blue dyed solution and yellow dyed solution were used to fill each independent fluid network until laminar flow exited the terminus

of the linear output channel. All extraneous microchannel inlets (*i.e.* those other than the one inlet to the upper channel of the left-most fluidic diode and the one inlet to the lower channel of the right-most fluidic diode) were plugged using stainless steel catheter plugs (model SP20/12, *Instech*). Segments of Tygon microbore tubing (model #06420-03, *Cole-Palmer*) were then connected to each inlet *via* stainless steel interconnecting couples (model SC20/15, *Instech*). The other end of the short segment of tubing ($\sim$1 cm) connected to the inlet of the prototype device (pre-filled with blue solution) was connected to a 3D printed 5mL reservoir filled with blue dyed fluid and serving as the fluidic source. The longer segment of tubing (up to $\sim$50 cm) connected to the outlet of the prototype device was used to visualize the output fluid from the device. To seal the air pressure source, steel plugs were used to block the two microchannel inlets to the pressure source channel. The experimental setup for each test consists of a white printer paper background to provide maximum contrast between the blue fluid filling the tubing and the background surface and the output segment of tubing linearly-positioned with a ruler placed above the tubing serving as a length reference.

4.3.4 Data Acquisition and Quantitative Video Processing

As mentioned in **Section 4.3.3**, a video analysis approach was chosen for data acquisition. It was experimentally-determined upon initial interfacing of the fluid output of the fabricated FPA prototypes that the rate of change of the instantaneous flow rates from the prototype devices at 1 Hz. Higher actuation frequencies exceeded the measurement capabilities of the FLOWELL microfluidic flow rate sensor platform (*Fluigent*, France) used in the laboratory for data acquisition. Since the sampling rate of an iPhone camera (30 frames-per-second) is higher than that of the FLOWELL platform (10 samples-per-second), a video recording method was employed to acquire raw data of the fluidic output performance of each prototype with different actuation frequencies. The experimental setup described in **Section 4.3.3** was used to collect the output fluid in a length of transparent tubing which enabled visualization of the rate of change of fluid volume within the tube with time. The operation of each prototype is recorded using an iPhone 10 camera running the iOS 11 operating system, and the video recording is subsequently analyzed using a custom Python video analysis script. The iPhone camera is supported using foam blocks to either side of the experimental setup, outside of the frame of the camera and positioned such that no shadow effects are generated. The lighting source was provided by an incandescent light bulb on a standing lamp positioned to the side of the iPhone as to deliver uniform light directed down upon the output tubing with no shadows or brilliant reflection on the tubing itself. Default frame rate, zoom and exposure settings for the iPhone 10 camera were used. The video recording is manually-started, a digital iPhone metronome app (Pro Metronome, *Xanin Tech, GmbH.*) is used to produce a sound at the desired frequency, and the prototype is then manually-actuated to match the desired actuation frequency produced by the metronome app, pushing with the pad of the index finger until the membrane is fully-depressed and being careful not to apply excess pressure to the sides of the membrane where the material is the weakest, which could result in fracture. The experiments

all run for up to one minute, or until the output tubing is completely filled (at higher Hz). When complete, the video recording is ended and the video file transferred to a computer and used in the following video analysis procedure. Analysis of the video recordings served to quantify fluid output parameters such as instantaneous fluid flow rate (one measurement every ∼33 milliseconds); average effective fluid flow rate over the course of the recording; the forward, reverse and net volume pumped per actuation cycle and with respect to time and with respect to actuation frequency.

To analyze the fluid output performance of the fabricated FPA_{V1}, FPA_{V2} and $\text{FPA}_{V2,in-line}$ prototypes (**Sections 4.4.3, 4.4.6 & 4.4.7**, respectively), a combination of Fiji image processing and data analysis using a custom Python script[1] were employed to extract raw data from each frame of a video recording of a given prototype operation experiment and to produce and plot the aforementioned quantifiable fluid flow parameters. See Appendix **Section 7.4**, *Image Analysis Protocol For Producing Raw Data From Videos of FPA Prototypes* for the video analysis protocol discussed in greater detail. Briefly, a raw .MOV video is imported into Fiji image analysis software, where it is then manually trimmed to appropriate beginning and ending times, the measurement scale is defined based on the size of a ruler in the frames of the video, an RGB stack is performed and the red channel selected and built-in software tools used to create a vectorized skeleton of the fluid path throughout the duration of the video. This skeleton (.txt file) along with video frames (.png files) at the beginning and ending of the video are then saved. The Python script is then used to import the skeleton, video frames and the video file itself. The program then analyzes the video to calculate the distance that the fluid has traveled along the path length of the tube at each frame of the video, then a a series of image processing codes calculate the instantaneous fluid flow rate and volume pumped at each frame (one-thirtieth of a second), taking into account the inner diameter of the tubing, and storing this data in a matrix. This data is then processed to produce and plot all of the quantified fluid flow parameters presented in **Figs. 4.5, 4.8 & 4.9**.

To produce the Q-P plot for the fabricated modular Diode_{V2} prototype in order to understand the fluid rectification behavior of this diode design and to calculate the diodicity value (**Section 4.4.5**), a LabSmith pressure sensor (μPS0250-T116-10, *LabSmith*, CA, USA; sampling rate of ∼60 samples-per-second) and the FLOWELL platform fluid flow rate sensor (*Fluigent*) were employed to measure the fluidic pressure (pressure sensor place in the upper channel of the fluidic diode as to mitigate the effect of any parasitic fluidic resistance inherent to the dynamic valve mechanism which can negatively-impact the diodicity calculation [115]) and fluid flow rate (sensor placed in the lower channel of the fluidic diode to measure the output fluid flow), respectively. The sensor data for one experiment with the brackets installed (*on*) and not installed (*off*) were then manually processed, aligned with calibration spikes at the beginning of each data set, plotted and the diodicity values calculated using Excel data analysis.

[1]The overall video analysis protocol as well as the Python script itself was primarily developed by Rudra Mehta, undergraduate student researcher in the Micro-Methods for Biology Laboratory Research Program. Rudra's dedication towards our group's research, especially as an undergraduate student, is much appreciated and admired.

Finally to produce the mixing index values for the fabricated FPA$_{V1,2fluid}$ two-fluid mixer prototype, device actuation at 1 Hz for a period of 10 seconds was recorded, centering the video on the output microchannel section of both smooth-walled control and μ-mixer integrated channel prototypes. The final frame of each video was then selected, manually imported into Fiji image analysis software, and the image analysis procedure used to calculate the mixing index at the outlet of the μ-mixer-integrated two-fluid mixer prototypes in **Chapter 2** (as described in **Section 2.3.5.2**) was employed to quantify the mixing index at the terminus of the microchannel outlet section. Three experimental mixing demonstrative experiments were performed and the mean mixing index, along with the standard deviation between experiments, were calculated.

4.4 Results and Discussion

4.4.1 Fabrication Results

Visualizations of the successfully-fabricated and post-processed single-fluid FPA prototype *via* Multijet additive manufacturing are shown in **Fig. 4.3**. The modular FPA prototype is shown (**Fig. 4.3a**) with all channels filled with blue dyed fluid for visualization purposes only, showing how fluids inside the device can be seen through the sufficiently-optically transparent 3D printed material. A cross-sectional view of the fabricated 3D fluidic diode operator (**Fig. 4.3b**, *top*) illustrates the successful resolution of the 150 μm thick dynamic check valve-like membrane separating upper and lower fluid chambers. The clearance between the central pillar and the sides of the aperture in the membrane is only 100 μm wide and so is too small to be clearly identified in this image. The image of the cross-section of the fabricated 3D air-fluid cavity (**Fig. 4.3b**, *middle*) reveals the successful resolution of the enclosed 150 μm thick membrane isolating the upper fluid and lower air channels from one another inside the fluid reservoir. Furthermore, the cross-section of the fabricated pressure source (**Fig. 4.3b**, *bottom*) reveals the successful fabrication of the hollow cavity and 150 μm thick finger-actuated membrane. Finally, the cross-sectional view of the fabricated pressure source channel (**Fig. 4.3c**) reveals the channel which bridges the pressure source and the lower channel of the fluidic reservoir. The membrane structures were deemed too fragile to be able to slice with a blade without damaging them, therefore all fabricated cross-sections were made possible by slicing the 3D solids model of each 3D fluidic operator element in half in the CAD design software and printing these cross-sectional 3D models separately for visualization purposes.

See Appendix **Fig. 7.34** for images of the fabricated FPA$_{V1}$ prototype before post-processing (**Fig. 7.34a**), a comparison of fabricated FPA$_{V1}$ prototypes before and after post-processing (**Fig. 7.34b**), a side-by-side visualization of fabricasted FPA$_{V2}$ and FPA$_{V2,in-line}$ prototypes after post-processing without brackets installed (**Fig. 7.34c**) and fabricated FPA$_{V2,in-line}$ prototypes with

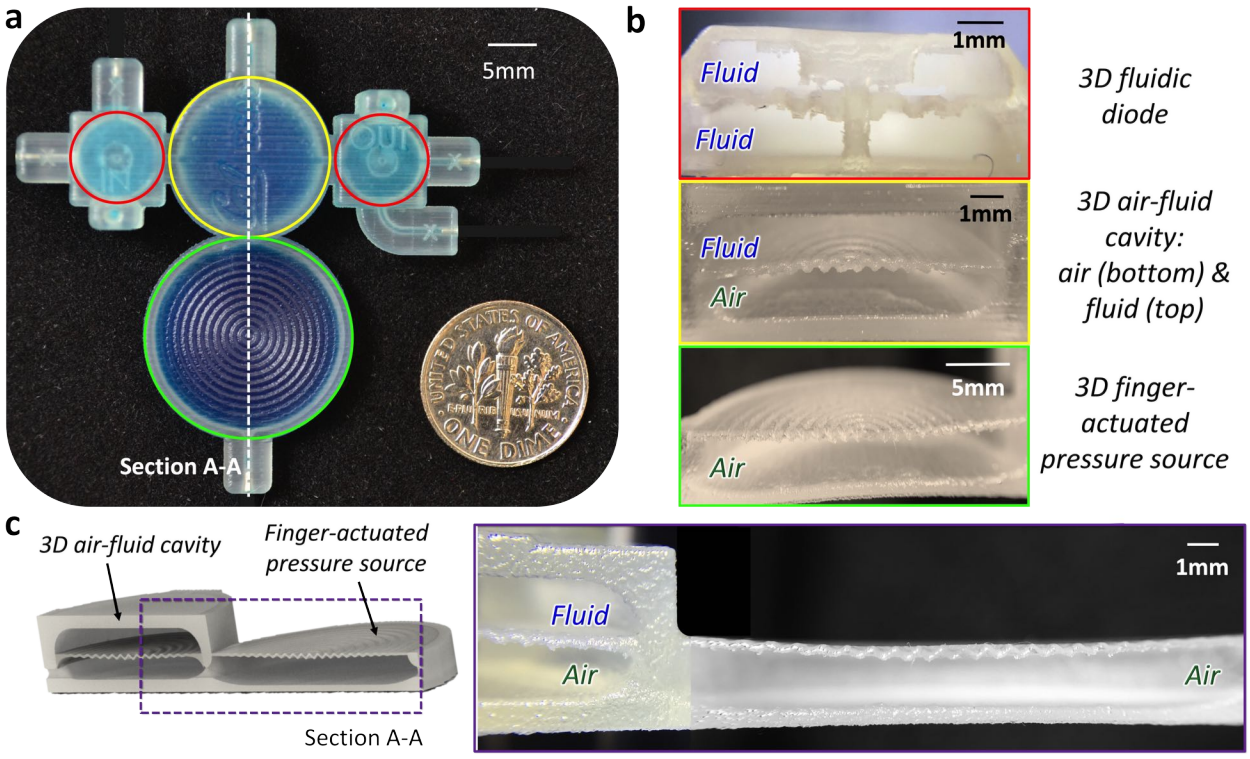

Figure 4.3: Fabrication results for the modular single-fluid 3D Printed FPA prototype. **(a)** Top-down image of the actual fabricated prototype with all channels filled with blue dyed fluid and a US dime for scale, and **(b)** physical cross-sections of the fabricated fluidic elements showing successful resolution of 3D printed microstructures. 3D fluidic diode (*red outline*), consisting of a circular 3D corrugated membrane separating upper and lower fluid channels connected by a circular aperture in the membrane; 3D air-fluid cavity (*yellow outline*), consisting of the 3D corrugated membrane isolating the upper fluid and lower air channels; and pressure source (*green outline*) consisting of the finger-actuated 3D corrugated membrane containing the air channel. **(c)** Cross-section of the 3D solids model rendering (*left*) and actual fabricated prototype (*right*) along Section A-A, showing the air channel comprising the 3D air-fluid cavity (*left*) and the finger-actuated pressure source (*right*).

and without brackets installed (**Fig. 7.34d**). Additionally, for a visualization of the surface quality and microstructural resolution of the finger-actuated membrane as compared to a flat surface, bot fabricated from Visjiet M3 material on the Projet 3000 3D printer using scanning laser microscopic imaging, see Appendix **Fig. 7.37**.

4.4.2 Visualization of Operational Fluid Actuation Results

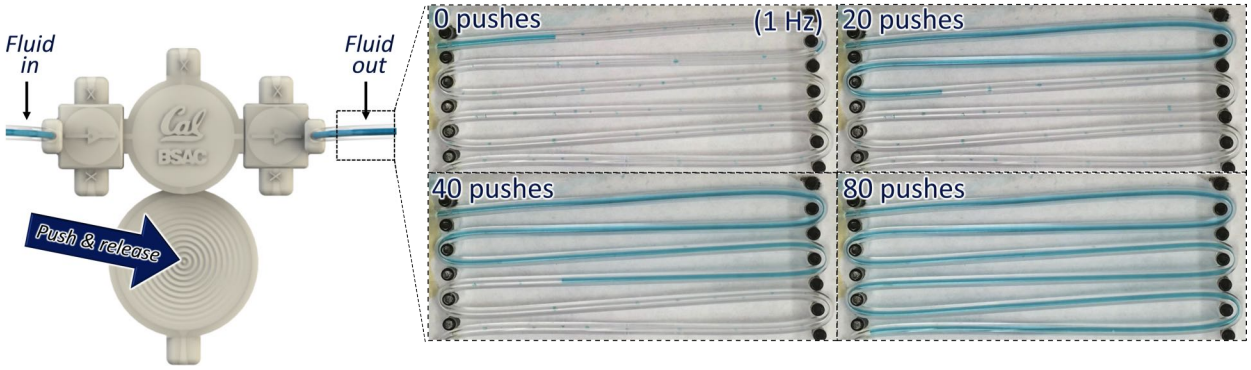

Figure 4.4: Experimental visualization of fluid actuation results from the single-fluid FPA prototype. (*Left*) Rendering of the fabricated prototype indicating the locations of the fluidic input and output from the device and the push-and-release operation on the finger-actuated pressure source. (*Right*) Actual blue dyed fluid output from the device filling transparent tubing resulting from device operation at one push-per-second (*i.e.* 1 Hz pushing frequency). Device output volume corresponding to 0, 20, 40 and 80 pushes on the finger-actuated membrane.

The results of operational actuation of the fabricated single-fluid FPA prototype at a frequency of 1 Hz is illustrated in **Fig. 4.4**. The experimental setup as described in **Section 4.3.3** was used to collect the generated device output in the form of an output volume of blue dyed fluid in a segment of transparent tubing arranged in a serpentine fashion. Each images shows the net fluid volume pumped after 0, 20, 40 & 80 actuation cycles, respectively. Qualitatively, larger net output volumes are generated with longer durations of actuation of the finger-powered pressure source.

4.4.3 Single-Fluid FPA Results (FPA_{V1})

Analysis of the experimental performance of the *initial* single-fluid FPA prototype design (FPA_{V1}) as featured in **Section 4.4.2** is presented in **Fig. 4.5**. The resulting output fluid flow rate from the device from an actuation frequency of 1 Hz is visualized with respect to time over 10 seconds of device actuation in **Fig. 4.5b**. Considering the raw flow rate data as representing the instantaneous *speed* of the fluid, each individual actuation cycle is visualized by a steep acceleration in the forward direction, forming a sharp peak in forward flow rate, followed by a very sharp deceleration leading to a sharp flow rate peak in the reverse direction, with a gradual decay in reverse flow rate back to a static condition. The area of underneath the forward flow rate data represents the volume pumped in the forward direction, while the area of above the reverse flow rate data represents the the result of back-flow in the system. The ratio of these volumes (*i.e.* volume transported in the forward direction : reverse direction) for the average actuation cycle is $\sim$1.5:1, indicating a

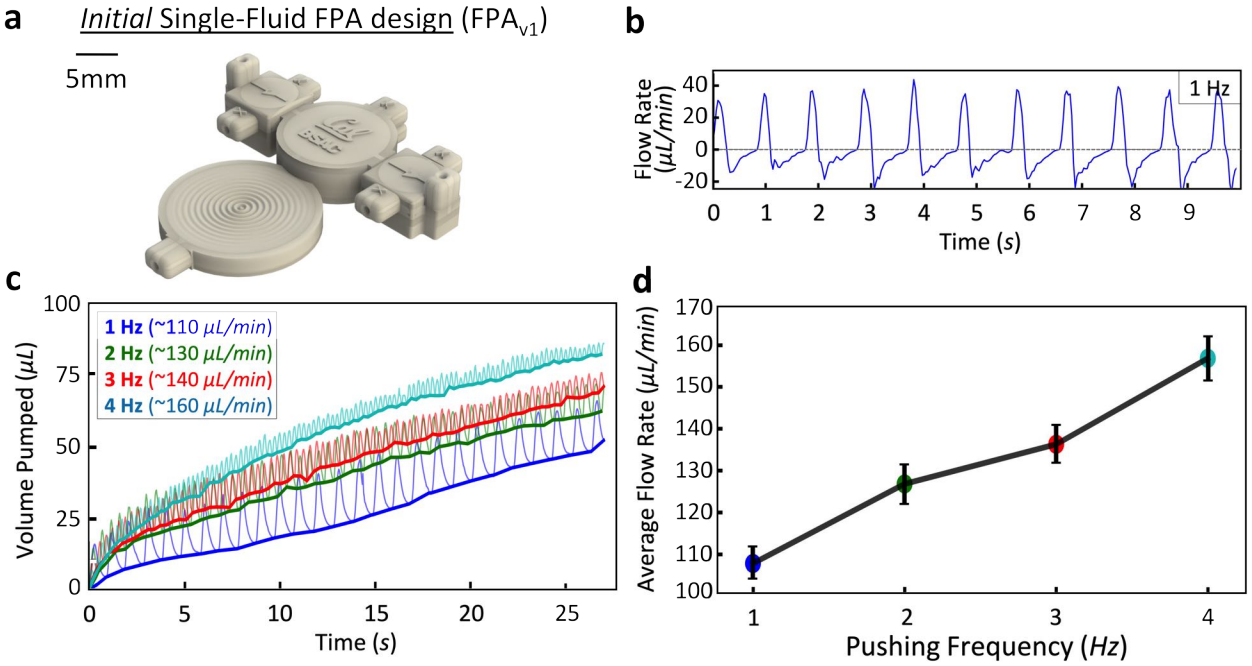

Figure 4.5: Experimental fluid actuation results from the *initial* single-fluid FPA prototype (FPA$_{V1}$). **(a)** Isometric view rendering of the prototype. **(b)** Raw flow rate *versus* time plot actuation at 1 Hz for a single operation, maximum forward flow rate per-push ∼40 μL/min, maximum reverse flow rate ∼20 μL/min. **(c)** Volume pumped *versus* time plot for individual operations at 1-4 Hz, raw data (*semi-transparent line*) and trend (*bold opaque*) line interpolated between actuation cycles representing net volume pumped with time, effective flow rate per Hz (*i.e.* net volume pumped per minute) shown in legend; larger forward volume pumped yet more back-flow per actuation cycle at lower actuation Hz's; less back-flow, less forward volume pumped, yet larger net forward volume pumped per actuation cycle at higher actuation frequencies. **(d)** Average effective flow rate *versus* actuation Hz for triplicate experiments at 1-4 Hz, error bars show standard deviation between experiments, average standard deviation of 10 μL/min; higher average flow rates with at higher actuation frequencies; minimum flow rate of ∼108 μL/min at 1 Hz, maximum flow rate of ∼156 μL/min at 4 Hz.

significant proportion of back-flow per-actuation cycle. Even so, over the course of any number of actuation cycles, a net fluidic volume is actuated out of the device in the forward direction. This is due to the lower effective fluidic resistance of the right-most fluidic diodes in the forward direction, resulting in a maximum forward flow rate of ∼40 μL/min; while the flow in the reverse direction in the system resulting in a maximum reverse flow rate of ∼20 μL/min is due to the back-flow in the right-most diode. Additionally, the observed decay in the reverse flow rate at the end of each actuation cycle is indicative of the settling time required for the dynamic membrane in the diode to restore back to its initial position, where a constant value of fluidic resistance exists which is a factor of the size of the annular aperture and the clearance between the membrane and the upper surface of the diode. The mechanisms of the fluidic diodes are discussed in **Section 4.4.4**.

The data representing the volume actuated out of the prototype device with respect to time over nearly 30 seconds for individual device actuation experiments at actuation frequencies from 1-4 Hz is presented in **Fig. 4.5c**. The net-volume actuated at the end of each actuation cycle, as indicated by the bold solid trend lines for each actuation frequency, reveal that total volume actuated out of the device over a certain period of time increases with higher actuation frequencies. Furthermore, at higher actuation frequencies (as indicated by the raw data represented by the lighter lines for each actuation frequency) lower amounts of back-flow and forward-actuated volume are produced per-actuation cycle due to the period of actuation being shorter than the setting time of the dynamic membrane inside the diode; yet simply due to the increased number of actuation cycles, a larger total volume of fluid is actuated over any given period of time. Moreover, **Fig. 4.5d** illustrates how the average effective flow rate from the prototype (*i.e.* the equivalent total volume pumped out of the device over a period of 60 seconds, averaged over experiments performed in triplicate) increases fairly linearly with increasing actuation frequency, producing $\sim$108 μL/min at 1 Hz, $\sim$126 μL/min at 2 Hz, $\sim$136 μL/min at 3 Hz & $\sim$156 μL/min at 4 Hz with an average standard deviation of $\sim$10 μL/min. For additional visualization of the raw flow rate output from FPA$_{V1}$ from 1-4 Hz, see Appendix **Fig. 7.38**.

4.4.4 Initial Fluidic Diode Results (Diode$_{V1}$)

The *initial* fluidic diode (Diode$_{V1}$) employed by the FPA$_{V1}$ prototype (**Fig. 4.6a**) was based on the 3D fluidic diode design previously developed by our group [115]. This 3D fluidic diode features a dynamic 3D corrugated membrane isolating an upper and a lower fluidic channel and consisting of a circular aperture in the center. A 100 μm clearance separates the aperture from a central post connected to the upper and lower surfaces of the interior of the diode. The interior of the fluidic diode is designed such that the upper surface extends deeper into the upper channel to within a fabricated clearance of 200 μm of the upper surface of the dynamic membrane, whereas the lower surface of the interior of the diode has a clearance of 750 μm from the bottom of the membrane. As a result, the effective fluidic resistance in the forward direction (*i.e.* fluid flow from the upper to the lower channel) is lower than in the reverse direction. Therefore under a positive applied fluidic pressure differential or *positive pressure* (*i.e.* higher pressure in the upper channel than in the lower channel, $P > 0$), forward fluid flow is permitted through the aperture in the *on* state. Under a negative fluidic pressure differential or *negative pressure* however (*i.e.* higher pressure in the lower channel than in the upper channel, $P < 0$), the membrane is deflected upwards until contact is made with the upper surface, which serves to close the mechanism and rectify fluid flow. It must be noted that this design, by nature, permits a certain degree of back-flow through the aperture under reverse pressure until the fluidic pressure become high enough to close the clearance and turn the diode to the *off* state. The results of experimental fluid rectification characteristics of a fabricated Diode$_{V1}$ prototype are presented in **Fig. 4.6b** (plot adapted from the figure in our group's previous publication [115]) as a flow rate *versus* pressure (QP) plot, which is the hydrodynamic equivalent of a current-voltage (IV) curve which is used to examine the electrical

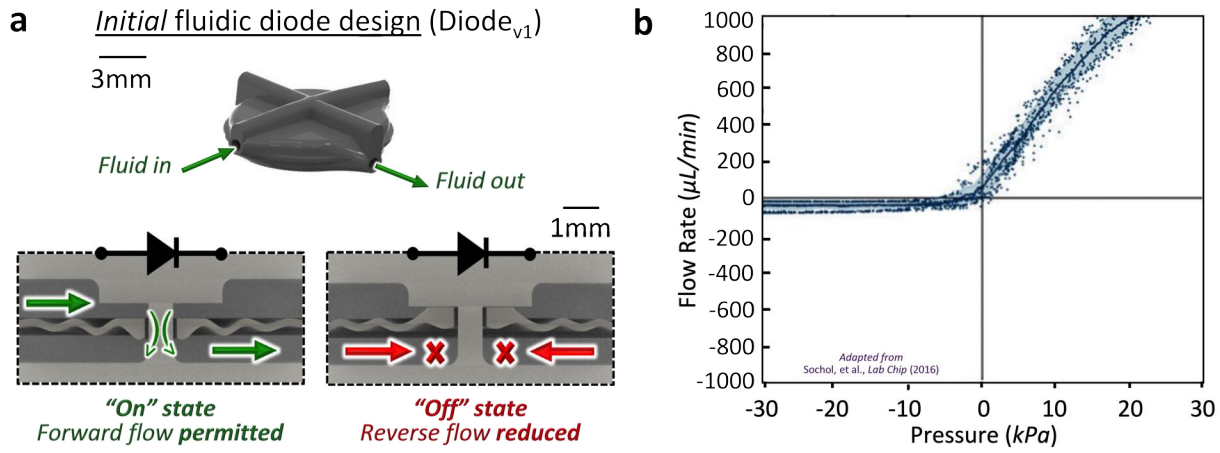

Figure 4.6: Experimental Q-P diagram showing output flow rates from a Diode$_{V1}$ prototype resulting from forward and reverse pressure sweeps. **(a)** Isometric view rendering of a modular Diode$_{V1}$ with four inlets for support material removal (*top*) and cross-section renderings of the interior of Diode$_{V1}$. In the *on* state (*bottom left*), a positive pressure (*i.e.* positive pressure into the upper fluid channel) drives fluid through the circular aperture in the corrugated membrane from the upper to the lower channel and deflects the membrane downwards, resulting in forward flow through the diode; in the *off* state (*bottom, right*), a negative pressure (*i.e.* positive pressure into the lower fluid channel) deflects the membrane upwards until contact is made with the upper surface, effectively closing the gap and reducing reverse flow through the diode. **(b)** Experimental Q-P diagram previously published by our group (see Sochol et al., *Lab Chip*, 2016 [115]) showing output flow rates from Diode$_{V2}$ resulting from forward and reverse pressure sweeps in triplicate experiments, moving average trend line and standard deviation, demonstrating experimental *diodicity* of ~80.6.

current rectification behavior of an electrical diode. The experimental setup used to collect this data is based on the process described in **Section 4.3.4**. The fabricated Diode$_{V1}$ prototype generates forward fluid flow rates up to $\sim$ 800 μL/min at ~15 kPa, while permitting back-flow regardless of the magnitude of the applied negative pressure with flow rates up to 45 kPa in the reverse direction due to applies negative pressure up to ~30 kPa. Furthermore, non-dimensional metric of fluidic *diodicity* (Di) was used to quantify the fluid rectification performance of the fabricated prototype and calculated using the data from the QP curve in **Fig. 4.6b** (excluding data in the transitional region, -5 kPa $<$ P $<$ 5 kPa around P = 0), as defined by Equation 4.1 [306]:

$$Di = \frac{R_{reverse}}{R_{forward}} \tag{4.1}$$

where $R_{reverse}$ represents the hydrodynamic resistance of the device in the reverse direction and $R_{forward}$ represents the hydrodynamic resistance of the device in the forward direction. Hydrodynamic resistance inside microfluidic channels can be defined by the equation: $\Delta P = R * Q$, where P is the applied fluidic pressure differential across a microchannel segment, Q is the resulting flow rate out of the microchannel segment. Therefore the value of $R_{reverse}$ was calculated by the slope

of the line of best fit between the average flow rate values at -5 kPa and -30 kPa and the value of $R_{forward}$ was calculated by the slope of the line of best fit between the average forward flow rate values at -5 kPa and -30 kPa, resulting in a diodicity value of ∼80.6.

4.4.5 Improved Fluidic Diode Results (Diode$_{V2}$)

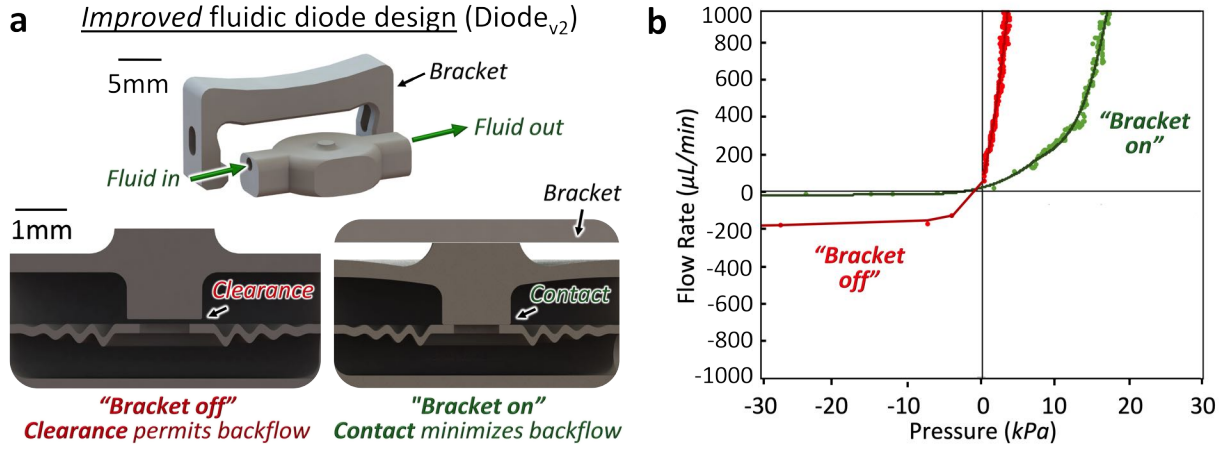

Figure 4.7: Experimental Q-P diagram showing output flow rates from a Diode$_{V2}$ prototype resulting from forward and reverse pressure sweeps. **(a)** Isometric view rendering of a modular Diode$_{V2}$ with one inlet and one outlet microchannel, as well as with an un-attached external bracket mechanism (*top*), and cross-section renderings of the interior of Diode$_{V2}$. With the bracket *off* (*bottom, left*), a clearance (∼100μm) between the surface of the rigid piston in the center of the upper channel and the aperture in the corrugated membrane permits forward and reverse flow, akin to the behavior of the internal mechanism of Diode$_{V1}$. With the bracket *on* (*bottom, right*), the knob on the exterior of the upper surface of the cavity is depressed and the upper surface elastically-deformed, deflecting the piston downwards such that contact with the corrugated membrane is established, eliminating the clearance and minimizing back-flow. **(b)** Experimental Q-P diagram showing output flow rate from Diode$_{V2}$ resulting from forward and reverse pressure sweeps, data points and solid trend lines for single experiments involving Diode$_{V2}$ with the bracket off (*red*) and on (*green*) demonstrating enhanced flow rectification with bracket on *versus* off, experimental *diodicity* values ∼1117.4 & ∼95.4, respectively.

An *improved* fluidic diode (Diode$_{V2}$) is proposed with an alternative morphology which enables *passive* fluid rectification, as opposed to the dynamic closure mechanism employed by the Diode$_{V1}$ design which permits inherent back-flow in the system. A conceptual Diode$_{V2}$ (**Fig. 4.7a**) consists of two distinct elements, the 3D fluidic diode itself, as well as a modular *bracket* component. The interior of the fluidic diode, similar to the interior of Diode$_{V1}$, entails a dynamic 3D corrugated membrane with a 1 mm diameter central circular aperture which divides upper and lower fluid channels. Additionally, upper surface extends deeper into the upper channel to within

an as-fabricated clearance of 100 μm of the upper surface of the dynamic membrane, whereas the lower surface of the interior of the diode has a clearance of 750 μm from the bottom of the membrane. Notably, this design lacks a central column (as is featured in the interior of Diode$_{V1}$) in order to permit lower fluidic resistance through the central aperture. Therefore when the bracket is in the *off* position, not installed on the diode, the as-fabricated clearance permits forward and reverse flow dynamics similar to those inherent to the the Diode$_{V1}$ design. Unique to Diode$_{V2}$, however, is the raised knob on the upper exterior surface of the diode. When the bracket is in the *on* position, installed on the diode (holes on each side of the bracket permit interfacing with the inlet and outlets of the diode using standard steel couples), the lower surface of the bracket contacts and depresses the knob on the upper surface of the diode (since the two surfaces overlap by 150 μm and the 5 mm thick bracket is much more rigid than the $\sim$500μm thick upper surface of the diode). Therefore the upper surface of the diode, and subsequently the protruding structure in the upper channel, is displaced downwards until the clearance between the membrane and the protruding structure is effectively eliminated. As a result, in the default fluidic state at P = 0 (*i.e.* equivalent fluid pressures in the upper and lower channels), back-flow through the aperture is prevented by the absence of clearance on the upper surface of the membrane. Therefore with the bracket installed, under positive pressure (P $>$ 0), an initial threshold pressure value must be reached in order to apply sufficient force on the membrane in order to cause downwards displacement and permit forward fluid flow through the aperture. Under negative pressure however (P $<$ 0) or at P = 0, the energy stored in the displaced membrane due to elastic strain restores the membrane back to its initial position, passively-eliminating the clearance between the membrane and the protruding surface which exists only under sufficient positive applied pressure, and preventing further back-flow in the system and rectifying reverse fluid flow more effectively than the closure mechanism of the Diode$_{V1}$ design.

The fluid rectification performance of a modular fabricated Diode$_{V2}$ prototype was experimentally characterized using the experimental setup described in **Section 4.3.4**. The results are presented by the QP plot shown in **Fig. 4.7b**. With the bracket *off*, the low fluidic resistance in the forward flow direction under positive pressure due to the large circular area of the aperture and as-fabricated resistance produces high forward flow rates at relatively low positive pressures, up to $\sim$930 μL/min at only $\sim$3.5 kPa. The as-fabricated clearance, however, also produces a low fluidic resistance in the reverse direction, resulting in a relatively high flow rate (back-flow) in the reverse direction under negative pressure as well, up to $\sim$186 μL/min at $\sim$12 kPa. With the bracket *on* and the clearance between the membrane and protruding surface eliminated, the build up of positive pressure in the upper channel necessary to displace the membrane downwards and initiate saturated forward flow is evident in the data as the increase in forward flow rate through the device is exponential up until $\sim$10 kPa, after which point the forward flow rate adopts a linear increase with a high slope up to $\sim$970 μL/min at $\sim$17 kPa, indicating that the diode transitionary pressure range in the forward direction extends to $\sim$10 kPa, as opposed to the forward transitionary pressure range of Diode$_{V1}$ up to $\sim$5 kPa. When subjected to negative pressure, however, the back-flow in the diode is effectively eliminated up to $\sim$5 kPa in the reverse direction, after which point the saturated back-flow in the system is significantly reduced as compared to that with the bracket off, only

reaching $\sim$12 μL/min at $\sim$30 kPa negative pressure. Therefore with the bracket on, the Diode$_{V2}$ prototype exhibits a $\sim$93.6% reduction in back-flow as compared to with the bracket off. Furthermore, the calculated experimental diodicity metrics of the Diode$_{V2}$ prototype with the bracket off and on are $\sim$95.4 & $\sim$1117.4, respectively. For additional analysis of the Q-P plots for Diode$_{V2}$ see Appendix **Fig. 7.39**. Finally, comparing the QP data for both Diode$_{V1}$ and Diode$_{V2}$ designs reveals that the passive fluid rectification mechanism employed by Diode$_{V2}$ with the bracket installed is more effective than the dynamic fluid rectification mechanism employed by Diode$_{V1}$. The maximum back-flow in Diode$_{V1}$ reaches $\sim$45 μL/min at $\sim$30 kPa negative pressure, whereas the back-flow in Diode$_{V2}$ reaches only $\sim$12 μL/min at $\sim$30 kPa negative pressure, demonstrating an $\sim$73.4% improvement in back-flow reduction as compared to Diode$_{V1}$.

4.4.6 Single-Fluid FPA with Improved Fluidic Diodes Results (FPA$_{V2}$)

As a demonstration of the beneficial application of the improved Diode$_{V2}$ design towards finger-actuated actuation systems, the experimental performance of the single-fluid FPA prototype design employing Diode$_{V2}$ designs (FPA$_{V2}$) is presented in **Fig. 4.8**. In all experiments involving this fabricated prototype device, brackets were installed in the *on* state on both fluidic diode operators (**Fig. 4.8a**). For visualization of a fabricated FPA$_{V2}$ (without brackets installed) prototype after post-processing see Appendix **Fig. 7.35a**. The raw output fluid flow rate from the prototype resulting from actuation at a frequency of 1 Hz is visualized over 10 seconds of device operation in **Fig. 4.8b**. Compared to the similar raw flow rate data characterizing the FPA$_{V1}$ prototype as shown in **Fig. 4.5b**, each individual actuation cycle of the FPA$_{V2}$ prototype produces a smaller magnitude of forward fluid flow rate (a maximum of only $\sim$28 μL/min compared to a maximum of $\sim$40 μL/min produced by FPA$_{V1}$) due to the higher internal fluidic resistance caused by the initially clearance-free internal mechanism of Diode$_{V2}$ and as a result higher transitionary pressure in the forward direction.However, the back-flow achieved per-actuation cycle for FPA$_{V2}$ is significantly reduced as compared to FPA$_{V1}$, as the area of underneath the forward flow rate data represents a much larger volume pumped in the forward direction than volume permitted to flow in the reverse direction, represented by the significantly-minimized area of above the reverse flow rate data, which exhibits a maximum of only $\sim$5 μL/min in the reverse direction (compared to a maximum of $\sim$20 μL/min produced by FPA$_{V1}$ in the reverse direction).

The volume output from the FPA$_{V2}$ prototype device with respect to time over nearly 30 seconds, determined for individual device actuation experiments at actuation frequencies from 1-4 Hz, is presented in **Fig. 4.8c**, which shows the raw volume actuated-with-time data from video analysis without any fitted trend lines. Additionally, for the individual experiments performed for which the results are plotted, the total volume actuated out of the device over a certain period of time increases with higher actuation frequencies, however there is less of an increase in net-volume pumped between 2-4 Hz than exists between 1 & 2 Hz, due to the fact that higher transitionary pressure caused by the high fluidic resistance in the forward direction likely has more of an appar-

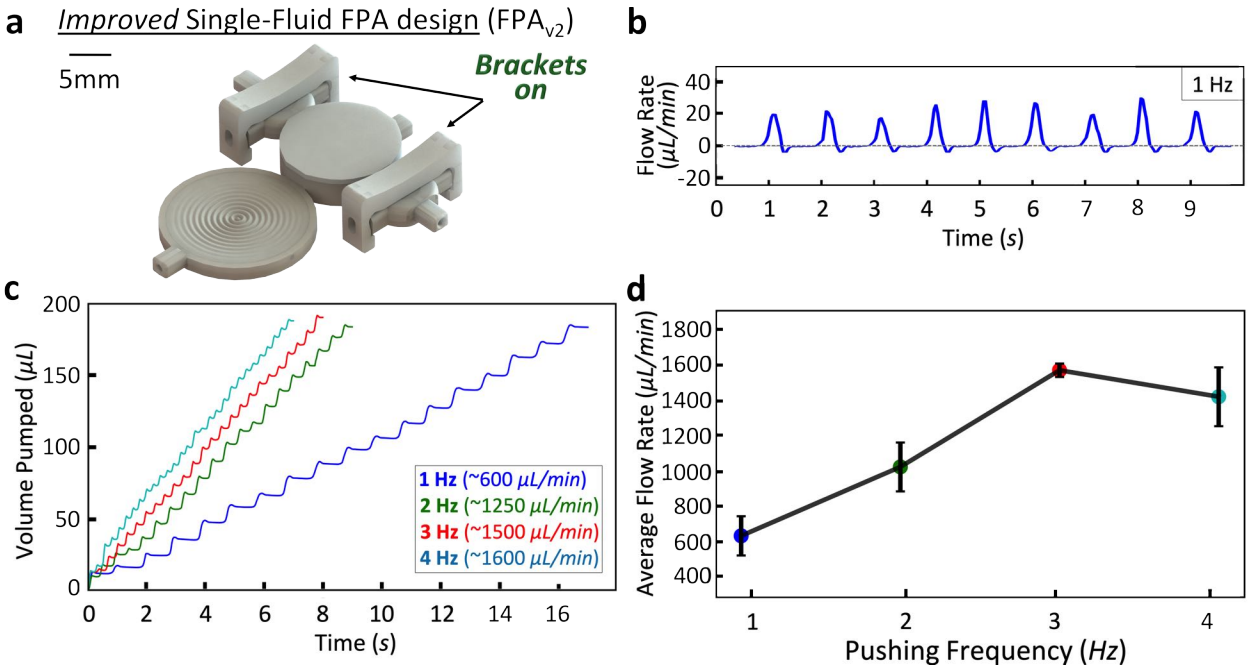

Figure 4.8: Experimental fluid actuation results from the single-fluid FPA prototype employing Diode$_{V2}$ designs, (FPA$_{V2}$). **(a)** Isometric view rendering of the prototype showing brackets *on*. **(b)** Raw flow rate *versus* time plot actuation at 1 Hz for a single operation, maximum forward flow rate per-push ∼28 μL/min; significant reduction in back-flow, maximum reverse flow rate ∼5 μL/min. **(c)** Volume pumped *versus* time plot for individual operations at 1-4 Hz, raw data plotted, effective flow rate per Hz (*i.e.* net volume pumped per minute) shown in legend; larger forward volume pumped yet more back-flow per actuation cycle at lower actuation Hz's; significantly less back-flow, less forward volume pumped, yet larger net forward volume pumped per actuation cycle at higher actuation frequencies. **(d)** Average effective flow rate *versus* actuation Hz for triplicate experiments at 1-4 Hz, error bars show standard deviation between experiments, average standard deviation of 225 μL/min; higher average flow rates with at higher actuation frequencies from 1-3 Hz, lower average flow rate from 3-4 Hz; minimum flow rate of ∼637 μL/min at 1 Hz, maximum flow rate of ∼1575 μL/min at 3 Hz.

ent damping effect on the pressure spikes at at higher actuation frequencies. Furthermore similar to the behavior observed for FPA$_{V1}$, at higher actuation frequencies lower amounts of back-flow and forward-actuated volume are produced per-actuation cycle due to the period of actuation being shorter than the setting time of the dynamic membrane inside the diode; yet simply due to the increased number of actuation cycles, a larger total volume of fluid is actuated over any given period of time. Moreover, **Fig. 4.8d** illustrates how the average effective flow rate from the prototype over a period of 60 seconds measured for experiments performed in triplicate increases fairly linearly with increasing actuation frequency, from 1 to 3 Hz, producing ∼637 μL/min at 1 Hz, ∼1027 μL/min at 2 Hz, ∼1575 μL/min at 3 Hz, roughly one order of magnitude higher than the average flow rates produced by the fabricated FPA$_{V1}$ prototype at these frequencies; however, the average

flow rate demonstrated at 4 Hz is roughly the same as at 3 Hz, $\sim$1450 μL/min, due to the damping effects of the high fluidic resistance in the forward direction at such high Hz's. The average standard deviation between the measured flow rates is $\sim$225 μL/min. For additional visualization of the raw flow rate output from FPA_{V1} from 1-4 Hz, see Appendix **Fig. 7.38**.

Comparing the raw flow rate *versus* time plots for the fabricated FPA_{V1} and FPA_{V2} prototype platforms also reveals more detailed information on the characteristics of the pressure waves at the device outlet which are the driving force of the fluid actuation. The peaks on the flow rate plot in the forward direction for each actuation cycle for FPA_{V1} (**Fig. 4.5b**) take the shape of sharp peaks with a maximum flow rate of $\sim$40 μL/min, whereas the peaks for FPA_{V2} (**Fig. 4.8b**) are all slightly wider but the maximum flow rate is lower, $\sim$28 μL/min, $\sim$50 μL/min. Since all of the fluidic operators are identical between these designs except for the design of the fluidic diodes, this behavior indicates a higher fluidic resistance in the forward direction for Diode_{V2} than for Diode_{V1}. Interestingly, the aperture on the membrane in Diode_{V1} is in fact smaller (represented by a clearance of 100 μm, outer diameter of 800 μm, inner diameter of 600 μm and annular area of $\sim$0.22 mm^2) than the aperture on the membrane in Diode_{V2} (represented by a through-hole diameter of 800 μm and area of $\sim$0.50 mm^2), and therefore creates a higher fluidic resistance to the fluid flowing through the aperture. The observed overall fluidic resistance behaviors are not in conflict with this fact, however, since the higher fluidic resistance in Diode_{V2} is due to the dynamic closure mechanism employed in the interior. Namely, the as-fabricated clearance between the aperture and the upper surface in the interior of Diode_{V1} provides a lower fluidic resistance in the forward direction than induced by the initial contact made between the aperture and upper surface inside the interior of Diode_{V2} when the bracket is installed onto the exterior of the diode. The higher fluidic resistance in the forward direction in the Diode_{V2} is due to the pressures that the fluid must (*i*) first exert onto the membrane to initially displace the membrane such that fluid can begin to flow through the aperture, followed by that which must resist the restorative force in the membrane, upon each actuation cycle. Therefore, the Diode_{V2} design experiences more of an energy loss per actuation cycle than the Diode_{V1} design.

The advantage of the Diode_{V2} design over the Diode_{V1} design, however, is revealed by the back-flow characteristics of each prototype. The overall back-flow in the system is predominantly due to the back-flow through the right-most diode when the pressure source is instantaneously *turned off* when the finger-actuated membrane is released. Analyzing the flow rate in the reverse direction for each actuation cycle for FPA_{V1} (**Fig. 4.5b**), the reverse flow rate adopts a decayed behavior with a maximum reverse flow rate of $\sim$20 μL/min, suggesting that the pressure drop across the membrane in the reverse direction possesses a restorative response time which is dependent on the mechanical properties of the membrane (*e.g.* elastic modulus). In other words, when the pressure source pressure is released, fluid flows from the device outlet through the lower channel of the right-most diode which flows through the aperture of the membrane. The gap between the membrane and the upper surface of the stationary piston in Diode_{V1} is at a maximum, therefore the fluidic resistance is at a minimum, at this point in time. As the elastic strain in the diode membrane and the vacuum pressure in the upper diode channel from the fluidic reservoir restores the

membrane back to its initial position, the fluidic resistance increases and saturates at a specific magnitude limited by the as-fabricated clearance between the membrane and upper surface. As a result, the back-flow in the diode decays is only stopped once the fluidic reservoir is completely filled with fluid and all membranes are restored back to their original position. As with the case of FPA_{V1} under back-flow, the peak-like behavior observed for the flow rate in the reverse direction for each actuation cycle of FPA_{V2} indicates that some back-flow occurs[2], but that very soon thereafter, contact is made between the membrane and the displaced upper stationary surface, effectively rectifying flow in the reverse direction with high fluidic resistance caused by the contact.

4.4.7 Single-Fluid FPA with In-Line Pressure Source Results ($\text{FPA}_{V2,in-line}$)

As an additional study into the optimization of the fluid actuation efficiency (*i.e.* how high of magnitudes of output flow rates can be generated by minimizing energy loss in the 3D fluidic operators as much as possible) of FPA prototypes, an alternative FPA design is proposed ($\text{FPA}_{V2,in-line}$), which utilizes a finger-actuated pressure source that is *in-line* with the two fluidic diodes, thereby eliminating energy lost due to the pressure force needed to expand of the membrane inside the fluid reservoir, such that the maximum force generated by the finger-actuated membrane is transferred directly to the fluid volume between the two fluidic diodes. The experimental performance of the fabricated $\text{FPA}_{V2,in-line}$ prototype is presented in **Fig. 4.9**. The $\text{FPA}_{V2,in-line}$ design is an extension of the FPA_{V2} design in that both designs utilize the improved Diode_{V2} fluidic diode designs with the brackets on (**Fig. 4.9a**) resulting in back-flow reduction in the system (as compared to the FPA_{V1} design) and therefore more efficient forward-driving fluid flow characteristics. Additionally, because the diameter (20 mm) and therefore area of the finger-actuated membrane are larger than those of the membrane contained inside the fluid reservoir in the FPA_{V2} design (15 mm in diameter), the larger displacing membrane will exert a higher pressure on the fluid volume in between the fluidic diodes, anyway, in addition to the increased pressure due to the reduction of energy loss by eliminating the membrane in the fluid reservoir. For visualization of a fabricated $\text{FPA}_{V2,in-line}$ (without brackets installed) prototype after post-processing see Appendix **Fig. 7.35b**. For a side-by-side visualization of the fabricated FPA_{V2} and $\text{FPA}_{V2,in-line}$ prototypes after post-processing, as well as fabricated $\text{FPA}_{V2,in-line}$ prototypes with and without brackets installed see Appendix **Fig. 7.34c,d**, respectively.

[2]In the ideal design, a perfect seal would exist between the flat and smooth surfaces in contact, effectively producing an infinitely-high flow rate and permitting zero back-flow. The nature of the fabrication surfaces, however is not ideal, as surface roughness on the order of $\sim$10's μm [185] exists on both surfaces; thus, when the peaks on the surfaces of each of the parallel surfaces are in contact, the membrane can displace no further upwards, yet a small volume of liquid is likely permitted to flow through the surface roughness peaks.

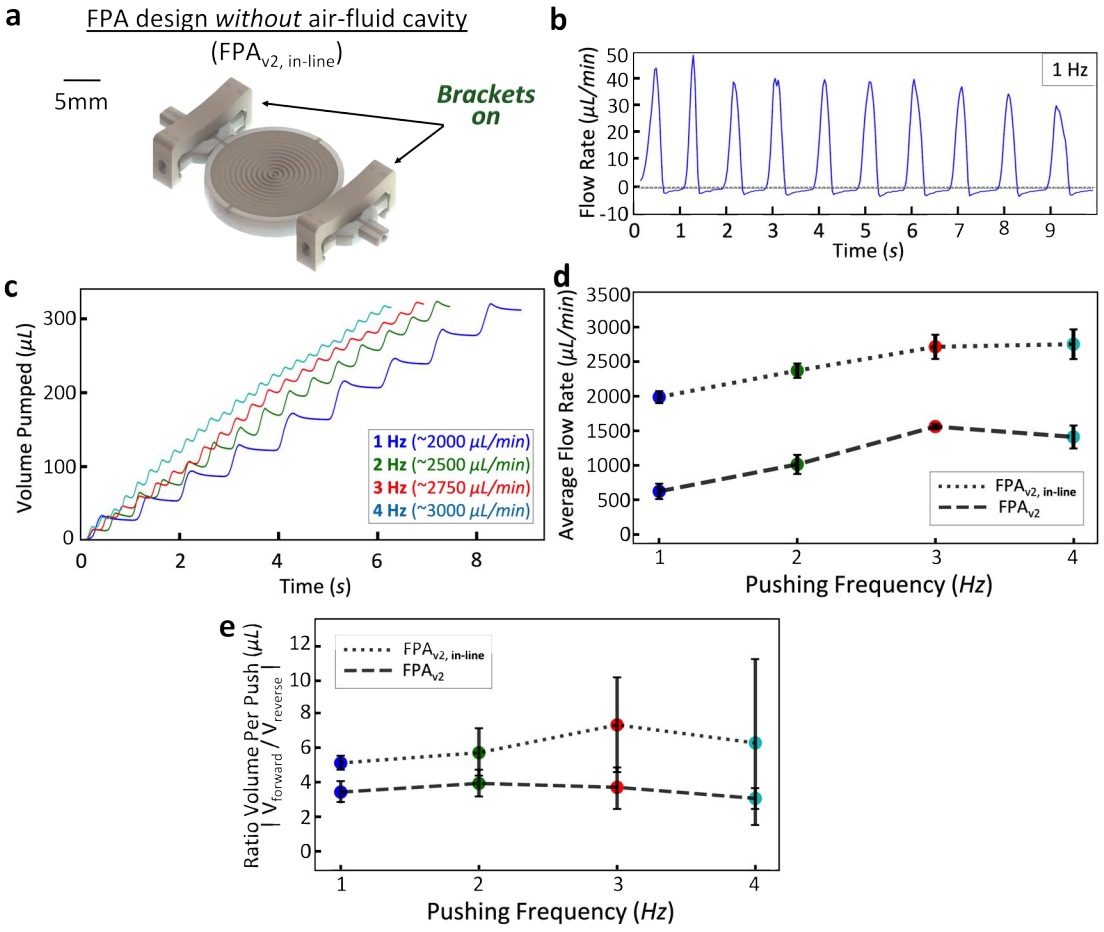

Figure 4.9: Experimental fluid actuation results from the single-fluid FPA prototype *with an in-line pressure source* (FPA$_{V2,in-line}$). **(a)** Isometric view rendering of the prototype showing brackets *on* and finger-actuated pressure source *in-line* with fluidic diodes. **(b)** Raw flow rate *versus* time plot actuation at 1 Hz for a single operation, maximum forward flow rate per-push ∼50 μL/min; significant reduction in back-flow, maximum reverse flow rate ∼3 μL/min. **(c)** Volume pumped *versus* time plot for individual operations at 1-4 Hz, raw data plotted, effective flow rate per Hz (*i.e.* net volume pumped per minute) shown in legend; larger forward volume pumped yet more back-flow per actuation cycle at lower actuation Hz's; significantly less back-flow, less forward volume pumped, yet larger net forward volume pumped per actuation cycle at higher actuation frequencies. **(d)** Average effective flow rate *versus* actuation Hz for triplicate experiments at 1-4 Hz for FPA$_{V2}$ and FPA$_{V2,in-line}$; error bars show standard deviation between experiments, average standard deviation of 292 μL/mins; higher average flow rates with at higher actuation frequencies from 1-4 Hz; minimum flow rate of ∼2000 μL/min at 1 Hz, maximum flow rate of ∼2775 μL/min at 4 Hz. **(e)** Ratio of volume per actuation cycle in forward to reverse directions *versus* actuation frequency for 1-4 Hz, data for FPA$_{V2}$ (decreasing from 2-4 Hz) and FPA$_{V2,in-line}$ (increasing from 1-3 Hz).

The raw output fluid flow rate from the prototype resulting from actuation at a frequency of 1 Hz is visualized over 10 seconds of device operation in **Fig. 4.9b**. Compared to the raw flow rate data characterizing the FPA_{V2} prototype as shown in **Fig. 4.8b**, each individual actuation cycle of the $\text{FPA}_{V2,in-line}$ prototype produces nearly a twice as large on average magnitude of forward fluid flow rate (a maximum of $\sim$50 μL/min compared to a maximum of $\sim$28 μL/min produced by FPA_{V2}) due to the significantly higher pressures created by the larger diameter membrane in between in-line with the two fluidic diodes which is displaced by the high force of the operator's finger with minimal energy loss. In addition, the average back-flow achieved per-actuation cycle for $\text{FPA}_{V2,in-line}$ is nearly the same as, or even slightly smaller than, that produced by the FPA_{V2} prototype, which exhibits a maximum of only $\sim$3 μL/min in the reverse direction (compared to a maximum of $\sim$5 μL/min produced by FPA_{V2} in the reverse direction). The volume output from the $\text{FPA}_{V2,in-lline}$ prototype device with respect to time over nearly 30 seconds, determined for individual device actuation experiments at actuation frequencies from 1-4 Hz, is presented in **Fig. 4.9c**, which shows the raw volume actuated-with-time data from video analysis without any fitted trend lines. Additionally, the total volume actuated out of the device over a certain period of time increases with higher actuation frequencies. Furthermore similar to the behavior observed for FPA_{V2}, at higher actuation frequencies, lower amounts of back-flow and forward-actuated volume are produced per-actuation cycle due to the period of actuation being shorter than the setting time of the dynamic membrane inside the diode; yet simply due to the increased number of actuation cycles, a larger total volume of fluid is actuated over any given period of time. Moreover, **Fig. 4.9d** illustrates how the average effective flow rate from the prototype over a period of 60 seconds measured for experiments performed in triplicate increases with a slightly positive fairly linear slope with increasing actuation frequency, from 1 to 4 Hz, producing $\sim$2000 μL/min at 1 Hz, $\sim$2378 μL/min at 2 Hz, $\sim$2717 μL/min at 3 Hz and $\sim$2775 μL/min at 4 Hz, roughly twice the magnitude of the average flow rates produced by the fabricated FPA_{V2} prototype at these frequencies. The average standard deviation between the measured flow rates is $\sim$292 μL/min. For additional visualization of the raw flow rate output from FPA_{V1} from 1-4 Hz, see Appendix **Fig. 7.38**. Moreover, the average ratio of volume transported in the forward direction to volume transported in the reverse direction per-actuation cycle for FPA_{V2} and $\text{FPA}_{V2,in-line}$ for 1-4 Hz are compared on the plot presented in **Fig. 4.8e**. At all actuation frequencies tested, the demonstrated $\text{FPA}_{V2,in-line}$ prototype produces higher volume ratios than the demonstrated FPA_{V2} prototype. At 4 Hz, both designs exhibit a slight reduction in the volume ratio from 3 Hz, as well as significantly high standard deviations, additional results of the damping effect of the internal membrane at such high Hz's. The FPA_{V2} prototype demonstrates a maximum volume ratio of $\sim$4:1 at 2 Hz and the $\text{FPA}_{V2,in-line}$ prototype demonstrates a maximum volume ratio of $\sim$7.4:1 at 3 Hz.

Moreover, measurements of the pressures generated in both the upper and lower channels of the right-most Diode_{V2} of the fabricated FPA_{V2} and $\text{FPA}_{V2,in-line}$ prototypes under both positive and negative pressure conditions reveal further information about the pressure wave created by each prototype design, as well as the effect of the in-line pressure source in the $\text{FPA}_{V2,in-line}$ design on the overall fluid output performance. See Appendix **Table 7.4** for tabulated maximum fluidic pressure and standard deviations (averages calculated over six independent experimental

trials actuating at 1 Hz for 60 seconds) as measured for the right-most diode (Diode_{V2} design; output of the lower channel produces the fluidic output of the device) for the fabricated FPA_{V2} and $\text{FPA}_{V2,in-line}$ prototypes with the brackets installed in the upper and lower channels under forward fluid flow (forward-driving pressure portion of the actuation cycle) and under reverse fluid flow (back-flow-driving pressure portion of the actuation cycle) conditions. All pressure measurements were created using the LabSmith pressure sensor (*LabSmith*) and all flow rate measurements were created using the FLOWELL platform fluid flow rate sensors (*Fluigent*). For the FPA_{V2} prototype design with the brackets on, analyzing the right-most diode under *forward flow* conditions, the maximum pressure generated in the *upper channel* is $\sim$17.1 kPa and in the *lower channel* is $\sim$8.2 kPa; whereas under *reverse flow* conditions, the maximum pressure generated in the *upper channel* is $\sim$-7.1 kPa and in the *lower channel* is $\sim$-2.9 kPa. And for the $\text{FPA}_{V2,in-line}$ prototype design with the brackets on, analyzing the right-most diode under *forward flow* conditions, the maximum pressure generated in the *upper channel* is $\sim$31.4 kPa and in the *lower channel* is $\sim$22.4 kPa; whereas under *reverse flow* conditions, the maximum pressure generated in the *upper channel* is $\sim$-11 kPa and in the *lower channel* is $\sim$-5.4 kPa. These measurements indicate that overall larger pressures in the right-most diode are generated using the in-line pressure source approach demonstrated by the $\text{FPA}_{V2,in-line}$ prototype as compared to using the fluid reservoir approach demonstrated by the FPA_{V2} prototype.

Overall, in applications where back-flow is permitted and a relatively-low effective throughput is required, $\sim$100 μL/min for example (*e.g.* for the simple transport of an *on-chip* volume of liquid to another location on a device), FPA_{V1} would be a suitable design to meet the needs of this application as this design can produce as low as $\sim$108 μL/min at 1 Hz actuation frequency, albeit with a significant amount of back-flow. In applications where back-flow would be detrimental for the successful completion of a given fluidic process (*e.g.* the handing of discrete fluids into a Y-junction where the fluids at the input microchannels should remain un-mixed as to be able to deliver pure volumes to the Y-junction on-demand) which also demands higher fluidic throughputs, $\sim$1000 μL/min for example, FPA_{V2} would suit the needs of such applications as it can produce anywhere from $\sim$600 - $\sim$1600 μL/min output flow rates depending on the actuation frequency. Furthermore, in applications where a very high fluidic throughput is required, $\sim$2 mL/min and greater for example (*e.g.* for collecting a liquid sample from an *off-chip* environment and filling of bulk fluid reservoirs either *on-* or *off-chip* for further *on-chip* analysis), $\text{FPA}_{V2,in-line}$ would be the most suitable design, as it produces the highest volumetric flow rate, as it is capable of producing upwards $\sim$2717 μL/min at 3 Hz actuation frequency.

Finally, in microfluidic device applications where as little back-flow as possible can be permitted yet lower effective fluid flow rates are required, to reduce the overall output flow rate from either the FPA_{V2} or $\text{FPA}_{V2,in-line}$ designs (beneficial as they both utilize the Diode_{V2} designs) can be accomplished by adding extra lengths of tubing to the end of the device to increase fluidic resistance of the interfacing hardware; highly-compact 3D printed resistor designs could be integrated into the body of the prototypes themselves at the outlet of the device to increase the pressure drop before the device outlet and therefore decrease the overall output flow rate; either devices could

be operated at smaller actuation frequencies (*e.g.* 0.5 or 0.25 Hz); and perhaps most rigorously, certain parameters of the 3D fluidic operators themselves can be redesigned to produce smaller flow rates at the same pumping frequencies. Regarding the latter option, from the ideal gas law, $P_1 * V_1 = P_2 * V_2$, where P_1 is equivalent to the initial starting pressure, P_0 = $P_{atmospheric}$; V_1 is equivalent to the as-fabricated volume of the pressure source cavity, V_0; P_2 is equivalent to the total pressure differential induced by the pressure source, P_{max}+P_0; and V_{min} is equivalent to the minimum volume inside the pressure source chamber when the membrane is depressed, which in the devices developed in this work is the result of the non-working air volume contained underneath the 3D corrugated microstructures comprising the finger-actuated membrane and is much smaller than V_1. **Eq. 4.2c** can be used to relate the maximum pressure generated by the pressure source to the volume change of the finger-actuated membrane,

$$(P_{max} + P_0) * V_{min} = P_0 * V_0 \tag{4.2a}$$

$$P_{max} + P_0 = \frac{P_0 * V_0}{V_{min}} \tag{4.2b}$$

$$P_{max} = (\frac{V_0}{V_{min}} - 1) * P_0 \tag{4.2c}$$

The as-fabricated volume of the hollow pressure cavity in this work (V_0) can be approximated by the volume of a spherical cap, $V_0 = \frac{1}{6}\pi h(3a^2 + h^2)$ where a is the radius of the base of the cap and h is the height of the cap, and is therefore a function of the diameter and thereby area of the finger-actuated pumping membrane. Therefore smaller membrane diameters and thereby smaller V_0 values, assuming the membrane can still be depressed to contact the bottom of the hollow cavity and keeping V_{min} constant, will result in smaller generated values of P_{max}, therefore slower device output flow rates. Likewise, larger membrane diameters and thereby larger V_0 values will result in larger generated values of P_{max}, therefore faster device output flow rates.

4.4.8 Integrated Two-Fluid FPA Results (FPA$_{V1,2fluid}$)

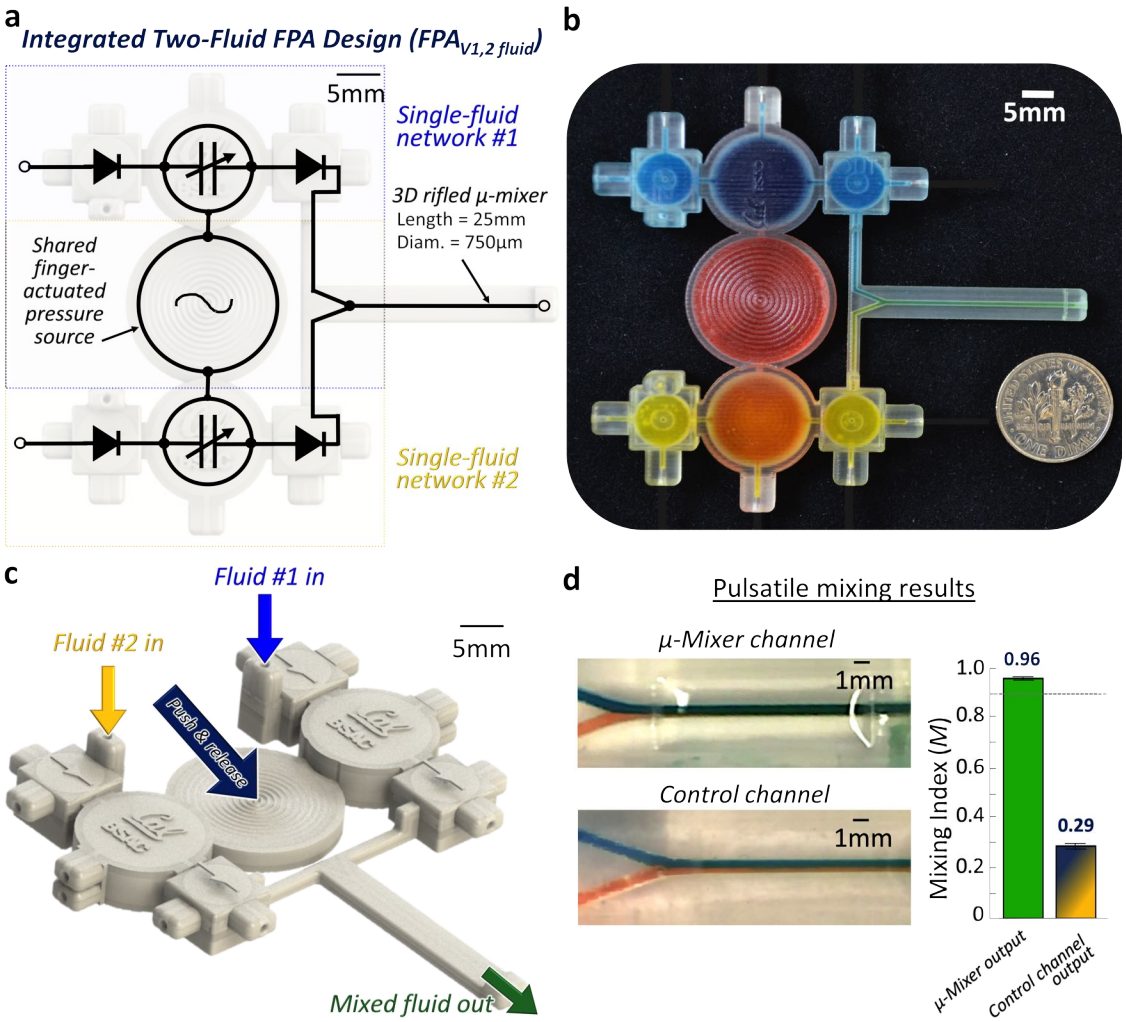

Figure 4.10: Demonstration of the integrated *two-fluid* FPA prototype (FPA$_{V1,2fluid}$) as a finger-powered, two-fluid pulsatile mixer. **(a)** Top-down rendering and fluidic circuitry schematic. **(b)** Top-down image of the fabrication results filled with color dyed solutions, two independent single-fluid networks (*blue* and *yellow*, respectively), a common finger-actuated pressure source air channel (*red*) and a 3D rifled μ-mixer-integrated mixing channel (*green*), with a US dime for scale. **(c)** Isometric view rendering illustrating working principle, two distinct input fluid sources are simultaneously-actuated by pulsatile pressure wave through the mixing channel. **(d)** Experimental pulsatile mixing results (1 Hz actuation frequency after 10 seconds); actual experimental images of the output region of fabricated prototypes with the μ-mixer-integrated channel (*left, top*) and a smooth-walled circular cross-section control channel (*left, bottom*); quantified mixing index at the terminus of each microchannel (*right*), average of three measurements with error bars denoting the standard deviation, 90% mixing threshold (*black* dotted line) shown; pulsatile two-fluid actuation through the μ-mixer structures results in enhanced fluid mixing (above 90%) *versus* the control.

The fluid actuation motion inherent to the demonstrated FPA prototypes can be described as *pulsatile* fluid motion. Even with back-flow reduction and conceptual elimination, the non-steady oscillatory pressure wave driving the fluid in the forward direction results in non-constant pulsatile fluid motion throughout the entire actuation cycle, thus the fluid motion possesses *time dependency*. In microfluidic applications which demand steady-state fluid flow, the FPA approach can be modified to deliver a more steady fluid output flow rate by the incorporation of 3D fluidic capacitor operators after the right-most diode near the outlet of the device [115] which serve to dampen the pressure wave driving the output fluid flow to a certain degree. The pulsatile nature of the FPA approach can also be used as an *advantage* towards certain microfluidic applications, however.

As a demonstration of the capability to integrate FPA-based designs *on-chip* into larger, more complex functional 3D printed microfluidic systems, a modular *two-fluid pulsatile mixer* design ($\text{FPA}_{V1,2fluid}$) is proposed, comprised of multiple *independent fluid channels* interconnected to a *common* finger-actuated pressure source, which utilizes the pulsatile mixing characteristics of the FPA approach to provide for completely-human powered mixing of microfluidic flows. The $\text{FPA}_{V1,2fluid}$ prototype (**Fig. 4.10a**) utilizes a single finger-actuated membrane to generate a pressure source which simultaneously actuates the dynamic membranes inside both fluid reservoirs in the two independent fluid channels (based off of the FPA_{V1} design). A fabricated $\text{FPA}_{V1,2fluid}$ prototype is shown in **Fig. 4.10b** with a U.S. dime for scale, filled with blue dyed fluid in the upper-most fluidic network, yellow dyed fluid in the lower-most fluidic network and red dyed fluid in the common pressure source channel, for visualization purposes. An additional visualization of the fabricated $\text{FPA}_{V1,2fluid}$ prototype after post-processing is presented in Appendix **Fig. 7.35c**.

As the $\text{FPA}_{V1,2fluid}$ prototype is operated at a given actuation frequency (**Fig. 4.10c**), both fluids are simultaneously actuated at the same flow rate, due to the geometric symmetry of the 3D fluidic operators in both fluidic networks, into a 3D Y-junction which leads to a single microchannel 25 mm in length enclosing intra-channel 3D μ-mixing structures (based off of the 3D rifled μ-mixer design as featured in **Chapter 2**). The *transient* pulsatile nature of the fluid flow inside the channel contributes additionally to the chaotic mixing induced by the intra-channel 3D μ-mixing structures, a principle previously-elucidated by asymmetric pulsatile microfluidic mixing approaches demonstrated inside smooth-walled microchannels fabricated *via* iMEMS-based fabrication methods [307]. In the fabricated prototype, during forward motion fluid flow passes through the channel with a maximum flow rate of $\sim$40 μL/min and during reverse fluid motion the accrued chaotic fluid advection is compounded by the additional contact with the 3D structures. The back-flow inherent to the FPA_{V1} 3D fluidic operators (resulting forward:reverse volume actuated per-cycle ratio of only $\sim$1.5:1) therefore permits the fluids to have a longer duration of contact with the intra-channel 3D μ-mixing structures over the course of device operation, thereby enhancing the degree of chaotic mixing as opposed to that achieved in fluid flow passing through the same length of a smooth-walled control microchannel.

The FPA$_{V1,2fluid}$ prototype operated at an actuation frequency of 1 Hz produces two independent fluid flows entering the Y-junction at ∼108 μL/min[3] which meet to form a co-laminar fluid flow. At this actuation frequency, the prototype produces a mixed segment of fluid, which has passed through the entire length of the 25 mm long output microchannel (∼11.0 μL), in 6 seconds. Therefore to experimentally-characterize the pulsatile mixing performance of the FPA$_{V1,2fluid}$ prototype, the experimental method as described in **Section 4.3.4** was used to quantify the mixing index (as first presented in **Section 2.3.5.2**) at the terminus of the outlet microchannel segment of the prototype after 10 seconds of actuation at 1 Hz. Furthermore an alternative FPA$_{V1,2fluid}$ prototype was designed and fabricated with an outlet microchannel segment possessing as smooth-walled inner geometry as a control. The mixing index at the outlet of this device as likewise determined using the same method. Experimental results (**Fig. 4.10d**) demonstrate that even given the pulsatile nature of fluid flow in the control FPA$_{V1,2fluid}$ prototype, since the flow rates of the two input fluids into the outlet microchannel are equivalent, a poorly-mixed (∼29% mixing) fluid output is generated from the device, limited by inter-species diffusive mixing; whereas by employing an intra-channel 3D μ-mixer-integrated outlet microchannel, the FPA$_{V1,2fluid}$ prototype generates significant mixing improvement (∼96% mixing) by employing chaotic mixing.

[3]In two-fluid microfluidic examples where *non-equivalent* forward-driven flow rates are desired from each of the fluids, the flow rates generated from each of the independent fluid channels can be altered with respect to one another by changing the size of the membranes inside each of the respective fluid reservoirs. **Eq. 4.2c** reveals that the numerical estimation of the generated pressure head from the finger-powered pressure source can be tailored by changing the as-fabricated volume of the pressure source cavity. Likewise, the pressure generated inside each *fluid reservoir* can be numerically determined using **Eq. 4.2c** as well, where V_0 represents the as-fabricated volume of the fluid reservoir, V_{min} represents the minimum volume inside the fluid reservoir when the internal membrane is displaced to its maximum extent upwards into the fluid channel (which can be minimized by designing an upper surface which reflects a spherical cap geometry similar to the lower surface of the pressure source chamber), P_0 represents the initial (at-rest) fluidic pressure inside the fluid chamber, and P_{max} is the maximum fluidic pressure generated in the fluidic channel from the volume reduction of the fluid reservoir. The extent to which the internal membrane displaces upwards into the fluid reservoir, and therefore as a result the generated maximum fluidic pressure, is dependent on the force on the internal membrane generated by the pressure exerted on the membrane from the pressure source channel. The force on the membrane can be related to the force applied to the finger-actuated pressure source membrane using **Eq. 4.3c**,

$$P_{psm} = P_{frm} \tag{4.3a}$$

$$\frac{F_{psm}}{A_{psm}} = \frac{F_{frm}}{A_{frm}} \tag{4.3b}$$

$$F_{frm} = \frac{A_{frm}}{A_{psm}} * F_{psm} \tag{4.3c}$$

where P_{psm} represents the pressure generated in the pressure source by the deflection of the finger-actuated membrane, P_{frm} represents the pressure exerted in the lower channel of the pressure source air channel on the bottom of the membrane contained in the fluid reservoir, F_{frm} is the force exerted on the fluid reservoir membrane, F_{psm} is the force exerted on the finger-actuated pressure source membrane, A_{frm} is the area of the fluid reservoir membrane and A_{psm} is the area of the finger-actuated pressure source membrane. Therefore by **Eq. 4.3c**, reducing the area of the fluid reservoir membrane relative to area of the finger-actuated pressure source membrane will reduce the force on the fluid reservoir membrane and therefore the overall fluid flow rate in that specific fluidic channel. In a two-fluid channel setup, reducing the area of one fluid reservoir membrane to the other will reduce the overall output fluid flow rate in that specific fluidic channel to the other fluidic channel.

These results demonstrate that multi-fluid FPA$_{V1,2fluid}$-based prototypes can enable entirely human-powered microfluidic mixing enhancement utilizing pulsatile fluid actuation and 3D μ-mixer-integration. These devices can be entirely-3D printed, thus eliminating the need for complex multi-step and lower-throughput conventional fabrication methods which are commonly used to manufacture conventional microfluidic mixing platforms. Furthermore, these devices enable completely human-powered fluidic actuation, eliminating the need for externally-powered complex fluidic micro-controllers and interfacing hardware, and making such 3D printed platforms suitable for portable, point-of-care applications where multi-fluid mixing is desired. Additionally, pulsatile fluid flow patterns have also been previously-demonstrated in other useful biomedical applications other than for mixing enhancement in conventionally-fabricated microfluidic devices, such as to elucidate more biophysiologically-relevant oscillatory shear stress states for organ-on-a-chip microfluidic platforms towards drug development and in fundamental *in-vitro* cardiac tissue research [67, 308]. Therefore such 3D printed for FPA$_{V1,2fluid}$ platforms have the potential to be advantageous tools as multi-fluid pulsatile flow generators towards even further alternative 3D printed microfluidic applications in the biomedical field.

Chapter 5

Entirely-3D Printed Biological Pathogen Detection Platform

5.1 Introduction

5.1.1 Motivation for *On-Site* Pathogen Detection

The ability to perform rapid point-of-need pathogen detection and point-of-care biological and molecular diagnostics in low-resource areas necessitates the use of completely *on-site* fluid sample collection, biological enrichment and detection. Most conventional approaches to detect sources of biological contamination of environmental liquid or biological fluid samples, for example, involve many time- and labor-intensive fluidic handling routines which must be performed in well-equipped laboratory settings and therefore often necessitates sample transportation to an *off-site* biological laboratory or healthcare clinic, which limits the overall speed of molecular diagnostics. Additionally, many microfluidic-based analytical approaches are not truly-compatible with point-of-need and point-of-care applications. Therefore, engineering of compact analytical platforms which can perform molecular diagnostics with the sensitivity, selectivity and speed of microfluidic-based approaches to perform fluidic actuation, biological enrichment and detection will enable truly-*on-site* analysis. As a result, the ability to perform rapid detection and diagnosis of pathogens *on-site* will enable recommendations for more effective medical treatments for pathogen-induced infections at earlier stages of treatment [309].

5.1.1.1 Water Quality Assessment Example

Contamination of potable sources of freshwater with pathogenic microbes such as enteric strains of *E. coli* and *Salmonella* bacteria is the leading cause of infectious disease outbreaks worldwide [310], resulting in the highest number of annual hospitalizations in the United States as well as the deaths of roughly 1.6 million children under the age of five worldwide, more than 80% of whom from rural communities in the developing world [311, 312]. Detection of pathogenic bacteria in

sources of drinking water as part of water quality assessment is therefore of the utmost importance for water utility providers, governmental and non-governmental organizations alike worldwide, due to the significant threat posed on human health; furthermore, organizations are focused on employing water quality assessment schemes to detect the presence of bacteria before the often rapid outbreak of disease [310]. Due to the general lack of high sensitivity point-of-need-compatible water-borne pathogen detection platforms, conventional methods of water quality testing involve many time-consuming, costly and labor-intensive separate fluidic handling processes. For example, he detection of drinking water-borne bacterial contaminants in liquid samples is usually performed using established laboratory-based biological enrichment and detection methods. One such gold-standard method, EPA Method 1604, necessitates collection of a $\sim$100 mL volume liquid sample; transportation of the sample to an *off-site* biological laboratory (particularly one certified to perform microbial analysis of potable water) equipped with cell culture equipment, supplies and well-trained personnel (a process which can take longer than 24 hours depending on the distance of the lab from the site of potential contamination); solution processing such as multiple filtration steps, plating on agar substrates and dilution with growth medium; biological enrichment in an incubator at 37°C for 24 hours; followed by analytical detection using fluorescence microscopy [313, 314]. While these methods demonstrate high sensitivity and accuracy, they often require 24-48+ hours for definitive results to be delivered back to the site of sample collection, which is too slow to deliver timely-predictions of pathogenic diseases [276, 315, 316].

In attempt to increase the overall throughput of such analysis (*i.e.* decreased incubation and detection times), microfluidic-based pathogen-detection techniques have been demonstrated towards rapid water quality assessments. Microscale approaches such as microchannel-integrated flow cytometry [317], microscale *on-chip* polymerase chain reaction [318], microelectronic-integrated microfluidic surface plasmon resonance [319] and enzyme-linked immunosorbent assay analysis [320] have been used to isolate and detect a variety of drinking water-borne pathogens [321–323], often demonstrating limits of detection (LoD), the lowest detectable concentration of an organism, which are comparable or even superior to conventional fluid handling processes in shorter periods of time (*i.e.* on the order of hours, *versus* days). The vast majority of these microfluidic techniques, however, entail high-cost and non-portable equipment for operation and quantitative detection, as well as multiple relatively complex fluidic operation procedures which are only practically applicable in well-controlled, high-resource laboratory settings, thereby limiting these approaches to laboratory settings and making them not inherently suitable for point-of-need applications [314]. For such water-borne pathogen detection applications, portable and cost-effective detection platforms for true point-of-need applications are lacking [324].

5.1.1.2 Clinical Urinary Tract Infection (UTI) Diagnostics Example

Urinary tract infections (UTI's) are a common healthcare concern across the globe, with costs associated with the diagnosis and treatment of UTI's in the United States alone exceeding $2.3 billion due to the hospitilization of upwards of 8 million patients for UTI-related complications annually. Current UTI diagnostic methods employed in clinical settings are performed by gold-standard clinical urine culture and analysis (urinalysis) techniques in order to detect the presence of particular strains of UTI-inducing bacteria in urine samples collected from patients, with *E. coli* responsible for up to 90% of all UTI's. Conventional microscopic urinalysis protocols, however, necessitate the use of complex laboratory-based bacteriological culture equipment and procedures which must be performed by highly-trained clinicians, with average diagnostic results taking 24-72 hours to be delivered back to the healthcare provider. Additionally, the current standard threshold for positive UTI diagnosis from urinalysis accomplished *via* both conventional and point-of-care UTI diagnostic approaches is $\sim 10^5$ cfu/mL. As a result, if a patient exhibits severe UTI-like symptoms, antibiotics are often prescribed before the diagnostic test results are received, which has lead to the development of certain strains of antibiotic-resistant UTI-causing bacteria in clinical settings.

The need therefore exists for more rapid and selective UTI detection methods, especially for point-of-care-based approaches which can be performed in low-resource medical clinics without access to complex urinalysis equipment. [215, 217, 325]. The most common UTI diagnostic tools designed for use in point-of-care applications take the form of immunoassay platforms, often paper-based test strips, which can deliver qualitative uropathogen detection in a few hours from the detection of nitrate and esterase molecules in urine, but such methods lack selectivity and sensitivity [326]. Therefore, novel rapid, easy-to-operate and sensitive point-of-care platforms are desperately needed towards detection of UTI-causing uropathogenic bacteria. Microfluidic approaches have previously been demonstrated for rapid urinalysis to identify UTI-causing uropathogens in isolated urine samples in healthcare clinics, for example lateral flow immunoassays [277], microfluidic nucleic-acid based detection [327], single-bacterium electrochemical detection [328], droplet-based microfluidics for single-bacterium detection [298] and ATP bioluminescence detection *via* fluorescence microscopy-compatible lab-on-a-chip platforms [329]; yet such platforms only demonstrate varying degrees of point-of-care applicability, as most still necessitate the use of laboratory-based fluidic interfaces, quantitative detection equipment and well-controlled experimental conditions in order to deliver higher selectivity and detection limits than those of clinical gold-standard methods [330].

5.1.2 Microfluidic Systems for Point-of-Need Pathogen Detection

An ever-increasing need exists, therefore, to develop technologies which enable truly-*on-site* pathogen detection in low-resource settings, such as rural clinics without access to the fluidic handing equipment and highly-trained operators. Most practically, such systems must ideally utilize portable and compact hardware to accomplish fluid sample collection, biological enrichment and detection completely-*on-site*, eliminating the time-consuming process of fluid sample transportation and laboratory-based fluidic handling [331]. Various microfluidic platforms have demonstrated the capability for enhanced multiplexed detection and quantification of pathogenic contamination in environmental and biological fluid samples. The majority of microfluidic systems, however, are not suitable to meet the demands of point-of-need and point-of-care applications. The development of compact biosensor platforms which possess the analytical capabilities and benefits of microfluidic-based approaches in truly *on-site* point-of-care clinical settings promise to have enormous impacts in disease treatment world-wide [17].

For example, with the objective of implementing portable schemes for quantitative detection, various platforms have been demonstrated utilizing portable cell phone-based imaging and quantitative detection schemes, promising in-field applicability. One such platform developed by Zhu et. al ([314]) utilizes anti-*E. coli* O157:H7 antibody-functionalized glass substrates to perform quantum dot-based sandwich assays utilizing LED light excitation hardware and a cell phone camera to image solutions in microchannels through a microscope lens, followed by image analysis using computer-based software. This system however, whilst utilizing a highly-sensitive quantum dot detection approach which enables a limit of detection (LoD) of *E. coli* comparable to that achieved using conventional fluidic processing standards, still requires multiple intricate fluid handling steps to load various solutions onto a microfluidic chip, necessitating the use of multiple independent fluid flow controllers restricted to use in laboratory settings and requires fluid handling by well-trained operators in order to achieve the promised detection accuracy, thereby limiting in-field portability. These limitations are commonplace with most point-of-need advertised platforms, such as an optofluidic sensor advertising low-cost 3D printed hardware, yet incorporating sensitive optical and electrical spectrofluorometry hardware [276]; cell phone-based optofluidic fluorescent imaging cytometry [332]; and battery-powered platforms which still rely upon non-inherently field-worthy microcontroller electronic setups to communicate with computer-based software [316]. Additionally, nearly all of these methods still require some form of biological enrichment, accomplished through incubation of a bacterial solution under optimal growth conditions, as to increase the cell density inside the sample, thereby increasing the efficiency and rate of biochemical reactions within the solution.

Moreover, various microfluidic approaches employing qualitative detection methods have also been demonstrated, with the objective of enabling detection which can be performed by un-trained personnel and requiring no external equipment. Such methods predominantly employ colorimetric detection methods which are used to identify the presence of a specific pathogen by inducing a

visible color change in a solution upon incubation of the fluid sample in the presence of enzyme-targeted colorimetric reagents. Many pathogenic bacteria species can be enzymatically-targeted to exhibit colorimetric changes, whereby upon biological enrichment, certain biochemical interactions between bacterial-specific enzymes (*i.e.* those expressed only be a particular strain of bacteria) and reagents result in clear and definitive color change in the molecule. The main objective with work utilizing such colorimetric detection approaches is the discovery, development and implementation of ever-higher sensitive enzyme-reagent pairs which can be used to constantly improve the LoD of the method. Due to the stability of most colorimetric reagents during device pre-treatment, storage and transport; relatively-minimal equipment is necessary to perform the single fluidic processing step (*i.e.* combining of a solid reagent with a liquid sample to form an enrichment and detection solution which can readily be performed passively, *on-chip*). Numerous point-of-need-targeted microfluidic approaches utilizing various colorimetric reagents have been previously-demonstrated, mainly utilizing paper-based microfluidic devices, as one of the most suitable approaches to meet requirements for point-of-need-targeted microfluidic applications. [278, 311, 333–335].

5.2 Design of the Hand-Held, Finger-Powered 3D Printed Pathogen Detection Platform

The proposal for a new class of microfluidic device is fundamentally motivated by the objective to engineer a simple-to-operate tool which eliminates the need for high-powered and bulky sources of fluidic operation and for un-trained personnel to use to perform completely-*on site* detection of liquid contamination by potentially-hazardous pathogenic organisms. The finger-powered fluid actuation approach previously demonstrated in **Chapter 4** serves as the inspiration for monolithically-fabricated 3D printed prototype structures to serve this role. Therefore, 3D printing was chosen as the fabrication method to engineer the proposed prototype due to the monolithic, simple and rapid fabrication additive manufacturing approach. This enables straight-forward and practical integration of power-less, finger-powered actuator systems with microchannel geometries which contain an easily-tailorable number of independent liquid sample analysis regions *on-chip*, facilitating multiplexed enrichment and detection of any desired number of target pathogens.

As illustrated in **Fig. 5.1**, the proposed hand-held device is intended to be held between the operator's thumb and index fingers, manually-inserted into an aqueous body of interest, and when actuated using solely the power of the human finger, used to uptake controlled volumes of fluid into discrete *on-chip* fluidic chambers. These chambers are pre-treated with bacterial enzyme-specific colorimetric reagents and nutrients, drop-casted into the device during fabrication and stored as a stable, dry coating inside each chamber, which will re-incorporate into each fluid sample. *On-chip* biological enrichment can then be performed utilizing various examples of commercially-available,

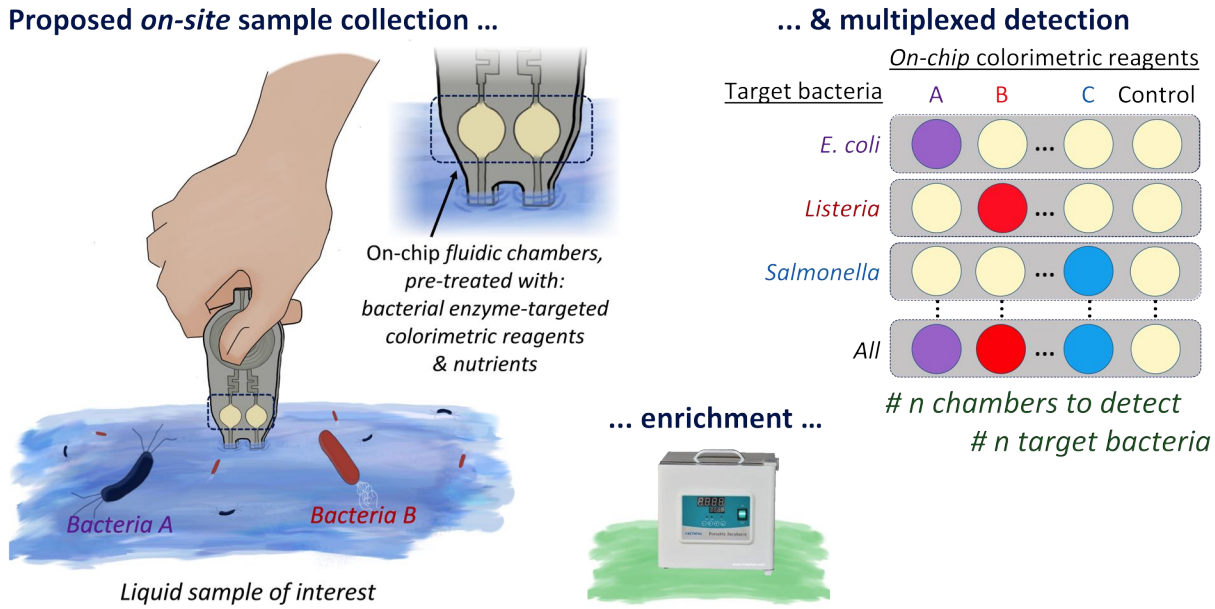

Figure 5.1: Conceptual illustrations of the proposed entirely-3D printed, hand-held microfluidic design targeting on-site fluid sample collection, enrichment and multiplexed pathogenic detection. **(a)** The proposed hand-held device is intended to be used to uptake fluid samples *on-site* from a potentially pathogen-contaminated aqueous body of interest into discrete on-chip fluidic chambers, powered solely by the actuation of the operator's finger (the singular application of water quality assessment is illustrated). Following **(b)** biological enrichment utilizing *on-site* hardware to incubate the entire device, the fluidic chambers, pre-treated with bacterial enzyme-specific reagents and nutrients stored *on-chip*, will enable **(c)** multiplexed detection of various pathogens using qualitative or semi-quantative approaches. The monolithically-fabricated 3D printed prototype, which eliminates the need for high-powered and bulky sources of fluidic operation and detection, is intended to serve as a simple-to-operate tool for un-trained personnel to use to perform completely-*on site* detection of contamination by potentially-hazardous pathogenic organisms.

field-ready rechargeable and portable incubation hardware, for example those currently used by non-governmental organizations to incubate biological fluid samples at 37°C for extended periods of time in rural clinical settings in low-resource areas, such as the Hach 12 VDC, 30-50°C Portable Incubator (*Hatch Electronics*, FL, USA) or Cooper G95 Portable Incubator (Cooper Surgical, CT, USA) [309]. Finally, after incubation, straightforward multiplexed colorimetric detection of an arbitrary number of distinct target bacterial pathogens in a single operation is accomplished utilizing a qualitative detection scheme which can be performed by un-trained personnel, resulting in analytical pathogen detection throughput in a matter of hours.

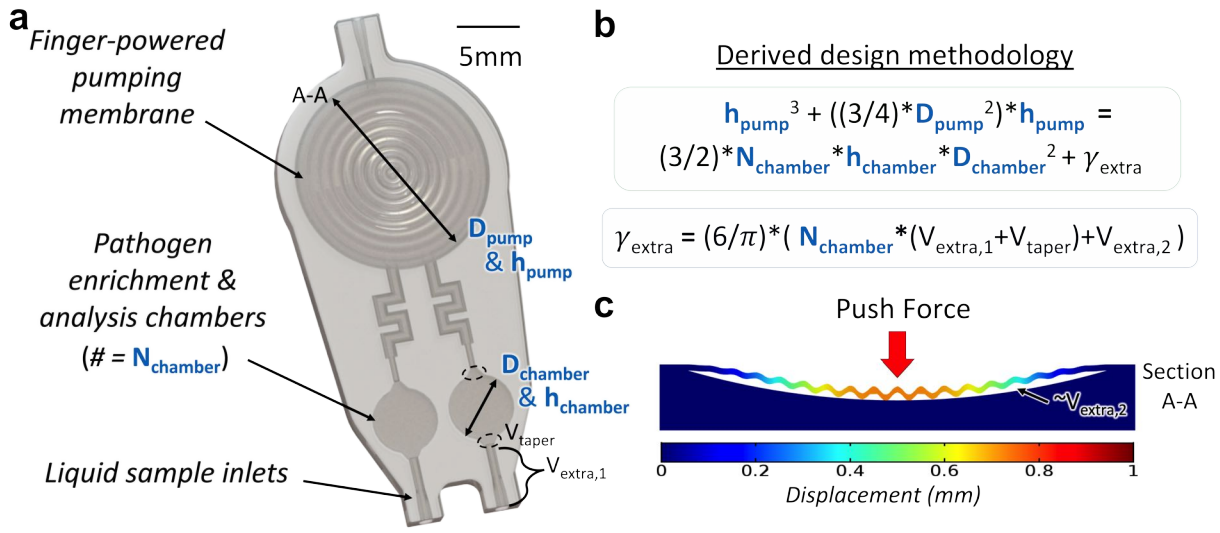

Figure 5.2: Diagram and design methodology of the proposed 3D printed pathogen detection platform. **(a)** Rendering of the 3D solids model illustrating the fundamental constituent design elements and as independent design parameters, *i.e.* the diameter of the finger-powered pumping membrane, D_{pump}, and the diameter and number of pathogen enrichment & analysis chambers, $D_{chamber}$ & $N_{chamber}$, respectively. **(b)** Derived design methodology equations in terms of the independent design parameters for which values are chosen, the constant volume of the liquid sample inlet, $V_{extra,1}$, as well as the approximate volume of space underneath the finger-powered pumping membrane when depressed, $V_{extra,2}$, which can be used to analytically determine the height of pressure source chamber, h_{pump}, such that the volume of the finger-powered pressure source is equivalent to that of the total volume of all chambers and liquid sample inlets. **(c)** Cross-section of a finite-element analysis simulation using COMSOL Multiphysics, visualizing the deformation of the finger-powered pumping membrane upon being pressed with a force of 10 N.

5.2.1 Design of the Integrated 3D Fluidic Network

The design of the proposed 3D pathogen detection platform targeting completely *on-site* pathogen detection is illustrated in **Fig. 5.2**. The proposed device design (**Fig. 5.2a**) consists of a solid 3D printed body containing hollow microchannels, cavities, inlets and a 3D fluidic operator serving as a human-powered pressure source, based off of the concept of the finger-actuated pressure source previously demonstrated for the FPA prototypes in **Chapter 4**. The *finger-powered pumping membrane* encloses a hollow *pressure source* cavity which adopts a spherical cap shape[1] as to roughly conform to the shape the fully depressed finger-actuated membrane, thereby minimiz-

[1] A spherical cap is formed by cutting a sphere by a plane which is perpendicular to the radius of the sphere intersecting the plane, is given by **Eq. 5.1**,

$$V = \frac{1}{6}\pi h(3a^2 + h^2) \tag{5.1}$$

ing the non-working volume of air between the 3D corrugated structures on the membrane and the lower surface of the cavity. The pressure source has a single microchannel inlet to facilitate support material removal on the top of the device and is connected to independent microchannels which lead to discrete *pathogen enrichment and analysis chambers* that are connected to the exterior of the device *via* liquid sample inlet microchannels. Conceptually, during operation the pressure source inlet microchannel is plugged such that when the membrane is depressed the enclosed volume of air is forced through the rest of the microchannel network, and when the membrane is released a vacuum pressure is generated which draws liquid in through the liquid sample inlets and into the *on-chip* chambers. The volumes of the pressure source cavity and the total volume of the microchannel regions which will be filled with liquid upon device operation must be designed carefully, such that they are *equivalent*, ensuring that the pressure source cavity is *no larger* in volume than that of the combined chambers and inlet volume (which would result in potential overflow of the system and fluid contamination of the pressure source) *nor smaller* in volume (which would result in incomplete filling of the chambers and decreased enrichment and detection efficiency). The height of the pressure source cavity should be sufficiently large as to maximize the volume of air displaced (through the microchannel network) by the membrane when fully-depressed, but be short enough as to ensure that when the membrane is displaced to its maximum state that contact is made with the bottom of the cavity before fracture can occur. The conceptual microchannel network design was broken down into discrete independent design variables: the diameter of the finger-powered pumping membrane (D_{pump}), the number of desired *on-chip* chambers ($N_{chamber}$), the diameter ($D_{chamber}$) and height ($h_{chamber}$) of each chamber and the height of the pressure source cavity (h_{pump}). The design is also broken down into design parameters which are assumed to be fixed (*i.e.* parameters which do not change when the independent design variables are changed). The volume inside each liquid sample collection inlet is chosen to represent the design constant $V_{extra,1}$, which is defined by the shape of the interfacing inlet used to facilitate support material removal and which during operation contains the volume of last portion of the fluid collected onto the device by the vacuum from the pressure source, $\sim$ 3.92 μL. This geometry is optimized to fit standard interfacing hardware and therefore will not change. Furthermore, The total volume of the slight tapered regions between the cylindrical volume of each chamber and the adjoining microchannels is defined as V_{taper}, $\sim$ 1.27 μL. In addition, the volume underneath the 3D corrugated features comprising the finger-actuated membrane which remains un-evacuated from the pressure chamber when the membrane is fully-depressed should not be considered as part of the functional air volume inside the pressure source; therefore, this value is chosen to represent the design constant $V_{extra,2}$ [2]. The value of this constant for the featured design was determined to be $\sim$7.82 μL

where a is the radius of the base of the cap and h is the height of the cap. In the 3D model of the pressure source cavity, the base of the cap is mated to the lower surface of the 3D corrugated finger-actuated membrane, and the height of the cap is represented by the perpendicular distance between the lowest point inside the cavity and the underside of the membrane.

[2]This value is *assumed* to be constant in the derivation of the design methodology. Indeed, changing the height of the cavity (textiti.e. changing only a single solids model) to produce a different chamber volume is subjectively more straightforward than adjusting the diameter of the membrane, since doing so would necessitate editing two different parts (*i.e.* designing an entirely new 3D corrugated membrane 2D profile and 3D part file in addition to changing the

using Solidworks solids modeling and solid volume geometric analysis following the procedure as described in **Section 5.3.1**. A detailed diagram of the hollow microchannel network, along with all dimensions of the microchannel network design developed in this work, as well as the design constants discussed in this chapter, are presented in Appendix **Fig. 7.44**. Setting the volume of the pressure source equivalent to that of the total combined volume of the desired number of liquid sample inlets and chambers, minus the non-working volume underneath the membrane when fully depressed, a design methodology represented by the equations shown in **Fig. 5.2b** was numerically derived. This derived design methodology not only enabled the design of the 3D printed platform featured in this work (by choosing $N_{chamber}$ = 2, $D_{chamber}$ = 5 mm, $h_{chamber}$ = 1 mm, D_{pump} = 15 mm to find the appropriate value of $h_{pump} \approx 0.67$ mm), but also enables the straightforward design recommendations to enable the design of any arbitrary number of target pathogen enrichment and detection chambers to perform multiplexed pathogen detection.

Additionally, a finite-element analysis simulation using COMSOL Multiphysics (**Fig. 5.2c**) is used to visualize the deflection of the finger-powered pumping membrane, which assumes material properties approximating those of the 3D printed material used in later prototyping, upon being pressed by a point-source with a force of 10 N, which is one of the lowest values (by a very conservative estimation) for the maximum thumb-index finger pinch forces that a typical human test subject is able to generate produce according to the Palmer pinch test [336]. This demonstrates that the membrane will deform sufficiently as to ensure that the lower surface establishes contact with the bottom surface of the pressure source chamber (before membrane fracture can occur); thus, the dead volume remaining underneath the membrane when fully-deformed is minimized, approximating $V_{extra,2}$.

5.3 Materials and Methods

5.3.1 Three Dimensional Modeling

The 3D microfluidic device design was created using Solidworks, following the example previously discussed in **Section 2.3.1**. The main body of the model was created using the same

diameter of the hollow cavity in the solid microchannel body part file). Even in light of the fact that with increasing chamber heights the membrane must elastically-deform to a greater extent and as a result the strain in the membrane and therefore the volume of air underneath the 3D corrugations will be slightly smaller since the membrane will be minutely more flat, it is assumed that this change is negligible and therefore the volume does not change with changing heights. When the diameter of the membrane instead changes, however, the geometry 3D corrugations changes accordingly as described by the equation presented in Appendix **Fig. 7.44c** which is a function of the outer diameter of the membrane. Therefore, if the decision is made to change the cavity volume by changing the diameter of the cavity (and membrane) instead of, or in addition to, the height of the cavity, the total volume of air underneath the structures will slightly change as well.

Solidworks cavity feature approach as was used to create the manufacturable *tetrahedral*-based 3D μ-CGG design, as described in **Section 3.3.1**. A 3D microchannel network design was first created, as is shown in Appendix **Fig. 7.44**, by assembling all of the individually-designed microchannel part models into a single assembly, from which a single part was created. This part was and used to create the 3D solids part file consisting of hollow 3D microchannel features inside the solid body. A new assembly was created from the hollow body part and a part file defining the 3D finger-actuated pressure source membrane was mated to the exposed circular rim defining the hollow pressure source cavity. This final manufacturable assembly was used to export the final .STL for fabrication, and was conceptually illustrated using PhotoView 360 to produce the device renderings throughout these sections. As mentioned in **Section 5.2.1**, Solidworks was also used to determine the value of the design constant defined as $V_{extra,2}$, which is represented by the volume underneath the fully-deformed membrane of the finger-powered pressure source. To determine this value, a 2D profile of the deformed membrane making contact with the bottom surface of the pressure source chamber was created in Solidworks, then a 3D solids model with a volume representing that of the empty space between the fully-deformed membrane and the bottom of the pressure source chamber was created using the revolve feature. The geometric volume of this model was then analytically determined using the volume analysis tool. The final manufacturable assembly file was also used to perform the basic finite element analysis (FEA) simulation to visualize the deflection of the finger-actuated membrane. A cross-section of the finger-actuated membrane and enclosed air cavity geometry (along section A-A, as shown in **Fig. 5.2a**) was taken and a 3D symmetry simulation was performed, using first-order adaptive element meshing and linear-elastic solid deformation assumptions. In the 2D view of the geometry, all edges were selected as solid boundaries, except for the corrugated membrane, which was defined as unfixed and was assigned material properties similar to those of the 3D-printed photocurable polymer used to fabricate the actual prototype device (VisiJet M3, *3D Systems*, ρ = 1.0210^3 kgm^{-3}; E = 1.2 GPa). Since the device is designed to be held between the user's thumb and index finger and actuated using the thumb pad, the study simulates a force applied at the center of the finger-actuated membrane of 10 N. The visual result of this simulation, illustrating the deflection of the membrane subjected this pushing force, is shown in **Fig. 5.2c**.

5.3.2 Fabrication and Post-Processing

The prototype device designs featured in this work were fabricated from the same materials, using the same equipment and were processed using the same post-processing procedure as previously detailed in **Section 2.3.3**. The support material was removed from the microchannel network by manually forcing heated mineral oil solution through each of the three microchannel inlets in the device, taking care not to apply so much pressure as to cause observable deformation in the membrane. Finally, as the pathogen enrichment and analysis chambers are intended to be used for dry-casting of colorimetric reagents and nutrients and bacterial cell culture, extra care was taken during the post-processing procedure to remove all of the support material and residual oil from

inside the microchannels, doubling the number of steps involving washing the microchannels with soapy and clean water. Additionally, one important concern with most 3D printed microfluidic systems developed for biological applications, and specifically taken into consideration in this work, is to ensure that post-processing measures are taken in order to minimize any cytotoxic effects of the 3D printed material (*i.e.* material characteristics which inhibit cellular growth and reproduction, and/or prove lethal to said organism), which could prove detrimental to the ability to successfully culture bacteria inside the fabricated prototype device [337]. One widely accepted definition of material biocompatibility is "the ability of a material to perform with an appropriate host response in a specific application" [338], which is a sufficiently broad definition which no doubt is intended to encourage or require individual case studies be performed on a given material towards a specific organism in order to claim biocompatibility in a specific context. Standard materials used to manufacture conventional microfluidic devices designed for cell culture are typically fabricated using materials proven to be biocompatible for most biological applications, such as PDMS, polystyrene (PS) and polymethylmethacrylate (PMMA) [87]. The biocompatibility of many polymers commonly used in additive manufacturing however, proprietary formulations not outwardly-advertised as meeting established biocompatiblity standards [86] in particular, has not been definitively proven [36]. Moreover, previous studies have shown that certain Multijet and SLA materials are proven to be cytotoxic to different cellular organisms during cell culture experiments and viability assays [33, 118].

Briefly, one of the primary mechanisms behind polymer cytotoxicity is the presence of unpolymerized residual monomers which are are statistically always present after the process of free radical polymerization of photocurable polymers and become trapped in the polymeric matrix at or near the material surface, eventually leaching into contacting aqueous solutions and proving cytotoxic to various cellular organisms contacting the exposed surface of the polymer matrix [339]. Developing various practical methods to reduce the cytotoxicity of commercially-available post-polymerized 3D printed polymers, without significantly altering other inherent mechanical properties of the material, is therefore one of the primary focuses in current research involving the engineering of 3D printed biomedical devices [340, 341]. Conveniently, the specific acrylate-based 3D printed Visijet M3 polymer used to fabricate the prototype in this work has been previously studied in the context of developing practical ethanol-treatment procedures to reduce the cytotoxicity of the post-polymerized material towards the culture of multi-cellular Zebrafish embryos. The results of this recent work showed that washing of the 3D printed material with a 99% aqueous-solution of ethanol, which is known to increase the solubility of residual acrylic monomers in solution, before cell culture resulted in nearly the same survival rate ($\tilde{9}0\%$ viable organisms at 72 hours) of multi-cellular Zebrafish embryos cultured inside 3D printed enclosed wells as was observed when culturing the same type of organism in a petri dish made from PS. The cytotoxicity of the 3D printed material was therefore shown to be significantly reduced using this ethanol-based material treatment procedure, as compared the same experiments performed using the 3D printed polymer without any ethanol treatment (showing practically 100% mortality at 72 hours). [129]

Therefore in order to reduce potential cytotoxicity of the fabricated 3D printed prototype device in this work in light of the results demonstrated by the aforementioned study [129], ethanol solution-based treatment was performed as the final step in the device post-processing protocol; whereby the nutrient and colorimetric reagents chambers are filled through the microchannel inlets with a solution of 99% ethanol in DI water. After 10 minutes the solution was evacuated from the microchannels and the device let to evaporate overnight.

5.3.3 Device Pre-Treatment and Operational Procedures

In order to enable *on-chip* pathogen enrichment and detection on the 3D printed platform, a custom chamber pre-treatment procedure was developed in order to pre-load the chambers on the prototype device with a combination of bacterial growth nutrients to facilitate rapid bacterial proliferation during enrichment and a colorimetric bacterial enzyme-specific reagent chemical enabling qualitative and quantitative pathogen detection. Immobilization of said chemicals inside the device chambers was accomplished by employing a *drop-casting*-like procedure, whereby a *pre-treatment solution* of both solids is loaded into the device and the solvent evaporated off as to leave behind a solid residue coating all surfaces inside the chambers. The pre-treatment solutions are formulated by combining certain combinations of the nutrient and colorimetric reagents in solid powdered form into a pure ethanol solution, following the experimental reagent preparation protocols discussed in **Section 5.3.6**. During the development of the drop-casting procedure, it was experimentally-determined that using DI water as a solvent was not optimal, as the slow evaporation rate of water resulted in a concentration of the particulates which had solidified at the device outlets while evaporation was taking place, and as a result none remained inside the chambers. The much higher evaporation rate of ethanol [342], on the other hand, resulted in a solid residue which remained inside the chambers, evenly coating all surfaces; thus, ethanol was chosen as the suitable solvent for the pre-treatment solutions. In the drop-casting portion of the pre-treatment procedure (*Fig. 5.3a*) the pre-treatment solution is manually loaded into liquid sample collection inlet on the fabricated prototype such that the solution visibly fills each chamber in its entirety. The ethanol solvent is then evaporated from the inside of all chambers (*Fig. 5.3b*) by placing the fabricated prototype into an oven set at 50°C for 3 hours to ensure that the ethanol solvent is completely evaporated, leaving a solid residue of solid nutrients and reagent coating the interior of the chambers and the liquid sample collection inlets. Conceptually, the device is now dried and can be transported in sealed packaging during transport and delivered to an *on-site* location for use. The stability of the solid residue overtime (*i.e.* change in sensitivity or degradation of the reagent or quality of the nutrient) was not studied in this work, and would need to be fully characterized experimentally pending scale-up of manufacturing, packaging and shipping of such a platform for use in real-world applications.

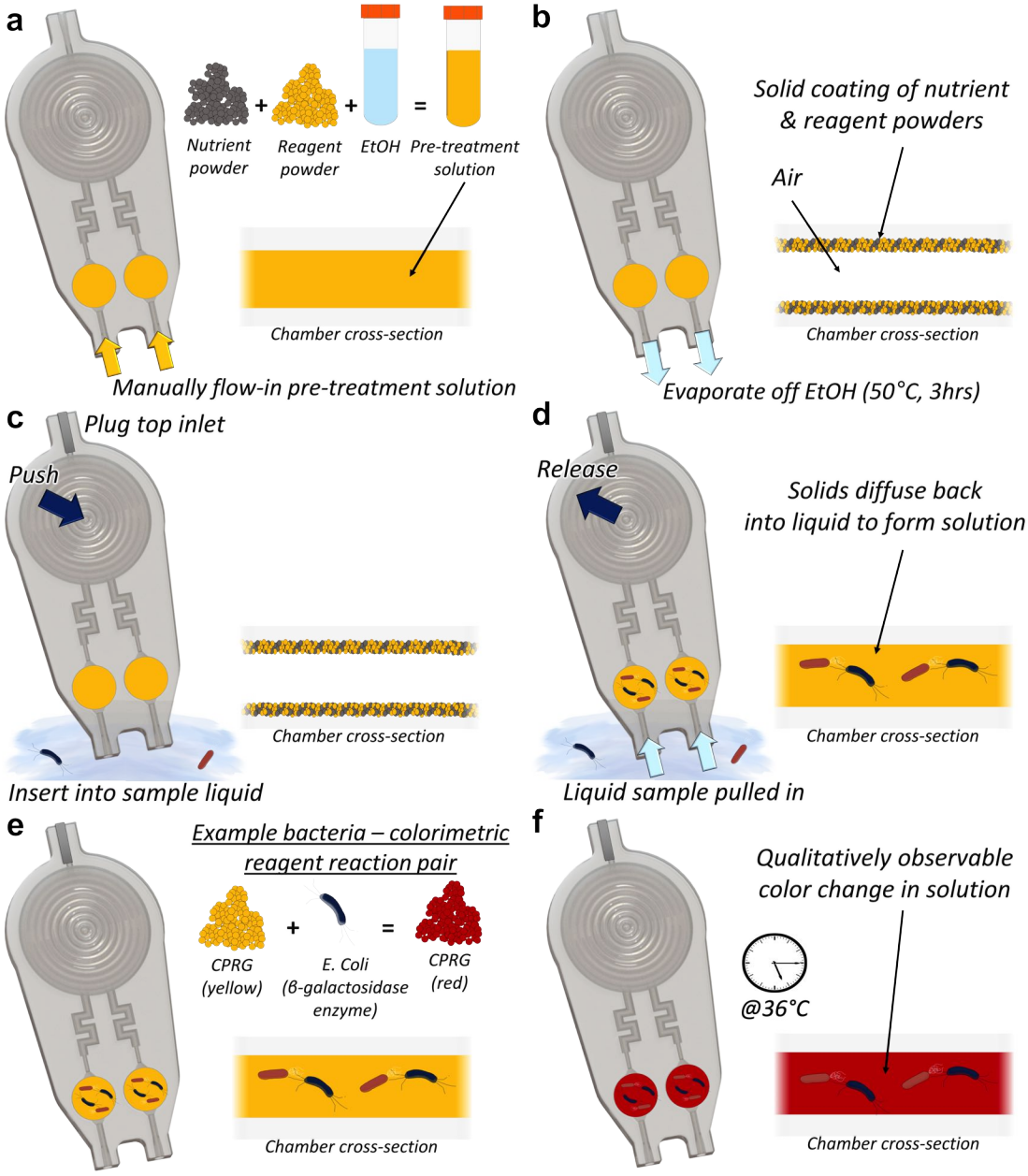

Figure 5.3: Illustration of the developed pre-treatment and conceptual operational procedures towards *on-chip* enrichment and colorimetric detection of pathogens present in isolated liquid samples. **(a)** Loading of pre-treatment solution followed by **(b)** evaporation of the solvent to immobilize solids inside the chambers. **(c)** Liquid sample collection and **(d)** re-suspension of pre-loaded solids. **(e)** Mechanisms of the proof-of-concept bacterial enzyme-colorimetric reagent pair and **(f)** detection scheme following *on-chip* enrichment as demonstrated in this work.

The device operation is as follows, which would conceptually be performed at an *on-site* location, but in this work was performed in a laboratory setting in the Bio Nanotechnology Center (BNC, Stanley Hall, UC Berkeley). When a liquid sample is desired to be tested, the external microchannel inlet on the 3D printed prototype's finger-powered pressure source is first plugged permanently using a stainless steel catheter plug (SP20/12, *Instech*) (conceptually the device will be removed from its packaging for transportation and will already have the pressure source inlet blocked) in order to create a vacuum pressure in the pressure source when the finger-actuated membrane is depressed. The liquid sample inlets are then inserted into the liquid body of choice (*Fig. 5.3c*) and the finger-actuated membrane depressed, which is then released (*Fig. 5.3d*), causing the vacuum pressure to drawn liquid through the inlets and into the chambers on the device, after which point the solid nutrient and reagent residue coating the chamber walls diffuses back into the liquid, re-creating a nutrient- and reagent-rich liquid solution. This work employs the chemical chlorophenol red-β-d-galactopyranoside (CPRG) as a proof-of-concept colorimetric reagent for the demonstration of *E. coli* pathogenic detection. CPRG is readily catalyzable by the β-galactosidase (β-gal) endogenous enzyme expressed exclusively by *E. coli* bacteria cells [343] which changes the color of the molecule from bright yellow to dark red, which is distinctly visible with the naked eye, especially when in a liquid solution (*Fig. 5.3e*). This project demonstrates the detection of a BL21 strain of *E. coli* bacteria for which CPRG is a suitable reagent to use for colorimetric detection. Therefore when the 3D printed platform is incubated (conceptually inside an *on-site* portable incubator) at 37°C, bacteria inside the solution metabolize the nutrients in the solution and proliferate. If the specific target bacterial strain is present inside the solution, the CPRG will begin to be metabolized, and after a certain period of time the color of the solution will turn from yellow to red (*Fig. 5.3f*), which can be qualitatively-observed through the relatively-transparent 3D printed material, or be quantified using image analysis. The rate of color change depends on a variety of factors including the initial starting cell density of bacteria inside the solution before incubation, the efficiency of heat transfer through the 3D printed material (*i.e.* the duration for thermal equilibrium to be reached between the solution and the 37°C environment), the rate and overall efficiency of diffusion of the solid residue into the solution, the presence of any interfering bacterium or chemicals inside the solution which would inhibit the growth of the bacteria or in some way degrade the colorimetric reagent, the inherent enzyme-reagent reaction rates, the pH and the temperature of the solution [343]. Therefore the implementation of a specific enzyme-reagent pair in determining the efficacy and limit of detection of the chosen detection scheme must first be well studied in a laboratory-setting, as is the focus of this project.

5.3.4 Experimental Setup

In order to experimentally-characterize the accuracy of the volume of fluid collected into each chamber for a given finger-actuation operation, a fluid verification uptake experiment (**Section 5.4.2**) was first performed. A glass petri dish was filled with blue dyed DI water. A 20 gauge stainless steel interconnecting couple (model SC20/15, *Instech*, USA) was inserted into the mi-

crochannel inlet connecting to the pressure source of the fabricated prototype such that when the finger-actuated membrane is depressed, air is evacuated from the pressure source through the microchannel network and out of the liquid sample inlets; when the inlets are inserted into a liquid sample and the finger-actuated membrane released, liquid is drawn through the inlets and into the fluidic chambers due to the vacuum pressure created in the pressure source. In this experiment, the finger-actuated membrane was depressed, the inlets inserted into the blue liquid, and the membrane released such that the fluid was drawn into the device, filling the *on-chip* chambers, and the collected volume was assessed using the image analysis protocol as described in **Section 5.3.5.1**.

The non-enrichment portions of the pre-treatment chemistry optimization and limit of detection experiments were all performed at temperatures of roughly 20 to 25 ° C and involved the use of three 3D printed 10-chamber microfluidic array components to perform each experiment in triplicate, simultaneously. Visualized in Appendix **Fig. 7.47**, the custom-designed array components have 10 chambers designed to the same specifications as the design of the chambers in the actual prototype platform itself (5 mm diameter, 1 mm height, 500 μm-thick upper surface) and were fabricated using a *Stratasys* Objet250 Connex3 3D printer from VeroClear polymer and FullCure720 support materials (*Stratasys*, MN, USA). The FullCure720 material is a hydrogel-based support material which is soluble in lye, therefore the support material was evacuated from the interior of each device by immersing the 3D printed components in a 200 mL volume of 1M KOH solution in a glass beaker contaning a magnetic stir bar, which was stirred and heated to 60°C for 12 hours on a heated stir plate, after which point the basic lye solution was neutralized using an appropriate concentration of HCl solution. The 3D printed components were then washed with DI water on the exterior, and DI water used to flush out the interior of each chamber, as to remove any basic or acidic ions remaining on the surfaces. A pure concentration of ethanol was then used to sanitize the interior of the chambers and the devices let to dry inside an oven at 50°C for 3 hours until the ethanol was completely evaporated from inside the chambers.

The pre-treatment chemistry optimization experiment (**Section 5.4.3**) studied the effects of different concentrations of growth nutrients on the proliferation of cells during incubation. Three different 3D printed arrays were used for each experiment to perform the experimental procedure in triplicate, simultaneously. Four different pre-treatment chemistries were prepared, following the procedures described in **Section 5.3.6**, containing the same concentration of the colorimetric reagent, CPRG, but different concentrations of growth nutrient from 0 to 125 g/L in ethanol as a solvent. These pre-treatment solutions were then manually loaded into each chamber on the 3D printed array using the syringe, tubing and interfacing steel coupling hardware as first referred to in **Section 2.3.3.2** until the entire chamber was filled. The ethanol was then evaporated from all of the chambers by placing all of the 3D printed arrays into an oven set at 50°C for 3 hours until the ethanol was completely evaporated. An inoculation of *E. coli* bacteria in liquid solution was prepared, transferred to phosphate buffer saline (PBS) solution, and diluted to a cell density of $\sim 10^6$ cfu/mL according to the procedures referred to in **Section 5.3.7**. As shown in the top image in **Fig. 5.6a**, the bacteria in PBS solution was then manually added to each chamber (except for Chamber #1 which was filled with $\sim 10^6$ cfu/mL bacteria in liquid LB solution with a concentration

of 25 g/L; and Chamber #2 which was filled with pure PBS solution with no bacteria present). Steel couples were then inserted into each inlet on the 3D printed device, two per-chamber, as to prevent solution evaporation during incubation and the 3D printed devices all placed inside a temperature- and CO_2-controlled bacteria incubator and incubated at 37°C in 4% CO_2. The 3D printed devices were removed from the incubator after 3 hours and 6 hours of incubation and imaged following the protocols described in **Section 5.3.5.2**. The result of this overall experiment is the recommendation of a certain nutrient concentration to be used in the optimal chamber pre-treatment solution chemistry.

The limit of detection (LoD) experiment (**Section 5.4.4**) was performed in order to determine how long of incubation was necessary in order to provide for sufficient bacterial proliferation as to induce a color change of the fluid inside each of the chambers from yellow to red, starting from different known initial concentrations of bacteria. Higher initial bacteria densities (*e.g.* $\sim 10^6$ cfu/mL) mean greater total amount of expressed bacterial enzymes are present in the solution, resulting in larger numbers of chemical reactions in a given period of time between the enzymes and the CPRG and therefore overall more rapid color change. The LoD value is defined as the initial starting concentration of bacteria present in the liquid sample before incubation as to produce color change in the solution in a given period of time; thus, different LoD values are reported, one for a given duration of enrichment. To perform this experiment, three different 3D printed arrays were used to perform the experimental procedure in triplicate, simultaneously. Chambers #1 & #2 were pre-loaded with a solution only containing 5 mM CPRG, and Chambers #3 - # 10 were pre-loaded with the with the optimal pre-treatment solution chemistry found in the previous experiment, then the ethanol was evaporated off using the same protocol as previously described. In this experiment, a serial dilution of bacteria in PBS was prepared according to the procedures referred to in **Section 5.3.7** to produce concentrations from $\sim 10^8$ cfu/mL down to $\sim 10^3$ cfu/mL. Each of the solutions was manually loaded into one chamber, in decreasing concentrations from Chamber #10 to Chamber #5. Chambers #1 - #4 were filled with PBS solution only. Steel couples were then inserted into each inlet on the 3D printed device, two per-chamber, and the 3D printed devices all placed inside the bacteria incubator and incubated at 37°C in 4% CO_2. Likewise with the previous experiment, the 3D printed devices were removed from the incubator after 3 hours and 6 hours of incubation and imaged following the protocols described in **Section 5.3.5.2**. The result of this overall experiment is the determination of both a quantitative LoD as determined by image analysis, as well as a qualitative LoD as determined by observation of color change with the naked-eye.

The prototype demonstration experiment (**Section 5.4.5**) demonstrated the real-world applicability of the 3D printed pathogen detection platform towards human-powered liquid sample collection and *on-chip* enrichment and detection. This experiment involved creating an $\sim$10 mL volume of *E. coli* in PBS solution diluted to the cell density as determined by the qualitative LoD found in the previous experiment, following the protocols referred to in **Section 5.3.7**. The device was used to collect the fluid into the *on-chip* chambers following the operational procedure used to perform the fluid uptake verification experiment. The liquid sample inlets on the device were then plugged with steel couples and the entire 3D printed prototype was incubated inside the bacteria incubator at 37°C in 4% CO_2. The prototype was removed from the incubator at the time reported for the LoD, and color change in the liquid samples qualitatively observed, the correlation to the LoD determined.

5.3.5 Data Acquisition and Quantitative Analysis

5.3.5.1 Fluid Uptake Verification Experiment

To visualize the volume of fluid collected into each *on-chip* chamber on the prototype device, the DSLR camera as previously-discussed in **Chapters 1 & 2** was used to capture one experimental image of the prototype device before fluid uptake, and one after fluid uptake, resulting in the actual experimental images as seen in **Fig. 5.5**. To quantify the volumes of fluid collected in the chambers, Fiji image analysis software as previously discussed in **Sections 2.3.5.2 & 3.3.5** was used to quantify the area of blue pixels in each chamber (including tapered regions), which was used to calculate the approximate volume of blue fluid collected in each region, according to the image analysis protocol described in Appendix **Section 7.5**, *Protocol For Calculating Volume of Fluid Collected Collected by the 3D Printed Prototype Platform From Fluid Uptake Verification Experimental Images*. The results of this image analysis protocol yielded the values presented in **Fig. 5.5c**.

5.3.5.2 Pre-Treatment Chemistry Optimization, Limit of Detection and Prototype Demonstration Experiments

For the pre-treatment chemistry optimization and limit of detection experiments, the same imaging setup as described in **Sections 2.3.4** was employed. When the color of the chambers on the 3D printed array devices is desired to be quantified at a given time before or during incubation, the incubation timer is stopped, the 3D printed array devices are removed from the incubator and are placed into the grooves in a custom-designed and laser-cut acrylic mount (as visualized in Appendix **Fig. 7.47b**), which is then placed into the light isolation imaging box. One of the 3D

printed array devices is aligned in the center of the view of the DSLR camera mounted into the ceiling of the box, and an LED light source inside the box is turned on and oriented as to shine directly down onto the 3D printed array device, minimizing shadows on the surface of the chambers created by the steel couples.The lens focus is manually-adjusted with the clearest focus on the upper surface of the chambers, and the image settings are manually-adjusted to create optimum brightness and contrast in the images (*e.g.* camera aperture f-stop of 1/5.6, ISO 800 and exposure of 0.25 seconds). One image is taken of the 3D printed array device, then the acrylic mount is slid such that the next device is in the view of the camera and a picture taken. A final picture is taken for the last 3D printed array device. The acrylic tray is then itself transported into the incubator as to continue the incubation cycle until the next desired round of experimental images is desired, at which point this process is repeated. For details of the image analysis protocol used to quantify the color change of the fluid inside each chamber, see Appendix **Section 7.5**, *Protocol For Calculating the R/G Ratio for Each Chamber on the 10-Chamber 3D Printed Array Devices For All Bacteriological Experiments* and Appendix **Fig. 7.33**. Briefly, for each image using Fiji: (*i*) a circle is drawn to enclose one chamber at a time avoiding air bubbles and shadows (the same area circle is drawn for each chamber) and (*ii*) the red and green pixel average intensity vales inside the circle are measured and recorded using a color histogram analysis. Using Excel, (*iii*) mean red and green values for the same chamber over three experimental images are calculated and a (*iv*) ratio of the red and green values is calculated for a given well and plotted. For the prototype demonstration experiment, a qualitative approach was used to assess the proliferation of *E. coli* in the *on-chip* chambers by which color change was optically observed. This approach demonstrates the benefits of the straightforward colorimetric detection method as a proof-of-concept, which facilitates ease-of-use by untrained personnel.

5.3.6 Preparation of Experimental Reagents

The blue dyed DI water solution used in the fluid verification uptake experiment was formulated by filling a 10mL glass petri dish with DI water and adding 10 drops of blue food-grade color dye, followed by incorporating the solution using a glass stir rod. In the pre-treatment chemistry optimization experiment, various chamber pre-treatment chemistries were developed. Formulation of all solutions began with adding CPRG powder (Chlorophenol red-β-D-galactopyranoside CPRG, item #10884308001, *Sigma-Aldrich*) to a 100% ethanol solution (Ethyl alcohol, Pure, item#E7023, *Sigma-Aldrich*) to concentration of 5 mM. To create the chemistries involving nutrient powder, the appropriate mass of LB broth powder (LB Broth, Miller, item #L3522, *Sigma-Aldrich*), the optimal growth nutrient for *E. coli* bacterial proliferation, was added to the CPRG in ethanol solution to create the necessary concentration of nutrient in the solution. Upon introduction of solid into liquid solution in test tubes, the tubes are aggravated using a vortex mixer (Vortex-Genie 2, *Scientific Industries*) in bursts of 5 seconds for roughly 30 seconds to ensure solution mixing.

5.3.7 Preparation of Cell Suspension

The specific terminology used to describe the growth of bacteria in this chapter are *bacterial growth* and *bacterial proliferation*, which both refer to the increase in the density of bacteria cells in a given volume of liquid bacterial culture media, where density is reported in *cfu/mL*. In all experiments, a strain of gram-negative *Escherichia coli* (*E. coli*) bacteria [344] (*Escherichia coli* (Migula) Castellani and Chalmers ATCC 25922, *American Type Culture Collection*, VA, USA) is used as the model organism for the demonstrative experiments performed in this work, chosen to represent the myriad of strains of *E. coli* which can be sources of water contamination [345] and UTI's [228]. The same procedures used to create a frozen-down stock of the original bacteria, a solid bacteria colony stock on an agar plate stored in a -4 $^\circ$ C refrigerator for use up to one month, and a fresh liquid bacteria culture stock solution from a single colony forming unit each time a new experiment was performed, as described in **Section 3.3.7**, were followed.

The experiment described in **Section 5.4.3** utilized a single bacteria culture stock concentration of around 10^6 cfu/mL, and the experiment described in **Section 5.4.4** featured a serial dilution of bacteria culture stock concentrations from around 10^3 to 10^8 cfu/mL. Each of the required bacteria culture stock concentrations were created following the serial dilution protocol as described in Appendix **Section 7.3**, *Spectrophotometric Bacteria Density Calculation and Growth Media Preparation Protocols*, with the exception of the additional step used in this work to suspend the bacteria cells in a PBS solution, instead of in a liquid LB media. To do so, referring to the specific methods detailed in the aforementioned protocol, a 2 mL centrifuge vial was filled with 1 mL of an initially-cloudy bacterial inoculation (density measured to be $\sim 10^8$ cfu/mL), which was spun down at 2,000 RPM on a bench top centrifuge until a pellet of bacteria was clearly visible on the base of the tube and the solution was translucent. The pellet was then harvested using a syringe and transferred to a 2 mL vial containing 1 mL of PBS solution (Phosphate Buffered Saline, 1X Solution, pH 7.4, *Fisher BioReagents*). The vial was then vibrated on a vortex mixer (Vortex-Genie 2, *Scientific Industries*) in bursts of 5 seconds for roughly 30 seconds to ensure the solution became cloudy, indicating the successful resuspension of bacteria in the PBS solution. The aforementioned protocols were followed to create the necessary densities and serial dilutions of the bacteria in PBS.

5.4 Results and Discussion

5.4.1 Fabrication Results

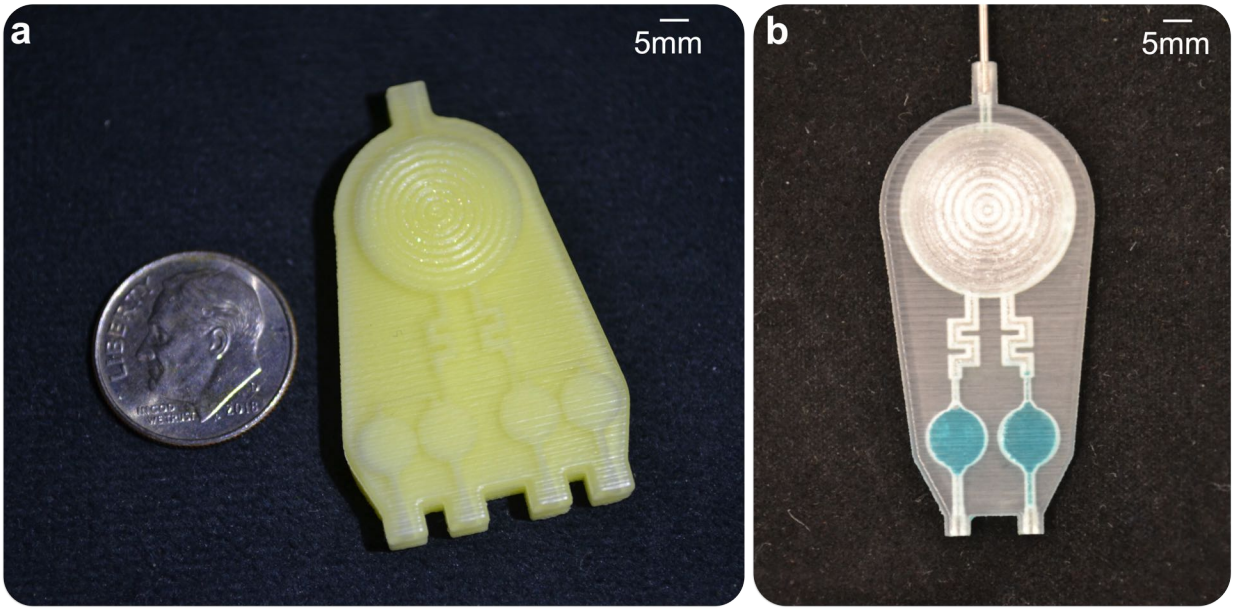

Figure 5.4: Fabrication result for the prototype 3D printed platform. **(a)** Image of a non-experimentally-characterized version (*i.e.* four *on-chip* chambers) of the 3D printed platform showing the yellow 3D printed sacrificial wax-based support material before removal during post-processing with a U.S. dime for scale. **(b)** Image of the final, experimentally-demonstrated, version of the 3D printed platform with blue dyed fluid filling the *on-chip* chambers for visualization and a steel plug blocking the pressure source chamber inlet.

A 3D printed prototype before post-processing (representing a preliminary design containing four chambers which was not pursued further than initial fabrication in this work) is shown in **Fig. 5.4a** with a U.S. dime for scale. The yellow wax-based support material is clearly visible on the bottom of the device as well as inside the chambers, microchannels and pressure source cavity. The actual prototype device demonstrated in all further experiments is shown in **Fig. 5.4b** following successful post-processing with a steel plug blocking pressure source inlet and blue dyed fluid filling the cavities for visualization purposes. The fabricated device is white in appearance, signifying the successful removal of all support material from the interior and exterior of the device.

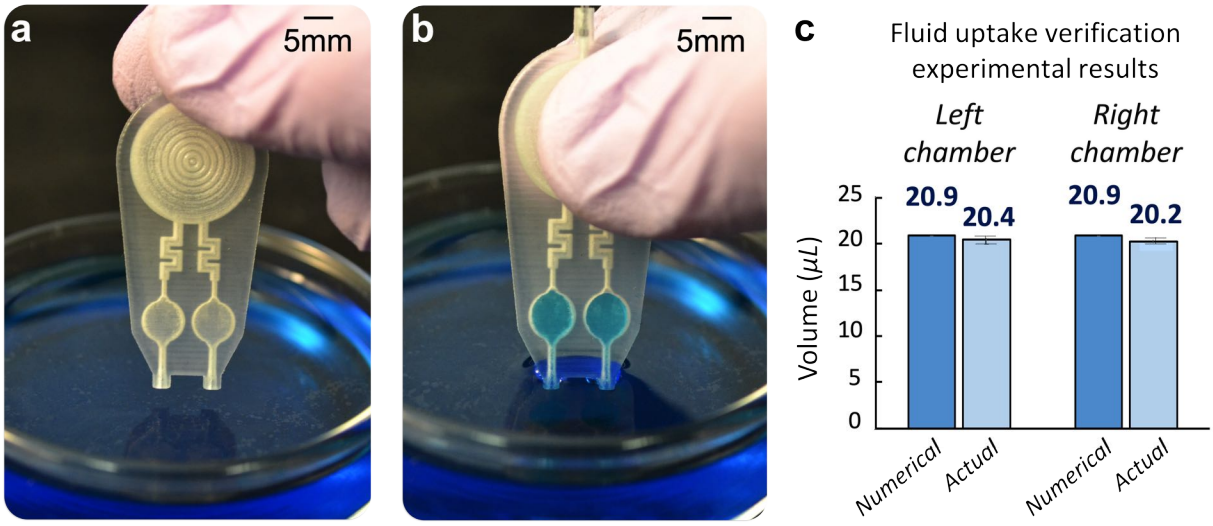

Figure 5.5: Experimental demonstration of the fluid uptake operation and verification of the collected fluid volume. **(a)** 3D printed prototype held between the researcher's thumb and forefinger and suspended over blue dyed DI water (inlet at the top of the pressure source chamber blocked with a steel plug). **(b)** Example experimental image of the fluid collected *on-chip* after inserting the prototype into the liquid, depressing and releasing the finger-actuated membrane. **(c)** Comparison between the analytically-determined chamber volume and the volume of liquid collected in each chamber quantified using image analysis; the average value of the experimental (labeled as *actual*) data from three uptake experiments is plotted with error bars representing the standard deviation between experiments, demonstrating results within a $\sim$3.0% difference.

5.4.2 Fluid Uptake Verification Experiment

The accuracy of the volume of fluid collected into each *on-chip* chamber on the prototype device during a single pressure source actuation procedure was experimentally-validated, as presented in **Fig. 5.5**, employing the experimental setup described in **Section 5.3.4**. The fabricated prototype platform is shown in **Fig. 5.5a** being held between the researcher's thumb and forefinger and suspended over blue dyed DI water, with the inlet at the top of the pressure source chamber blocked with a steel plug. The volume collected in the *on-chip* chambers after the prototype was inserted into the solution, the membrane depressed and then released, is visualized in **Fig. 5.5b**. Qualitatively, fluid volume appears to completely fill each of the chambers, but does not extend into the microchannel networks themselves, as intended. The image analysis procedure as described in **Section 5.3.5.1** was used to determine a quantitative approximation of the volumes of fluid in each chamber (**Fig. 5.5c**), which revealed no more than a $\sim$3% error between the collected fluid volumes and the as-designed spatial volumes of each of the chambers.

5.4.3 Development of Chamber Pre-Treatment Chemistry

To enable *on-chip* biological enrichment, the concentration of the LB nutrient in the pre-treatment chemistry was optimized. A nutrient-rich growth medium is necessary for bacterial growth, therefore if the concentration of nutrient in the chamber pre-treatment chemistry is too low the *E. coli* bacteria will not proliferate, defeating the purpose of the enrichment procedure. The experimental setup described in **Section 5.3.4**, namely three 3D printed 10-chamber array devices, was employed to evaluate multiple different pre-treatment chemistries containing different concentrations of growth nutrient (but the same 5 mM concentration of CPRG reagent), simultaneously. The *top* image in **Fig. 5.6a** shows the actual experimental image of the 3D printed array following pre-treatment, and all chambers filled with a $\sim 10^6$ cfu/mL concentration of *E. coli* in PBS buffer solution, before incubation. Almost immediately upon introduction of the bacterial solution to the chambers, the solid residue was qualitatively-observed to dissolve into the solution lending the liquid a yellow color (this was confirmed by initial experiments where solutions were removed from chambers after sitting inside the chambers for roughly one minute, and indeed the color of

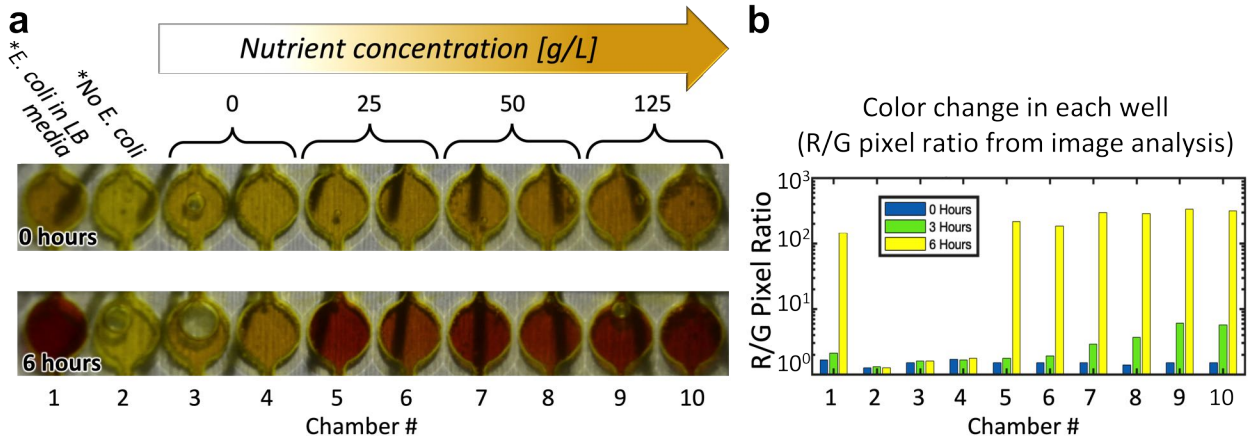

Figure 5.6: Experimental development of the custom pre-treatment chemistry used to pre-load nutrient & reagent solids into *on-chip* chambers. **(a)** Images of an example 3D printed 10-chamber array before (*top*) and after (*bottom*) incubation at 37°C for 6 hours, chambers pre-treated with different chemistries; a solution of 5 mM metabolic-indicator (CPRG) powder in ethanol (Chambers #1-#4), and a solution of 5 mM CPRG & different concentrations of nutrient (LB) powder in ethanol (Chambers #5-10). Following ethanol evaporation, chambers are filled with *E. coli* solutions; $1*10^6$ cfu/mL in 25 g/L LB media (Chamber #1), phosphate buffer solution, PBS, only (Chamber #2), and $1*10^6$ cfu/mL in PBS (Chambers #3-#10). **(b)** Red/green (R/G) pixel ratio in the center of each chamber quantified using image analysis at 0 hours, 3 hours and 6 hours after incubation, mean R/G values are plotted for experiments performed in triplicate by simultaneous incubation of three identical prepared 3D printed arrays. All pre-treatment chemistries induce roughly equivalent color change after 6 hours. 125 g/L LB and 5 mM CPRG in ethanol (in Chambers #9 & #10) exhibits the most color change after only 3 hours, therefore is the optimal pre-treatment chemistry.

the solution as viewed through transparent tubing was yellow). Different experimental parameters and pre-treatment chemistries were evaluated using the different chambers. Upon incubation in a laboratory incubator at 37°C, the three 3D printed arrays were removed from the incubator and imaged after 3 and 6 hours. The experimental image of an example 3D printed array after 6 hours incubation (*bottom* image in **Fig. 5.6a**) reveals the bacterial proliferation in the presence of different pre-treatment chemistries in the form of color change from yellow to red. The color changes of each well were qualitatively-observed, as well as quantitatively-assessed following the image analysis protocol described in **Section 5.3.5.2**, producing R/G data (**Fig. 5.6b**).

Chamber #1 contains the laboratory-standard optimal LB concentration (25 g/L) in liquid solution, which provides the optimal growth conditions for bacterial proliferation. As expected, after 6 hours incubation this chamber exhibits strong color change from light yellow ($\sim 10^0$ R/G ratio) to dark red ($\sim 10^2$ R/G ratio). This represents the baseline color change for the optimal bacterial proliferation in liquid media and serves as a control to study the efficacy of LB diffusion into solution starting from different pre-loaded LB coating concentrations by comparing the color changes of each of the chambers with different starting pre-treated concentrations of CPRG to the color change in this chamber. Chamber #2 contains only PBS solution and no model bacteria, therefore serving as a control to detect any possible solution contamination or any background color change in the CPRG solution over the course of incubation. The color of this chamber does not change over the course of incubation, therefore no contamination is present and the CPRG delivers a stable background colorimetric response over the course of the entire experiment. Chambers #3-#4 are duplicates, having been pre-treated with a chemistry containing no growth nutrients, only CPRG, and therefore serve as controls to study the proliferation of bacteria in the absence of any growth nutrients (*i.e.* any color change in these wells would indicate the colorimetric sensitivity of the CPRG to the metabolism of a constant $\sim 10^6$ cfu/mL concentration during incubation, and therefore the importance of *on-chip* nutrients for bacterial proliferation). These chambers both exhibit practically-no color change over 6 hours of incubation, therefore no bacterial proliferation is present. The concentration of LB powder in the pre-treatment chemistries increases from 25 g/L (Chambers #5 & #6) to 50 g/L (Chambers #7 & #8) to 125 g/L (Chambers #9 & #10). At 0 hours, Chambers #5-#10 all appear a similar degree of orange in appearance as Chamber #1 (containing an optimal concentration of LB media), indicating the successful diffusion of solid LB into media. This is further supported by the fact that after 6 hours incubation all LB-containing pre-treatment chemistries induce roughly equivalent color change from $\sim 10^0$ to $\sim 10^2$ R/G ratio. Furthermore, definitive color change is observed in Chambers #9 & #10 at only 3 hours (the largest increase in R/G ratio of all chambers, from $\sim$100 - $\sim$600). As a result, Chambers #9 & #10 represent what is defined as the optimal developed pre-treatment chemistry for *on-chip* enrichment: a solution of 125 g/L LB and 5 mM CPRG.

5.4.4 Proof-of-Concept Determination of Limit of Detection

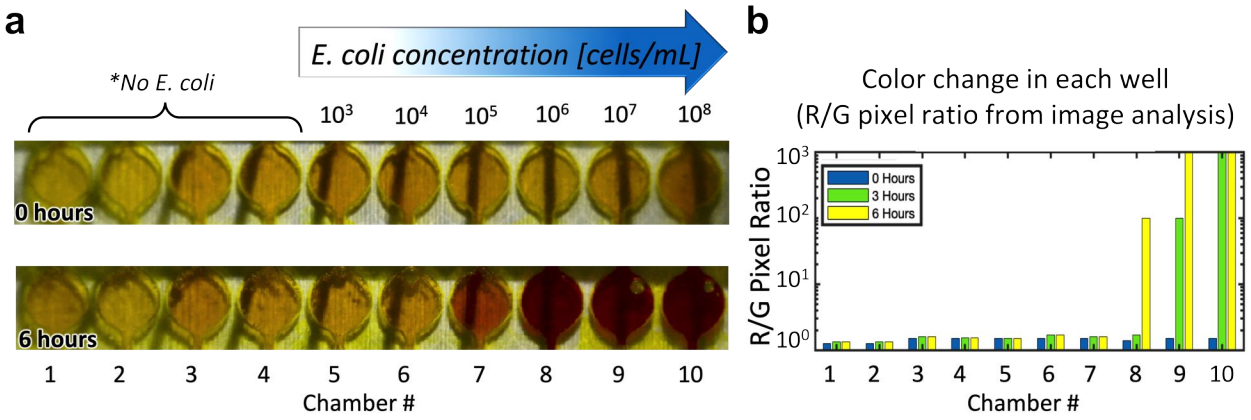

Figure 5.7: Experimental determination of the limit of detection (LoD) for the employed proof-of-concept colorimetric detection scheme towards the model *E. coli*. **(a)** Images of the 3D printed 10-chamber array before (*top*) and after (*bottom*) incubation at 37°C for 6 hours. Pre-treatment solution of 5 mM CPRG powder in ethanol (Chambers #1-#2), and solution of 5 mM CPRG & 125 g/L LB powder in ethanol (Chambers #3-#10). Following ethanol evaporation, chambers are filled with PBS only (Chambers #1-#4), and a serial dilution of *E. coli* in ethanol from $1*10^3$ cfu/mL (Chamber #5) to $1*10^8$ (Chamber #10). **(b)** R/G pixel ratio in the center of each chamber quantified using image analysis at 0, 3 and 6 hours after incubation, mean R/G values are plotted for experiments performed in triplicate by simultaneous incubation of three identical prepared 3D printed arrays. Lowest quantitative LoD of $1*10^6$ cfu/mL ($\sim 10^2$ R/G ratio in Chamber #8), lowest qualitative LoD of $1*10^5$ cfu/mL (orange in Chamber #7) both in 6 hours.

One of the most important characteristics of any biological detection scheme to understand is the limit of detection (LoD), which is defined by the lowest detectable concentration of an organism (*e.g.* bacterial density) in a certain period of time. To enable experimental determination of the LoD of the employed proof-of-concept pathogen detection scheme demonstrated in this work, the same experimental setup, data acquisition and quantitative processing approaches as those used in the previously-discussed experiment were employed, incorporating three newly-fabricated and post-processed 3D printed 10-chamber array devices. The *top* image in **Fig. 5.7a** shows the actual experimental image of an example 3D printed array following pre-treatment before incubation used to evaluate the proportional bacterial proliferation rates at fixed points in time using serial dilution of *E. coli* in PBS buffer solution. Chambers #1-#2 were pre-treated with a solution of only 5 mM CPRG powder in ethanol, serving as a control to observe any color change in the CPRG over time, whilst Chambers #3-#10 were all pre-treated with the optimal pre-treatment chemistry, as determined in **Section 5.4.3** (a solution of 125 g/L LB and 5 mM CPRG). Chambers #1-#4 were all filled with pure PBS buffer solution such that Chambers #3-#4 would indicate any contamination during the experiment. Chambers #5-#10 were filled with a serial dilution of *E. coli* in ethanol from $\sim 10^3$ cfu/mL (Chamber #5) to $\sim 10^8$ cfu/mL (Chamber #10).

The quantitative color change data (**Fig. 5.7b**) reveal that Chambers #9 & #10, with $\sim 10^7$ cfu/mL and $\sim 10^8$ cfu/mL of *E. coli*, respectively, exhibit definitive bacterial proliferation at 3 and 6 hours. Furthermore, Chamber #8 with $\sim 10^6$ cfu/mL of *E. coli* exhibits definitive bacterial proliferation at at 6 hours. Moreover, from the quantitative data, Chamber #7 with $\sim 10^5$ cfu/mL of *E. coli* does not indicate any significant increase in R/G ratio at 6 hours, therefore the metric of R/G ratio analysis indicates a *quantitative* LoD of $\sim 10^6$ cfu/mL in 6 hours. However upon qualitative analysis, compared to the lack of color change in the control chambers with no *E. coli* present, the image of Chamber #7 does present clear color change from light yellow to dark orange, despite the fact that the R/G ratio of this shade of orange is not significantly higher than for light yellow. Therefore, Chamber # 7 demonstrates what is defined as the *qualitative* LoD in this work of $\sim 10^5$ cfu/mL of *E. coli* in 6 hours. This quantitative LoD value is larger than that which has been demonstrated for *E. coli* detection in drinking water samples utilizing alternative microfluidic bacterial detection schemes, such as optical turbidity measurements using microchannel-interfacing spectrophotometry [310], complex microfluidic PCR platforms [346], or fluorescence *in-situ* hybridization microscopic detection [324], techniques; yet these approaches demonstrate limited portability and practical applicability for point-of-need water quality assessment applications. One of the inherent advantages of the proposed platform, therefore is the lack of external equipment necessary to perform quantitative detection, therefore the developed prototype would be more suitable for portable, point-of-need applications such as detection of bacteria in drinking water samples from a perspective of practicality and ease-of-use.

At the same time, the quantitative LoD demonstrated in this experiment is in agreement with the state-of-the-art LoD as evaluated for the CPRG compound for the detection of *E. coli* from previous studies [343, 347], and similar to what was observed in these previous studies, no noticeable color change in the chambers containing $\sim 10^4$ cfu/mL of *E. coli* and lower concentrations was observed up to 24 hours of incubation. The LoD evaluated for this proof-of-concept *E. coli* detection method is therefore a limitation of the catalysis efficiency of the β-gal enzyme towards CPRG. Various methods have been attempted by previous groups to enhance the sensitivity of CPRG to *E. coli* detection, such as engineering bacteriophages to interact with the bacteria in a liquid sample, causing them to over-express the β-gal enzyme in solution, thereby generating an enzyme-amplified colorimetric signal, which has reduced the LoD of CPRG for *E. coli* down to $\sim 10^2$ cfu/mL in 7 hours [348]. Additional recently-developed techniques utilizing antibody-tagged gold nanoparticles, which when bound to bacteria in solution *via* enzyme-antigen binding change the optical color and fluorescence signal of the solution and produce highly-sensitive qualitative colorimetric as well as quantitative immunofluorescence signals, have demonstrated the detection of smaller concentrations of *E. coli* in solution, as low as *e.g.* $\sim 10^2$ cfu/mL [349, 350]. Such an additional analytical methods could be employed towards enhancing the LoD exhibited by the prototype 3D printed platform developed in this work as pre-treatment chemistry. Developing a method to maintain bacteriophage viability and stability during solvent evaporation, device storage and transport would be necessary. Moreover, exploring alternative colorimetric reagents which exhibit higher sensitivity to *E. coli*-expressed enzymes, as well as evaluating different bacterial enzyme-reagents pairs (Appendix **Fig. 7.46**) have the potential to elucidate even lower LoD's [333, 334]. Finally,

redesigning and optimizing the geometry of the *on-chip* chambers themselves could prove a fairly straight-forward method to improve LoD; assuming that higher concentrations of diffused nutrients and reagents in the liquid solution exist towards the chamber surfaces than in the center of the volume during incubation, reducing the volume of the chamber (smaller height and diameter) would increase the surface area-to-volume ratio of the chambers, thereby increasing overall bacterial contact with the diffused nutrients and reagents and potentially increasing the sensitivity of the detection method [351].

Furthermore, these previous CPRG-*E. coli* detection experiments were performed in enclosed vials of solution and the experiments performed in this work were performed in air-tight microfluidic channels plugged by steel couples. *E. coli* cells are capable of both aerobic and anaerobic respiration, and therefore proliferate in such air-tight volumes [352]; however culture of μL-volumes of *E. coli* in channels fabricated from oxygen- permeable materials (such as PDMS), thereby creating an environment for aerobic respiration, has been shown to increase the proliferation rate and overall achievable cell density of the bacteria [351]. Therefore, further improvement of the proposed 3D printed platform in this work should seek to develop approaches to integrate oxygen-permeable materials (*i.e.* constructing *on-chip* chambers with exposed upper and lower surfaces such that thin PDMS membranes can be incorporated into the device post-3D printing and secured in a water-tight fashion as to enclose the chambers with an oxygen-permeable layer [353]), facilitating aerobic biological enrichment *on-chip*, which has the potential to increase the LoD and/or decrease the overall times necessary for pathogen detection. Moreover, improved pathogen detection can be additionally facilitated by including an extra bacterial pre-concentration step before collecting the liquid samples on the device. For example, by incorporating *on-chip* micro-pore filtration (*i.e.* by designing a 3D printed mating structure used to interface with such a piece of commercially-available hardware which is installed onto the device), the starting concentration of bacteria collected into the chambers could be increased, thereby reducing analysis time.

Additionally, the experiments in this work demonstrating the proposed 3D printed pathogen detection platform all feature the use of a laboratory-based bacterial incubator to achieve incubation of the prototype devices. In conceptual device operation as mentioned in **Section 5.2**, multiple portable incubation schemes which are often in low resource areas, for example in rural clinics at the site of patient care detection, can be employed to perform *on-site* pathogen detection. Furthermore, mechanical schemes of integrating battery-powered micro-Jule heater technology *on-chip* [49] (*i.e.* after the main body of the 3D printed platform is fabricated) would be a potential method to directly apply a heat flux to the *on-chip* pathogen enrichment and detection chambers to generate a *localized* elevated temperature of 37°C for truly-*on-chip* bacterial incubation, completely eliminating the need for external incubation hardware and further expanding the point-of-need and point-of-care applicability of the proposed platform.

5.4.5 Demonstration of Actual Prototype Device

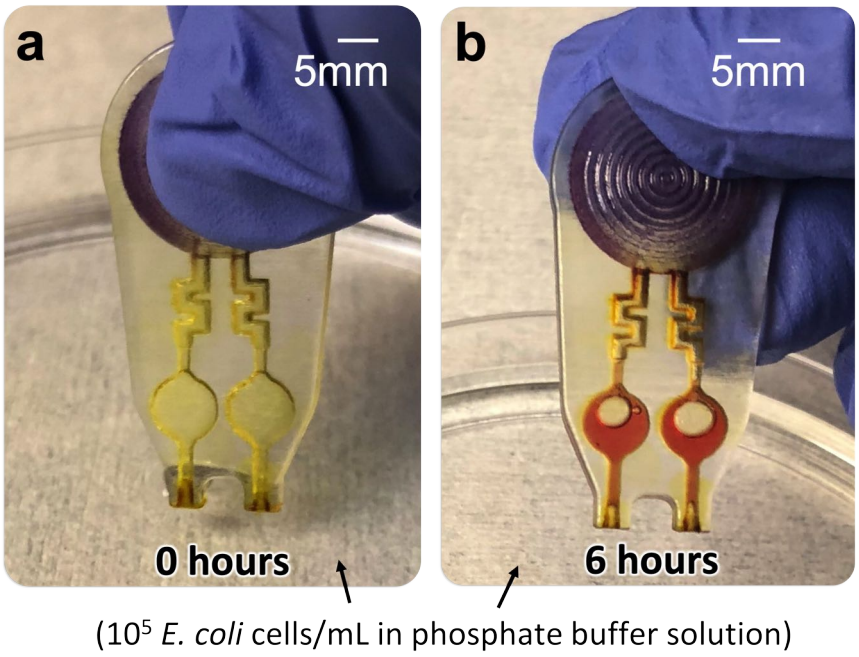

Figure 5.8: Demonstration of *on-chip* human-powered liquid sample collection, bacterial enrichment and pathogen detection using the actual hand-held 3D printed platform prototype. All device chambers pre-loaded with the optimal chamber pre-treatment chemistry (125 g/L LB & 5 mM CPRG in ethanol solution as determined in **Fig. 5.6b**). **(a)** Prototype held between the researcher's thumb and forefinger inserted into a solution of 10^5 cfu/mL *E. coli* in PBS (representing model *E. coli*-contaminated drinking water). **(b)** Same device held in the same position after being used to collect liquid samples and following incubation at 37°C for 6 hours, exhibiting definitive pathogen detection results in agreement with the qualitative LoD results previously-demonstrated in **Fig. 5.7b**.

To demonstrate the complete experimental procedure using the actual fabricated entirely-3D printed pathogen detection platform towards *E. coli.* detection, the experimental setup described in **Section 5.3.4** was employed, whereby a solution of $\sim 10^5$ cfu/mL of *E. coli* in PBS buffer was prepared, and the fabricated device (**Fig. 5.8a**) was used to manually-collect liquid samples, after which the device was incubated at 37°C in a laboratory incubator for 6 hours. At that time, the device was removed from the incubator and color change in the chambers observed. Indeed, the solution in the chambers changed color from light yellow to dark orange (**Fig. 5.8b**) after 6 hours of incubation, which confirms the qualitative LoD result as determined in **Section 5.4.4**. As discussed in **Section 5.1**, the clinical state-of-the-art LoD of *E. coli* in urine samples towards UTI clinical diagnostics is $\sim 10^5$ cfu/mL in 24 hours, which is used to define the clinical standard to declare a patient *positive* for a UTI [217]. In this work, the qualitative LoD is determined to be $\sim 10^5$ cfu/mL in only 6 hours, therefore the proposed 3D printed pathogen detection platform employing the proof-of-concept CPRG-*E. coli* detection scheme already demonstrates the potential to

yield enhanced diagnostic capabilities towards clinical UTI detection. Experimental investigation of device pre-treatment would be necessary to demonstrate the applicability of the platform, at this stage in its development, towards such diagnostic application, upon which further enhancement of the device pre-treatment procedure or liquid sample handing procedure might be warranted in order to enable pathogen detection inside minimally- or non-processed urine samples. Moreover, the portability, ease-of-use and qualitative detection approach demonstrate the applicability of the proposed platform to be used as an enhanced UTI diagnostic tool for use in point-of-care settings, such as in low-resource rural clinics. Overall, this experiment demonstrates that an entirely-3D platform, pre-treated with the optimal chemistry of nutrient and reagent powders in *on-chip* chambers, can enable the human-powered liquid sample collection, and *on-chip* biological enrichment and simple qualitative colorimetric detection necessary to perform *on-site* detection of pathogenic bacteria.

Chapter 6

Conclusions and Future Directions

Research into the use of alternative manufacturing approaches towards the fabrication of microfluidic devices is of particular interest in the field of microfluidic device engineering. Additive manufacturing-based methods demonstrate the inherent capability to fabricate *three dimensionally*-complex sub-millimeter microstructures. High-resolution 3D printing, such as Multijet modeling, therefore enables the engineering of novel truly-3D microfluidic systems incorporating microchannel and microstructure designs, capabilities and functionalities which are otherwise impossible to achieve using conventional MEMS-based microfluidic manufacturing approaches. Additive manufacturing also enables the scalability of dynamic and passive 3D fluidic operators, 3D microchannel networks and integrated 3D fluidic systems into compact entirely-3D printed microfluidic platforms while similar 2D structures would require a significantly greater amount of design and manufacturing skill, time and labor. Furthermore, the single-step, monolithic fabrication process affords microfluidic device engineers the ability to rapidly-prototype their designs, enabling iteration of the fabrication, evaluation and improvement of novel 3D microfluidic designs at an un-precedented pace compared to using conventional MEMS-based microfluidic fabrication methods. Moreover, the ease-of-use and flexibility in the CAD design process used to model 3D printable microfluidic designs enables an un-paralleled degree of user-customizability and tailorability of specific designs and functionalities suited to meet the needs of a given application. This flexibility, in addition to the increasingly-wide spread accessibility to high-resolution commercial 3D printing technologies promises to usher in a paradigm shift in the design and manufacturing of microfluidic device. Professionals ranging from microfluidic device engineers, to biomedical researchers and healthcare providers with limited engineering skills, alike, working in facilities all over the globe with access to an *on-site* 3D printer (*e.g.* in a research laboratory, hospital or clinical setting) will be able to *download* and *tailor* (*i.e.* from a *cloud*-like repository of digital, easily-editable 3D models) a desired microfluidic biomedical or diagnostic tool to meet the needs of their specific experiment, and will be able to fabricate their microfluidic hardware *in-house*, *on-demand*.

In this dissertation, several new classes of *three dimensionally*-complex, integrated microfluidic systems were developed and fabricated using Multijet 3D printing, their unique fluidic handling capabilities were investigated through various characterization methods, and their functional advantages towards addressing various challenges currently faced by conventional microfluidic platforms in relevant clinical biomedical and diagnostic applications were experimentally-demonstrated.

6.1 Low Reynolds Number 3D Micromixers

Two different 3D μ-mixer conceptual designs incorporating truly-3D intra-channel microstructures *via* additive manufacturing approaches were developed and employed in order to tackle the fundamental challenge of homogenous mixing of co-laminar fluids under low Reynolds Number (*Re*) conditions. The *3D rifled* μ-mixer design employs a 3D split-and-recombination (SaR) twist and 3D helical rifling; the *3D bulbous* μ-mixer design employs a 3D undulating side-wall and 3D helical rifling. These 3D microstructures induce chaotic advection in *three-dimensions*, thereby enhancing chaotic co-laminar fluidic mixing efficiency inside 3D printed microchannels.

Simulations of the 3D μ-mixer models demonstrated the ability of the 3D intra-channel microstructures to induce transverse fluid velocities and helical rotation in *three-dimensions* inside each design, resulting in increased twisting and folding of the co-laminar fluid boundary layer and enhanced inter-species fluidic mixing *via* chaotic advection. As a result, 1-5 unit-length versions of both 3D μ-mixer designs demonstrated enhanced mixing efficiency per-unit length over smooth-walled μ-channel designs at low *Re* conditions ($0.01 \leq Re \leq \sim 50$) typically experienced in conventional microfluidic device applications.Furthermore, a Multijet additive manufacturing approach was then employed to fabricate entirely-3D printed modular two-fluid microfluidic mixing devices incorporating various length 3D μ-mixer and control μ-channel designs. Experimental fluorescence imaging of the devices operating in a low to moderately-low *Re* regime ($0.1 \leq Re \leq \sim 10$) was performed, and an image analysis protocol was developed and used to quantify the mixing quality at the outlet of each device. The experimental results reveal that the most efficient overall mixing performances observed (*i.e.* reaching or surpassing 90% mixing in the shortest unit-length device tested) was exhibited by both 1 unit-length 3D rifled and 3D bulbous μ-mixer prototype devices at $Re \approx 10$. Furthermore, the most efficient mixing demonstrated in the low *Re* regime was accomplished by the 3 unit-length 3D rifled and 3D bulbous μ-mixer prototypes, 90% mixing at $Re \approx 0.1$. Moreover, none of the control μ-channel prototypes of any length achieved 90% mixing for any of the *Re*'s tested. Compared to the simulated mixing performances, all control μ-channel prototypes exhibited lower quality mixing at all *Re*, and both μ-mixer prototypes demonstrated greater mixing performances for the 1 unit-length device at $Re \approx 10$ and for the 3 unit and 5 unit-length devices at all *Re*'s tested. Finally, compared to various examples of previously-demonstrated conventional 2D and 3D μ-mixer designs, the experimental results demonstrated in this work suggest that by employing entirely-3D printed intra-channel 3D μ-mixing structures, such as the fabricated 3D SaR, 3D helical rifling and 3D undulation microstructures, enhanced mixing at lower *Re*'s in more compact microchannels is possible.

Moving forward, the applicability of 3D printed μ-mixer structures can be theoretically studied more in-depth towards specific applications. For example, in the study of the efficacy of such μ-mixers to mix whole blood and reagent solutions, the properties of the input fluidic species will need to be adapted to model fluids containing particles with different diffusivity constants (*e.g.* modeling blood cells or other macro-molecules in whole blood) in various concentrations. This will inherently change the species convection-diffusion dynamics in the simulation, ultimately resulting in μ-mixers demonstrating different mixing performances based on the application. Therefore future application-specific theoretical simulations can be performed. Moreover, higher-complexity 3D printed microfluidic systems will no doubt be designed which will incorporate even more complex intra-channel 3D μ-mixing structures. Towards this end, alternative 3D microstructure designs can be explored to enhance even further the degree of chaotic mixing induced in future 3D printed μ-mixer designs. For example, non-repeating physical elements increase the degree of randomness in fluid motion inside a microchannel, which induces a greater degree of chaotic fluid mixing [174]. To increase the randomness of the physical 3D elements demonstrated in this work, an improved 3D rifled μ-mixer-based design could employ: (*i*) additional SaR elements in-series used to bisect and recombine the boundary layer at different angles, (*ii*) additional sections of 3D rifling in-series with randomly-alternating pitch length, edge size, cross-section shape (*i.e.* square, oval, non-equillateral triangle) and direction of twist, and (*iii*) a non-linear microchannel axial path (*i.e.* spiral orientation [354]). Additionally, an improved 3D bulbous μ-mixer-based design could employ: (*i*) hollow spherical regions in-series with randomly changing inner-diameter, (*ii*) non-symmetric hollow shaped-regions, (*iii*) 3D rifling with randomly-alternating pitch length, edge size and cross-section shape, and (*iv*) a non-linear microchannel axial path. Furthermore, the flexibility in the digital 3D design process of 3D printable-microfluidic systems permits the straight-forward integration of 3D μ-mixers designs at any location along the length of an arbitrary 3D microchannel. This freedom permits microfluidic device engineers an un-paralleled degree of customization of the localized mixing performance, an ability which will help usher in the development of the next generation of even more geometrically-complex, high mixing-efficiency and 3D printed microfluidic platforms tailored to various biomedical applications such as point-of-care blood serum analysis.

6.2 Microfluidic Concentration Gradient Generators for Antimicrobial Drug Screening

The throughput of microfluidic-based antibiotic susceptibility testing (AST) to combat antibiotic-resistant bacterial infections in clinical and research settings is limited by the inability of conventional concentration gradient generation (CGG) microchannel networks to generate gradients of more than two antibiotic inputs at a time due to the inherent planar nature of fluidic routing in conventional microchannels, which renders symmetric gradients of three or more antibiotics im-

possible to achieve. Multiple-antibiotic combination drug screening CDS procedures must therefore be performed manually with significantly lower throughput, which contributes to the lack of comprehensive CDS studies of combinations of three or more clinically-relevant antibiotics to treat emerging antibiotic-resistant infections. In this work, two different conceptual 3D microfluidic concentration gradient generator (3D μ-CGG) prototype devices were proposed and designed, each capable of performing 3D fluidic routing only possible to achieve using an additive manufacturing approach, to generate symmetric concentration gradients between three input fluids.

Analytical modeling of each 3D μ-CGG design demonstrated that functionally-useful fluidic output *μ-drug cocktails* are produced, representing a 3D generated gradient of three input fluids, which can be used for *off-chip* experimental studies. Theoretical simulation results from computational fluid dynamics (CFD) models revealed output concentrations well within 10% of the analytically-predicted values. Prototypes of each 3D μ-CGG design were then fabricated using Multijet 3D printing. Experimental validation of the 3D gradient generation performance of each prototype were performed using fluorescence imaging of generated gradients of fluorophore dye solutions. The experimental gradients produced by the *layer*-based 3D microchannel network were represented by 15 discrete μ-drug cocktails containing approximate proportional concentrations of each input fluidic species, *i.e.* $\sim$100%, 75%, 50%, 10% & 0%, three of which contained different approximate proportions of all three input fluids, *i.e.* $\sim$32% of one species and $\sim$11% of the other two. The experimental gradients produced by improved *tetrahedral*-based 3D microchannel network performs geometrically-symmetric fluid routing in *three dimensions*, were represented by 13 discrete μ-drug cocktails each containing potentially more useful approximate proportional concentrations of each input fluidic species within 10% of the analytically and theoretically-predicted values, *i.e.* $\sim$100%, 70%, 50%, 30% & 0%, one of which containing equivalent-proportions of all three input fluidic species, *i.e.* $\sim$35% of two of the fluidic species and $\sim$32% of the other. Furthermore, CFD simulation results demonstrated that the inclusion of integrated 3D rifled μ-mixer-based intra-channel structures in the vertical microchannels inside the *tetrahedral*-based 3D μ-CGG design improve the accuracy of the generated gradient up to $\sim$88%. Moreover, the biomedical application of the fabricated 3D μ-CGG prototypes towards higher-throughput AST evaluation, in particular the unique capability of for three-antibiotic gradient generation, was demonstrated through various bacteriological studies of clinically-relevant antibiotic compounds against an ampicillin-resistant strain of *E. coli* bacteria as a model. The AST approach employed in this work achieved definitive results in only 5 hours, demonstrating higher analytical throughput than conventional AST methods and meeting the standard for rapid optical detection-based microfluidic AST evaluation. The *single-antibiotic* minimum inhibitory concentration (MIC) values for five different antibiotic compounds were determined, as well as *pair-wise* and *three-antibiotic* combination drug screening studies performed to evaluate the *synergistic*, *additive* and *antagonistic* properties of the various antibiotics in combination, validating known combinatorial effects for the antibiotics as determined in previous AST studies, and providing demonstrative clinically-relevant antibiotic dosages and combinatorial treatment recommendations to treat antibiotic-resistant bacterial infections caused by the model bacteria.

Moving forward, 3D printing approaches, such as the Multijet technique demonstrated in this work, will enable biomedical researchers to simply modify the digital designs of different classes of 3D μ-CGG devices to tailor the 3D gradient generation performance and number of discrete fluidic inputs and outputs of their CGG biomedical tools. These devices can then be rapidly-prototyped and fabricated in-house using a commercially-available 3D printer, in a clinical point-of-care setting, customizing μ-drug cocktail concentrations to meet the needs of specific experimental applications, *on-demand*, such as for replicating specific chemokine gradient environments and producing specific combinations of sensitive chemotherapeutic drugs to study precisely-dosed multi-drug cancer cell growth inhibition, *on-chip*. Future 3D μ-CGG designs should utilize the 3D geometric symmetry as demonstrated by the *tetrahedral*-based 3D μ-CGG design, avoiding the vertical microchannels which linearly-interconnect the fluidic inlets to outlet microchannels, in order to produce more uniform fluidic distribution throughout the complex 3D fluidic network and to produce more useful proportions of input fluidic species. Furthermore, the flexibility in the 3D solids modeling procedure renders the design of larger 3D μ-CGG fluidic networks (*i.e* additional structural layers, numbers of inlet and outlet microchannels and different 3D arrangements such as cubic shapes with four fluidic inlets, pentagonal shapes with five fluidic inlets or hexagonal shapes with six fluidic inlets) rather trivial. The primary concern when designing larger 3D μ-CGG devices is the fluidic resistance encountered by fabricated microchannel network prototypes. Additional measures to facilitate complete removal of support materials from such networks during post-processing might be necessary to completely post-process larger fluidic networks, such as the addition of wax-removal inlets as demonstrated with the *layer*-based 3D μ-CGG prototype, increasing the hydraulic diameters of the microchannels, or the implementation of automated pressure-driven mineral oil actuation employing a system such as the Fluigent micro-controller used in this work. Furthermore, optimization of the overall device operational setup should be focused on reducing the overall length of tubing required to interface with the device, making the apparatus more compact, and reducing the overall effective fluidic resistance of the network. Such an approach would render the interfacing hardware easier for the operator to operate and allow the hardware to be more portable and travel to different point-of-need settings. Additionally, shortening the overall lengths of the interfacing tubing would allow lower operational flow rates to be used in experiments, allowing dynamic tailoring of the generated concentration gradient to produce flow rate-dependent concentrations at the outlets. Finally, the throughput of AST using additively-manufactured 3D μ-CGG devices will be even further increased by incorporating the 3D gradient generating microfluidic networks into a larger, monolithically-fabricated 3D printed multi-drug microfluidic AST micro-total analytical system (μ-TAS). These integrated platforms would incorporate 3D μ-CGG microchannel networks into the device itself and perform automated routing of the fluidic outputs to designated regions on the device to perform *on-chip* bacterial incubation and quantification of bacterial proliferation inhibition. The miniaturization of the bacterial enrichment and quantitative detection steps performed *off-chip* in this work into future 3D printed 3D μ-CGG-integrated μ-TAS platforms promises to significantly increase the analytical throughput of biomedical and diagnostic AST applications.

6.3 Integrated Finger-Powered Microfluidic Actuators

Various entirely-3D printed, hand-held modular microfluidic finger-powered actuators (FPA's) have been developed, serving as human-powered sources of forward-driving pressure heads. Individual 3D fluidic operators, including 3D fluidic diodes, fluid reservoirs with enclosed dynamic 3D corrugated membranes, and isolated pressure source channels were designed as integrated 3D microfluidic networks, and fabricated as entirely monolithically-3D printed prototype devices. Parameters of the fluidic output of all fabricated prototypes, such as instantaneous flow rate, volume pumped over time and average effective output flow rate, due to cyclic actuation frequencies from 1-4 Hz were experimentally-characterized in order to compare the performance of each design.

An initial FPA design (FPA_{V1}) was fabricated incorporating one-way valve operators of a 3D fluidic diode design ($Diode_{V1}$) for which a certain degree of back-flow through the diode is necessary to actively shut-off the diode in the reverse direction to enable reverse flow rectification. As a result, the fabricated FPA_{V1} prototype exhibited slightly greater volumetric flow rate in the forward direction than in the reverse direction for each actuation cycle, achieving net-forward output fluid flow rates ranging from $\sim$108 μL/min at 1 Hz to $\sim$156 μL/min at 4 Hz actuation frequencies, albeit with a significant degree of back-flow throughout the device during operation. In order to reduce the back-flow throughout the system, thereby making such FPA devices more suitable for microfluidic applications where minimal back-flow is required as well as enabling generation higher forward-driven fluid flow rates, the 3D fluidic diode was redesigned. The new 3D fluidic diode design ($Diode_{V2}$) employs a passive fluid rectification mechanism, consisting of a modular bracket component installed onto the exterior of the diode in order to establish contact between the dynamic membrane and the upper surface on the interior of the diode in the default state, which experimentally-demonstrated a $\sim$73.4% enhancement in reverse fluid flow rectification (*diodicity* of $\sim$1117.4) as compared to the $Diode_{V1}$ design (*diodicity* of $\sim$80.6). $Diode_{V2}$ designs were then incorporated into FPA models and fabricated, resulting in two improved FPA prototypes, one design incorporating the isolated pressure source channel (FPA_{V2}) and one design employing finger-actuated membrane and pressure source directly in-line between the two 3D fluidic diodes ($FPA_{V2,in-line}$). Due to the reduction in back-flow of the $Diode_{V2}$ operators, the FPA_{V2} prototype demonstrated larger effective fluid flow rates than the otherwise-similar FPA_{V1} prototype of $\sim$637 μL/min at 1 Hz up to $\sim$1450 μL/min at 4 Hz. Furthermore, due to the increased pressure head generated by the in-line pressure source per-actuation cycle, the $FPA_{V2,in-line}$ prototype demonstrated the largest effective fluid flow rates, from $\sim$2000 μL/min at 1 Hz up to $\sim$2775 μL/min at 4 Hz. Finally, an integrated two-fluid FPA design was developed ($FPA_{V1,2fluid}$) which accomplished simultaneous actuation of two independent fluids through a single 3D μmixer-integrated output channel at the same flow rate and demonstrated the ability to perform complete, entirely human-powered, two-fluid pulsatile mixing at 1 Hz actuation frequency in 10 seconds.

Moving forward, employing a single *on-chip* finger-powered pressure source channel isolated from the fluidic network by dynamic membranes inside fluid reservoirs enables the actuation of multiple independent fluid sources through a microfluidic device using a single operational pressure source. Simultaneously actuating multiple fluids through more complicated microchannel networks at the same fluid flow rate has applications towards multi-fluid microfluidic pulsatile mixing; however if different forward-driven flow rates are desired on such a platform, the 3D geometries of the individual 3D fluidic operators can be tailored in order to produce variable flow rates in each of the independent fluid channels whilst still utilizing the same shared finger-powered pressure source. Moreover, the FPA designs featured in this work, while fabricated and experimentally-demonstrated as modular, stand-alone actuators, also have the potential to be integrated into the 3D digital solids model design of general 3D printable microfluidic devices at any arbitrary location to provide entirely-electrical power-free fluidic actuation. Such integrated FPA's have the ability to power larger, entirely-3D printable μ-TAS platforms without the need for externally-powered fluidic actuation sources, making such 3D printed devices better capable of meeting the compact, portable and electrical power-free demands of various point-of-need diagnostic applications.

6.4 Entirely-3D Printed, On-Site Biological Pathogen Detection Platform

Finally, an entirely-3D printed, hand-held microfluidic platform targeting completely-*on-site* fluid sample collection, biological enrichment and straight-forward qualitative detection was developed, fabricated, experimentally-tested and demonstrated towards the detection of *E. coli* bacteria in model drinking water towards water quality assessment applications.

A manually-actuated liquid sample collection mechanism was designed, made possible by the design of a finger-actuated pressure source, with the capability of human-powered uptake of liquid samples on to *on-chip* pathogen enrichment and detection chambers. A comprehensive multiplexed design methodology was developed for which analytical equations were derived relating all of the independent design parameters defining the 3D solids model, enabling uptake of precise volumes of fluid sufficient to fill any desired number of discrete *on-chip* chambers, thereby enabling the multiplexed detection of any desired number of target pathogens. A fabricated prototype consisting of two chambers was designed and fabricated, and the experimental fluid uptake performance validated to within $\sim$3% of the analytically predicted value. Furthermore, to facilitate completely *on-chip* biological enrichment and detection, a custom device pre-treatment procedure was developed which accomplished drop-casting of enzymatically-targeted colorimetric reagents and bacterial growth nutrients and immobilization of a solid surface coating inside each of the *on-chip* chambers. The chemistry of the pre-treatment solution was experimentally-optimized to a composition of 125 g/L concentration of nutrient, LB powder, and 5 mM concentration of the *E.*

coli-targeted colorimetric reagent, CPRG. Moreover, the limit of detection of the proof-of-concept colorimetric detection scheme employing the *E. coli*-CPRG bacteria-reagent pair was qualitatively-determined to be a concentration of $\sim 10^5$ cfu/mL of *E. coli* in buffer solution in 6 hours. Finally, the human-powered bacteria sample uptake, *on-chip* enrichment and detection of *E. coli* in buffer solution was then experimentally-demonstrated using the actual 3D printed prototype platform. The capability to perform truly-*on-site* pathogen detection is possible using the demonstrated platform by employing portable incubator hardware to accomplish enrichment at the site of liquid sample collection.

Moving forward, the application of the 3D pathogen detection platform towards water quality assessment is challenged by other previously-demonstrated microfluidic devices towards pathogen detection in drinking water which have demonstrated smaller limits of detection for *E. coli*, albeit with significantly-less point-of-care applicability. Towards the detection of *E. coli* in UTI diagnostic applications, however, the 3D platform demonstrates great promise, as the current platform achieves the state-of-the-art limit of detection for UTI-causing bacteria in clinical point-of-care settings. Regardless of the end application, exploring alternative pathogen-colorimetric reagent pairs for which device pre-treatment can be used to pre-load the chemicals *on-chip* has the potential to further reduce the limit of detection of the system. Furthermore, incorporating additional components to the pre-treatment chemistry which have been shown to induce bacterial enzyme over-expression also has the potential to enhance the limit of detection, whilst still preserving the unique straightforward qualitative detection aspect of the demonstrated pathogen detection approach. Alternatively, future integration of such a 3D printed bioreactor design with portable quantitative detection schemes as well as compact microelectronic-integrated hardware to achieve *on-chip*, localized bacterial incubation has the potential to extend the platform demonstrated in this work towards truly-*on-site* point-of-need pathogen detection applications.

Chapter 7

Appendix

7.1 Introduction Appendix

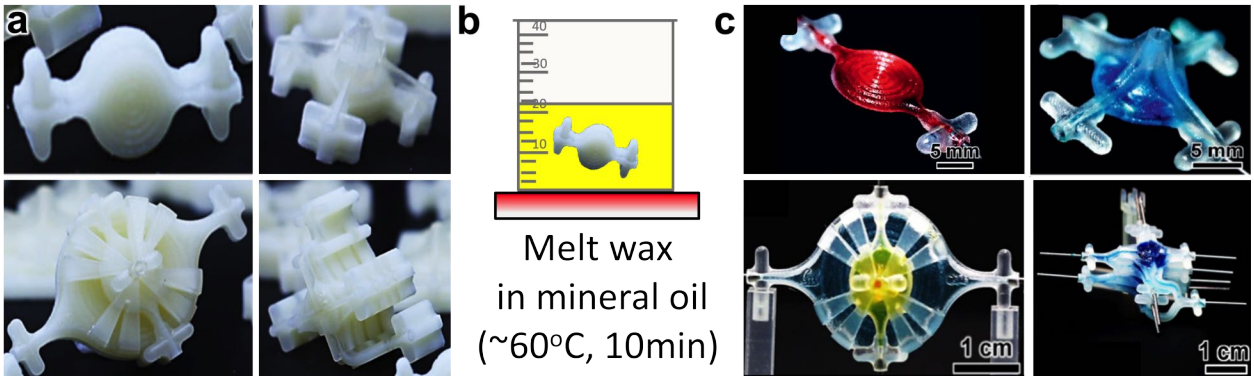

Figure 7.1: Prototype devices featured in Sochol, Lab on a Chip, 2016 [115] before and after custom post-processing technique to remove wax-based support material from inside fabricated prototypes.

	Soft lithography	3D printing
Setup cost	~$80k[a]	$1–20k
Cost per print/materials	High	High
Turn-around time	~24 h	<2 h
3D capability	Layered 2D designs	3D digital designs
Fluid automation	Routine	Demonstrated
Throughput	Low	Medium
Manufacturability	Poor	Good

Figure 7.2: Comparison of microfluidics fabrication *via* soft lithography and 3D printing [89].

a Equipment	Technology	Resolution (Z; XY)	Materials (Structural; Support)	Cost [$/g]
3D Systems Projet 3500	MultiJet	16; ~50 um	*Rigid* resins; *(Mineral oil) dissolvable* wax	$0.20-$0.30
Stratasys Objet260	PolyJet	16; ~50 um	*Rigid & flexible* polymers; *(KOH) soluble* gel	$0.13-$0.30
Carbon3D M1	Stereo-Lithography (SLA)	75; ~75 um	*Rigid & flexible* polymers; None*	$0.15-$0.20
Stratasys Dimension 1200es	Fused Deposition Modeling (FDM)	300; ~200 um	*Rigid* ABS polymers; *(KOH) soluble* polymer	$0.13-$0.20

b Property	PDMS	PolyJet Materials
Wettability (Droplet generation)	Hydrophobic (Water-in-oil)	Hydrophilic (Oil-in-water)
Tensile strength	2 MPa (Isotropic)	Rigid: 50-60 MPa (Anisotropic) Flexible: 0.8-1.5 MPa (Anisotropic)
Young's Modulus	0.5-3.5 Mpa (Isotropic)	Rigid: 2-3 GPa (Anisotropic) Flexible: 0.1-0.3 MPa (Anisotropic)
Cytocompatibility	Yes	MED610 (USP VI & ISO 10993-1:2009) (*Stratasys*)
Gas Permeability	High	Poor
Refractive Index	1.43	1.47 (VeroClear, *Stratasys*)* (PDMS thin coat inside microchannel fills roughness, improving optical clarity)

c Property	*3D Systems Projet3000* VisiJetEX200	*Stratasys Objet260* VeroClear (Tango+)
Tensile strength	42 MPa (Anisotropic)	Rigid: 50-60 MPa (Anisotropic) Flexible: 0.8-1.5 MPa (Anisotropic)
Young's Modulus	1.2 GPa (Anisotropic)	Rigid: 2-3 GPa (Anisotropic) Flexible: 0.1-0.3 MPa (Anisotropic)
Poisson's Ratio	~0.35	~0.35

[1] http://www.mediacopy.co.uk/3d_printing_material_properties.htm#white
[2] http://pubs.rsc.org/en/content/articlepdf/2016/lc/c6lc00163g?page=search
[3] http://cdn-pubs.acs.org/doi/full/10.1021/acs.analchem.5b01202?src=recsys

Figure 7.3: 3D printing technologies, materials investigated in this work.

7.2 Low Reynolds Number 3D Micromixers Appendix

Variable	Value
ρ	1000 kg/m^3
μ	8.9x10^{-4} Pa s
d_h	750x10^{-6} m
A_d	π ($\frac{d_h}{2}$)^2 m^2
$D_{fluorescein}$	4.25x10^{-6} cm^2 s^{-1}

Table 7.1: Parameters used in theoretical simulations and experimental data processing for the 3D μ-mixers

Flow Rate (Q, μL/min)	Reynolds Number (Re)	Péclet Number (Pe)
0.3146	0.01	20.9444
0.5555	0.0177	36.9822
0.9809	0.0312	65.303
1.732	0.0551	115.3072
3.0582	0.0972	203.5985
5.4	0.1717	359.5029
10.4	0.3306	692.376
20.4	0.6485	1358.1222
31.455	1	2094.1046
157.28	5.0001	10470.8557
310.4	9.868	20664.761
314.55	9.9999	20941.0457
405.4	12.8882	26989.3496
510.4	16.2263	33979.6844
629.1	19.9999	41882.0914
1572.8	50.0013	104708.5572

Table 7.2: Flow rates and corresponding Reynolds and Péclet Numbers (as calculated using variables in Table 1.1) used as input parameters for theoretical simulations and experimental data acquisition for the 3D μ-mixers

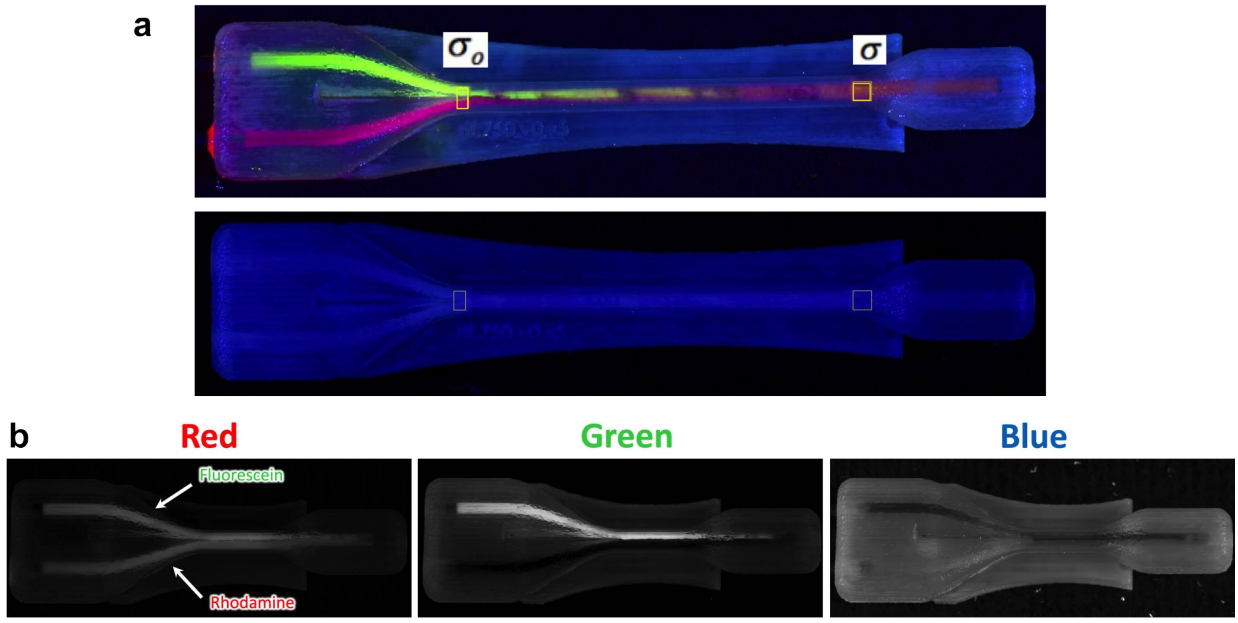

Figure 7.4: Example images from the Fiji image analysis software during the raw image data collection procedure to analyze the RMI of each experimental image of the prototype mixer devices; see Appendix Protocols: *Protocol For Calculating Mixing Index From Experimental Fluorescent Images of μ-Mixers* and *Image Analysis Protocol For Producing Raw Data From Experimental Fluorescent Images of μ-Mixers*. **(a)** Illustration of squares drawn in Fiji to select region for RGB raw data measurement, drawn at the microchannel input (*image, left*) and outlet (*image right*). Example images of a 5 unit long 3D rifled μ-Mixer device, empty (*top*) used for calculating noise intensity, and with input flow rate of 5.4 μL/min (*bottom*). Yellow boxes labeled with which box is used generate raw data used to calculate the standard deviation in the unmixed state at the device inlet, σ_o, and in the mixed state at the outlet, σ. Equations used to calculate **(b)** standard deviation at each location and **(c)** RMI value from each set of images (empty and at a single input flow rate) for each device [184]. **(d)** Visualizations of separate RGB Stack channels from Fiji image analysis software. Produced from the identical raw image ($1M_control_5.4uL.png$). The most distinctive difference in light intensity emitted from Fluorescein (*upper microfluidic channel*) and Rhodamine (*lower microfluidic channel*) is in the green wavelength of light, therefore raw data for the green light channel was used in the RMI calculations.

7.2.1 Image Analysis Protocol For Producing Raw Data From Experimental Fluorescent Images of μ-Mixers

1. Open raw image file (file name *i.e.* $1M_Rifled_5.4uL$, $DeviceLength_MixerType_FlowRate$) in Fiji (Fiji is an open-source distribution of ImageJ image processing package, that includes specific plugins for ImageJ designed to facilitate image analysis for scientific purposes).

2. Open ROI Manager.

3. Create an RGB stack of the image. Select the Green stack, as the difference in intensity of the fluorescent wavelength of light emitted between the Fluorescein, background (mostly blue reflection) and the Rhodamine (nearly pure red emission) is for the green wavelength, see Appendix Fig.7.4d.

4. On the Green stack, draw a square at the input of the device at the intersection of the two input fluid microchannels, capturing the region of the "initial" fluid mixing quality. Ensure that the drawn height of the square is no taller than the width of the microchannel.

5. A Python script is created and loaded into the Macros programming extension on Fiji that enables automated data collection. In the ROI manager, run this script and update the source file directory to the folder where the image is stored and the output directory to a manually created folder with the title "$[Devicelength]_[Devicetype]$". When run, the script records the value from the drawn rectangle in a .csv file.

6. In the ROI Manager, draw another square on the outlet section of the microchannel with roughly the same dimensions as the initial square, capturing the mixing quality of the fluids at the outlet, and run the script again.
   The first time the script is run on an image, the script reads the title of the image and names the .csv file "$[Devicelength]_[Devicetype]_[Flowrate]_[input1]$". The second time the script is run, the .csv file is saved with the title "$[Devicelength]_[Devicetype]_[Flowrate]_[output1]$".

7. In order to account for the variation in the data from the specific dimension of rectangle drawn and the positioning on the image, repeat the preceding steps twice more (draw rectangle and run script) to have three separate measurements of the inlet and outlets of the device. The third and fourth times that the script is run, the .csv files are saved with the titles "$[Devicelength]_[Devicetype]_[Flowrate]_[input2]$" and "$[Devicelength]_[Devicetype]_[Flowrate]_[output2]$", respectively. The likewise, the fourth and fifth times that the script is run, the .csv files are saved with the titles "$[Devicelength]_[Devicetype]_[Flowrate]_[input3]$" and "$[Devicelength]_[Devicetype]_[Flowrate]_[output3]$", respectively.

8. Repeat the above steps for each image taken.

7.2.2 Protocol For Calculating Mixing Index From Experimental Fluorescent Images of μ-Mixers

1. Run the additional Python script that was created to calculate the RMI value from a single device at a given steady state flow rate.
2. Change the input directory of the Python script to the folder labeled "$[Devicelength]_[Devicetype]$" containing all of the .csv files for a given device of a given length.
3. Run the script, which performs the calculations as described in Section 2.3.5.2, which calculates one RMI value for a single device of a certain length at each steady state flow rate that was experimentally tested, storing all of the values in a single matrix saved as a data file in that folder.
4. Repeat the above procedures for each folder labeled "$[Devicelength]_[Devicetype]$", generating all RMI values.
5. Use an additional custom Python script to plot the data, which reads all of the RMI values matrices for each device of a given length.

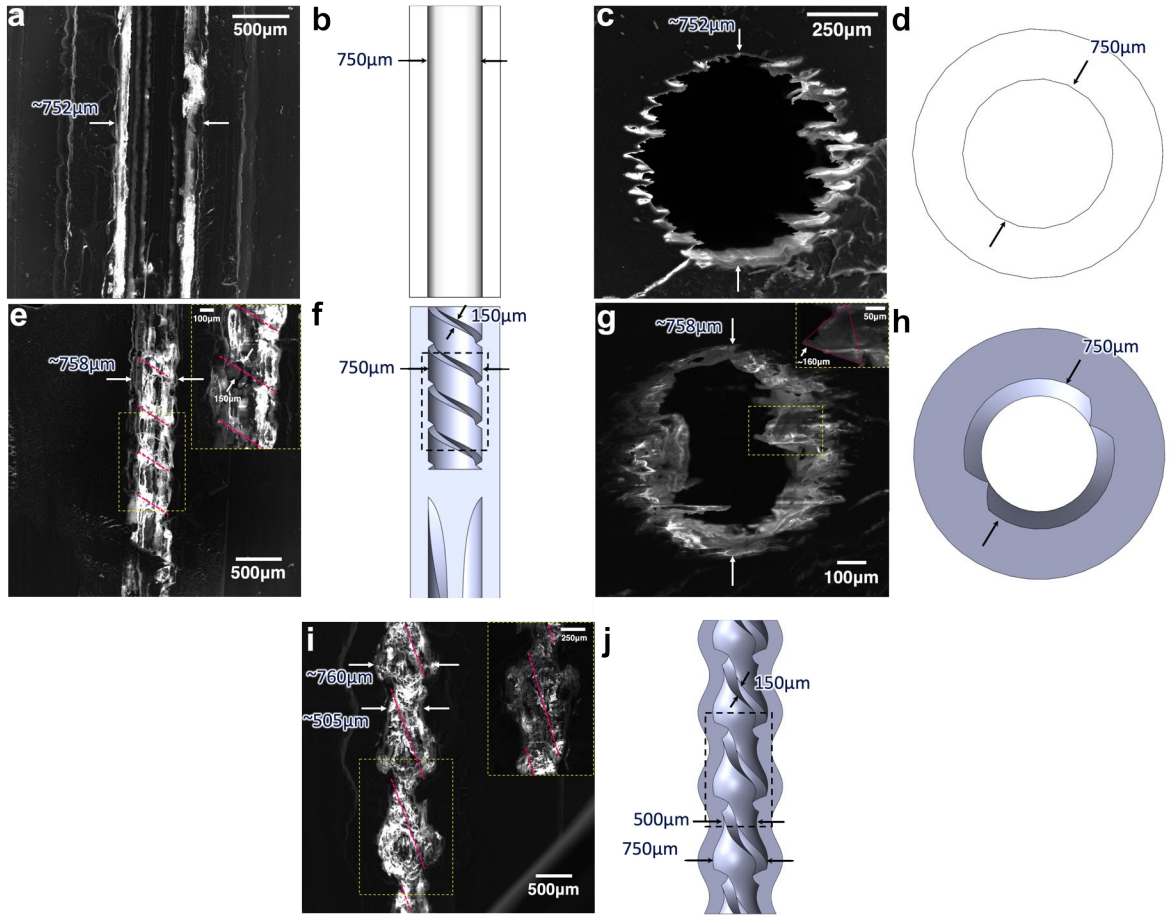

Figure 7.5: SEM images of modular μ-mixer prototypes. **(a-b)** Control μ-channel top-down view; **(c-d)** control μ-channel profile view; **(e-f)** 3D rifled μ-mixer top-down view; **(g-h)** 3D rifled μ-mixer profile view; **(i-j)** 3D bulbous μ-mixer top-down view

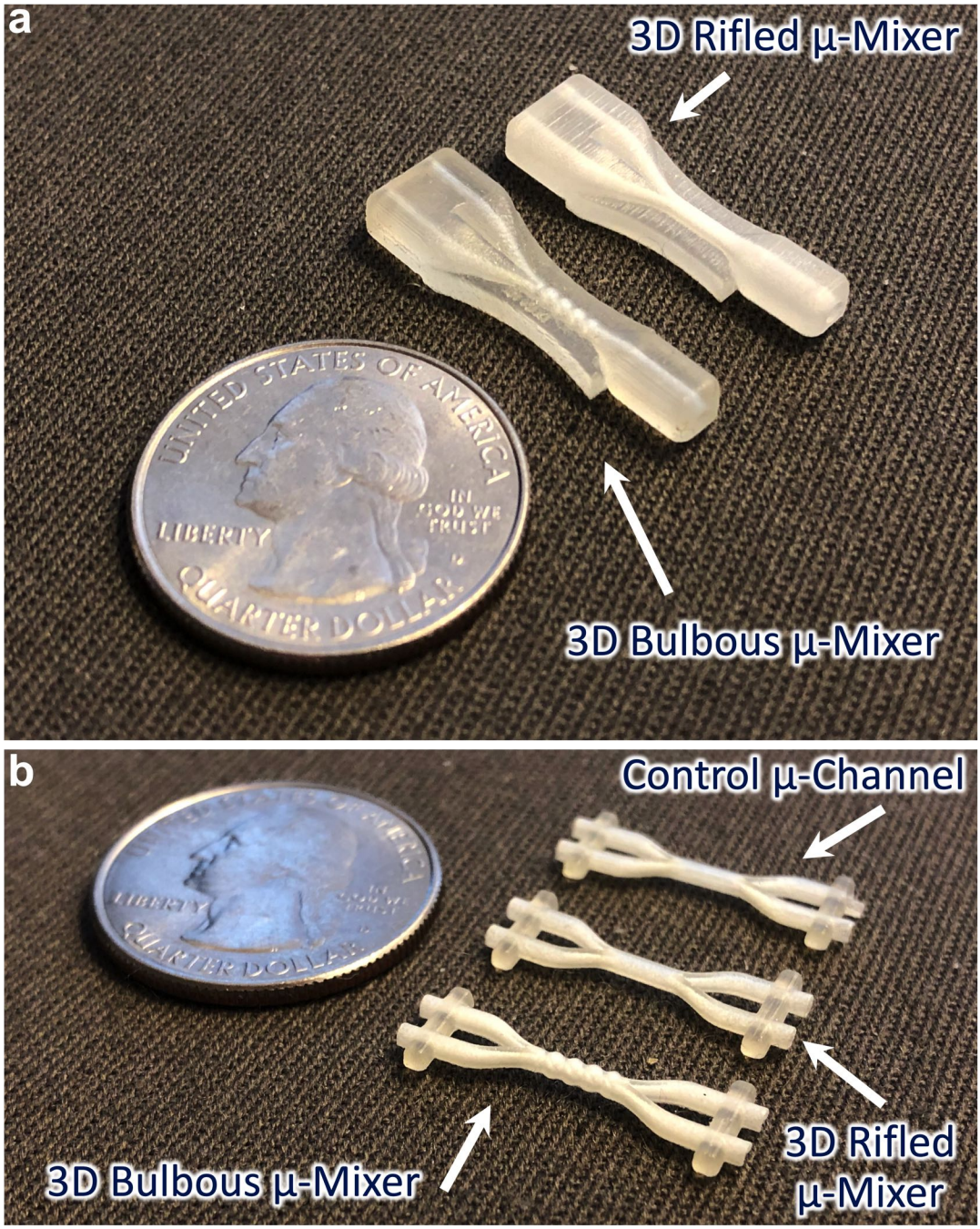

Figure 7.6: Fabricated μ-mixer prototypes. **(a)** 3D rifled and 3D bulbous μ-mixers. **(b)** Control μ-channel and 3D rifled and 3D bulbous μ-mixer prototypes with two inlets and two outlets.

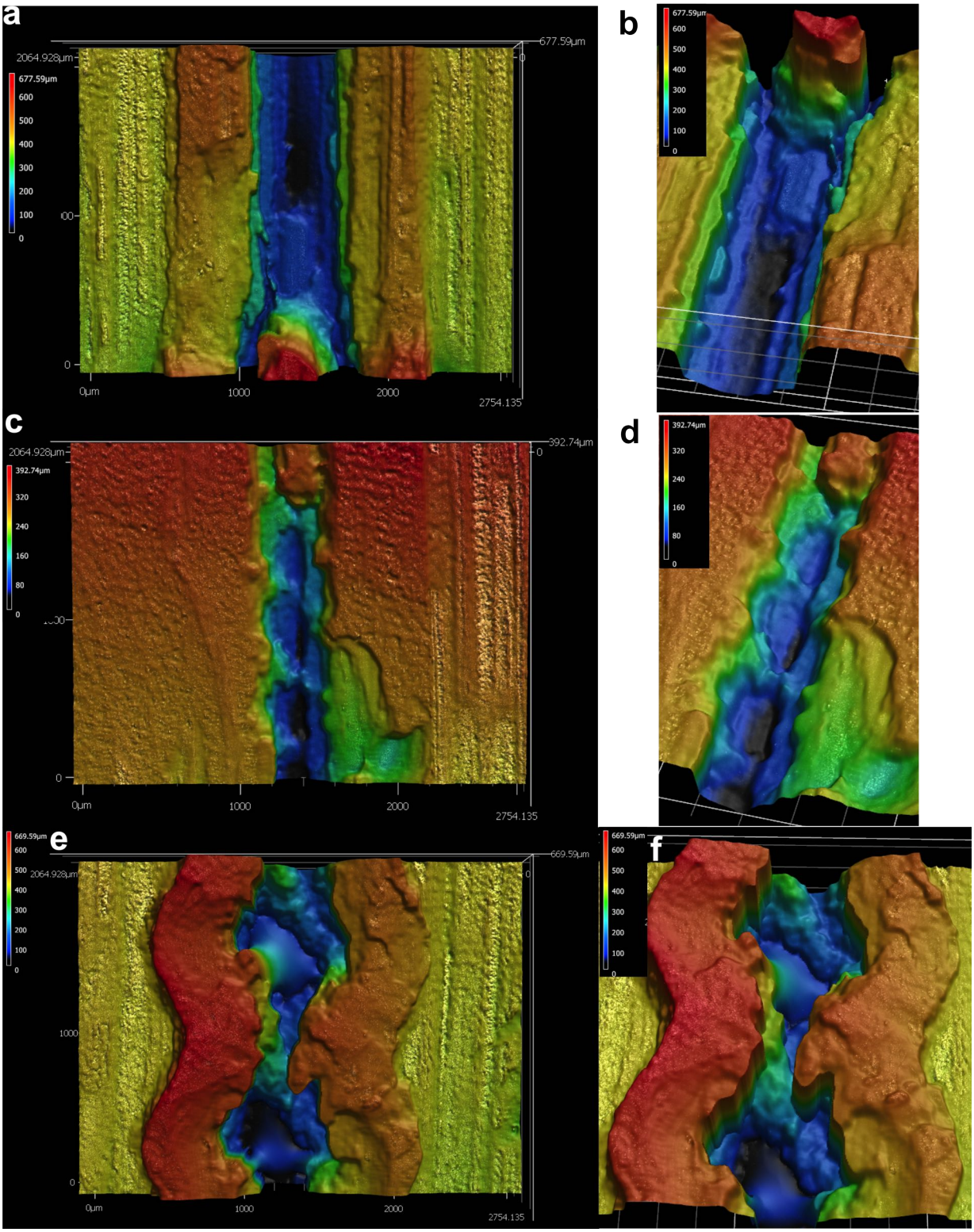

Figure 7.7: Scanning laser microscopy images of fabricated μ-mixer prototypes. **(a-b)** Control μ-channel. **(c-d)** 3D rifled μ-mixer. **(e-f)** 3D bulbous μ-mixer.

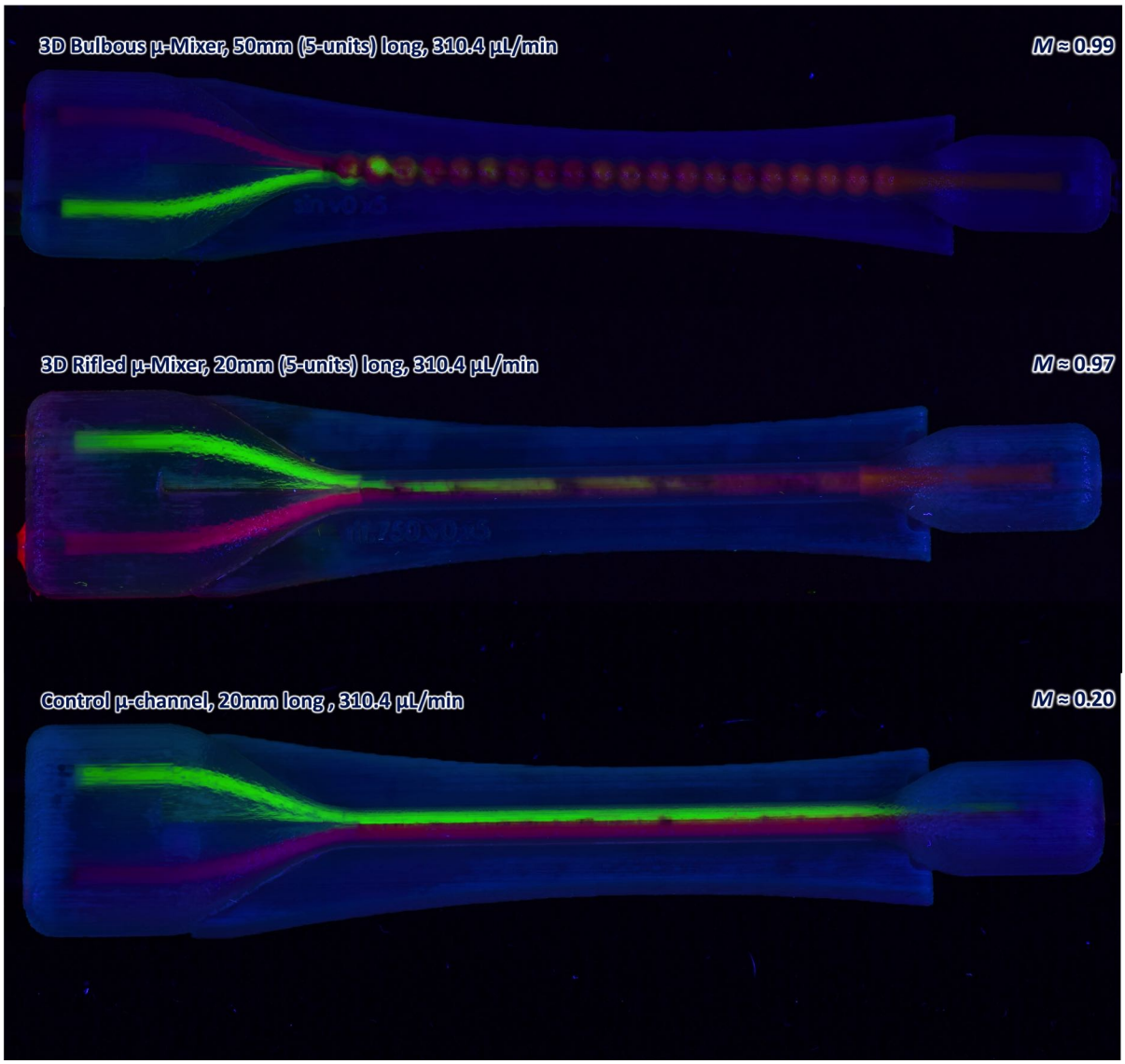

Figure 7.8: Additional experimental images of μ-mixer prototypes visualizing mixing.

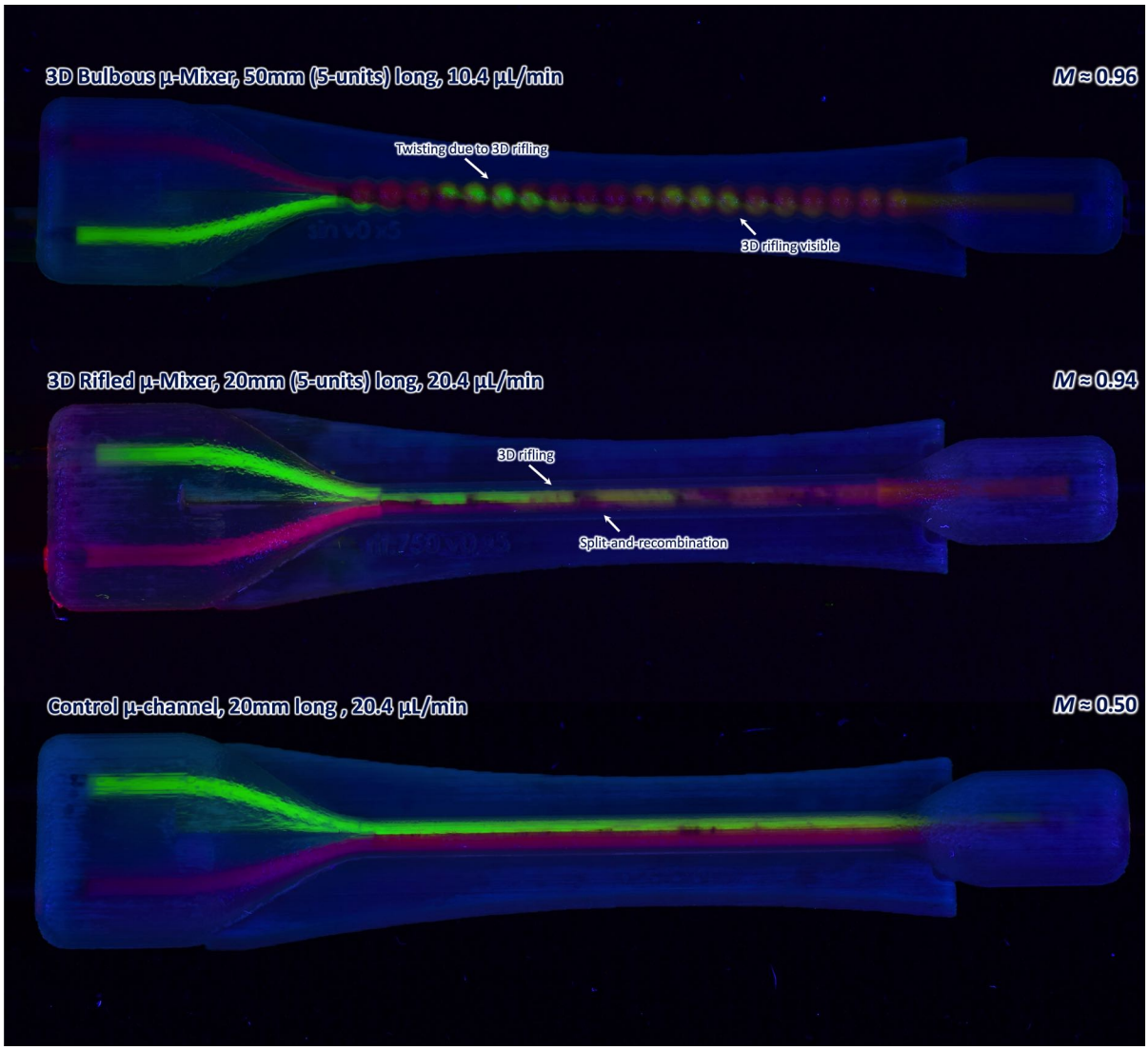

Figure 7.9: Additional experimental images of μ-mixer prototypes.

7.3 Microfluidic Concentration Gradient Generators for Antimicrobial Drug Screening

Flow Rate (Q, μL/min)	Reynolds Number (Re)	Péclet Number (Pe)
10	0.3179	2665.7462
50	1.5896	3328.7308
100	3.1791	6657.4617
150	4.7687	9986.1925
250	7.9478	16643.6542
500	15.8956	33287.3084
1000	31.7912	66574.6167
1500	47.6869	199861.9251
2000	63.5825	133149.2334
2500	79.4781	166436.5418
3000	95.3737	199723.8502
4000	127.165	266298.4669

Table 7.3: Flow rates and corresponding Reynolds and Peclet Numbers (as calculated using variables in Table 1.1) used as input parameters for theoretical simulations of the 3D *tetrahedral*-based μ-CGG designs.

7.3.1 Protocol For Producing Normalized Fluorescent Concentration Values from Flow Verification Experimental Fluorescent Image Analysis

To begin:

1. Create one folder for each set of images from a single well plate tested, which contains: an excel data file (for storage of raw data), all of the raw images (.jpeg files taken from the SD card from the DSLR camera) and the processed images produced by Fiji.
2. Sets of experimental images (one centered over each well on the fluid receptacle) analyzed for the *layer*-based μ-CGG design:
    - Fluorescein into device Inlet #1 (DI water into all other inlets)
    - Separate well containing a 30 μL aliquot of pure DI water (0% control well)
    - Separate well containing a 30 μL aliquot of pure fluorescein stock solution (100% control well)
3. Sets of experimental images (one centered over each well on the fluid receptacle) analyzed for the *tetrahedral*-based μ-CGG design:
    - Rhodamine into device Inlets #1 (DI water into all other inlets)
    - Rhodamine into device Inlet #2 (DI water into all other inlets)
    - Rhodamine into device Inlet #3 (DI water into all other inlets)
    - Separate well containing a 30 μL aliquot of pure DI water (0% control well)
    - Separate well containing a 30 μL aliquot of pure rhodamine stock solution (100% control well)

Extracting raw data using Fiji from each individual image from a given set of experimental images:

1. Open Fiji software.
2. Process $\rightarrow$ Batch $\rightarrow$ Macro.
3. Select as Input the location of the raw image to be analyzed.
4. Select as Output the location where the processed image is to be saved.
5. Select as Output Format as .TIFF

6. In the coding block, if analyzing **fluorescein** fluorescent images, type the following code:
$title = getTitle();$
$index = lastIndexOf(title, ".");$
$out_path = path + substring(title, 0, index) + "_avg.csv";$
$run("RemoveOverlay");$
$selectWindow(title);$
$makeOval(2040, 700, 380, 380);$
$drawOval(2040, 700, 380, 380);$
$roiManager("add");$
$run("SplitChannels");$
$selectWindow(title + "(\textbf{green})");$
$roiManager("select", 0);$
$run("SetMeasurements...", "areamean");$
$run("Measure");$

7. In the coding block, if analyzing **rhodamine** fluorescent images, type the following code:
$title = getTitle();$
$index = lastIndexOf(title, ".");$
$out_path = path + substring(title, 0, index) + "_avg.csv";$
$run("RemoveOverlay");$
$selectWindow(title);$
$makeOval(2040, 700, 380, 380);$
$drawOval(2040, 700, 380, 380);$
$roiManager("add");$
$run("SplitChannels");$
$selectWindow(title + "(\textbf{red})");$
$roiManager("select", 0);$
$run("SetMeasurements...", "areamean");$
$run("Measure");$

8. Click Test. A new image is displays that shows a yellow circle drawn in the location and of the size programmed in the above code, which should be very close to the well in the center of each image. Adjust these values until the yellow circle fits perfectly centered to each well and fits completely inside the wall of the well.

9. When the yellow circle appropriately fits the well, hit Process. This action takes the green (for fluorescein) or red (for rhodamine) RGB stack channel (best enhancing the contrast of the fluorescence intensity of the emission from the respective florophore from the background), measures the average pixel intensity inside the circular area and saves the data in a .csv text file.

10. Open the .csv text file and copy and paste the data into the Excel document, labeling the name of the file, thereby the location of the fluid sample well on the fluid receptacle.

11. Repeat this action for every experimental image. Once finished, the data in the Excel document represents the magnitude of fluorescence intensity in each well.

As a visual aid, for example images of the various stages of Fiji image analysis of a matrix of wells representing a gradient of rhodamine on a 96-well plate, see Appendix Fig.7.33: **(a)** raw image of 96-well plate used for analysis; **(b)** raw image of 96-well plate imaged under a 585 nm bandpass filter; **(c)** Fiji-processed image of the red RGB stack channel of this image; **(d)** raw image of 96-well plate imaged under a red bandpass filter; **(c)** Fiji-processed image of the red RGB stack channel of this image. **(b)-(c)** Show four circles overlaid on the images as drawn by Fiji.

Calculating the Normalized Fluorescent Concentration value for each device output fluid sample from a given experimental collection:

1. Open the Excel document representing the experimental data from a given experimental collection
2. The normalized fluorescent concentration value (arbitrary units) is calculated by normalizing the magnitude of fluorescence intensity of a given fluid sample containing the fluid sample generated from the gradient generator device, containing a certain percentage of the input florophore concentration, to that present in the 100% control well, in this case the maximum concentration of florophore [266].
3. Therefore in Excel define in a new region of the spreadsheet the following equation for Mixing Index calculation:
   = ((well of interest) - (0% control well)) / ((100% control well) - (0% control well))
   which defines the Normalized Fluorescent Concentration for a given well of interest as the magnitude of the average pixel intensity from said well, minus the average pixel intensity from the 0% control well representing background fluorescence noise, divided by the magnitude of the average pixel intensity from the 100% control well representing the pure concentration of florophore emission, minus the average pixel intensity from the 0% control well.
4. Apply this equation to all cells representing all fluid receptacle wells.
5. For the data from the experimental tests of the *tetrahedral*-based μ-CGG design, take an average and standard deviation of the normalized fluorescent concentration values previously calculated.
6. These data can now be plotted using Excel.

7.3.2 Protocol For Producing Normalized Growth Values from Bacteriological Experimental Fluorescent Image Analysis

To begin:

1. Create one folder for each set of images from a single well plate tested, which contains: an excel data file (for storage of raw data), all of the raw images (.jpeg files taken from the SD card from the DSLR camera) and the processed images produced by Fiji.
2. Sets of experimental images (one centered over each well on the fluid receptacle) analyzed for the *layer*-based μ-CGG design:
    - Nitrofurantoin into device Inlet #1 (LB media into all other inlets)
    - Tetracycline into device Inlet #1 (LB media into all other inlets)
    - Trimethoprim into device Inlet #1 (LB media into all other inlets)
    - Nitrofurantoin into device Inlet #1, Tetracycline into device Inlet #2, Trimethoprim into device Inlet #3
    - Separate well containing a 30 μL aliquot of pure LB media (0% control well)
    - Separate well containing 30 μL LB media, 30 μL resazurin solution and 30 μL antibiotic solution (100% control well)
3. Sets of experimental images (one centered over each well on the fluid receptacle) analyzed for the *tetrahedral*-based μ-CGG design:
    - Tetracycline into device Inlet #1 (LB media into all other inlets)
    - Ciprofloxacin into device Inlet #1 (LB media into all other inlets)
    - Amikacin into device Inlet #1 (LB media into all other inlets)
    - Tetracycline into device Inlet #1, Ciprofloxacin into device Inlet #2
    - Amikacin into device Inlet #1, Ciprofloxacin into device Inlet #2
    - Tetracycline into device Inlet #1, Amikacin into device Inlet #2
    - Amikacin into device Inlet #1, Ciprofloxacin into device Inlet #2, Tetracycline into device Inlet #3
    - Separate well containing a 30 μL aliquot of pure LB media (0% control well)
    - Separate well containing 30 μL LB media, 30 μL resazurin solution and 30 μL antibiotic solution (100% control well)

Extracting raw data using Fiji from each individual image from a given set of experimental images:

1. Open Fiji software.
2. Process → Batch → Macro.
3. Select as Input the location of the raw image to be analyzed.
4. Select as Output the location where the processed image is to be saved.
5. Select as Output Format as .TIFF
6. In the coding block, type the following code:
$title = getTitle();$
$index = lastIndexOf(title, ".");$
$out_path = path + substring(title, 0, index) + "_avg.csv";$
$run("RemoveOverlay");$
$selectWindow(title);$
$makeOval(2040, 700, 380, 380);$
$drawOval(2040, 700, 380, 380);$
$roiManager("add");$
$run("SplitChannels");$
$selectWindow(title + "(green)");$
$roiManager("select", 0);$
$run("SetMeasurements...", "areamean");$
$run("Measure");$
7. Click Test. A new image is displays that shows a yellow circle drawn in the location and of the size programmed in the above code, which should be very close to the well in the center of each image. Adjust these values until the yellow circle fits perfectly centered to each well and fits completely inside the wall of the well.
8. When the yellow circle appropriately fits the well, hit Process. This action takes the green RGB stack channel (best enhancing the contrast of the fluorescence intensity of the resorufin emission isolated by the 585 nm filter from the background), measures the average pixel intensity inside the circular area and saves the data in a .csv text file.
9. Open the .csv text file and copy and paste the data into the Excel document, labeling the name of the file, thereby the location of the fluid sample well on the fluid receptacle.
10. Repeat this action for every experimental image. Once finished, the data in the Excel document represents the magnitude of fluorescence intensity in each well.

Calculating the Normalized Growth value for each device output fluid sample from a given experimental collection:

1. Open the Excel document representing the experimental data from a given experimental collection
2. The normalized growth value (arbitrary units) is calculated by normalizing the magnitude of fluorescence intensity of a given fluid sample containing the fluid sample generated from the gradient generator device, containing a certain percentage of the input antibiotic concentration, to that present in the 100% control well, in this case the maximum growth present in the case where no antibiotic is present [266].
3. Therefore in Excel define in a new region of the spreadsheet the following equation for Mixing Index calculation:
   = ((well of interest) - (0% control well)) / ((100% control well) - (0% control well))
   which defines the normalized growth value for a given well of interest as the magnitude of the average pixel intensity from said well, minus the average pixel intensity from the 0% control well representing background fluorescence noise, divided by the magnitude of the average pixel intensity from the 100% control well representing the maximum concentration of resorufin produced possible, minus the average pixel intensity from the 0% control well.
4. Apply this equation to all cells representing all fluid receptacle wells.
5. For the data from the experimental tests of the *tetrahedral*-based μ-CGG design, take an average and standard deviation of the normalized growth values previously calculated.
6. These data can now be plotted using Excel.

7.3.3 Agar Plating Protocols

MicroMethods for Biology **(M3B) Research Program Protocols**

How to make agar from scratch for plating

1. Mix 500mL DI water, 12.5g LB media powder & 7.5g agar powder in a 1L bottle
2. Autoclave media for 20 minutes. Remove and place in an oven @ ~50C degrees for ~20 minutes (just for the solution to cool down to ~50C). Pour enough agar to fill bottom of all plates, but not too thick (to save volume). Let sit for ~10 minutes, while completing next step, or until plates solidify.
3. Immediately clean out bottle with water.

How to make an agar plate with cell colonies

- Way to make sure that new cell solutions (in LB media) come from a single bacteria cell colony (i.e. are healthy, alive, and non-mutated)
    1. Make an agar plate. See above.
    2. Remove a scrape of frozen bacteria from one of the micro K12 amp resistant E Coli tubes stored in the -80 degrees C freezer with a glass stir rod or disposable hook.
    3. Draw 3 lines at the top of the plate. Turn plate 90 degrees, scrape some of these lines across the top. Turn 90 degrees and repeat twice.
    4. Incubate ~24 hours (overnight)
    5. Last scrapes should have diluted the concentration of cells such that only a few isolated colonies are present.
    6. Store plate in -4 C refrigerator for 1 months
    7. When need to make new solution, take a single colony from plate using a hook, place into LB media. Incubate overnight or until cloudy (~10^8).

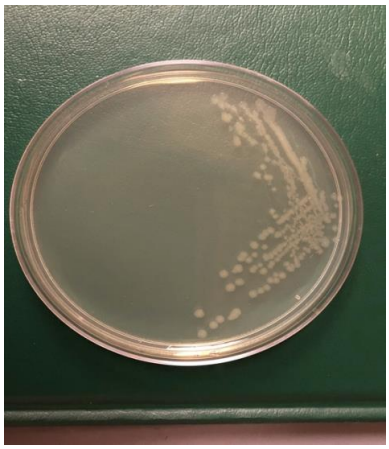

    8.

Agar Plate Single Colony Growth Method (<10^2 - 10^4)

- *Pros*: most precise & robust method, preferred by MCB & biology journals
- *Cons*: can only determine cfu/mL ***24 hours after using cells in experiment***
    1. Culture cells in LB overnight in LB media until cloudy. ***Assume*** ~10^8.
        a. Need to make 16 plates: ~10^8 → ~10^1, 2 plates per concentration.
        b. Autoclave agar with 8 autoclavable ~1.5mL tubes (or grab some that are clean and have already been autoclaved).
    2. Dilute cells down to ~10^5 (***assumed***) & use in experiment. Save some of the original cell solution.
    3. Make agar. See below.

4. Pour enough agar to fill bottom of all plates, but not too thick (to save volume). Let sit for ~10 minutes, while completing next step, or until plates solidify. Label 2 plates for each concentration: 8, 7, 6, 5, 4, 3, 2, 1.
5. Label the 8 tubes 8, 7, 6, 5, 4, 3, 2, 1. Each tube represents a (10^1) dilution. (Therefore *ex*: tube 8 = ~10^8; tube 7 = ~10^7, etc…)
6. Add 100uL of the ***original*** (~10^8) cell solution + 900uL of PBS in "tube 8". Vortex tube.
7. Add 100uL of tube 8 to tube 7, add 900uL of PBS. Vortex tube.
8. Repeat Step 7 until tube 1 is filled.
9. Add 100uL of each tube to each of the plates matching the number.
10. Spread the liquid evenly using cell spreader on the whole plate.
11. Repeat Steps 9-10 for all concentrations.
12. Incubate the plates overnight (~24 hours). Place plates upside down (so condensation doesn't rest on the surface).
13. Next day, remove from incubator, keep plates closed. Count number of individual colonies. Mark each colony with a sharpie. Count # of colonies for all plates. Take average colony numbers between both plates for each concentration.
14. ***Look for the plate number with 25-250 colonies. This is the final plate!***
    a. <25 colonies or >250 colonies → uncertain about count.
    b. Average colonies number * 10 * 10^(# labeled plate)
        i. *e.g.* 49 is average colony number of plates labeled "6"
        ii. e.g. 49 * 10 * 10^6 = 4.9*10^8
        iii. ***4.9*10^8 was the concentration of the original stock. Figure out what this was diluted to that was used in the experiment (24 hours before).***

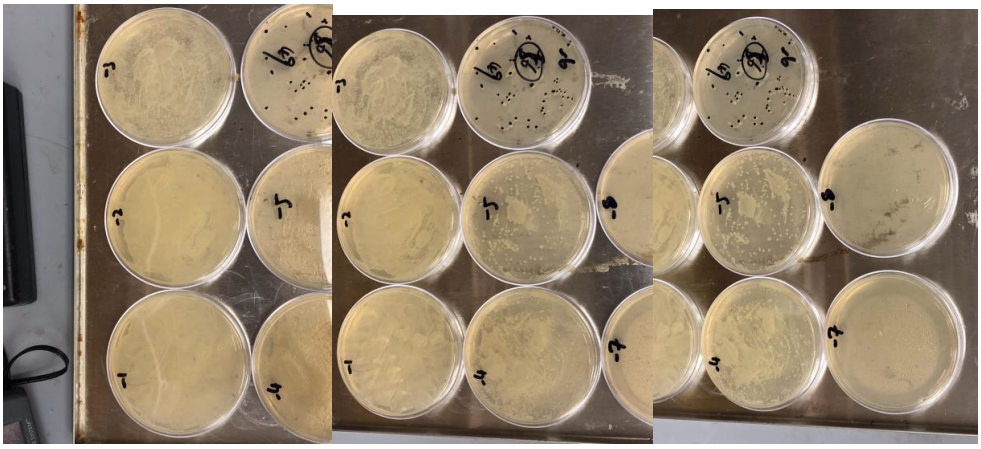

7.3.4 Spectrophotometric Bacteria Density Calculation and Growth Media Preparation Protocols

***MicroMethods for Biology* (M3B) Research Program Protocols**

Lessons for working with cells & cfu/mL determination

- Cannot use cell stock solution older than 1-2 days old
  - Nutrients in LB all used up, cells mostly dead, remaining cells likely mutated
  - Start new cell solution every week, dilute ~100uL of old solution in fresh LB every ~2 days, incubate overnight
- Keep colony plate (see below) in 4 degree C freezer for 1-2 months, take 1 colony everytime you want to start a new cell stock solution
- *Ex.* 2*10^6 cfu/mL
  - Coefficient (2) does not matter, only exponent. In manuscripts, just report "...we diluted our E Coli. cell solution to ~1e6 cfu/mL using an OD600 method"

How to make fresh LB media from scratch

- Better than buying LB from scratch if you make a lot in bulk (store in separate containers, make enough to last whole month, at least).
  1. Mix 1000mL DI water & LB media powder in a 1L bottle (follow bottle directions)
  2. Autoclave media & four 250mL empty bottles for 20 minutes.
  3. Transfer liquid into the four bottles, store with tight lids.

OD600 Method (10^5 - 10^9)

- This method is sufficient for our antimicrobial testing experiments, diluting cells to 10^5
- *Pros*: Instantaneous determination. Dilute down to the target concentration for use.
- *Cons*: "Approximate" method, not the "confident standard" determination method. **However → usually appropriate for engineering publications!**
  1. Culture cells in LB media overnight (either from a single colony on agar plate or from an old LB stock of cells) until solution is visibly cloudy.
  2. Take OD600 measurement using quartz cuvettes, calibrate using fresh LB.
  3. Reading should be ~1.00 (→ corresponds to ~1*10^8 cfu/mL)
  4. Dilute to 1*10^8 cfu/mL → final concentration
     a. OD600 ~1.152
     b. 1/1.152 = 0.87
     c. Make stock: 0.87mL cells + 0.13 mL LB → "confident" 1*10^8 cfu/mL
     d. Dilute down to final concentration (*e.g.* 1*10^5 cfu/mL)

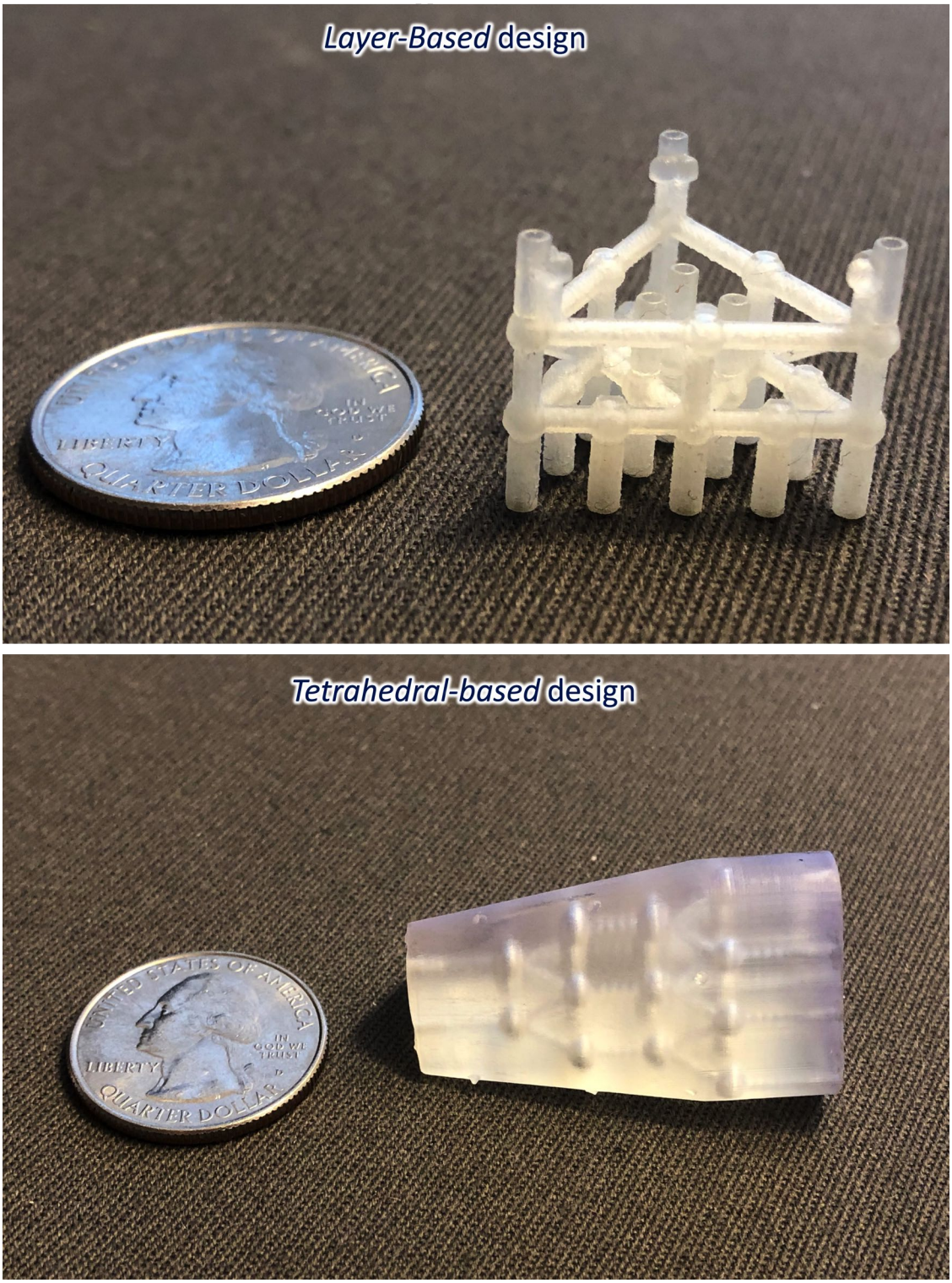

Figure 7.10: Fabricated μ-CGG prototypes. **(Top)** 3D *layer*-based μ-CGG design. **(Bottom)** 3D *tetrahedeal*-based μ-CGG design with integrated 3D μ-mixer vertical channels.

Figure 7.11: Experimental setup for operation of the *layer*-based 3D μ-CGG prototype.

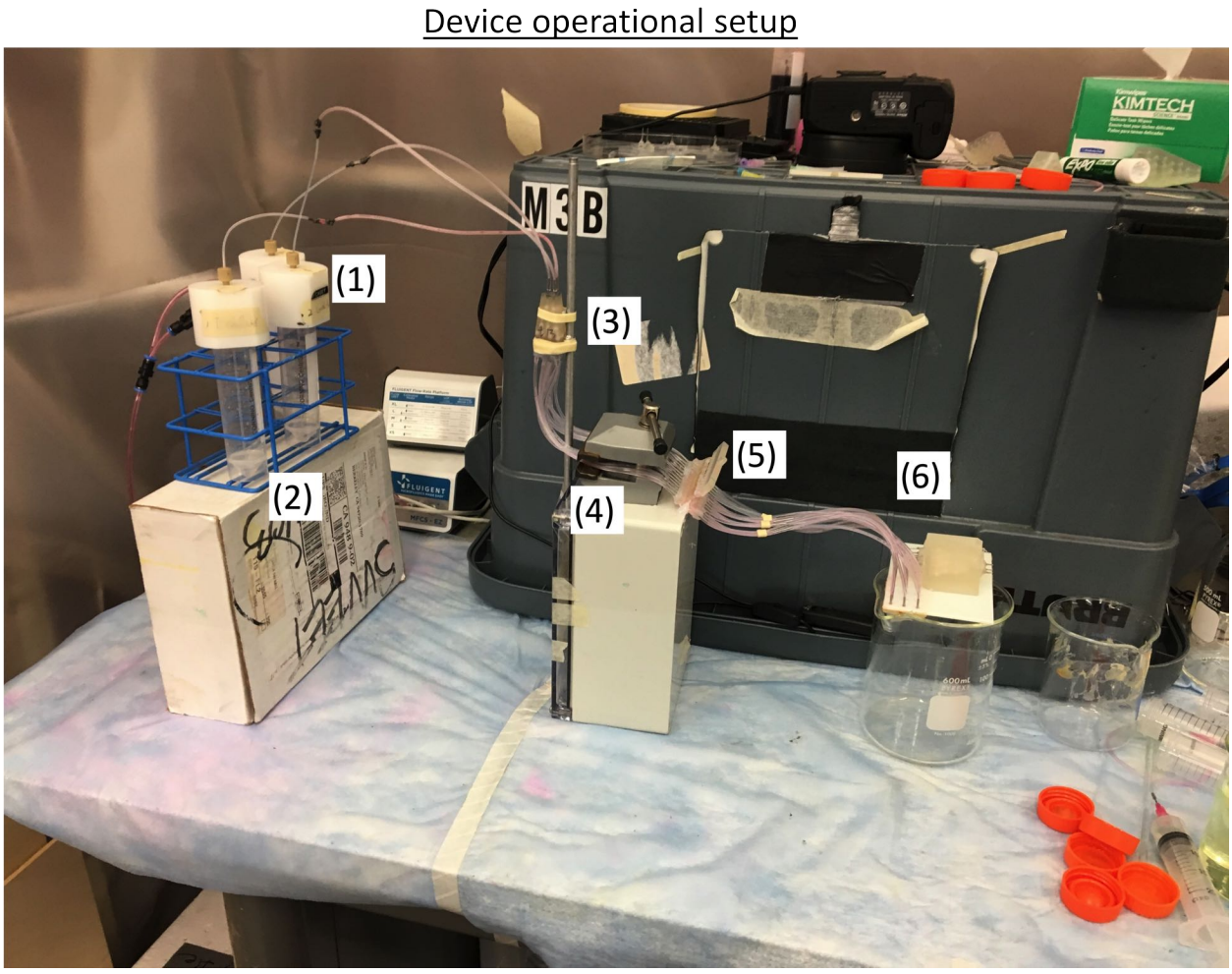

Figure 7.12: Experimental setup for operation of the *tetrahedral*-based 3D μ-CGG prototype. **(1-2)** Fluid reservoirs; **(3)** prototype device; **(4)** 3D printed T-junctions; **(5)** fluid outputs; **(6)** aligner to arrange output tubing to fit for a 96 well plate.

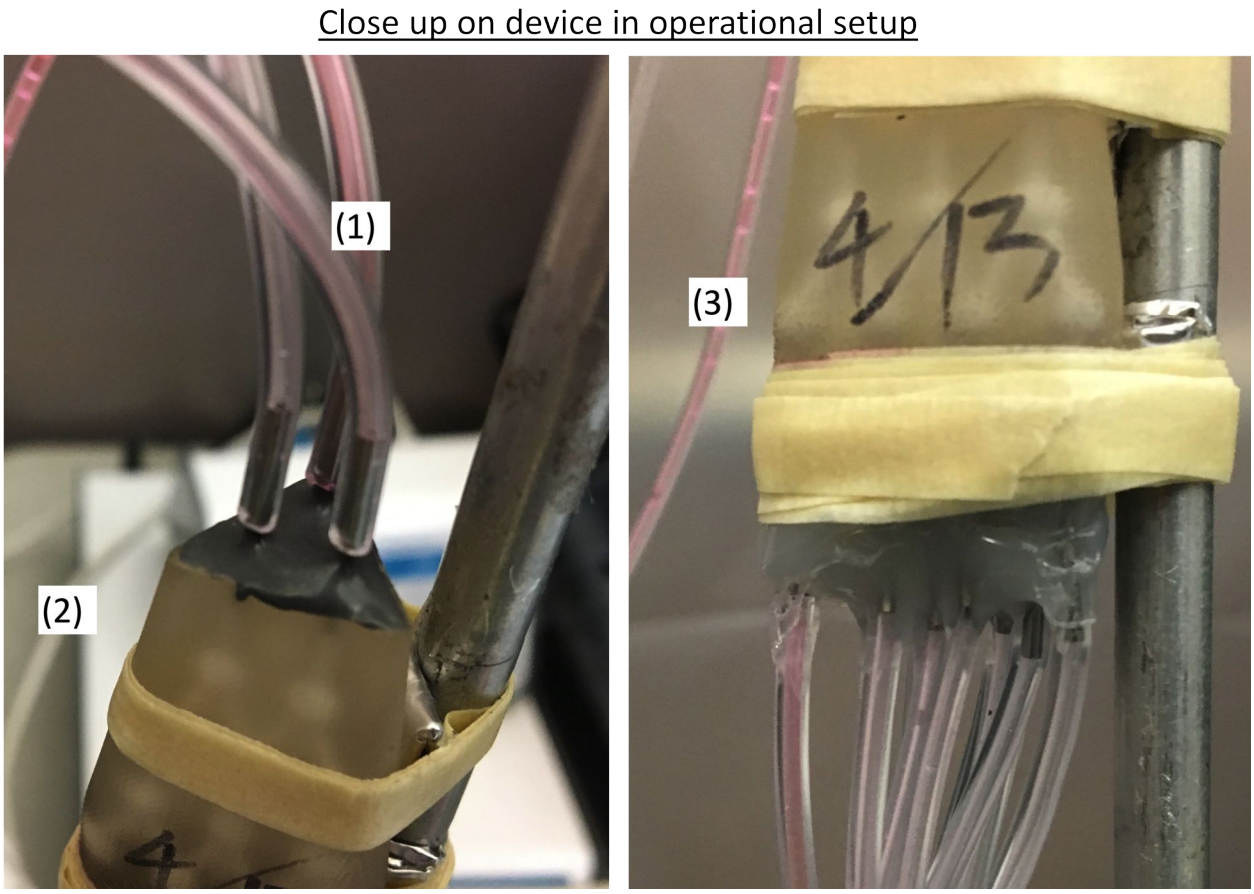

Figure 7.13: Close up view of the inlet and outlet interfaces with the prototype device. **(1)** Three distinct inlet tubes into the prototype with epoxy forming water tight connection between the steel couples and the 3D printed device. **(2)** 3D printed prototype device. **(3)** 13 discrete outlet tubes from the prototype device.

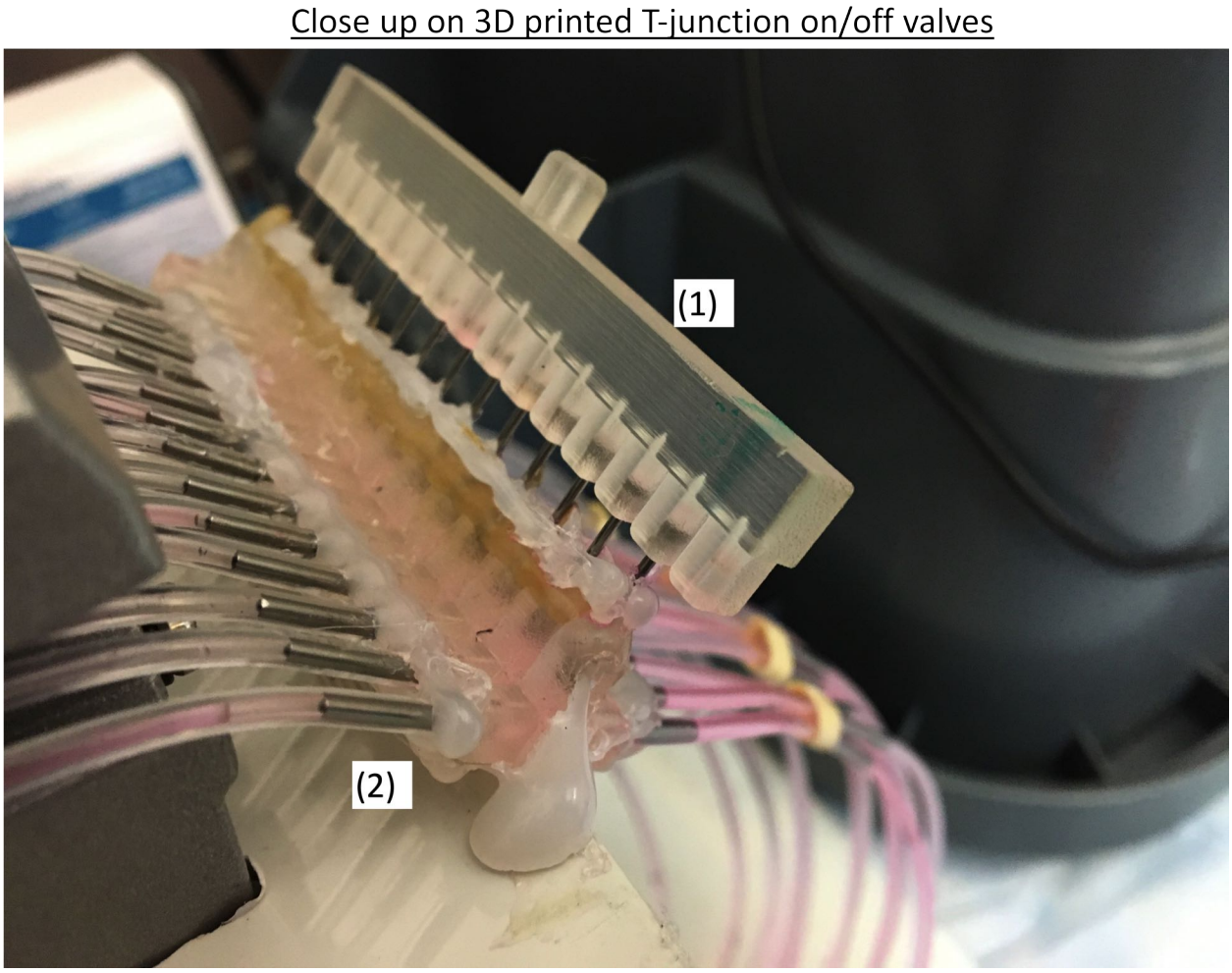

Figure 7.14: 3D printed T-junction. **(1)** Removable 3D printed block. **(2)** 13 discrete ”on-off” valve T-junctions controlling the flow out of each of the output tubing from the device. Tubing from the left comes from the device, tubing to the right routes fluid to the 96 well plate.

Close up on 96 well plate used for device output fluid collection

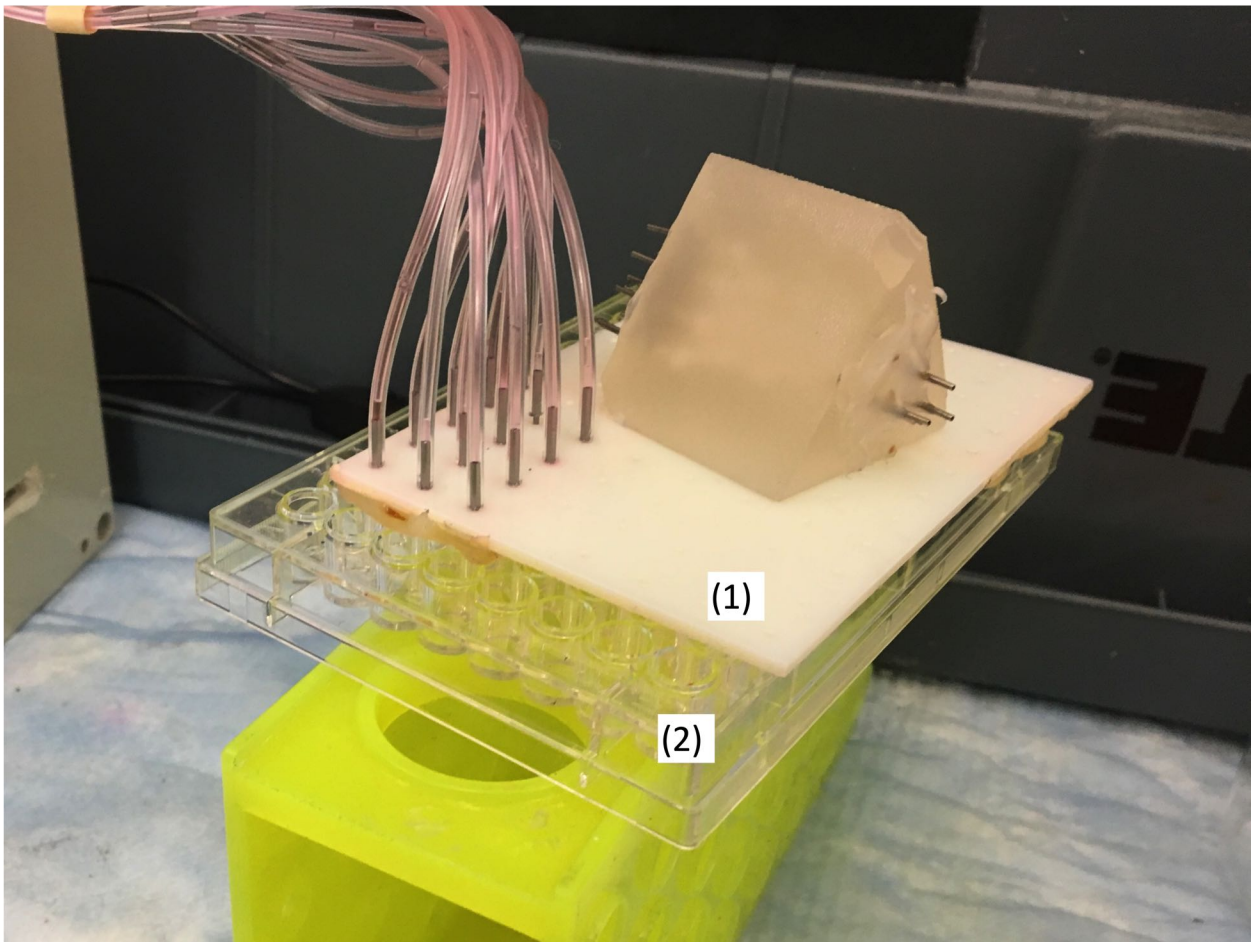

Figure 7.15: 3D printed aligner arranging outlet tubing to a 96 well plate. **(1)** Aligner. **(2)** 96-well plate.

Close up on light blocking imaging setup

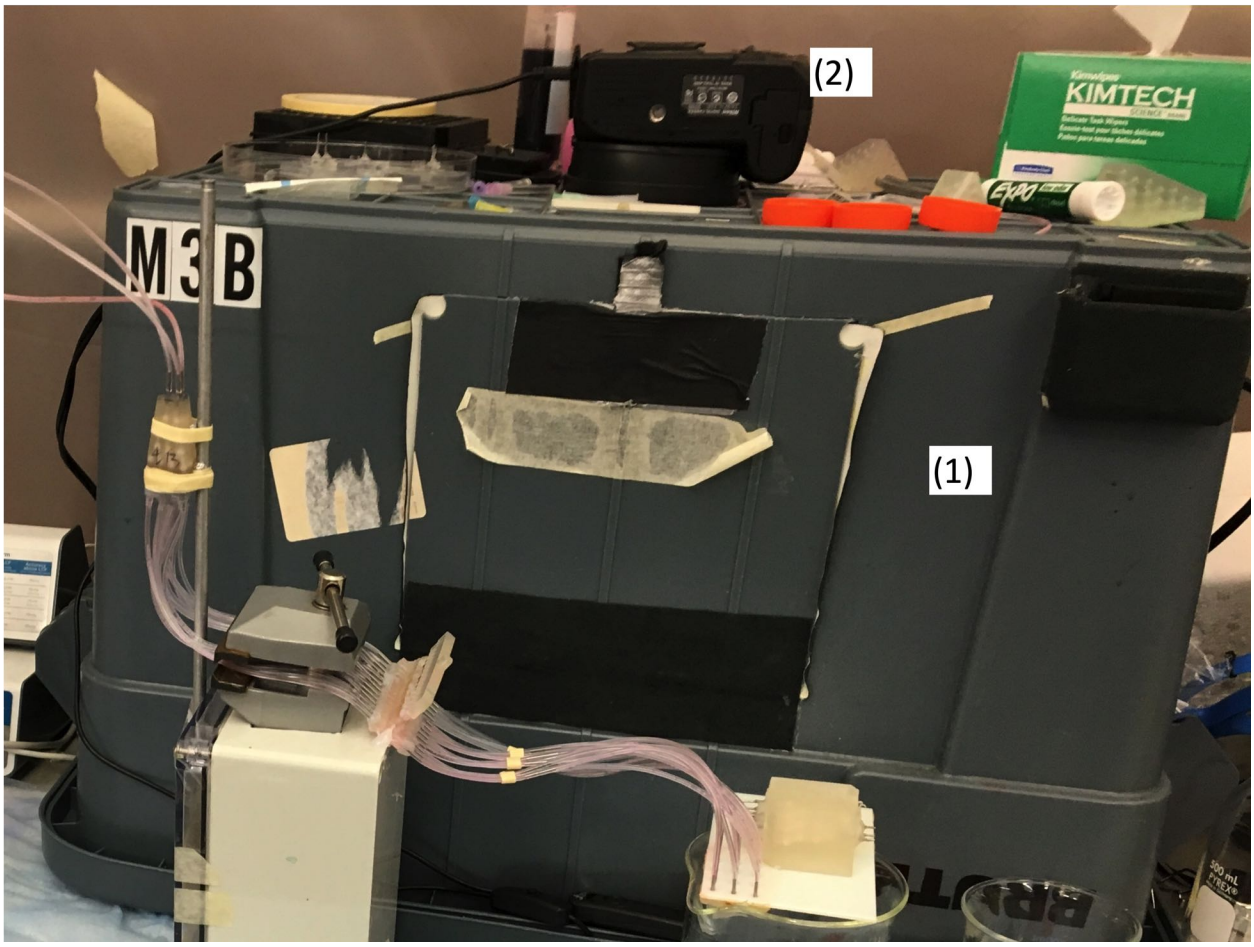

Figure 7.16: Fluorescence imaging setup. **(1)** Light-isolation box. **(2)** DSLR camera.

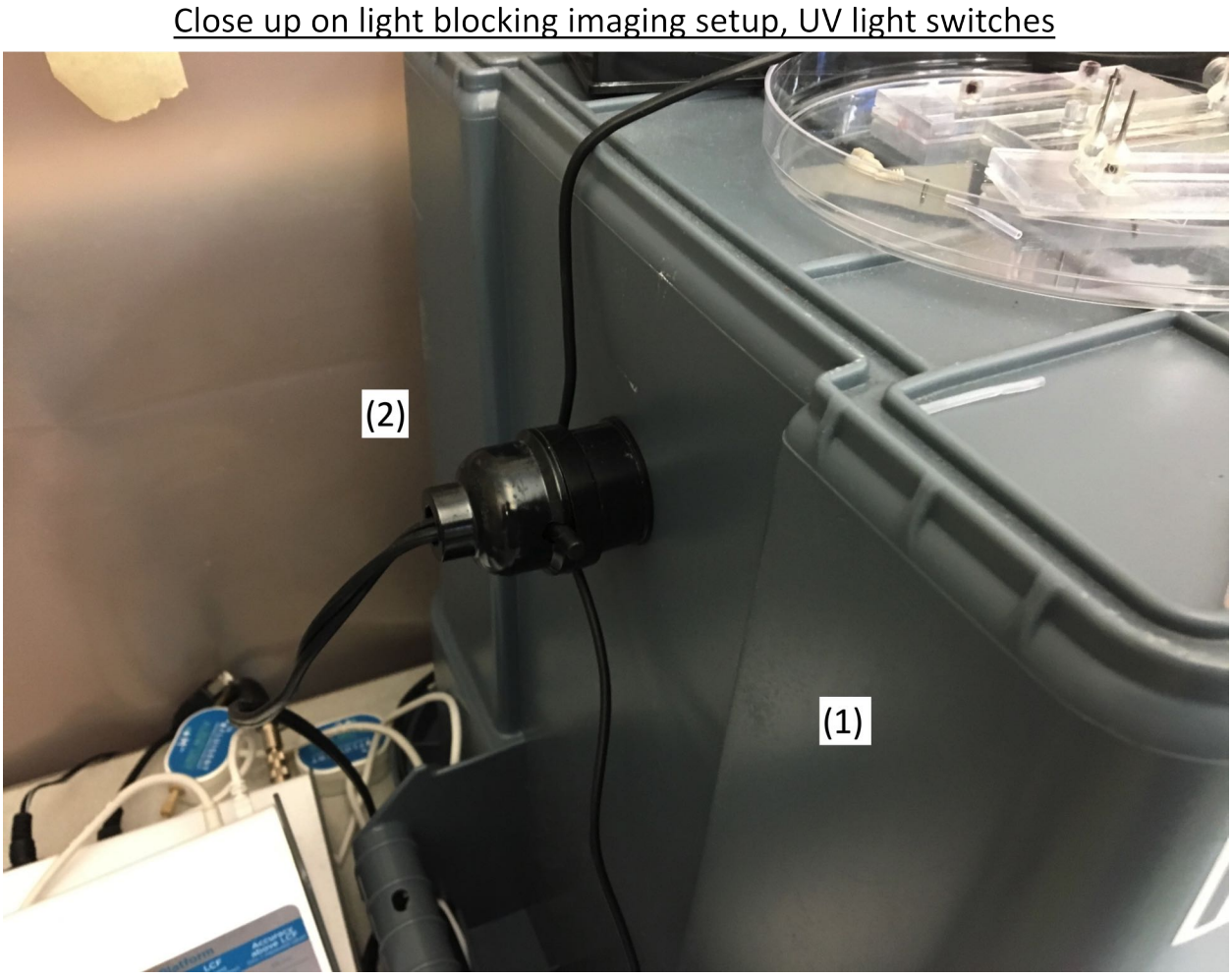

Figure 7.17: Light source for the fluorescence imaging setup. **(1)** Light-isolation box. **(2)** UV light bulb switch.

Close up on light isolation box & imaging setup, camera view

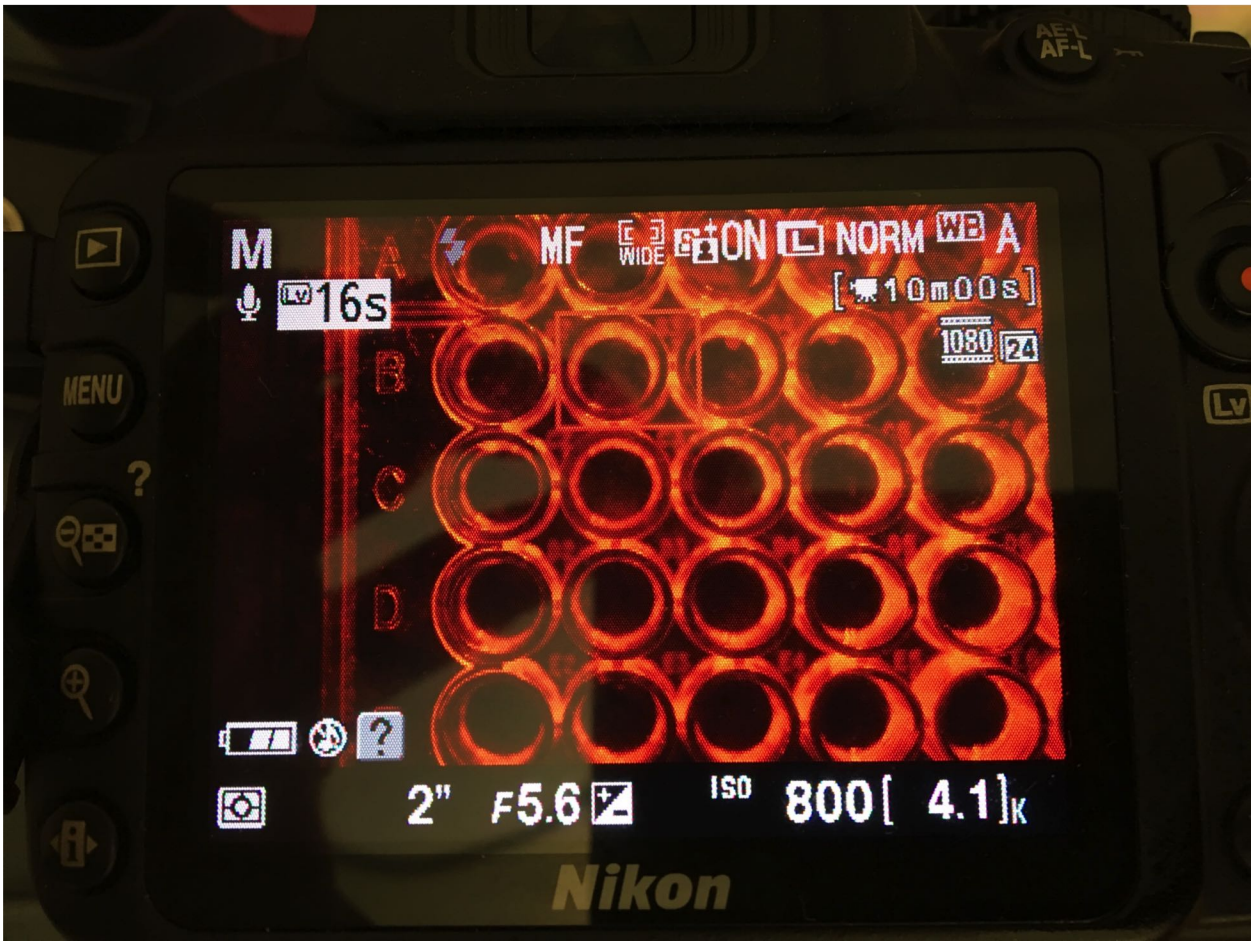

Figure 7.18: Example fluorescent imaging view through the DSLR camera with the red filter over lens and excitation by the UV light source.

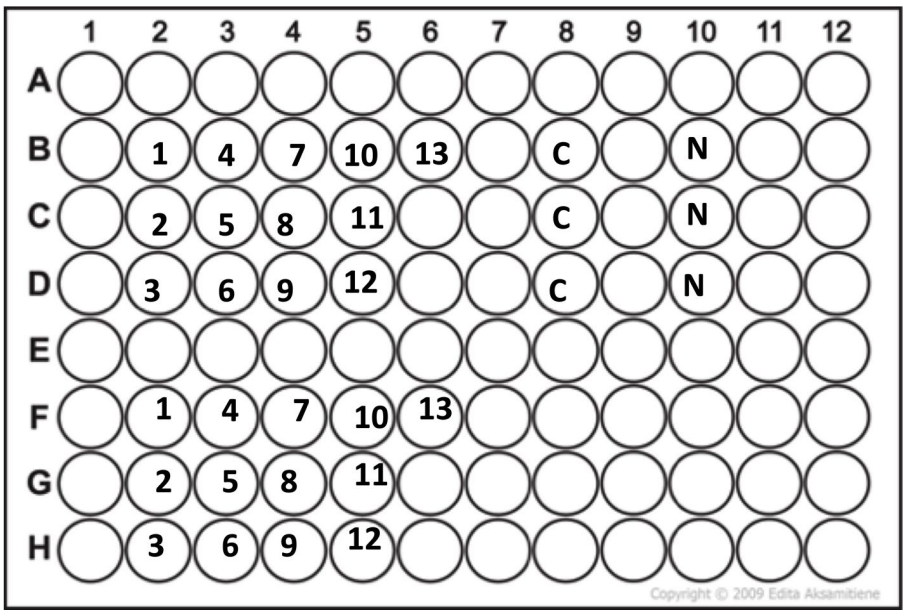

Figure 7.19: Diagram of the layout of the orientation of the fluidic outputs from the *tetrahedral*-based 3D μ-CGG device prototype, routed via segments of tubing, onto discrete wells on a conventional 96-well plate. In addition to the 13 device output fluid samples, three samples of bacteria without any antibiotic present serve as a positive control, and three samples of just resazurin indicator solution are used to subtract any effects from background fluorescence of reaszurin with no bacteria growth present. Showing how the results of two separate fluid collections can fit on a single well plate. In practice each fluid collection experiment for a specific combination of input fluidic samples was performed in triplicate and collected on two 96-well plates in total.

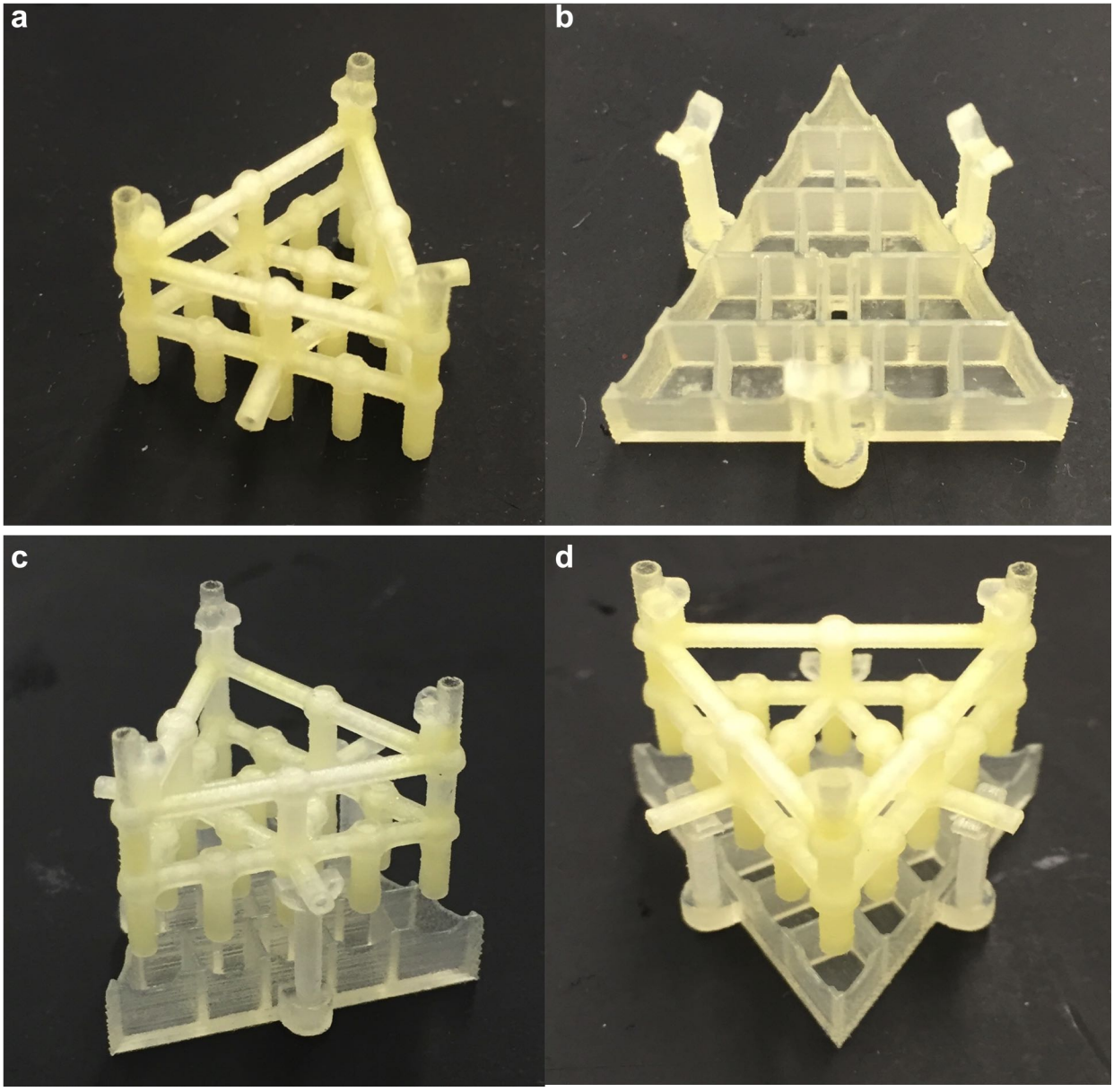

Figure 7.20: Fabricated 3D *layer*-based μ-CGG prototypes. **(a)** 3D *layer*-based μ-CGG prototype. **(b)** Experimental 3D printed fluid output collection receptacle, not pursued in this work, but shown for illustration purposes. **(c)** 3D *layer*-based μ-CGG prototype placed on top of 3D printed receptacle.

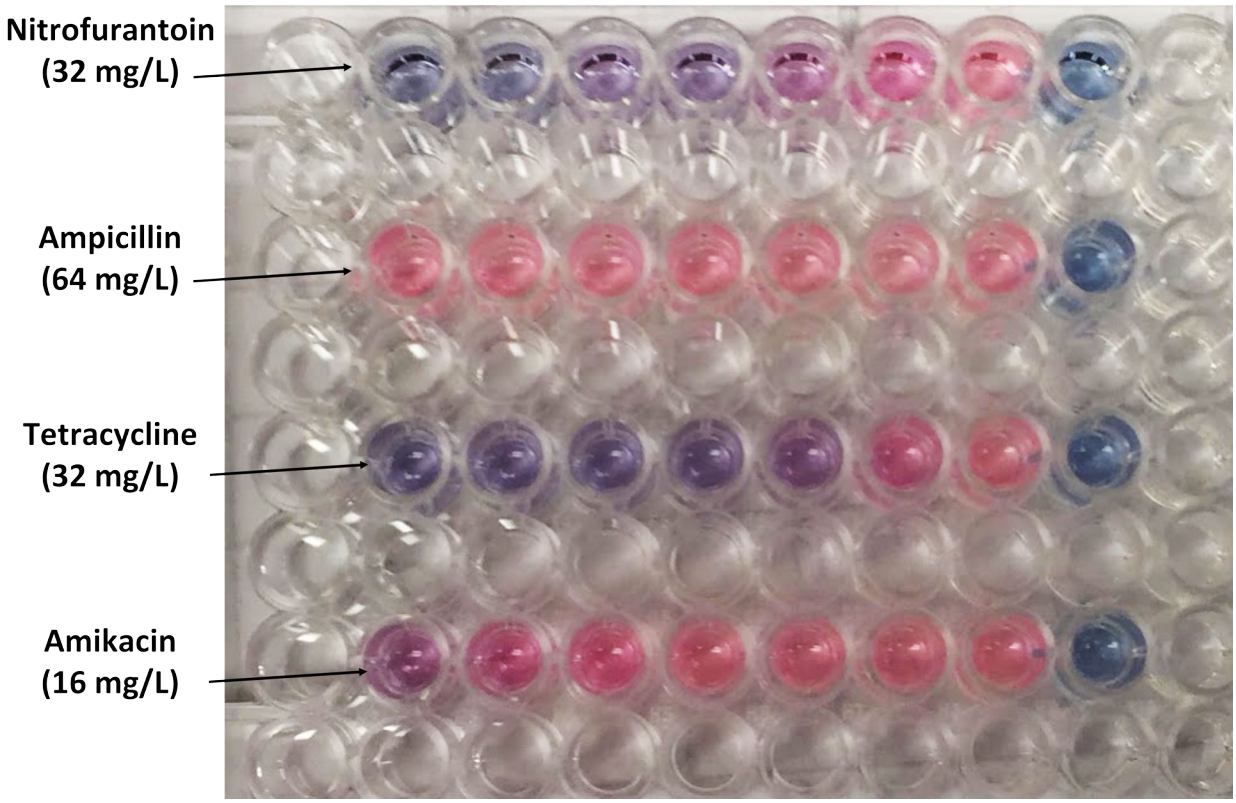

Figure 7.21: Bulk antibiotic serial dilution experiment on 96 well plate showing bacterial growth in high antibiotic concentrations (left) to low antibiotic concentrations (right). Demonstrates antibiotic resistance of *E. coli* bacteria in ampicillin.

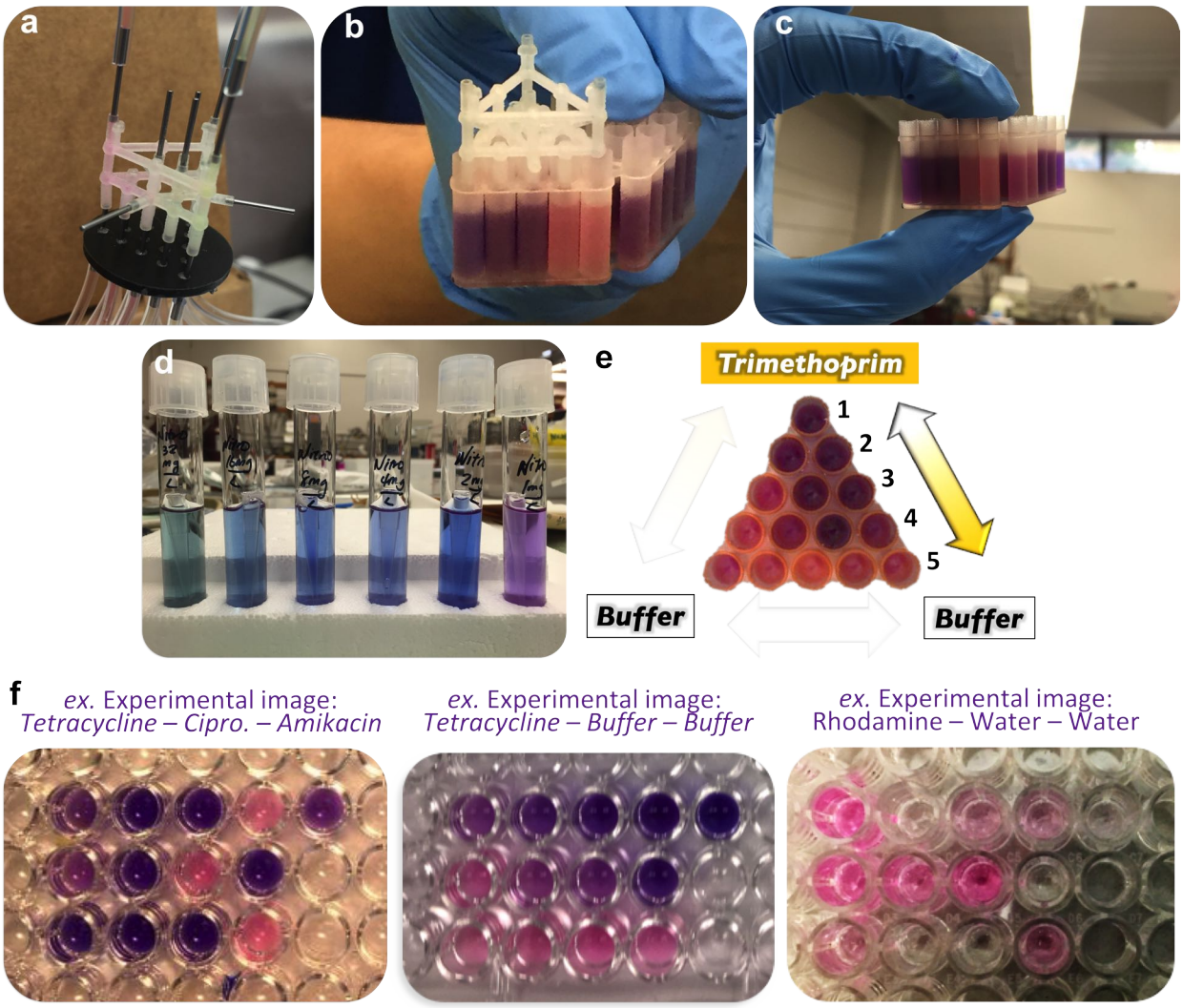

Figure 7.22: Miscellaneous images from 3D μ-CGG experiments. **(a-c)** 3D *layer*-based μ-CGG prototype. **(d)** Bulk antibiotic testing in test tubes. **(e)** Example experimental image after bacterial incubation off the fluid receptacle for the testing of the 3D *layer*-based μ-CGG prototype. **(f)** Example experimental images after bacterial incubation of 96 well plates for the resting of the 3D *tetrahedral*-based μ-CGG prototype showing bacterial growth in the presence of different concentrations of antibiotic.

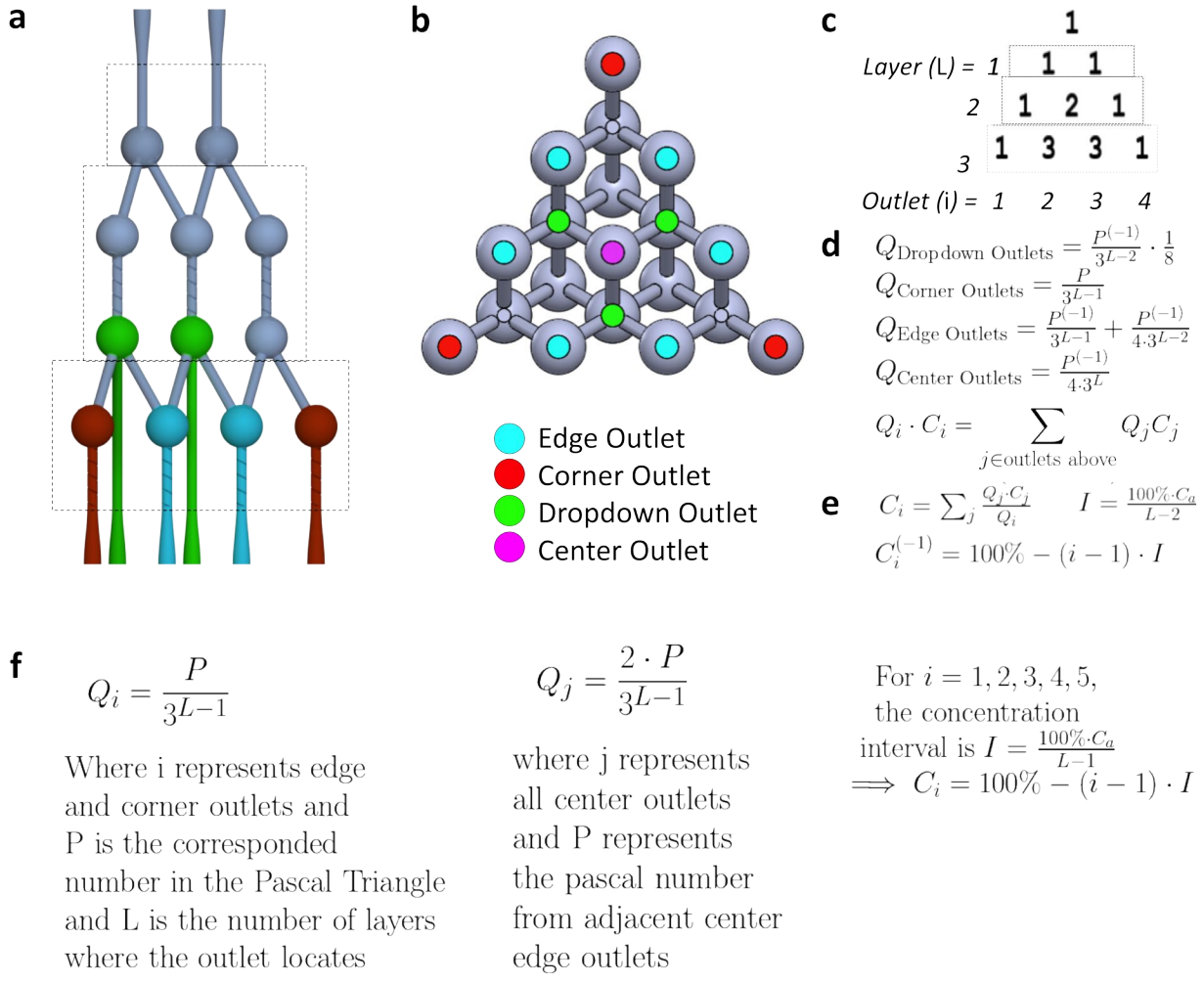

Figure 7.23: Diagram of the later-based analytical design of the 3D *tetrahedral*-based μ-CGG. **(a-b)** Microchannel network and outlets labels. **(c)** Pascal's triangle representing the labeling of the outlets on each side of the microchannel network. **(d)** Analytical flow rate out of each device outlet. **(e)** Conservation of mass equations. **(f)** Derived design equations.

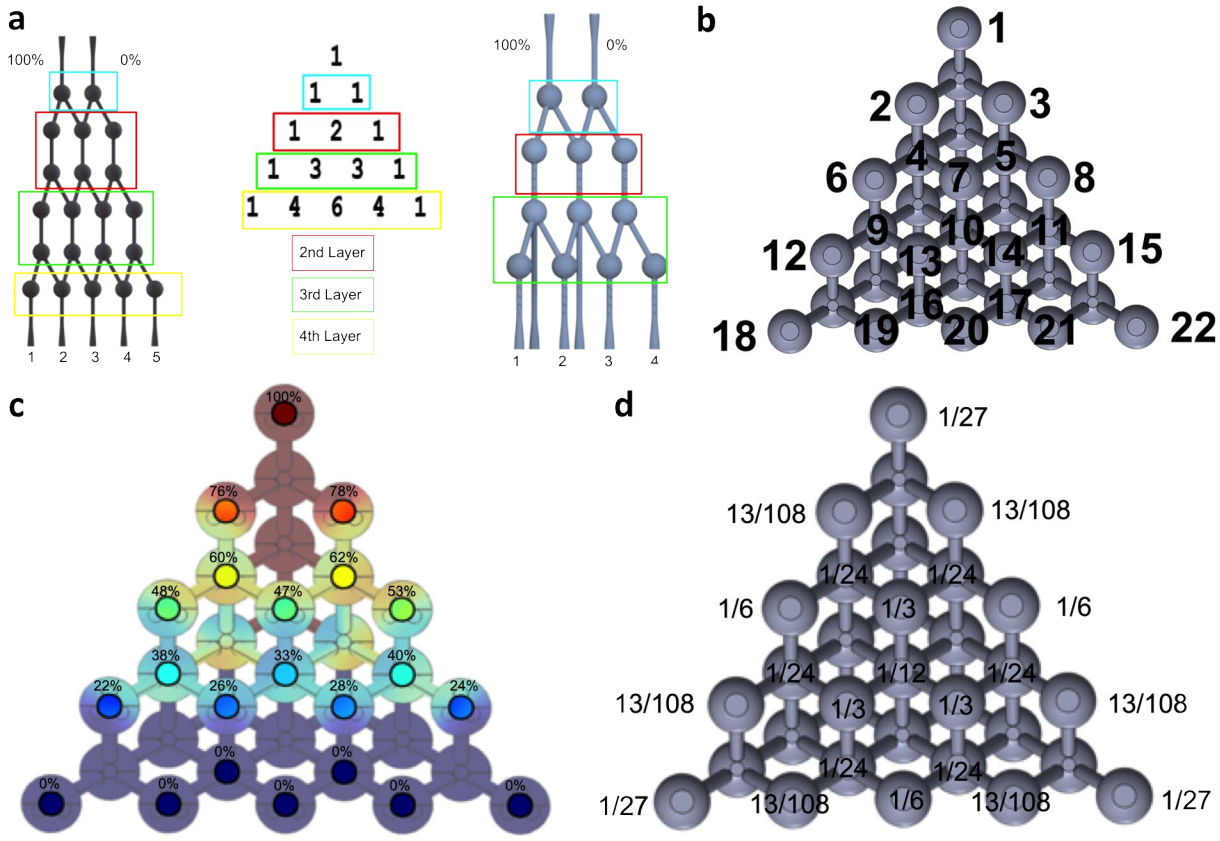

Figure 7.24: Diagram of the analytical design of a four-layer 3D *tetrahedral*-based μ-CGG. **(a)** Layer arrangement. **(b)** Outlet numbering. **(c)** Theoretical concentration of each input concentration at each outlet. **(d)** Analytically-calculated output flow rate at each outlet.

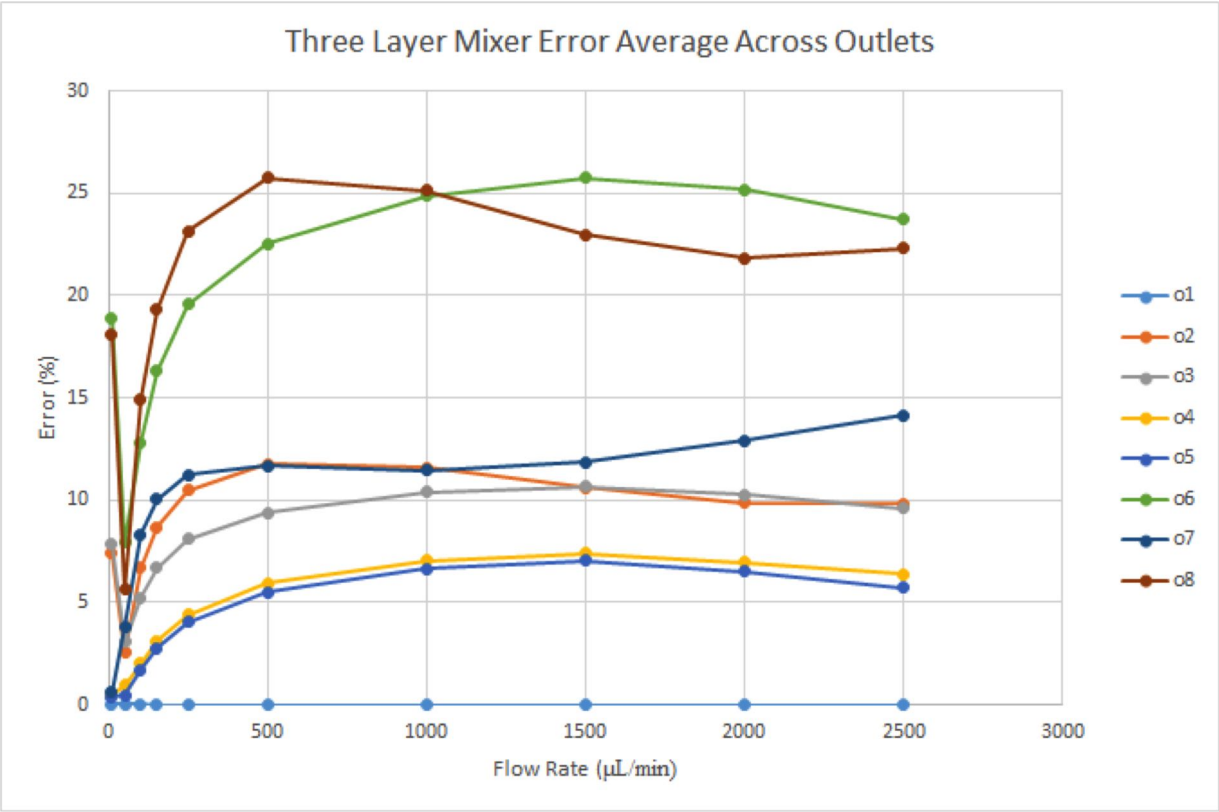

DEFINITION OF ERROR:
error = abs(predicted - actual)/predicted

Figure 7.25: COMSOL results for error from the mean value of concentration at each device outlet for the simulated output of the 3D *tetrahedral*-based μ-CGG design with 3D rifled vertical channels.

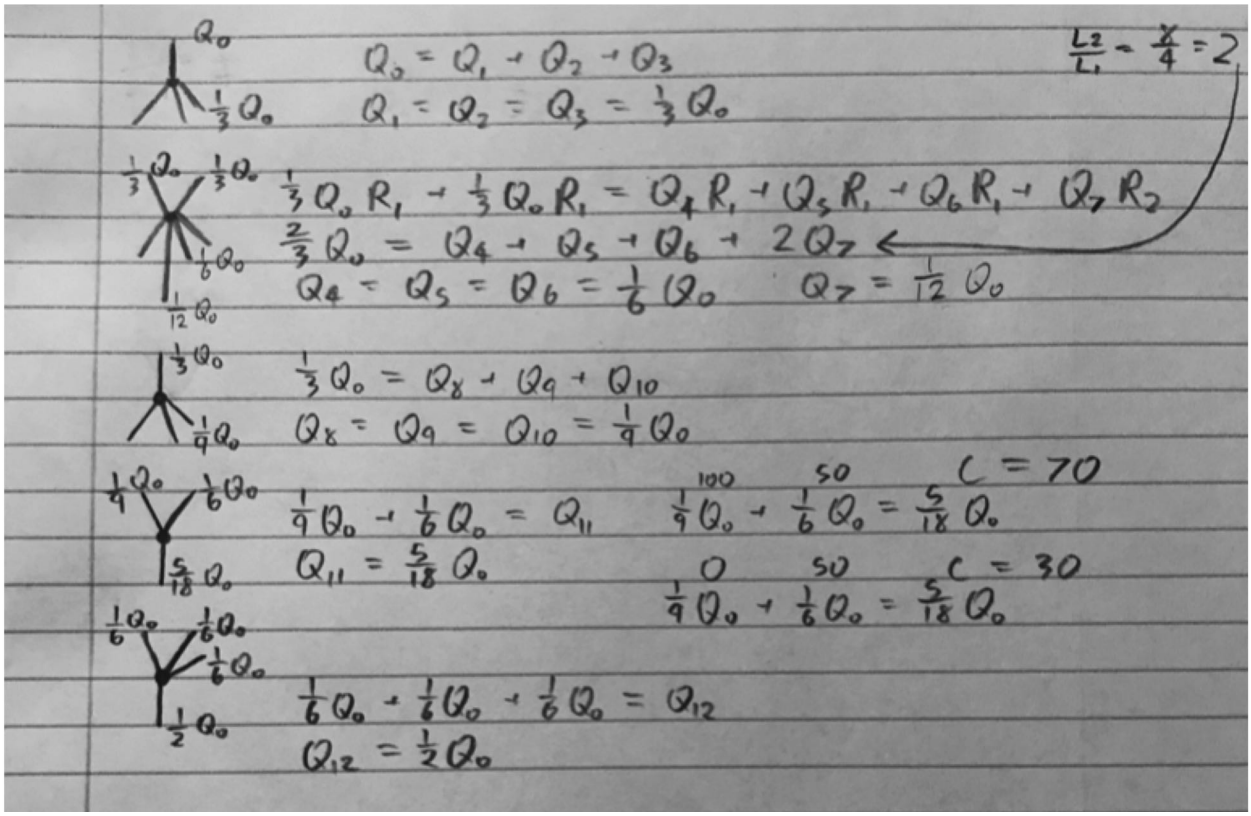

Figure 7.26: Example analytical calculations of flow rate throughout the fluidic network of the 3D *tetrahedral*-based μ-CGG design.

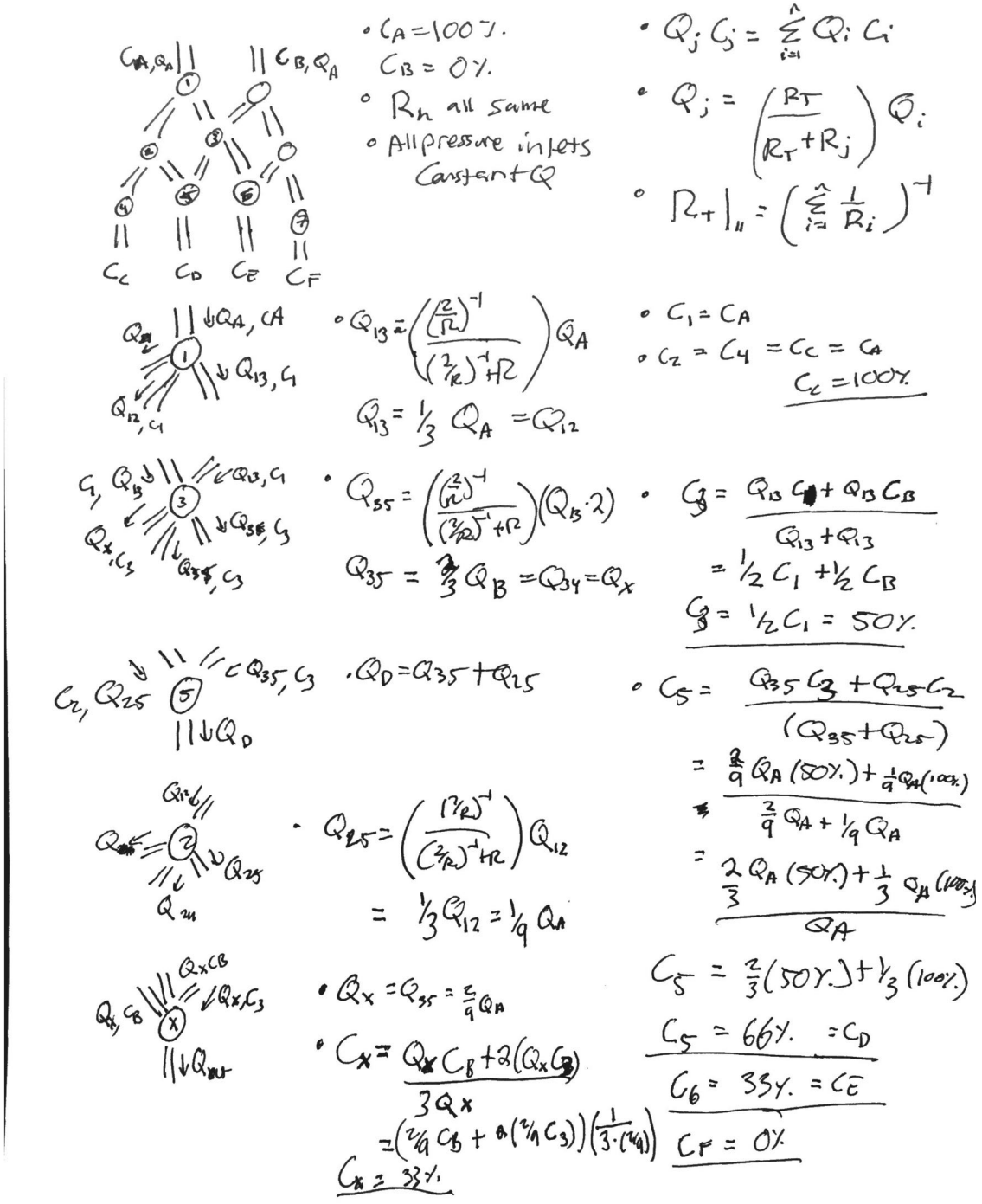

Figure 7.27: Example analytical calculations of concentration throughout the fluidic network of the 3D *tetrahedral*-based μ-CGG design.

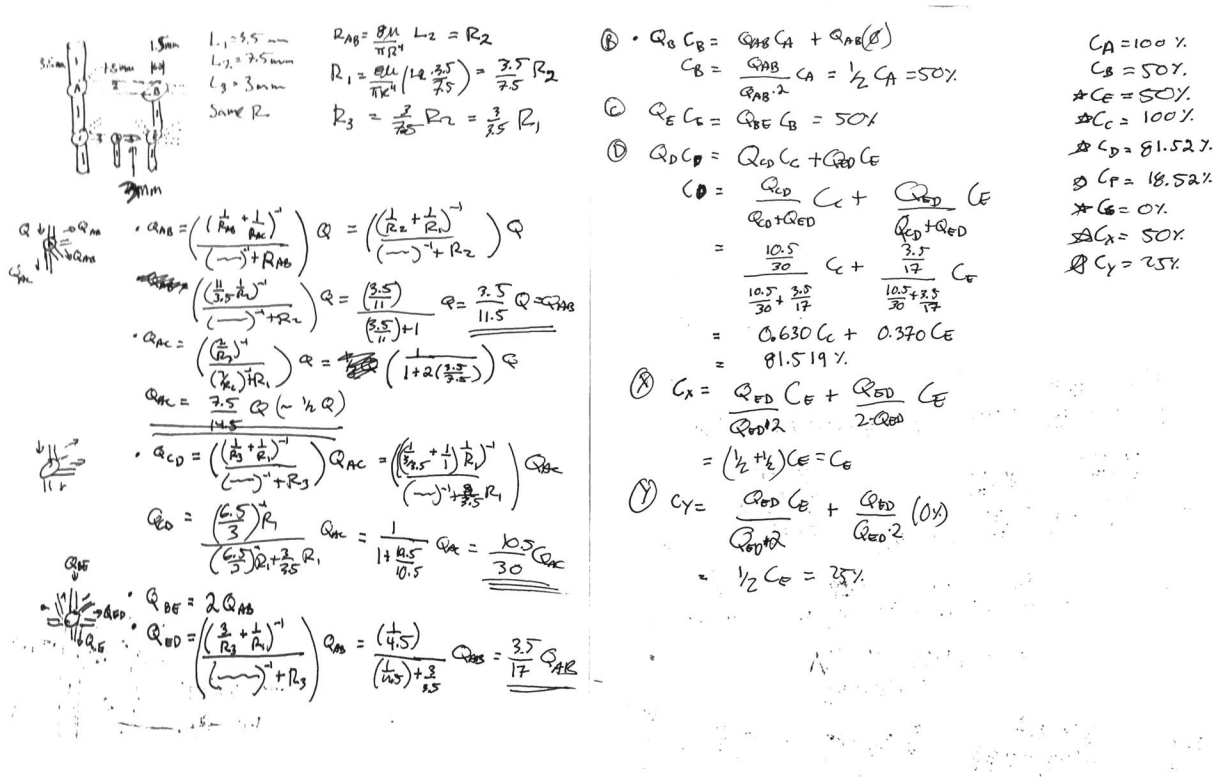

Figure 7.28: Example analytical calculations of concentration, 3D *layer*-based μ-CGG design.

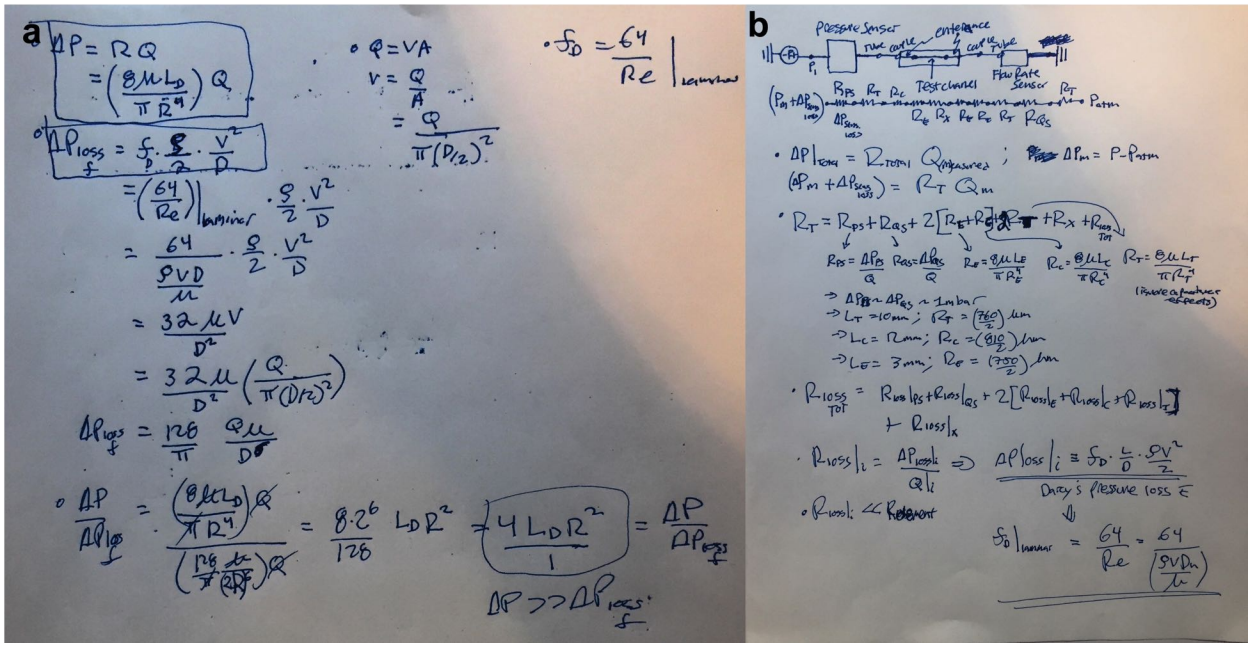

Figure 7.29: Example derivations of fluidic resistance inside circular microchannels.

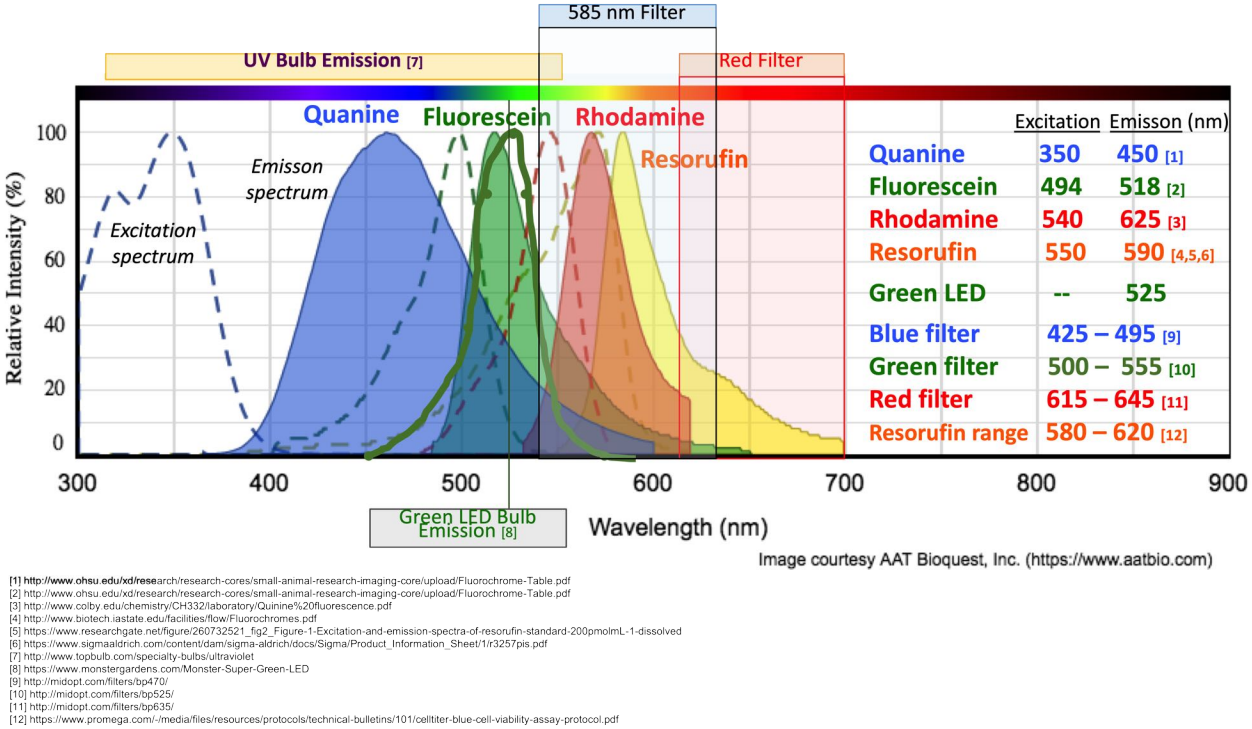

[1] http://www.ohsu.edu/xd/research/research-cores/small-animal-research-imaging-core/upload/Fluorochrome-Table.pdf
[2] http://www.ohsu.edu/xd/research/research-cores/small-animal-research-imaging-core/upload/Fluorochrome-Table.pdf
[3] http://www.colby.edu/chemistry/CH332/laboratory/Quinine%20fluorescence.pdf
[4] http://www.biotech.iastate.edu/facilities/flow/Fluorochromes.pdf
[5] https://www.researchgate.net/figure/260732521_fig2_Figure-1-Excitation-and-emission-spectra-of-resorufin-standard-200pmolmL-1-dissolved
[6] https://www.sigmaaldrich.com/content/dam/sigma-aldrich/docs/Sigma/Product_Information_Sheet/1/r3257pis.pdf
[7] http://www.topbulb.com/specialty-bulbs/ultraviolet
[8] https://www.monstergardens.com/Monster-Super-Green-LED
[9] http://midopt.com/filters/bp470/
[10] http://midopt.com/filters/bp525/
[11] http://midopt.com/filters/bp635/
[12] https://www.promega.com/-/media/files/resources/protocols/technical-bulletins/101/celltiter-blue-cell-viability-assay-protocol.pdf

Figure 7.30: Visual excitation and emission spectra for all chemicals used in this work.

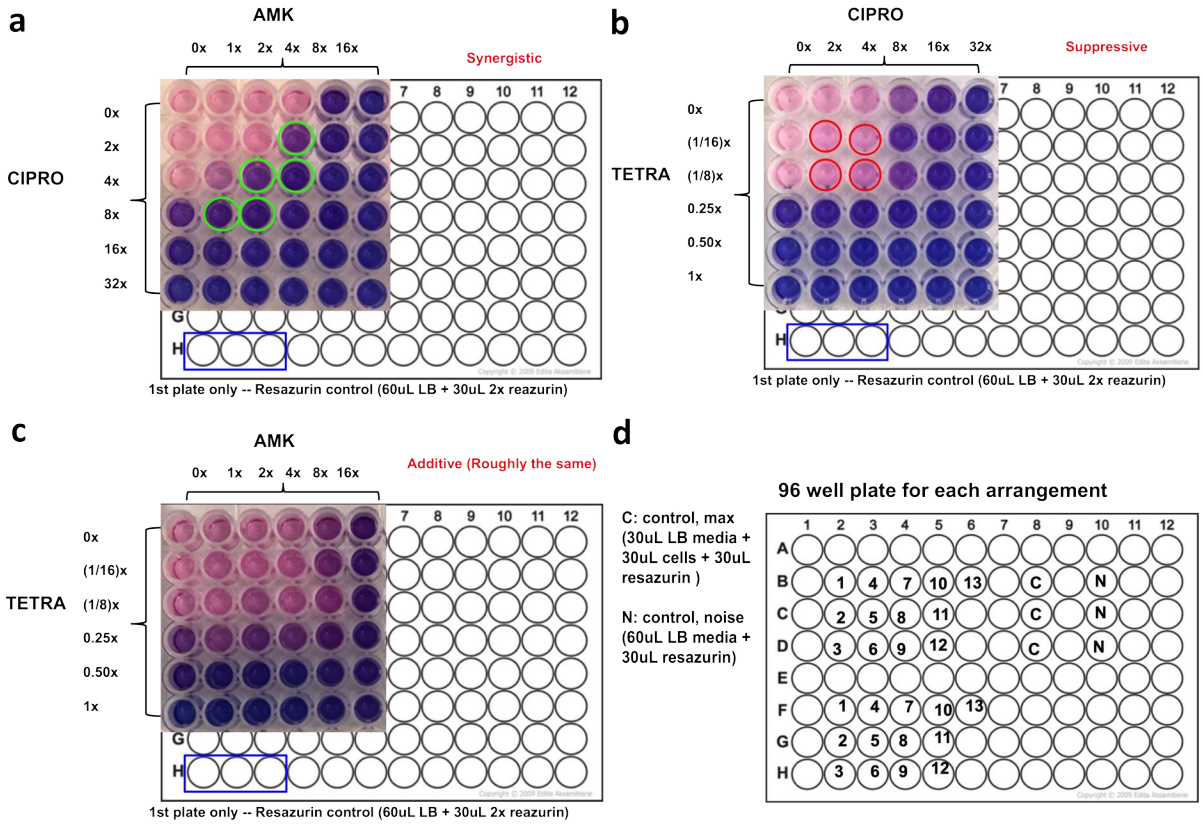

Figure 7.31: Bulk two-antibiotic combination drug screening experimental results of bacterial growth in manually-pipetted antibiotic solutions. **(a)** Ciprofloxacin and amikacin showing synergistic behavior in the green wells. **(b)** Ciprofloxacin and tetracycline showing antagonistic behavior in the green wells. **(c)** Tetracycline and amikacin showing additive behavior. **(d)** 96 well plate arrangement.

***Layer-based* Device**

Base Molecule / Species	Stock Solution	In 100% Output Well
Nitrofurantoin	~48 mg/L	~16 mg/L
Tetracycline	~12 mg/L	~4 mg/L
Trimethoprim	~1.5 mg/L	~0.50 mg/L
Resazurin	~100 mg/L	~33 mg/L
K12 Ampicillin-resistant *E. coli*	~$1*10^6$ cfu/mL	~$1*10^6$ cfu/mL

Antibiotic	Documented MIC	MIC (Device)
Nitrofurantoin	~4-8[e,f] mg/L	~8.3 mg/L
Tetracycline	~1-2[e,f] mg/L	~2.2 mg/L
Trimethoprim	~0.25[d,e] -1[f] mg/L	~0.26 mg/L

***Tetrahedral-based* Device**

Base Molecule / Species	Stock Solution	In 100% Output Well[1]
Amikacin	~48 mg/L	~16 mg/L
Tetracycline	~1.5 mg/L	~0.50 mg/L
Ciprofloxacin	~0.19 mg/L	~0.096 mg/L
Ampicillin	~96 mg/L	~32 mg/L
Resazurin	~125 mg/L	~42 mg/L
K12 Ampicillin-resistant *E. coli*	~$3*10^6$ cfu/mL	~$1*10^6$ cfu/mL

Antibiotic	Documented MIC	MIC (Bulk)	MIC (Device)
Ampicillin	~4-8[b,c,d,e] mg/L	N/A	N/A
Amikacin	~16[g] - 20[d] mg/L	~16.00 mg/L	~11 mg/L
Ciprofloxacin	< ~1[a,c,d,e,f] mg/L	~0.064 mg/L	~0.050 mg/L
Tetracycline	~1-2[e,f] mg/L	~0.50 mg/L	~0.26 mg/L

[1]Determined from bulk MIC well plating study experiments; 90µL total

Figure 7.32: Antibiotic stock solution and MIC value concentrations used in all experiments.

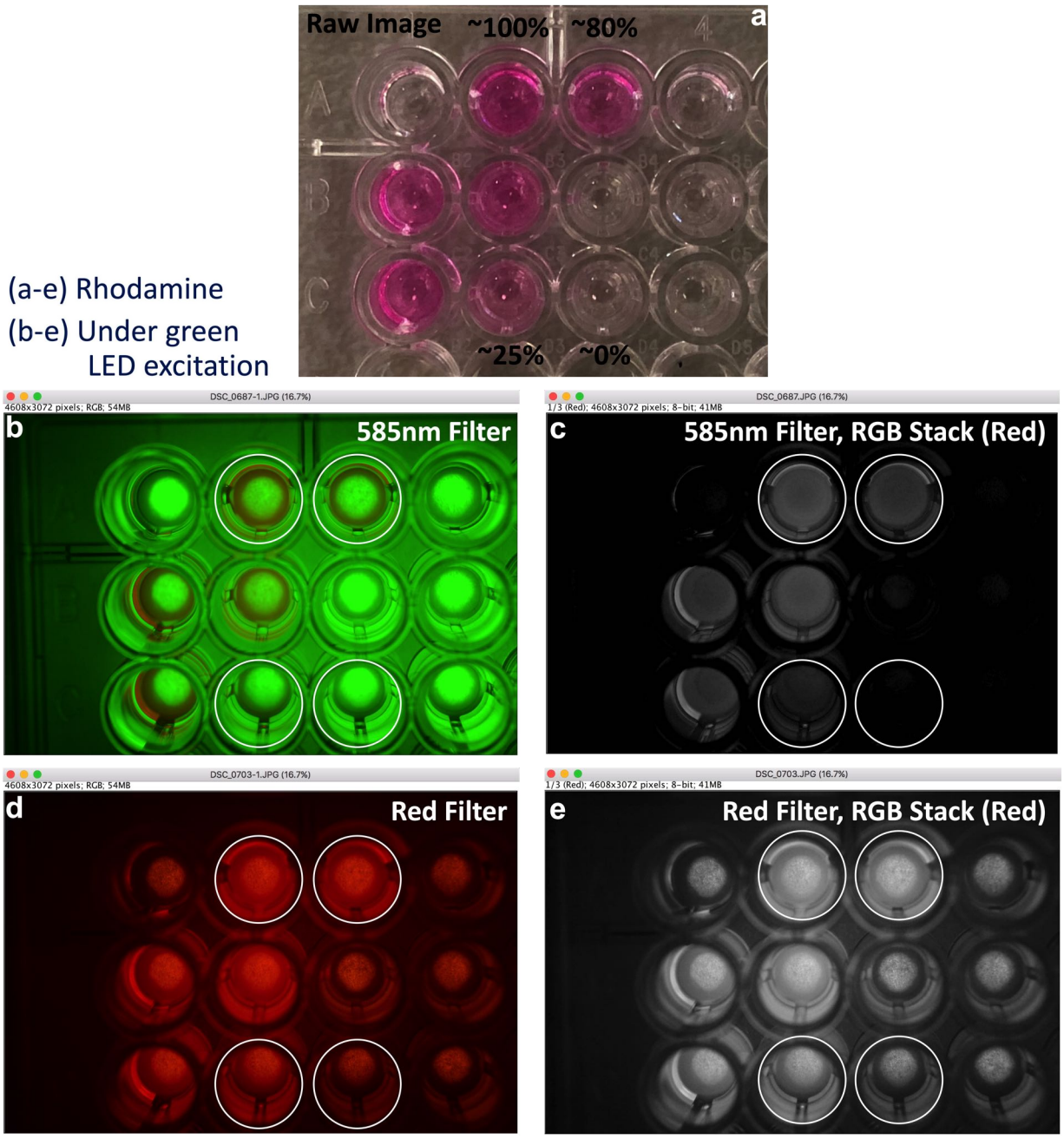

Figure 7.33: Visual aid showing example images of various stages of Fiji image analysis of a matrix of wells representing a gradient of rhodamine on a 96-well plate. **(a)** raw image of 96-well plate used for analysis; **(b)** raw image of 96-well plate imaged under a 585 nm bandpass filter; **(c)** Fiji-processed image of the red RGB stack channel of this image; **(d)** raw image of 96-well plate imaged under a red bandpass filter; **(c)** Fiji-processed image of the red RGB stack channel of this image. **(b)-(c)** Show four circles overlaid on the images as drawn by Fiji.

7.4 Integrated Finger-Powered Microfluidic Actuators Appendix

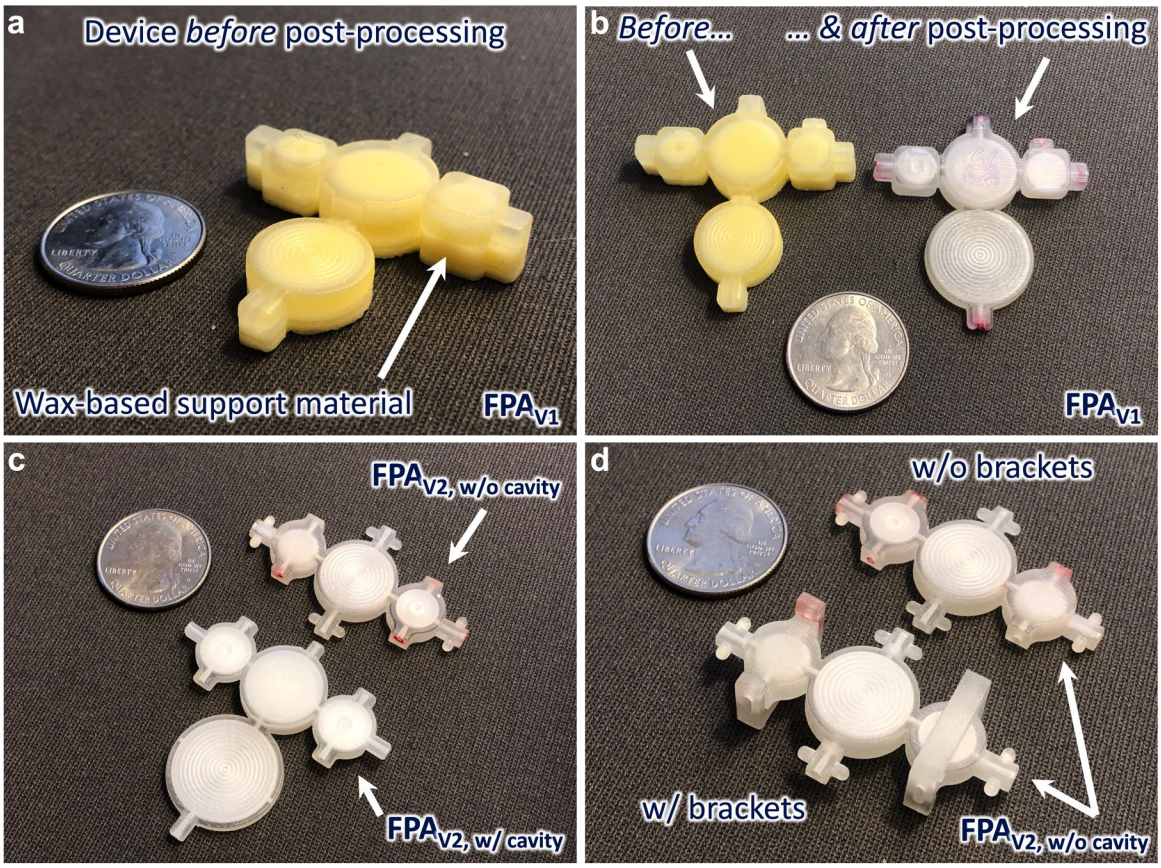

Figure 7.34: 3D printed fabrication results, FPA prototypes. **(a-b)** FPA$_{V1}$, **(c)** FPA$_{V2}$, **(d)** FPA$_{V2,in-line}$

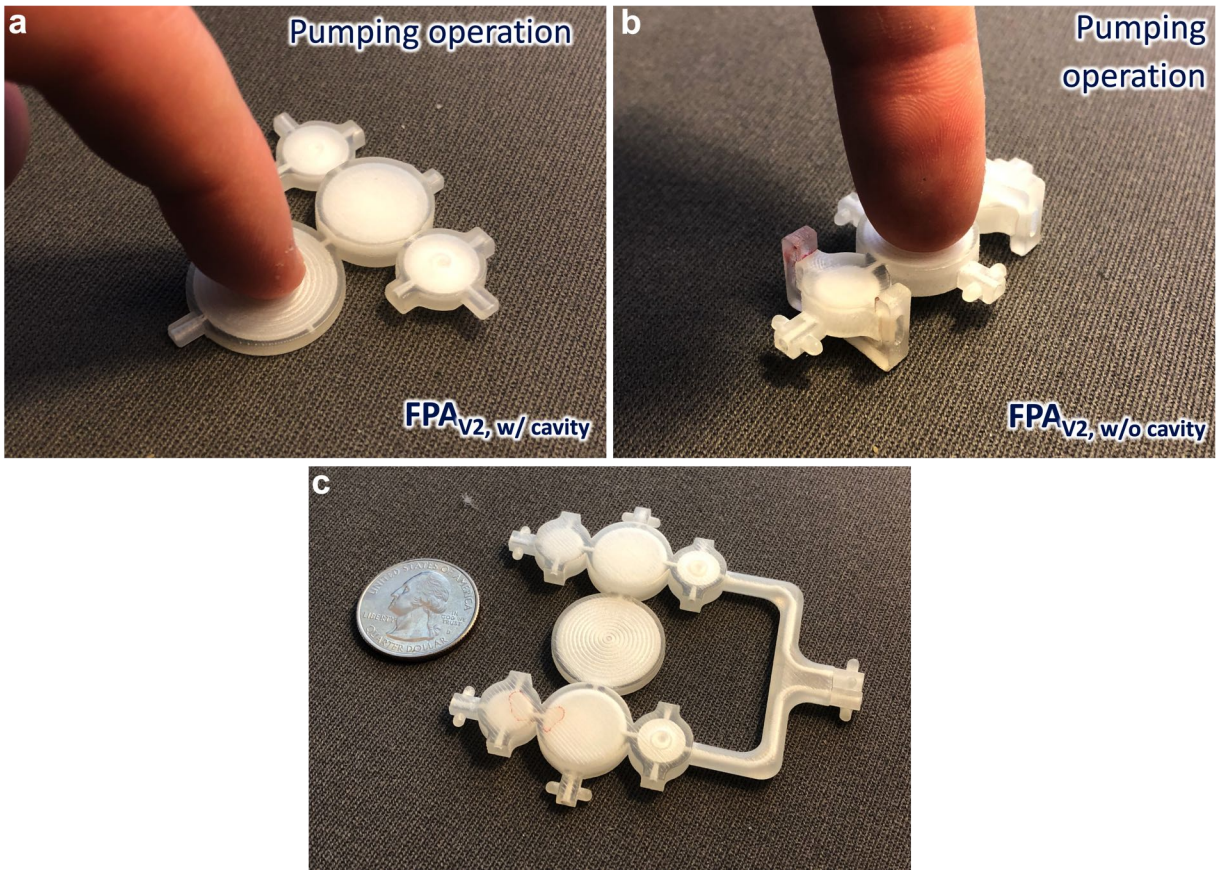

Figure 7.35: 3D printed fabrication results, FPA prototypes, showing finger-powered actuation. **(a)** FPA$_{V2}$, **(b)** FPA$_{V2,in-line}$, **(c)** FPA$_{V1,2fluid}$.

Figure 7.36: Experimental setup used to collect fluid output from each FPA prototype.

7.4.1 Image Analysis Protocol For Producing Raw Data From Experimental Fluorescent Images of FPA Prototypes

Rudra Mehta

To run this protocol, you'll need the following programs/packages:

- Python
  - Numpy
  - Matplotlib
- ImageJ
- OpenCV
- FFMPEG

Step 1. Obtain video of test as a `.mov` file. Find the number of pumps and save this value

Step 2. Trim the video to the desired start/stop times

Step 3. Convert the video to a raw `.avi` file

a. Run the following command from terminal:

```
ffmpeg -i [input_name].mov -an -vcodec rawvideo -filter:v
fps=30 -y [output_name].avi
```

b. Place the `.avi` file in a folder named `[output_name]`. This name will be referred to as `video_name` from here on.

Step 4. Open the `.avi` file with ImageJ as a stack

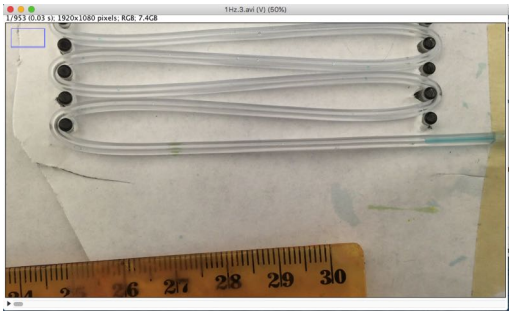

Step 5. Draw a line between 2 of the cm marks on the ruler, and press `m` to measure it. Grab the pixel distance reported, and convert it to a μm/pixel ratio. Save this value for later.

Step 6. [ImageJ] Crop video to region of interest (Note: takes a while for long videos)

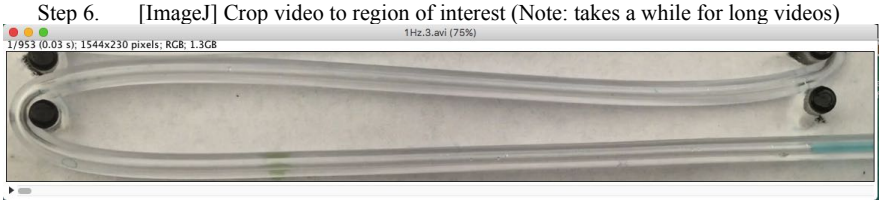

Step 7. [ImageJ] Split channels, keep the red channel window, close the others. Save this as an AVI, no compression, with the name `[video_name]_r.avi`.

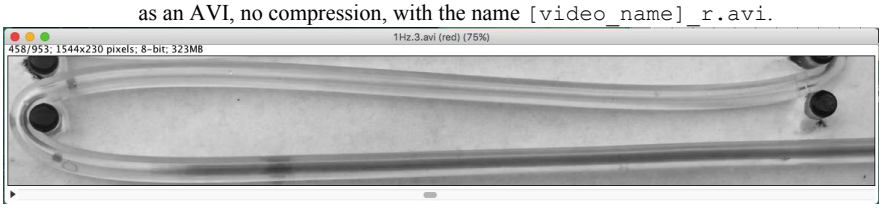

Step 8. [ImageJ] Save the first time slice as a PNG, and save the time slice where the fluid goes the farthest as another PNG. Then open both with ImageJ.

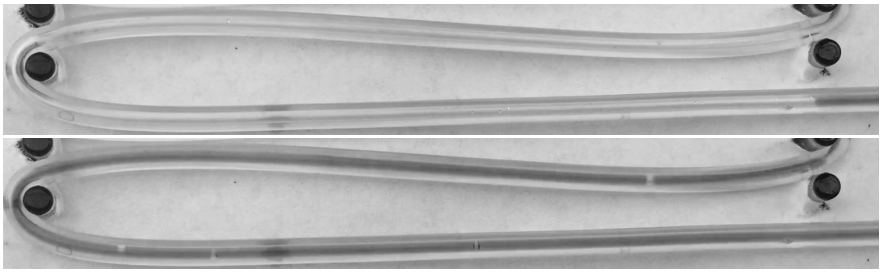

Step 9. [ImageJ] Go [Process]→[Image Calculator] and select the 'Difference' option.

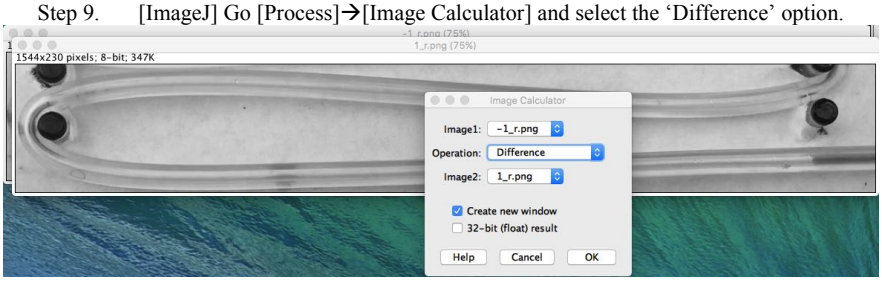

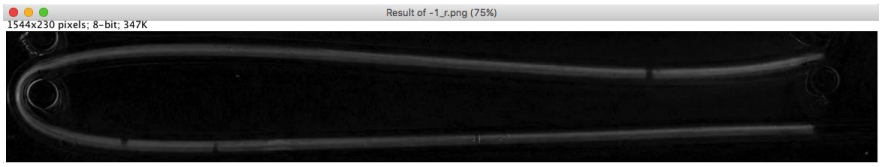

Step 10. [ImageJ] On the resulting image, go [Process]→[Binary]→[Make Binary]. You should see a white line, though the image might have some other white areas and the line might not be fully connected.

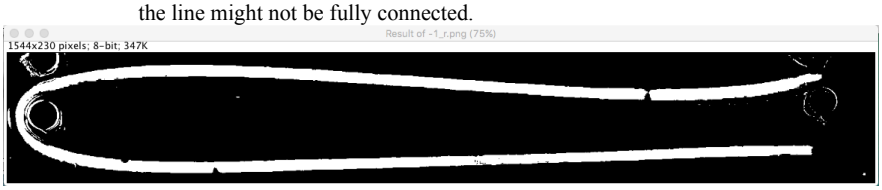

Step 11. [ImageJ] Go to color picker, and click on a white region of the image. Then, select the pencil tool, and draw in lines to connect the line.

Then if you go [Process]→[Binary]→[Fill Holes], it should result in one pure white line.

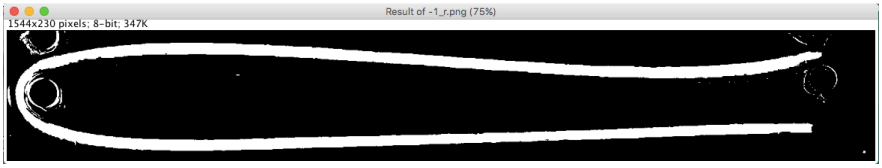

Step 12. [ImageJ] Go [Process]→[Binary]→[Open], then [Process]→[Binary]→[Dilate], and finally [Process]→[Binary]→[Skeletonize] to get a skeleton (single pixel-wide line) of the path the fluid takes in the video. However, the skeleton isn't perfect yet; we have to clean it up.

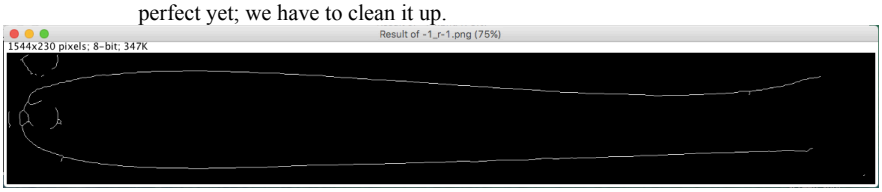

Step 13. [ImageJ] Using the drawing tools, clean up the skeleton. You should only be left with one white line (one pixel thick in all places). Each white pixel should be touching exactly 2 other white pixels when you look at all 8 contact points (edges + corners), excluding the first and last white pixel in the path. Also, extend both the beginning and ending of the path by at least 10 pixels.

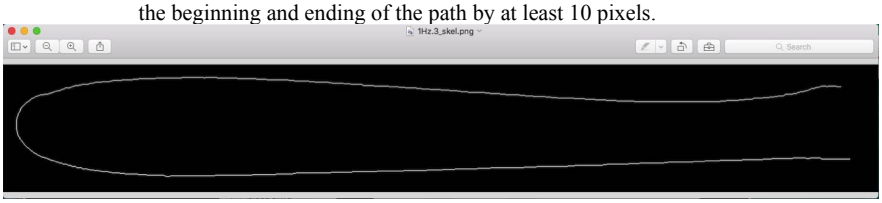

Save this skeleton as both a PNG and Text Image. The names should be `[video_name]_skel.png` and `[video_name]_skel.txt`

Step 14. [ImageJ, Python] Figure out the x,y coordinates of the first point in the path. Open the python file `FPP_skeleton.py` and locate the `valsPerVid` dictionary at the top. Add an entry to the dictionary, with the format

`"[video_name]":([x-coord],[y-coord])`

and filling in the regions inside the [ ]. Additionally, change the variable `name` to the `[video_name]` you entered in the dictionary.

```
# name : initial point (x,y)
valsPerVid = { "test1":(345,519), "1Hz.3":(1474,164)}

# Change this line for each video
name = "1Hz.3"
```

Step 15. [Python] Run `FPP_skeleton.py`. Make sure the equality printed out makes sense, or else you have an error in your skeleton. If you do, the smaller number is the pixel where something went wrong. Usually, the issue will be that you have an extra pixel along the path in that location.

```
calvisitor-10-105-164-142:fpp rudramehta$ python FPP_skeleton.py
2929 == 2929?
```

Step 16. [Python] Next, open `FPP_analyze.py`. Again, locate the `valsPerVid` dictionary at the top, and add another entry. This time, the format is

`"[video_name]":[image_threshold]`

Image threshold is the pixel brightness value that the program will use to determine if a given pixel contains fluid or not. You can determine this value by opening the [video_name]_r.avi file you saved in ImageJ, and inspecting pixel values for pixels containing and not containing fluid, and select an appropriate threshold from there. Run `FPP_analyze.py`.

```
# name : threshold
valsPerVid = { "test1":125, "1Hz.3":50 }

# Change this line to choose a video
name = "1Hz.3"
```

Step 17. [Python] Finally, open `FPP_graph.py`. Locate the `valsPerVid` dictionary at the top, and add another entry. This time, the format is

`"[video_name]":([num_pumps],[μm_per_pixel])`

where `num_pumps` and `μm_per_pixel` are from steps 1 and 2, respectively.

```
# name : (number of pumps, um per pixel)
valsPerVid = { "test1":(83, 84), "1Hz.3":(29,51.26)  }

# Change this line for each video
name = "1Hz.3"
```

Step 18. Run `FPP_graph.py`. The result will be placed in the folder you created in step 3.

To change the results displayed:

If you want to see different results, you can edit the file `FPP_graph.py`. It relies on a lot on Numpy and Matplotlib to create the graphs.

How it works:

The file's input is an array called `lens`. `lens` contains the length that the flow travelled, in pixels, every frame. Using `µm_per_pixel` and `radius`, these values are converted to µL pumped per frame. Furthermore, using `fps` (frames per second` when graphing, you can get a graph of Volume pumped (µL) vs Time (s).

Other possibilities with data:

Another thing you can do with the data is use numpy's gradient function to generate a derivative. If this is done after the unit conversion to get `lens` to a volume, you can graph the gradient vs time to get a Volume Flow Rate (µL/s) vs Time (s) graph.

You can also use the `num_pumps` value to plot Volume pumped (µL) vs Push.

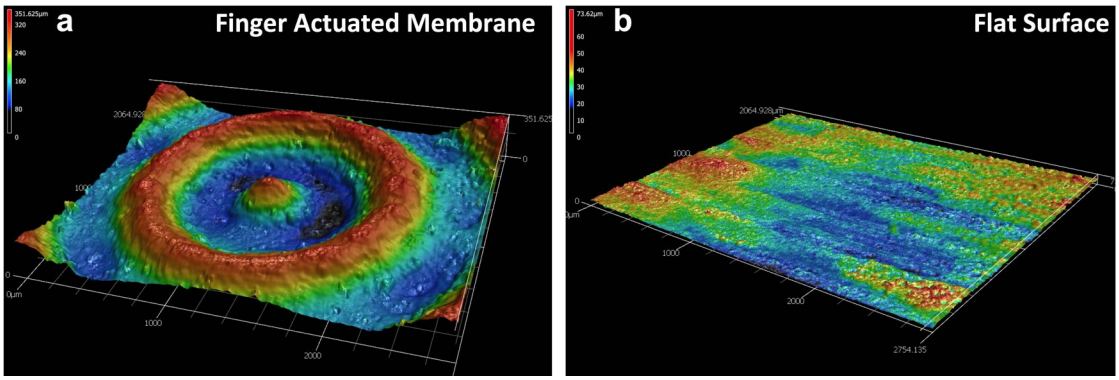

Figure 7.37: Scanning laser microscope images of fabrication results. **(a)** Finger-actuated 3D corrugated membrane. **(b)** Flat 3D printed surface.

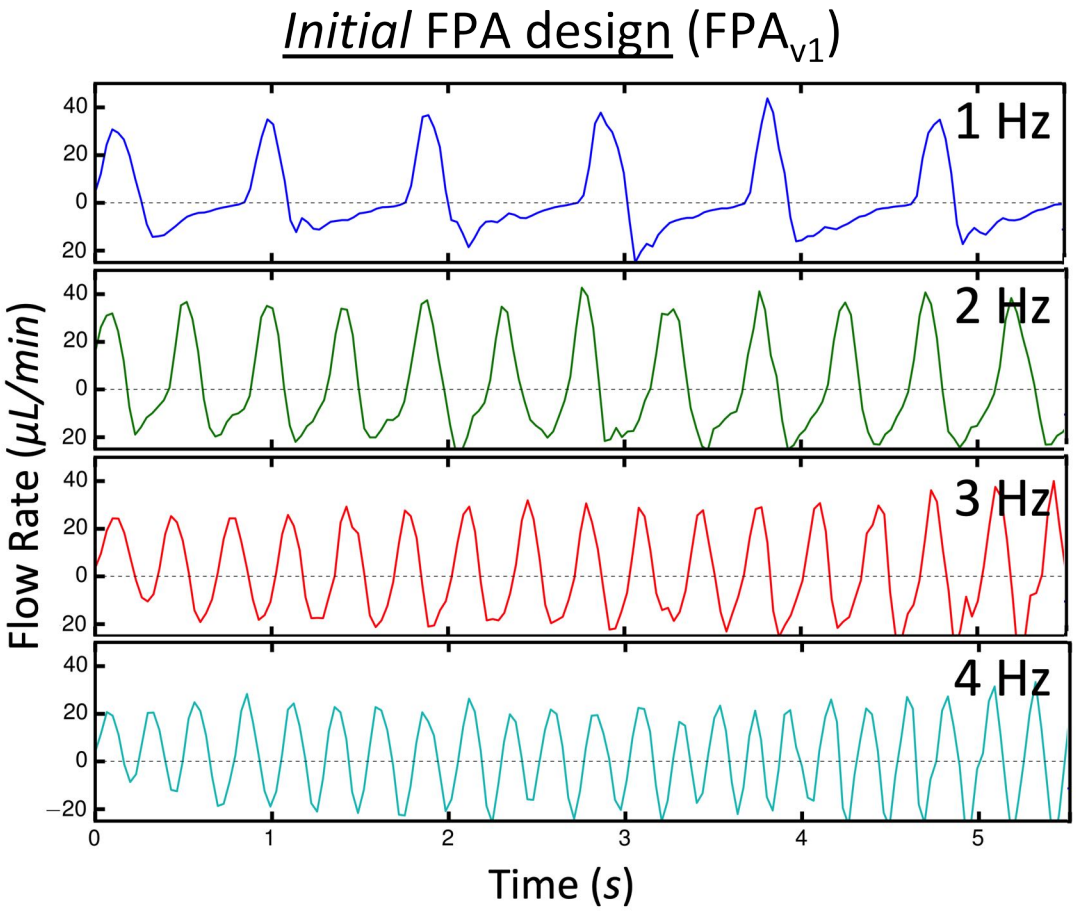

Figure 7.38: FPA$_{V1}$, raw flow rate *versus* time data for 1-4 Hz.

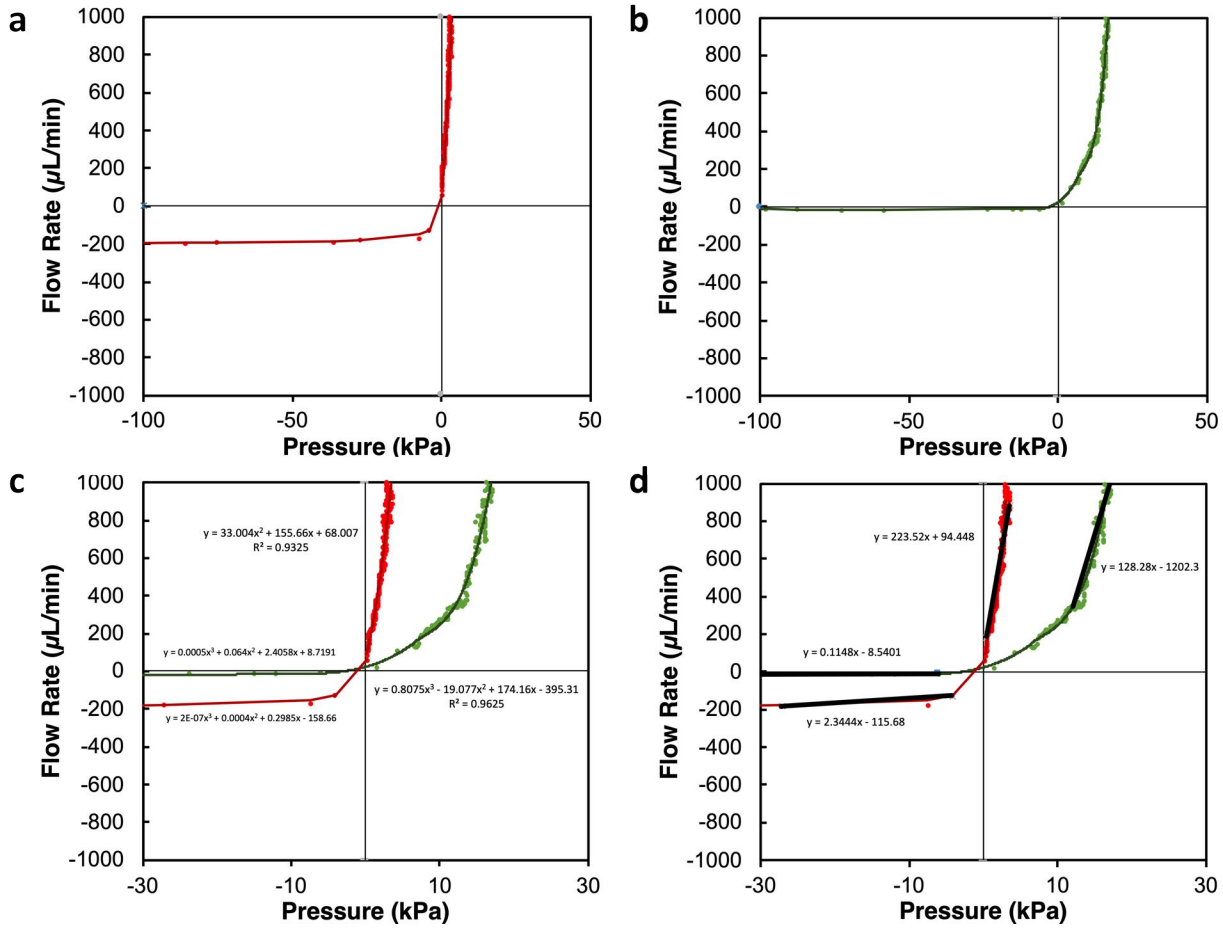

Figure 7.39: Fluidic diode experimental characterization results, Q-P plots. **(a)** Diode$_{V2}$ with bracket off. **(b)** Diode$_{V2}$ with bracket on. **(c)** Diode$_{V2}$ both states showing equations of approximate lines of best fit. **(d)** Diode$_{V2}$ both states showing equations of approximate linear lines of best fit for calculation of diodicity.

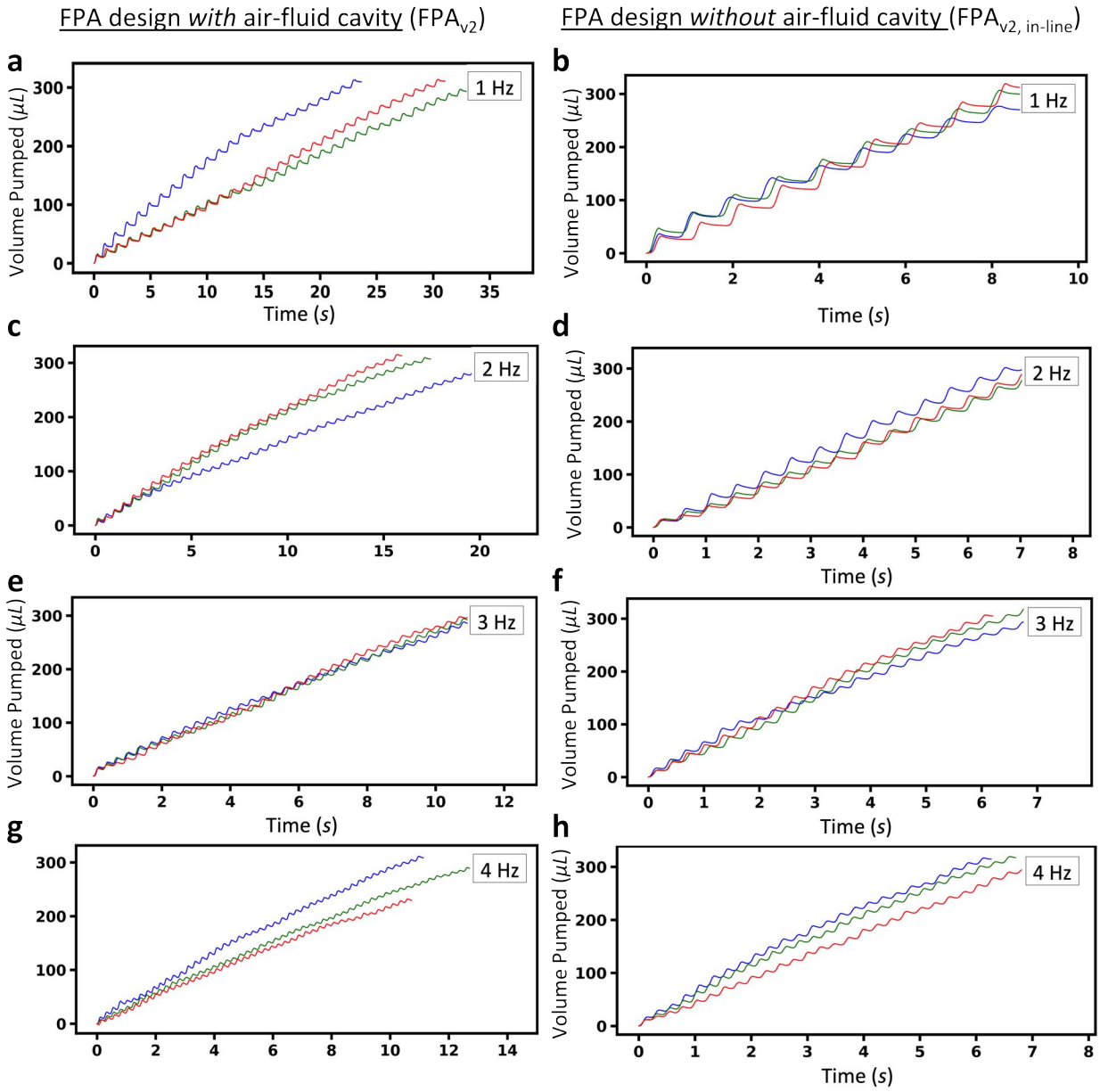

Figure 7.40: Experimental results for FPA$_{V2}$ and FPA$_{V2,in-line}$ prototypes, volume pumped *versus* time.

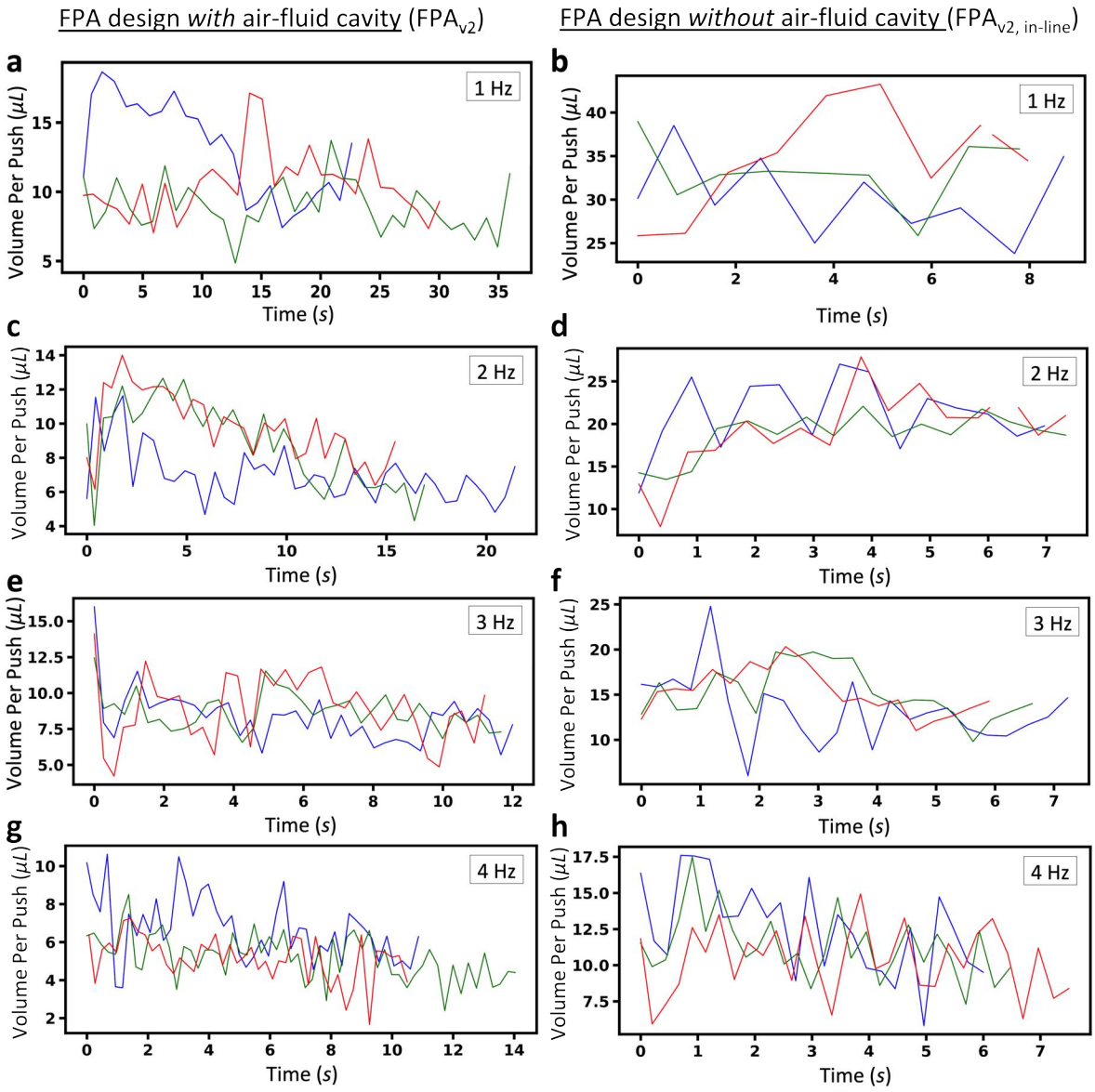

Figure 7.41: Experimental results for FPA$_{V2}$ and FPA$_{V2,in-line}$ prototypes,volume per push *versus* time.

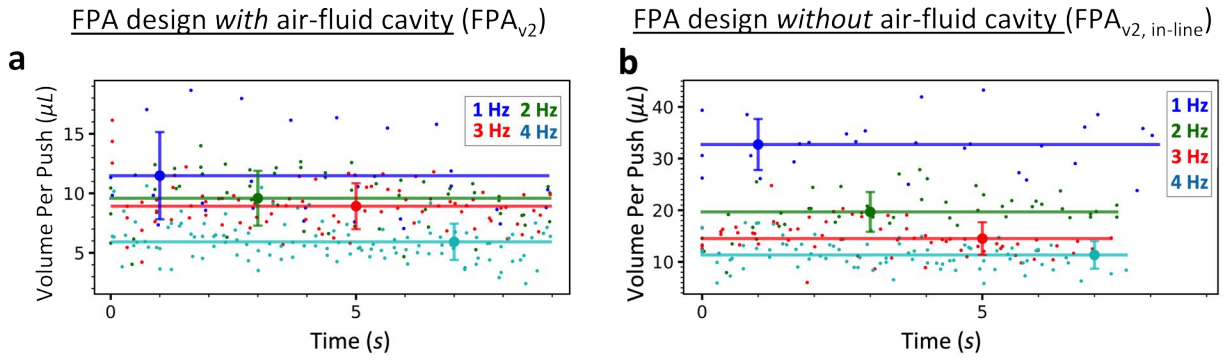

Figure 7.42: Experimental results for FPA$_{V2}$ and FPA$_{V2,in-line}$ prototypes, average volume per push.

Ratio of Volume Per Push (μL) in Forward to Reverse Directions ($V_{forward}$ / $V_{reverse}$)

FPA design *with* air-fluid cavity (FPA$_{v2}$)

a	Forward Flow (uL)	Standard Dev	Reverse Flow (uL)	Standard Dev
1Hz	14.62	3.13	4.38	0.87
2Hz	11.28	2.53	2.91	0.53
3Hz	12.04	2.05	3.40	0.70
4Hz	8.47	1.87	2.81	0.56

FPA design *without* air-fluid cavity (FPA$_{v2,\ in\text{-}line}$)

b	Forward Flow (uL)	Standard Dev	Reverse Flow (uL)	Standard Dev
1Hz	40.71	5.54	7.96	0.82
2Hz	23.86	6.19	4.67	2.03
3Hz	16.98	3.47	2.45	0.57
4Hz	13.88	2.98	2.52	0.62

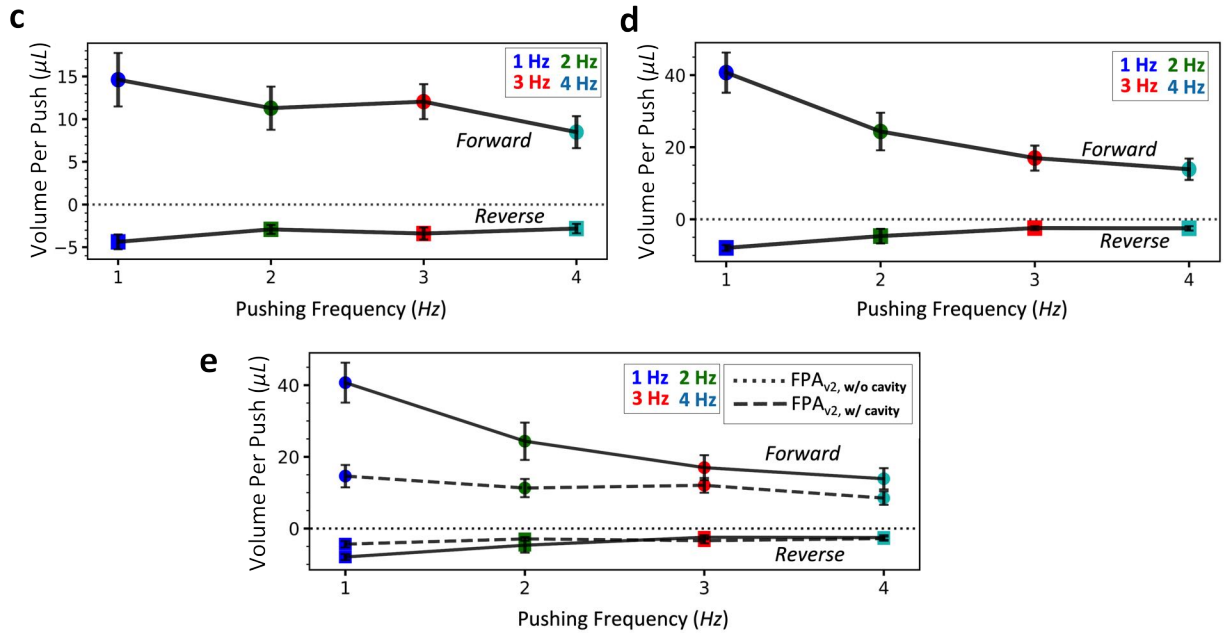

Figure 7.43: Experimental results for FPA$_{V2}$ and FPA$_{V2,in-line}$ prototypes, ratio of volume per push.

		FPA_{V2}		$FPA_{V2,in-line}$	
		Max (kPa)	Stdev (kPa)	Max (kPa)	Stdev (kPa)
Upper Channel	Forward Flow	17.107	5.216	31.353	5.377
	Reverse Flow	-7.062	2.231	-11.010	1.994
Lower Channel	Forward Flow	8.185	2.470	22.423	11.906
	Reverse Flow	-9.925	1.410	-5.409	3.189

Table 7.4: Mean maximum pressure values (average calculated from *six* experimental trials and standard deviations (*Stdev*) in units of kPa for FPA_{V2} and $FPA_{V2,in-line}$ prototypes with brackets installed.

7.5 Entirely-3D Printed, On-Site Biological Pathogen Detection Platform Appendix

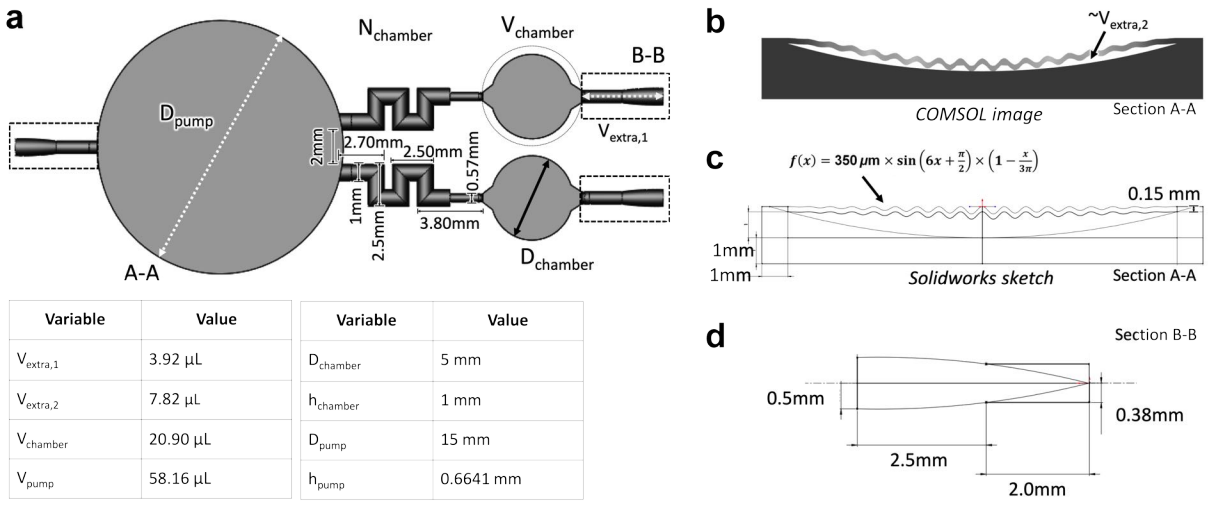

Variable	Value
$V_{extra,1}$	3.92 µL
$V_{extra,2}$	7.82 µL
$V_{chamber}$	20.90 µL
V_{pump}	58.16 µL

Variable	Value
$D_{chamber}$	5 mm
$h_{chamber}$	1 mm
D_{pump}	15 mm
h_{pump}	0.6641 mm

Figure 7.44: Diagram of the 3D pathogen detection platform design. **(a)** Microchannel network. **(b)** Illustration of membrane deformation from COMSOL results. **(c)** Cross-section of pressure source cavity. **(d)** Cross-section of liquid inlet.

7.5.1 Protocol For Calculating Volume of Fluid Collected Collected by the 3D Printed Prototype Platform From Fluid Uptake Verification Experimental Images

To calculate the volume of fluid collected into each chamber and tapered hollow regions on the 3D printed platform prototype, the following analytical protocol was used, analyzing the image of the prototype with collected fluid *on-chip* (**Fig. 5.5b**).

1. Open the raw image file corresponding to the prototype after fluid collection was performed in the Fiji image analysis software.
2. Set the measurement scale on the image. First measure the width of one of the 3D printed microchannel inlet structures on the fabricated prototype device using a pair of digital calipers and record this value in mm. In Fiji, draw a horizontal line on the image of the prototype of the microchannel inlet structure just measured physically between each of the edges. Then, click Analyze, Set Scale to define this line length as the dimension measured on the actual device, in mm. This now enables Fiji to calculate the size and area of each pixel on the image in terms of the approximate realistic length on the actual prototype.
3. Click Image, Type, RGB stack, and view the Blue Channel Stack image which shows the greatest contrast between the blue pixels of the fluid and the white pixels of the 3D printed material. All of the pixels now appear on greyscale between 1 and 255.
4. Draw circle around one of regions on the image which includes the chamber and each of the tapered regions that lead to the microchannels leading into and exiting the chamber. This is the analytical volume of interest. Crop the image to view only this region, which includes some of the background material surrounding this region.
5. Using Solidworks, analytically calculate the volume of the 3D solids model corresponding to this specific portion of the microchannel network using the volumetric analysis tool. This volume is experimentally determined to be 20.9 mm^3, which is equivalent to 20.9 μL.
6. In Fiji, click Analyze, Set measurements to open the measurement settings window. Check the boxes labeled *area*, *pixel min/max values* and *limit to threshold*. Close the window.
7. Click Image, Adjust, Threshold. In the open window, adjust the Limit Threshold sliders to isolate pixel magnitudes from 0 to 200, which isolates all of the blue pixels inside region from the white pixels defining the side walls of the chamber region. Click Ok, and the result is a group of white pixels representing all of the pixels corresponding to the color blue on the original image within this area.

8. Define a closed loop boundary using the manual line drawing tool to draw a random line through the black region on the image corresponding to the side wall of the region to isolate all of the white pixels. This now ensure that all white pixels within this defined geometry represent the blue pixels only corresponding to the fluid in the chamber and tapered regions.

9. Click Measure. The open window displays the total number of white pixels within the region and their total area (A) in units of mm^2.

10. Calculate the approximate volume of blue fluid inside the region assuming a uniform height (h) of the hollow region of 1mm, using the equation: $V = A*h$. The result of this calculation represents the approximate volume of blue fluid inside the region.

11. Repeat this procedure starting from the same raw experimental image, but analyzing the other of two hollow regions.

12. Repeat the experimental fluid collection and above analytical procedures thrice. The mean volume for the fluid collected in each region from experiments performed in triplicate, along with the standard deviation between the individual calculations, are shown in **Fig. 5.5c**.

7.5.2 Protocol For Calculating the R/G Ratio for Each Chamber on the 10-Chamber 3D Printed Array Devices For All Bacteriological Experiments

1. Open the raw image file of the 3D printed array part in the Fiji image analysis software.
2. Draw a circle around one chamber at a time, ensuring to enclose as much of the area as possible without capturing any air bubbles or shadows from the steel plugs.
3. Click Color Histogram. A new window appears showing the mean, mode and standard deviation of the red, green and blue magnitude intensities of all of the pixels in the area enclosed in the circle.
4. Manually record the mean red and green intensity values for that chamber in an Excel spreadsheet.
5. In Excel, calculate the ratio of the mean red and green intensity values.
6. Repeat this procedure on the same raw experimental image analyzing all of the other of chambers, saving all of the mean red and green intensity values and the ratio between them in the same Excel file.
7. Repeat this procedure for all three images from the three separate 3D printed array devices from experiments performed in triplicate.
8. Calculate a mean R/G ratio value for each chamber from all three experimental images.
9. Plot all mean R/G ratios for each chamber number on a log-scale using MATLAB; results are shown in **Fig. 5.5c, 5.6c**.

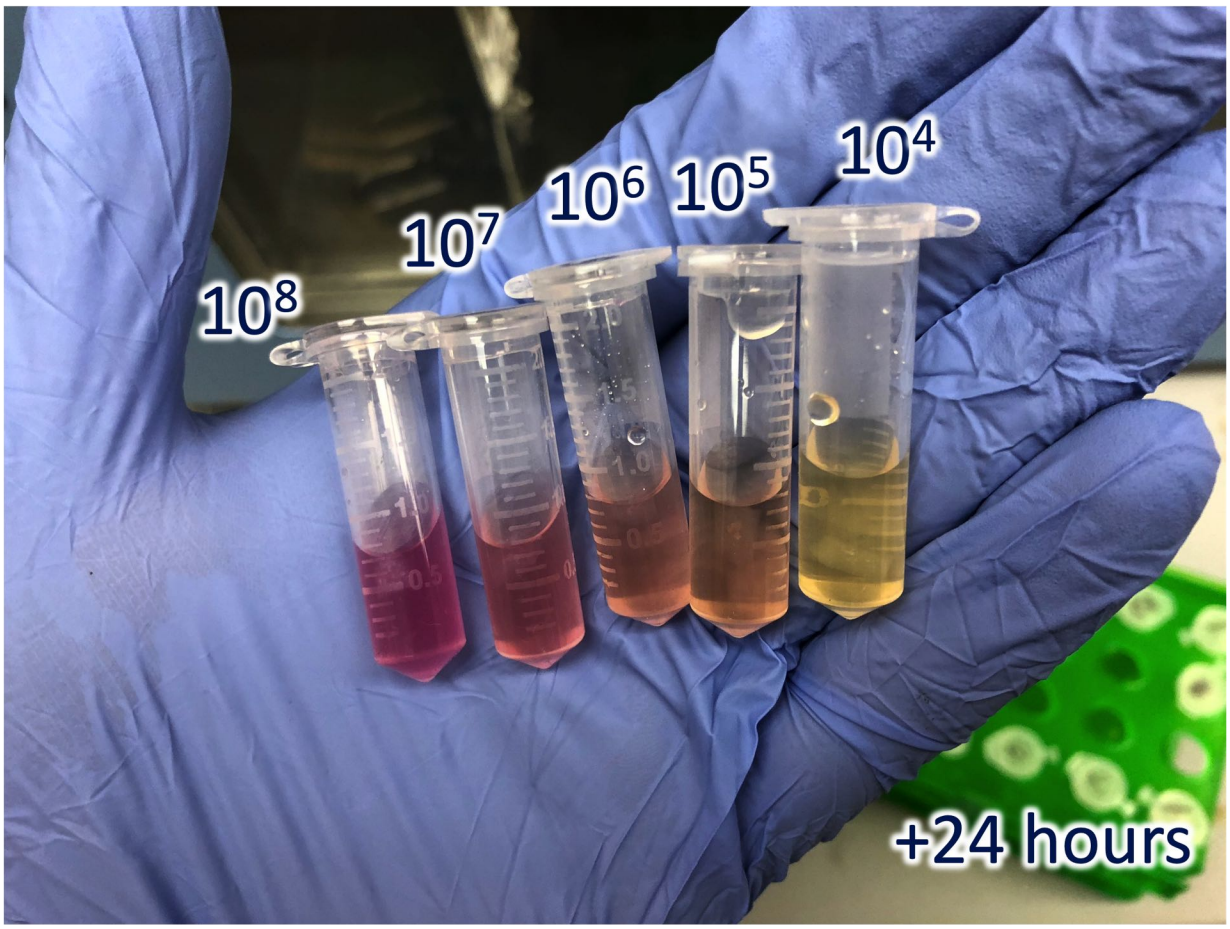

Figure 7.45: Results of bacteria growth in tubes after 24 hours, containing bacteria solution, CPRG colorimetric reagent and LB growth media.

Known *enzyme-specific* colorimetric reagent-bacteria pairs:

Bacteria	Reagent	Target Enzyme	Color Change
E. coli	Chlorophenol red β-galactopyranoside (CPRG)	β- galactosidase	
Salmonella enterica	5-bromo-6-chloro-3-indolyl caprylate	37–39 & esterase	
Listeria monocytogenes	Phospholipase C (PI-PLC) + 5-bromo-4-chloro-3- indolyl-myo-inositol phosphate (X-InP)	35,36 phosphatidylinositol	

Jokerst et al., *Analytical* Chemistry, 2012
Adkins et al., *Analytical* Chemistry, 2017

Figure 7.46: Different known bacterial enzyme-colorimetric reagent pairs.

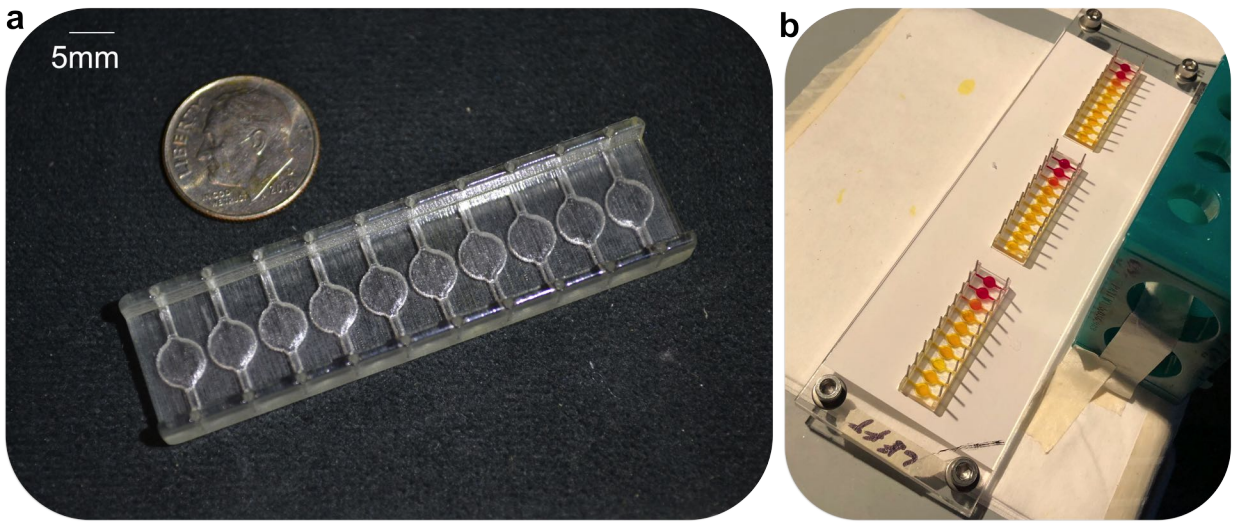

Figure 7.47: 3D printed 10-chamber arrays used for bacteriological experiments.

7.6 Bonus Features

Figure 7.48: MEMS 2017 conference awards ceremony, Las Vegas, NV, January 2017. Eric winning the Outstanding Student Paper Award.

Figure 7.49: Alison Long, Josh Chen, Professor Liwei Lin, Eric Sweet and Ilbey Karakurt, co-authors on the MEMS 2017 paper, February 2017.

Figure 7.50: Logos

Figure 7.51: Fluorescent solutions.

Figure 7.52: Thank you, Cal! Go Bears!

Bibliography

[1] M Kleiber et al. *Advances in Mechanics: Theoretical, Computational and Interdisciplinary Issues: Proceedings of the 3rd Polish Congress of Mechanics (PCM) and 21st International Conference on Computer Methods in Mechanics (CMM), Gdansk, Poland, 8-11 September 2015*. CRC Press, 2016. ISBN: 9781315645063. URL: https://books.google.com/books?id=u-gbDAAAQBAJ.

[2] Felix J H Hol and Cees Dekker. "Zooming in to see the bigger picture: Microfluidic and nanofabrication tools to study bacteria". In: *Science* 346.6208 (2014). ISSN: 0036-8075. DOI: 10.1126/science.1251821. URL: http://science.sciencemag.org/content/346/6208/1251821.

[3] Chandra M. Pandey et al. "Microfluidics Based Point-of-Care Diagnostics". In: *Biotechnology Journal* 13.1 (2018). ISSN: 18607314. DOI: 10.1002/biot.201700047.

[4] Xiaojun Chen et al. "3D printed microfluidic chip for multiple anticancer drug combinations". In: *Sensors and Actuators, B: Chemical* 276.January (2018), pp. 507–516. ISSN: 09254005. DOI: 10.1016/j.snb.2018.08.121. URL: https://doi.org/10.1016/j.snb.2018.08.121.

[5] Wei-Heong Tan and Shoji Takeuchi. "A trap-and-release integrated microfluidic system for dynamic microarray applications". In: *Proceedings of the National Academy of Sciences* 104.4 (Jan. 2007), 1146 LP –1151. DOI: 10.1073/pnas.0606625104. URL: http://www.pnas.org/content/104/4/1146.abstract.

[6] Adam Bange, H Brian Halsall, and William R Heineman. "Microfluidic immunosensor systems". In: *Biosensors and Bioelectronics* 20.12 (2005), pp. 2488–2503. ISSN: 0956-5663. DOI: https://doi.org/10.1016/j.bios.2004.10.016. URL: http://www.sciencedirect.com/science/article/pii/S095656630400483X.

[7] Alexander R Jafek et al. "Instrumentation for xPCR Incorporating qPCR and HRMA". In: *Analytical Chemistry* 90.12 (June 2018), pp. 7190–7196. ISSN: 0003-2700. DOI: 10.1021/acs.analchem.7b05176. URL: https://doi.org/10.1021/acs.analchem.7b05176.

[8] Carl L Hansen et al. "A robust and scalable microfluidic metering method that allows protein crystal growth by free interface diffusion". In: *Proceedings of the National Academy of Sciences* 99.26 (Dec. 2002), 16531 LP –16536. DOI: 10.1073/pnas.262485199. URL: http://www.pnas.org/content/99/26/16531.abstract.

[9] Shuichi Takayama et al. "Subcellular positioning of small molecules". In: *Nature* 411.6841 (2001), p. 1016. ISSN: 1476-4687. DOI: 10.1038/35082637. URL: https://doi.org/10.1038/35082637.

[10] Majid Ebrahimi Warkiani et al. "Membrane-less microfiltration using inertial microfluidics". In: *Scientific Reports* 5.1 (2015), p. 11018. ISSN: 2045-2322. DOI: 10.1038/srep11018. URL: https://doi.org/10.1038/srep11018.

[11] Wei-Heong Tan and Shoji Takeuchi. "Dynamic microarray system with gentle retrieval mechanism for cell-encapsulating hydrogel beads". In: *Lab on a Chip* 8.2 (2008), pp. 259–266. ISSN: 1473-0197. DOI: 10.1039/B714573J. URL: http://dx.doi.org/10.1039/B714573J.

[12] Kaori Kuribayashi-Shigetomi, Hiroaki Onoe, and Shoji Takeuchi. "Cell Origami: Self-Folding of Three-Dimensional Cell-Laden Microstructures Driven by Cell Traction Force". In: *PLOS ONE* 7.12 (Dec. 2012), e51085. URL: https://doi.org/10.1371/journal.pone.0051085.

[13] Andrew Evan Kamholz and Paul Yager. "Theoretical analysis of molecular diffusion in pressure-driven laminar flow in microfluidic channels". In: *Biophysical Journal* 80.1 (2001), pp. 155–160. ISSN: 00063495. DOI: 10.1016/S0006-3495(01)76003-1. URL: http://dx.doi.org/10.1016/S0006-3495(01)76003-1.

[14] Chunfei Hu et al. "Microfluidic Platforms for Gradient Generation and its Applications". In: *Biochemistry and Analytical Biochemistry* 06.02 (2017). DOI: 10.4172/2161-1009.1000320.

[15] Douglas P Holmes. "Confined Fluid Flow: Microfluidics and Capillarity". In: *Mechanical Engineering, Boston University* Sapienza U (2015).

[16] Skarphedinn Halldorsson et al. "Advantages and challenges of microfluidic cell culture in polydimethylsiloxane devices". In: *Biosensors and Bioelectronics* 63 (2015), pp. 218–231. ISSN: 18734235. DOI: 10.1016/j.bios.2014.07.029. URL: http://dx.doi.org/10.1016/j.bios.2014.07.029.

[17] Kathleen E. Mach, Pak Kin Wong, and Joseph C. Liao. "Biosensor diagnosis of urinary tract infections: A path to better treatment?" In: *Trends in Pharmacological Sciences* 32.6 (2011), pp. 330–336. ISSN: 18733735. DOI: 10.1016/j.tips.2011.03.001. URL: http://dx.doi.org/10.1016/j.tips.2011.03.001.

[18] Ali Asgar S Bhagat, Erik T K Peterson, and Ian Papautsky. "A passive planar micromixer with obstructions for mixing at low Reynolds numbers". In: *Journal of Micromechanics and Microengineering* 17.5 (2007), pp. 1017–1024. ISSN: 09601317. DOI: 10.1088/0960-1317/17/5/023.

[19] Jonathan Knight. "Honey, I shrunk the lab". In: *Nature* 418.6897 (2002), pp. 474–475. ISSN: 00280836. DOI: 10.1038/418474a.

[20] S. Hardt et al. "Passive micromixers for applications in the microreactor and microTAS fields". In: *Microfluidics and Nanofluidics* 1.2 (2005), pp. 108–118. ISSN: 16134982. DOI: 10.1007/s1040400400290.

[21] Jessica Melin and Stephen R. Quake. "Microfluidic large-scale integration: the evolution of design rules for biological automation." In: *Annual review of biophysics and biomolecular structure* 36 (2007), pp. 213–231. ISSN: 1056-8700. DOI: 10.1146/annurev.biophys.36.040306.132646. arXiv: arXiv:1011.1669v3. URL: http://www.ncbi.nlm.nih.gov/pubmed/17269901.

[22] K Plevniak, M Campbell, and M He. "3D printed microfluidic mixer for point-of-care diagnosis of anemia". In: *2016 38th Annual International Conference of the IEEE Engineering in Medicine and Biology Society (EMBC)*. 2016, pp. 267–270. ISBN: VO -. DOI: 10.1109/EMBC.2016.7590691.

[23] Jae Hwan Jung, Gha-Young Kim, and Tae Seok Seo. "An integrated passive micromixer magnetic separation capillary electrophoresis microdevice for rapid and multiplex pathogen detection at the single cell level". In: *Lab on a Chip* 11.20 (2011), pp. 3465–3470. ISSN: 1473-0197. DOI: 10.1039/C1LC20350A. URL: http://dx.doi.org/10.1039/C1LC20350A.

[24] Armando Cosentino et al. "An efficient planar accordion-shaped micromixer: from biochemical mixing to biological application". In: *Scientific Reports* 5 (Dec. 2015), p. 17876. URL: https://doi.org/10.1038/srep17876%20http://10.0.4.14/srep17876%20https://www.nature.com/articles/srep17876#supplementary-information.

[25] Paul Yager et al. "Microfluidic diagnostic technologies for global public health". In: *Nature* 442.7101 (2006), pp. 412–418. ISSN: 1476-4687. DOI: 10.1038/nature05064. URL: https://doi.org/10.1038/nature05064.

[26] Werner Karl Schomburg. "Introduction to Microsystem Design". In: 1 (2011). DOI: 10.1007/978-3-642-19489-4. URL: http://link.springer.com/10.1007/978-3-642-19489-4.

[27] David C Duffy et al. "Rapid Prototyping of Microfluidic Systems in Poly(dimethylsiloxane)". In: *Analytical Chemistry* 70.23 (1998), pp. 4974–4984. DOI: 10.1021/ac980656z. URL: http://dx.doi.org/10.1021/ac980656z.

[28] G D Aumiller et al. "Submicrometer resolution replication of relief patterns for integrated optics". In: *Journal of Applied Physics* 45.10 (Oct. 1974), pp. 4557–4562. ISSN: 0021-8979. DOI: 10.1063/1.1663087. URL: https://doi.org/10.1063/1.1663087.

[29] Marc A Unger et al. "Monolithic Microfabricated Valves and Pumps by Multilayer Soft Lithography". In: *Science* 288.5463 (2000), pp. 113–116. ISSN: 0036-8075. DOI: 10.1126/science.288.5463.113. URL: http://science.sciencemag.org/content/288/5463/113.

[30] Todd Thorsen, Sebastian J Maerkl, and Stephen R Quake. "Microfluidic Large-Scale Integration". In: *Science* 298.5593 (2002), pp. 580–584. ISSN: 0036-8075. DOI: 10.1126/science.1076996. URL: http://science.sciencemag.org/content/298/5593/580.

[31] M. L. Adams et al. "Polydimethylsiloxane based microfluidic diode". In: *Journal of Micromechanics and Microengineering* 15.8 (2005), pp. 1517–1521. ISSN: 09601317. DOI: 10.1088/0960-1317/15/8/020.

[32] James A Weaver et al. "Static control logic for microfluidic devices using pressure-gain valves". In: *Nat Phys* 6.3 (2010), pp. 218–223. URL: http://dx.doi.org/10.1038/nphys1513.

[33] Bruce Gale et al. "A Review of Current Methods in Microfluidic Device Fabrication and Future Commercialization Prospects". In: *Inventions* 3.3 (2018), p. 60. DOI: 10.3390/inventions3030060.

[34] Peter Tseng et al. "Research highlights: printing the future of microfabrication". In: *Lab Chip* 14.9 (2014), pp. 1491–1495. DOI: 10.1039/C4LC90023E. URL: http://dx.doi.org/10.1039/C4LC90023E.

[35] J Y Kim et al. "Automatic aligning and bonding system of PDMS layer for the fabrication of 3D microfluidic channels". In: *Sensors and Actuators A: Physical* 119.2 (2005), pp. 593–598. ISSN: 0924-4247. DOI: http://dx.doi.org/10.1016/j.sna.2004.09.023. URL: http://www.sciencedirect.com/science/article/pii/S0924424704007071.

[36] Tuan D. Ngo et al. "Additive manufacturing (3D printing): A review of materials, methods, applications and challenges". In: *Composites Part B: Engineering* 143.December 2017 (2018), pp. 172–196. ISSN: 13598368. DOI: 10.1016/j.compositesb.2018.02.012. URL: https://doi.org/10.1016/j.compositesb.2018.02.012.

[37] P F ONeill et al. "Advances in three-dimensional rapid prototyping of microfluidic devices for biological applications". In: *Biomicrofluidics* 8.5 (2014). DOI: http://dx.doi.org/10.1063/1.4898632. URL: http://scitation.aip.org/content/aip/journal/bmf/8/5/10.1063/1.4898632.

[38] Feng Li et al. "One-Step Fabrication of a Microfluidic Device with an Integrated Membrane and Embedded Reagents by Multimaterial 3D Printing". In: *Analytical Chemistry* 89.8 (2017), pp. 4701–4707. ISSN: 15206882. DOI: 10.1021/acs.analchem.7b00409.

[39] Liangcai Xiong, Peng Chen, and Quansheng Zhou. "Adhesion promotion between PDMS and glass by oxygen plasma pre-treatment". In: *Journal of Adhesion Science and Technology* 28.11 (2014), pp. 1046–1054. ISSN: 15685616. DOI: 10.1080/01694243.2014.883774.

[40] Say Hwa Tan et al. "Oxygen plasma treatment for reducing hydrophobicity of a sealed polydimethylsiloxane microchannel". In: *Biomicrofluidics* 4.3 (2010), pp. 1–8. ISSN: 19321058. DOI: 10.1063/1.3466882.

[41] Martin D. Brennan, Megan L. Rexius-Hall, and David T. Eddington. "A 3D-printed oxygen control insert for a 24-well plate". In: *PLoS ONE* 10.9 (2015), pp. 1–9. ISSN: 19326203. DOI: 10.1371/journal.pone.0137631. URL: http://dx.doi.org/10.1371/journal.pone.0137631.

[42] Chia Wen Tsao and Don L. DeVoe. "Bonding of thermoplastic polymer microfluidics". In: *Microfluidics and Nanofluidics* 6.1 (2009), pp. 1–16. ISSN: 16134982. DOI: 10.1007/s10404-008-0361-x.

[43] Gregory W. Bishop. "3D printed microfluidic devices". In: *Microfluidics for Biologists: Fundamentals and Applications* 8.2 (2016), pp. 103–113. ISSN: 1758-5090. DOI: 10.1007/978-3-319-40036-5_4. URL: http://dx.doi.org/10.1088/1758-5090/8/2/022001.

[44] Ho Nam Chan et al. "Direct, one-step molding of 3D-printed structures for convenient fabrication of truly 3D PDMS microfluidic chips". In: *Microfluidics and Nanofluidics* 19.1 (2015), pp. 9–18. ISSN: 16134990. DOI: 10.1007/s10404-014-1542-4.

[45] Chengpeng Chen et al. "3D-printed microfluidic devices: fabrication, advantages and limitations-a mini review". In: *Analytical Methods* 8 (2016), pp. 6005–6012. ISSN: 1759-9660. DOI: 10.1039/c6ay01671e. URL: http://dx.doi.org/10.1039/C6AY01671E.

[46] Ryan D Sochol et al. "Unidirectional mechanical cellular stimuli via micropost array gradients". In: *Soft Matter* 7.10 (2011), pp. 4606–4609. DOI: 10.1039/C1SM05163F. URL: http://dx.doi.org/10.1039/C1SM05163F.

[47] Ryan D Sochol et al. "Continuous flow multi-stage microfluidic reactors via hydrodynamic microparticle railing". In: *Lab Chip* 12.20 (2012), pp. 4168–4177. DOI: 10.1039/C2LC40610A. URL: http://dx.doi.org/10.1039/C2LC40610A.

[48] Ryan D Sochol et al. "Dual-mode hydrodynamic railing and arraying of microparticles for multi-stage signal detection in continuous flow biochemical microprocessors". In: *Lab Chip* 14.8 (2014), pp. 1405–1409. DOI: 10.1039/C4LC00012A. URL: http://dx.doi.org/10.1039/C4LC00012A.

[49] Ryan D. Sochol et al. "3D printed microfluidics and microelectronics". In: *Microelectronic Engineering* 189 (2018), pp. 52–68. ISSN: 01679317. DOI: 10.1016/j.mee.2017.12.010.

[50] Alireza Ahmadian Yazdi et al. "3D printing: an emerging tool for novel microfluidics and lab-on-a-chip applications". In: *Microfluidics and Nanofluidics* 20.3 (2016), pp. 1–18. ISSN: 16134990. DOI: 10.1007/s10404-016-1715-4.

[51] Anthony K. Au et al. "3D-Printed Microfluidics". In: *Angewandte Chemie - International Edition* 55.12 (2016), pp. 3862–3881. ISSN: 15213773. DOI: 10.1002/anie.201504382.

[52] Anthony K Au et al. "3D-printed microfluidic automation". In: *Lab Chip* 15.8 (2015), pp. 1934–1941. DOI: 10.1039/C5LC00126A. URL: http://dx.doi.org/10.1039/C5LC00126A.

[53] Yongha Hwang, Omeed H. Paydar, and Robert N. Candler. "3D printed molds for non-planar PDMS microfluidic channels". In: *Sensors and Actuators, A: Physical* 226 (2015), pp. 137–142. ISSN: 09244247. DOI: 10.1016/j.sna.2015.02.028. URL: http://dx.doi.org/10.1016/j.sna.2015.02.028.

[54] A K Au, N Bhattacharjee, and A Folch. "3D-Printed Microvalves and Micropumps". In: c (2014), pp. 210–212.

[55] A. Del Campo and C. Greiner. "SU-8: A photoresist for high-aspect-ratio and 3D submicron lithography". In: *Journal of Micromechanics and Microengineering* 17.6 (2007). ISSN: 09601317. DOI: 10.1088/0960-1317/17/6/R01.

[56] J Cooper McDonald et al. "Fabrication of microfluidic systems in poly(dimethylsiloxane)". In: *ELECTROPHORESIS* 21.1 (Jan. 2000), pp. 27–40. ISSN: 0173-0835. DOI: 10.1002/(SICI)1522-2683(20000101)21:1<27::AID-ELPS27>3.0.CO;2-C. URL: https://doi.org/10.1002/(SICI)1522-2683(20000101)21:1%3C27::AID-ELPS27%3E3.0.CO%20http://2-c.

[57] Ryan D Sochol et al. "Hydrodynamic resettability for a microfluidic particulate-based arraying system". In: *Lab on a Chip* 12.23 (2012), pp. 5051–5056. ISSN: 1473-0197. DOI: 10.1039/C2LC40704C. URL: http://dx.doi.org/10.1039/C2LC40704C.

[58] Hoang Tuan Nguyen et al. "Low-cost, accessible fabrication methods for microfluidics research in low-resource settings". In: *Micromachines* 9.9 (2018), pp. 1–10. ISSN: 2072666X. DOI: 10.3390/mi9090461.

[59] I. D. Johnston et al. "Mechanical characterization of bulk Sylgard 184 for microfluidics and microengineering". In: *Journal of Micromechanics and Microengineering* 24.3 (2014). ISSN: 13616439. DOI: 10.1088/0960-1317/24/3/035017.

[60] Young Shik Shin et al. "PDMS-based micro PCR chip with Parylene coating". In: *Journal of Micromechanics and Microengineering* 13.5 (2003), pp. 768–774. ISSN: 0960-1317. DOI: 10.1088/0960-1317/13/5/332.

[61] G. Casquillas et al. "PDMS thickness vs spin-coating speed". In: *Elveflow* 1 (2005), pp. 2–3. URL: https://www.elveflow.com/microfluidic/PDMS%20thickness%20VS%20spin%20speed.pdf.

[62] Mengying Zhang et al. "A simple method for fabricating multi-layer PDMS structures for 3D microfluidic chips". In: *Lab on a Chip* 10.9 (2010), pp. 1199–1203. ISSN: 14730189. DOI: 10.1039/b923101c.

[63] Janelle R Anderson et al. "Fabrication of Topologically Complex Three-Dimensional Microfluidic Systems in PDMS by Rapid Prototyping". In: *Analytical Chemistry* 72.14 (July 2000), pp. 3158–3164. ISSN: 0003-2700. DOI: 10.1021/ac9912294. URL: https://doi.org/10.1021/ac9912294.

[64] Hua Gong et al. "High density 3D printed microfluidic valves, pumps, and multiplexers". In: *Lab on a chip* 16.13 (2016), pp. 2450–2458. ISSN: 1473-0197. DOI: 10.1039/C6LC00565A. URL: http://xlink.rsc.org/?DOI=C6LC00565A.

[65] Transon V Nguyen et al. “Semi-autonomous liquid handling via on-chip pneumatic digital logic”. In: *Lab Chip* 12.20 (2012), pp. 3991–3994. DOI: 10.1039/C2LC40466D. URL: http://dx.doi.org/10.1039/C2LC40466D.

[66] Daniel C. Leslie et al. “Frequency-specific flow control in microfluidic circuits with passive elastomeric features”. In: *Nature Physics* 5.3 (2009), pp. 231–235. ISSN: 17452481. DOI: 10.1038/nphys1196. URL: http://dx.doi.org/10.1038/nphys1196.

[67] Yangfan Chen et al. “A microfluidic circulatory system integrated with capillary assisted pressure sensors”. In: *Lab on a Chip* 17.4 (2017), pp. 653–662. ISSN: 14730189. DOI: 10.1039/c6lc01427e. URL: http://dx.doi.org/10.1039/C6LC01427E.

[68] J C Loetters et al. “The mechanical properties of the rubber elastic polymer polydimethylsiloxane for sensor applications”. In: *Journal of Micromechanics and Microengineering* 7.3 (1999), pp. 145–147. ISSN: 0960-1317. DOI: 10.1088/0960-1317/7/3/017.

[69] Zhixin Wang, Alex A. Volinsky, and Nathan D. Gallant. “Crosslinking effect on polydimethylsiloxane elastic modulus measured by custom-built compression instrument”. In: *Journal of Applied Polymer Science* 41050 (2014), pp. 1–4. ISSN: 00218995. DOI: 10.1002/app.41050.

[70] Dongeun Huh et al. “Microfabrication of human organs-on-chips.” In: *Nature protocols* 8.11 (2013), pp. 2135–57. ISSN: 1750-2799. DOI: 10.1038/nprot.2013.137. URL: http://www.ncbi.nlm.nih.gov/pubmed/24113786.

[71] G. Firpo et al. “Permeability thickness dependence of polydimethylsiloxane (PDMS) membranes”. In: *Journal of Membrane Science* 481 (2015), pp. 1–8. ISSN: 18733123. DOI: 10.1016/j.memsci.2014.12.043. URL: http://dx.doi.org/10.1016/j.memsci.2014.12.043.

[72] Mark J. Mondrinos et al. “Native extracellular matrix-derived semipermeable, optically transparent, and inexpensive membrane inserts for microfluidic cell culture”. In: *Lab on a Chip* 17.18 (2017), pp. 3146–3158. ISSN: 14730189. DOI: 10.1039/c7lc00317j. URL: http://dx.doi.org/10.1039/C7LC00317J.

[73] Neil J Graf and Michael T Bowser. “Effect of cross sectional geometry on PDMS micro peristaltic pump performance: comparison of SU-8 replica molding vs. micro injection molding”. In: *Analyst* 138.19 (2013), pp. 5791–5800. ISSN: 0003-2654. DOI: 10.1039/C3AN00671A. URL: http://dx.doi.org/10.1039/C3AN00671A.

[74] Larry J Kricka et al. “Fabrication of plastic microchips by hot embossing”. In: *Lab on a Chip* 2.1 (2002), pp. 1–4. ISSN: 1473-0197. DOI: 10.1039/B109775J. URL: http://dx.doi.org/10.1039/B109775J.

[75] Julien Giboz, Thierry Copponnex, and Patrice Mele. “Microinjection molding of thermoplastic polymers: a review”. In: *Journal of Micromechanics and Microengineering* 17.6 (2007), R96–R109. ISSN: 0960-1317. DOI: 10.1088/0960-1317/17/6/r02. URL: http://dx.doi.org/10.1088/0960-1317/17/6/R02.

[76] Giuliano Bissacco et al. “Precision manufacturing methods of inserts for injection molding of microfluidic systems.” In: *Proceedings - ASPE Spring Topical Meeting on Precision Micro/Nano Scale Polymer Based Component and Device Fabrication, ASPE 2005* (2005), pp. 57–63.

[77] Kosuke Iwai et al. “Finger-powered microfluidic systems using multilayer soft lithography and injection molding processes.” In: *Lab on a chip* 14.19 (2014), pp. 3790–9. ISSN: 1473-0189. DOI: 10.1039/c4lc00500g. URL: http://www.ncbi.nlm.nih.gov/pubmed/25102160.

[78] Chia Wen Tsao. “Polymer microfluidics: Simple, low-cost fabrication process bridging academic lab research to commercialized production”. In: *Micromachines* 7.12 (2016). ISSN: 2072666X. DOI: 10.3390/mi7120225.

[79] M Heckele and W K Schomburg. “Review on micro molding of thermoplastic polymers”. In: *Journal of Micromechanics and Microengineering* 14.3 (2003), R1–R14. ISSN: 0960-1317. DOI: 10.1088/0960-1317/14/3/r01. URL: http://dx.doi.org/10.1088/0960-1317/14/3/R01.

[80] S Ghosh et al. “A mass manufacturarle thermoplastic based microfluidic droplet generator using rapid injection molding and solvent bonding method”. In: *2017 19th International Conference on Solid-State Sensors, Actuators and Microsystems (TRANSDUCERS)*. 2017, pp. 1758–1761. ISBN: 2167-0021 VO -. DOI: 10.1109/TRANSDUCERS.2017.7994408.

[81] Ke Liu and Z. Hugh Fan. “Thermoplastic microfluidic devices and their applications in protein and DNA analysis”. In: *Analyst* 136.7 (2011), pp. 1288–1297. ISSN: 00032654. DOI: 10.1039/c0an00969e.

[82] Jing-Song Chu, Michael D Gilchrist, and Nan Zhang. “Microinjection Molding for Microfluidics Applications BT, Encyclopedia of Microfluidics and Nanofluidics”. In: ed. by Dongqing Li. New York, NY: Springer New York, 2015, pp. 2085–2101. ISBN: 978-1-4614-5491-5. DOI: 10.1007/978-1-4614-5491-5_694. URL: https://doi.org/10.1007/978-1-4614-5491-5_694.

[83] C Szydzik et al. “An automated optofluidic biosensor platform combining interferometric sensors and injection moulded microfluidics”. In: *Lab on a Chip* 17.16 (2017), pp. 2793–2804. ISSN: 1473-0197. DOI: 10.1039/C7LC00524E. URL: http://dx.doi.org/10.1039/C7LC00524E.

[84] Niall P. Macdonald et al. “Comparing Microfluidic Performance of Three-Dimensional (3D) Printing Platforms”. In: *Analytical Chemistry* 89.7 (2017), pp. 3858–3866. ISSN: 15206882. DOI: 10.1021/acs.analchem.7b00136.

[85] Usama M. Attia. “Micro-Injection Moulding of Three-Dimensional Integrated Microfluidic Devices”. In: *Engineering* 2009.1 (2009), pp. 2–3. ISSN: 03781127. DOI: 10.1260/095745604288020O. URL: http://scholar.google.com/scholar?hl=en&btnG=Search&q=intitle:Cranfield+university#5.

[86] Anthony K. Au, Wonjae Lee, and Albert Folch. "Mail-order microfluidics: Evaluation of stereolithography for the production of microfluidic devices". In: *Lab on a Chip* 14.7 (2014), pp. 1294–1301. ISSN: 14730189. DOI: 10.1039/c3lc51360b.

[87] Yuksel Temiz et al. "Lab-on-a-chip devices: How to close and plug the lab?" In: *Microelectronic Engineering* 132 (2015), pp. 156–175. ISSN: 01679317. DOI: 10.1016/j.mee.2014.10.013. URL: http://dx.doi.org/10.1016/j.mee.2014.10.013.

[88] Andrew C. Lamont, Abdullah T. Alsharhan, and Ryan D. Sochol. "Geometric Determinants of In-Situ Direct Laser Writing". In: *Scientific Reports* 9.1 (2019), pp. 1–12. ISSN: 20452322. DOI: 10.1038/s41598-018-36727-z. URL: http://dx.doi.org/10.1038/s41598-018-36727-z.

[89] Nirveek Bhattacharjee et al. "The upcoming 3D-printing revolution in microfluidics". In: *Lab Chip* 16.10 (2016), pp. 1720–1742. DOI: 10.1039/C6LC00163G. URL: http://dx.doi.org/10.1039/C6LC00163G.

[90] S Scot Crump. *Apparatus and method for creating three-dimensional objects*. 1992.

[91] Bok Yeop Ahn et al. "Printed origami structures". In: *Advanced Materials* 22.20 (2010), pp. 2251–2254. ISSN: 09359648. DOI: 10.1002/adma.200904232.

[92] Nirveek Bhattacharjee et al. "The upcoming 3D-printing revolution in microfluidics". In: *Lab on a Chip* 16.10 (2016), pp. 1720–1742. ISSN: 14730189. DOI: 10.1039/c6lc00163g. URL: http://dx.doi.org/10.1039/C6LC00163G.

[93] Daniel Therriault, Scott R. White, and Jennifer A. Lewis. "Chaotic mixing in three-dimensional microvascular networks fabricated by direct-write assembly". In: *Nature Materials* 2.4 (2003), pp. 265–271. ISSN: 14761122. DOI: 10.1038/nmat863.

[94] J. A. Lewis. "Direct Ink Writing of 3D Functional Materials". In: *Advanced Functional Materials* 16.17 (Nov. 2006), pp. 2193–2204. ISSN: 1616-301X. DOI: 10.1002/adfm.200600434. URL: https://doi.org/10.1002/adfm.200600434.

[95] Bok Y Ahn et al. "Omnidirectional Printing of Flexible, Stretchable, and Spanning Silver Microelectrodes". In: *Science* 323.5921 (Mar. 2009), 1590 LP –1593. DOI: 10.1126/science.1168375. URL: http://science.sciencemag.org/content/323/5921/1590.abstract.

[96] Willie Wu, Adam DeConinck, and Jennifer A Lewis. "Omnidirectional Printing of 3D Microvascular Networks". In: *Advanced Materials* 23.24 (2011), H178–H183. ISSN: 1521-4095. DOI: 10.1002/adma.201004625. URL: http://dx.doi.org/10.1002/adma.201004625.

[97] Jordan S Miller et al. "Rapid casting of patterned vascular networks for perfusable engineered three-dimensional tissues". In: *Nat Mater* 11.9 (2012), pp. 768–774. URL: http://dx.doi.org/10.1038/nmat3357.

[98] Matthew K Gelber and Rohit Bhargava. "Monolithic multilayer microfluidics via sacrificial molding of 3D-printed isomalt". In: *Lab on a Chip* 15.7 (2015), pp. 1736–1741. ISSN: 1473-0197. DOI: 10.1039/C4LC01392A. URL: http://dx.doi.org/10.1039/C4LC01392A.

[99] David B Kolesky et al. "3D Bioprinting of Vascularized, Heterogeneous Cell-Laden Tissue Constructs". In: *Advanced Materials* 26.19 (May 2014), pp. 3124–3130. ISSN: 0935-9648. DOI: 10.1002/adma.201305506. URL: https://doi.org/10.1002/adma.201305506.

[100] Zong'an Li et al. "Fabrication of PDMS microfluidic devices with 3D wax jetting". In: *RSC Advances* 7.6 (2017), pp. 3313–3320. DOI: 10.1039/C6RA24884E. URL: http://dx.doi.org/10.1039/C6RA24884E.

[101] Hideo Kodama. "Automatic method for fabricating a three dimensional plastic model with photo hardening polymer". In: *Review of Scientific Instruments* 52.11 (Nov. 1981), pp. 1770–1773. ISSN: 0034-6748. DOI: 10.1063/1.1136492. URL: https://doi.org/10.1063/1.1136492.

[102] Charles W. Hull. *Apparatus for production of three-dimensional objects by stereolithography*. 1986.

[103] Zahra Faraji Rad et al. "High-fidelity replication of thermoplastic microneedles with open microfluidic channels". In: *Nature Publishing Group* 3.April (2017), pp. 1–11. ISSN: 2055-7434. DOI: 10.1038/micronano.2017.34. URL: https://www.nature.com/articles/micronano201734.pdf.

[104] Chad I. Rogers et al. "3D printed microfluidic devices with integrated valves". In: *Biomicrofluidics* 9.1 (2015). ISSN: 19321058. DOI: 10.1063/1.4905840.

[105] Anthony K Au et al. "3D-Printed Microfluidic Automation". In: 15.8 (2015), pp. 1934–1941. DOI: 10.1039/c5lc00126a.3D-Printed.

[106] Krisna C Bhargava, Bryant Thompson, and Noah Malmstadt. "Discrete elements for 3D microfluidics". In: *Proceedings of the National Academy of Sciences* 111.42 (2014), pp. 15013–15018. DOI: 10.1073/pnas.1414764111. URL: http://www.pnas.org/content/111/42/15013.abstract.

[107] Rujing Zhang and Niels B Larsen. "Stereolithographic hydrogel printing of 3D culture chips with biofunctionalized complex 3D perfusion networks". In: *Lab on a Chip* 17.24 (2017), pp. 4273–4282. ISSN: 1473-0197. DOI: 10.1039/C7LC00926G. URL: http://dx.doi.org/10.1039/C7LC00926G.

[108] Sidra Waheed et al. "3D printed microfluidic devices: Enablers and barriers". In: *Lab on a Chip* 16.11 (2016), pp. 1993–2013. ISSN: 14730189. DOI: 10.1039/c6lc00284f. URL: http://dx.doi.org/10.1039/C6LC00284F.

[109] Arturo Urrios et al. "3D-printing of transparent bio-microfluidic devices in PEG-DA". In: *Lab on a Chip* 16.12 (2016), pp. 2287–2294. ISSN: 1473-0197. DOI: 10.1039/C6LC00153J. URL: http://dx.doi.org/10.1039/C6LC00153J.

[110] Aliaa I. Shallan et al. "Cost-effective three-dimensional printing of visibly transparent microchips within minutes". In: *Analytical Chemistry* 86.6 (2014), pp. 3124–3130. ISSN: 15206882. DOI: 10.1021/ac4041857.

[111] Michael J. Beauchamp, Gregory P. Nordin, and Adam T. Woolley. "Moving from millifluidic to truly microfluidic sub-100-μm cross-section 3D printed devices". In: *Analytical and Bioanalytical Chemistry* 409.18 (2017), pp. 4311–4319. ISSN: 16182650. DOI: 10.1007/s00216-017-0398-3.

[112] Hua Gong et al. "Custom 3D printer and resin for 18 x 20 micron microfluidic flow channels". In: *Lab on a Chip* 17.17 (2017), pp. 2899–2909. ISSN: 1473-0197. DOI: 10.1039/C7LC00644F. URL: http://dx.doi.org/10.1039/C7LC00644F.

[113] Franziska Klein et al. "Elastic Fully Three-dimensional Microstructure Scaffolds for Cell Force Measurements". In: *Advanced Materials* 22.8 (Feb. 2010), pp. 868–871. ISSN: 0935-9648. DOI: 10.1002/adma.200902515. URL: https://doi.org/10.1002/adma.200902515.

[114] John R Tumbleston et al. "Continuous liquid interface production of 3D objects". In: *Science* 347.6228 (Mar. 2015), 1349 LP –1352. DOI: 10.1126/science.aaa2397. URL: http://science.sciencemag.org/content/347/6228/1349.abstract.

[115] R. D. Sochol et al. "3D printed microfluidic circuitry via multijet-based additive manufacturing". In: *Lab on a Chip* 16.4 (2016), pp. 668–678. ISSN: 14730189. DOI: 10.1039/c5lc01389e.

[116] M Yamane. *Apparatus and method for forming three-dimensional article*. 1991.

[117] T Almquist. *Thermal stereolithography*. 1997.

[118] Feng Zhu et al. "Three-dimensional printed millifluidic devices for zebrafish embryo tests". In: *Biomicrofluidics* 9.4 (2015). ISSN: 19321058. DOI: 10.1063/1.4927379.

[119] Pengju Yin et al. "Engineering of removing sacrificial materials in 3D printed microfluidics". In: *Micromachines* 9.7 (2018), pp. 1–12. ISSN: 2072666X. DOI: 10.3390/mi9070327.

[120] W M Lee et al. "Fabricating low cost and high performance elastomer lenses using hanging droplets." In: *Biomedical optics express* 5.5 (2014), pp. 1626–35. ISSN: 2156-7085. DOI: 10.1364/BOE.5.001626. URL: http://www.pubmedcentral.nih.gov/articlerender.fcgi?artid=4026886&tool=pmcentrez&rendertype=abstract.

[121] Eric C. Sweet et al. "Finger powered, 3D printed microfluidic pumps". In: *TRANSDUCERS 2017 19th International Conference on Solid-State Sensors, Actuators and Microsystems* (2017), pp. 1766–1769. DOI: 10.1109/TRANSDUCERS.2017.7994410.

[122] Eric C. Sweet et al. “3D printed three-flow microfluidic concentration gradient generator for clinical E. Coli-antibiotic drug screening”. In: *Proceedings of the IEEE International Conference on Micro Electro Mechanical Systems (MEMS)* Figure 1 (2017), pp. 205–208. ISSN: 10846999. DOI: 10.1109/MEMSYS.2017.7863376.

[123] J G Dawson et al. “Bioinspired vascular structures via 3D printing and suspended microfluidics”. In: *2017 IEEE 30th International Conference on Micro Electro Mechanical Systems (MEMS)*. 2017, pp. 426–429. ISBN: null VO -. DOI: 10.1109/MEMSYS.2017.7863433.

[124] Nicholas W Bartlett et al. “A 3D-printed, functionally graded soft robot powered by combustion”. In: *Science* 349.6244 (July 2015), 161 LP –165. DOI: 10.1126/science.aab0129. URL: http://science.sciencemag.org/content/349/6244/161.abstract.

[125] Kari B Anderson et al. “A 3D Printed Fluidic Device that Enables Integrated Features”. In: *Analytical Chemistry* 85.12 (June 2013), pp. 5622–5626. ISSN: 0003-2700. DOI: 10.1021/ac4009594. URL: https://doi.org/10.1021/ac4009594.

[126] Rafal Walczak et al. “Inkjet 3D Printing Studies on Applicability for Lab on a chip Technique”. In: *Procedia Engineering* 168 (2016), pp. 1362–1365. ISSN: 18777058. DOI: 10.1016/j.proeng.2016.11.377. URL: http://dx.doi.org/10.1016/j.proeng.2016.11.377.

[127] Eric C Sweet et al. “Entirely-3D Printed Microfluidic Platform for on-Site Detection of Drinking Waterborne Pathogens”. In: *Proceedings of the IEEE International Conference on Micro Electro Mechanical Systems (MEMS)* January (2019), pp. 79–82.

[128] Eric C Sweet et al. “3D PRINTED CHAOTIC MIXER FOR LOW REYNOLDS NUMBER MICROFLUIDICS”. In: *2019 20th International Conference on Solid-State Sensors, Actuators and Microsystems and Eurosensors XXXIII (TRANSDUCERS and EUROSENSORS XXXIII)* June (2019), pp. 2258–2261.

[129] N. P. MacDonald et al. “Assessment of biocompatibility of 3D printed photopolymers using zebrafish embryo toxicity assays”. In: *Lab on a Chip* 16.2 (2016), pp. 291–297. ISSN: 14730189. DOI: 10.1039/c5lc01374g. URL: http://dx.doi.org/10.1039/C5LC01374G.

[130] Nurul Mohd Fuad et al. “Characterization of 3D-printed moulds for soft lithography of millifluidic devices”. In: *Micromachines* 9.3 (2018), pp. 1–11. ISSN: 2072666X. DOI: 10.3390/mi9030116.

[131] Xiaojun Chen et al. “3D printed microfluidic chip for multiple anticancer drug combinations”. In: *Sensors and Actuators, B: Chemical* 276.January (2018), pp. 507–516. ISSN: 09254005. DOI: 10.1016/j.snb.2018.08.121. URL: https://doi.org/10.1016/j.snb.2018.08.121.

[132] Nadine Philippin et al. “3D-Printed Microfluidic Chip System for Dielectrophoretic Manipulation of 3D-Printed Microfluidic Chip System for Dielectrophoretic Manipulation of Colloids”. In: February 2019 (2018).

[133] R. Walczak. “Inkjet 3D printing - towards new micromachining tool for MEMS fabrication”. In: *Bulletin of the Polish Academy of Sciences: Technical Sciences* 66.2 (2018), pp. 179–186. ISSN: 23001917. DOI: 10.24425/122098.

[134] Bethany C. Gross et al. “Polymer Coatings in 3D Printed Fluidic Device Channels for Improved Cellular Adherence Prior to Electrical Lysis”. In: *Analytical Chemistry* 87.12 (2015), pp. 6335–6341. ISSN: 15206882. DOI: 10.1021/acs.analchem.5b01202.

[135] Steven J Keating et al. “3D Printed Multimaterial Microfluidic Valve”. In: *PLOS ONE* 11.8 (Aug. 2016), e0160624. URL: https://doi.org/10.1371/journal.pone.0160624.

[136] Daniel C Leslie et al. “Frequency-specific flow control in microfluidic circuits with passive elastomeric features”. In: *Nat Phys* 5.3 (2009), pp. 231–235. URL: http://dx.doi.org/10.1038/nphys1196.

[137] Joshua D. Tice et al. “Control of pressure-driven components in integrated microfluidic devices using an on-chip electrostatic microvalve”. In: *RSC Advances* 4.93 (2014), pp. 51593–51602. ISSN: 20462069. DOI: 10.1039/c4ra10341f. URL: http://dx.doi.org/10.1039/C4RA10341F.

[138] Bobak Mosadegh et al. “Integrated elastomeric components for autonomous regulation of sequential and oscillatory flow switching in microfluidic devices”. In: *Nat Phys* 6.6 (2010), pp. 433–437. URL: http://dx.doi.org/10.1038/nphys1637.

[139] Bobak Mosadegh et al. “Next-generation integrated microfluidic circuits”. In: *Lab Chip* 11.17 (2011), pp. 2813–2818. DOI: 10.1039/C1LC20387H. URL: http://dx.doi.org/10.1039/C1LC20387H.

[140] Frederick K Balagaddé et al. “Long-Term Monitoring of Bacteria Undergoing Programmed Population Control in a Microchemostat”. In: *Science* 309.5731 (2005), pp. 137–140. ISSN: 0036-8075. DOI: 10.1126/science.1109173. URL: http://science.sciencemag.org/content/309/5731/137.

[141] Chung-Cheng Lee et al. “Multistep Synthesis of a Radiolabeled Imaging Probe Using Integrated Microfluidics”. In: *Science* 310.5755 (2005), pp. 1793–1796. ISSN: 0036-8075. DOI: 10.1126/science.1118919. URL: http://science.sciencemag.org/content/310/5755/1793.

[142] Anton Enders et al. “3D Printed Microfluidic Mixers, A Comparative Study on Mixing Unit Performances”. In: *Small* 15.2 (2019), pp. 1–9. ISSN: 16136829. DOI: 10.1002/smll.201804326.

[143] Chia Yen Lee et al. “Microfluidic mixing: A review”. In: *International Journal of Molecular Sciences* 12.5 (2011), pp. 3263–3287. ISSN: 14220067. DOI: 10.3390/ijms12053263.

[144] Yong Kweon Suh and Sangmo Kang. "A review on mixing in microfluidics". In: *Micromachines* 1.3 (2010), pp. 82–111. ISSN: 2072666X. DOI: 10.3390/mi1030082.

[145] Lang Nan, Zhuangde Jiang, and Xueyong Wei. "Emerging microfluidic devices for cell lysis: A review". In: *Lab on a Chip* 14.6 (2014), pp. 1060–1073. ISSN: 14730189. DOI: 10.1039/c3lc51133b.

[146] Gerson R. Aguirre et al. "Integrated micromixer for incubation and separation of cancer cells on a centrifugal platform using inertial and dean forces". In: *Microfluidics and Nanofluidics* 18.3 (2015), p. 513 526. ISSN: 16134990. DOI: 10.1007/s10404014145 07.

[147] Ying Zhang, Hon Fai Chan, and Kam W Leong. "Advanced materials and processing for drug delivery The past and the future". In: *Advanced Drug Delivery Reviews* 65.1 (2013), pp. 104–120. ISSN: 0169-409X. DOI: https://doi.org/10.1016/j.addr.2012.10.003. URL: http://www.sciencedirect.com/science/article/pii/S0169409X12003213.

[148] Leslie Y Yeo et al. "Microfluidic Devices for Bioapplications". In: *Small* 7.1 (Jan. 2011), pp. 12–48. ISSN: 1613-6810. DOI: 10.1002/smll.201000946. URL: https://doi.org/10.1002/smll.201000946.

[149] Chia Yen Lee and Lung Ming Fu. "Recent advances and applications of micromixers". In: *Sensors and Actuators, B: Chemical* 259 (2018), pp. 677–702. ISSN: 09254005. DOI: 10.1016/j.snb.2017.12.034. URL: http://dx.doi.org/10.1016/j.snb.2017.12.034.

[150] Yong Kweon Suh and Sangmo Kang. "A review on mixing in microfluidics". In: *Micromachines* 1.3 (2010), pp. 82–111. ISSN: 2072666X. DOI: 10.3390/mi1030082.

[151] Moien Alizadehgiashi et al. "3D Printed Microfluidic Devices for Materials Science". In: *Advanced Materials Technologies* 3.7 (2018), pp. 1–8. ISSN: 2365709X. DOI: 10.1002/admt.201800068.

[152] Ashleigh B. Theberge et al. "Microdroplets in Microfluidics, An Evolving Platform for Discoveries in Chemistry and Biology". In: *Angewandte Chemie International Edition* 49.34 (Aug. 2010), pp. 5846–5868. ISSN: 1433-7851. DOI: 10.1002/anie.200906653. URL: https://doi.org/10.1002/anie.200906653.

[153] Alicia G.G. Toh et al. "Engineering microfluidic concentration gradient generators for biological applications". In: *Microfluidics and Nanofluidics* 16.1-2 (2014), pp. 1–18. ISSN: 16134990. DOI: 10.1007/s10404-013-1236-3.

[154] Sky Tang and Gm Whitesides. "Basic microfluidic and soft lithographic techniques". In: *Optofluidics, Fundamentals, Devices, and Applications* (2010), p. 1. ISSN: 0071601562.

[155] Laurie E. Locascio. "Microfluidic mixing". In: *Analytical and Bioanalytical Chemistry* 379.3 (2004), pp. 325–327. ISSN: 1618-2642. DOI: 10.1007/s00216-004-2630-1.

[156] Dino Di Carlo. "Inertial microfluidics". In: *Lab on a Chip* 9.21 (2009), pp. 3038–3046. ISSN: 14730189. DOI: 10.1039/b912547g.

[157] H A Stone, A D Stroock, and A Ajdari. "Engineering Flows in Small Devices, Microfluidics Toward a Lab on a Chip". In: *Annual Review of Fluid Mechanics* 36.1 (2004), pp. 381–411. DOI: 10.1146/annurev.fluid.36.050802.122124. URL: https://doi.org/10.1146/annurev.fluid.36.050802.122124.

[158] Todd M Squires and Stephen R Quake. "Microfluidics, Fluid physics at the nanoliter scale". In: *Rev. Mod. Phys.* 77.3 (Oct. 2005), pp. 977–1026. DOI: 10.1103/RevModPhys77977. URL: https://link.aps.org/doi/10.1103/RevModPhys.77.977.

[159] Nhut Tran Minh, Tao Dong, and Frank Karlsen. "An efficient passive planar micromixer with ellipse like micropillars for continuous mixing of human blood". In: *Computer Methods and Programs in Biomedicine* 117.1 (2014), pp. 20–29. ISSN: 18727565. DOI: 10.1016/j.cmpb.2014.05.007. URL: http://dx.doi.org/10.1016/j.cmpb.2014.05.007.

[160] Christopher T. Culbertson, Stephen C. Jacobson, and J. Michael Ramsey. "Diffusion coefficient measurements in microfluidic devices". In: *Talanta* 56.2 (2002), pp. 365–373. ISSN: 00399140. DOI: 10.1016/S0039-9140(01)00602-6.

[161] S. P. Adiga et al. "Absolute Diffusion Coefficients: Compilation of Reference Data for FCS Calibration Peter". In: *Biophysical journal* 5.1 (2010), pp. 4021–4032. ISSN: 0006-3002. DOI: 10.1038/srep04424. URL: http://ci.nii.ac.jp/naid/130003362507/%5Cnhttp://www.ncbi.nlm.nih.gov/pubmed/22577821%5Cnhttp://www.ncbi.nlm.nih.gov/pubmed/18654251%5Cnhttp://www.ncbi.nlm.nih.gov/pubmed/18988237%5Cnhttp://scitation.aip.org/content/aip/journal/apl/85/15/10.1063/1.1805712.

[162] Mihret Woldemariam et al. "Mixing performance evaluation of additive manufactured milli-scale reactors". In: *Chemical Engineering Science* 152 (2016), pp. 26–34. ISSN: 00092509. DOI: 10.1016/j.ces.2016.05.030. URL: http://dx.doi.org/10.1016/j.ces.2016.05.030.

[163] Vimal Kumar, Marius Paraschivoiu, and K. D P Nigam. "Single-phase fluid flow and mixing in microchannels". In: *Chemical Engineering Science* 66.7 (2011), pp. 1329–1373. ISSN: 00092509. DOI: 10.1016/j.ces.2010.08.016. URL: http://dx.doi.org/10.1016/j.ces.2010.08.016.

[164] Wei Feng Fang and Jing Tang Yang. "A novel microreactor with 3D rotating flow to boost fluid reaction and mixing of viscous fluids". In: *Sensors and Actuators, B: Chemical* 140.2 (2009), pp. 629–642. ISSN: 09254005. DOI: 10.1016/j.snb.2009.05.007.

[165] Javier Atencia, Jayne Morrow, and Laurie E. Locascio. "The microfluidic palette: A diffusive gradient generator with spatio-temporal control". In: *Lab on a Chip* 9.18 (2009), pp. 2707–2714. ISSN: 14730189. DOI: 10.1039/b902113b.

[166] Ayoola Brimmo et al. "3D Printed Microfluidic Probes". In: *Scientific Reports* 8.1 (2018), pp. 1–8. ISSN: 20452322. DOI: 10.1038/s41598-018-29304-x. URL: http://dx.doi.org/10.1038/s41598-018-29304-x.

[167] Abraham D Stroock. "Chaotic Mixer for Microchannels". In: *Science* 295.5555 (2002), pp. 647–651. ISSN: 00368075. DOI: 10.1126/science.1066238. URL: http://www.sciencemag.org/cgi/doi/10.1126/science.1066238.

[168] Bengt Wunderlich et al. "Microfluidic mixer designed for performing single-molecule kinetics with confocal detection on timescales from milliseconds to minutes". In: *Nature Protocols* 8.8 (2013), pp. 1459–1474. ISSN: 17542189. DOI: 10.1038/nprot.2013.082.

[169] James B Knight et al. "Hydrodynamic Focusing on a Silicon Chip: Mixing Nanoliters in Microseconds". In: *Physical Review Letters* 80.17 (Apr. 1998), pp. 3863–3866. DOI: 10.1103/PhysRevLett.80.3863. URL: https://link.aps.org/doi/10.1103/PhysRevLett.80.3863.

[170] A. M. Guzman and C. H. Amon. "Dynamical flow characterization of transitional and chaotic regimes in converging diverging channels". In: *Journal of Fluid Mechanics* 321 (1996), pp. 25–57. ISSN: 00221120. DOI: 10.1017/S002211209600763X.

[171] Virginie Mengeaud, Jacques Josserand, and Hubert H Girault. "Mixing Processes in a Zigzag Microchannel, Finite Element Simulations and Optical Study". In: *Analytical Chemistry* 74.16 (Aug. 2002), pp. 4279–4286. ISSN: 0003-2700. DOI: 10.1021/ac025642e. URL: https://doi.org/10.1021/ac025642e.

[172] Keyin Liu et al. "Design and analysis of the cross-linked dual helical micromixer for rapid mixing at low Reynolds numbers". In: *Microfluidics and Nanofluidics* 19.1 (2015), pp. 169–180. ISSN: 16134990. DOI: 10.1007/s10404-015-1558-4. URL: http://dx.doi.org/10.1007/s10404-015-1558-4.

[173] Hassan Aref. "Stirring by chaotic advection". In: *Journal of Fluid Mechanics* 143 (1984), pp. 1–21. ISSN: 0022-1120. DOI: DOI:10.1017/S0022112084001233. URL: https://www.cambridge.org/core/article/stirring-by-chaotic-advection/7B32CACE61D5AD79077846D7ACF4A31E.

[174] Brian Hama et al. "Evolution of mixing in a microfluidic reverse staggered herringbone micromixer". In: *Microfluidics and Nanofluidics* 22.5 (2018), p. 1. ISSN: 16134990. DOI: 10.1007/s10404-018-2074-0. URL: http://dx.doi.org/10.1007/s10404-018-2074-0.

[175] F Jiang et al. "Helical flows and chaotic mixing in curved micro channels". In: *AIChE Journal* 50.9 (Sept. 2004), pp. 2297–2305. ISSN: 0001-1541. DOI: 10.1002/aic.10188. URL: https://doi.org/10.1002/aic.10188.

[176] Abraham D Stroock et al. "Patterning Flows Using Grooved Surfaces". In: *Analytical Chemistry* 74.20 (Oct. 2002), pp. 5306–5312. ISSN: 0003-2700. DOI: 10.1021/ac0257389. URL: https://doi.org/10.1021/ac0257389.

[177] Jia Ou, Geoffrey R. Moss, and Jonathan P. Rothstein. "Enhanced mixing in laminar flows using ultrahydrophobic surfaces". In: *Physical Review E - Statistical, Nonlinear, and Soft Matter Physics* 76.1 (2007), pp. 1–10. ISSN: 15393755. DOI: 10.1103/PhysRevE.76.016304.

[178] Sung Jin Park et al. “Rapid three dimensional passive rotation micromixer using the breakup process”. In: *Journal of Micromechanics and Microengineering* 14.1 (2004), pp. 6–14. ISSN: 09601317. DOI: 10.1088/0960-1317/14/1/302.

[179] Xiaole Mao et al. “Milliseconds microfluidic chaotic bubble mixer”. In: *Microfluidics and Nanofluidics* 8.1 (2010), pp. 139–144. ISSN: 16134982. DOI: 10.1007/s10404-009-0496-4.

[180] Wonjae Lee et al. “3D printed microfluidic device for the detection of pathogenic bacteria using size based separation in helical channel with trapezoid cross section.” In: *Scientific Reports* 5 (2015), p. 7717. ISSN: 2045-2322. DOI: 10.1038/srep07717. URL: http://www.pubmedcentral.nih.gov/articlerender.fcgi?artid=4289896&tool=pmcentrez&rendertype=abstract.

[181] H. M. Xia et al. “Chaotic micromixers using two-layer crossing channels to exhibit fast mixing at low Reynolds numbers”. In: *Lab on a Chip* 5.7 (2005), pp. 748–755. ISSN: 14730189. DOI: 10.1039/b502031j.

[182] Z. Chen et al. “Performance analysis of a folding flow micromixer”. In: *Microfluidics and Nanofluidics* 6.6 (2009), pp. 763–774. ISSN: 16134982. DOI: 10.1007/s10404-008-0351-z.

[183] Jue Nee Tan and Adrian Neild. “Microfluidic mixing in a Y-junction open channel”. In: *AIP Advances* 2.3 (2012). ISSN: 21583226. DOI: 10.1063/1.4750483.

[184] Ali Hashmi and Jie Xu. “On the Quantification of Mixing in Microfluidics”. In: *Journal of Laboratory Automation* 19.5 (2014), pp. 488–491. ISSN: 22110690. DOI: 10.1177/2211068214540156.

[185] Casey C. Glick et al. “Rapid assembly of multilayer microfluidic structures via 3D printed transfer molding and bonding”. In: *Microsystems and Nanoengineering* 2.July (2016), p. 16063. ISSN: 20557434. DOI: 10.1038/micronano201663. URL: http://www.nature.com/articles/micronano201663.

[186] ProJet and 3D Systems. “VisiJet EX200 Plastic Material for 3D Modeling”. In: May (2009).

[187] 3D Systems. “Safety Data Sheet, VisiJet EX 200, VisiJet M3 Crystal”. In: 1.1 (2016), pp. 1–7. URL: http://infocenter.3dsystems.com/materials/sites/default/files/sds-files/professional/VisiJet_EX200/24184-S12-02-B,SDS%20GHS,English,VisiJet%20EX%20200%20and%20M3%20Crystal.pdf.

[188] 3DSystems. “Safety Data Sheet, VisijetS100”. In: 1910.2 (2012), pp. 8–10.

[189] 3D Systems. *High Definition 3D Modeling, Projet HD 3000*. Tech. rep. 800. 2009.

[190] Sung-Yueh Wu et al. “3D printed microelectronics for integrated circuitry and passive wireless sensors”. In: *Microsystems and Nanoengineering* 1.April (2015), p. 15013. ISSN: 2055-7434. DOI: 10.1038/micronano.2015.13. URL: http://www.nature.com/articles/micronano201513.

[191] Mehdi Rafeie et al. “An easily fabricated three dimensional threaded lemniscate shaped micromixer for a wide range of flow rates”. In: *Biomicrofluidics* 11.1 (2017). ISSN: 19321058. DOI: 10.1063/1.4974904.

[192] Takao YASUI et al. “Confocal Microscopic Evaluation of Mixing Performance for Three Dimensional Microfluidic Mixer”. In: *Analytical Sciences* 28.1 (2012), p. 57. ISSN: 0910-6340. DOI: 10.2116/analsci.28.57.

[193] Yu Cheng Lin, Yung Chiang Chung, and Chung Yi Wu. “Mixing enhancement of the passive microfluidic mixer with J-shaped baffles in the tee channel”. In: *Biomedical Microdevices* 9.2 (2007), pp. 215–221. ISSN: 13872176. DOI: 10.1007/s10544-006-9023-5.

[194] Elmabruk A. Mansur et al. “A State of the Art Review of Mixing in Microfluidic Mixers”. In: *Chinese Journal of Chemical Engineering* 16.4 (2008), pp. 503–516. ISSN: 10049541. DOI: 10.1016/S1004954108601147.

[195] National Center for Biotechnology Information. *Fluorescein, CID=16850*. Tech. rep.

[196] National Center for Biotechnology Information. *Rhodamine B, CID=6694*. Tech. rep.

[197] Chia Yen Lee and Lung Ming Fu. “Recent advances and applications of micromixers”. In: *Sensors and Actuators, B: Chemical* 259 (2018), pp. 677–702. ISSN: 09254005. DOI: 10.1016/j.snb.2017.12.034. URL: http://dx.doi.org/10.1016/j.snb.2017.12.034.

[198] Jun Yang et al. “Design and fabrication of a three dimensional spiral micromixer”. In: *Chinese Journal of Chemistry* 31.2 (2013), pp. 209–214. ISSN: 1001604X. DOI: 10.1002/cjoc201200922.

[199] Alexa M Melvin and Thomas J Roussel. “Design and Simulation of 3D Printed Check Valves Using Fluid- Structure Interaction”. In: ().

[200] Jorge Nicolas Cabrera et al. “Increased surface roughness in polydimethylsiloxane films by physical and chemical methods”. In: *Polymers* 9.8 (2017), p. 331. ISSN: 20734360. DOI: 10.3390/polym9080331.

[201] Donghee Lee and Sung Yang. “Surface modification of PDMS by atmospheric-pressure plasma-enhanced chemical vapor deposition and analysis of long-lasting surface hydrophilicity”. In: *Sensors and Actuators, B: Chemical* 162.1 (2012), pp. 425–434. ISSN: 09254005. DOI: 10.1016/j.snb.2011.12.017. URL: http://dx.doi.org/10.1016/j.snb.2011.12.017.

[202] Toyohiro Naito et al. “Three dimensional fabrication for microfluidics by conventional techniques and equipment used in mass production”. In: *Micromachines* 7.5 (2016). ISSN: 2072666X. DOI: 10.3390/mi7050082.

[203] Tae Woo Lim et al. “Three dimensionally crossing manifold micro mixer for fast mixing in a short channel length”. In: *Lab on a Chip* 11.1 (2011), pp. 100–103. ISSN: 14730189. DOI: 10.1039/c005325m.

[204] Chao Liu et al. "Rapid three-dimensional microfluidic mixer for high viscosity solutions to unravel earlier folding kinetics of G-quadruplex under molecular crowding conditions". In: *Talanta* 149 (2016), pp. 237–243. ISSN: 00399140. DOI: 10.1016/j.talanta.2015.11.036. URL: http://dx.doi.org/10.1016/j.talanta.2015.11.036.

[205] Jonathan Avesar et al. "Rapid phenotypic antimicrobial susceptibility testing using nanoliter arrays". In: *Proceedings of the National Academy of Sciences* 114.29 (July 2017), E5787 LP –E5795. DOI: 10.1073/pnas.1703736114. URL: http://www.pnas.org/content/114/29/E5787.abstract.

[206] CDC. "Antibiotic Resistance Threats in the United States". In: *U.S. Department of Health and Human Services.* 114 (2013).

[207] Nishant A. Dafale et al. "Selection of appropriate analytical tools to determine the potency and bioactivity of antibiotics and antibiotic resistance". In: *Journal of Pharmaceutical Analysis* 6.4 (2016), pp. 207–213. ISSN: 20951779. DOI: 10.1016/j.jpha.2016.05.006. URL: http://dx.doi.org/10.1016/j.jpha.2016.05.006.

[208] Claude Saint Ruf et al. "Antibiotic susceptibility testing of the gram negative bacteria based on flow cytometry". In: *Frontiers in Microbiology* 7.JUL (2016), pp. 1–13. ISSN: 1664302X. DOI: 10.3389/fmicb.2016.01121.

[209] Sibhghatulla Shaikh et al. "Antibiotic resistance and extended spectrum betalactamase types, epidemiology and treatment". In: *Saudi Journal of Biological Sciences* 22.1 (2015), pp. 90–101. ISSN: 1319562X. DOI: 10.1016/j.sjbs.2014.08.002. URL: http://dx.doi.org/10.1016/j.sjbs.2014.08.002.

[210] Otto Cars, Anna Hedin, and Andreas Heddini. "The global need for effective antibiotics, Moving towards concerted action". In: *Drug Resistance Updates* 14.2 (2011), pp. 68–69. ISSN: 1368-7646. DOI: https://doi.org/10.1016/j.drup.2011.02.006. URL: http://www.sciencedirect.com/science/article/pii/S1368764611000227.

[211] Roberta J Worthington and Christian Melander. "Combination Approaches to Combat Multi-Drug Resistant Bacteria, The problem of multi drug-resistant bacteria". In: *Trends in Biotechnology* 31.3 (2012), pp. 177–184. DOI: 10.1016/j.tibtech.2012.12.006. URL: https://www.ncbi.nlm.nih.gov/pmc/articles/PMC3594660/pdf/nihms437593.pdf.

[212] Adult Infectious and Disease Notes. "Conly". In: 16.3 (2005), pp. 159–160.

[213] Samuel Kim et al. "Miniaturized Antimicrobial Susceptibility Test by Combining Concentration Gradient Generation and Rapid Cell Culturing". In: *Antibiotics* 4.4 (2015), pp. 455–466. DOI: 10.3390/antibiotics4040455.

[214] Chris Wilkerson et al. “Antibiotic Resistance and Distribution of Tetracycline Resistance Genes in Escherichia coli O157H7 Isolates from Humans and Bovines”. In: *Antimicrobial Agents and Chemotherapy* 48.3 (2004), pp. 1066–1067. ISSN: 00664804. DOI: 10.1128/AAC.48.3.1066-1067.2004.

[215] Sumera Sabir et al. “Isolation and antibiotic susceptibility of E. coli from urinary tract infections in a tertiary care hospital”. In: *Pakistan Journal of Medical Sciences* 30.2 (2014), pp. 389–392. ISSN: 1682024X. DOI: 10.12669/pjms.302.4289.

[216] Dionex. “Analysis of the Aminoglycoside Antibiotics Kanamycin and Amikacin Matches USP Requirements”. In: *Application Note 267* (2011), pp. 1–6.

[217] Erique Jose Peixoto De Miranda et al. “Susceptibility To Antibiotics in Urinary Tract Infections in a Secondary Care Setting in Sao Paulo, Brazil, From Urine Cultures”. In: *Revista do Instituto de Medicina Tropical de Sao Paulo* 56.4 (2014), pp. 313–324. DOI: 10.1590/s0036-46652014000400009.

[218] Jan Hudzicki. “Kirby-Bauer Disk Diffusion Susceptibility Test Protocol Author Information”. In: *American Society For Microbiology* December 2009 (2012), pp. 1–13. URL: https://www.asm.org/Protocols/Kirby-Bauer-Disk-Diffusion-Susceptibility-Test-Pro.

[219] Steven D. Dallas et al. “Development of doxycycline MIC and disk diffusion interpretive breakpoints and revision of tetracycline breakpoints for Streptococcus pneumoniae”. In: *Journal of Clinical Microbiology* 51.6 (2013), pp. 1798–1802. ISSN: 00951137. DOI: 10.1128/JCM.00125-13.

[220] CLSI. “Performance Standards for Antimicrobial Susceptibility Testing Performance Standards for Antimicrobial Susceptibility Testing Suggested Citation”. In: *CLSI document M02-A11* (2018), pp. 100–125. URL: https://clsi.org/media/2663/m100ed29_sample.pdf.

[221] Jennifer Campbell et al. “Microfluidic advances in phenotypic antibiotic susceptibility testing”. eng. In: *Biomedical microdevices* 18.6 (Dec. 2016), p. 103. ISSN: 1572-8781. DOI: 10.1007/s10544-016-0121-8. URL: https://www.ncbi.nlm.nih.gov/pubmed/27796676%20https://www.ncbi.nlm.nih.gov/pmc/articles/PMC5473355/.

[222] J M Andrews. “Determination of minimum inhibitory concentrations.” In: *The Journal of antimicrobial chemotherapy* 48 (2001), pp. 5–16. ISSN: 0305-7453. URL: http://www.ncbi.nlm.nih.gov/pubmed/11420333.

[223] Christer Malmberg et al. “A novel microfluidic assay for rapid phenotypic antibiotic susceptibility testing of bacteria detected in clinical blood cultures”. In: *PLoS ONE* 11.12 (2016), pp. 1–15. ISSN: 19326203. DOI: 10.1371/journal.pone.0167356.

[224] Irith Wiegand, Kai Hilpert, and Robert E W Hancock. "Agar and broth dilution methods to determine the minimal inhibitory concentration (MIC) of antimicrobial substances". In: *Nature Protocols* 3.2 (2008), pp. 163–175. ISSN: 17542189. DOI: 10.1038/nprot.2007.521.

[225] Eucast. "Determination of minimum inhibitory concentrations of antibacterial agents by broth dilution". In: *Clinical Microbiology and Infection* 9.8 (2003), pp. 1–7. ISSN: 1469-0691. DOI: 10.1046/j.1469-0691.2003.00790.

[226] Amanda K. Kidsley et al. "Antimicrobial susceptibility of escherichia coli and salmonella spp. Isolates from healthy pigs in Australia". In: *Frontiers in Microbiology* 9.JUL (2018), pp. 1–11. ISSN: 1664302X. DOI: 10.3389/fmicb.2018.01207.

[227] Zakariya Al-Muharrmi et al. "Antibiotic combination as empirical therapy for extended spectrum Beta-lactamase." In: *Oman medical journal* 23.2 (2008), pp. 78–81. ISSN: 1999-768X. URL: http://www.ncbi.nlm.nih.gov/pubmed/22379542%0Ahttp://www.pubmedcentral.nih.gov/articlerender.fcgi?artid=PMC3282419.

[228] Pranita D. Tamma, Sara E. Cosgrove, and Lisa L. Maragakis. "Combination therapy for treatment of infections with gram-negative bacteria". In: *Clinical Microbiology Reviews* 25.3 (2012), pp. 450–470. ISSN: 08938512. DOI: 10.1128/CMR.05041-11.

[229] Nate J. Cira et al. "A self-loading microfluidic device for determining the minimum inhibitory concentration of antibiotics". In: *Lab on a Chip* 12.6 (2012), pp. 1052–1059. ISSN: 14730189. DOI: 10.1039/c2lc20887c.

[230] A. J. Watkinson et al. "Novel method for rapid assessment of antibiotic resistance in Escherichia coli isolates from environmental waters by use of a modified chromogenic agar". In: *Applied and Environmental Microbiology* 73.7 (2007), pp. 2224–2229. ISSN: 00992240. DOI: 10.1128/AEM.02099-06.

[231] Anat Zimmer et al. "Prediction of multidimensional drug dose responses based on measurements of drug pairs". In: *Proceedings of the National Academy of Sciences* 113.37 (2016), pp. 10442–10447. ISSN: 0027-8424. DOI: 10.1073/pnas.1606301113.

[232] Spoorthi N Jain and Aishwarya Sampath. "Antibiotic Synergy Test: Checkerboard Method on Multidrug Resistant Pseudomonas Aeruginosa". In: *Research Journal of Pharmacy* 2.12 (2011), p. 2011. URL: www.irjponline.com.

[233] Funmilola Oluyemi Omoya and Kehinde Oluyemi Ajayi. "Synergistic Effect of Combined Antibiotics against Some Selected Multidrug Resistant Human Pathogenic Bacteria Isolated from Poultry Droppings in Akure, Nigeria". In: *Advances in Microbiology* 06.14 (2016), pp. 1075–1090. ISSN: 2165-3402. DOI: 10.4236/aim.2016.614100.

[234] Pamela Yeh, Ariane I. Tschumi, and Roy Kishony. "Functional classification of drugs by properties of their pairwise interactions". In: *Nature Genetics* 38.4 (2006), pp. 489–494. ISSN: 10614036. DOI: 10.1038/ng1755.

[235] Tobias Bollenbach. "Antimicrobial interactions: Mechanisms and implications for drug discovery and resistance evolution". In: *Current Opinion in Microbiology* 27 (2015), pp. 1–9. ISSN: 18790364. DOI: 10.1016/j.mib.2015.05.008. URL: http://dx.doi.org/10.1016/j.mib.2015.05.008.

[236] Tobias Bollenbach et al. "Nonoptimal Microbial Response to Antibiotics Underlies Suppressive Drug Interactions". In: *Cell* 139.4 (2009), pp. 707–718. ISSN: 00928674. DOI: 10.1016/j.cell.2009.10.025. URL: http://dx.doi.org/10.1016/j.cell.2009.10.025.

[237] Yi Lu et al. "Single Cell Antimicrobial Susceptibility Testing by Confined Microchannels and Electrokinetic Loading". In: *Analytical Chemistry* 85.8 (Apr. 2013), pp. 3971–3976. ISSN: 0003-2700. DOI: 10.1021/ac4004248. URL: https://doi.org/10.1021/ac4004248.

[238] Sachidevi Puttaswamy et al. "A Comprehensive Review of the Present and Future Antibiotic Susceptibility Testing (AST) Systems". In: *Archives of Clinical Microbiology* 09.03 (2018), pp. 1–9. DOI: 10.4172/1989-8436.100083.

[239] Ikram Ullah Khan et al. "Microfluidics: A focus on improved cancer targeted drug delivery systems". In: *Journal of Controlled Release* 172.3 (2013), pp. 1065–1074. ISSN: 0168-3659. DOI: https://doi.org/10.1016/j.jconrel.2013.07.028. URL: http://www.sciencedirect.com/science/article/pii/S0168365913004380.

[240] James Q Boedicker et al. "Detecting bacteria and determining their susceptibility to antibiotics by stochastic confinement in nanoliter droplets using plug-based microfluidics." In: *Lab Chip* 8.8 (2008), pp. 1265–1272. ISSN: 1473-0197. DOI: 10.1039/b804911d. URL: http://dx.doi.org/10.1039/b804911d.

[241] Nam-Trung Nguyen et al. "Design, fabrication and characterization of drug delivery systems based on lab-on-a-chip technology". In: *Advanced Drug Delivery Reviews* 65.11 (2013), pp. 1403–1419. ISSN: 0169-409X. DOI: https://doi.org/10.1016/j.addr.2013.05.008. URL: http://www.sciencedirect.com/science/article/pii/S0169409X13001270.

[242] Dami An, Kwangmi Kim, and Jeongyun Kim. "Microfluidic system based high throughput drug screening system for curcumin/TRAIL combinational chemotherapy in human prostate cancer PC3 cells". In: *Biomolecules and Therapeutics* 22.4 (2014), pp. 355–362. ISSN: 20054483. DOI: 10.4062/biomolther.2014.078.

[243] Samar Damiati et al. "Microfluidic devices for drug delivery systems and drug screening". In: *Genes* 9.2 (2018). ISSN: 20734425. DOI: 10.3390/genes9020103.

[244] Dileep Daniel Monie and Sujata Kumari Bhatia. "Bioprinting of Dynamic Human Organs-on-Chips: Enabling Technologies for Rapid Drug Development and Personalized Medicine". In: *Bioprinting in Regenerative Medicine*. Ed. by Kursad Turksen. Cham: Springer International Publishing, 2015, pp. 123–137. ISBN: 978-3-319-21386-6. DOI: 10.1007/978-3-319-21386-6_6. URL: http://dx.doi.org/10.1007/978-3-319-21386-6_6.

[245] Edmond W K Young and David J Beebe. "Fundamentals of microfluidic cell culture in controlled microenvironments". In: *Chemical Society Reviews* 39.3 (2010), pp. 1036–1048. ISSN: 0306-0012. DOI: 10.1039/B909900J. URL: http://dx.doi.org/10.1039/B909900J.

[246] Kathleen E. Mach et al. "A biosensor platform for rapid antimicrobial susceptibility testing directly from clinical samples". In: *Journal of Urology* 185.1 (2011), pp. 148–153. ISSN: 00225347. DOI: 10.1016/j.juro.2010.09.022. URL: http://dx.doi.org/10.1016/j.juro.2010.09.022.

[247] Janine Bates et al. "Point of care testing for urinary tract infection in primary care (POETIC): Protocol for a randomised controlled trial of the clinical and cost effectiveness of FLEXICULT informed management of uncomplicated UTI in primary care". In: *BMC Family Practice* 15.1 (2014), pp. 1–9. ISSN: 14712296. DOI: 10.1186/s12875-014-0187-4.

[248] Hongying Zhu et al. "Cost-effective and compact wide-field fluorescent imaging on a cell-phone." In: *Lab on a Chip* 11.2 (2011), pp. 315–322. ISSN: 1473-0189. DOI: 10.1039/c0lc00358a. URL: http://pubs.rsc.org/en/Content/ArticleHTML/2011/LC/C0LC00358A.

[249] Yoshimi Matsumoto et al. "A microfluidic channel method for rapid drug-susceptibility testing of Pseudomonas aeruginosa". In: *PLoS ONE* 11.2 (2016), pp. 1–17. ISSN: 19326203. DOI: 10.1371/journal.pone.0148797.

[250] Dertinger SKW et al. " Generation of gradients having complex shapes using microfluidic networks". In: *Analytical Chemistry* 73.6 (2001), pp. 1240–1246.

[251] Choong Kim et al. "A serial dilution microfluidic device using a ladder network generating logarithmic or linear concentrations". In: *Lab on a Chip* 8.3 (2008), pp. 473–479. ISSN: 14730189. DOI: 10.1039/b714536e.

[252] S H Zigmond and S J Sullivan. "Sensory adaptation of leukocytes to chemotactic peptides." In: *The Journal of Cell Biology* 82.2 (Aug. 1979), 517 LP –527. DOI: 10.1083/jcb.82.2.517. URL: http://jcb.rupress.org/content/82/2/517.abstract.

[253] Bahige G. Abdallah et al. "Protein Crystallization in an Actuated Microfluidic Nanowell Device". In: *Crystal Growth and Design* 16.4 (2016), pp. 2074–2082. ISSN: 15287505. DOI: 10.1021/acs.cgd.5b01748.

[254] Nachiket Shembekar et al. “Droplet-based microfluidics in drug discovery, transcriptomics and high-throughput molecular genetics”. In: *Lab Chip* 16 (2016), pp. 1314–1331. ISSN: 1473-0197. DOI: 10.1039/C6LC00249H. URL: http://pubs.rsc.org/en/Content/ArticleLanding/2016/LC/C6LC00249H.

[255] Federica Eduati et al. “A microfluidics platform for combinatorial drug screening on cancer biopsies”. In: *Nature Communications* 9.1 (2018), p. 2434. ISSN: 2041-1723. DOI: 10.1038/s41467-018-04919-w. URL: https://doi.org/10.1038/s41467-018-04919-w.

[256] Bo Hong et al. “A concentration gradient generator on a paper-based microfluidic chip coupled with cell culture microarray for high-throughput drug screening”. In: *Biomedical Microdevices* 18.1 (2016), pp. 1–8. ISSN: 15728781. DOI: 10.1007/s10544-016-0054-2.

[257] Minghui Tang et al. “A linear concentration gradient generator based on multi-layered centrifugal microfluidics and its application in antimicrobial susceptibility testing”. In: *Lab on a Chip* 18.10 (2018), pp. 1452–1460. ISSN: 14730189. DOI: 10.1039/c8lc00042e. URL: http://dx.doi.org/10.1039/C8LC00042E.

[258] Ping Cui and Sicen Wang. “Application of microfluidic chip technology in pharmaceutical analysis: A review”. In: *Journal of Pharmaceutical Analysis* 9.4 (2019), pp. 238–247. ISSN: 20951779. DOI: 10.1016/j.jpha.2018.12.001. URL: http://dx.doi.org/10.1016/j.jpha.2018.12.001.

[259] Kelly Flentie et al. “Microplate-based surface area assay for rapid phenotypic antibiotic susceptibility testing”. In: *Scientific Reports* 9.1 (2019), pp. 1–9. ISSN: 20452322. DOI: 10.1038/s41598-018-35916-0. URL: http://dx.doi.org/10.1038/s41598-018-35916-0.

[260] Jang Ho Ha et al. “Analysis of 3D multi-layer microfluidic gradient generator”. In: *Electrophoresis* 38.2 (2017), pp. 270–277. ISSN: 15222683. DOI: 10.1002/elps.201600443.

[261] Yunhuan Zheng et al. “Development of a novel perfusion microfluidic cell culture device for cell-based assays”. In: *4th IEEE International Conference on Nano/Micro Engineered and Molecular Systems, NEMS 2009* January (2009), pp. 257–260. DOI: 10.1109/NEMS.2009.5068572.

[262] Yong He et al. “Developments of 3D Printing Microfluidics and Applications in Chemistry and Biology: a Review”. In: *Electroanalysis* 28.8 (2016), pp. 1658–1678. ISSN: 15214109. DOI: 10.1002/elan.201600043.

[263] Jing Dai, Morgan Hamon, and Sachin Jambovane. “Microfluidics for Antibiotic Susceptibility and Toxicity Testing”. In: *Bioengineering* 3.4 (2016), p. 25. ISSN: 2306-5354. DOI: 10.3390/bioengineering3040025. URL: http://www.mdpi.com/2306-5354/3/4/25.

[264] Kwang W. Oh et al. “Design of pressure-driven microfluidic networks using electric circuit analogy”. In: *Lab on a Chip* 12.3 (2012), pp. 515–545. ISSN: 14730189. DOI: 10.1039/c2lc20799k.

[265] Noo Li Jeon et al. “Generation of solution and surface gradients using microfluidic systems”. In: *Langmuir* 16.22 (2000), pp. 8311–8316. ISSN: 07437463. DOI: 10.1021/la000600b.

[266] Krzysztof Churski et al. “Rapid screening of antibiotic toxicity in an automated microdroplet system”. In: *Lab on a Chip* 12.9 (2012), pp. 1629–1637. ISSN: 14730189. DOI: 10.1039/c2lc21284f.

[267] Product Description. “in Vitro”. In: *Water Research* 800 ().

[268] Promega Corporation. “CellTiter Blue Cell Viability Assay recommended controls for resazurin”. In: (), pp. 608–277.

[269] Satyajit D. Sarker, Lutfun Nahar, and Yashodharan Kumarasamy. “Microtitre plate based antibacterial assay incorporating resazurin as an indicator of cell growth and its application in the in vitro antibacterial screening of phytochemicals”. In: *Methods* 42.4 (2007), pp. 321–324. ISSN: 10462023. DOI: 10.1016/j.ymeth.2007.01.006. URL: http://dx.doi.org/10.1016/j.ymeth.2007.01.006.

[270] Lila Ruangpan. “Chapter 3. Minimal inhibitory concentration (MIC) test and determination of antimicrobial resistant bacteria”. In: *Laboratory manual of standardized methods for antimicrobial sensitivity tests for bacteria isolated from aquatic animals and environment* Mic (2004), pp. 31–55.

[271] Omega Optical. “Omega Optical 585BP90 Data Sheet”. In: *Data Sheet* (2017), pp. 6–7.

[272] A.M. Cauce. “Bacterial Counts - Quantitative Analysis of Microbes”. In: *University of Washington* (2012), pp. 1–5.

[273] M. D. EWELL. “Counting Bacteria”. In: *Science* ns-15.384 (2006), pp. 362–362. ISSN: 0036-8075. DOI: 10.1126/science.ns-15.384.362-a.

[274] B L De. “BL21(DE3) Competent E coli C2527H”. In: 21 (), pp. 20–21.

[275] Agilent Technologies. “BL21(DE3) Competent Cells, BL21(DE3)pLysS Competent Cells, and BL21 Competent Cells”. In: 21 (2019).

[276] Joao Simoes and Tao Dong. “Continuous and real-time detection of drinking water pathogens with a low cost fluorescent optofluidic sensor”. In: *Sensors (Switzerland)* 18.7 (2018). ISSN: 14248220. DOI: 10.3390/s18072210.

[277] Yongmo Yang, Sangpyeong Kim, and Junseok Chae. “Separating and detecting escherichia coli in a microfluidic channel for urinary tract infection applications”. In: *Journal of Microelectromechanical Systems* 20.4 (2011), pp. 819–827. ISSN: 10577157. DOI: 10.1109/JMEMS.2011.2159095.

[278] Ping Yao et al. “3D printed pneumatic microfluidic mixer for colorimetric detection of Listeria monocytogenes”. In: (2018), pp. 1–10. DOI: 10.13031/aim.201800524.

[279] P. Pletnev et al. “Survival guide: Escherichia coli in the stationary phase”. In: *Acta Naturae* 7.4 (2015), pp. 22–33. ISSN: 20758251.

[280] *Pouring LB Agar Plates*. URL: https://www.addgene.org/protocols/pouring-lb-agar-plates/ (visited on 10/10/2019).

[281] Klas I. Udekwu et al. “Functional relationship between bacterial cell density and the efficacy of antibiotics”. In: *Journal of Antimicrobial Chemotherapy* 63.4 (2009), pp. 745–757. ISSN: 14602091. DOI: 10.1093/jac/dkn554.

[282] Bradley J Gardiner et al. “Nitrofurantoin and fosfomycin for resistant urinary tract infections, old drugs for emerging problems”. eng. In: *Australian prescriber* 42.1 (Feb. 2019), pp. 14–19. ISSN: 0312-8008. DOI: 10.18773/austprescr.2019.002. URL: https://www.ncbi.nlm.nih.gov/pubmed/30765904%20https://www.ncbi.nlm.nih.gov/pmc/articles/PMC6370609/.

[283] C Duployez, J Robert, and A Vachee. “Trimethoprim susceptibility in E. coli community acquired urinary tract infections in France”. In: *Medecine et Maladies Infectieuses* 48.6 (2018), pp. 410–413. ISSN: 0399-077X. DOI: https://doi.org/10.1016/j.medmal.2018.03.010. URL: http://www.sciencedirect.com/science/article/pii/S0399077X17307266.

[284] Pamela Yeh, Ariane I. Tschumi, and Roy Kishony. “Functional classification of drugs by properties of their pairwise interactions”. In: *Nature Genetics* 38.4 (2006), pp. 489–494. ISSN: 10614036. DOI: 10.1038/ng1755.

[285] George M Eliopoulos and Claudie T Eliopoulos. “Ciprofloxacin in combination with other antimicrobials”. In: *The American Journal of Medicine* 87.5 (Nov. 1989), S17–S22. ISSN: 0002-9343. DOI: 10.1016/0002-9343(89)90013-2. URL: https://doi.org/10.1016/0002-9343(89)90013-2.

[286] “Amikacin Sulfate”. In: *Amikacin Sulfate Monograph for Professionals* (2017), pp. 1–23.

[287] Christina A. Sutherland, Jamie E. Verastegui, and David P. Nicolau. “In vitro potency of amikacin and comparators against E. coli, K. pneumoniae and P. aeruginosa respiratory and blood isolates”. In: *Annals of Clinical Microbiology and Antimicrobials* 15.1 (2016), pp. 1–7. ISSN: 14760711. DOI: 10.1186/s12941-016-0155-z.

[288] J. Zhao et al. “Protothecosis successfully treated with amikacin combined with tetracyclines. Fallbericht. Protothecose erfolgreich mit Amikacin plus Tetracyclinen behandelt”. In: *Mycoses* 47.3-4 (2004), pp. 156–158. ISSN: 0933-7407. DOI: 10.1046/j.1439-0507.2003.00955.x.

[289] Joseph L Kuti et al. “Defining the potency of amikacin against Escherichia coli, Klebsiella pneumoniae, Pseudomonas aeruginosa, and Acinetobacter baumannii”. eng. In: *Infection and drug resistance* 11 (May 2018), pp. 783–790. ISSN: 1178-6973. DOI: 10.2147/IDR.S161636. URL: https://www.ncbi.nlm.nih.gov/pubmed/29872328%20https://www.ncbi.nlm.nih.gov/pmc/articles/PMC5975598/.

[290] M Azhar and D Dendukuri. "Microfluidic platforms for point of care (POC) medical diagnostics". In: ed. by Roger J B T - Medical Biosensors for Point of Care (POC) Applications Narayan. Woodhead Publishing, 2017, pp. 255–273. ISBN: 978-0-08-100072-4. DOI: https://doi.org/10.1016/B978-0-08-100072-4.00011-3. URL: http://www.sciencedirect.com/science/article/pii/B9780081000724000113.

[291] Srikrishnan Pillai Raju and Xiaogang Chu. "Rapid Low-Cost Microfluidic Detection in Point of Care Diagnostics". In: *Journal of Medical Systems* 42.10 (2018), p. 184. ISSN: 1573-689X. DOI: 10.1007/s10916-018-1043-1. URL: https://doi.org/10.1007/s10916-018-1043-1.

[292] Frank A. Gomez. "The future of microfluidic point-of-care diagnostic devices". In: *Bioanalysis* 5.1 (2013), pp. 1–3. ISSN: 17576180. DOI: 10.4155/bio.12.307.

[293] Elisabetta Primiceri et al. "Key enabling technologies for point-of-care diagnostics". In: *Sensors (Switzerland)* 18.11 (2018). ISSN: 14248220. DOI: 10.3390/s18113607.

[294] Sunitha Nagrath et al. "Isolation of rare circulating tumour cells in cancer patients by microchip technology". In: *Nature* 450.7173 (2007), pp. 1235–1239. ISSN: 1476-4687. DOI: 10.1038/nature06385. URL: https://doi.org/10.1038/nature06385.

[295] Samuel K Sia and Larry J Kricka. "Microfluidics and point-of-care testing". In: *Lab on a Chip* 8.12 (2008), pp. 1982–1983. ISSN: 1473-0197. DOI: 10.1039/B817915H. URL: http://dx.doi.org/10.1039/B817915H.

[296] Kathleen David. "Point-of-Care Versus Lab-Based Testing, Striking a Balance". In: *Clinical Laboratory News* 1 (2016).

[297] Ann E. Stapleton et al. "Performance of a New Rapid Immunoassay Test Kit for Point-of-Care Diagnosis of Significant Bacteriuria". In: *Journal of Clinical Microbiology* 53.9 (2015), pp. 2805–2809. ISSN: 0095-1137. DOI: 10.1128/jcm.00353-15.

[298] Dong Ku Kang et al. "Rapid detection of single bacteria in unprocessed blood using Integrated Comprehensive Droplet Digital Detection". In: *Nature Communications* 5 (2014), pp. 1–10. ISSN: 20411723. DOI: 10.1038/ncomms6427. URL: http://dx.doi.org/10.1038/ncomms6427.

[299] Alphonsus H.C. Ng and Aaron R. Wheeler. "Next-generation microfluidic point-of-care diagnostics". In: *Clinical Chemistry* 61.10 (2015), pp. 1233–1234. ISSN: 15308561. DOI: 10.1373/clinchem.2015.240226.

[300] Adel Pourmand et al. "Fabrication of whole-thermoplastic normally closed microvalve, micro check valve, and micropump". In: *Sensors and Actuators, B: Chemical* 262 (2018), pp. 625–636. ISSN: 09254005. DOI: 10.1016/j.snb.2017.12.132. URL: https://doi.org/10.1016/j.snb.2017.12.132.

[301] Bei Zhao et al. "A Controllable and Integrated Pump-enabled Microfluidic Chip and Its Application in Droplets Generating". In: *Scientific Reports* 7.1 (2017), pp. 1–8. ISSN: 20452322. DOI: 10.1038/s41598-017-10785-1. URL: http://dx.doi.org/10.1038/s41598-017-10785-1.

[302] Ivan K. Dimov et al. "Stand-alone self-powered integrated microfluidic blood analysis system (SIMBAS)". In: *Lab on a Chip* 11.5 (2011), pp. 845–850. ISSN: 14730189. DOI: 10.1039/c0lc00403k.

[303] K. Iwai, R. D. Sochol, and L. Lin. "Finger-powered, pressure-driven microfluidic pump". In: *Proceedings of the IEEE International Conference on Micro Electro Mechanical Systems (MEMS)* (2011), pp. 1131–1134. ISSN: 10846999. DOI: 10.1109/MEMSYS.2011.5734629.

[304] Juhwan Park, Hyewon Roh, and Je Kyun Park. "Finger-actuated microfluidic concentration gradient generator compatible with a microplate". In: *Micromachines* 10.3 (2019). ISSN: 2072666X. DOI: 10.3390/mi10030174.

[305] Yuan Sheng Lee, Nirveek Bhattacharjee, and Albert Folch. "3D-printed Quake-style microvalves and micropumps". In: *Lab on a Chip* 18.8 (2018), pp. 1207–1214. ISSN: 14730189. DOI: 10.1039/c8lc00001h. URL: http://dx.doi.org/10.1039/C8LC00001H.

[306] Eric Christopher Sweet. "3D Printed Integrated Fluidic Circuitry via Multijet Additive Manufacturing: A New Class of Three Dimensional Microfluidic Operators". Masters of Science Thesis. University of California, Berkeley, 2015, pp. 1–46.

[307] Aa Deshmukh. "Continuous micromixer with pulsatile micropumps". In: *Technical Digest of the ...* (2000), pp. 2–5. URL: http://www.me.berkeley.edu/faculty/liepmann/bio.html/assets/deshmukh_HiltonHead.pdf.

[308] Jianbo Shao et al. "Integrated microfluidic chip for endothelial cells culture and analysis exposed to a pulsatile and oscillatory shear stress". In: *Lab on a chip* 9.21 (2009), pp. 3118–25. ISSN: 1473-0197. DOI: 10.1039/b909312e. URL: http://www.ncbi.nlm.nih.gov/pubmed/19823728.

[309] Behzad Nasseri et al. "Point-of-care microfluidic devices for pathogen detection". In: *Biosensors and Bioelectronics* 117 (2018), pp. 112–128. ISSN: 0956-5663. DOI: https://doi.org/10.1016/j.bios.2018.05.050. URL: http://www.sciencedirect.com/science/article/pii/S0956566318304044.

[310] Samendra Masaaki. "Rapid Detection Technologies for Monitoring Microorganisms in Water". In: *Biosensors Journal* 03.01 (2014), pp. 1–8. DOI: 10.4172/2090-4967.1000109.

[311] Jaclyn A. Adkins et al. "Colorimetric and Electrochemical Bacteria Detection Using Printed Paper- and Transparency-Based Analytic Devices". In: *Analytical Chemistry* 89.6 (2017), pp. 3613–3621. ISSN: 15206882. DOI: 10.1021/acs.analchem.6b05009.

[312] P. Gwimbi. "The microbial quality of drinking water in Manonyane community: Maseru district (Lesotho)". In: *African Health Sciences* 11.3 (2011), pp. 474–480. ISSN: 16806905.

[313] USEPA. "Method 1604: Total Coliforms and Escherichia coli in Water by Membrane Filtration Using a Simultaneous Detection Technique (MI Medium). U.S. Environmental Protection Agency Office of Water. Washington. EPA-821-R-02-024." In: September (2002), p. 18. DOI: EPA-821-R-02-024. URL: http://www.epa.gov/nerlcwww/1604sp02.pdf.

[314] Hongying Zhu, Uzair Sikora, and Aydogan Ozcan. "Quantum dot enabled detection of Escherichia coli using a cell-phone". In: *Analyst* 137.11 (2012), pp. 2541–2544. ISSN: 13645528. DOI: 10.1039/c2an35071h.

[315] Pramod K. Pandey et al. "Contamination of water resources by pathogenic bacteria". In: *AMB Express* 4.1 (2014), pp. 1–16. ISSN: 21910855. DOI: 10.1186/s13568-014-0051-x.

[316] Ke Yang et al. "Novel developments in mobile sensing based on the integration of microfluidic devices and smartphones". In: *Lab on a Chip* 16.6 (2016), pp. 943–958. ISSN: 14730189. DOI: 10.1039/c5lc01524c. URL: http://dx.doi.org/10.1039/C5LC01524C.

[317] R B Raybourne, M Tortorello, and M Y Deng. "Microscopy techniques: DEFT and flow cytometry". In: *Detecting pathogens in food* 33.8 (2003), 2188 LP –2191.

[318] P M Fratamico et al. "Detection of Escherichia coli O157:H7 by multiplex PCR." In: *Journal of Clinical Microbiology* 33.8 (Aug. 1995), 2188 LP –2191. URL: http://jcm.asm.org/content/33/8/2188.abstract.

[319] William E Aldeen et al. "Evaluation of a commercially available ELISA assay for detection of Giardia lamblia in fecal specimens". In: *Diagnostic Microbiology and Infectious Disease* 21.2 (1995), pp. 77–79. ISSN: 0732-8893. DOI: https://doi.org/10.1016/0732-8893(94)00142-J. URL: http://www.sciencedirect.com/science/article/pii/073288939400142J.

[320] Joon Myong Song and Tuan Vo-Dinh. "Miniature biochip system for detection of Escherichia coli O157:H7 based on antibody-immobilized capillary reactors and enzyme-linked immunosorbent assay". In: *Analytica Chimica Acta* 507.1 (2004), pp. 115–121. ISSN: 0003-2670. DOI: https://doi.org/10.1016/j.aca.2003.11.072. URL: http://www.sciencedirect.com/science/article/pii/S0003267003015083.

[321] D J Wright, P A Chapman, and C A Siddons. "Immunomagnetic separation as a sensitive method for isolating Escherichia coli O157 from food samples". In: *Epidemiology and Infection* 113.1 (1994), pp. 31–39. ISSN: 0950-2688. DOI: DOI:10.1017/S0950268800051438. URL: https://www.cambridge.org/core/article/immunomagnetic-separation-as-a-sensitive-method-for-isolating-escherichia-coli-o157-from-food-samples/AEBBE7E82980FADB5D63937F85FAB0

[322] Fidel G Perez et al. “Immunomagnetic Separation with Mediated Flow Injection Analysis Amperometric Detection of Viable Escherichia coli O157”. In: *Analytical Chemistry* 70.11 (June 1998), pp. 2380–2386. ISSN: 0003-2700. DOI: 10.1021/ac970715t. URL: https://doi.org/10.1021/ac970715t.

[323] Y Yang, S Kim, and J Chae. “Separating and Detecting Escherichia Coli in a Microfluidic Channel for Urinary Tract Infection Applications”. In: *Journal of Microelectromechanical Systems* 20.4 (2011), pp. 819–827. ISSN: 1941-0158 VO - 20. DOI: 10.1109/JMEMS.2011.2159095.

[324] Flor Yazmin Ramirez Castillo et al. “Waterborne pathogens: Detection methods and challenges”. In: *Pathogens* 4.2 (2015), pp. 307–334. ISSN: 20760817. DOI: 10.3390/pathogens4020307

[325] Betsy Foxman. “Urinary Tract Infection Syndromes: Occurrence, Recurrence, Bacteriology, Risk Factors, and Disease Burden”. In: *Infectious Disease Clinics of North America* 28.1 (2014), pp. 1–13. ISSN: 0891-5520. DOI: https://doi.org/10.1016/j.idc.2013.09.003. URL: http://www.sciencedirect.com/science/article/pii/S0891552013000743.

[326] Raymond N Blum and Richard A Wright. “Detection of pyuria and bacteriuria in symptomatic ambulatory women”. In: *Journal of General Internal Medicine* 7.2 (1992), pp. 140–144. ISSN: 1525-1497. DOI: 10.1007/BF02598002. URL: https://doi.org/10.1007/BF02598002.

[327] Ayokunle Oluwafemi Olanrewaju et al. “Microfluidic Capillaric Circuit for Rapid and Facile Bacteria Detection”. In: *Analytical Chemistry* 89.12 (2017), pp. 6846–6853. ISSN: 15206882. DOI: 10.1021/acs.analchem.7b01315.

[328] Vural Kara et al. “Microfluidic detection of movements of: Escherichia coli for rapid antibiotic susceptibility testing”. In: *Lab on a Chip* 18.5 (2018), pp. 743–753. ISSN: 14730189. DOI: 10.1039/c7lc01019b.

[329] Shilun Feng, Tao Dong, and Zhaochu Yang. “Detection of Urinary Tract Infections on lab-on-chip device by measuring photons emitted from ATP bioluminescence”. In: *2014 36th Annual International Conference of the IEEE Engineering in Medicine and Biology Society, EMBC 2014* (2014), pp. 3114–3117. DOI: 10.1109/EMBC.2014.6944282.

[330] M S Kumar et al. “Recent advances in biosensor based diagnosis of urinary tract infection”. In: *Biosensors and Bioelectronics* 80 (2016), pp. 497–510. ISSN: 0956-5663. DOI: https://doi.org/10.1016/j.bios.2016.02.023. URL: http://www.sciencedirect.com/science/article/pii/S0956566316301300.

[331] S Lori Busa et al. *Advances in Microfluidic Paper-Based Analytical Devices for Food and Water Analysis*. 2016. DOI: 10.3390/mi7050086.

[332] Hongying Zhu et al. “Optofluidic Fluorescent Imaging Cytometry on a Cell Phone”. In: *Anal Chem.* 83.17 (2011), pp. 6641–6647. DOI: 10.1021/ac201587a.Optofluidic.

[333] Jana C. Jokerst et al. “Development of a paper-based analytical device for colorimetric detection of select foodborne pathogens”. In: *Analytical Chemistry* 84.6 (2012), pp. 2900–2907. ISSN: 00032700. DOI: 10.1021/ac203466y.

[334] J C Jokerst et al. “a Paper-Based Analytical Device for the Colorimetric Detection of Foodborne Pathogenic Bacteria”. In: *Analytical Chemistry* 84 (2011), pp. 2116–2118. DOI: dx.doi.org/10.1021/ac203466y.

[335] Terry L Riss et al. “Cell Viability Assays”. In: *Assay Guidance Manual* (2004), pp. 1–31. URL: http://www.ncbi.nlm.nih.gov/pubmed/23805433.

[336] Angela Didomenico Astin. “Finger force capability measurement and prediction using anthropometric and myoelectric measures”. In: (1999), pp. 1–103.

[337] Matthew E. Walsh et al. “3D-Printable Materials for Microbial Liquid Culture”. In: *3D Printing and Additive Manufacturing* 3.2 (2016), pp. 113–118. ISSN: 2329-7662. DOI: 10.1089/3dp.2016.0007.

[338] David F. Williams. “On the mechanisms of biocompatibility”. In: *Biomaterials* 29.20 (2008), pp. 2941–2953. ISSN: 01429612. DOI: 10.1016/j.biomaterials.2008.04.023.

[339] Cristina B. Neves et al. “Ethanol postpolymerization treatment for improving the biocompatibility of acrylic reline resins”. In: *BioMed Research International* 2013 (2013). ISSN: 23146133. DOI: 10.1155/2013/485246.

[340] C. G.Y. Ngan et al. “Optimising the biocompatibility of 3D printed photopolymer constructs in vitro and in vivo”. In: *Biomedical Materials (Bristol)* 14.3 (2019). ISSN: 1748605X. DOI: 10.1088/1748-605X/ab09c4.

[341] Russell Y. Neches et al. “On the intrinsic sterility of 3D printing”. In: *PeerJ* 4 (2016), e2661. DOI: 10.7717/peerj.2661.

[342] Ibrahim Sadek Khattab et al. “Density, viscosity, and surface tension of water and ethanol mixtures from 293 to 323K”. In: *Korean Journal of Chemical Engineering* 29.6 (2012), pp. 812–817. ISSN: 1975-7220. DOI: 10.1007/s11814-011-0239-6. URL: https://doi.org/10.1007/s11814-011-0239-6.

[343] Juhong Chen et al. “Development of Engineered Bacteriophages for Escherichia coli Detection and High Throughput Antibiotic Resistance Determination”. In: *ACS Sensors* 2.4 (2017), pp. 484–489. ISSN: 23793694. DOI: 10.1021/acssensors.7b00021.

[344] Product Sheet. “Escherichia coli ATCC 25922”. In: *Product Sheet* (2013), pp. 1–2.

[345] T. A. Edge et al. “Occurrence of waterborne pathogens and escherichia coli at offshore drinking water intakes in lake Ontario”. In: *Applied and Environmental Microbiology* 79.19 (2013), pp. 5799–5813. ISSN: 00992240. DOI: 10.1128/AEM.00870-13.

[346] G. Czilwik et al. “Rapid and fully automated bacterial pathogen detection on a centrifugal-microfluidic LabDisk using highly sensitive nested PCR with integrated sample preparation”. In: *Lab on a Chip* 15.18 (2015), pp. 3749–3759. ISSN: 14730189. DOI: 10.1039/c5lc00591d.

[347] Juhong Chen et al. “Detection of Escherichia coli in Drinking Water Using T7 Bacteriophage-Conjugated Magnetic Probe”. In: *Analytical Chemistry* 87.17 (2015), pp. 8977–8984. ISSN: 15206882. DOI: 10.1021/acs.analchem.5b02175.

[348] Juhong Chen et al. “Lyophilized Engineered Phages for Escherichia coli Detection in Food Matrices”. In: *ACS Sensors* 2.11 (2017), pp. 1573–1577. ISSN: 23793694. DOI: 10.1021/acssensors.7b00561.

[349] Huan Peng and Irene A Chen. “Rapid Colorimetric Detection of Bacterial Species through the Capture of Gold Nanoparticles by Chimeric Phages”. In: *ACS Nano* 13.2 (Feb. 2019), pp. 1244–1252. ISSN: 1936-0851. DOI: 10.1021/acsnano.8b06395. URL: https://doi.org/10.1021/acsnano.8b06395.

[350] Qi You et al. “Colorimetric and test stripe-based assay of bacteria by using vancomycin-modified gold nanoparticles”. In: *Sensors and Actuators B: Chemical* 281 (2019), pp. 408–414. ISSN: 0925-4005. DOI: https://doi.org/10.1016/j.snb.2018.10.103. URL: http://www.sciencedirect.com/science/article/pii/S0925400518318811.

[351] Skarphedinn Halldorsson et al. “Advantages and challenges of microfluidic cell culture in polydimethylsiloxane devices”. In: *Biosensors and Bioelectronics* 63 (2015), pp. 218–231. ISSN: 18734235. DOI: 10.1016/j.bios.2014.07.029. URL: http://dx.doi.org/10.1016/j.bios.2014.07.029.

[352] M. Blondeau et al. “Correlating biological methods to assess Escherichia coli bacteria viability in silica gels”. In: *Analytical Methods* 6.8 (2014), pp. 2429–2431. ISSN: 17599679. DOI: 10.1039/c4ay00111g.

[353] Soichiro Tsuda et al. “Customizable 3D printed ’Plug and Play’ millifluidic devices for programmable fluidics”. In: *PLoS ONE* 10.11 (2015), pp. 1–13. ISSN: 19326203. DOI: 10.1371/journal.pone.0141640.

[354] A. P. Sudarsan and V. M. Ugaz. “Multivortex micromixing”. In: *Proceedings of the National Academy of Sciences* 103.19 (2006), pp. 7228–7233. ISSN: 0027-8424. DOI: 10.1073/pnas.0507976103.